ICAP2015

Jointly organized by Shanghai Institute of Applied Physics (SINAP), CAS,
SLAC National Accelerator Laboratory (SLAC) and Tsinghua University

October 12 -16, Shanghai

http://icap2015.csp.escience.cn

12th International Computational Accelerator Physics Conference

ICAP2015 Co-Chairs

Zhentang Zhao, SINAP
Kwok Ko, SLAC
Chuanxiang Tang, Tsinghua University

Scientific Program Committee (SPC)

Ohmi Kazuhiito, KEK, Japan
Kwok Ko (SPC Co-Chair), SLAC, USA
Ursula van Rienen, Universität Rostock, Germany
Chuanxiang Tang (SPC Co-Chair), Tsinghua University, China
Thomas Weiland, Technische Universität Darmstadt, Germay

Organizing Committee (OC)

Martin Berz, Michigan State University, USA
Oliver Boine-Frankenheim, GSI, Germany
Sarah M. Cousineau, ORNL, USA
Kyoko Makino, Michigan State University, USA
Cho-Kuen Ng, SLAC, USA
Dmitri Ovsyannikov, St.-Petersburg State University, Russia
Chris Prior, Rutherford Appleton Laboratory, UK
Stephan Russenschuck, CERN, Switzerland
Rob Ryne, Lawrence Berkeley National Laboratory, USA
Frank Schmidt, CERN, Switzerland

ICAP15
ICAP2015

Contents

Scientific Programme Committee (SPC)

Kazuhito Ohmi	KEK, Japan
Kwok Ko (SPC Co-Chair)	SLAC, USA
Ursula van Rienen	Universität Rostock, Germany
Chuanxiang Tang (SPC Co-Chair)	Tsinghua University, China
Thomas Weiland	Technische Universität Darmstadt, Germay

Organizing Committee (OC)

Martin Berz	Michigan State University, USA
Oliver Boine-Frankenheim	GSI, Germany
Sarah M. Cousineau	ORNL, USA
Kyoko Makino	Michigan State University, USA
Cho-Kuen Ng	SLAC, USA
Dmitri Ovsyannikov	St.-Petersburg State University, Russia
Chris Prior	Rutherford Appleton Laboratory, UK
Stephan Russenschuck	CERN, Switzerland
Rob Ryne	Lawrence Berkeley National Laboratory, USA
Frank Schmidt	CERN, Switzerland

Local Organizing Committee (LOC)

Yongbin Leng (Chair)	SINAP, China
Chuanxiang Tang (Co-Chair)	Tsinghua University, China
Heping Yan (Technical Editor)	SINAP, China
Bocheng Jiang	SINAP, China
Zhengchi Hou	SINAP, China
Xin Han	SINAP, China

COMPUTATION REQUIREMENT TOWARDS THE FUTURE ELECTRON ION COLLIDER, eRHIC*

Yue Hao†, C-A Dept. Brookhaven National Laboratory, Upton, NY 11973, USA

Abstract

eRHIC is the proposed electron ion collider(EIC) in Brookhaven National Laboratory, an upgrade of RHIC, the only operating collider in US. The demand of high luminosity (10^{33} to 10^{34} $cm^{-2}s^{-1}$) impels the adoption of an innovative linac-ring collision scheme, i.e. an ERL as the new electron accelerator. The design of eRHIC requires detailed numerical studies on various aspects, which include the start-to-end tracking of multi-pass ERL, special beam-beam study of linac-ring scheme, various beam dynamics issues, spin tracking, novel orbit/optics correction scheme. We will review the eRHIC simulation studies and discuss the challenges of the precise numerical modeling, in order to reduce the design risk.

INTRODUCTION

Electron-ion collider is a power tool of deep inelastic scattering for probing the inner structure of the hadrons. To get a much greater insight of the nucleon structure, including the distribution of the momentum, spin and flavor of the quarks and gluons, a high luminosity electron ion collider (EIC) is required.

In an EIC, the ion beam is accelerated to desired energy and stored in an synchrotron ring, while the electron accelerators has two options. An electron storage ring, together with its injector and booster, can be built and form a 'ring-ring' collision scheme with the ion ring. Alternatively, an energy recovery linac (ERL) can serve as electron accelerator, and form a 'ERL-ring' scheme. In an ERL, the electron beam gain energy from the RF cavities (usually superconducting) with the accelerating phase. After the electron beam collides with the ion beam, it will be decelerated in the same RF cavity, with the decelerating phase which is ensured by the pass length of the electron beam. The energy is then used to accelerate the new electron bunches. This energy recovery process enables high collision rate, hence high luminosity. Therefore in an ERL based collider, the electron beam is always fresh, however, its energy is re-used.

eRHIC [1] is the upgrade of RHIC, the only operating collider in US. RHIC provides up to 250 GeV proton and 100 GeV/n heavy ion. The new electron accelerator will provide polarized electron beam up to ~20 GeV. The ERL-ring scheme of eRHIC is the baseline design of eRHIC, since it has several benefits over a 'ring-ring' counterpart, which include:

- The beam-beam limit of the electron beam is removed due to a single collision for every electron bunch, which leads to an higher luminosity. The ERL-ring scheme eRHIC will achieve 4×10^{33} $cm^{-2}s^{-1}$ luminosity from collision of 250GeV proton and 15.9 GeV electron beam.
- The electron can be dumped at a much lower energy,
- The simpler synchronization of the electron beam with various ion energies.
- Much less synchrotron radiation power

eRHIC ERL adopts a multi-pass ERL design to save cost on the expensive Superconducting RF structure, i.e. the electron beam passes the linac with accelerating phase several times to accumulate energy before collision. To avoid building large number of energy recirculation passes, eRHIC also takes advantage of the concept of FFAG [2], which has enormous momentum acceptance (up to 4x in the design), to reduce the number of recirculation beamline to two lines. The FFAG based ERL reduce the cost of the transport lines significantly. Table 1 lists the baseline parameter of ERL-ring eRHIC and the Figure 1 shows its layout.

Despite the advantages of the ERL-ring scheme, it also presents a higher risk, which includes

- The electron beam current has to be provided from the source. Therefore a 50mA polarized electron source has to be demonstrated.
- Multi-pass high energy ERL with FFAG transport and related beam dynamics.
- The new beam-beam effect in ERL-ring scheme.

Table 1: The Baseline Parameters of ERL-ring eRHIC

Parameters	eRHIC	
	e	p
Energy (GeV)	15.9	250
Bunch spacing (ns)	106	
Intensity, 10^{11}	0.07	3.0
Current (mA)	10	415
rms norm. emit. (mm-mrad)	23	0.2
$\beta^*_{x/y}$ (cm)	5	5
rms bunch length (cm)	0.4	5
IP rms spot size (μm)	6.1	
Beam-beam parameter		4×10^{-3}
Disruption parameter	36	
Polarization, %	80	70
Luminosity, 10^{33} $cm^{-2}s^{-1}$	4.9	

Besides the experimental R&D efforts, detailed simulations of the ERL-ring eRHIC are the best tool to retire the design risks. We will present the current simulation progress and the necessary improvements in the future.

* Work supported by Brookhaven Science Associates, LLC under Contract No. DE-AC02-98CH10886 with the U.S. Department of Energy.

† yhao@bnl.gov

ISBN 978-3-95450-136-6

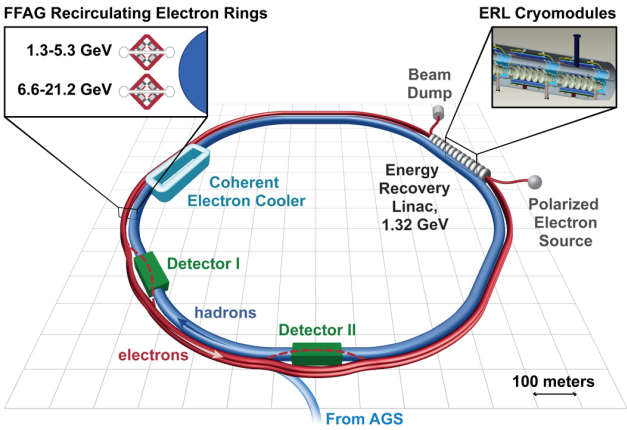

Figure 1: The layout of ERL-ring scheme eRHIC, the blue ring represents the existing RHIC ring and red ring represents the FFAG transport lines.

eRHIC ERL DESIGN OVERVIEW AND START-TO-END SIMULATION

eRHIC ERL adopts a multi-pass (12 or 16 passes) design to reach the desired collision energy of the electron beam (15.9 GeV or 21.2 GeV). It adopts a 1.322 GeV main linac, including the second harmonic cavity for energy loss compensation and optional fifth harmonic cavity for energy spread compensation. The electron beam will pass the linac 24 or 32 times before it is transported to beam dump. To avoid large number of recirculation passes, two non-scaling FFAG recirculating passes are designed to accommodate all the energies. The non-scaling FFAGs use simple FODO like cells with two shifted quadrupoles. Electron beams with different energies has different orbits with smaller orbit deviations, different optics functions and time of fight, compare with the scaling FFAGs.

The FFAG cells has to be optimized for the application as the recirculating passes of the multi-pass ERL. The optimization includes:

- Minimized the total synchrotron radiations,
- Small orbit deviations to simplify the magnet design,
- Control the chromaticity.

Two FFAGs is planned to accommodates all the energies of up-to-16-pass ERL. The first FFAG covers the first four energies and the second covers the rest of the energy. The particle with this energy takes the reference orbit , which is roughly circular in the arc. The orbit and optics of different energies are shown in the top sub-figures of Figure 3. The tune for each energies are kept in the lower half range of 0.0-0.5 to reduce the chromaticity for the lower energy passes in the FFAG, as shown in the bottom left of the Figure 3. The energy dependence of pass length and the compaction factor are shown in the bottom middle figure. The choice of the reference energy of the FFAG lattice, counterintuitively not the highest energy, optimizes the total radiation power of all energies. The radiation power dependence on energy largely differs from the fourth power of energy dependence, since the local radius is different for all energies.

To modify the curvature of the FFAG baselines, the offsets of the quadrupoles in certain cells of the FFAG (named transition cells) can be changed adiabatically. Therefore the FFAG recirculating passes can fit into the existing RHIC tunnel, which does not has unique curvature. Since we can only use finite number of cells to make the curvature transition, the fine-tuning using the dipole corrector of each magnet is necessary to reduce the residue orbit errors of each energy due to the curvature transition.

A pair of splitter and combiner are required to connect the ERL recirculating passes to the linac. They are designed to fulfill the following tasks:

- Transport the beam between the recirculating pass and the entrance/exit linac,
- Match the optics of each pass to the linac,
- Adjust the time of flight of each energy so that proper acceleration and deceleration can be achieved,
- Play important role in orbit correction.

The splitter and combiner are needed for all multi-pass ERL designs, since the task 1 and 2 are common. The task 3 and 4 are special for the FFAG recirculating passes which make its splitter and combiner more complicated. A 16-line spreader and combiner design is finished for eRHIC to fulfill those requirement, the geometric design of the splitter/combiner is shown in Figure 3.

It is the first time that FFAG-based multi-pass ERL is proposed. Therefore, no existing simulation packages can directly simulate the whole accelerating and decelerating processes, i.e. a start-to-end simulation. There are multiple beam dynamics issues to be addressed in the simulation, such as the longitudinal and transverse dynamics with various wake fields and the synchrotron radiation effects, the beam break-up studies with undamped cavity HOMs and the spin tracking to ensure the polarization at the interaction point. In addition, the correction scheme for such machine does not exist and need special treatments.

To address the above needs, we implement a python commander layer to coordinate the ERL start-to-end simulation, while use the existing and well-tested beam dynamics codes for individual beam-dynamics tasks. In one hand, the python layer collect the lattice of each parts and connect them in the start-to-end order and form a 120-km long lattice. Each individual magnet gets unique name and the errors of the each magnet are associated to it's name, which guarantees the bunch experiences same element errors when it travels through multiple times. On the other hand, the python layer does not perform the actual tracking work. It rewrite the lattice to various format of inputs and using existing code to track the macro-particles. For instance, ELEGANT [3] is used for 6-D particle tracking with wake-fields, CSR effect and the synchrotron radiation effect; Zgoubi/PyZgoubi [4] is used for start-to-end spin tracking; and GBBU [5] is used to evaluate beam current threshold of the transverse beam break-up instability. The new algorithm of the orbit and optics correction will be also implemented in the python layer.

ISBN 978-3-95450-136-6

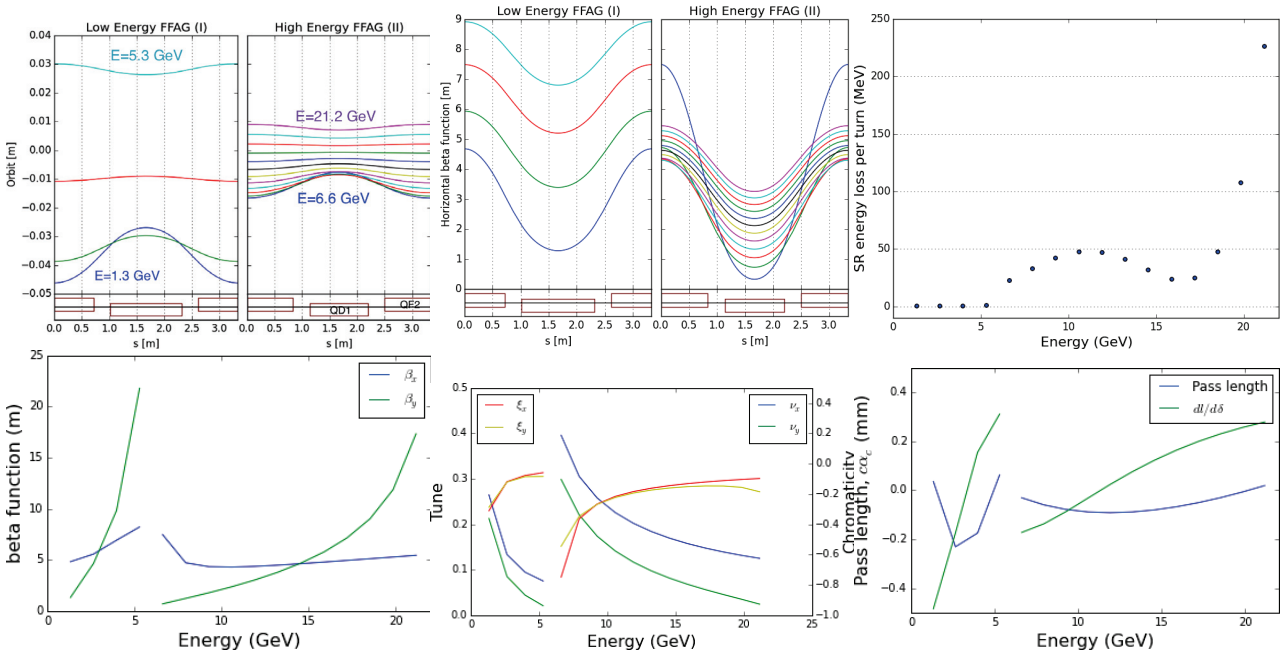

Figure 2: The orbit, optics, time of flight and radiation power of the optimized FFAG double cell.

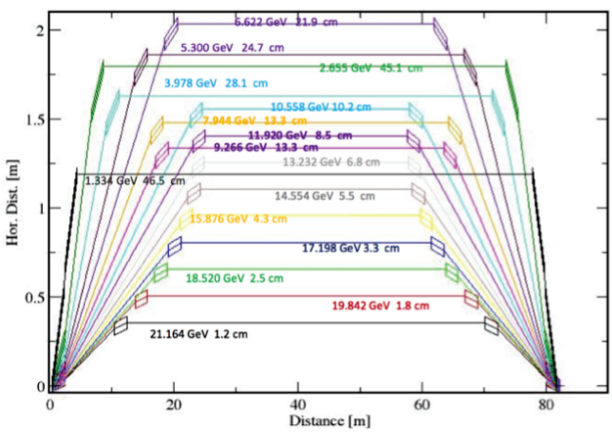

Figure 3: Layout of the splitter/combiner

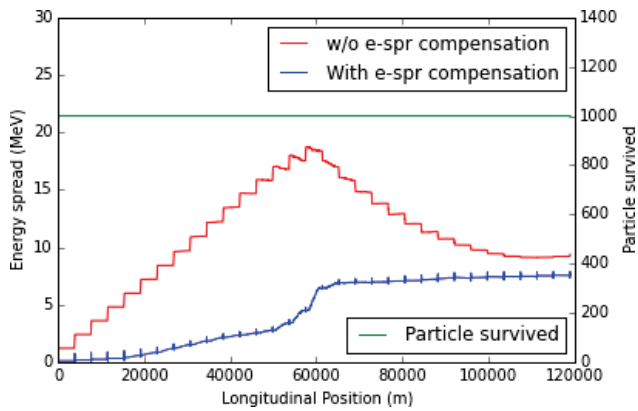

Figure 4: Comparison of the energy spread with (blue line) and without (redline) the energy spread compensator cavities . The green curve indicates the survived particle in the start-to-end tracking.

Using 6-D symplectic matrix to represent the unfinished beamlines, we established a 'skeleton version' of the start-to-end simulation frame for the eRHIC ERL. It includes the main linac with the options of including the energy loss compensating cavities (2^{nd} harmonic cavities) and the energy spread compensating cavities (5^{th} harmonic cavities), the 6-D symplectic matrices with constant vector for spreader and combiners for each energy and the two FFAG beam lines which consists of 720 FFAG cells. The constant vector in the spreader and combiner are used to provide proper transverse shift for the entrance of the FFAGs and the proper pass length adjustment to ensure the energy recovery process. In the simulation, the electron bunches starts at the injection energy of the ERL with accelerating phase, then pass through the linac, and the corresponding spreader/combiners and FFAGs. With correct length adjustments, the bunch will gain energy in multiple passes and reach the collision energy. With the extra half wavelength in the highest energy spreader/combiner, the bunch will be decelerated to the dump energy.

The first study on this skeleton model is the longitudinal dynamics study. We present one example which studies whether the energy spread compensation cavities can be removed. The main challenge of removing the cavity is the increased energy spread due to the RF curvature. The electron-ion collision does not pose a strong requirement on the energy spread at IP as long as the the spread won't cause noticeable chromatic emittance growth. However, the energy spread at the beam dump must be well controlled to prevent beam loss before the dump.

Figure 4 compares the electron beam accelerated to and decelerated from 21.2 GeV top energy, with (shown in the

ISBN 978-3-95450-136-6

blue line) or without (shown in the red line) the energy spread compensating cavity. When no energy spread compensation is present, the energy spread is accumulating in the accelerating stage, mainly due to the RF curvature. In the decelerating stage, the energy spread cannot be fully compensated by the negative curvature due to the nonlinearity of the FFAG with respect to beam energy and synchrotron radiation. We have to optimize the R_{56} in the low energy spreader/combiners from its initial values to reach comparable energy spread at the beam dump, as the case with the energy spread compensation. Green lines indicates in both cases, no beam loss can be observed in the tracking.

BEAM-BEAM EFFECT IN ERL BASED EIC

Beam beam effects present one of the major restrictions in achieving the higher luminosities. The special 'linac-ring' scheme removes the beam-beam parameter limitation of the electron beam, hence higher luminosity can be achieved [6]. This also bring new challenges due to the beam-beam effect in the 'linac-ring' scheme, including the electron disruption effect, the electron pinch effect, the ion-beam kink instability and the ion beam heating due to the electron beam noise.

The electron disruption effect and the pinch effect rise due to the large beam-beam parameter of the electron beam. The strong nonlinear beam interaction field will distort the electron beam distribution and the large linear beam-beam tune shift leads to significant mismatch between the design optics and the electron beam distribution. Figure 5 shows the beam distribution after the collision and Figure 6 illustrates the electron beam size shrinking in the opposing ion beam (the pinch effect) and the electron beam rms emittance growth. The pinch effect in one hand will enhance the luminosity from 3.3×10^{33} cm^{-2}s^{-1} to 4.9×10^{33} cm^{-2}s^{-1}, a factor of 1.48. However, this effect also boosts the local beam-beam force to the opposing ions beam, which may affects the dynamics aperture of the ion beam.

To model the beam-beam force from the 'pinched electron bunch', it is not sufficient to model the transverse beam distribution as Gaussian and calculated the force using the second order moment of the beam distribution. The transverse distribution of the electron beam forms a dense core and a long tail due to to strong beam-beam force from the ion beam, as shown in Figure 5. Figure 7 compares the beam force calculated from the distribution and from the rms beam size. It indicates that a poisson solver is needed to precisely model the pinch effect on the ion beam.

For the ion beam, the largest challenge is the kink instability [7, 8], which arise due to the effective wake field of the beam-beam interaction with the electron beam. The electron beam is affected by the head of the ion beam and passes the imperfection of the head portion to its tail. The threshold of the instability can be estimated by the head-tail model as:

$$\xi_i d_e < 4\nu_s/\pi$$

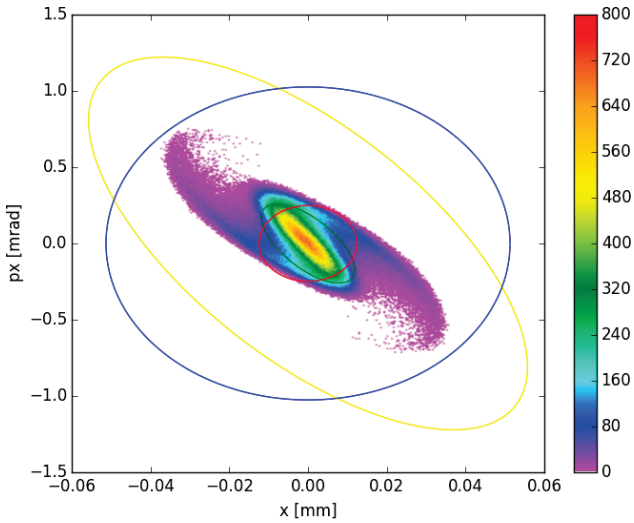

Figure 5: The electron beam distribution after the electron ion collision, with the parameter of the baseline eRHIC design.

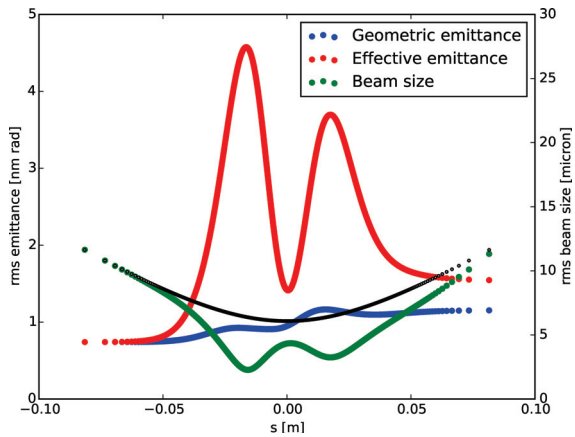

Figure 6: The electron beam distribution after the electron ion collision, with the parameter of the baseline eRHIC design.

The eRHIC parameter exceeds the threshold, therefore a fast deterioration of the ion beam quality is expected if no countermeasure is implemented. Simplified simulation study also predict that the instability will occur and can not be suppressed by the current chromaticity in RHIC [8]. A pickup-kicker type feedback system is studied in [9]. The inner-bunch modes of the instability can be picked up, amplified through a broad-band amplifier and corrected by the high band-width kicker. For the 5 cm eRHIC ion bunch length, the bandwidth of the feed-back system should be no narrower than 50-300 MHz.

Another important effect, which has not been studied, is the interplay of the space charge effect and the beam-beam effect. Both effects will cause complicate nonlinear resonance and reduce the beam life time. Previous beam experiments in RHIC shows that the beam with large space charge tune shift suffers short beam life time even with small beam-beam parameter. However, in electron-ion colliders, the beam-

ISBN 978-3-95450-136-6

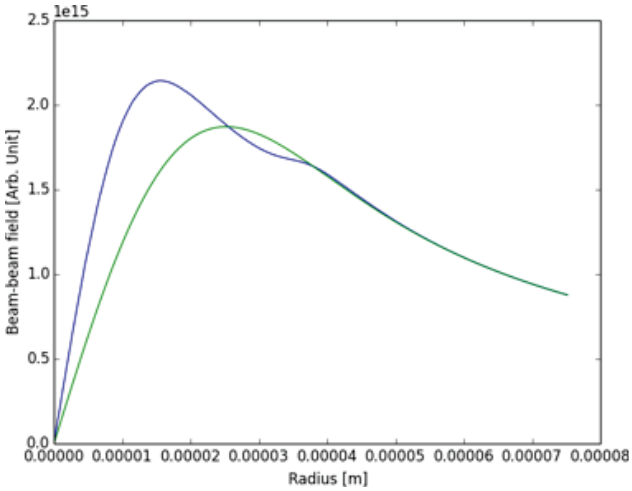

Figure 7: Comparison of the beam-beam force from a 'pinched' electron beam. The blue curve represents the force calculated from the beam distribution, while the green one is calculated from the rms beam size if the beam is assumed to have transverse Gaussian distribution.

beam parameter is the opposite sign as in the hadron/lepton colliders. A thorough simulation is required to study the interplay of the space charge effect and beam-beam effect from a pinched electron beam and find the maximum allowable space charge tune shift for the desire beam-beam parameter. The eRHIC luminosity is limited due to these effects, a recent method of space charge compensation [10] can be considered. However detail simulation of this method is required to ensure the beam stability.

COMPUTATION FOR COOLING CONCEPTS

To achieve the high luminosity, effective cooling methods for the ion beam are necessary. Coherent electron cooling (CEC) [11] is the promising method for high energy ion beam. It consists the modulator, FEL amplifier and kicker sections. Currently a proof-of-principle experiment is being prepared to prove the feasibility. A precise numerical model can not only guide the experiment, but also help to extrapolate the CEC proof-of-principle results to the cooling for eRHIC.

The delta-f PIC simulation [12, 13] is used to model the modulator and kicker section. In between, Genesis [14] can be use for the simulation of FEL amplifier. The simulation of the modulator with uniform transverse density shows very good agreement with the 1-D theory. However, a 3-D modulator model is still in an immature stage to simulate the finite beam sized effect as well as the presence of the focusing elements for the electron beam. To evaluate the cooling time precisely, we are also exploring the available 3-D self-consistent space charge libraries for the precise modulator and kicker modeling and benchmark with the delta-f PIC simulations.

SUMMARY

This article only highlighted several computation challenges of an ERL-ring scheme eRHIC. There are other essential requirements of beam dynamics studies such as the 3-D space charge modeling of the electron injector, the BBU simulation with harmonic cavities, the ion trapping effects.

The design of ERL-ring eRHIC is largely supported by the detailed simulation of the design, tracking and beam dynamics simulations. Through the numerical studies we already identified many challenges and found the corresponding countermeasures. More detailed numerical studies are demanded to further reduce the risks of the new concepts in the ERL-ring eRHIC design.

REFERENCES

[1] arXiv:1409.1633

[2] D. Trbojevic et al., 'Non-Scaling Fixed Field Alternating Gradient ERL for eRHIC', in proceedings of IPAC 2015, Richmond, VA, USA.

[3] M. Borland, 'elegant: A Flexible SDDS-Compliant Code for Accelerator Simulation', Advanced Photon Source LS-287, September 2000.

[4] Zgoubi website: http://sourceforge.net/projects/zgoubi/; PyZgoubi website: http://www.hep.man.ac.uk/u/sam/pyzgoubi/

[5] E. Pozdeyev, Phys. Rev. ST-AB 8, 054401, (2005).

[6] Y. Hao and V. Ptitsyn, Phys. Rev. ST Accel. Beams 13, 071003 (2010)

[7] R. Li, B.C. Yunn, V. Lebedev, J.J. Bisognano, "Analysis of Beam-beam Kink Instability in a Linac- Ring Electron-Ion Collider", PAC'01, Chicago, IL, (2001).

[8] Y. Hao and V. Ptitsyn, Phys. Rev. ST Accel. Beams 16, 101001 (2010)

[9] Y. Hao, M. Blaskiewicz, V. N. Litvinenko, and V. Ptitsyn., "Kink Instability Suppression With Stochastic Cooling Pickup And Kicker", IPAC'12, New Orleans, Louisiana, USA, (2012).

[10] V.N. Litvinenko and G. Wang, Phys. Rev. ST-AB 17, 114401, (2014).

[11] V.N.Litvinenko, Y.S Derbenev, Physical Review Letters 102, 114801 (2009). D. Ratner, Physical Review Letters 111, 084802 (2013).

[12] G.I. Bell et al., "Vlasov and PIC simulations of a modulator section for coherent electron cooling", in the proceedings of PAC11, New York, NY, USA.

[13] G.I. Bell et al., 'High-Fidelity 3D Modulator Simulations of Coherent Electron Cooling Systems', in the proceedings of IPAC2012, New Orleans, LA, USA.

[14] S. Reiche, "GENESIS 1.3: a fully 3D time-dependent FEL simulation code," Nucl. Instrum. Methods Phys. Res., Sect. A, 429, 243 (1999).

ISBN 978-3-95450-136-6

USING BIG DATA IN NSLS-II STORAGE RING COMMISSIONING*

Y. Li#, L. Yang, W. Cheng, BNL, NY, USA

Abstract

Big data from both beam position monitor turn-by-turn readings and the designed model are intensively used in the NSLS-II storage ring commissioning. From beam-based data, various beam parameters, including Twiss parameters, tune, dispersion, chromaticity, linear coupling, are characterized and compared against the design model. Then, iterative optimizations yield very promising results, such as, nearly 100% injection efficiency, small Beta-phase beat, a diffraction limit vertical beam size, etc. within a short period of time. Various lattice configurations of w/o damping wigglers, high linear chromaticity have been optimized and commissioned successfully also.

NSLS-II STORAGE RING

The NSLS-II storage ring is a 30-cell (15-superperiod) double-bend achromat structure (with 30 dispersive straights): 15 low-βx (short) straights of length 6.6m and 15 high-βx (long) straights of length 9.3 m. The designed linear optics for one cell is illustrated in Fig. 1. One long straight is used for injection and two are used for RF cavities. Three long straights are used for damping wigglers (1.8T peak field, 2×3.4 m length each), which lower the horizontal emittance down from 2 to 1 nm rad. In-vacuum undulators with full-gaps as small as 5 mm can provide very high brightness x-ray sources. Elliptically polarized undulators will also provide important sources for user research.

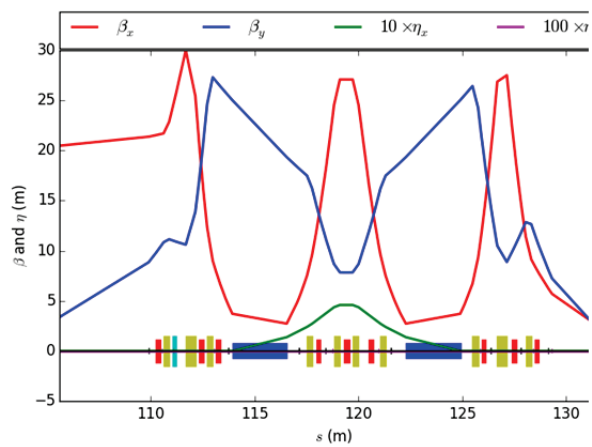

Figure 1: NSLS-II storage ring linear optics for one cell.

The storage ring commissioning began since March 2014. After several months of commissioning, a promising agreement between measured linear optics parameters and the designed model was achieved. The injection efficiency was verified to be above 95%. Three pairs of damping wigglers, four in-vacuum undulators and two elliptically polarized undulators have been successfully incorporated into the ring lattice. Electron beam with an emittance as low as 1 nm rad was seen on a pinhole x-ray camera in December 2014.

COMMISSIONG TOOLS

Development Tools and Libraries

Python was chosen as the main developing tool, which is a powerful programming language with huge community support [1, 2]. Many well-developed tool-boxes provide powerful and convenient numeric and interface capabilities during the commission process, such as scipy and numpy [3] used for scientific application, matplotlib to produce publication quality figures in a variety of hard-copy formats and interactive environments across platforms, ipython-notebook [4] used as an interactive computational environment, in which user can combine code execution, rich text, mathematics, plots and rich media. A typical ipython notebook interface to obtain tune from turn-by-turn data is shown in Fig. 2.

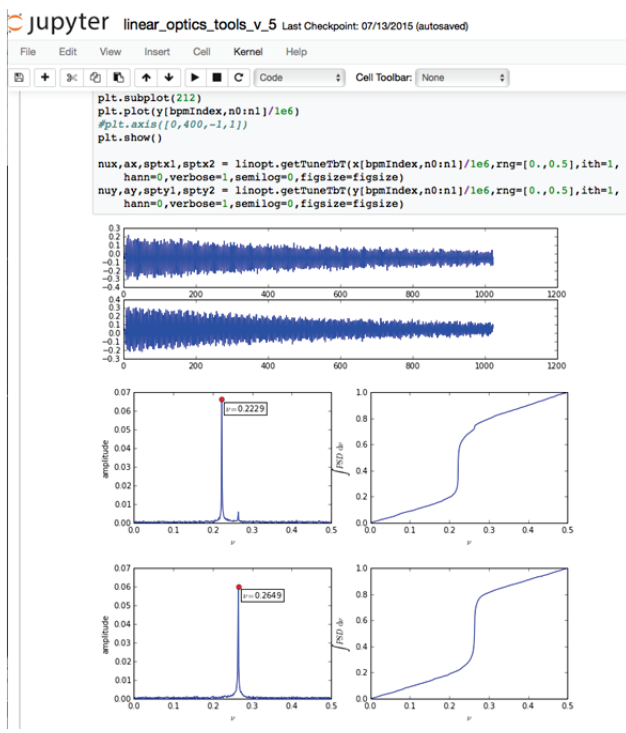

Figure 2: IPython notebook interface for TbT data analysis.

Accelerator Physics High Level Application (APHLA) is a python library developed for accelerator commissioning and beam study. It takes advantages of NSLS-II service oriented architecture, e.g. channel finder service, model service and unit conversion service, to become a

* Supported by DOE, US under contract No. DE-AC02-98CH10886
# yli@bnl.gov

ISBN 978-3-95450-136-6

package more than equipment control. It can be imported as a standard python library,

```
   >>> import aphla as ap
   >>> ap.machines.load("nsls2","SR")
>>> ap.getOrbit(spos=True)
```

Data Storage and Access

Before and during commission, big data are created from either the design model or beam-based measurement. Some of them need to be accessed for optimization, or stored and archived for off-line analysis. Hierarchical Data Format (HDF) is adopted for this purpose, which provides a data model, library, and file format for storing and managing data. It supports an unlimited variety of datatypes, and is designed for flexible and efficient I/O and for high volume and complex data. A python library - h5py, can support python to communicate with HDF5 files flexibly. HDF5 files can be transferred and viewed among different operation platforms. A typical HDF5 file including NSLS-II storage ring lattice parameters and various response matrices is shown in Fig. 3.

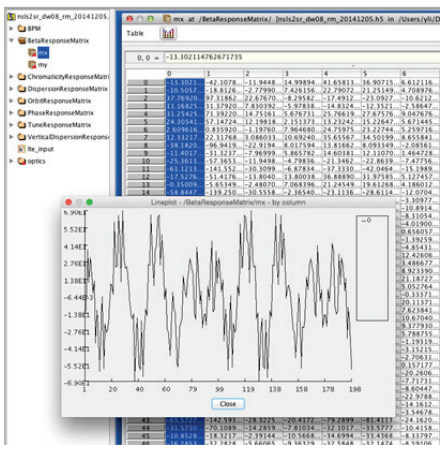

Figure 3: View of a HDF5 files including NSLS-II storage ring lattice and various response matrices.

BIG COMMISSIONING DATA

There are two sources of commissioning data. First data source is the design model. The linear optics model, including, beta-function, phase, dispersion, etc., at each observation point was pre-calculated, which are used as the optimization goals. All measurable parameters dependency on controllable variables (basically, the magnets power suppliers DC currents, or AC voltage settings), are also pre-calculated and saved as various response matrices for computing correction strength. Second data source is real-time beam-based measurement, basically BPM turn-by-turn data. With some algorithms, the actual real-time beam parameters are extracted from these data, and compared against the design model, a suitable corrections are calculated by inversing the corresponding response matrices, then implementing through APHLA, which is integrated with all necessary unit conversions.

Since there are numerous BPMs, beam diagnostics outputs, and controllable parameters, real-time beam information is usually redundant. Therefore, in most case, we can identify some errors or exceptions due to hardware malfunctions, like bad BPMs, etc. A big data allows us to characterize beam parameters, and then to implement optimization more precisely.

COMMISSIONING ACHIEVEMENTS

Hardware Failure Identification

When stored beam was first established, it must follow an ugly closed orbit. Any attempts of improving the orbit leaded to beam dump. Thus, we suspected that some physical obstacles inside vacuum chamber actually block beam trajectory. A moving orbit bump was created with the pre-calculated design orbit response matrix to localize these obstacles. This application helped us to localize two hanging RF springs as illustrated in Fig. 4. In the meantime, BPM sum signal provides similar beam loss information to indicate the location of hanging RF spring at cell 10.

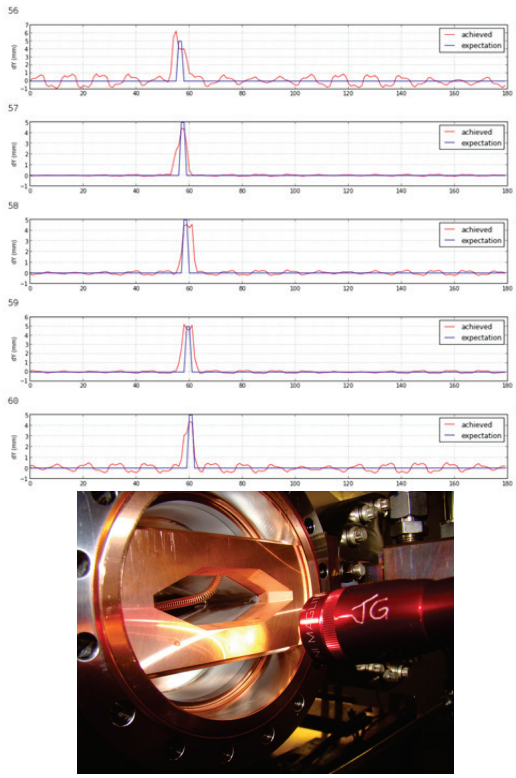

Figure 4: Moving bump to localize the physical obstacle in vacuum chamber.

Linear Optics Optimization

Beam position monitor's turn-by-turn capability synchronized with injection kickers or pingers provides sufficient information to characterize the linear lattice [5]. The uncorrected beta-beat was 20-30%. After implementing beam-based alignment [6] as shown in Fig. 5, the linear optics was optimized to 1-2% (see Fig. 6), and injection efficiency was achieved close to 100%.

ISBN 978-3-95450-136-6

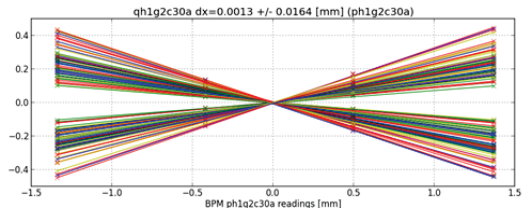

Figure 5: Beam-based alignment for one of quadrupoles.

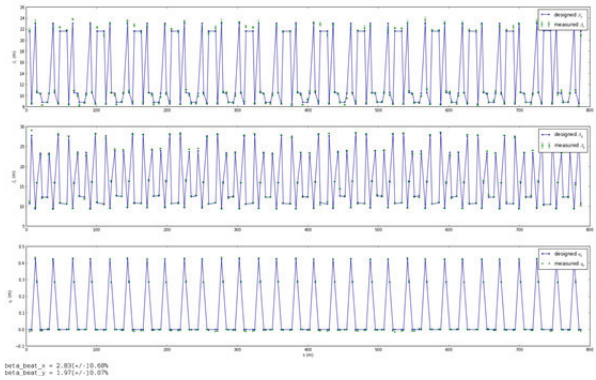

Figure 6: Corrected linear optics (horizontal, vertical beta-functions, and horizontal dispersion).

Diffraction-Limit Vertical Beam Size

A new application of measuring symplectic generators to characterize and control the linear betatron coupling was used to achieve diffraction-limit beam size in the vertical plane. Figure 7 illustrates the transverse x-ray beam profiles as seen by a pinhole camera before and after coupling correction. From synchronized and consecutive TbT readings, symplectic and coupled Lie generators describing the coupled linear dynamics are extracted. Four plane-crossing terms in the generators directly characterize the coupling between the horizontal and the vertical planes. Coupling control can be accomplished by utilizing the dependency of these plane-crossing terms on skew quadrupoles. This method can be automatized to realize linear coupling feedback control with negligible disturbance on machine operation.

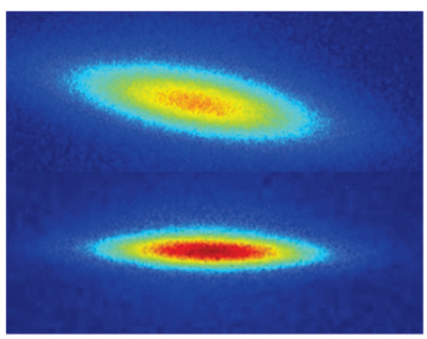

Figure 7: X-ray beam profiles seen by a pinhole camera before/after coupling correction.

In the meantime, the coupled beta-function was extracted by fitted one-turn map. It can be found the two coupling modes were effectively suppressed around the whole ring after correction, as illustrated in Fig. 8.

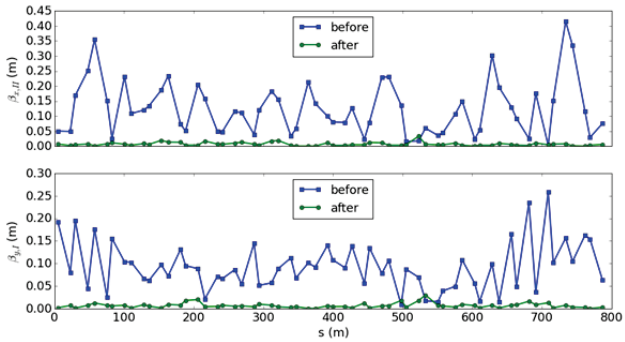

Figure 8: Comparison of the coupled beta-function before and after correction.

SUMMARY

The big data pool holding both the design model and real-time measurement is helpful in the commissioning the newly built NSLS-II ring. With the powerful python scripts and libraries, we achieved many promising results within the project time budget

ACKNOWLEDGMENT

We would like to thank NSLS-II colleagues for many helpful and stimulating discussions, and continuous support from operation group.

REFERENCES

[1] http://www.python.org
[2] J.M Perkel, Programming: Pick up Python, Nature, Vol. 518 (2015) 7537.
[3] http://www.scipy.org
[4] http://www.ipython.org/notebook.htm
[5] P. Castro-Garcia, Doctoral Thesis (1996)
[6] G. Portmann, Automated Beam Based Alignment of the ALS Quadrupoles, PAC95

ISBN 978-3-95450-136-6

HIGH LUMINOSITY LHC HOLLOW ELECTRON LENS COLLIMATION USING MERLIN*

H. Rafique†, R. J. Barlow, University of Huddersfield, Huddersfield, UK
R. B. Appleby, S. C. Tygier, Cockcroft Institute and The University of Manchester, Manchester, UK
R. Bruce, S. Redaelli, J. F. Wagner, CERN, Geneva, Switzerland

Abstract

The high luminosity large hadron collider (HL LHC) upgrade envisions an unprecedented stored beam energy of up to 700 MJ. To protect the machine during operation, an efficient collimation system is vital. The hollow electron lens (HEL) is being explored as a possible collimation enhancer for the LHC, based on Tevatron designs and operational experience [1], for active halo control. A HEL produces a hollow cylindrical beam of electrons through which the accelerator (proton) beam travels, particles that overlap undergo an electromagnetic interaction. As they can operate close to the beam core without being damaged, HELs may serve as soft scraper devices [2]. For the first time a HEL in high luminosity configuration is simulated in the HL LHC using the recently updated MERLIN 5 accelerator libraries [3–5]. The effects on the LHC beam halo are observed for various HEL operation modes.

INTRODUCTION

The LHC collimation system has operated efficiently over Run I, with stored beam energies of up to 150MJ, and continues to do so in the current Run II. The HL LHC upgrade aims to increase the luminosity of the LHC by reducing the emittance and doubling the beam current. Thus it is prudent to investigate methods of improving the LHC collimation system for the HL LHC upgrade.

HELs have been identified as a possible means of active halo control [6]. It has been shown at the Tevatron that HELs can increase the diffusion of halo particles onto an aperture restriction such as the primary collimator (TCP) of the LHC collimation system [1]. HELs can operate closer to the beam core than a solid scraper, as there is no impedence effect and no material damage is incurred [2]. This makes them ideal for use with beams of unprecedented stored energy.

A conceptual design report followed advanced studies of a HEL in the nominal LHC [7], more recently plans have been prepared to integrate a HEL into the LHC, with the indication to prepare a technical design for implementation beginning in 2018, based on Run II operational experience [6].

PROPOSED LHC HEL

It is proposed to integrate a superconducting HEL in IR4, where it has access to high pressure He for cooling, and there is the required space between beamlines. Inevitably two HELs will be required, one for each beam. Two candidate locations have been identified as RB-44 and RB-46, both in IR4, either side of the RF insertion [7].

Using MERLIN, a HEL was implemented into the LHC lattice at RB-46. The optics parameters for both the nominal and HL-LHC are shown in Table 1. Both the Tevatron HEL [1], and proposed LHC HEL [7] parameters are modelled. As HL integration studies are ongoing, the position used is a first case study to test the MERLIN implementation.

Table 1: Optics Parameters Calculated at the HEL in MERLIN for the Nominal LHC and HL LHC, HEL Parameters for the Tevatron and LHC HELs

Parameter [Unit]	**LHC**	**HL-LHC**
s [m]	10037	10037
β_x [m]	183.6	144.0
β_y [m]	175.5	259.6
σ_x [μm]	293.5	259.9
σ_y [μm]	286.9	349.0
μ_x [deg]	222.1	215.7
μ_y [deg]	202.4	202.8
E_p [TeV]	7	7
HEL Parameter [Unit]	**Tevatron**	**LHC**
E_e [keV]	5	10
I [A]	1.2	5
L [m]	2	3

MERLIN HEL PROCESS

Assuming an azimuthally symmetric e^- beam, no edge effects or fringe fields, and only considering the active part of the HEL (not the bending fields for injection and extraction of the e^- beam), the HEL is modelled in MERLIN 5 [4, 5] as follows.

For a HEL of length L, with electron beam current I, the kick for a particle at a transverse displacement r, is given by Eq. (1) [8].

$$\theta_{max}(r) = \frac{1}{4\pi\epsilon_0 c^2} \frac{2LI(1+\beta_e\beta_p)}{(B\rho)_p \beta_e \beta_p} \frac{1}{r} \qquad (1)$$

where β_e and β_p are the Lorentz β of the HEL electron beam, and machine proton beam respectively, and $(B\rho)_p$ is the proton beam rigidity.

For a perfect radial HEL distribution (uniform between the HEL beam transverse radii R_{min} and R_{max} and axially symmetric), the kick exerted on a particle is a function of its transverse position, and is given by Eq. (2) [8].

* Research supported by FP7 HiLumi LHC (Grant agreement 284404)
† haroon.rafique@hud.ac.uk

ISBN 978-3-95450-136-6

$$\theta_{kick} = \begin{cases} 0, & r < R_{min} \\ \frac{r^2 - R_{min}^2}{R_{max}^2 - R_{min}^2}\theta_{max}, & R_{min} < r < R_{max} \\ \theta_{max}, & r > R_{max} \end{cases} \quad (2)$$

A measured beam profile [9] is parameterised and included in MERLIN as well as the perfect profile detailed in Eq. (2).

As in the SixTrack [10] HEL routine [11], the MERLIN HollowElectronLensProcess offers 4 operation modes;

1. DC: HEL constantly at maximum.
2. AC: HEL beam current is modulated to resonate with the betatron tune.
3. Diffusive: HEL is randomly switched on/off on a turn by turn basis.
4. Turnskip: HEL is switched on every n turns, where n is an integer.

As discussed in previous work [8, 11, 12], the most interesting cases for collimation enhancement are the AC and diffusive modes.

SIXTRACK COMPARISON

To compare MERLIN's HEL process with SixTrack's elens routine, a simple bunch of 64 protons was generated in SixTrack, populating horizontal phase space between 1-10σ_x. This bunch is shown in green in Fig. 1, and was run for the nominal LHC (lattice v6.503, squeeze and separation on), in both MERLIN and SixTrack. The Poincaré sections at the HEL, which is operating in AC mode, are compared in Fig. 2. The HELs used in Fig. 2 are based on Tevatron hardware, and thus operate with the Tevatron paramaters shown in Table 1.

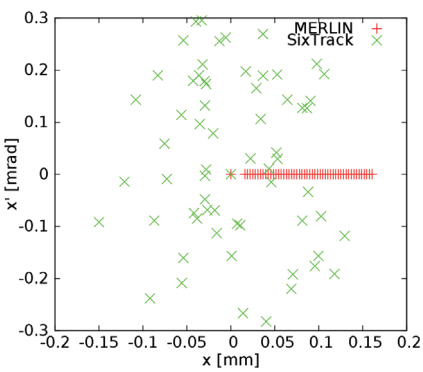

Figure 1: Distributions generated in SixTrack (green) and MERLIN (red) for similar bunches populated between 1-10 σ_x.

As the closed orbits in both programs are not the same, the slight difference shown in Fig. 2 is expected. It is clear however, that the MERLIN HEL process is operating similarly to the SixTrack elens routine. To clarify this comparison, it is repeated for the DC mode in Fig. 3, in this case MERLIN generates its own distribution, which is a purely horizontal bunch between 1-10 σ_x, but of 50 equally spaced protons,

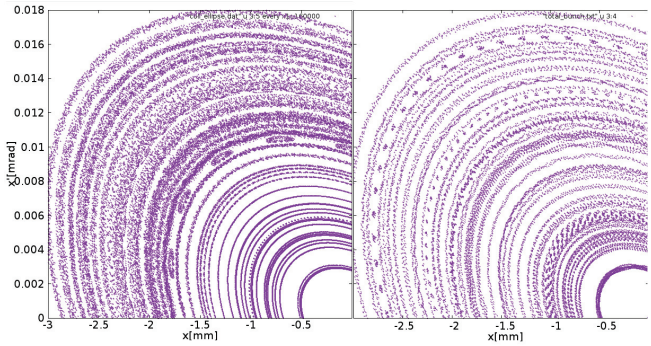

Figure 2: Poincaré sections at an AC Tevatron HEL in SixTrack (left) and MERLIN (right) for an identical bunch populated between 1-10 σ_x, shown in green in Fig. 1.

and a reference proton at (0,0), as shown in red in Fig. 1. The SixTrack bunch has a small non-zero momentum component, whereas this is zero in the MERLIN bunch. In spite of this difference it is clear that both codes are producing resonances in phase space, which perturb the protons by a similar amount.

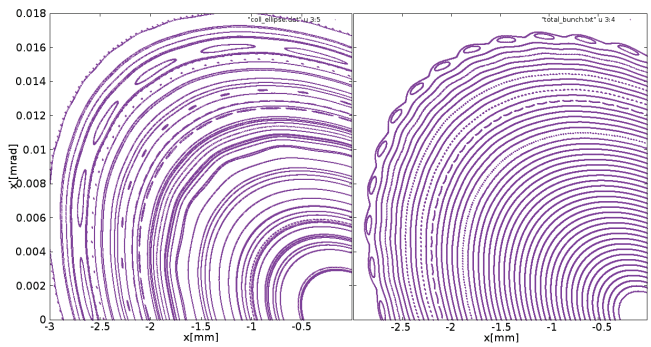

Figure 3: Poincaré sections at a DC Tevatron HEL in SixTrack (left) and MERLIN (right) for similar bunches populated between 1-10 σ_x, which are shown in Fig. 1.

HL LHC

As the LHC has a larger beam rigidity than the Tevatron, it is clear from Eq. (1) that using a Tevatron HEL in the LHC would result in a smaller effect on the protons that interact with the HEL. Thus an LHC HEL has been proposed, that should operate as a collimation enhancer in both the nominal and HL LHC [7]. Using the LHC HEL parameters, which are set out in Table 1, the previous plots are repeated; using the MERLIN generated bunch shown in Fig. 1, in both the nominal and HL LHC. Figure 4 illustrates that the optics differences in these two machines have a large impact upon the position and size of resonances that the HEL creates.

For collimation enhancement, the most promising modes of HEL operation are AC and diffusive. To illustrate why this is the case, both were run in the HL LHC lattice (v1.2) using the MERLIN bunch from Fig. 1, and the result is shown in Fig. 5. It is clear that the AC widens the Poincaré section of a given particle, thus making it more likely to impact upon

ISBN 978-3-95450-136-6

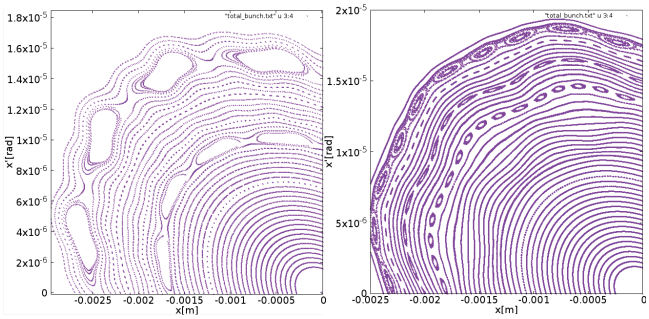

Figure 4: Poincaré sections at the position of a DC LHC HEL in the nominal (left) and HL (right) LHC using the MERLIN bunch from Fig. 1.

a collimator if it is already near one. The diffusive mode however shows a massive spread of particle coordinates in phase space, meaning that it should aid in collimation more than the AC mode.

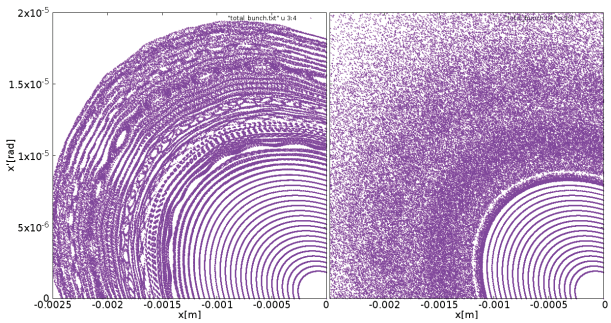

Figure 5: Poincaré sections at the position of an AC (left), and a diffusive (right) LHC HEL in the HL LHC using the MERLIN bunch from Fig. 1.

In all cases, the HEL does not interfere with particles with a transverse displacement smaller than the minimum radius. In order to estimate the HEL's impact on collimation, a simulation was set up such that a halo bunch populating 4-5.9 σ_x in x was tracked for 10^5 turns, with various or no HELs operating between 4-8 σ_x in the HL LHC lattice. Only a single primary collimator, TCP.C6L7 was present, with a jaw opening of 6.2 σ_x. The results are shown in Fig. 6.

As expected from this simulation, with no HEL present, the particles remain stable and never impact upon the TCP. It is clear also that with a DC HEL, cleaning enhancement is negligible. The AC mode appears to remove only particles that are closest to the TCP, in only a few hundred turns, this makes sense as from Fig. 5 we see that the Poincaré section is widened by a small amount - thus only particles close to the TCP location of 6.2 σ_x are likely to be excited onto it, leaving particles closer to the core intact. This is in agreement with past studies using SixTrack [8].

The diffusive case appears the most promising for cleaning enhancement, in fact nearly all halo particles have been excited onto the TCP after 10^5 turns (around 10 s of machine time), this is desirable as the collimation system exists to clean halo particles from the bunch. As the diffusive mode

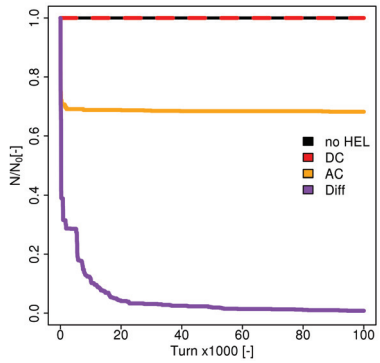

Figure 6: Normalised particle survival after 10^5 turns in the HL LHC with a single TCP at 6.2 σ_x, and a bunch populated between 4-5.9 σ_x.

gives each particle a random kick at each turn, particles do not remain stable, and may be focussed or defocussed by large amounts. It has been observed previously [8] that the diffusive HEL shows a steady decrease in the halo particle population - this is still the case, however now as we use the LHC HEL parameters, the particle kicks are larger and thus cleaning enhancement occurs over fewer turns.

Previous work found that the AC mode enhanced cleaning more than the diffusive [11], however we find that the diffusive case enhances cleaning more. There are differences between the simulations that could account for this. Firstly the distributions used are different - the lack of a transverse momentum component in MERLIN will equate to different particle tracks in the accelerator. Also the calculated machine tunes will be slightly different as one is done using thin lens (SixTrack), and the other thick lens (MERLIN) tracking, this is important as the AC mode requires accurate knowledge of the machine tune.

CONCLUSION

A HEL physics process has been included in the new version of MERLN, the effects of which have been demonstrated for the LHC, in its nominal and HL configurations. The effect of 3 HEL modes and 2 sets of HEL hardware parameters have been observed in many turn simulations. While the DC HEL mode in the HL LHC appears not to effect any cleaning enhancement, both the AC and diffusive modes show significant collimation enhancement. The diffusive case appears to be the more promising for cleaning a purely horizontal halo, exciting almost 100% of particles onto the primary collimator in around 10 s. Whereas the AC mode appears to leave particles closer to the beam core intact, the diffusive mode removes all particles that interact with the HEL. This is because the AC mode widens a particle's Poincaré section in $x\ x'$ phase space, whereas the diffusive mode can create large focussing or defocussing effects.

ISBN 978-3-95450-136-6

REFERENCES

[1] V. Shiltsev *et al.*, "Electron Lenses for Particle Collimation in LHC", FERMILAB-CONF-07-698-APC

[2] G. Stancari *et al.*, Phys. Rev. Lett. 107, 084802 (2011)

[3] `http://merlin-pt.sourceforge.net/`

[4] `https://sites.google.com/site/haroonrafiquemerlin/`

[5] H. Rafique *et al.*, "MERLIN for LHC Collimation", presented at ICAP'15, Shanghai, China, paper TUCBC1, these proceedings.

[6] S. Redaelli *et al.*, "Plans for deployment of hollow electron lenses at the LHC for enhanced beam collimation", Proc. IPAC15, Richmond, Virginia, 2015

[7] G. Stancari *et al.*, "Conceptual Design of Hollow Electron Lenses for Beam Halo Control in the Large Hadron Collider", FERMILAB-TM-2572-APC

[8] V. Previtali *et al.*, "Numerical Simulations of a Hollow Electron Lens as a Scraping Device for the LHC", Proc. IPAC13, China, 2013

[9] V. Moens, "Experimental and Numerical Studies on the Proposed Application of Hollow Electron Beam Collimation for the LHC at CERN", CERN-THESIS-2013-126

[10] `http://sixtrack.web.cern.ch/SixTrack/`

[11] V. Previtali *et al.*, "Hollow Electron Lens Simulations for the SPS", Proc. IPAC13, China, 2013

[12] H. Rafique *et al.*, "Simulation of hollow electron lenses as LHC beam halo reducers using MERLIN", Proc. IPAC15, Richmond, Virginia, 2015

ISBN 978-3-95450-136-6

IMPLEMENTATION OF BENCHMARKS FOR PRECISION TRACKING IN STORAGE RINGS*

R. Hipple†, M. Berz, Michigan State University, East Lansing, Michigan, USA

Abstract

Currently, there is a much interest in making precision measurements utilizing storage rings [1]. For example, the Muon g-2 experiment at Fermilab [2] and the Electric Dipole Moment (EDM) program of the JEDI Collaboration [3] require measurements of sub-ppm precision. Of particular importance is the ability to treat all nonlinear effects arising from detailed field distributions, including fringe fields.

In this paper, we track existing and proposed storage ring lattices using multiple codes and compare the results. The storage rings in question are the COSY Jülich ring at Forschungzentrum Jülich [4] and the High Energy Storage Ring (HESR) [5] to be constructed as part of FAIR at GSI. We present new results of tracking of the HESR lattice with COSY INFINITY [6], including full fringe fields, and the resulting dynamic aperture is estimated.

Finally, a set of benchmarks has been proposed [7] to test the accuracy and speed of codes used for tracking orbital and spin dynamics in storage rings. We present a comparison of the results of such benchmarks with the codes COSY INFINITY, an eight-order Runge-Kutta Integrator, MADX, MAD8, and ZGOUBI tracking.

COMPARATIVE TRACKING

In a previous paper [8] we performed a comparative analysis of repetitive tracking for the storage ring Cosy Jülich with both COSY INFINITY and ZGOUBI [9], both of which can treat fringe fields. Despite the fact that ZGOUBI tracking is nonsymplectic, qualitative agreement between the tracking pictures was found. COSY INFINITY was an order of magnitude faster while producing comparable results.

HESR

Continuing work begun with COSY Jülich, we turned our attention to a future storage ring, the High Energy Storage Ring (HESR), part of the Facility for Antiproton and Ion Research (FAIR) at GSI in Darmstadt, Germany [5]. Following a similar line of analysis as for COSY Jülich, we perform comparative tracking experiments between COSY INFINITY, MADX [10] and MAD8 [11]. We present first results below.

General Layout of HESR

HESR is a racetrack storage ring similar to COSY Jülich, but of larger scale. The circumference of the ring is 575 m consisting of two 123m straight sections connecting two 157 m arcs. The momentum of the antiproton beam ranges from 1.5 GeV/c to 15 GeV/c. The number of elements is much larger than that of COSY Jülich; HESR consists of 44 bending elements and 84 focusing elements. This requires precise agreement amongst the transfer matrices of the various codes.

First Order Transfer Matrices

After implementing the given lattice in COSY INFINITY, the first check is to compare the first order transfer matrices with those of MADX and MAD8. Here are the matrix from MAD v8.51 Win32 and COSY.

$$\begin{bmatrix} -1.0456753 & -1.7327760 \\ 0.18033015 & -0.65749692 \end{bmatrix}$$

$$\begin{bmatrix} -1.046011 & -1.730853 \\ .1803385 & -.6576032 \end{bmatrix}$$

On the other hand, computing the transfer matrix with MAD-X 5.02.00 (64 bit, Linux), gives the following result:

$$\begin{bmatrix} 1.2664075 & 3.6824325 \\ -.077346854 & .56472775 \end{bmatrix}$$

The apparent difference is due to the fact that MAD-X uses kick approximation for the particle optical elements. Representing each of the elements by slicing into 128 sub-elements, we obtain good agreement with the matrices of MAD8 and COSY:

$$\begin{bmatrix} -1.0456753 & -1.7327760 \\ .18033015 & -.65749692 \end{bmatrix}$$

A further detailed study of the influence of the number of slices shows that the discrepancy follows an inverse square law (Figure 1), as expected from a kick approximation. In the following we therefore choose a large number of slices (128) for these simulations since CPU time was not the primary concern. The remaining discrepancy is likely attributable to slightly different values for natural constants and similar matters, the effect of which is amplified here due to large numerical cancellation effects arising particularly due to large drifts in the system.

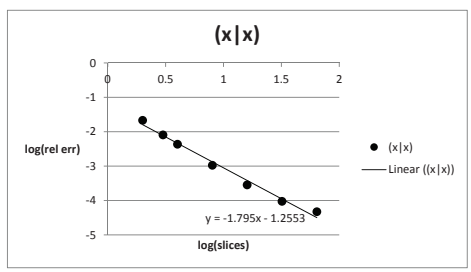

Figure 1: Relative matrix element discrepancy vs. number of slices.

* This work is supported by the U.S. Department of Energy under grant number DE-FG02-08ER41546.

† hipple@msu.edu

ISBN 978-3-95450-136-6

Having good baseline agreement in the transfer matrix, we can proceed to tracking with confidence. Here is the result of turning on fringe fields in COSY INFINITY:

$$\begin{bmatrix} -1.061066 & -1.462613 \\ .1675836 & -.7114451 \end{bmatrix}$$

Contrary to the case for COSY Jülich, in which the fringe fields rendered the lattice unstable, for HESR the lattice remains stable. We can thus proceed to tracking without re-fitting of the lattice. Figure 2 shows a tracking picture with fringe fields turned off. The orbits are at 1 cm increments, extending out to 6 cm, which is actually larger than the physical aperture of the beam elements. When we turn on fringe fields and repeat the tracking (Figure 3), we clearly see beam loss at radii greater than 4 cm. Confirmation of this is given by examining closely the region from 3–5 cm, Figure 4. These effects purely due to fringe fields are not apparent in tracking by MAD8 or MAD-X.

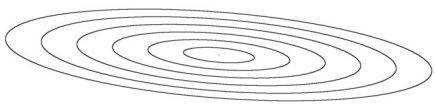

Figure 2: COSY INFINITY HESR tracking with no fringe fields.

Figure 3: COSY INFINITY HESR tracking with full fringe fields.

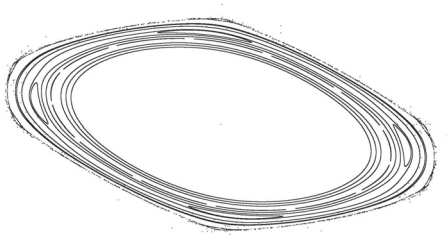

Figure 4: COSY INFINITY HESR tracking beam loss region.

BENCHMARKING

Recently a set of benchmarks for tracking software based on high precision analytical estimates for spin tracking has been proposed [7]. Our group at Michigan State University is actively engaged in implementing these benchmark tests in a variety of codes. Here we present some early results of this effort.

A straightforward test, easy to implement in any code, is off-reference motion through a dipole. The motion of a cosine-like ray through such a constant field is diagrammed in Figure 5. The solid circle is the reference orbit of radius R, and the location of the test particle is represented by the dashed circle and angle θ. The dashed circle is offset from the reference orbit by the quantity x_0. The 16 radial lines in the circle of the reference orbit denote the locations where the coordinates of the test particles will be plotted. A tracking code will calculate the position of the displaced particle by the particle optical coordinates x and a which can be derived from geometric considerations:

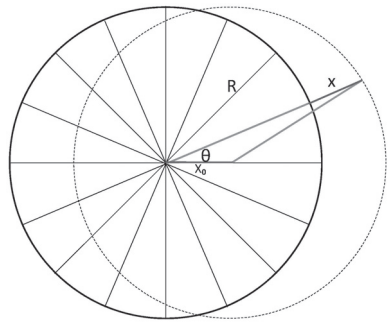

Figure 5: (x,a) coordinate of an off-axis cosine-like trajectory in a dipole.

$$\begin{aligned} x &= x_0 \cos\theta + \sqrt{(R^2 - x_0^2 \sin^2\theta} - R \\ x' &= x_0 \sin\theta - x_0^2 \sin\theta \cos\theta / \sqrt{R^2 - x_0^2 \sin^2\theta} \end{aligned}$$

Here x' is the derivative with respect to polar angle, which can be used to obtain the respective particle optical coordinate for slope or relative momentum.

The main appeal of this test lies in the fact that regardless of the launching position x_0, the orbit will return to exactly this point after one revolution through the lattice. Any deviation from this shows a limitation of the code, either due to numerics, or more importantly, through approximations in the dynamics.

The first test is a comparison of a Runge-Kutta integrator written in-house at MSU with COSY INFINITY at 19th order. Figure 6 shows the results of Runge-Kutta tracking (10000 turns @ $\approx$ 300 seconds CPU time). This is in excellent agreement with the analytic solution all the way out to $.9R$. Figure 7 is a plot of the same system tracked to 19th order by COSY INFINITY for 10000 turns. What is apparent is the loss of fidelity at approximately $.9R$. This is to be expected, as COSY INFINITY tracking is based on a Taylor

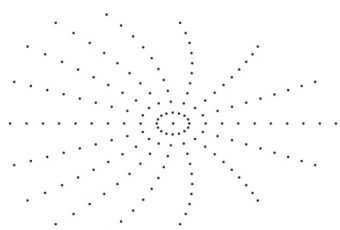

Figure 6: (x,a) coordinate tracking by Runge-Kutta of a cosine-like trajectory through a dipole at 7-70% radius (courtesy Eremey Valetov, MSU).

ISBN 978-3-95450-136-6

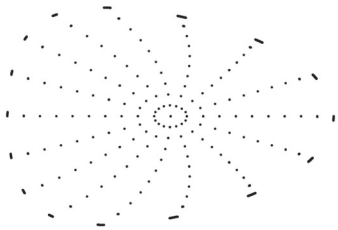

Figure 7: (x,a) coordinate tracking by COSY INFINITY of a cosine-like trajectory in a dipole from 7–70% radius (courtesy Eremey Valetov, MSU).

expansion about the reference orbit, and there will always be some radius beyond which a Taylor expansion will lose its accuracy. On the other hand, a Runge-Kutta integrator suffers no such limitation. We therefore expect the accuracy of an RK integrator to be independent of R. Nonetheless, even at $.9R$, agreement of COSY INFINITY with the analytic solution is on the order of 10^{-5}. Additionally, COSY INFINITY is an order of magnitude faster; this plot took only $\approx 30s$.

Similar benchmarking was performed using ZGOUBI (Figure 8). This tracking picture is substantially different from that of COSY INFINITY; it is worthwhile to investigate why. To see whether particles indeed return to their start-

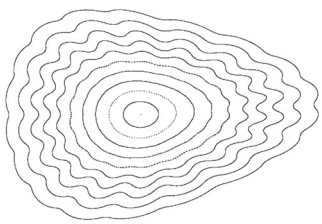

Figure 8: (x,a) ZGOUBI tracking of a cosine-like trajectory through a dipole at 7-70% radius

ing position, Figure 9 shows the result of eight single turns through the dipole. The initial locations of the particles are along the horizontal. The successive turns form branches which spiral away from the horizontal. The increasing curvature of the particle configuration causes the phase space orbits to fill out and become solid lines. Another interesting observation is the behavior of the first 5 particles from the center. These particles do not share in the spiraling motion; thus we suspect a software-related discrepancy between the handling of particles at $x < 5$ cm and those for which $x > 5$ cm. Figure 10 shows the same tracking test for MAD8. This tracking uses thick elements, which yield qualitatively similar orbits to ZGOUBI. The nonlinear features apparent in the ZGOUBI tracking picture of Figure 8 are not apparent in the MAD8 tracking.

Finally, we repeat the same benchmark test with MADX, which does not use thick elements for tracking. Figure 11 shows the tracking picture. The asymmetrical nature of the orbits is lacking, which is due to approximations in the Hamiltonian MADX makes to allow the use of kicks. Again

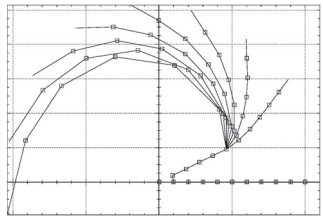

Figure 9: ZGOUBI locations of particles after first 8 turns. Each branch is a successive turn.

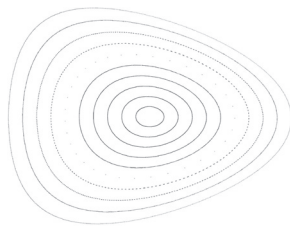

Figure 10: (x,a) MAD8 tracking of a cosine-like trajectory through a dipole at 7-70% radius

the orbits are filled, as we found in ZGOUBI. If we study the first few turns and plot the location of the particles after each turn, we observe a similar "spiraling" as present in ZGOUBI.

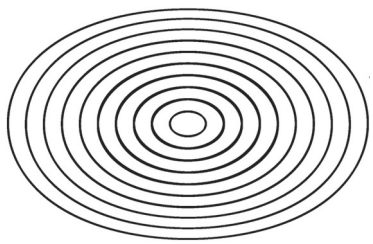

Figure 11: (x,a) MADX tracking of a cosine-like trajectory through a dipole at 7-70% radius

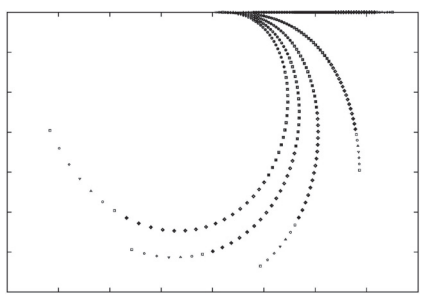

Figure 12: MADX locations of particles after first 4 turns. Each branch is a successive turn.

ISBN 978-3-95450-136-6

REFERENCES

[1] Andreas Lehrach, presented at ICAP'15, Shanghai, China, THAJI1, these proceedings.

[2] J. Grange et al., Muon g-2 Technical Design Report, 2015, arXiv:1501.06858

[3] JEDI Collaboration. collaborations.fz-juelich.de/ikp/jedi

[4] U. Bechstedt et al., Nucl. Instrum. Methods Phys. Res. B 113 (1996) 26-29

[5] B. Lorentz et al., "HESR Linear Lattice Design", EPAC'08, Genoa, June 2008, MOPC112 (2008), www.jacow.org

[6] M. Berz, K. Makino, "COSY INFINITY 9.2 Beam Physics Manual", MSUHEP-151103 (2015)

[7] E.M. Metodiev et al., Nucl. Instrum. Methods Phys. Res., Sect. A 797, 311 (2015)

[8] R.Hipple, M. Berz, Microscopy and Microanalysis 21 Suppl. 4 (2015)

[9] F. Méot, S. Valero, "ZGOUBI Users' Guide" -, CEA DSM DAPNIA-02-395 (2013)

[10] H. Grote et al., "The MAD-X Program (Methodical Accelerator Design) Version 5.03.00, User's Reference Manual", mad.web.cern.ch/mad/

[11] Hans Grote, F. Christoph Iselin, "The MAD Program (Methodical Accelerator Design), Version 8, User's Reference Manual", CERN/SL/90-13 (AP) (Rev. 4)

ISBN 978-3-95450-136-6

INVESTIGATION OF LATTICE FOR DEUTERON EDM RING

Yu. Senichev*, IKP, Forschugszentrum Jülich, Germany
S.Andrianov, A. Ivanov, St. Petersburg State University, St. Petersburg, Russia
S. Chekmenev, III. Physikalisches Institut, RWTH Aachen, Aachen, Germany
M. Berz, E. Valetov, Michigan State University, East Lansing, MI 48824, USA
on behalf of the JEDI Collaboration

Abstract

The quasi-frozen spin (QFS) concept of a storage ring for deuteron EDM measurement is based on the fact that the anomalous magnetic moment has a small negative value. Due to this fact, the rotation of spin in two parts of ring with the magnetic and electric fields relative to the momentum can compensate each other. In contrast to the concept of frozen spin we have the freedom to choose the ring parameters and also greatly simplified lattice. We consider two possible options for the lattice based on QFS concept and compare them with the frozen spin lattice where the elements with the combined electric and magnetic fields proposed by BNL are used. In the first QFS option, we use completely separate electric and magnetic parts that form a structure. In the second option, we suggest using only two magnetic arcs with two straight sections having the straight elements with magnetic and electric fields. The straight elements have a horizontal electric field of 120 kV/cm and a vertical magnetic field of 80 mT. They provide the compensation for the spin rotation in the arc and at the same time allow having straight electric plates without the higher orders field. This scheme could be tested in the COSY ring at FZ Juelich to prove the quasi-frozen spin concept.

FROZEN AND QUASI-FROZEN SPIN CONCEPT

In the frozen spin method [1], the main objective is to maximize the EDM signal growth, which is provided by the frozen orientation of spin along the momentum, i.e. by zero spin frequency $\vec{\omega} = 0$ relative to the momentum due to the magnetic dipole moment (hereinafter called MDM precession) in $\vec{E} \times \vec{B}$ fields:

$$\vec{\omega}_G = -\frac{e}{m}\left\{G\vec{B} + \left(\frac{1}{\gamma^2 - 1}\right)\frac{\vec{\beta} \times \vec{E}}{c}\right\}, \qquad (1)$$

where $G = (g-2)/2$ is the anomalous magnetic moment and g is the gyromagnetic ratio.

However, if the spin oscillates in the horizontal plane with respect to the frozen spin direction with amplitude Φ_s, then the EDM growth decreases proportionally to the factor $J_0(\Phi_s) \approx 1 - \frac{\Phi_s^2}{4}$.

Taking into account that the deuterons anomalous magnetic moment $G = -0.142$ has a small value and the fact that the spin oscillates around the momentum direction within half value of the advanced spin phase $\pi \cdot \gamma G/2n$, each time returning back by special optics with n-periodicity, it is obvious that the effective contribution to the expected EDM effect is reduced only by a few percent. This allows us to proceed to the concept of quasi-frozen spin [2], where the spin is not frozen with respect to the momentum vector, but continually oscillates around momentum with a small amplitude.

TWO POSSIBLE OPTIONS OF QUASI-FROZEN SPIN LATTICE

In [1], it has been shown how to implement a variable MDM spin precession in the storage ring and to provide a sufficient EDM signal growth. Due to the fact that there is an energy region, where the MDM spin oscillation in the electric field is several times faster than in the magnetic field, the idea of quasi-frozen structure can be implemented on the basis of two lattice structure options. The first option is based on two types of arcs: magnetostatic and electrostatic with inverse curvature of the later. That is, the lattice is created by two parts: two magnetic arcs with bend magnets, rotating the particle by angle $\Phi^B = (\pi + 2\alpha)$ per arc and providing the MDM spin rotation in horizontal plane relative to the momentum by an angle $\Phi_s^B = \nu_s^B \cdot \Phi^B$, where ν_s^B is spin tune in magnetic field, and two electrostatic arcs with electric deflectors of negative curvature, rotating the beam by an angle $\Phi^E = -2\alpha$ per arc and providing the MDM spin rotation in the horizontal plane relative to the momentum in opposite direction by an angle $\Phi_s^E = \nu_s^E \cdot \Phi^E$, where ν_s^E is spin tune in electric field. To realize the quasi-frozen spin concept, we have to fulfil the condition $\Phi_s^E = -\Phi_s^B$. Since in the electrostatic deflector the spin is rotated relative to the momentum with frequency that is by the factor of $K = \nu_s^E/\nu_s^B$ faster than in magnetostatic structure, we have the basic relation for two different arcs:

$$\nu_s^B \cdot (\pi + 2\alpha) = \nu_s^E \cdot 2\alpha$$
$$\alpha = \frac{0.5 \cdot \pi}{\nu_s^E/\nu_s^B - 1}. \qquad (2)$$

Following the principles of this idea, it is obvious that the electrostatic and magnetostatic parts have an arbitrary geometry with the single condition:

*y.senichev@fz-juelich.de

ISBN 978-3-95450-136-6

$$\sum_i \Phi_i^E \nu_s^E = \sum_j -\Phi_j^B \nu_s^B, \quad (3)$$

where Φ_i^E, Φ_j^B are the momentum angle rotations in i-th electrostatic and j-th magnetostatic element of structure respectively. The sequence of magnetic and electrostatic elements in the ring is also arbitrary and determined by the beam dynamics. So, turn by turn, the MDM spin rotation in magnetostatic part is compensated by MDM spin rotation in electrostatic part.

Obviously, this oscillation should lead to EDM signal reduction. However, due to the small amplitudes of Φ_s^E and Φ_s^B, the growth of EDM signal is reduced in comparison to the fixed spin direction case by the factor:

$$J_0(\Phi_s^{E,B}) \approx 1 - \frac{(\Phi_s^{E,B})^2}{4}, \quad (4)$$

which is ~ 0.98 in our case.

Figure 1 shows a visual appearance example of the first option of the ring for the deuteron energy 270 MeV based on QFS concept.

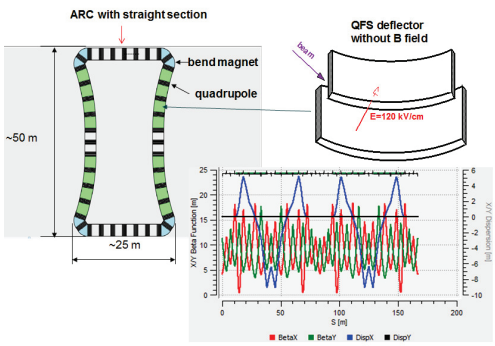

Figure 1: First option of ring lattice based on QFS concept with TWISS.

The free dispersion straight sections are placed between the magnetic arcs and are necessary to accommodate the polarimeter, the beam extraction and injection systems and RF cavity. The separation of bend elements on the magnetic and electrostatic components simplifies the common construction and allows adjusting them separately.

However, this concept inherits one drawback of cylindrical electrodes, namely the whole set of high-order nonlinearities. Therefore, we introduced a magnetic field of small value $\sim$ 80 mT, compensating the Lorentz force of the electric field. Thus, in the second option of lattice, we use the straight elements placed on the straight sections with incorporated E and B fields to recover MDM spin rotation in the magnetic arcs. The lattice consists of two magnetic arcs and two straight sections with the straight $\vec{E} \times \vec{B}$ elements, where Lorentz force equals to zero, and the total length of these elements is defined by the required spin recovery condition.

Figure 2 shows second option of the ring for the deuteron energy 270 MeV based on this concept.

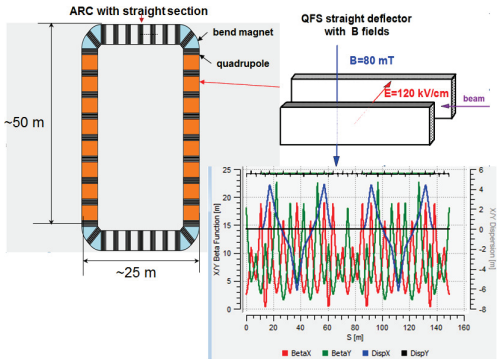

Figure 2: Second option of ring lattice based on QFS concept with TWISS.

As in the previous option, the lattice includes the straight sections with zero dispersion in the middle of magnetic arcs for the polarimeter, the beam extraction and injection systems, and the RF cavity. Thus, in the magnetic arc, the particles are rotated by the angle Φ_{arc}^B, with simultaneous MDM spin rotation in horizontal plane relative to momentum by the angle $\Phi_s^{arc} = \gamma G \cdot \Phi_{arc}^B$. On the straight section, the straight elements with E and B fields provide MDM spin rotation in the horizontal plane in the opposite direction relative to the momentum in E field by an angle $\Phi_s^E = -\left(\gamma G + \frac{\gamma}{\gamma+1}\right)\beta^2 \cdot \Phi_{ss}^E$, where Φ_{ss}^E is momentum rotation in electric field, and in B field by an angle $\Phi_s^B = (\gamma G + 1)\Phi_{ss}^B$, where Φ_{ss}^B is momentum rotation in magnetic field. Since the Lorenz force is zero, the angles $\Phi_{ss}^E = \Phi_{ss}^B$ are equal to each other. Therefore, they could be defined through one of them, for instance through magnetic field $\Phi_{ss}^B = \frac{eB_{ss}}{m\gamma v} \cdot L_{ss}$, where B_{ss}, L_{ss} are the magnetic field and length of the straight element. To realize the quasi-frozen spin concept, we have to fulfil the condition $\Phi_{ss}^B - \Phi_{ss}^E = \Phi_{arc}^B$, i.e.

$$(\gamma G + 1) \cdot \Phi_{ss}^B - \left(\gamma G + \frac{\gamma}{\gamma+1}\right)\beta^2 \cdot \Phi_{ss}^E = \gamma G \cdot \pi. \quad (5)$$

Carrying out simple transformations, we obtain the basic relation for the straight element parameters:

$$L_\sum E_{ss} = \frac{G}{G+1} \cdot \frac{mc^2}{e} \cdot \pi\beta^2\gamma^3$$
$$B_{ss} = -\frac{E_{ss}}{c\beta}, \quad (6)$$

where $L_\sum$ is the total length of straight elements in one straight section.

Thus, taking maximum electric field at level 120 kV/cm requires a magnetic field below 80 mT.

It opens prospects for simplifying the general construction. In particular, a permanent magnet or an air core electric coil may be used.

Finally for comparison, we have designed lattice based on the BNL deflector on arc with incorporated E and B fields (see Fig. 3).

ISBN 978-3-95450-136-6

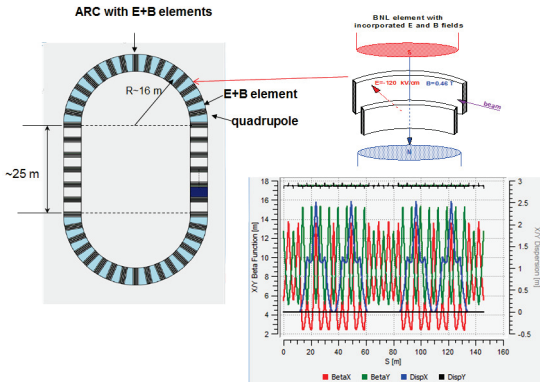

Figure 3: Option of lattice based on BNL element with TWISS functions.

Despite the difference in the concepts, the basic parameters, namely the size of the rings, the length of the straight sections, the number of focusing periods, and the number of deflecting and focusing elements and sextupoles all remain approximately the same.

As a special role is given to sextupoles, all structures have at least 6 families of sextupoles for a flexible control of spin coherence time and chromaticity in all coordinates, and each family carries out its own functions. Besides, since sextupoles are non-linear elements and, in addition to useful functions, distort phase trajectories and may induce nonlinearity in the dependence of orbit lengthening versus particle coordinates, we have studied all families from the point of view of spin coherence time correction and phase trajectories.

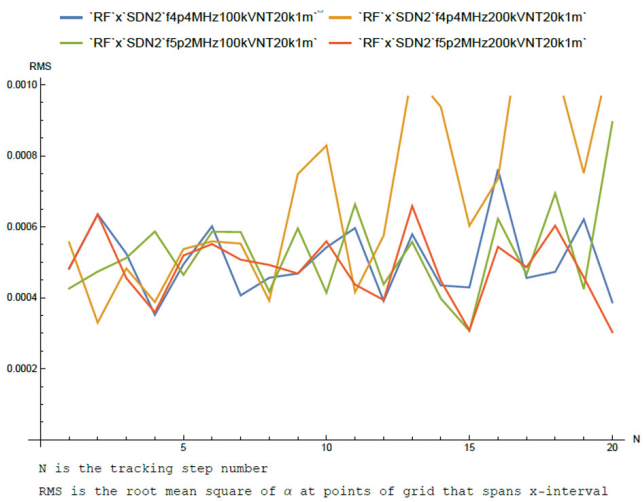

Figure 4: RMS spin deviation vs turn number

Figure 4 shows an example of how the rms spin deviation over whole bunch changes with turn number (up to one million turns). For some families, deviation remains practically at the same level. More details of these studies are given in [3].

CONCLUSION

The proposed quasi-frozen spin method could simplify the lattice and would allow diagnosis of the presumably existing EDM signal. The structures based on QFS concept are much easier and cheaper. The QFS lattice meets to all requirements of EDM search. This scheme can be applied in any existing ring with energy of at least 270 MeV and with deuteron polarized sources. To confirm the feasibility of the structure, we have done a numerical simulation of 3D spin-orbital motion using two codes, COSY-Infinity [4] and MODE [5].

REFERENCES

[1] D. Anastassopoulos et al., "AGS Proposal: Search for a permanent electric dipole moment of the deuteron nucleus at the 10^{29} e · cm level", BNL Report, 2008.

[2] Yu. Senichev et al., "Quasi-frozen spin method for EDM deuteron search", Proceedings of IPAC2015, Richmond, USA, pp. 213-215 http://accelconf.web.cern.ch/AccelConf/IPAC2015/papers/mopwa044.pdf.

[3] E. Valetov et al., "Search for the optimal spin decoherence effect in QFS lattice", presented at ICAP'15, Shanghai, China, THDBC2, *these proceedings*, 2015.

[4] M. Berz, "Computational Aspects of Design and Simulation: COSY INFINITY", NIM A298, p. 473 (1990).

[5] A. Ivanov et al., "Matrix Integration of ODEs for Spin-orbit Dynamics Simulation", Proc. of IPAC2014, Dresden, Germany, pp. 400402 (2014).

ISBN 978-3-95450-136-6

DYNAMIC KERNEL SCHEDULER (DKS) – ACCELERATING THE OBJECT ORIENTED PARTICLE ACCELERATOR LIBRARY (OPAL)

U. Locāns, University of Latvia, Riga, Latvia and PSI, Villigen, Switzerland
A. Adelmann, A. Suter, PSI, Villigen, Switzerland

Abstract

Hardware accelerators, such as graphical processing units (GPU) and Intel Many Integrated Core (MIC) processors, provide a huge performance potential for HPC applications. However, due to different hardware architectures and development frameworks, developing fast and manageable code for these devices is a challenging task, especially when integrating the usage of co-processors in large applications, such as OPAL. DKS provides a slim software layer that separates device specific code from the host application and provides a simple interface to communicate and schedule task execution on the device. Algorithms in DKS are implemented using CUDA, OpenCL, and OpenMP to target different devices. The first version of DKS was integrated in OPAL to speed up the FFT based Poisson solver and Monte Carlo simulations for particle matter interaction. The concepts of DKS and its integration with OPAL will be presented, as well as results showing speedups in the range of 9x to 150x for OPAL simulations using GPU or Intel MIC.

INTRODUCTION

Dynamic Kernel Scheduler (DKS) and its integration in Object Oriented Particle Accelerator Library (OPAL) is presented in this work. The aim of DKS is to ease the use of hardware accelerators in large host applications, such as OPAL. This is achieved by seperating all the accelerator and framework specific code in a seperate layer and providing a simple interface that can be implemented in the host application. This interface allows host application to communicate with DKS to schedule memory management, data transfer and kernel execution on the device. DKS contains function implementations writeen using CUDA, OpenCL, and OpenMP to allow the targeting of different accelerators that may be available on the system.

The ability of DKS to have implementations using different frameworks and libraries, and switch between them from the host applications allows not only to target hardware accelerators of different types and fine tune code to gain the maximum performance from each device, but also provides some software investment protection. In case some hardware architecture is no longer manufactured or some new architecture or development framework emerges only DKS needs to be updated.

The first version DKS was integrated into OPAL to accelerate its FFT based Poisson solver and Monte Carlo simulations. This DKS version uses CUDA kernels and OpenMP offload pragms to allow OPAL to accelerate the code using GPU or Intel Many Integrated Core devices.

DKS CONCEPT AND ARCHITECTURE

DKS is a slim software layer between the host application and the hardware accelerator, as depicted in Figure 1. The aim of the DKS is to allow the creation of fast fine tuned kernels using device specific frameworks such as CUDA, OpenCL, and OpenMP. On top of that, DKS allows the easy use of these kernels in host applications without providing any device or framework specific details. This approach facilitates the integration of different types of devices in the existing applications with minimal code changes and makes the device and the host code a lot more manageable.

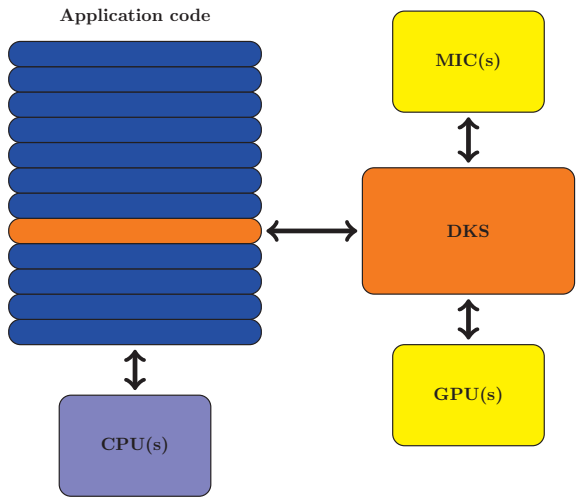

Figure 1: The concept of the Dynamic Kernel Scheduler.

DKS architecture is split into three seperate parts:

1. Communication functions, that handle memory allocation and data transfer to, and from, the device. All the memory management is left up to the user so the data transfers and memory allocation can be scheduled only when necessary. GPU streams are suported so asynchronous data transfer and kernel execution can be implemented.
2. Function library, witch contains algorithms written in CUDA, OpenCL and OpenMP to target different devices and DKS can switch between implementations based on the hardware that is available.
3. Auto-tuning functionality, which is not part of the first DKS version. The aim of auto-tuning is to select the appropriate implementation of the algorithm and change the launch parameters according to the devices that are available on the system in order to gain the maximum performance.

ISBN 978-3-95450-136-6

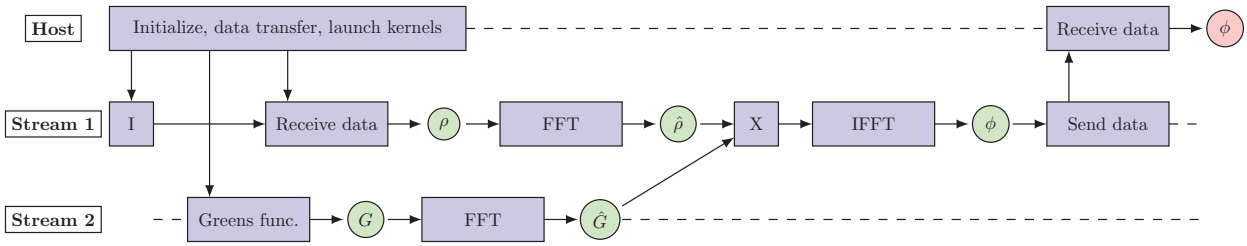

Figure 2: Sequence diagram of the FFT Poisson Solver run with DKS.

OPAL AND DKS

OPAL (Object Oriented Particle Accelerator Library) is a parallel, open source C++ framework for general particle accelerator simulations which includes 3D space charge, short range wake fields, and particle matter interaction. OPAL is based on IPPL (Independent Parallel Particle Layer) which adds parallel capabilities. Main functions inherited from IPPL are structured rectangular grids, fields, parallel FFT, and particles with the respective interpolation operators. Other features are expression templates, and massive parallelism (up to 65000 processors) which allows it to tackle the largest problems in the field.

FFT Poisson Solver in OPAL

The Poisson solver is an essential part of any self-consistent electrostatic beam dynamics code. From the – time to solution – point of view, we observe that in the order of 1/3 of the computational time is spend in this algorithm.

In many of the physics application, the bunch can be considered as small compared to the transverse size of the surrounding beam pipe ($\partial\Omega$). If this is the case the conducting walls can be neglected and, we can solve an open boundary problem. Here we follow the method of Hockney and compute the potential on a grid of size $2^3 M_x M_y M_z$, assuming 3 spatial dimensions of the problem. The calculation then is making use of Fast Fourier Transform (FFT) techniques, with a computational effort scaling as $O(2^3 M_x M_y M_z (\log_2 2 M_x M_y M_z)^3)$ [1–3].

FFT Poisson Solver in DKS

In DKS the FFT Poisson solver is implemented using CUDA to target NVIDIA's GPUs. It uses NVIDIA's cuFFT library to perform the FFT, separate kernels to calculate the Greens function and perform the multiplication on the GPU. To overlap the computation of the Green's function and the transfer of the charge density, ρ, CUDA streams are used. The implementation in DKS allows for multiple CPUs on the same node to share one GPU device, this is achieved using CUDA inter process communications. For the FFT Poisson solver one of the MPI processes acts as a main process and initializes memory allocation and kernel execution on the device. The other MPI processes meanwhile only send and receive data to and from the GPU. The sequence diagram in Figure 2 shows the steps executed for the FFT Poisson solver on the host and GPU.

Particle Matter Interaction in OPAL

One of the features in OPAL is the ability to perform Monte Carlo simulations of the particle beam interaction with matter. This is mostly used for simulations of degrader for proton therapy. A fast charged particle moving through the material undergoes collisions with the atomic electrons and loses energy. In addition, particles are also deflected from their original trajectory due to the Coulomb scattering with nuclei, as shown in Figure 3. The energy loss in OPAL is calculated using Bethe-Bloch formula and the change of particle trajectory is simulated using Multiple Coulomb Scattering and Single Rutherford Scattering [4–6].

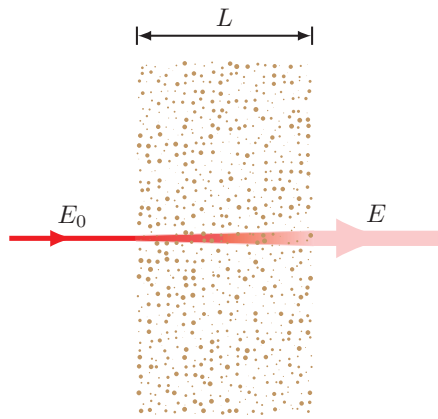

Figure 3: Particle matter interaction, final energy $E < E_0$ and larger momenta spread due to Coulomb scattering and the large angle Rutherford scattering.

At every time step when the particle beam is inside a material the following steps are executed.

- calculate the energy loss of the beam
- delete the particle if the particle's kinetic energy is smaller than a given threshold
- apply Coulomb & Rutherford scattering to the beam

Particle Matter Interaction in DKS

DKS contains CUDA and OpenMP implementations allowing OPAL to offload the simulations of particle matter interactions to GPUs and Intel MIC devices. DKS contains algorithms to allow offload the simulations of energy loss, Coulomb scattering and Rutherformd scattering. In adition particle drift before and after the material using time integration scheme can also be offload to the device.

ISBN 978-3-95450-136-6

Communication between host and device is minimized as much as possible by keeping the particles that are moving through the material in the device memory. They are only transfered to the host once they exit the material. To get the correct distributions for energy loss and scattering NVIDIAS's cuRand and Intels MKL VSL libraries are used. In order to improve the data access paterns of the algorithm and assist with the vectrorization for the Intel MIC, data layout of the particles is organized in structure of arrays format.

RESULTS

To test OPAL with DKS a series of test simulations where run. First the simulations where run on the CPU, where original OPAL's implementations of FFT Poisson solver and Monte Carlo simulations are used. Additional test runs where OPAL uses DKS to offload these tasks to GPU or Intel MIC where perfomed to test the performance of the algorithms in DKS. The test system consists of host with two Intel Xeon e5-2609 v2 processors with total 8 CPU cores, a Nvidia Tesla K20, Nvidia Tesla K40 and a Intel Xeon Phi 5110p.

To test the OPAL FFT Poisson solver performance with DKS, a similar problem setup as reported in [7, 8] was used. Results in Table 1 show the results from CPU simulations run on 8 cores and simulations using GPU. For larger grid sizes where the calculation of Greens function can be overlaped with data transfer we can observe a speedup of up to ×12 compared to the CPU version.

Table 1: OPAL FFT Poisson Solver Results

FFT size	DKS	FFTPoisson Time (s)	FFTPoisson speedup
64×64×32	no	22.53	
	K20	**7.42**	**×3**
	K40	**7.32**	**×3**
128×128×64	no	206.73	
	K20	**32.15**	**×6.5**
	K40	**25.87**	**×8**
256×256×128	no	1879.84	
	K20	**202.63**	**×9.3**
	K40	**160.87**	**×11.7**

To test the Monte Carlo simulations for particle matter interaction a test case where particle beam moves through a $L = 1$ cm thick graphite slab, mimicking a degrader device used in proton therapy. Table 2 shows the benchmark results for these simulations using varios number of particles. Due to current limitations of OPAL CPU simulations where run only on one CPU core. The results show that significant speedup in these simulations can be achieved on the accelerators compared to the host, but it is also observed that GPU significanlty outperforms Intel MIC.

Table 2: OPAL Degrader Results

Particles	DKS	Degrader time(s)	Degrader speedup	Integration time(s)	Integration speedup
10^5	no	20.30		3.46	
	MIC	**2.29**	**×8**	**0.89**	**×4**
	K20	**0.28**	**×72**	**0.15**	**×23**
	K40	**0.19**	**×107**	**0.14**	**×24**
10^6	no	206.77		34.93	
	MIC	**5.38**	**×38**	**4.62**	**×7.5**
	K20	**1.41**	**×146**	**1.83**	**×19**
	K40	**1.18**	**×175**	**1.21**	**×29**
10^7	no	2048.25		351.64	
	K20	**14.4**	**×142**	**17.21**	**×20**
	K40	**12.79**	**×160**	**11.43**	**×30**

SUMMARY

In this paper we presented the first version of Dynamic Kernel Scheduler whitch provides a software layer between host application and hardware accelerators. This allows to create a fine tuned code for different hardware accelerators using different frameworks and easily integrate it into existing host applications. DKS was integrated into OPAL to offload FFT based Poisson solver and Monte-Carlo simulations for particle matter interaction to GPU and Intel MIC using either CUDA or OpenMP. The results of this work show that DKS can be used to substantially speed up existing host applications with minimal additions and changes to host code. Seperating the device specific code in a different layer allows managing and fine tunining the code more easily and it also keeps the host application a lot more portable since all the device and framework specific details are handled by DKS.

REFERENCES

[1] R.W. Hockney, Methods Comput. Phys. 9, 136-210 (1970).

[2] J.W. Eastwood and D.R.K. Brownrigg, J. Comp. Phys, 32, 24-38 (1979).

[3] R.W. Hockney and J.W. Eastwood, "Computer Simulation using Particles," Taylor & Francis Group (1988).

[4] *Stopping Powers and Ranges for Protons and Alpha Particles*, ICRU Report 49 (1993).

[5] K.A. Olive et al., *Particle Data Group*, Chin. Phys. C, 38, 090001 (2014).

[6] W.R. Leo, *Techniques For Nuclear And Particle Physics Experiments*.

[7] Y. Bi, A. Adelmann, et al., Phys. Rev. STAB **14**(5) 054402 (2011).

[8] J. Yang, Adelmann, et al., Phys. Rev. STAB **13**(6) 064201 (2010).

ISBN 978-3-95450-136-6

PYTHON-BASED HIGH-LEVEL APPLICATIONS DEVELOPMENT FOR SHANGHAI SOFT X-RAY FREE-ELECTRON LASER

T. Zhang*, J. Chen, B. Liu, D. Wang, SINAP, Shanghai 201800, China

Abstract

Shanghai soft x-ray free-electron laser is currently being built at SSRF campus of SINAP. At the same time, the development of the high-level applications are on-going, with the intention of building a fully open source and robust software ecosystem, Python has been chosen as the essential developing programming language. Up to now, the software framework has been readily established, multiple physics-related high-level applications are under development. Additionally, EPICS soft-IOC applications has been built for the software debugging. The development are taken in a distributed manner, i.e. git is used to organize the source code and for the ease of team collaboration, specific applications are built into Python modules and finally integrated into a single Python package named 'felapps' for deployment. In this paper, details about the Python-based software development at SXFEL and the future ideas are covered.

INTRODUCTION

Shanghai soft x-ray free-electron laser (SXFEL) facility is designed to be a two-staged seeded FEL, which baseline physics operation mode is cascaded high-gain harmonic generation (HGHG), as such the fully coherent radiations with ultra-high brilliance at the wavelength around 8.8 nm could be generated at the end of the second HGHG stage. It is now under construction at the northeast of SSRF campuse site of SINAP, CAS (see Fig. 1), the first lasing is expected to be at the end of 2017. SXFEL also has the potential to radiate at even high frequencies, e.g. after the beam energy upgrading up to 1.1 GeV, FEL radiations within the water window regime could be privided to the users [1].

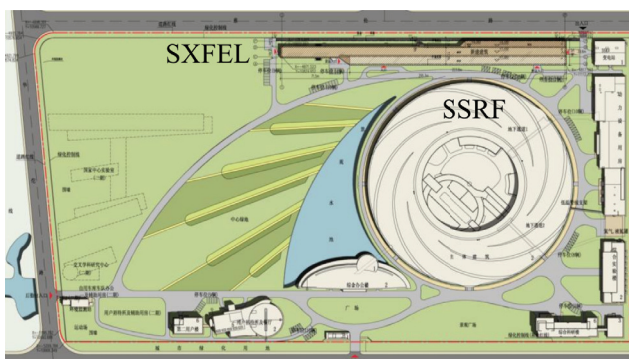

Figure 1: Buiding sketch of SXFEL and SSRF.

Meanwhile, the high-level applications for SXFEL are now under development, the mission is to build a user-friendly, extensible, maintainable system to make the usage of such kind of large scientific facilities be easier. To achieve such purposes, Python has been choosed to be the main developing programming language, since it is a fully object-oriented designed, could be much more powerful when incorporating third-party modules [2]. Numpy and Scipy Python packages are used to handle complex numerical computing issues, such as matrix manipulations, numerical integration as well as other general mathematical calculations [3]. The matplotlib package is used to handle the data visualization jobs, which provides matlab-like commands to deal tasks like figure plotting, but with a much more flexible and extensible manner [4]. So the core Python, together with Numpy, Scipy and matplotlib, actually makes an excellent alternative for matlab.

Since the control system of SXFEL relys on EPICS [5], all the raw data streaming come up to the high-level applications are from the lower EPICS levels. PyEpics is used to be the interface between the lower-level and high-level [6]. The hdf5 self-explantory scientific data format is used to be as the standard format throughout the whole high-level applications [7, 8].

Efficient and nice-looking graphical user interface (GUI) is of much great importance to imporve the user experience, here we choose wxPython as the main GUI builder toolkits, which is the python wrapper for C++ GUI class named wxWidget [9]. The fully open-sourced developing environment definitely make it quite flexible and also means could save a lot budget.

SOFTWARE FRAMEWORK OF FELAPPS

The python-based high-level applications for SXFEL is named felapps, the framework is shown in Fig. 2. The general view is divided into two parts, the left grey part is for applications developed for non-python, for example, legacy apps, and the right orange part is the incubated python world. There are apps with general purposes, like imageviewer, dataworkshop, etc., which could be invoked and served as universal task-handler; and the apps that designed for specific goals are basicly physics-related ones, which be used to solve the corresponding physics problem, such as laser-beam interaction, beam lattice matching, etc.; all these apps are behaving as subpackages or submodules in the python interpretation, integrating into felapps package.

Generally speaking, the design philosophy behind felapps is trying to make the complex suff into the packages, but the simply interface to the users, as well as the sustainable, maintainable development procudure. In order to debug and test the software, an intentionally designed EPICS soft IOC is deployed. Version control system git is utilized to manage the source code, and for the ease of team collaborations [10].

* zhangtong@sinap.ac.cn

ISBN 978-3-95450-136-6

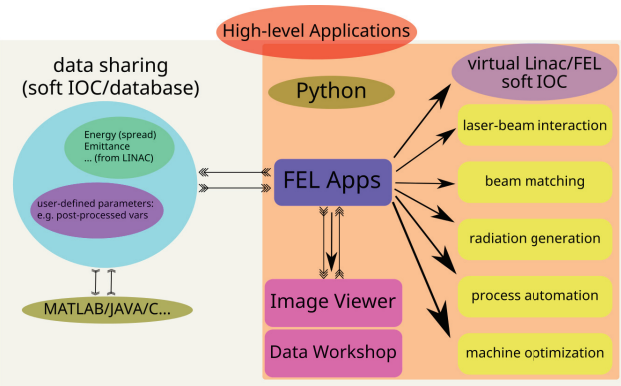

Figure 2: General framework of felapps.

DEVELOPMENT STATUS OF FELAPPS

Trying to make the development extensible and maintainable, Fig. 3 illustrates the project structure. The utils subpackage of felapps actually serves as the infrastructure, providing verious classes/functions, e.g. the parseutils module is responsible for the configuration file parsing tasks, and GUI components & data visulization classes/functions could be found in pltutils module, etc., newly added modules could be classified according to the functions.

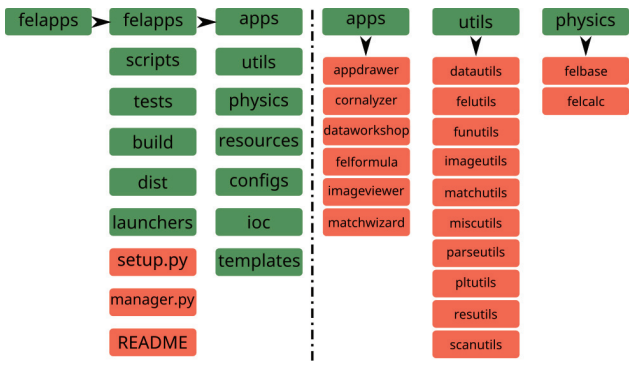

Figure 3: felapps project structure.

Up to now, multiple general purpose apps have built for the felapps package, alphabetically, they are appdrawer, cornalyzer, dataworkshop, felformula, imageviewer and matchwizard, please note that every app could be further feature-improved.

Appdrawer is also aliased as runfelpps, this is the main portal to the apps that felapps package contains. Figure 4 shows the graphical interface when appdrawer is invoked, from which other apps could be called by pushing the corresponding button, the alphabet list could be extended when new apps are created.

Imageviewer is a general purpose designed application for data or image acquisition (Fig. 5), rich properties could be user-defined in the Configurations menu item, once the input EPCIS PV name is connected, data acquisition routine could be started by clicking DAQ Start button, the acquisition frequency could also be configured, data and image could be saved, advanced saving function could be issued through

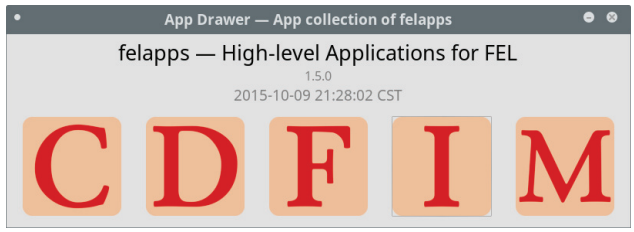

Figure 4: Subpackage of felapps: appdrawer.

Auto Save menu item in Operations menu, into which, saving data format e.g. hdf5, saving path and saving frequency could be defined. The saved data could be post-processed by Dataworkshop, which is a general purpose data post-processor for felapps.

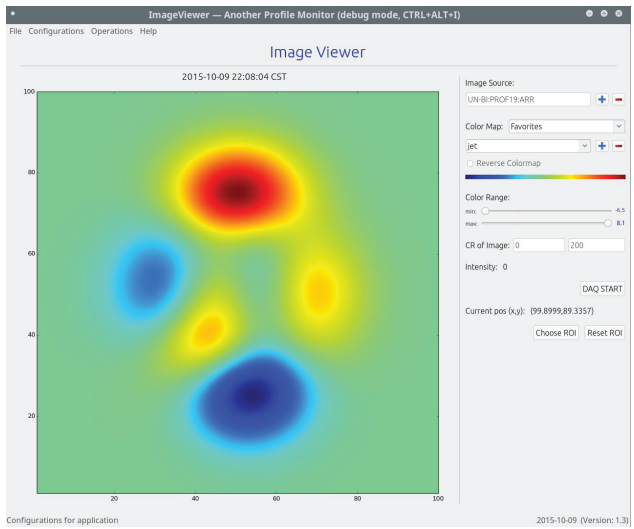

Figure 5: Subpackage of felapps: imageviewer.

After data files are imported into Dataworkshop (Fig. 6), the corresponding images are shown on the right image grid panel, sophisticated functions could be applied to the loaded images/data to get processed informations.

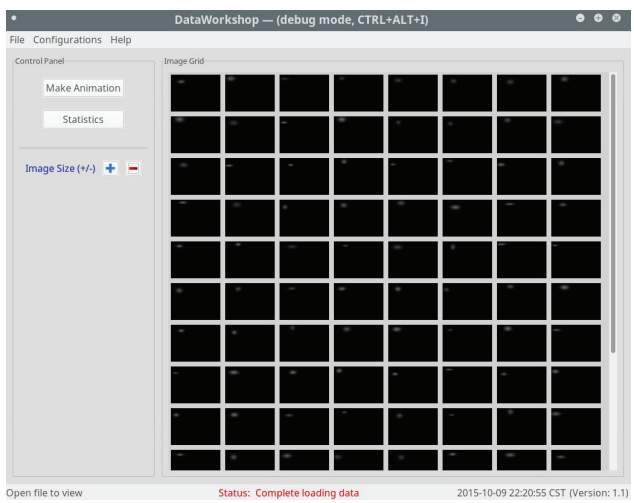

Figure 6: Subpackage of felapps: dataworkshop.

ISBN 978-3-95450-136-6

Felformula app is designed to handle FEL calculations (Fig. 7), after the user completes filling the electron beam parameters, felformula shows the primary properties of FEL radiations, parameter scan could be enabled when optimization is demanding.

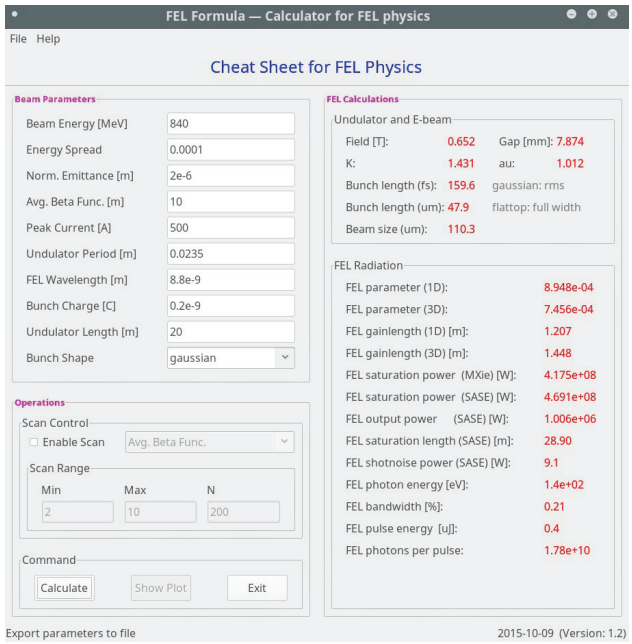

Figure 7: Subpackage of felapps: felformula.

The parameter correlation and scan feature could be handled by app cornalyzer, which is brief for correlation analyzer, also designed with a flexible configurable manner (Fig. 8).

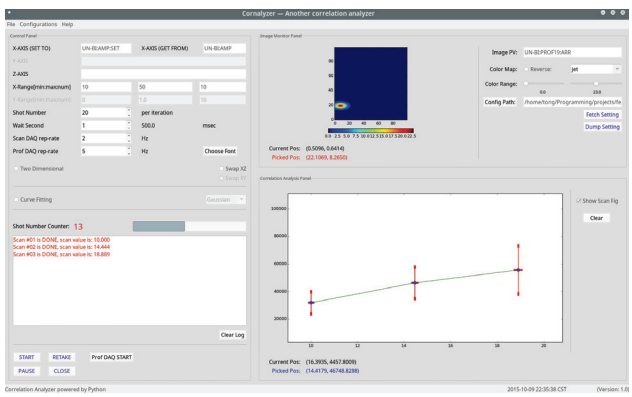

Figure 8: Subpackage of felapps: cornalyzer.

Matchwizard is the app for handling the lattice matching tasks, however it only has the ability to do lattice visulization, which incorporates the python package — beamline to parse

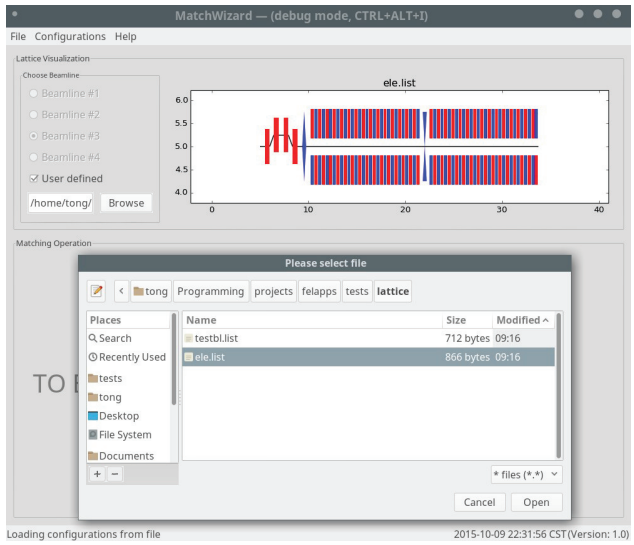

Figure 9: Subpackage of felapps: matchwizard.

and visualize the lattice file, e.g. MAD format lattice, see Fig. 9.

It is significant to note that the initial design consideration of felapps is trying to make the whole software easy to develop and maintain, as well as to delopment. Thanks to the great python module: setuptool, the deployment is really easy and clear now. We can build the .whl package to directly dictribute felapps, or upload onto PyPI web server [11] and deploy onto other system by issing 'pip install felapps'.

CONCLUSIONS

In general, the python-based high-level applications for SXFEL are under development, whole picture is on the way to build an fully-featured aigle python ecosystem, and it is envisioned that verious applications should be benefited from such kind of python-based infrastructure.

REFERENCES

[1] B. Liu et al., "Status of SXFEL and DCLS," FEL'15, Daejeon, August 2015, WEA02, (2015); http://www.JACoW.org
[2] https://docs.python.org/
[3] http://docs.scipy.org/doc/
[4] http://matplotlib.org/
[5] http://www.aps.anl.gov/epics/tech-talk/
[6] http://cars9.uchicago.edu/software/python/pyepics/
[7] https://www.hdfgroup.org/HDF5/
[8] http://docs.h5py.org/en/latest/
[9] http://www.wxpython.org/Phoenix/docs/html/main.html
[10] http://www.git-scm.com/
[11] https://pypi.python.org/

ISBN 978-3-95450-136-6

ADVANCED MODELING OF ACCELERATORS FOR NEXT GENERATION LIGHT SOURCES*

J. Qiang#, C. Mitchell, R. Ryne, M. Venturini, LBNL, Berkeley, CA94720, U.S.A.

Abstract

Next generation light sources are critical to scientific discovery in numerous fields such as materials science, chemistry, and the biosciences. In this paper, we will review status of accelerator modeling of next generation light sources and report on the progress that we have made in developing advanced computational tools for high fidelity start-to-end simulation and optimization of these sources. We will present numerical methods and application examples for modeling of a next generation FEL-based light source.

INTRODUCTION

Next generation high brightness FEL X-ray light sources provide great opportunity for scientific discovery in many fields. Some grand challenges in basic energy science research involve controlling material processes at the electron level, designing energy efficient synthesis of new matter with desired properties, understanding the effects of complex correlation between the atomic and the electronic constituents on matter properties, mastering energy and information on the nanoscale, and characterizing and controlling matter away or far away from equilibrium [1]. To meet those challenges, one needs ultrafast, ultrabright, tunable X-ray light sources. A next generation FEL-based X-ray light source with its high spatial and temporal coherence provides many orders of magnitude higher peak brightness than a conventional third generation light source. A number of next generation FELs were built and are under construction or design. The performance of those next generation light sources depends critically on the quality of the electron beam entering the radiation undulator. However, the presence of collective effects (space-charge, coherent synchrotron radiation (CSR), structure and resistive wakefields) inside the beam can significantly degrade the beam quality. Figure 1 shows the longitudinal phase space distribution of an electron beam at the entrance to an undulator with and without space-charge and CSR effects. It is seen that the presence of those collective effects causes large phase space modulation, increases energy spread and significantly degrades the beam quality. Advanced computational methods are needed in order to accurately model those effects.

ADVANCED COMPUTATIONAL METHODS

The simulation of a next generation light source starts with an initial particle distribution behind the cathode. In this study, we developed a second-order computational model to simulate the generation of photo-electrons from a photo-cathode driven by an external laser. For a given laser temporal pulse distribution and spatial distribution, a number of electrons carrying the total emitted charge are generated behind the cathode with the same transverse distribution as the laser's and the same longitudinal distribution as the laser's temporal profile times a reference longitudinal velocity v_0. Those electrons are moved outside the photocathode using N time steps. Here, the time step size is $\Delta t = t_{laser}/N$, where t_{laser} is the total laser pulse length. Figure 2 shows a schematic plot of the emission process in the simulation. In the second-order photo-electron emission model, the positions and the velocities of an electron after emission are given by

$$\begin{aligned} x &= x_0 + v_{x0}\delta t + \frac{1}{2}a_x(\delta t)^2 \\ v_x &= v_{x0} + a_x\delta t \\ z &= v_{z0}\delta t + \frac{1}{2}a_z(\delta t)^2 \\ v_z &= v_{z0} + a_z\delta t \end{aligned} \quad (1)$$

where $\delta t = z/v_0$, z is the electron longitudinal coordinate out of the photocathode right after emission during the time step Δt, and $\boldsymbol{a}$ is the acceleration that can be calculated using the field at the photo-cathode surface. As a comparison, we generate *300* pC photo electrons from a photo-injector gun using the second-order emission model and the first-order emission model (without including acceleration). The current profile of the beam shortly after emission is shown in Fig. 3 using different numbers of emission steps in the above emission models. It is seen that the crude first order emission model can introduce artificial modulation of the beam. A much larger number of emission steps (a factor of 4) i.e. smaller emission step size, are needed in order to achieve the same level smoothness of the current profile.

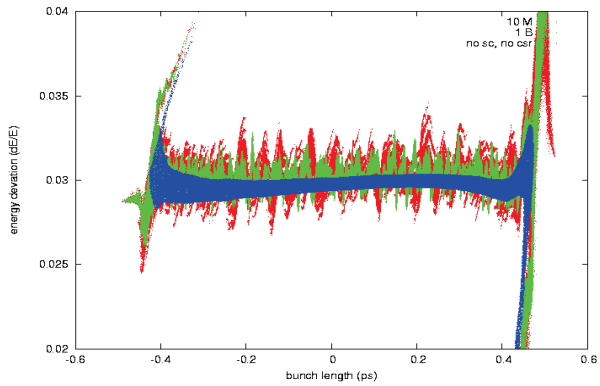

Figure 1: Final longitudinal phase space without (blue) and with longitudinal space-charge and CSR effects (green and red).

*Work supported by the Director of the Office of Science of the US Department of Energy under Contract no. DEAC02-05CH11231 and Contract no. DE-AC02-76SF00515.

#jqiang@lbl.gov

ISBN 978-3-95450-136-6

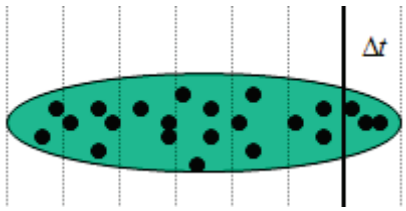

Figure 2: A schematic plot of the electron emission process at the photocathode.

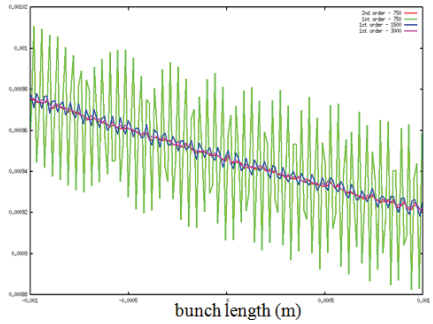

Figure 3: A section of current profile of the beam after emission using the second-order emission model (red) and the first-order emission model with different numbers of emission steps.

Efficient methods to calculate 3D space-charge effects, 1D longitudinal CSR effects, structure and resistive wall wakefields were developed in past studies [2,3,4]. However, a brute force approach to resolve the fine structure microbunching below optical wavelength throughout the entire electron beam can be computationally expensive. A multi-level Poisson solver with adaptive mesh refinement in selected regions of the beam will be more efficient. An illustration plot of this method with three levels of refinement in the longitudinal direction is shown in Fig. 4. In the multi-level solver, the potential on a grid i at level n is given as

$$\phi^n(x^i) = \sum_{j\in mesh(n-1)} G^{n-1}(x^i,x^j)\rho^j - \sum_{j\in mesh(n)(n-1)} G^{n-1}(x^i,x^j)\rho^j + \sum_{j\in mesh(n)} G^n(x^i,x^j)\rho^j$$

where *mesh(n-1)* denotes the mesh grid on level *n-1*, *mesh(n)(n-1)* denotes the mesh grid at level *n* also belonging to level *n-1*, and *mesh(n)* denotes the mesh grid on level *n*. For *n* less than or equal to *1*, the Green function *G* is *0*. In the above equation, the first two terms correspond to the long-range forces contributed by electrons on the parent grid level *n-1*. The third term denotes the short-range force on the child grid level *n*. For the open boundary condition assumed here, each convolution in the above equation can be computed by using an FFT-based method after zero padding. This results in a computational complexity of *O(Nlog(N)),* where *N* is the number of mesh grid points at each level. In the multi-level particle-mesh method, the convolution at child mesh grid level *n* can be further decomposed into the summation of a long-range force at level *n* and a short-range force at level *n+1* in a selected domain. Such a decomposition process can be repeated for many levels until the desired resolution is achieved in the desired region. The field for particles located inside the computational domain at level *n* is equal to the summation of field values interpolated from this level and the levels below the level *n*.

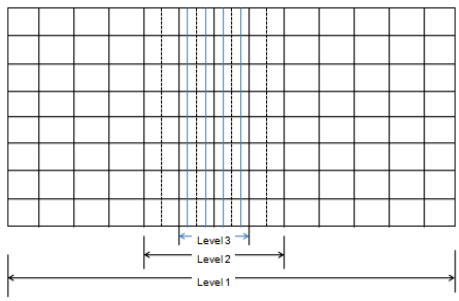

Figure 4: An illustration plot of multi-level particle mesh refinement.

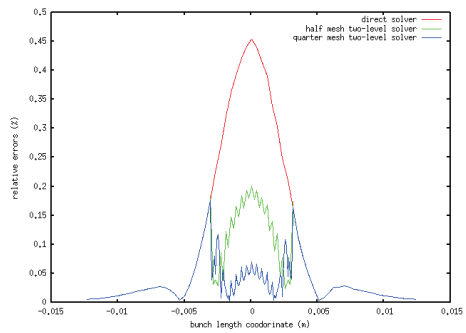

Figure 5: Relative electric potential errors across the beam using direct Poisson solver (red) and the multi-level Poisson solver (green and blue).

As a test, we calculated the electric potential in the middle of a beam with the direct Poisson solver and the above new multi-level Poisson solver. The relative errors of the solution from both methods are given in Fig. 5. It is seen that the new multi-level Poisson solver results in about a factor of four less errors in comparison to the direct solver. Such a multi-level Poisson solver with high accuracy in the selected region can significantly save the computational time in the simulation.

Numerical integration is used to advance the particle spatial and momentum coordinates with given space-charge and external fields. A widely used numerical integrator in the literature is the so-called Boris integrator [5]. The Boris integrator has 2nd order numerical accuracy and works well at lower energy when the relativistic factor γ is small. As the electron beam energy increases, there is a strong cancellation between the electric space-charge force and the magnetic space-charge force in the laboratory frame. In the case of a large γ factor for a relativistic electron beam, the numerical errors in computing the cancellation between the electric space-charge force and the magnetic space-charge force using the Boris integrator become worse due to the fact that the magnetic force and the electric force are not calculated in the same time step. In the limit as γ goes to infinity, the Boris integrator requires that both the magnetic field and the electric field disappear with any given time step size, which is unphysical. Here, we developed a new numerical integra-

ISBN 978-3-95450-136-6

tor that has 2nd-order numerical accuracy but works correctly for the relativistic electron beam. The one step update in particle coordinates for the new numerical integrator is given as:

$$x^{i+1/2} = x^{i-1/2} + \Delta t\, v^i$$
$$(\gamma v)_1^{i+1} = (\gamma v)^i + \Delta t \frac{q}{m}(E^{i+1/2} + v^i \times B^{i+1/2})$$
$$u^i = (v_1^{i+1} + v^i)/2$$
$$(\gamma v)^{i+1} = (\gamma v)^i + \Delta t \frac{q}{m}(E^{i+1/2} + u^i \times B^{i+1/2})$$

The new numerical integrator computes the electric force and the magnetic force in the same time step and correctly handles the cancellation of the two forces in the laboratory frame. As a test example, we simulated a *1* nC, *250* MeV bunch that is spherical in the beam frame and that freely expands in vacuum. Due to the symmetry of the space-charge forces in the beam frame, the beam should stay spherical. Figure 6 shows the evolution of the horizontal, vertical and longitudinal rms sizes in the beam frame from the simulation using the Boris integrator and the new proposed integrator with the same time step size. It is seen that the Boris integrator gives a wrong prediction of the transverse X and Y sizes while the new algorithm correctly predicts the rms size evolution.

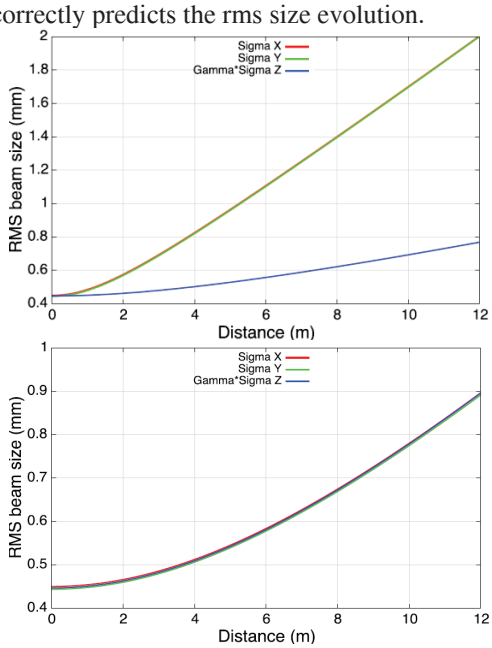

Figure 6: Transverse and longitudinal rms sizes evolution from the Boris integrator (top) and from the new integrator (bottom) in a freely expanding sphere beam.

APPLICATIONS*

The advanced computational tools developed here were implemented into a parallel 3D particle-in-cell tracking code suite, IMPACT [2, 6, 7]. IMPACT has become an essential tool for the design of the LCLS-II [8], and in particular for the investigation of the microbunching instability [9]. As a way to illustrate the code capabilities, we briefly discuss the application of the IMPACT to a specific problem of LCLS-II lattice-design optimization.

Figure 7 shows a schematic layout of the LCLS-II beam delivery system [10]. The combination of the long *(>2* km) transport beam line following the L3-Linac and leading to the FEL undulators, the presence of several doglegs, and a relatively low electron-beam energy *(4 GeV),* aggravates the microbunching effects. To mitigate the problem it was proposed to insert weak chicanes adjacent to the doglegs' dipoles to provide local R_{56}-compensation [9]. Specifically, two local compensation chicanes have been designed to compensate R_{56} in the first dogleg (DL1), with three more compensation chicanes inserted after the spreader in the hard x-ray transport line, and two more inserted in the soft x-ray transport line. Because of an interesting 3D space-charge effect [11], it turns out that exact local R_{56}-compensation does not provide maximum suppression of the microbunching instability. To find the optimum setting of the compensating chicanes we scanned the bending angle of all dipole magnets in all compensation chicanes by a same scaling factor; with *0%* corresponding to the nominal design setting for exact R_{56}-compensation. As a measure of the instability we considered the rms current fluctuations along the bunch core relative to a smoothened current profile fitted to a cubic polynomial, as observed at the entrance of the FEL undulators.

Figure 8 shows the rms current fluctuation as a function of the percentage increase from nominal of the compensating chicanes' bend angle (for transport of *100 pC* bunches to the hard x-ray FEL). It is seen that *20%* increase, corresponding to about 1.5 times larger $|R_{56}|$, yields the least current fluctuation.

Figure 9 shows the final longitudinal phase space and current profile with the nominal compensation setting and 20% increase of bend angle. Notice how the *20%* setting results in much reduced microbunching as seen in both longitudinal phase space and current profile.

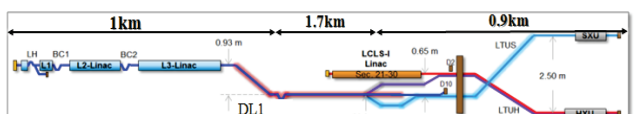

Figure 7: Schematic of the LCLS-II beam delivery system.

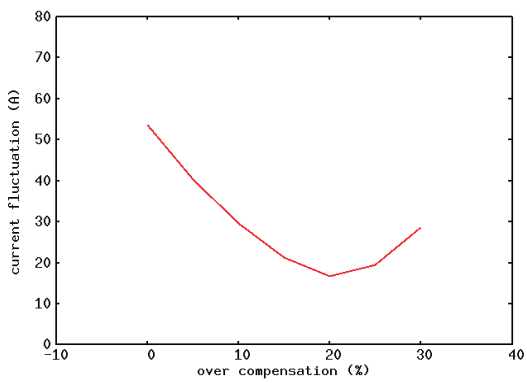

Figure 8: RMS bunch current-profile fluctuations as a function of relative deviation from nominal of the compensation chicanes' bend angle (entrance of the hard x-ray FEL; *100* pC charge) .

ISBN 978-3-95450-136-6

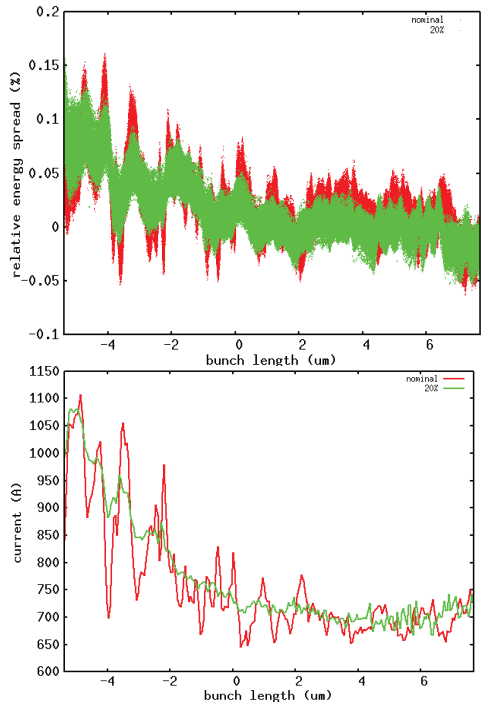

Figure 9: Longitudinal phase space (top) and current profile (bottom) with nominal (red) and *20%* (green) larger bend angle in the compensating chicanes (*100* pC, entrance of hard x-ray FEL)

PARALLEL DESIGN PARAMETER OPTIMIZATION

Differential evolution is a simple yet efficient population-based, stochastic, evolutionary algorithm for global parameter optimization [12]. In a number of studies, the differential evolution algorithm performed effectively in comparison to several stochastic optimization methods such as simulated annealing, controlled random search, evolutionary programming, the particle swarm method, and genetic algorithm.

The differential evolution algorithm starts with a population initialization. A group of NP solutions in the control parameter space is randomly generated to form the initial population. This initial population can be generated by sampling from a uniform distribution within the parameter space if no prior information about the optimal solution is available, or by sampling from a known distribution (e.g., Gaussian) if some prior information is available. After initialization, the differential evolution algorithm updates the population from one generation to the next generation until reaching a convergence condition or until the maximum number of function evaluations is reached. At each generation, the update step consists of three operations: mutation, crossover, and selection. The mutation and the crossover operations produce new candidates for the next generation population and the selection operation is used to select from among these candidates the appropriate solutions to be included in the next generation. During the mutation operation stage, for each population member (target vector) x_i, $i = 1, 2, 3, \bullet\bullet\bullet, NP$ at generation G, a new mutant vector v_i is generated by following a mutation strategy. Some commonly used mutation strategies in past studies are [12]:

$$\text{DE/rand/1}: \ \vec{v}_i = \vec{x}_{r_1} + F_{xc}(\vec{x}_{r_2} - \vec{x}_{r_3})$$

$$\text{DE/rand/2}: \ \vec{v}_i = \vec{x}_{r_1} + F_{xc}(\vec{x}_{r_2} - \vec{x}_{r_3}) + F_{xc}(\vec{x}_{r_4} - \vec{x}_{r_5})$$

$$\text{DE/best/1}: \ \vec{v}_i = \vec{x}_b + F_{xc}(\vec{x}_{r_1} - \vec{x}_{r_2})$$

$$\text{DE/best/2}: \ \vec{v}_i = \vec{x}_b + F_{xc}(\vec{x}_{r_1} - \vec{x}_{r_2}) + F_{xc}(\vec{x}_{r_3} - \vec{x}_{r_4})$$

$$\text{DE/current-to-best/1}: \ \vec{v}_i = \vec{x}_i + F_{cr}(\vec{x}_b - \vec{x}_i) + F_{xc}(\vec{x}_{r_1} - \vec{x}_{r_2})$$

$$\text{DE/current-to-best/2}: \ \vec{v}_i = \vec{x}_i + F_{cr}(\vec{x}_b - \vec{x}_i) + F_{xc}(\vec{x}_{r_1} - \vec{x}_{r_2}) + F_{xc}\,(\vec{x}_{r_3} - \vec{x}_{r_4})$$

$$\text{DE/current-to-rand/1}: \ \vec{v}_i = \vec{x}_i + F_{cr}(\vec{x}_{r_1} - \vec{x}_i) + F_{xc}\,(\vec{x}_{r_2} - \vec{x}_{r_3})$$

$$\text{DE/current-to-rand/2}: \ \vec{v}_i = \vec{x}_i + F_{cr}(\vec{x}_{r_1} - \vec{x}_i) + F_{xc}\,(\vec{x}_{r_2} - \vec{x}_{r_3}) + F_{xc}\,(\vec{x}_{r_4} - \vec{x}_{r_5})$$

$$\text{DE/rand-to-best/1}: \ \vec{v}_i = \vec{x}_{r_1} + F_{cr}(\vec{x}_b - \vec{x}_i) + F_{xc}\,(\vec{x}_{r_2} - \vec{x}_{r_3})$$

$$\text{DE/rand-to-best/2}: \ \vec{v}_i = \vec{x}_{r_1} + F_{cr}(\vec{x}_b - \vec{x}_i) + F_{xc}(\vec{x}_{r_2} - \vec{x}_{r_3}) + F_{xc}(\vec{x}_{r_4} - \vec{x}_{r_5})$$

where the integers r_1, r_2, r_3, r_4 and r_5 are chosen randomly from the interval *[1,NP]* and are different from the current index i, F_{xc} is a real scaling factor that controls the amplification of the differential variation, x_b is the best solution among the *NP* population members at the generation G, and F_{cr} is a weight for the combination between the original target vector and the best parent vector or the random parent vector.

The use of multiple mutation strategies makes the differential evolution algorithm complicated to implement and use appropriately. In this study, we developed a new adaptive unified differential evolution (AuDE) algorithm for global optimization [13]. This algorithm uses only a single mutation expression, but encompasses almost all commonly-used mutation strategies as special cases. It is mathematically simpler than the conventional algorithm with its multiple mutation strategies, and also provides users the flexibility to explore new combinations of conventional mutation strategies during optimization. By making the control parameters in the mutation and crossover stages self-adaptive, it also sets the user free from choosing an appropriate set of control parameters for each optimization problem.

This single unified mutation expression can be written as:

$$\vec{v}_i = \vec{x}_i + F_1(\vec{x}_b - \vec{x}_i) + F_2(\vec{x}_{r_1} - \vec{x}_i) + F_3(\vec{x}_{r_2} - \vec{x}_{r_3}) + F_4(\vec{x}_{r_4} - \vec{x}_{r_5})$$

This unified mutation expression represents a combination of exploitation (from the best found solution) and exploration (from the random solutions) to generate a new mutant solution. For example, one can see that for $F_1 = 0$, $F_2 = 1$, and $F_4 = 0$, this equation reduces to DE/rand/1; for $F_1 = 1$, $F_2 = 0$, and $F_4 = 0$, it reduces to DE/best/1. Using the single unified expression the ten mutation strategies of the standard differential evolution algorithm can be written as a single mutation expression. This new expression provides an opportunity to explore more broadly the space of mutation operators. By using a different set of parameters F_1, F_2, F_3, F_4, a new mutation strategy can be achieved.

ISBN 978-3-95450-136-6

The goal of multi-objective optimization is to find the Pareto front in the objective function solution space. The Pareto optimal front is a collection of all non-dominated solutions in the whole feasible solution space. Any other solution in the feasible solution space will be dominated by those solutions on the Pareto optimal front. In the multi-objective optimization, a solution A is said to dominate a solution B if all components of A are at least as good as those of B (with at least one component strictly better). The solution A is non-dominated if it is not dominated by any solution within the group. In this study, we have developed a new parallel multi-objective differential evolution algorithm with variable population size and external storage. The algorithm in each generation and external storage can be summarized in the following steps:

- Step 0: Define the minimum parent size, NPmin and the maximum size, NPmax of the parent population. Define the maximum size of the external storage, NPext.
- Step 1: An initial population of NPini parameter vectors is chosen randomly to cover the entire solution space.
- Step 2: Generate the offspring population using the adaptive unified differential evolutionary algorithm.
- Step 3: Check the new population against boundary conditions and constraints.
- Step 4: Combine the new population with the existing parent population from external storage. Nondominated solutions (Ndom) are found from this group of solutions and min(Ndom, NPext) of solutions are put back into external storage. Pruning is used if Ndom > NPext. NP parent solutions are selected from this group of solutions for next generation production. If NPmin ≤ Ndom ≤ NPmax, NP = Ndom. Otherwise, NP = NPmin if Ndom < NPmin and NP = NPmax if Ndom > NPmax. The elitism is emphasized through keeping the non-dominated solutions while the diversity is maintained by penalizing the over-crowded solutions through pruning.
- Step 5: If the stopping condition is met, stop. Otherwise, return to Step 2.

As a test of above algorithm, we used the following two objective functions:

$$f_1(\mathbf{x}) = 1 - \exp\left(-\sum_{i=1}^{3}\left(x_i - \frac{1}{\sqrt{3}}\right)^2\right)$$
$$f_2(\mathbf{x}) = 1 - \exp\left(-\sum_{i=1}^{3}\left(x_i + \frac{1}{\sqrt{3}}\right)^2\right)$$

The distance to the Pareto front as a function of function evaluation number is shown in Fig. 10. It is seen that new proposed algorithm ("variation population with external storage" or VPES) can converge significantly faster than a widely used genetic algorithm NSGA-II [14].

The above population based differential evolutionary optimization algorithm naturally leads to a multi-level parallel implementation. Our method contains two levels of parallelization. First, the whole population is distributed among a number of groups of parallel processors. Each group of processors contains a subset of the whole population. Different sets of the sub-population can be tracked simultaneously. Second, each objective function evaluation corresponds to an accelerator simulation, for which parallel simulation codes are available. A good scalability of the parallel differential evolution algorithm has been demonstrated on a Cray XT5 computer using 100, 000 processors using this method.

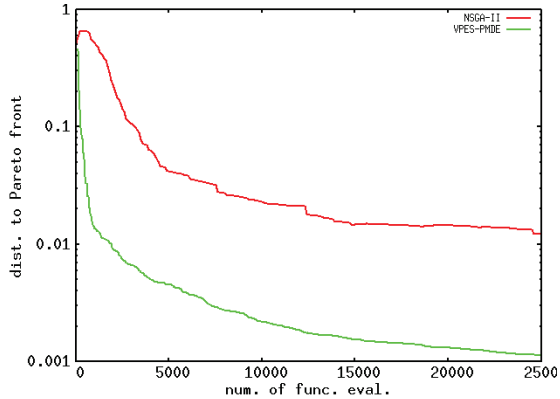

Figure 10: Distance to the Pareto front as a function of number of function evaluation using the genetic algorithm (NSGA-II) and the new proposed algorithm (VPES-PMDE).

ACKNOWLEDGMENTS

We would like to thank the support of the LCLS-II design team in the application study.

REFERENCES

[1] J. Hemminger, et al., "Directing matter and energy: five challenges for science and the imagination," Report from Basic Energy Sciences Advisory Committee, 2007.
[2] J. Qiang, et al., PRST-AB 9, 044204 (2006).
[3] J. Qiang, et al, NIMA 682, 49 (2012).
[4] C. Mitchell, et al, NIMA 715, 119 (2013).
[5] J. P. Boris, "Relativistic plasma simulation-optimization of a hybrid code," in Proceedings of the Fourth Conference on Numerical Simulation Plasmas Naval Research Laboratory, Washington, D.C., 1970, pp. 3–67.
[6] J. Qiang, et al., J. of Comp. Phys., 163, 434 (2000).
[7] J. Qiang, et al., PRST-AB 12, 100702 (2009).
[8] T. O. Raubenheimer, "Technical challenges of the LCLS-II CW X-ray FEL," in proceedings of IPAC2015, Richmod, VA, USA.
[9] M. Venturini, et al., IPAC 2015, p. 1843 (2015).
[10] P. Emma et al., in proceedings of FEL'14, THP025.
[11] M. Venturini and J. Qiang, PRST-AB, 18, 054401, (2015).
[12] R. Storn and K. Price, J. of Global Optimization, 11, p. 341 (1997).
[13] J. Qiang and C. Mitchell, in Optimization Online digest, Feb. 2015.
[14] K. Deb, et al., IEEE Trans. Evolutionary Computation 6, p. 183 (2002).

ISBN 978-3-95450-136-6

HIGH-PERFORMANCE MODELING OF PLASMA-BASED ACCELERATION USING THE FULL PIC METHOD*

J.-L. Vay†, R. Lehe, LBNL, Berkeley, CA 94720, USA
H. Vincenti, CEA, Saclay, France
B. B. Godfrey, I. Haber, U. Maryland, College Park, MD 20742, USA
P. Lee, LPGP, CNRS, Université Paris-Saclay, 91405, Orsay, France

Abstract

Numerical simulations have been critical in the recent rapid developments of plasma-based acceleration concepts. Among the various available numerical techniques, the Particle-In-Cell (PIC) approach is the method of choice for self-consistent simulations from first principles. The fundamentals of the PIC method were established decades ago, but improvements or variations are continuously being proposed. We report on several recent advances in PIC-related algorithms that are of interest for application to plasma-based accelerators, including: (a) detailed analysis of the numerical Cherenkov instability and its remediation for the modeling of plasma accelerators in laboratory and Lorentz boosted frames, (b) analytic pseudo-spectral electromagnetic solvers in Cartesian and cylindrical (with azimuthal modes decomposition) geometries, (c) novel analysis of MaxwellÕs solversÕ stencil variation and truncation, in application to domain decomposition strategies and implementation of Perfectly Matched Layers in high-order and pseudo-spectral solvers.

INTRODUCTION

Laser-driven plasma based electron accelerators (LPAs) have demonstrated the production of high-quality electron beams at energies ranging from 1 MeV [1] to 4 GeV [2] in cm-scale distances, fulfilling the need for compact acceleration. Numerical simulations have been critical in the recent rapid developments of plasma-based acceleration concepts, and among the various available numerical techniques, the electromagnetic Particle-In-Cell (PIC) approach is the method of choice for self-consistent simulations from first principles.

Electromagnetic Particle-In-Cell method

In the electromagnetic Particle-In-Cell method [3], the electromagnetic fields are solved on a grid, usually using Maxwell's equations

$$\frac{\partial \mathbf{B}}{\partial t} = -\nabla \times \mathbf{E} \quad (1)$$

$$\frac{\partial \mathbf{E}}{\partial t} = \nabla \times \mathbf{B} - \mathbf{J} \quad (2)$$

$$\nabla \cdot \mathbf{E} = \rho \quad (3)$$

$$\nabla \cdot \mathbf{B} = 0 \quad (4)$$

given here in natural units, where t is time, $\mathbf{E}$ and $\mathbf{B}$ are the electric and magnetic field components, and ρ and $\mathbf{J}$ are the charge and current densities. The charged particles are advanced in time using the Newton-Lorentz equations of motion

$$\frac{d\mathbf{x}}{dt} = \mathbf{v}, \quad (5)$$

$$\frac{d(\gamma \mathbf{v})}{dt} = \frac{q}{m}(\mathbf{E} + \mathbf{v} \times \mathbf{B}). \quad (6)$$

where m, q, $\mathbf{x}$, $\mathbf{v}$ and $\gamma = 1/\sqrt{1 - v^2}$ are respectively the mass, charge, position, velocity and relativistic factor of the particle. The charge and current densities are interpolated on the grid from the particles' positions and velocities, while the electric and magnetic field components are interpolated from the grid to the particles' positions for the velocity update.

Various methods are available for solving Maxwell's equations on a grid, based on finite-differences, finite-volume, finite-element, spectral, or other discretization techniques that apply most commonly on single structured or unstructured meshes and less commonly on multiblock multiresolution grid structures. In the following subsections, we summarize the widespread second order finite-difference time-domain (FDTD) algorithm, as well as the pseudo-spectral analytical time-domain (PSATD) and pseudo-spectral time-domain (PSTD) algorithms. Extension to multiresolution (or mesh refinement) PIC is described in, e.g. [4, 5].

Finite-Difference Time-Domain The most popular algorithm for electromagnetic PIC codes is the Finite-Difference Time-Domain solver

$$D_t \mathbf{B} = -\nabla \times \mathbf{E} \quad (7)$$

$$D_t \mathbf{E} = \nabla \times \mathbf{B} - \mathbf{J} \quad (8)$$

$$[\nabla \cdot \mathbf{E} = \rho] \quad (9)$$

$$[\nabla \cdot \mathbf{B} = 0]. \quad (10)$$

The differential operator is defined as $\nabla = D_x \hat{\mathbf{x}} + D_y \hat{\mathbf{y}} + D_z \hat{\mathbf{z}}$ and the finite difference operators in time and space are

* Work supported in part by the Director, Office of Science, Office of High Energy Physics, U.S. Dept. of Energy under Contract No. DE-AC02-05CH11231 and the US-DOE SciDAC ComPASS collaboration, and used resources of the National Energy Research Scientific Computing Center.
† jlvay@lbl.gov

ISBN 978-3-95450-136-6

defined respectively as $D_t G|^n_{i,j,k} = \left(G|^{n+1/2}_{i,j,k} - G|^{n-1/2}_{i,j,k}\right)/\Delta t$ and $D_x G|^n_{i,j,k} = \left(G|^n_{i+1/2,j,k} - G|^n_{i-1/2,j,k}\right)/\Delta x$, where Δt and Δx are respectively the time step and the grid cell size along x, n is the time index and i, j and k are the spatial indices along x, y and z respectively. The difference operators along y and z are obtained by circular permutation. The equations in brackets are given for completeness, as they are often not actually solved, thanks to the usage of a so-called charge conserving algorithm. The quantities are given on a staggered (or "Yee") grid [6], where the electric field components are located between nodes and the magnetic field components are located in the center of the cell faces.

Pseudo Spectral Analytical Time Domain (PSATD) Maxwell's equations in Fourier space are given by

$$\frac{\partial \tilde{\mathbf{E}}}{\partial t} = i\mathbf{k}\times\tilde{\mathbf{B}} - \tilde{\mathbf{J}} \quad (11)$$

$$\frac{\partial \tilde{\mathbf{B}}}{\partial t} = -i\mathbf{k}\times\tilde{\mathbf{E}} \quad (12)$$

$$[i\mathbf{k}\cdot\tilde{\mathbf{E}} = \tilde{\rho}] \quad (13)$$

$$[i\mathbf{k}\cdot\tilde{\mathbf{B}} = 0] \quad (14)$$

where $\tilde{a}$ is the Fourier Transform of the quantity a. As with the real space formulation, provided that the continuity equation $\partial\tilde{\rho}/\partial t + i\mathbf{k}\cdot\tilde{\mathbf{J}} = 0$ and $\mathbf{k}\cdot\mathbf{k}\times\tilde{\mathbf{E}}$ are satisfied, then the last two equations will automatically be satisfied at any time if satisfied initially and do not need to be explicitly integrated.

Decomposing the electric field and current between longitudinal and transverse components $\tilde{\mathbf{E}} = \tilde{\mathbf{E}}_L + \tilde{\mathbf{E}}_T = \hat{\mathbf{k}}(\hat{\mathbf{k}}\cdot\tilde{\mathbf{E}}) - \hat{\mathbf{k}}\times\hat{\mathbf{k}}\times\tilde{\mathbf{E}}$ and $\tilde{\mathbf{J}} = \tilde{\mathbf{J}}_L + \tilde{\mathbf{J}}_T = \hat{\mathbf{k}}(\hat{\mathbf{k}}\cdot\tilde{\mathbf{J}}) - \hat{\mathbf{k}}\times\hat{\mathbf{k}}\times\tilde{\mathbf{J}}$ gives

$$\frac{\partial \tilde{\mathbf{E}}_T}{\partial t} = i\mathbf{k}\times\tilde{\mathbf{B}} - \tilde{\mathbf{J}}_\mathbf{T} \quad (15)$$

$$\frac{\partial \tilde{\mathbf{E}}_L}{\partial t} = -\tilde{\mathbf{J}}_\mathbf{L} \quad (16)$$

$$\frac{\partial \tilde{\mathbf{B}}}{\partial t} = -i\mathbf{k}\times\tilde{\mathbf{E}} \quad (17)$$

with $\hat{\mathbf{k}} = \mathbf{k}/k$.

If the sources are assumed to be constant over a time interval Δt, the system of equations is solvable analytically and is given by (see [7] for the original formulation and [8] for a more detailed derivation):

$$\tilde{\mathbf{E}}^{n+1}_T = C\tilde{\mathbf{E}}^n_T + iS\hat{\mathbf{k}}\times\tilde{\mathbf{B}}^n - \frac{S}{k}\tilde{\mathbf{J}}^{n+1/2}_T \quad (18)$$

$$\tilde{\mathbf{E}}^{n+1}_L = \tilde{\mathbf{E}}^n_L - \Delta t\tilde{\mathbf{J}}^{n+1/2}_L \quad (19)$$

$$\tilde{\mathbf{B}}^{n+1} = C\tilde{\mathbf{B}}^n - iS\hat{\mathbf{k}}\times\tilde{\mathbf{E}}^n + i\frac{1-C}{k}\hat{\mathbf{k}}\times\tilde{\mathbf{J}}^{n+1/2} \quad (20)$$

with $C = \cos(k\Delta t)$ and $S = \sin(k\Delta t)$.

Combining the transverse and longitudinal components, gives

$$\tilde{\mathbf{E}}^{n+1} = C\tilde{\mathbf{E}}^n + iS\hat{\mathbf{k}}\times\tilde{\mathbf{B}}^n - \frac{S}{k}\tilde{\mathbf{J}}^{n+1/2} + (1-C)\hat{\mathbf{k}}(\hat{\mathbf{k}}\cdot\tilde{\mathbf{E}}^n) + \hat{\mathbf{k}}(\hat{\mathbf{k}}\cdot\tilde{\mathbf{J}}^{n+1/2})(\frac{S}{k} - \Delta t), \quad (21)$$

$$\tilde{\mathbf{B}}^{n+1} = C\tilde{\mathbf{B}}^n - iS\hat{\mathbf{k}}\times\tilde{\mathbf{E}}^n + i\frac{1-C}{k}\hat{\mathbf{k}}\times\tilde{\mathbf{J}}^{n+1/2}. \quad (22)$$

Considering the fields generated by the source terms without the self-consistent dynamics of the charged particles, this algorithm is free of numerical dispersion and is not subject to a Courant condition. Furthermore, this solution is exact for any time step size subject to the assumption that the current source is constant over that time step.

As shown in [8], by expanding the coefficients S_h and C_h in Taylor series and keeping the leading terms, the PSATD formulation reduces to the better known pseudo-spectral time-domain (PSTD) formulation [9, 10]:

$$\tilde{\mathbf{E}}^{n+1} = \tilde{\mathbf{E}}^n + i\Delta t\mathbf{k}\times\tilde{\mathbf{B}}^{n+1/2} - \Delta t\tilde{\mathbf{J}}^{n+1/2}, \quad (23)$$

$$\tilde{\mathbf{B}}^{n+3/2} = \tilde{\mathbf{B}}^{n+1/2} - i\Delta t\mathbf{k}\times\tilde{\mathbf{E}}^{n+1}. \quad (24)$$

The dispersion relation of the PSTD solver is given by $\sin(\frac{\omega\Delta t}{2}) = \frac{k\Delta t}{2}$. In contrast to the PSATD solver, the PSTD solver is subject to numerical dispersion for a finite time step and to a Courant condition that is given by $c\Delta t \le 2/\pi\sqrt{\frac{1}{\Delta x^2} + \frac{1}{\Delta y^2} + \frac{1}{\Delta x^2}}$.

The PSATD and PSTD formulations that were just given apply to the field components located at the nodes of the grid. As noted in [11], they can also be easily recast on a staggered Yee grid by multiplication of the field components by the appropriate coefficients to shift them from the collocated to the staggered locations. The choice between a collocated and a staggered formulation is application-dependent.

Modeling in a Lorentz boosted frame

Modeling the interaction including the laser and the entire plasma in the simulation box is neither practical nor needed, as a window following the beam and the wake (a standard and widespread technique in accelerator physics) is sufficient to capture the physics. However, the large range of scale separations between the plasma column length and the driving laser wavelength still demands tens of millions of time steps for the modeling of a meter long plasma capable of boosting the energy of an electron or positron beam in the range of 10 GeV. The numerical cost can be alleviated by using one or more of: (i) the quasistatic approximation [12], which takes advantage of the separation of time scales in the dynamics of the laser and plasma electrons, (ii) envelope models of the laser, (iii) running the simulation in a Lorentz boosted frame co-propagating in the direction of the laser, rather than in the laboratory frame [13]. We will focus here on the last approach. When using this approach,

ISBN 978-3-95450-136-6

the plasma column is drifting at relativistic velocity relative to the grid, leading to the numerical Cherenkov instability (NCI) [14] that needs to be understood and controled. The next section summarizes the most recent developments in the understanding and mitigation of NCI.

ANALYSIS AND MITIGATION OF THE NUMERICAL CHERENKOV INSTABILITY

The numerical Cherenkov instability [14] is the most serious numerical instability affecting multidimensional PIC simulations of relativistic particle beams and streaming plasmas [15–17]. It arises from coupling between possibly numerically distorted electromagnetic modes and spurious beam modes, the latter due to the mismatch between the Lagrangian treatment of particles and the Eulerian treatment of fields [18]. In recent papers we derived and solved electromagnetic dispersion relations for the numerical Cherenkov instability for both FDTD [19, 20] and PSATD [21, 22] algorithms, developed methods for significantly reducing growth rates, and successfully compared results with those of the Warp simulation code [23].

For either algorithm the dispersion relation can be written in the high energy limit as

$$C_0 + n\sum_{m_z} C_1 \csc\left[\left(\omega - k_z'\right)\frac{\Delta t}{2}\right] + n\sum_{m_z} C_2 \csc^2\left[\left(\omega - k_z'\right)\frac{\Delta t}{2}\right] = 0, \tag{25}$$

with coefficients C_0, C_1, C_2 defined by Eqs. (29) – (31) of [24] for the FDTD algorithm and by Eqs. (40) – (42) of [25] for the PSATD algorithm. Numerical solutions of the complete dispersion relations indicate that Eq. (25) is quantitatively accurate for γ as small as 10 and qualitatively useful for γ as small as 3. At still lower beam energies, the well known electrostatic numerical instability [26, 27] dominates.

Equation (25) involves sums over numerical aliases, $k_z' = k_z + m_z\, 2\pi/\Delta z$, for wave numbers aligned with the direction, z, of beam propagation. In the limit of vanishingly small time-steps and cell-sizes, Eq. (25) simplifies to $C_0 = n$, as expected, with n the beam density divided by γ (*i. e.*, the density of the beam in its rest frame). Thus, all beam resonances in Eq. (25) are numerical artifacts, even $m_z = 0$.

Not surprisingly, the numerical Cherenkov instability is fastest growing at resonances between the spurious beam modes and electromagnetic modes. The resonant instability scales roughly as the cube root of $n\,C_2/\Delta t$, evaluated at $\omega = k_z' v$, and can be destructively fast. The non-resonant instability, on the other hand, scales roughly as the square root of of $n\,C_2$, again evaluated at $\omega = k_z' v$. Although slower growing, it also is troublesome, because it can occur at smaller wave numbers.

Numerical instability growth rates can be unacceptably large if no special measure is taken. They can be reduced by using higher order current and field interpolation, by digital filtering, and by numerical damping of the electromagnetic fields (numerical damping is not explored further in this paper and the reader is refered to [15, 28–30] for more information). Cubic interpolation, for instance, is effective at suppressing higher order modes of the numerical Cherenkov instability and, to a lesser extent, $m_z = 0, -1$ modes. Digital filtering, on the other hand, effectively zeroes fields at large wave numbers, eliminating resonant numerical Cherenkov instabilities there.

A "magic time step" first was observed for the so-called "Galerkin field interpolation" [31] in LPA simulations [15, 17] and subsequently was explained analytically in [24]. It arises from approximate cancellation of the coefficients of E_x and B_y in C_2 for wave numbers near the dominant numerical Cherenkov resonance. The exact location of the "magic time step" depends on details of the field solver. In contrast, a "magic time step" was discovered analytically for the "Uniform field interpolation" [31]. It occurs because C_2 vanishes identically at $v\Delta t/\Delta z = 0.5$ in the high γ limit. One can concoct other, more complicated interpolation schemes with "magic time steps", but the value of doing so seems small. Definitions of the three FDTD interpolation schemes discussed here were provided in Sec. 2.4 and also can be found in [19, 32], and of PSATD variants (a) and (b) of the Esirkepov current conservation algorithm [33] in [25, 34].

The numerical Cherenkov instability can be viewed as the result of numerically induced mismatches between transverse fields as seen by the particles or, more or less equivalently, by mismatches between transverse currents and charge density. Correcting those mismatches, at least as they occur in coefficient C_2 at large γ, can in principle make every value of Δt a "magic time step". A plethora of approaches are provided in [22, 25], from which PSATD options (b1) and (b2) of the second reference are presented here. Option (b1) adjusts the ratio E_x/B_y as seen by the particles so that C_2 vanishes analytically for $v = 1$. The resulting growth rates are significantly reduced, especially for $v\Delta t/\Delta z > 1$. In fact, the residual growth at $v\Delta t/\Delta z > 1$ scales roughly as $1/\gamma$, although higher order numerical modes also play a role.

Implementing these and other schemes in the PSATD algorithm is straightforward, because currents and fields are known in k-space. Analogous schemes can be implemented readily in the FDTD algorithm, if one is willing to transform currents and fields to k-space. But, one would then be better off to use the PSATD algorithm throughout, because it is more accurate and often less unstable. It is, however, possible to set C_2 approximately equal to zero (accurate to six significant figures) by approximating the desired E_x/B_y ratio with a fourth-order rational interpolation function, as described in [32]. Sample simulations indicate that this approach is economical, requires minimal additional digital filtering, and apparently has no adverse effect on physical results at wavelengths long compare to the simulation axial cell size. Although derived for highly relativistic flows, it works reasonably well down to γ of order 3, below which the

ISBN 978-3-95450-136-6

numerical Cherenkov instability ceases to be the dominant numerical effect.

In [35], new field correction factors have been derived that completely eliminate the $m_z = 0$ numerical Cherenkov instability for the generalized PSTD algorithm, including the PSATD algorithm. When combined with a sharp cut-off digital filter at large k, these correction factors reduce peak growth rates to less (often much less) than 0.01 of the beamÕs relativistic plasma frequency. These coefficients are optimal in the sense that they differ from unity only slightly over a broad portion of k-space while eliminating both $m_z = 0$ numerical instability branches. A disadvantage from the implementation perspective is that the coefficients must be computed numerically for each set of simulation parameters.

Software to calculate the rational interpolation coefficients, as well as phase diagrams and resonance curves, are available in Computable Document Format [36] at http://hifweb.lbl.gov/public/BLAST/Godfrey/. The extensive analyses involved in deriving and solving the dispersion relations discussed in this section were performed with *Mathematica* [37].

EXTENSION AND PARALLELIZATION OF PSATD-PIC

A quasi-cylindrical version of the PSATD algorithm

When modeling 3D physical situations, the standard PSATD algorithm typically uses a 3D Cartesian mesh, which can be computationally expensive. However, when the physical situation has close-to-cylindrical symmetry, the calculations can in principle be reduced to a few 2D *quasi-cylindrical*[1] grids, and the resulting simulations can be much faster. This idea has been implemented in FDTD PIC, for instance by [38], and resulted in a speedup of one to two orders of magnitude.

In [39], we extended this idea to the PSTAD algorithm. Instead of the three-dimensional Fourier transform which is used in the standard 3D PSATD, the quasi-cylindrical PSATD algorithm uses the combination of a Hankel transform (radially) and a one-dimensional Fourier transform (longitudinally).

In this Fourier-Hankel formalism, the equations of the Maxwell solver are structurally very similar to (21) and (22), and thus many of the advantages of the standard 3D PSATD carry over to the quasi-cylindrical PSATD. In particular, the quasi-cylindrical algorithm has no Courant condition, and has an ideal dispersion relation in vacuum. In [39], we also benchmarked this algorithm in situations that are relevant to laser-plasma acceleration, and we showed that it avoids a number of numerical artifacts that are otherwise present in FDTD PIC codes.

[1] Here, the term *quasi*-cylindrical refers to the azimuthal decomposition which is generally used (see e.g. [38]), and which can take into account small departures from the purely cylindrical symmetry.

Parallelization and detailed analysis of the effects of stencil spatial variations with arbitrary high-order finite-difference Maxwell solver.

One possible drawback for the use of pseudo-spectral solvers is the difficulty in scaling them to a large number of cores on existing and, even more so on upcoming, supercomputers. To alleviate the problem, we proposed in [8] to take advantage of the finite-speed of light that is an intrinsic property of Maxwell's equations, and use domain decomposition with local FFTs on each subdomain. While initial tests of the method were succesfully conducted, the use of a finite number of guard cells surrounding each subdomain inevitably entails a small approximation when using the PSTD or PSATD algorithm that inevitably leads to a a small error when using pseudo-spectral solvers, which may sometimes result in a growing instability. Using the property that the PSTD and PSATD solvers can be viewed as the limit of FDTD solvers when the stencil order tends to infinity, we presented in [40] a general analytical approach that enables the evaluation of numerical discretization errors of fully three-dimensional arbitrary order finite-difference Maxwell solver, with arbitrary modification of the local stencil in the simulation domain. This model can be used to determine the minimum number of guard cells required to achieve a given numerical accuracy. It is validated against simulations with domain decomposition technique and Perfectly Matched Layers (PMLs), when these are used with a very high-order Maxwell solver, as well as in the infinite order limit of pseudo-spectral solvers. Results confirm that the new analytical approach enables exact predictions in each case. It also confirms that the domain decomposition technique can be used with a very high-order Maxwell solver and a reasonably low number of guard cells with negligible effects on the whole accuracy of the simulation. It also provides a more accurate framework for analyzing the efficiency of PMLs with high-order stencils and pseudo-spectral solvers, confirming earlier results obtained in [41].

CONCLUSION

The Particle-In-Cell (PIC) method continues to be the method of choice for detailed fully kinetic modeling of plasma accelerators. Modeling in a Lorentz boosted frame can provide orders of magnitude speedup, provided that the numerical Cherenkov instability (NCI) is under control. Recent work has led to a full understanding of the instability and to the development of efficient mitigation techniques. The studies have also shown that PIC methods utilizing pseudo-spectral electromagnetic field solvers are inherently more stable to NCI, generating renewed interest into these solvers, that used to be very popular until the replacement of vector supercomputers by massively parallel supercomputers. This has also prompted the development of a novel pseudo-spectral solver with azimuthal Fourier decomposition, and a composition of Fourier and Hankel transforms for fast simulations. The difficulty of scaling pseudo-spectral solvers to many cores is addressed through the use of domain de-

ISBN 978-3-95450-136-6

composition, prompting the development of a novel analytic method for studying the effect of stencil variations.

ACKNOWLEDGMENT

This document was prepared as an account of work sponsored in part by the United States Government. While this document is believed to contain correct information, neither the United States Government nor any agency thereof, nor The Regents of the University of California, nor any of their employees, nor the authors makes any warranty, express or implied, or assumes any legal responsibility for the accuracy, completeness, or usefulness of any information, apparatus, product, or process disclosed, or represents that its use would not infringe privately owned rights. Reference herein to any specific commercial product, process, or service by its trade name, trademark, manufacturer, or otherwise, does not necessarily constitute or imply its endorsement, recommendation, or favoring by the United States Government or any agency thereof, or The Regents of the University of California. The views and opinions of authors expressed herein do not necessarily state or reflect those of the United States Government or any agency thereof or The Regents of the University of California.

REFERENCES

[1] C. G. R. Geddes, K. Nakamura, G. R. Plateau, C. Toth, E. Cormier-Michel, E. Esarey, C. B. Schroeder, J. R. Cary, W. P. Leemans, Plasma-density-gradient injection of low absolute-momentum-spread electron bunches, Phys. Rev. Lett. 100 (2008) 215004. doi:10.1103/PhysRevLett.100.215004.

[2] W. P. Leemans, A. J. Gonsalves, H.-S. Mao, K. Nakamura, C. Benedetti, C. B. Schroeder, C. Tóth, J. Daniels, D. E. Mittelberger, S. S. Bulanov, J.-L. Vay, C. G. R. Geddes, E. Esarey, Multi-gev electron beams from capillary-discharge-guided subpetawatt laser pulses in the self-trapping regime, Phys. Rev. Lett. 113 (2014) 245002. doi:10.1103/PhysRevLett.113.245002.

[3] C. Birdsall, A. Langdon, Plasma Physics Via Computer Simulation, Adam-Hilger, 1991.

[4] J.-L. Vay, D. Grote, R. Cohen, A. Friedman, Novel methods in the particle-in-cell accelerator code-framework warp, Computational Science and Discovery 5 (2012) 014019 (20 pp.).

[5] J.-L. Vay, J.-C. Adam, A. Heron, Asymmetric pml for the absorption of waves. application to mesh refinement in electromagnetic particle-in-cell plasma simulations, Computer Physics Communications 164 (1-3) (2004) 171–177. doi:10.1016/J.Cpc.2004.06.026.

[6] K. Yee, Numerical solution of initial boundary value problems involving maxwells equations in isotropic media, Ieee Transactions On Antennas And Propagation Ap14 (3) (1966) 302–307.

[7] I. Haber, R. Lee, H. Klein, J. Boris, Advances in electromagnetic simulation techniques, in: Proc. Sixth Conf. Num. Sim. Plasmas, Berkeley, Ca, 1973, pp. 46–48.

[8] J.-L. Vay, I. Haber, B. B. Godfrey, A domain decomposition method for pseudo-spectral electromagnetic simulations of plasmas, Journal of Computational Physics 243 (2013) 260–268. doi:10.1016/j.jcp.2013.03.010.

[9] J. Dawson, Particle simulation of plasmas, Reviews Of Modern Physics 55 (2) (1983) 403–447. doi:10.1103/RevModPhys.55.403.

[10] Q. Liu, The pstd algorithm: A time-domain method requiring only two cells per wavelength, Microwave And Optical Technology Letters 15 (3) (1997) 158–165. doi:10.1002/(Sici)1098-2760(19970620)15:3<158::Aid-Mop11>3.3.Co;2-T.

[11] Y. Ohmura, Y. Okamura, Staggered grid pseudo-spectral time-domain method for light scattering analysis, Piers Online 6 (7) (2010) 632–635.

[12] P. Sprangle, E. Esarey, A. Ting, Nonlinear-theory of intense laser-plasma interactions, Physical Review Letters 64 (17) (1990) 2011–2014.

[13] J.-L. Vay, Noninvariance of space- and time-scale ranges under a lorentz transformation and the implications for the study of relativistic interactions, Physical Review Letters 98 (13) (2007) 130405/1–4.

[14] B. B. Godfrey, Numerical cherenkov instabilities in electromagnetic particle codes, Journal of Computational Physics 15 (4) (1974) 504–521.

[15] J. L. Vay, C. G. R. Geddes, E. Cormier-Michel, D. P. Grote, Numerical methods for instability mitigation in the modeling of laser wakefield accelerators in a lorentz-boosted frame, Journal of Computational Physics 230 (15) (2011) 5908–5929. doi:10.1016/J.Jcp.2011.04.003.

[16] L. Sironi, A. Spitkovsky, private Communication (2011).

[17] X. Xu, P. Yu, S. F. Martins, F. Tsung, V. K. Decyk, J. Vieira, R. A. Fonseca, W. Lu, L. O. Silva, W. B. Mori, Numerical instability due to relativistic plasma drift in em-pic simulations, Computer Physics Communications 184 (2013) 2503–2514.

[18] B. B. Godfrey, Canonical momenta and numerical instabilities in particle codes, Journal of Computational Physics 19 (1) (1975) 58–76.

[19] B. B. Godfrey, J.-L. Vay, Numerical stability of relativistic beam multidimensional {PIC} simulations employing the esirkepov algorithm, Journal of Computational Physics 248 (0) (2013) 33 – 46. doi:http://dx.doi.org/10.1016/j.jcp.2013.04.006.

[20] B. B. Godfrey, J.-L. Vay, Suppressing the numerical cherenkov instability in {FDTD} {PIC} codes, Journal of Computational Physics 267 (0) (2014) 1 – 6. doi:http://dx.doi.org/10.1016/j.jcp.2014.02.022.

[21] B. B. Godfrey, J.-L. Vay, I. Haber, Numerical stability analysis of the pseudo-spectral analytical time-domain {PIC} algorithm, Journal of Computational Physics 258 (0) (2014) 689 – 704. doi:http://dx.doi.org/10.1016/j.jcp.2013.10.053.

[22] B. B. Godfrey, J.-L. Vay, I. Haber, Numerical stability improvements for the pseudo-spectral em pic algorithm, IEEE Transactions on Plasma Science 42 (2014) 1339–1344. doi:10.1109/TPS.2014.2310654.

[23] D. Grote, A. Friedman, J.-L. Vay, I. Haber, The warp code: Modeling high intensity ion beams, in: Aip Conference Proceedings, no. 749, 2005, pp. 55–8.

ISBN 978-3-95450-136-6

[24] B. B. Godfrey, J.-L. Vay, Numerical stability of relativistic beam multidimensional pic simulations employing the esirkepov algorithm, Journal of Computational Physics 248 (2013) 33–46. doi:10.1016/j.jcp.2013.04.006.

[25] B. B. Godfrey, J.-L. Vay, I. Haber, Numerical stability analysis of the pseudo-spectral analytical time-domain pic algorithm, Journal of Computational Physics 258 (2014) 689–704. doi:10.1016/j.jcp.2013.10.053.

[26] A. B. Langdon, Nonphysical modifications to oscillations, fluctuations, and collisions due to space-time differencing, in: Proceedings of the fourth conference on numerical simulation of plasmas, 1970, pp. 467–495.

[27] H. Okuda, Nonphysical instabilities in plasma simulation due to small debye length, in: Proceedings of the fourth conference on numerical simulation of plasmas, 1970, pp. 511–525.

[28] B. Godfrey, Time-biased field solver for electromagnetic pic codes, Proceedings of the Ninth Conference on Numerical Simulation of Plasmas.

[29] A. Friedman, A 2nd-order implicit particle mover with adjustable damping, Journal of Computational Physics 90 (2) (1990) 292–312.

[30] A. Greenwood, K. Cartwright, J. Luginsland, E. Baca, On the elimination of numerical cerenkov radiation in pic simulations, Journal of Computational Physics 201 (2) (2004) 665–684. doi:10.1016/J.Jcp.2004.06.021.

[31] J.-L. Vay, B. B. Godfrey, Modeling of relativistic plasmas with the particle-in-cell method, Comptes Rendus MÃľcanique 342 (10âĂŞ11) (2014) 610 – 618, theoretical and numerical approaches for Vlasov-maxwell equations. doi:http://dx.doi.org/10.1016/j.crme.2014.07.006.

[32] B. B. Godfrey, J.-L. Vay, Suppressing the numerical cherenkov instability in fdtd pic codes (2014).

[33] T. Esirkepov, Exact charge conservation scheme for particle-in-cell simulation with an arbitrary form-factor, Computer Physics Communications 135 (2) (2001) 144–153.

[34] J.-L. Vay, I. Haber, B. B. Godfrey, A domain decomposition method for pseudo-spectral electromagnetic simulations of plasmas, Journal of Computational Physics 243 (2013) 260–268. doi:10.1016/j.jcp.2013.03.010.

[35] B. B. Godfrey, J.-L. Vay, Improved numerical cherenkov instability suppression in the generalized {PSTD} {PIC} algorithm, Computer Physics Communications 196 (2015) 221 – 225. doi:http://dx.doi.org/10.1016/j.cpc.2015.06.008.

[36] Computable document format (cdf) (2012). URL http://www.wolfram.com/cdf/

[37] Mathematica, version nine (2012). URL http://www.wolfram.com/mathematica/

[38] A. Lifschitz, X. Davoine, E. Lefebvre, J. Faure, C. Rechatin, V. Malka, Particle-in-cell modelling of laserâĂŞplasma interaction using fourier decomposition, Journal of Computational Physics 228 (5) (2009) 1803 – 1814. doi:http://dx.doi.org/10.1016/j.jcp.2008.11.017.

[39] R. Lehe, M. Kirchen, I. A. Andriyash, B. B. Godfrey, J.-L. Vay, A spectral, quasi-cylindrical and dispersion-free particle-in-cell algorithm, arXiv:1507.04790.

[40] H. Vincenti, J.-L. Vay, Detailed analysis of the effects of stencil spatial variations with arbitrary high-order finite-difference maxwell solver, arXiv:1507.05572.

[41] P. Lee, J.-L. Vay, Efficiency of the perfectly matched layer with high-order finite difference and pseudo-spectral maxwell solvers, Computer Physics Communications 194 (2015) 1 – 9. doi:http://dx.doi.org/10.1016/j.cpc.2015.04.004.

ISBN 978-3-95450-136-6

MERLIN FOR LHC COLLIMATION*

H. Rafique†, R. J. Barlow, University of Huddersfield, Huddersfield, UK
R. B. Appleby, S. C. Tygier, Cockcroft Institute and The University of Manchester, Manchester, UK
R. Bruce, S. Redaelli, CERN, Geneva, Switzerland

Abstract

MERLIN version 5 delivers a new tool for Large Hadron Collider (LHC) collimation. Significant upgrades and optimisation have been performed to bring forth a new release of the C++ accelerator physics library. Version 5 offers modularity, including scattering routines with many physics models, which may be user supplemented trivially. The extensibility of MERLIN offers the ad hoc addition of; physics processes such as collimation, lattice elements such as the hollow electron lens (HEL), and tracking integrators. Accurate beam physics, including: synchrotron motion, symplectic tracking, and proton collimation are demonstrated. Using the LHC collimation system to produce loss maps at a beam energy of 7 TeV we validate the capabilities of MERLIN 5.

INTRODUCTION

MERLIN [1, 2] is a C++ library used for accelerator physics. Originally developed by Nick Walker *et. al.* at DESY to study the ILC [3]. For the past few years it has been developed in collaboration with the LHC collimation group for simulation of the LHC collimation system. Until recently, two code strands existed, the HEL version [4, 5], and the loss map version [6]. The two strands have now been merged into release 5, adding functionality, better structure, optimisation, and user friendliness. Here we concentrate only on MERLIN's use in LHC collimation, though as a library it has may other capabilities.

LHC COLLIMATION

The ultimate goal when simulating the LHC collimation system is the production of loss maps, which record the likely location of proton losses in the LHC to a 10 cm resolution. For loss map production, a simulation must include many elements. As well as accurate tracking, synchrotron motion, and proton scattering, a complete model of the LHC, it's apertures, and all collimator settings and materials are required. `Monospace` text denotes MERLIN classes.

Using a MADX [7] generated TFS table, MERLIN's `MADInterface` class constructs an `AcceleratorModel`, which holds a vector of `AcceleratorComponent`s. Each `AcceleratorComponent` has an `Aperture`, an `AcceleratorGeometry`, and an `EMField`. Aditionally, collimator elements have a `Material`.

As the LHC is a synchrotron, many turn simulations require accurate modelling of RF cavities, this is illustrated in Fig. 1, where a bunch is populated in *dp ct* phase space and simulated in the nominal 7 TeV LHC. The colour gradient runs from yellow to red, where yellow is initial turns and red final turns. Only stable particles inside the bucket will survive long enough to be plotted in red, the others being lost.

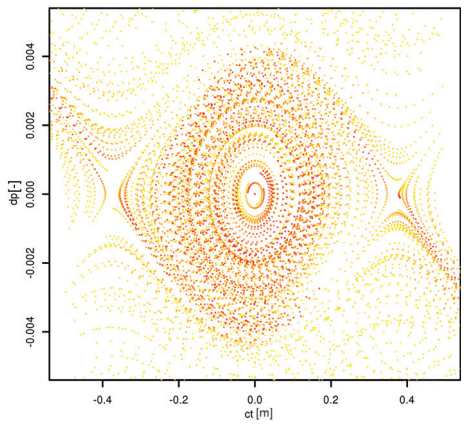

Figure 1: Poincaré section in *dp ct* phase space of the RF bucket for the nominal LHC. The colour gradient from yellow to red indicates the turn that the particle is recorded at.

A file containing the jaw openings, rotation, and material of all collimators is read by the `CollimatorDatabase` class, which sets these variables in the `AcceleratorModel` collimators. As the MADX TFS table doesn't contain an accurate aperture model an aperture file is read by the `ApertureConfiguration` class which iterates through each element in the `AcceleratorModel`, and sets the appropriate `Aperture` for it. An `InterpolatedAperture` exists to provide a better representation of the machine aperture, for example if multiple apertures are recorded within a single element. An example of the apertures created, for IR7 in the nominal LHC, is shown in Fig. 2.

As SixTrack [8] apertures are taken from the post-processing files they do not display the collimators, however these are identical as they are set using an identical collimator input file. We see that all other apertures are near identical.

Proton Bunch

The `LatticeFunction` class uses the `AcceleratorModel` to calculate the optics functions of the machine at each element, including; the β and α functions, fractional phase advance, and the closed orbit. A separate `Dispersion` and `PhaseAdvace` class exists, the latter to include the full phase advance μ, and the phase advance between any two accelerator elements. The lattice functions of the high luminosity (HL) LHC calculated in MERLIN, are shown in Fig. 3,

* Research supported by FP7 HiLumi LHC (Grant agreement 284404)
† haroon.rafique@hud.ac.uk

ISBN 978-3-95450-136-6

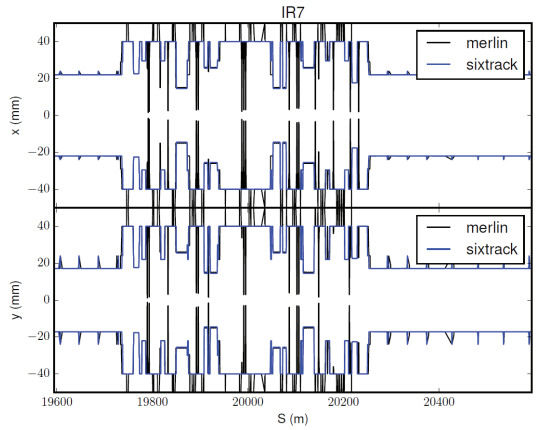

Figure 2: Apertures in IR7 in the nominal LHC, comparing MERLIN with SixTrack.

where they are compared, and seen to be identical to those calculated in MADX.

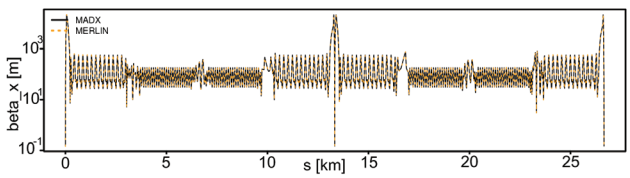

Figure 3: β_x functions for the HL LHC, comparing MERLIN (orange), and MADX (black).

A BeamData class uses the LatticeFunctions to define a ProtonBunch that accurately represents the machine bunch at any point in the accelerator.

Tracker

The ParticleTracker class takes the AcceleratorModel and the ProtonBunch as arguments, and iterates the ProtonBunch through each AcceleratorComponent in the AcceleratorModel.

The modular nature of Merlin extends to the integrators used for tracking. An integrator set, for example TRANSPORT, consists of a number of classes that each implement an integration algorithm for a set of elements, e.g. drift, bend, quadrupole etc. The tracker can be configured to use a complete integrator set or a mix of implementations, for example the user may wish to swap in a specific algorithm for some element types. MERLIN provides TRANSPORT (the default) [9], THIN_LENS and SYMPLECTIC integrator sets. A comparison of the TRANSPORT and SYMPLECTIC trackers is shown in Fig. 4.

If any PhysicsProcesses are attached to the tracker, they are called before tracking at the required elements. The structure of an LHC collimation run is shown in Fig. 5.

COLLIMATION PROCESS

The collimation process flow is shown in Fig. 6. CollimateParticleProcess identifies first whether or not the AcceleratorComponent is a Collimator and contains a

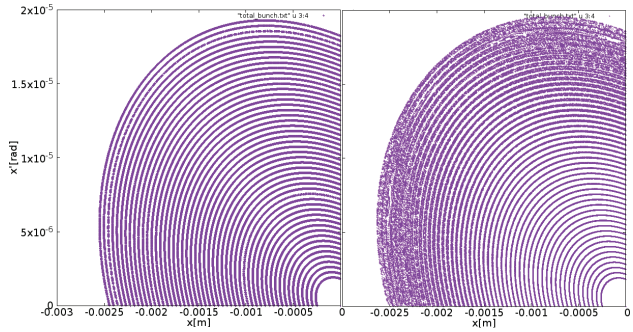

Figure 4: Poincaré section in the nominal LHC for particles with x values between 1-10σ_x, comparing the TRANSPORT (left) and SYMPLECTIC (right) integrators.

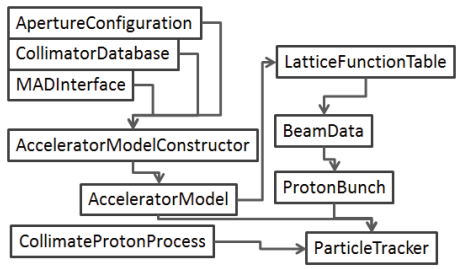

Figure 5: Flow of a standard LHC collimation simulation.

ScatterAtCollimator flag. When set to true, full collimation is performed at collimator elements, when false (the case for all non collimator elements), all particles outside the aperture are absorbed. Next we check if any particles hit the collimator jaw. When this is the case, we iterate through the rest of the particles and perform collimation.

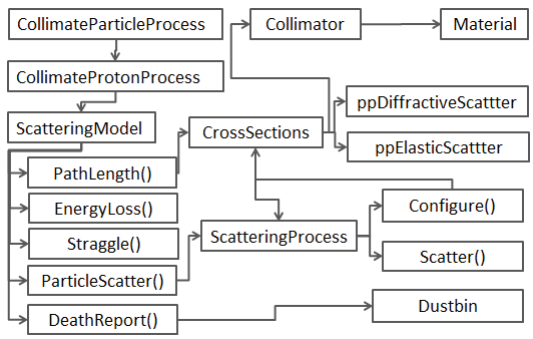

Figure 6: Flow of the collimation process.

The CollimateProtonProcess holds a pointer to the ScatteringModel class, which contains the main collimation functions. First the PathLength function is used to initialise the CrossSections class, which obtains all relevant information from the process, element, and bunch, to calculate cross sections for all ScatteringProcesses. This initialisation is done only once for each collimator jaw material, and the CrossSections object is stored for later referral, thus optimising the run. Next, energy loss and multiple coulomb scattering are performed, followed by point like processes (ScatteringProcesses).

ISBN 978-3-95450-136-6

A dictionary of standard materials is present in MERLIN, the user may add their own material by specifying certain properties, this includes mixtures which will be useful when studying novel jaw materials for HL LHC collimation.

MERLIN contains nine `ScatteringProcesse`s; SixTrack+K2 [8], and advanced versions of; proton nucleon elastic, proton nuclear elastic, single diffractive, Rutherford, as well as inelastic scattering. MERLIN's own elastic and single diffractive scattering have recently undergone rigorous improvements [10]. As well as this, the ionisation process contained in the EnergyLoss function has the option of the simple SixTrack+K2 like, and advanced implementation.

As shown in Table. 1, there exist five preset combinations of `ScatteringProcesse`s and ionisation functions. The combination may either be specifically chosen by the user, or a preset may be selected using the `ScatteringModel`::SetScatterType(n) function, where n is the enumerator corresponding to the column headings shown in Table 1.

Table 1: Preset Combinations of `ScatteringProcesse`s and Ionisation. Note that all combinations include an inelastic process

Process	0	1	2	3	4
Rutherford	ST	ST	ST	ST	M
pn Elastic	ST	M	ST	ST	M
pN Elastic	ST	M	ST	ST	M
Single Diffractive	ST	ST	M	ST	M
Ionisation	ST	ST	ST	M	M

As well as a proton collimation process, MERLIN 5 contains two new processes related to LHC collimation. The first, the HEL process, has been used to study the effect of HELs as collimation enhancers in the nominal and HL LHC [4, 5]. The second, a crab cavity failure process (`CCFailureProcess`), is under development, and will allow for the simulation of voltage and phase failures of crab cavities, which are present in the HL LHC.

Performance enhancements have been made in MERLIN 5, including optimisations to memory access. This has resulted in an approximate 40% increase in throughput. For 200 turn LHC loss maps MERLIN tracks around 57 protons per second per core on a 3.3 GHz Xeon E5-2643, making a full 6.4 million particle loss map take around 30 CPU hours. Multiple processes or MPI can be used to distribute MERLIN to hundreds of cores.

LOSS MAPS

MERLIN loss maps are comparable with SixTrack generated loss maps, as shown in Fig. 7, in which both codes are run for 200 turns in the nominal LHC, SixTrack with $6.4 \cdot 10^6$ particles, MERLIN with $3 \cdot 10^7$. MERLIN's advanced scattering routines, increased speed, and multiple trackers, mean that it is perfectly adapted for LHC collimation studies. This will soon include a study of loss maps for points in the squeeze for the HL LHC.

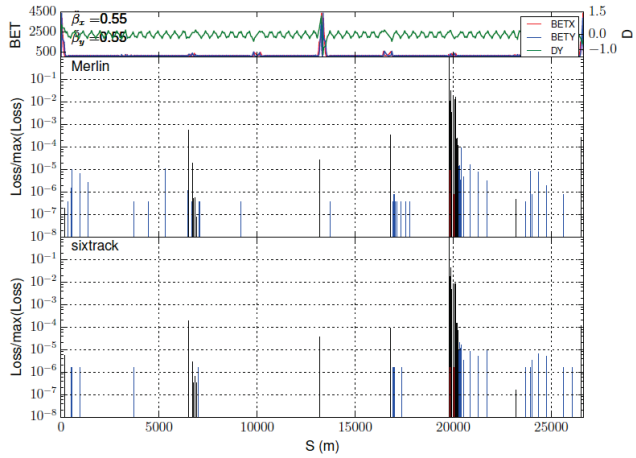

Figure 7: Nominal LHC loss map, comparing MERLIN (above), with SixTrack (below). The topmost plot shows the optics functions.

CONCLUSION

MERLIN 5 includes new; collimation structure, physics processes (HEL and CCFailure), scattering, and optimisation. Together with handling of composite materials, synchrotron motion, and symplectic tracking, MERLIN is a complete tool for LHC collimation studies, and after successful comparisons, may be used for nominal and HL physics cases. In particular, MERLIN may be exploited to study novel materials and collimation schemes for the HL LHC upgrade, including use of HELs as enhancers [5], and the impact of crab cavity failures on collimation.

ACKNOWLEDGMENT

The authors would like to acknowledge the significant contribution to MERLIN by former developers James Molson and Maurizio Serluca over the past few years.

REFERENCES

[1] `http://merlin-pt.sourceforge.net/`

[2] `https://sites.google.com/site/haroonrafiquemerlin/`

[3] D. Kruecker, F. Poirier, N. Walker, "Merlin-based start-to-end simulations of luminosity stability for the ILC", Proc. PAC2007.

[4] H. Rafique *et al.*, "Simulation of hollow electron lenses as LHC beam halo reducers using MERLIN", Proc. IPAC15, Richmond, Virginia, 2015.

[5] H. Rafique *et al.*, "High luminosity LHC hollow electron lens collimation using MERLIN", presented at ICAP'15, Shanghai, China, paper MODBC2, these proceedings.

[6] J. Molson *et al.*, "Advances with MERLIN - a beam tracking code", Proc. IPAC10, Kyoto, Japan, 2010.

[7] `http://madx.web.cern.ch/madx/`

[8] `http://sixtrack.web.cern.ch/SixTrack/`

[9] K. L. Brown *et al.*, SLAC-91, Rev. 3, 1983.

[10] J. Molson, "Proton scattering and collimation for the LHC and LHC luminosity upgrade", PhD Thesis, The University of Manchester, 2014.

ISBN 978-3-95450-136-6

HIGH-FIDELITY SIMULATIONS OF LONG-TERM BEAM-BEAM DYNAMICS ON GPUs

B. Terzić*, K. Arumugam, M. Aturban, C. Cotnoir, A. Godunov, D. Ranjan, M. Stefani, M. Zubair
Old Dominion University, Norfolk, Virginia, USA
F. Lin, V. Morozov, Y. Roblin, H. Zhang, Jefferson Lab, Newport News, Virginia, USA

Abstract

Future machines such as the Electron Ion Collider (MEIC), linac-ring machines (eRHIC) or LHeC are particularly sensitive to beam-beam effects. This is the limiting factor for long-term stability and high luminosity reach. The complexity of the non-linear dynamics makes it challenging to perform such simulations typically requiring millions of turns. Until recently, most of the methods have involved using linear approximations and/or tracking for a limited number of turns. We have developed a framework which exploits a massively parallel Graphical Processing Units (GPU) architecture to allow for tracking millions of turns in a sympletic way up to an arbitrary order. The code is called GHOST for GPU-accelerated High-Order Symplectic Tracking. Our approach relies on a matrix-based arbitrary-order symplectic particle tracking for beam transport and the Bassetti-Erskine approximation for the beam-beam interaction.

INTRODUCTION AND BACKGROUND

The proper magnetic optics design and performance of a storage ring or a collider—such as the LHC, RHIC, LHeC, and electron-ion colliders—crucially depends on its its long-term dynamics. Approaches which approximate the long-term dynamical stability based on relatively short-term simulations do not provide the necessary level of confidence. Ultimately, to simulate accurately the beam dynamics in a storage ring or a collider, it is necessary to track the beam particles for millions to billions of turns—comparable to the beam lifetime. However, until the recent advent of the GPU technology, such long-term simulations have been prohibitively expensive computationally.

Long-term simulations require the tracking to be symplectic—invariants of motion must be explicitly preserved. A constant linear transfer map can be made trivially symplectic by ensuring that it satisfies the symplecticity criterion. Indeed, many "kick-drift" codes take advantage of this fact to perform a symplectic step-by-step integration of the particle's equations of motion through a ring represented by a piecewise constant Hamiltonian. However, this approach is not suitable for long-term tracking due to the inherently large number of steps required for each particle turn around the ring. In order to attain the required efficiency, our new Gpu-accelerated Higher-Order Symplectic Tracking (GHOST) code uses a truncated single-turn non-linear Taylor map to track a particle while explicitly enforcing the symplecticity by solving a set of associated implicit, non-linear set of equations.

The beam collisions are described by the Poisson equation which can be solved by a number of methods at a high computational cost. To reduce the computational load, a number of approximations have been proposed. BEAM-BEAM3D [1] uses a shifted integrated 2D Green's function method to solve the equation on a grid. The 2D approximation is made possible by dividing the beams in thin slices. Another approximation can be to assume a gaussian beam distribution which leads to a one-dimensional integration [2]. Finally Bassetti-Erskine (BE) [3] approach introduces one more level of approximation by assuming that the beams have vanishing length and a Gaussian transverse distribution. This reduces the Poisson equation to a single evaluation of a complex error function, which is computationally efficient. In GHOST, we use the BE formalism for beam interaction, generalized to an arbitrary geometry, which may also include upright and round beams (as opposed to flat beams originally derived in BE).

GHOST: ALGORITM DESCRIPTION

In GHOST, the beam bunches are represented by an appropriate Gaussian distribution of point particles, while the effect of the collision is computed using the generalized BE approximation. The new code is SDDS-compliant [4], which can be readily post-processed with the powerful SDDS tools.

Particle Tracking

Various established particle tracking codes feature lattice map generation techniques. Our code relies on maps generated by the well-established algorithms of COSY Infinity [5]. COSY Infinity generates Taylor maps of an arbitrary order for a given optical system by numerically integrating the equations of motion in the system using differential algebraic techniques. As a result, it generates coefficients $M(x|\alpha\beta\gamma\eta\lambda\mu)$ of the Taylor expansion of the form

$$x = \sum_{\alpha\beta\gamma\eta\lambda\mu} \mathcal{M}(x|\alpha\beta\gamma\eta\lambda\mu) x^\alpha a^\beta y^\gamma b^\eta l^\lambda \delta^\mu, \qquad (1)$$

for each of the six phase-space coordinates: x, $a \equiv p_x/p_0$, y, $b \equiv p_y/p_0$, l, and δ where x and y are the transverse particle positions, a and b are the transverse momentum components p_x and p_y, respectively, normalized to the reference momentum p_0, $l = -(t - t_0)v_0\gamma_0/(1 + \gamma_0)$ and $\delta = (K - K_0)/K_0$. Here t, K, v_0, and γ_0 are the time of flight, kinetic energy, velocity, and Lorentz factor, respectively. The subscript 0

* bterzic@odu.edu

ISBN 978-3-95450-136-6

indicates the reference value. The six variables form three canonically conjugate pairs.

For symplectic tracking, the initial and final coordinates must satisfy the symplectic condition, described as a partial differential equation constructed from the generating function of the dynamic system. Taking the second kind of generating function as an example, assuming the initial coordinates of a symplectic system are $(\boldsymbol{q}_i, \boldsymbol{p}_i)$ and the final coordinates of it are $(\boldsymbol{q}_f, \boldsymbol{p}_f)$, the coordinates satisfy

$$(\boldsymbol{q}_f, \boldsymbol{p}_i) = \mathbf{J}\nabla F_2(\boldsymbol{q}_i, \boldsymbol{p}_f), \tag{2}$$

where

$$\mathbf{J} = \begin{bmatrix} 0 & -\mathbf{I} \\ \mathbf{I} & 0 \end{bmatrix}. \tag{3}$$

One can perform symplectic tracking by solving the above equations. The generating function F_2 can be derived from the truncated map $\mathbf{M}$ [6]. With $\mathbf{M}$ and F_2 known, first one calculates $(\boldsymbol{q}'_f, \boldsymbol{p}'_f)$ applying $\mathbf{M}$ on $(\boldsymbol{q}_i, \boldsymbol{p}_i)$, and then use $(\boldsymbol{q}_i, \boldsymbol{p}_i, \boldsymbol{q}'_f, \boldsymbol{p}'_f)$ as a start point to solve Eq. (2) numerically. Because $(\boldsymbol{q}'_f, \boldsymbol{p}'_f)$ is very close to $(\boldsymbol{q}_f, \boldsymbol{p}_f)$, Eq. (2) can be solved to machine accuracy in a few iterations [6].

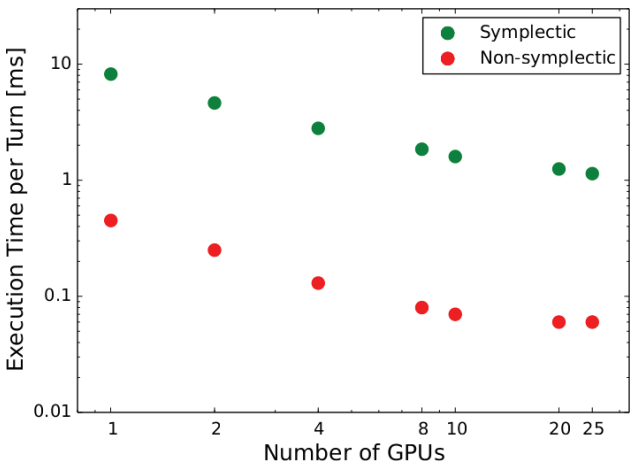

Figure 1: Execution time per turn as a function of the number of GPU devices for symplectic (green dots) and non-symplectic (red) tracking of 3rd order for 100000 particles.

Beam Collision

Because of this efficiency, the BE model [3] at the heart of a beam-beam code gives us the best chance of accurately studying the long-term dynamics in colliders. BE approximation greatly reduces the computational cost of the beam-beam interaction when the interacting bunches are: (i) well-approximated by a Gaussian transverse distribution, (ii) infinitesimally short and (iii) transversally flat. In that case, the computationally expensive Poisson equation exactly reduces to an inexpensive complex error function.

The first approximation—that the bunches are Gaussian—is reasonable because we are interested in the steady-state solution for which we have a stable long-term behavior. Some machines, such as LHC, exhibit strong beam-beam distortions on both beams produced by coherent and incoherent effects as well as long-range interactions. We plan to extend GHOST by implementing a hybrid fast multipole method to address these cases.

The second approximation—that the bunches are infinitesimally short—is resolved by dividing bunches into several transverse slices and treating each as infinitesimally short. GHOST then employs the synchro-beam mapping, the symplectic beam-beam map usable for the long bunch [7,8]. The collision between the two beams at the interaction point is simulated by collisions of individual slices.

The third approximation—that the bunches are flat—is relaxed by deriving the generalized solutions for upright and (nearly) round bunches.

GPU Implementation

The amount of computations required to track and collide bunches over $10^7 - 10^9$ turns is prohibitive. In serial mode, the problem would simply be computationally intractable, with simulation taking years to run. This clearly motivates the use of sophisticated, finely-tuned algorithms running on massively-parallel platforms.

The parallel particle tracking in GHOST is implemented on a hybrid CPU-GPU platform using CUDA (Compute Unified Device Architecture), taking full advantage of the highly repetitive nature of calculations performed. In particular, one portion of the code—the setup, initialization and I/O—run on the traditional CPU platform, while computationally intensive components of the beam tracking and collision execute on a cluster of NVIDIA's GPUs. Cluster parallelization is implemented through MPI.

Our numerical experiments were carried out on a cluster of Kepler K20 GPUs with GK110 processor equipped with 5GB of GDDR5 memory. In tracking mode, GHOST achieves maximum speedup (CPU time/GPU time) on a single GPU device of over 280. The speedup scales nearly linearly with multiple GPU devices.

Figure 1 shows the scalability of tracking code on a cluster of GPUs when tracking 100000 particles with a 3rd order map. Symplectic tracking is, as expected, consistently more expensive because of the symplectic correction at each step (which requires solving a non-linear set of equations). The particles are equally distributed between the available GPUs in the cluster and the absence of communication between the threads and also between the GPUs provides a linear scalability with the number of GPUs. The scalability continues to be linear until the number of particles assigned to each GPU is sufficient enough to keep the device busy by maximizing the utilization.

At this level of performance, tracking 100000 particles for 400 million turns—corresponding, for instance, to one hour of beam lifetime of the proposed MEIC—on 25 GPUs takes about 4.5 days in symplectic and about 7 hours in non-symplectic 3rd order tracking mode. It is expected that the performance improves with each new GPU models (at this time there are two more recent and more powerful GPUs on the market — Tesla K40 and Tesla K80).

ISBN 978-3-95450-136-6

BENCHMARKING

At this stage of the development, only the tracking (symplectic and non-symplectic) mode of GHOST is GPU-optimized. The collision mode has been fully developed as a prototype and is currently being implemented and optimized in CUDA. Therefore, the results for tracking (Figs. 1 and 2) have been done in GHOST, and the results for beam-beam collision (Figs. 3 and 4) on the serial prototype. While the simulations reported here are for a generic collider ring design (tracking figures) and the electron-ion design similar to the proposed MEIC [9] (beam-beam figures), the results are general.

We successfully carried out these benchmarks for GHOST:

- Particle tracking—both symplectic and non-symplectic—in GHOST is equivalent to that in COSY Infinity, as illustrated in Fig. 2.
- In beam-beam simulations, the results—for example, luminosity shown in Fig. 3—converge as the number of transverse slices in the simulation are increased.
- In beam-beam simulations, the reduction factor in luminosity due to the hourglass effect shows excellent agreement with the analytic estimate [8, 10] (Fig. 4).

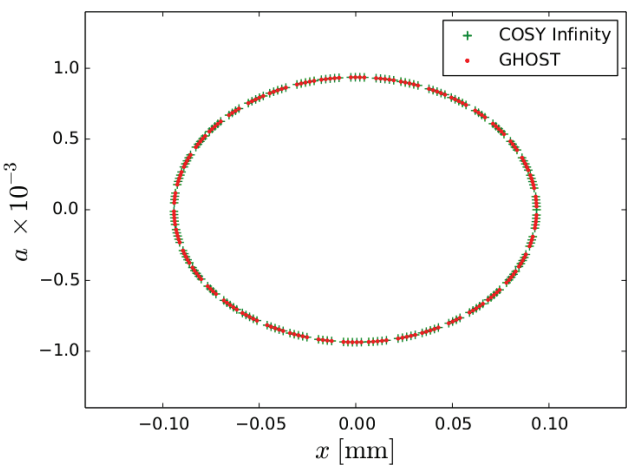

Figure 2: A particle tracked using 3rd order symplectic tracking for 2 million turns and recorded every 10000 turns with COSY Infinity (green crosses) and GHOST (red dots).

DISCUSSION

MEIC envisions a synchronization scheme which involves having different harmonic numbers for the electron and ion rings. This will give raise to gear changing effects which will have to be studied carefully to assess stability and proper damping of these resonances. GHOST will allow for an arbitrary pattern of bunches for both rings. As a benefit one also will be able to account for clearing gaps in the ion bunch pattern.

Additional features currently under development that will be a part of the next iteration include: synchrotron damping, cooling of the proton beam by a low-energy electron beam, intra-beam scattering and crabbing.

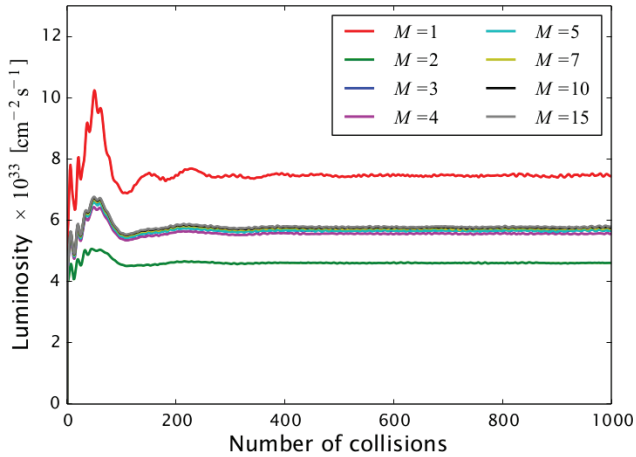

Figure 3: Luminosities computed with GHOST for different numbers of slices M with 40000 particles for the MEIC parameters [9] in which the beam bunches are three times longer than the nominal values, with the reduction factor due to hourglass of 23% (the third point from the left on the red curve in Fig. 4).

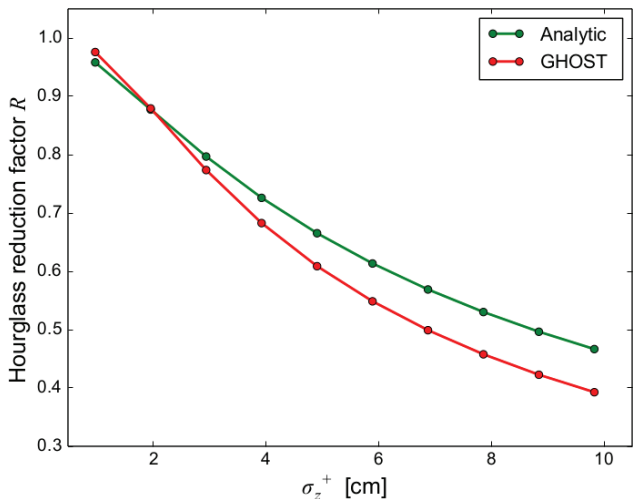

Figure 4: The hourglass effect as a function of the initial beam size, computed in a simulation with 128000 particles and 10 slices in each beam using GHOST (red line) and the analytic expression [8, 10] (green line). The layout used is that of the MEIC [9], with the constant ratio σ_z^+/σ_z^-.

ACKNOWLEDGMENT

We are thankful for the generous support of the Old Dominion University Research Foundation through the Research Seed Funding Program 15-492. We gratefully acknowledge the support of NVIDIA Corporation with the donation of the Tesla K40 GPU used for this research. This paper is authored by Jefferson Science Associates, LLC under U.S. Department of Energy (DOE) Contract No. DE-AC05-06OR23177.

ISBN 978-3-95450-136-6

REFERENCES

[1] J. Qiang, R. Ryne and M. Furman, PR STAB 5, 104402 (2002).

[2] R. Wanzenberg, Tech. Rep. DESY M 10-01, DESY (2010).

[3] M. Bassetti and G. Erskine, Tech. Rep. CERN-IRS-TH/80-06, CERN (1980).

[4] M. Borland, Proceedings of ICAP (1998).

[5] K. Makino and M. Berz, *COSY INFINITY version 8*, Nuclear Instruments and Methods, A427:338–343 (1999).

[6] M. Berz, *Nonlinear Problems in Future Particle Accelerators*, World Scientific Publishing, Hackensack, NJ (1991).

[7] K. Hirata, H. Moshammer and F. Ruggerio, Particle Accelerators 40, 205 (1993).

[8] A. W. Chao and M. Tigner, *Handbook of Accelerator Physics and Engineering*, World Scientific Publishing, Hackensack, NJ (2009).

[9] Y. Roblin, V. Morozov, B. Terzić, M. Aturban, D. Ranjan and M. Zubair, Proceedings of IPAC (2013).

[10] M. Furman, Proceedings of PAC (1991).

ISBN 978-3-95450-136-6

AN IMPROVED PARALLEL POISSON SOLVER FOR SPACE CHARGE CALCULATION IN BEAM DYNAMICS SIMULATION

Dawei Zheng*, Ursula van Rienen, University of Rostock, Rostock, Germany
Ji Qiang, LBNL, Berkeley, CA, USA

Abstract

In numerous beam dynamics simulations of particle accelerators, the space charge calculation is a critical issue. The ways to calculate the space charge force vary in different kinds of methods. A common method based on Green's function in free space is often implemented in various PIC (particle-in-cell) simulation codes for beam tracking. However, the calculation time of the Poisson solver for both, serial and parallel cases can reach a high percentage of the whole simulation time consumption. In this paper, we present an improved parallel Poisson solver. The enhanced solver focuses on three aspects of efficiency improvement: using the reduced integrated Green's function, using the discrete cosine transform for Green's function, using a novel fast implicitly zero-padded convolution routine. The amended, parallel Poisson solver is implemented using MPI and Open MP. We study the strong scaling and the weak scaling for the scalability property of the Poisson solver, too. The novel solver is integrated into the IMPACT-T code in order to compare it with the commonly used Poisson solver.

INTRODUCTION

For the particle accelerator research, simulations are critical tools from the design to the operation. Furthermore, the space charge calculation constitutes a major part of the beam dynamics simulation, which considers the low energy region of the accelerators. Applying the mid-point rule on an equidistant grid for the numerical integration of Poisson's equation, the method based on Green's function in free space is often given as:

$$\varphi(\mathbf{r_l}) \approx \frac{1}{4\pi\varepsilon_0} \cdot \sum_{\mathbf{l'}=(1,1,1)}^{(N_x,N_y,N_z)} \rho(\mathbf{r'_{l'}})\tilde{G}(\mathbf{r_l}, \mathbf{r'_{l'}}), \qquad (1)$$

where $\mathbf{l} = (i, j, k)$, $\mathbf{l'} = (i', j', k')$ and $\tilde{G}(\mathbf{r_l}, \mathbf{r'_{l'}}) = h_x h_y h_z G(\mathbf{r_l}, \mathbf{r'_{l'}})$. The discrete $\varphi(\mathbf{r_l})$ is obtained by Fourier convolution theorem. Additionally, Hockney and Eastwood [1] have published an efficient way to extend the charge density, which is required for the Fourier convolution. A further study of an integrated Green's function method which is suitable for the novel Free Electron Lasers (FELs) is described in [2] [3]. For this kind of 3D FFT-typed Poisson solver, the time and memory consumption may easily reach the limit for PC simulation. The parallel implementation of the routine is preferred for a higher level computing performance. In this paper, we present an improved parallel Poisson solver, which differs from the commonly used routine. The efficiency improvement is impressive and valuable referenced for other parallel FFT-typed Poisson solver codes in the community.

* dawei.zheng@uni-rostock.de

THE IMPROVED PARALLEL POISSON SOLVER

The improved parallel Poisson solver is based on the efficient serial Poisson solver outlined in [4]. Three aspects of efficiency improvement are enhanced:

1. Using the reduced integrated Green's function (RIGF):

$$\tilde{G}_{\mathrm{RIGF}}(\mathbf{r}_{(i,j,k)}) = \begin{cases} \tilde{G}_{\mathrm{IGF}}(\mathbf{r}_{(i,j,k)}) & 1 \le w \le R_w; \\ h_x h_y h_z G(\mathbf{r}_{(i,j,k)}) & R_w \le N_w + 1; \end{cases}$$

where $\tilde{G}_{\mathrm{IGF}}$ is described in [2] [3] and R_w is determined by an adaptive method in [4], where w represents the indices x, y, z.

2. Using the discrete cosine transform (DCT) for Green's function: define $g = \{g_1, g_2, \ldots g_{n+1}\}$, and the real even symmetric extension (RESE) of g is g_{ex}, i.e. $g_{ex} = \{g_1, g_2, \ldots g_{n+1}, g_n, g_{n-1}, \ldots g_2\}_{2n}$. Then

$$\mathrm{FFT}_{2n}(\mathrm{RESE}(g)) = 2 \cdot \mathrm{RESE}(\mathrm{DCT}_{n+1}(g)).$$

The same result succeeds by replacing the factor 2 to a factor 8 for 3D extension case. The complexity reduces significantly from $O((\log_2 2n)^3)$ to $O((\log_2 n)^3)$ besides RESE.

3. Using a novel fast implicitly zero-padded convolution routine: define the unit: $\omega_m^m = 1$. We achieve a FFT without the last bit reversal stage named FFTPADBACKWARD and FFTPADFORWARD as in Alg. 1.

Algorithm 1 FFTPADBACKWARD, FFTPADFORWARD

Input: f
Output: f, u
1: **function** FFTPADBACKWARD
2: **for** $k = 1 \to n$ **do**
3: $u(k) \leftarrow \omega_{2n}^{k-1} f(k)$;
4: **end for**
5: $f(:) \leftarrow \mathrm{IFFT}[f(:)]$;
6: $u(:) \leftarrow \mathrm{IFFT}[u(:)]$;
7: **end function**

Input: f, u
Output: f
1: **function** FFTPADFORWARD
2: $f(:) \leftarrow \mathrm{FFT}[f(:)]$;
3: $u(:) \leftarrow \mathrm{FFT}[u(:)]$;
4: **for** $k = 1 \to n$ **do**
5: $f(k) \leftarrow f(k) + \omega_{2n}^{-k+1} u(k)$;
6: **end for**
7: **end function**

In principle, the FFTPADBACKWARD and FFTPADFORWARD transforms are deformed inverse FFT (IFFT) and FFT, respectively. The two outputs of the FFTPADBACKWARD are the same as those obtained by separating the even-odd indices of the $2n$ sized FFT of the explicitly zero padded f, i.e. we define $f_{ex} = \begin{bmatrix} f \\ 0 \end{bmatrix}_{2n}$ and $[f, u]_n = \mathrm{fftpadBackward}_n(f)$, which results in $[\mathrm{IFFT}_{2n}(f_{ex})_{\mathrm{odd}}, \mathrm{IFFT}_{2n}(f_{ex})_{\mathrm{even}}] = [f, u]$. The FFTPADFORWARD transform is obtained by the inverse procedure.

The 2D and 3D FFTPADBACKWARD (FFTPADFORWARD) are the same procedures as 2D and 3D IFFT (FFT), i.e. they

ISBN 978-3-95450-136-6

execute a 1D transform along each direction, serially. The improved 3D parallel Poisson solver is further developed to suit a real to complex (R2C) 1D FFT along the first direction in order to reduce the number of further deformed FFTs in other directions.

THE IMPROVED PARALLEL POISSON SOLVER'S ROUTINE

All processors utilized in the solver are mapped onto a 2D process grid. Each process owns a unique ID (RowID, ColID) as the element of a matrix.

The charge density $\rho(i, j, k)$ is distributed to the process grid by filling (j, k)s into the (RowID,ColID)s as (j_{local}, k_{local})s equally. Only the is are free to be utilized. Since the indices of j, k are distributed to the grid, the elements ordered by the two directions can not be used directly, e.g. for the Fourier transforms in the other two directions. Communications and transports of data are therefore a special challenge in supercomputers. Unlike the shared-memory computer programming (as PCs), the transport of data is a serious problem in parallel programming (as supercomputers). This problem requires intensive concern. We use the *MPI_alltoall* for the high dimension transpose. The specified transpose function rearranges the 3D vector by exchanging the order of direction e.g. ijk to jik or kji for each time. The time consumption of the data transpose can reach a high percentage of the total CPU time comparing to the pure computing time for high dimension Fourier transforms.

The programming routine is organized by four parts:

1. The RIGF calculation and the related DCT (Fig.1) – the Green's function values G, which is distributed in the 2D grid processes by the order (k, j, i) (k(blue), j(red), i(green)) in each process, are calculated by the RIGF method; the 3D DCT of G is implemented. The results are extended in j direction in demand for further multiplication in Part 3.

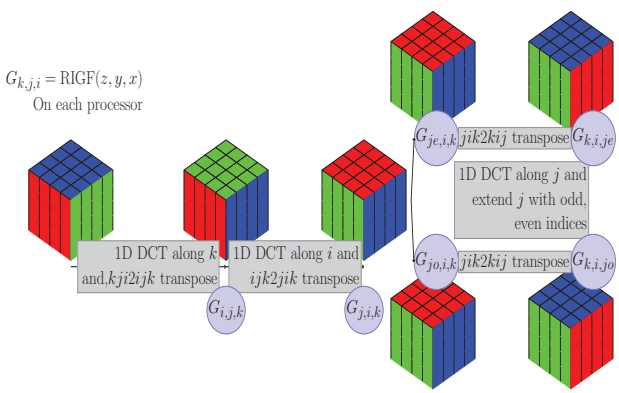

Figure 1: The RIGF calculation and the related 3D DCT.

2. The 3D backward deformed FFT routine (Fig.2) – the ρ is firstly padded with the same size zeros in i direction as $\mathrm{Ex}\rho_{i,j,k}$. The following deformed 3D FFTs is constructed by the *R2C* FFTs from the real vectors $\mathrm{Ex}\rho_{i,j,k}$ to the complex vectors $C\rho_{i,j,k}$ along i, the FFTPADBACKWARDS along j, and the FFTPADBACKWARDS along k.

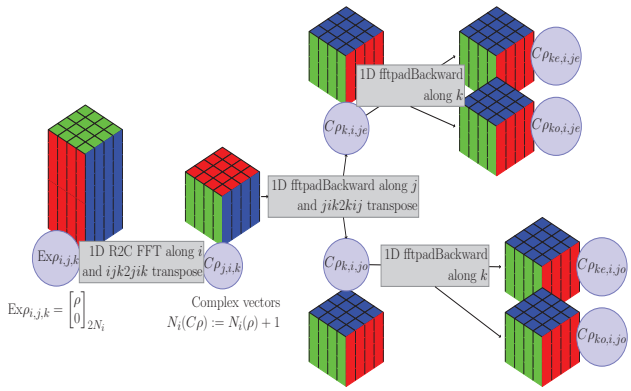

Figure 2: The 3D backward deformed FFT routine.

3. Multiplication in spectral domain – the results from Part1 and Part2 are multiplied element by element according to the following rule:

$$C\rho_{ke,i,jx} = \mathrm{RESE}(\tilde{G}_{k,i,jx})_{\mathrm{even}} * C\rho_{ke,i,jx}, \text{ and}$$
$$C\rho_{ko,i,jx} = \mathrm{RESE}(\tilde{G}_{k,i,jx})_{\mathrm{odd}} * C\rho_{ko,i,jx},$$

where x expresses e (even) or o (odd).

4. The 3D forward deformed FFT routine part (Fig.3) – the inverse procedure of Part 2 is performed.

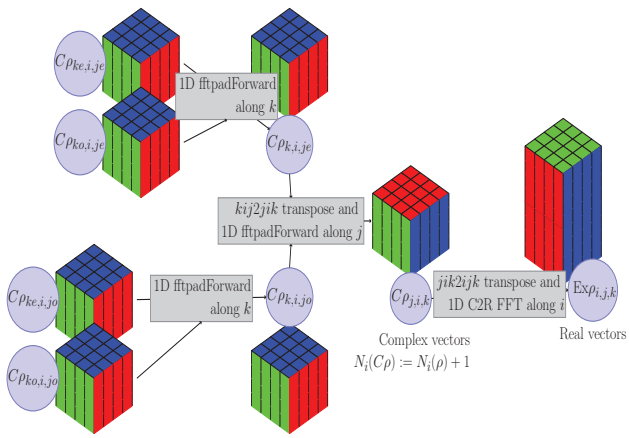

Figure 3: The 3D forward deformed FFT routine.

STUDY OF THE IMPROVED PARALLEL POISSON SOLVER

The parallel Poisson solver is written in Fortran 90 with the Open MPI, compiled by the Intel compiler, and executed on the Edison supercomputer at the NERSC (National Energy Research Scientific Computing Center).

1. We carry out the strong scaling and weak scaling study of the solver. The results are shown in Fig.4. The weak scaling figures (above) are plotted by fixing the ratio between the size of the problem and the cores in order to keep it constant. The starting points are 32^3/core (left) and 64^3/core (right), respectively. The strong scaling figures (below) are

ISBN 978-3-95450-136-6

plotted by fixing the size of the problem, 128^3 (left) and 256^3 (right), as well as increasing the number of cores in processing. Therefore, the problem is more like a cpu-bound rather than a memory-bound problem.

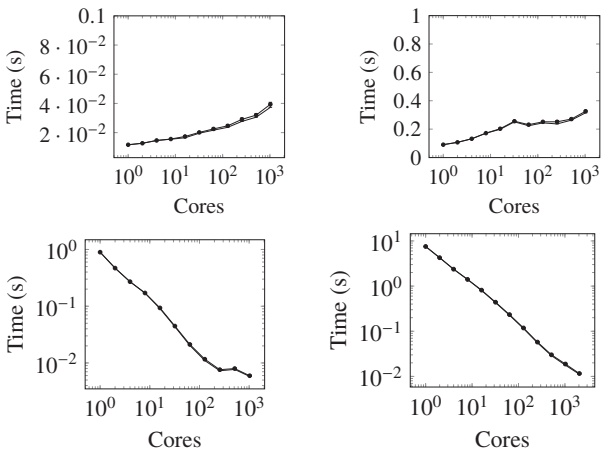

Figure 4: The weak scaling (top) and strong scaling (bottom) study.

2. The OpenMP is a shared memory multiprocessing API, which cooperates with the OpenMPI process together in the same computational node. Probably, the best choice may be 1-4 MPI processes per NUMA node (each processor (12 cores) constitutes a NUMA node, and each node has two processors) with 12-3 OpenMP threads each node on Edison. Additionally, there is a time cost in the preparation of OpenMP when we link the OpenMP library. The OpenMP parallel parts are mainly developed for "do-loops". The SIMD, up to the date, is not further optimized. In Fig. 5, the process numbers N_p in use are fixed by 96, and the thread number per node varies from 1 to 6. For $N_{x,y,z} = 512$ (left) and $N_{x,y,z} = 256$ (right), we plot all the CPU time for different OpenMP threads per process in use (for two memory affinity situation: numa_node and depth).

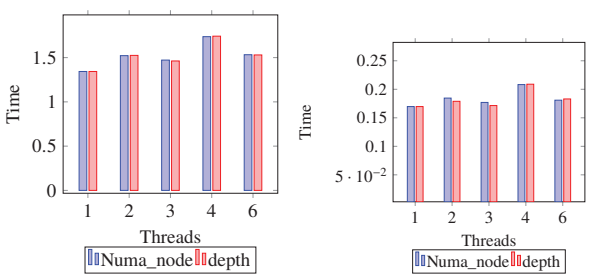

Figure 5: CPU time for different OpenMP threads per process in use.

As shown in Fig.5, the Open MPI obtains better results than the hybrid Open MPI+OpenMP case with the same number of cores in use.

3. Comparing the factors of time consumption and accuracy, the improved Poisson solver computes faster than the commonly used Poisson solver, whereas their calculations are equally accurate.

Example 1: We track an extreme long bunch with the transverse aperture size $R_{x,y} = 0.15$m, longitudinal size $L_z = 1.0e5$m, at the initial sections of a virtual accelerator. Some simulation parameters are $dt = 1.0e-12$, s, $t_{\text{step}}20,000,000$, $N_{x,y,z} = 64$, $N_{\text{col}} = 8$, $N_{\text{row}} = 8$. In Fig. 6, we have shown a perfect match in RMS bunch size and RMS emittance in x direction between the improved parallel Poisson solver and the commonly used Poisson solver routine. For the other directions, y and z, the results match perfectly.

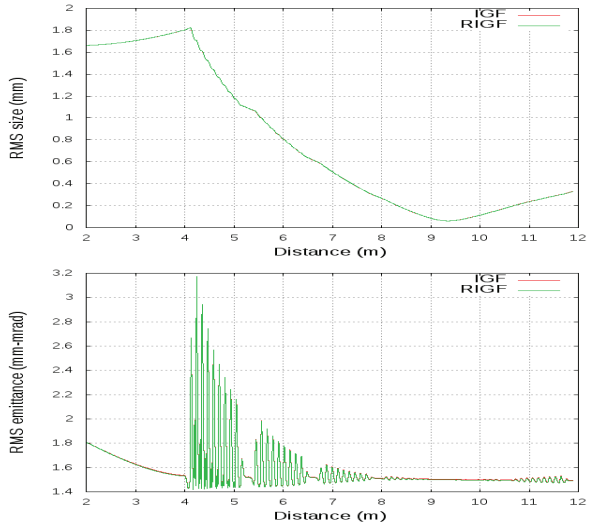

Figure 6: A schematic plot of comparison of the RMS size and RMS emittance in x direction.

Example 2: We compare the efficiency improvement of the new solver. As shown in Tab.1, the speed-up is as high as 2, which is significant. For small size problems with a large number of processes, the speed-up is not obvious. This may be because the data transports occupy a high percentage of the whole time consumption in both solvers.

Table 1: Comparison of the Common IGF and Novel RIGF Solvers

N_w	N_p	t_{RIGF}	t_{IGF}	N_w	N_p	t_{RIGF}	t_{IGF}
64	4	93.57 s	221.9 s	64	256	7.136 s	8.311 s
64	16	26.82 s	64.73 s	128	256	25.95 s	40.45 s
64	64	9.871 s	20.28 s	256	256	198.5 s	298.8 s

In conclusion, the new improved parallel Poisson solver proves to be more efficient than the commonly used routine in the calculation of space charge for beam dynamics simulations.

ACKNOWLEDGMENT

Dawei Zheng is supported by the China Scholarship Council. This research was partially supported by the U.S. Department of Energy under Contract no.DE-AC02-05CH11231.

ISBN 978-3-95450-136-6

REFERENCES

[1] R.W. Hockney and J.W. Eastwood, Computer Simulation Using Particles, Institut of Physics Publishing, Bristol, (1992).

[2] J. Qiang, S. Lidia, R.D. Ryne, and C. Limborg-Deprey, Phys. Rev. ST Accel. Beams, vol 9, 044204 (2006).

[3] J.Qiang, S. Lidia, R.D. Ryne, and C. Limborg-Deprey, Phys. Rev. ST Accel. Beams, vol 10, 129901 (2007).

[4] D. Zheng, G. Pöplau and U. van Rienen, "Efficiency optimization of fast Poisson solver in beam dynamics simulation", Computer Physics Communications, In press (2015).

ISBN 978-3-95450-136-6

COMPUTATION OF BEAM COUPLING IMPEDANCE IN THE FREQUENCY DOMAIN BY MEANS OF FIT AND FEM

U. Niedermayer*, O. Boine-Frankenheim, and H. De Gersem
Technische Universität Darmstadt, Institut für Theorie Elektromagnetischer Felder (TEMF),
Schlossgartenstraße 8, 64289 Darmstadt, Germany

Abstract

A detailed knowledge of transverse and longitudinal beam coupling impedance is required to quantify intensity thresholds due to coherent instabilities and beam induced heating in ion synchrotrons. Particularly at low frequencies, where the beam pipe dominates the impedance spectrum, analytical calculations are widely used since contemporary time domain methods are inapplicable. We present two different ways to compute beam coupling impedance in the frequency domain. One is based on the Finite Integration Technique (FIT) and it is implemented in 2D and 3D. The staircase FIT approximates curved structures only poorly, therefore another solver is implemented in 2D based on the Finite Element Method (FEM). The unstructured triangular FEM mesh allows to approximate curved structures better. Moreover, it allows to compute the space charge impedance, since the shape of the beam and the beam's dipole moment can be represented properly, such that the direct space charge force can be subtracted and only the coherent force remains. Space charge and resistive wall impedance results for GSI and the upcoming FAIR project and the impedance of the beam pipe for the Future Circular Collider (FCC-hh) design study are presented as applications.

INTRODUCTION

The beam in a synchrotron is modeled as a disc with radius a and surface charge density σ traveling with velocity βc. The displacement d_x of the beam (i.e. a coherent dipole oscillation) can be approximated to first order by

$$\sigma(\varrho,\varphi) \approx \frac{q}{\pi a^2}(\Theta(a-\varrho)+\delta(a-\varrho)d_\mathrm{x}\cos\varphi). \quad (1)$$

The force acting back on the beam is described by the coupling impedance [1]

$$\underline{Z}_\parallel(\omega) = -\frac{1}{q^2}\int_\mathrm{beam}\underline{\vec{E}}\cdot\underline{\vec{J}}^*_\parallel \mathrm{d}V \quad (2)$$

$$\underline{Z}_{\perp,\mathrm{x}}(\omega) = -\frac{\beta c}{(qd_\mathrm{x})^2\omega}\int_\mathrm{beam}\underline{\vec{E}}\cdot\underline{\vec{J}}^*_{d_\mathrm{x}} \mathrm{d}V. \quad (3)$$

where the beam current in frequency domain (FD) is obtained from Eq. (1) as

$$\underline{J}_{\mathrm{s,z}}(\varrho,\varphi,z;\omega) = \underline{J}_\parallel + \underline{J}_{d_\mathrm{x}} = (\sigma_\parallel+\sigma_{d_\mathrm{x}})e^{-i\omega z/\beta c} \quad (4)$$

such that its magnitude is independent of the beam velocity. Equations (2), (3) can be interpreted as functionals of the solution of Maxwell's equations recast in the curl-curl equation

$$\nabla\times\underline{\nu}\nabla\times\underline{\vec{E}} - \omega^2\underline{\varepsilon}\,\underline{\vec{E}} = -i\omega\underline{\vec{J}}_\mathrm{s}, \quad (5)$$

with the complex reluctivity $\underline{\nu} = \underline{\mu}^{-1} = (\mu'+i\mu'')/|\underline{\mu}|^2$, and the complex permittivity $\underline{\varepsilon} = \varepsilon_0\varepsilon_r - i\kappa/\omega$ (conductivity κ) as functions of position and frequency.

FINITE INTEGRATION TECHNIQUE

The FIT discretizes Eq. (5) as

$$\widetilde{\mathbf{C}}\mathbf{M}_{\underline{\nu}}\mathbf{C}\underline{\widehat{\mathbf{e}}} - \omega^2\mathbf{M}_{\underline{\varepsilon}}\underline{\widehat{\mathbf{e}}} = -i\omega\underline{\widehat{\widehat{\mathbf{j}}}}_\mathrm{s}, \quad (6)$$

usually on a rectangular (staircase) mesh of size $n_p = N_xN_yN_z$. This represents a complex (non-Hermitean) ill conditioned system of size $3n_p \times 3n_p$. A simple way to include the beam entry and exit is to use a Floquet boundary condition, i.e. the longitudinal partial derivative matrix of size $n_p \times n_p$ becomes

$$[\mathbf{P}_z]_{m,n} = \begin{cases} -1, & \text{if } m = n \\ 1, & \text{if } m = n - N_xN_y \\ e^{-i\omega L/v}, & \text{if } m = n - N_xN_y + n_p \\ 0, & \text{else.} \end{cases} \quad (7)$$

Note that $\widetilde{\mathbf{P}} = -\mathbf{P}^\mathrm{H}$ and thus $\widetilde{\mathbf{C}} = \mathbf{C}^\mathrm{H}$, but in the presence of losses Eq. (6) remains non-Hermitean. In the case of only one cell in longitudinal direction one obtaines a 2D scheme, i.e. $\mathbf{P}_z = -1 + \exp(-i\omega\Delta z/v)$ becomes a scalar. Due to the numerical simplicity, it is advantageous to treat distributed impedances of long (2D) structures by means of direct solvers (see [2] and references therein for details). However, as visible in Fig. 1, the dipole source to compute

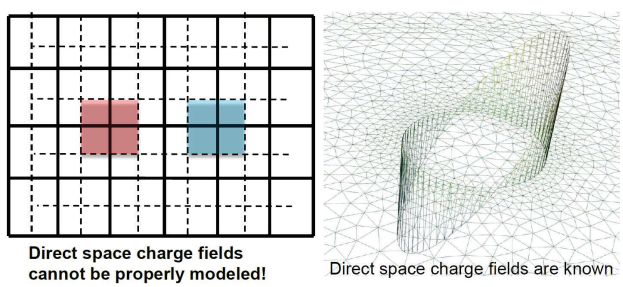

Figure 1: Modeling of the dipole source in the FIT (left) and FEM (right) approach.

the transverse impedance cannot be modeled accurately by the staircase FIT. Thus the direct space charge fields, which depend on the shape of the dipole cannot be removed. This issue is solved by using an unstructured mesh and the finite element method.

* niedermayer@temf.tu-darmstadt.de

ISBN 978-3-95450-136-6

FINITE ELEMENT METHOD

In 2D, Eq. (5) can be solved by the FEM using nodal functions for the longitudinal and Nédélec edge functions [3] for the transverse components (see [4] for details). The implementation is done in Python using the FEniCS package [5, 6]. The mesh originates from Gmsh [7]. Edge functions are advantageous because the tangential electric field on a material boundary is continuous, while the normal one is allowed to have a jump (as is physically correct). Since lowest order edge functions are incapable to representing functions with nonzero divergence, a Helmholtz split has to be applied to Eq. (5). Apart from the additional Poisson system, the curlcurl system presents for lowest order elements an (ill conditioned) complex system of size $n_n + n_e$, which is solved by a direct solver from PETSc, see [8]. The hereby presented code ('BeamImpedance2D', see also [4]) includes also a surface impedance boundary condition (SIBC) $\vec{n}\times\vec{n}\times\vec{E} = \underline{Z}_s\vec{n}\times\vec{H}$. This allows to simulate the impedance of resistive beam pipes at high frequency without resolving the extremely small skin depth δ in the mesh.

AN APPLICATION FOR FAIR

The extraction kickers for the SIS100 synchrotron consist of a 80 cm long ferrite (Ferroxcube 8C11 [9]) yoke with about 10 cm aperture and 6 cm thickness. The beam scenario with highest intensity and shortest bunch length (single 2E13 protons bunch, $\sigma_s = 3.7$ m) causes the highest stationary heat power as

$$P = \omega_0 \frac{q^2 v^2}{2\pi^2} \int_0^\infty \mathrm{Re}\{\underline{Z}_\parallel(\omega)\}|\underline{\lambda}(\omega)|^2 \mathrm{d}\omega. \qquad (8)$$

The impedance of such a kicker device can be strongly reduced by interrupting the magnetic circuit by means of copper sheets in the magnet gap(s). Computation results indicate that for 2.8 mm magnet gaps the heat load is 7327 W with open gaps and 48 W with the gaps filled by a copper sheet (see [10] for more details). As visible in Fig. 2, the FIT and FEM codes obtain roughly the same impedance results. However, note that for curved structures, the staircase FIT code supposedly gives inaccurate results.

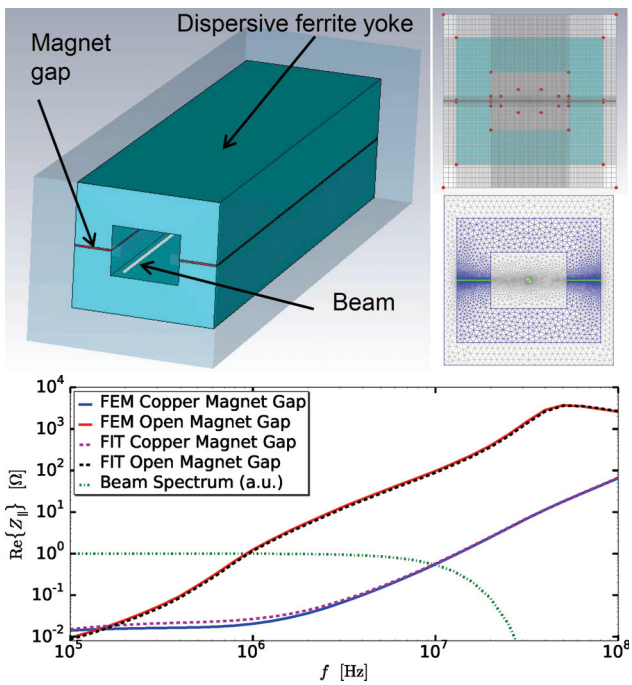

Figure 2: SIS100 transfer kicker magnet, FIT and FEM meshes, and longitudinal impedance results.

AN APPLICATION FOR THE FCC-HH DESIGN STUDY

The future circular collider (FCC) design study aims for a post-LHC accelerator. The hadron-hadron (hh) scenario is outlined for proton collisions up to 100 TeV c.o.m. and a circumference of roughly 100 km [11]. It will be the first hadron accelerator project where synchrotron radiation plays a significant role. Therefore, the beam pipe is designed with a slit and a reflector (see Fig. 3), in order to lead the synchrotron radiation away from the beam (otherwise photo-electrons could build up an unstable electron cloud). Moreover, an impedance reduction is obtained by adding a copper layer of 80μm to the inner surface of the Titanium beam screen.

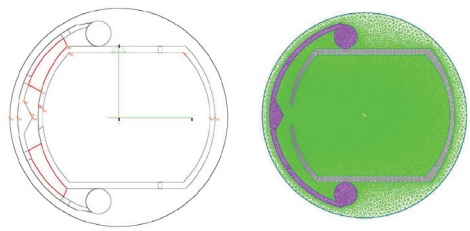

Figure 3: Technical drawing (R. Kersevan, CERN) and Gmsh mesh of the proposed FCC-hh beam pipe.

The transverse impedance of such a complicated structure is computed with BeamImpedance2D. Since only highly conducting materials at low temperature ($RRR \approx 100$) are involved, the SIBC is valid for frequencies down to 100 Hz. However, in order to model the thin copper layer on the titanium pipe, a two-layer SIBC, i.e.

$$\underline{Z}_s(\omega) = \left.\frac{\underline{E}_x}{\underline{H}_y}\right|_{z=0} = \frac{1+i}{\kappa_1\delta_1}\frac{Me^{ik_{z1}d} + Ne^{-ik_{z1}d}}{Me^{ik_{z1}d} - Ne^{-ik_{z1}d}} \qquad (9)$$

$$M = 1 + \sqrt{\frac{\mu_1\kappa_2}{\mu_2\kappa_1}}, \quad N = 1 - \sqrt{\frac{\mu_1\kappa_2}{\mu_2\kappa_1}} \qquad (10)$$

$$\delta_p = \sqrt{\frac{2}{\mu_p\kappa_p\omega}}, \quad k_{zp} = \frac{1-i}{\delta_p}, \quad p = 1, 2 \qquad (11)$$

which is the analytic solution of a 1D diffusion problem, is required. A plot of the surface impedance for the cold titanium pipe with copper coating can be seen in Fig. 4.

ISBN 978-3-95450-136-6

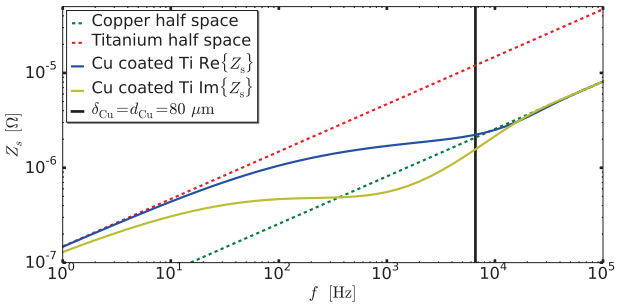

Figure 4: Surface impedance for Copper (κ = 6E7 S/m) coated Titanium (κ = 1.8E6 S/m) with both RRR = 100.

Figure 5 shows the transverse impedance of the pipe, where only the inner vacuum part was meshed and the two-layer SIBC was employed. The results are compared to analytic ones by the Mathematica [12] code Rewall [13] for a round multilayer pipe. As expected, the thick wall impedance lies between the one for minimal and maximal pipe radius. Moreover, the vertical impedance must be larger than the horizontal one, since the vertical aperture is smaller (for a round pipe the transverse impedance scales as $\propto b^{-3}$). The bump of the imaginary part at high frequency is artificial and originates from improper cancellation of space charge impedance at very high γ = 50000, i.e. the error of the space charge impedance is larger than the imaginary part of the resistive wall impedance.

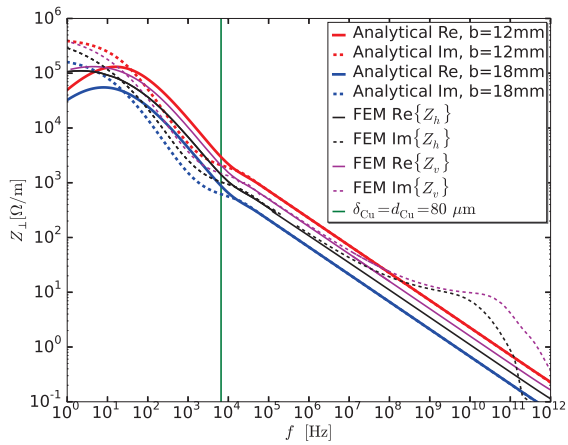

Figure 5: Transverse impedance result for the pipe in Fig. 3 (1 m length) relevant for the Coupled Bunch (at low frequencies) and TMCI (broadband at high frequency) instabilities.

CONCLUSION AND OUTLOOK

Two beam coupling impedance solvers were presented. One is based on FIT and implemented in 2D and 3D using a Floquet boundary condition. The staircase FIT is, however, inappropriate to model curved structures. This is particularly a problem for the transverse impedance at $\beta < 1$, since the direct space charge impedance which outshines the overall imaginary impedance result, is not known for a twin-pencil-beam excitation (Fig. 1) and can thus not be removed. When using an unstructured mesh and the FEM, the source for the dipolar transverse impedance can be modeled as a dipole ring, which has analytically known fields inside. These contributions can be removed up to the accuracy of the field computation. The transverse wall impedance can thus be computed for arbitrary beam velocity. Moreover, the SIBC avoids meshing the wall, which makes this approach applicable up to very high frequencies.

The development of a 3D FEM solver is outlined for the future. Since the Floquet boundary conditions cannot be applied on an unstructured mesh so easy, special beam port boundary conditions will be implemented (see e.g. [14]). The Floquet boundary conditions with FIT, however, can also be employed to compute the impedance of periodic structures. Examples of such are dielectric gratings, which are used in Dielectric Laser Acceleration (DLA), see [15].

ACKNOWLEDGMENT

The authors wish to thank Thilo Egenolf and Fedor Petrov (TEMF) and Xavier Buffat and Daniel Schulte (CERN) for input on the FCC-hh pipe design and Udo Blell (GSI) for input on the SIS100 kicker design.

REFERENCES

[1] R. Gluckstern, CERN Accelerator School (2000).

[2] U. Niedermayer and O. Boine-Frankenheim, Proc. of ICAP'12 (2012).

[3] J.C. Nedelec, Numer. Math. 35, 315-341 (1980).

[4] U. Niedermayer et al., Phys. Rev. –STAB 18, 032001 (2015).

[5] A. Logg, K.-A. Mardal, G.N. Wells, et al., Automated Solution of Differential Equations by the Finite Element Method, Springer (2012).

[6] `www.fenicsproject.org`

[7] C. Geuzaine and J.-F. Remacle, GMSH 2.8.4, `www.geuz.org/gmsh` (2014).

[8] Portable, Extensible Toolkit for Scientific Computation, `http://www.mcs.anl.gov/petsc/`.

[9] Ferroxcube 8C11 Material specification (2002).

[10] U. Niedermayer and O. Boine-Frankenheim, GSI Scientific Report (2013).

[11] `http://www.fcc.web.cern.ch`

[12] Wolfram *Mathematica 9.0®*, `www.wolfram.com` (2013).

[13] N. Mounet and E. Metral, CERN-BE-2009-039, see also `www.cern.ch/imp`

[14] M. Balk, PhD thesis at TU-Darmstadt, Cuvillier Verlag (2005).

[15] J. England et al., Review of Modern Physics (2014).

ISBN 978-3-95450-136-6

DEVELOPMENT STATUS OF A THIN LENS MODEL FOR FRIB ONLINE MODEL SERVICE*

G. Shen, Z. He#, FRIB, Michigan State University, East Lansing, 48864 USA

Abstract

FRIB (Facility for Rare Isotope Beams) is a heavy ion linac facility under construction, which has various specific features in its beam dynamics design to achieve the world highest beam power for heavy ion linacs. It is a challenge to develop an online model which covers all those specific features and satisfies the requirement for execution speed at the same time. An online model named TLM (Thin Lens Model) is under active development at FRIB to address its all major beam dynamics issues. This paper describes the latest status of TLM code, the infrastructure to integrate the TLM into FRIB beam commissioning environment.

INTRODUCTION

FRIB [1, 2] is a new project funded by DOE and MSU (Michigan State University), and under construction on the campus of MSU and will be a new national user facility for nuclear science. Its driver accelerator is designed to accelerate all stable ions to energies > 200 MeV/u with beam power on the target up to 400 kW. It consists of 2 ECR (Electron Cyclotron Resonance) ion sources, a low energy beam transport, a RFQ (Radio Frequency Quadrupole) linac, 3 Linac segments, 2 folding segments to confine the footprint and facilitate charge selection, and a beam delivery system to transport to the target. The beam is stripped to higher charge states in the first LS section (LS1).

TLM ONLINE MODEL

As mentioned in [3], an online model is under active development at FRIB to meet its needs. The emphasis of the development is put on the execution speed and coverage of FRIB specific needs. The FRIB lattice is designed with some specific features as summarized below:

- Solenoid focusing lattice;
- Non-axisymmetric field components at QWRs (Quarter Wave Resonators). The non-axisymmetric nature of QWR induces dipole and quadrupole components, which has significant contribution to FRIB beam dynamics;
- Multi-charge-state beam acceleration. FRIB is designed to accelerate up to five charge states simultaneously to achieve high beam intensity. It is a challenge to meet stringent beam-on-target requirements especially for multi-charge-state beams;
- Achromat arc sections between linac segments;
- Second order achromat with sextupole magnets.

To commission the beam effectively and efficiently, an online model named TLM (Thin Lens Model) is under active development at FRIB to address those issues. It currently supports optical elements including dipole magnet, quadrupole magnet, solenoid magnet, axisymmetric RF cavity and non-axisymmetric RF cavity, corrector magnet, stripper, electrostatic optical elements (dipole and quadrupole), and diagnostic devices.

RF Cavity

There are 2 major considerations about FRIB cavity modelling, which are 1) significant velocity change especially in low energy range, and 2) multipole field component effect caused by the non-axisymmetric geometry of its cavity.

A full implementation of FRIB RF cavity has been published in [4,5]. In short, because FRIB needs to accelerate up to 5 different beams simultaneously, traditional one gap approach, which has been widely used in many envelope-tracking codes, does not apply to FRIB, especially for its low-energy part. Therefore, TLM adopts field integration to track the reference particle, and two-gap model for transfer matrix calculation.

Solenoid

The FRIB adopts solenoid lattice instead of quadrupole lattice acting as the only focusing component for all four cryomodules. Solenoid focusing lattice introduces strong coupling effect between horizontal and vertical directions. A realistic solenoid has fringe effect, which has to be modeled properly.

With the rotating Larmor frame, the transfer matrix of solenoid can be decomposed into two commuting transfer matrix: one rotating and one constant focusing. The solenoid is treated as a constant focusing element when in the Larmor frame. Figure 1 shows an example of transverse design for oxygen lattice when using Larmor frame to simplify designing procedure.

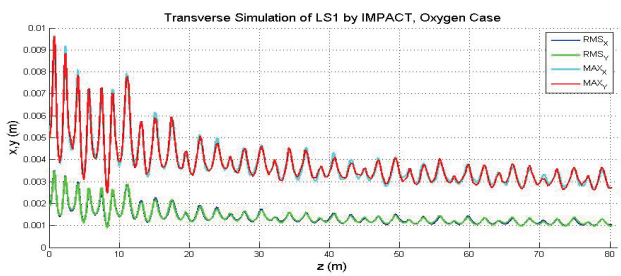

Figure 1: example of transverse design for oxygen lattice using Larmor frame and confirmation of beam envelope using IMPACT-Z [6].

There are two main effects of solenoid fringe field, one is decreasing of focusing strength, and another is decreas-

*Work supported by the U.S. Department of Energy Office of Science under Cooperative Agreement DE-SC0000661
#hez@frib.msu.edu

ISBN 978-3-95450-136-6

ing of rotating Larmor angle. Decrease of Larmor angle is proportional to field integration and is easy to calculate. We model the focusing reducing effect by adding two defocusing thin lens kick described as Eq. (1) [7].

$$M_{edge} = \begin{bmatrix} 1 & 0 & 0 & 0 & 0 & 0 \\ -\Phi & 1 & 0 & 0 & 0 & 0 \\ 0 & 0 & 1 & 0 & 0 & 0 \\ 0 & 0 & -\Phi & 1 & 0 & 0 \\ 0 & 0 & 0 & 0 & 1 & 0 \\ 0 & 0 & 0 & 0 & 0 & 1 \end{bmatrix} \quad (1)$$

Where $\Phi = \frac{-g^2 a}{2}$, g is focusing strength proportional to B and a is aperture size. An estimated solenoid fringe effect using Eq. (1) shows that adding fringe effect results in significant envelope blow up as illustrated in Fig. 2:

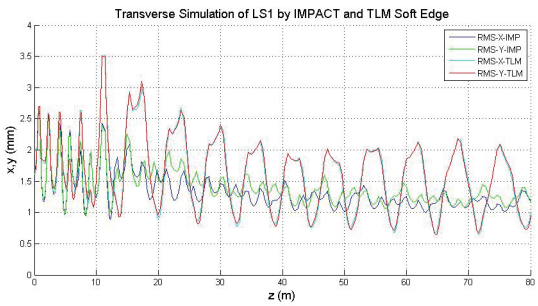

Figure 2: Horizontal and vertical envelope with (blue and green) and without (cyan and red) solenoid fringe.

Electrostatic Element

The electrostatic optical elements include dipole and quadrupole component and are used in FRIB front-end section. The transfer matrix of an electrostatic quadrupole is basically the same as magnetic quadrupole after changing definition of focusing strength into Eq. (2) [8]:

$$k^2 = \frac{q}{\beta^2 \gamma E_s} \frac{V_0}{R^2} \quad (2)$$

Where V_0 is the voltage of electrode and R is the radius. The transfer matrix for a hardedge spherical electrostatic bend is Eq. (3) [8]:

$$\begin{bmatrix} x_2 \\ x_2' \\ \delta_K \\ \delta_m \end{bmatrix} = \begin{bmatrix} c_x & s_x & d_x N_k & d_x N_m \\ -s_x k_x^2 & c_x & (s_x/\rho_0) N_k & (s_x/\rho_0) N_m \\ 0 & 0 & 1 & 0 \\ 0 & 0 & 0 & 1 \end{bmatrix} \begin{bmatrix} x_1 \\ x_1' \\ \delta_K \\ \delta_m \end{bmatrix}$$

$$\begin{bmatrix} y_2 \\ y_2' \end{bmatrix} = \begin{bmatrix} c_y & s_y \\ -s_y k_y^2 & c_y \end{bmatrix} \begin{bmatrix} y_1 \\ y_1' \end{bmatrix} \quad (3)$$

Where $c_x = \cos(k_x L)$, $s_x = \sin(k_x L)/k_x$, $d_x = \frac{1-\cos(k_x L)}{\rho_0 k_x^2}$, $c_y = \cos(k_y L)$, $s_y = \frac{\sin(k_y L)}{k_y}$, $N_K = \frac{(1+2\eta_0)^2+1}{2(1+\eta_0)(1+2\eta_0)}$, $N_m = \frac{(1+2\eta_0)-1}{2(1+\eta_0)(1+2\eta_0)}$, $\eta_0 = \frac{m-m_0}{2m_0}$, $\delta_k = \frac{K}{K_0} - 1$, $\delta_m = \frac{(m/z)}{(m/z_0)} - 1$, $k_x^2 \rho_0^2 = 1 - n_1 + \frac{1}{(1+2\eta_0)^2}$, $k_y^2 \rho_0^2 = n_1$, for spherical electrostatic bend, n_1=1, ρ_0 is bending radius, m is particle mass, m_0 is static mass, K is particle kinetic energy, K_0 is reference particle kinetic energy, z is particle charge state, z_0 is reference particle charge state.

Stripper

There exists three effects needed to take into consideration to model a stripper, which are 1) change in charge state, 2) energy straggling, and 3) blow up in phase space respectively.

Charge states distribution after stripping is calculated by Baron's formula [9]:

$$\frac{\bar{Q}}{Z} = 1 - exp\left(-83.275 \frac{\beta}{Z^{0.447}}\right)$$
$$Q_{ave} = \bar{Q}\left(1 - exp(-12.905 + 0.2124Z - 0.00122Z^2)\right)$$
$$d = \sqrt{\bar{Q}(0.07535 + 0.19Y - 0.2654Y^2)}, Y = \bar{Q}/Z \quad (4)$$

Q_{ave} is the average output charge state and d is standard deviation. Gaussian distribution of output charge state is assumed. Baron's formula can be benchmarked with NSCL data, for Uranium Z=92, E_k=9.92MeV/u (Fig. 3):

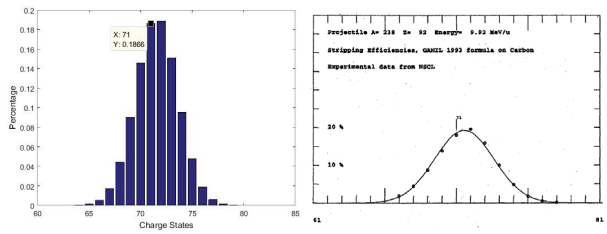

Figure 3: charge state distribution calculated using Baron's formula and benchmark with NSCL data.

Modelling of energy straggling effect and phase-space blow-up effect starts with SRIM [10] Monte-Carlo simulation. SRIM is able to calculate particle energy and momentum after particles injected into a certain stripper material. Then, an empirical formula in Eq. (5) is adopted to fit the results and the obtained parameters are used for stripper modelling:

$$f(\theta, E) = (\theta/\theta_N) \cdot e^{-\left(\frac{\theta}{\theta_2}\right)^u} \cdot e^{-\frac{1}{2}\left[\frac{(E-E_0)}{E_1}\right]^2} \quad (5)$$

The energy straggling effect can be get from parameter E_0, and the envelope blow up effect can be estimated using Eq. (6):

$$\sigma_h = \sqrt{\sigma_f^2 + \sigma_g^2} \quad (6)$$

σ_f is the standard deviation of original beam; σ_g is an extra standard deviation added solely with stripper; σ_h is the resulting standard deviation. The model is then benchmarked with a particle tracking code IMPACT-Z, results are shown in Fig. 4.

Multi-charge State

FRIB is simultaneously accelerating multiple charge states in order to enhance the beam current. Instead of conventional particle tracking method, TLM is utilizing a divide-and conquer three-step-scheme to track multi-charge state beam.

- Step 1: Machine initialization by reference charge state: An ideal particle with a center charge state is used to initialize the whole machine, mainly the cavity phase;

ISBN 978-3-95450-136-6

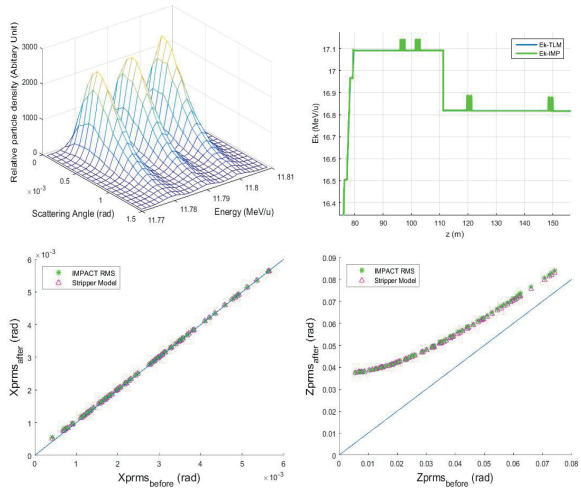

Figure 4: (a) Energy and angle distribution simulated by SRIM (b) Energy straggling effect benchmarked with IMPACT (c) Transverse momentum rms blow up and benchmark with IMPACT (d) Longitudinal momentum rms blow up and benchmark with IMPACT-Z.

- Step 2: Reference orbit initialization of the reference particle for each charge states: single particle tracking is used for a reference particle for each charge states and the result is recorded for reference
- Step3: Envelope tracking for each charge state: transfer matrix is adjusted according to different charge states and its different reference orbit.

The method and benchmark has been thoroughly discussed in [11].

BENCHMARK

The result of TLM simulation has been benchmarked with some well-recognized codes to crosscheck its result. We choose our lattice design codes, which is DIMAD for our front-end and IMPACT-Z for main linac, to verify the simulation results.

For the main linac, the results are compared including both transverse plane and longitudinal plane within acceptable error range. Two typical examples are as shown in Fig. 5, which are for central beam orbit for LS1 segment, and energy for LS1 and FS1 segments. The accumulated error is within 2% for orbit, and 0.005% for energy.

For the front-end, the results are benchmarked against DIMAD [12] code, and results for both horizontal and vertical envelope are shown in Fig. 6. The accumulated RMS error has been achieved within 0.01%.

CONCLUSION

An online model is under active development at FRIB to support FRIB specific requirements. Implementation of major functions and optical elements are finished and the simulation results are benchmarked against various well-recognized simulation such as IMPACT-Z and DIMAD, and a good agreement has achieved within acceptable error range. The online model has been now integrated

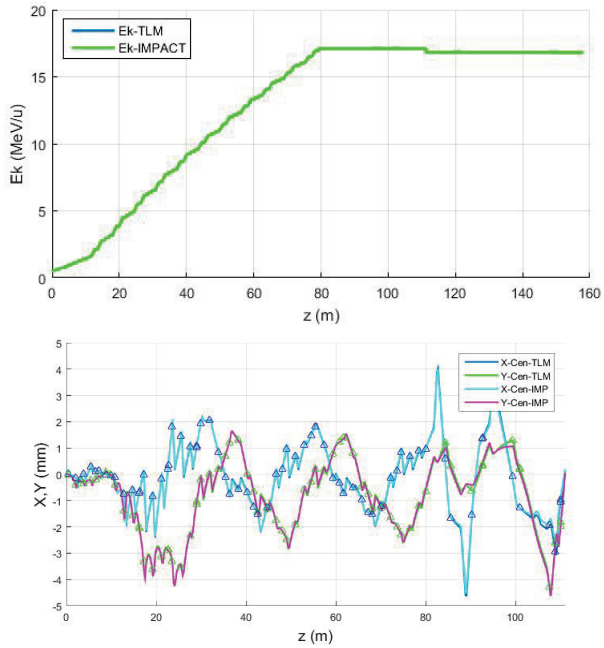

Figure 5: Benchmark results against IMPACT-Z of central beam trajectory (top) for LS1 segment, and beam energy for LS1 and FS1 segments (bottom).

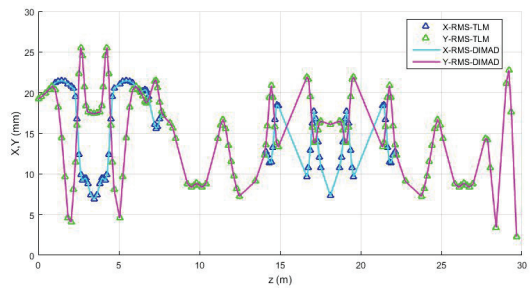

Figure 6: Benchmark results against DIMAD of X/Y envelope for FRIB FE using the lattice of Artemis IS.

into FRIB commissioning software framework, and the development of physics application has been started with the support of the online model.

ACKNOWLEDGMENT

The authors would thank our FRIB colleagues, especially M. Ikegami, S. Lund, E. Pozdeyev, J. Wei, Y. Yamazaki, Q. Zhao, Y. Zhang, for their helpful discussions and suggestions. They want to thank D. Bailey and Z. Zheng for providing the field maps for RF cavity and for electrostatic bend. They also would like to thank Prof M. Berz at MSU and his group for sharing the COSY code.

REFERENCES

[1] http://www.frib.msu.edu
[2] J. Wei et al, "FRIB Accelerator: Design and Construction Status", MOM1I02, proceedings of HIAT'15, Yokohama, Japan (2015)

ISBN 978-3-95450-136-6

[3] M. Ikegami, G. Shen, “Development Plan for Physics Application Software for FRIB Driver Linac”, MOPWI023, proceedings of IPAC15, VA, US (2015)

[4] Z. He et al., “An Analytical Cavity Model for Fast Linac-Beam Tuning”, TUPB058, proceedings of LINAC2012, Tel-Aviv, Israel (2012)

[5] Z. He et al., “Beam Dynamic Influence From Quadrupole Components in FRIB Quarter Wave Resonators”, MOPAB35, proceedings of HB2014, East-Lansing, MI, USA (2014)

[6] J. Qiang et al., Impact. In Proceedings of the 1999 ACM/IEEE conference on Supercomputing, page 55. ACM, 1999.

[7] Aslaninejad, M. et al "Solenoid fringe fields effects for the Neutrino Factory linac-MADX investigation." IPAC 10 (2010): 3963.

[8] Wollnik, Hermann. Optics of charged particles. Elsevier, 2012.

[9] E. Baron, G ANIL Report 79R/146/TF14

[10] Ziegler, James F., Matthias D. Ziegler, and Jochen P. Biersack. SRIM. Cadence Design Systems, 2008.

[11] Z. He et al., "Linear envelope model for multicharge state linac." Physical Review Special Topics-Accelerators and Beams 17, no. 3 (2014): 034001.

[12] R. Servranckx, K. Brown, L. Schachinger, and D. Douglas, “User’s Guide to the Program DIMAD”, SLAC Report 285, UC-28, May 1985.

ISBN 978-3-95450-136-6

MAXIMUM ENTROPY TOMOGRAPHY RECONSTRUCTION

Shuoyu Zheng, CIAE, Beijing, China
Y.-N. Rao, Thomas Planche, TRIUMF, Vancouver, Canada

Abstract

The goal of tomography is to reconstruct a higher dimensional distribution from a series of projections measured in a lower dimensional subspace. In the absence of large number of projections, the maximum entropy algorithm can reconstruct a distribution that maximizes the entropy and simultaneously reproduce all the measured projections exactly. The MENT algorithm [1] has been applied to the reconstruction of the transverse and longitudinal phase space distributions at particle accelerators. Only one- dimensional intensity profiles of different beam transfer matrices have to be measured. The article mainly completed the code for the tomographic reconstruction of the longitudinal phase space where non-linear transformations have to be taken into account, and finally introduced the test result of the real data taken from accelerator in TRIUMF for transverse tomography [3].

MAXIMUM ENTROPY TOMOGRAPHY

Tomography

We will only be dealing with 2-D distribution here. Let f(x,y) be the source distribution defined over an area. It satisfies

$$f(x,y) \geq 0 \quad and \quad \iint f(x,y)dxdy = 1 \qquad (1)$$

The projection P(x) of this distribution on the x-axis is defined by

$$\mathrm{P}(x) = \int_{-\infty}^{+\infty} f(x,y)dy \qquad (2)$$

The input data for tomographic reconstruction is a set of such projection onto N different s-axes defined by a set of transformation matrices

$$\begin{pmatrix} s \\ t \end{pmatrix} = R_i \begin{pmatrix} x \\ y \end{pmatrix} = \begin{pmatrix} a & b \\ c & d \end{pmatrix}_i \begin{pmatrix} x \\ y \end{pmatrix} \qquad (3)$$

The transformation matrix Ri can be a rotation matrix, used for real space reconstruction, or the beam transport matrices for reconstruction of phase space. It conserves the area of the source distribution because $\det(R_i)=1$. Using the inverse transformation from the ith projection coordinates (s,t) back to the source plane (x,y), The ith projection is represented as

$$P_i(s) = \int_{-\infty}^{+\infty} f[x_i(s,t), y_i(s,t)]dt \qquad (4)$$

The goal is to invert Eq. (4) and determine the function f(x,y). However, the inversion is not unique unless the number of projections I is infinite. For a finite number of the measurements, many different distributions exist that can reproduce all the measured projections. Out of these distributions, the one that has the maximum entropy and satisfies the boundary conditions of Eq. (4) is the most appropriate one, because it contains the least information.

Maximum Entropy Algorithm

In the thermodynamics entropy is defined as a measure of the multiplicity of system. For the continuous distribution f(x,y), the entropy is written as

$$\mathrm{E}(f) = -\int_{-\infty}^{+\infty}\int_{-\infty}^{+\infty} f(x,y)\ln f(x,y)dxdy \qquad (5)$$

For a system of a large number of particles, the most probable distribution will be the distribution of the highest entropy.

Taking into account the boundary conditions, the extended entropy function is written as

$$(f,\lambda) = E(f) - \sum_{i=1}^{I}\int_{-\infty}^{+\infty} \lambda_i(s)[P_i - f(x_i,y_i)dt]ds \qquad (6)$$

Where x_i and y_i are functions of s,t, and where the $\lambda_i(s)$ denotes the Lagrange multiplier functions. The conditions for the stationary solution are

$$\frac{\partial\varepsilon(f,\lambda)}{\partial\lambda_i} = 0 \quad and \quad \frac{\partial\varepsilon(f,\lambda)}{\partial f} = 0 \qquad (7)$$

The first condition in Eq. (7) is in fact equivalent to the constraints defined by Eq. (4), whereas the second one gives

$$-\ln[f(x,y)] - 1 + \sum_{i=1}^{I}\lambda_i = 0 \quad or \quad f(x,y) = \prod_{i=1}^{I} H_i \qquad (8)$$

Where the unknown Lagrange multipliers λ_i have been replaced by the equally unknown function $\mathrm{H_i} = \exp(\lambda_i - 1/N)$. The arguments of these functions are $\mathrm{s_i} = a_i x + b_i y$, completely determined by the projection. So, the task is merely to find these H-values for the equation.

Since the measured projections are received as discrete rather than continuous distributions, it's natural to formulate a binned projection as follows

$$\mathrm{G_{ij}} = \int_{s_{ij}}^{s_{i(j+1)}} P_i(s)ds = \int_{-\infty}^{+\infty}\int_{-\infty}^{+\infty} f(x,y)\Gamma_{ij}dxdy \qquad (9)$$

Where the coordinate transformation from (s,t) to (x,y) with Jacobian equal to 1 is applied, and $\Gamma_{ij}(j = 1,2,\ldots,J_i)$ denotes a characteristic function

$$\Gamma_{ij}(s) = \begin{cases} 1 & s_{ij} \leq s \leq s_{i(j+1)} \\ 0 & otherwise \end{cases} \qquad (10)$$

ISBN 978-3-95450-136-6

Therefore, Eq. (8) can be written as

$$f(x,y)=\prod_{i=1}^{I}\sum_{j=1}^{J_i}H_{ij}\Gamma_{ij} \tag{11}$$

Substituting Eq. (11) into Eq. (9) gives an iteration relation for the factors H_{ij}

$$G_{ij}=H_{ij}\int_{-\infty}^{+\infty}\int_{-\infty}^{+\infty}dxdy\Gamma_{ij}\left\{\prod_{k\neq i}^{I}\sum_{l=1}^{J_k}H_{kl}\Gamma_{kl}\right\} \tag{12}$$

So

$$Hij=\frac{G_{ij}}{\iint dxdy\Gamma_{ij}\{\prod_{k\neq i}^{I}\sum_{l=1}^{J_k}H_{kl}\Gamma_{kl}\}} \tag{13}$$

After the H-factors are computed, they can be substituted back into Eq. (11) to compute the distribution function f(x,y).

Longitudinal Phase Space Tomography

For longitudinal tomography, the final result we get is about ΔE and Δt

$$\begin{aligned}\Delta E &= \Delta E_i + qU_a(\cos(\phi)-\cos(\varphi_0))\\ &= \Delta E_i - qU_a\sin(\phi 0)(\phi-\phi 0)\\ &\quad -\frac{1}{2}qU_a\cos(\phi 0)(\phi-\phi 0)\,\hat{}\,2+\cdots\end{aligned} \tag{14}$$

where

$$\phi\text{-}\phi 0=2\pi f\Delta t$$

as we all know, Δt is not that easy to measure, but we can easily measure ΔE, if we use the tomography reconstruction, we can easily get the distribution of the ΔE and Δt.

TEST RESULTS FOR LONGITUDINAL TOMOGRAPHY

Test Resulto of Longitudinal Tomography for Short Bunches

For short bunches, the ΔE we test is between -0.1 keV~0.4 keV, the Δt is between -0.4 ps~0.4 ps. We test the tomography program using 12 projections. Figure 1 is the original figure. And we use 12 different transformed matrixes to transform the figure.

And after we get the transformed figures, we do projections on x axis, and we get 12 different projections and 12 transformed matrixes corresponding to the projections, and these are the data we input to the tomography program. Figure 2 is the reconstructed figure we get from tomography. This result matches pretty well with the original input figure.

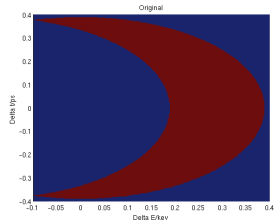

Figure 1: Original figure of short bunches.

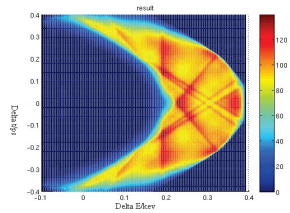

Figure 2: The reconstructed figure of short bunches.

Test Result of Longitudinal Tomography for Long Bunches

For long bunches, the ΔE we test is still between -0.1kev~0.4kev, but the Δt is between -40ps~40ps. As the same with the short bunches test, we still run the tomography using 12 projections. Figure 3 is the original figure. And we still use 12 different transformed matrixes to transform the figure. Figure 4 is the reconstructed figure we get from tomography. As we can see, this result match pretty well with the original input figure.

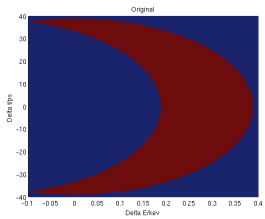

Figure 3: The original figure of long bunches.

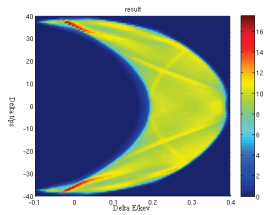

Figure 4: The reconstructed figure of long bunches.

Longitudinal Tomography for no Taylor Expansion

For real data, if the bunch of the particle is too long, then we cannot do Taylor expansion, because we do Taylor expansion of cos(phi) at phi0, and keep up to the 2nd order term of (phi-phi0) while omitting the other higher order terms. This implies that (phi-phi0) must be much smaller than 1 in magnitude, that means

$$\phi\text{-}\phi 0=2\pi f\Delta t<1$$

$$\Delta t=<\frac{1}{2\pi f}=\frac{1}{2\pi\times 0.0013\text{THz}}=122\text{ ps}$$

Therefore, when the bunch is too long, the Taylor expansion cannot be properly used. So I improve the code, and change the definition of the matrix, and change the code of coordinate transformation. And finally we succeed solving the problem. And there is no Taylor expansion for long bunch. And I test the code, and it can work perfectly and the result of reconstruction is nearly the same as above we test.

ISBN 978-3-95450-136-6

APPLICATION OF TRANSVERSE TOMOGRAPHY

The real data we taken from real machine is the viewscreen like Fig. 5, and we can change the work current of the magnet to change the shape of the beam bunches just like Fig. 6. We can use the viewscreen to record the different x-y shapes of the beam bunches.

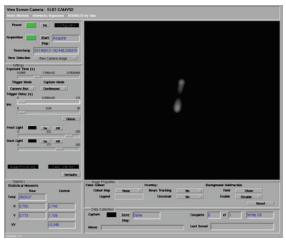

Figure 5: Viewscreen figure of bunches.

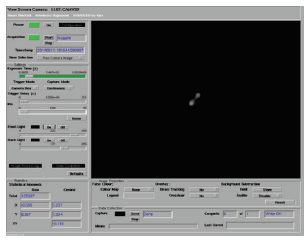

Figure 6: Viewscreen figure of bunches.

After processing the viewscreen figure, we can get the x-y figure of the beam. Then we can do projections on x axis and y axis. And the projections we input to the tomography are showed in Fig. 7 and Fig. 8

Figure 7 is projections on y axis, so we can use these data to get the result figure of y and y'. Figure 8 is projections on x axis, so we can use these data to get the result figure of x and x'.

Figures 9 and 10 are the results of y and y'. Figures 11 and 12 are the results of x and x'.

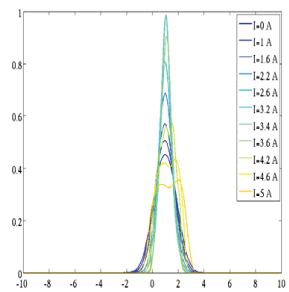

Figure 7: Projections on y-axis.

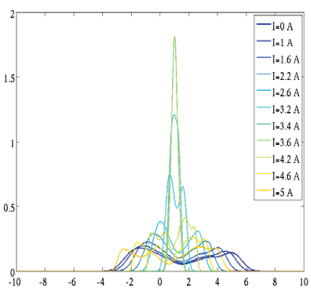

Figure 8: Projections on x-axis.

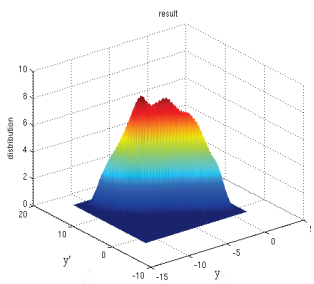

Figure 9: Results of y and y'.

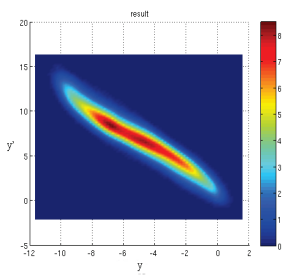

Figure 10: Results of y and y' (top view).

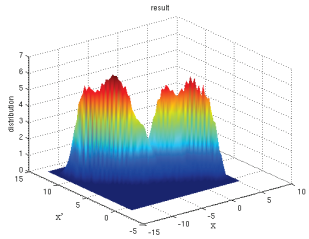

Figure 11: Results of x and x'.

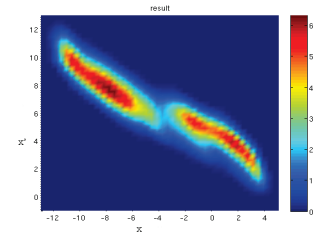

Figure 12: Results of x and x'(top view).

ACKNOWLEDGMENTS

The authors would like to thank J. Scheins from FZ Juelich and F. Loehl from DESY for kindly providing their MENT code.

REFERENCES

[1] G. Minerbo, MENT: A Maximum Entropy Algorithm for Reconstructing a Source from Projection Data, Computer Graphics and Image Processing, 10, 48-68, 1979.

[2] J.J. Scheins, Tomographic Reconstruction of Transverse and Longitudinal Phase Space Distributions using the Maximum Entropy Algorithm, TESLA Report 2004-08. 2004

[3] Ivan Tashev, Y.-N. Rao, R. Baartman, Program for Tomographic Reconstruction of Beam Distribution in Real Space, TRIUMF Design Note TRI-DN-07-29, October 17, 2007.

ISBN 978-3-95450-136-6

THE ELECTRO-MAGNETIC FIELD SIMULATION AND CAVITY DESIGN OF RIDGETRON FOR HIGH POWER ELECTRON IRRADIATION ACCELERATOR

Chunguang Li, Jinhai Li, Ziqiang Zeng, Shuoyu Zheng
China Institute of Atomic Energy, Beijing 102413, China

Abstract

Ridgetron is designed with a frequency of 100 MHz and electron energy of 10 MeV and power of 50 kW. It used for disinfection and sterilization of medical appliers. The electro-magnetic field simulation and cavity design of the Ridgetron is carried out by CST code. The influences of the cavity length, accelerating gap and electrode head on electric field and effective shunt impedance are analyzed, and cavity structure is determined. After that, we calculate the energy gain, analyse influence of different acceleration times on shunt impedance and energy gain. The results show that with the same cavity length, the more the acceleration times, the greater the shunt impedance, but the cavity diameter is greater too. Finally according to the objective of the design requirements, we optimize the accelerating times to obtain electron energy of 10 MeV.

APPLICATION OF IRRADIATION PROCESSING

Irradiation processing is the application of low-energy charged particle beam or x-rays produced by irradiation facility to deal with material. At present, irradiation processing is widely used in sterilization of medical supplies, food irradiation, environmental science, and high polymer material modification, etc. Especially in terms of disinfection and sterilization of medical and health supplies, irradiation is replacing conventional chemical disinfection methods. Electron irradiation accelerator is one of the vital devices of irradiation processing. The higher of irradiation accelerator power, the stronger of processing ability. As growing about 18% one year of irradiation processing industry, high-power irradiation accelerator is in great demand. For high-power irradiation device, there are Rhodotron [1, 2], 10 MeV/20 kW electron linac. This paper made a design of a high power electron accelerator called Ridgetron with working frequency of 100 MHz, output energy of 10 MeV and beam power of 50 kW. Ridgetron is first proposed by Japan [3, 4] with output energy of 2.5 MeV and beam power of 6.5 kW. But there was no more research after that.

RIDGETRON WORKING PRINCIPLE

Ridgetron is shown as Figure 1. The two same ridge are placed in a cylindrical cavity. Electron beam produced by electron gun is accelerated in the gap. After passing the channel, it is deflected 180 degrees by magnets and into another channel, accelerated again in the gap successively. it is extracted after passing the last channel. It is convenient to adjust output energy by controlling accelerating times.

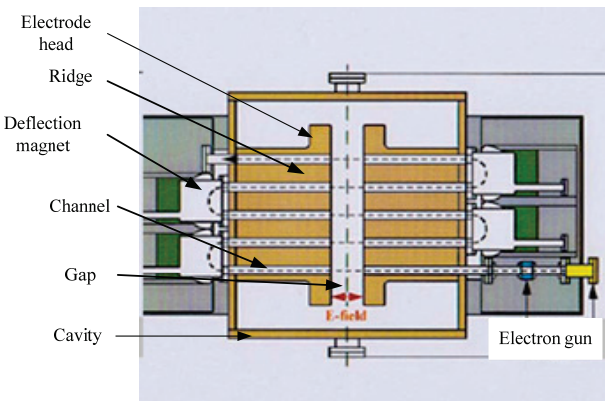

Figure 1: Working principle of Ridgetron.

Ridgetron's development is mainly divided into four parts including electromagnetic analysis, beam deflection system design, cooling system, and mechanical and electrical design, etc. This paper uses Microwave CST code to make electromagnetic analysis. Through simulation and analysis to determine structure parameters of cavity at the biggest shunt impedance, analyze influences of cavity structure on shunt impedance and optimize electrode head and acceleration times.

SIMULATION MODEL

The electric field distribution is shown as Figure 2, its excitation is TE110 mode. The electric field strength is the strongest in the gap and almost close to zero in other space. The magnetic field distribution is shown as Figure 3, it parallels round ridge board along the direction of the cavity length, and the magnetic field intensity is strong around ridge board and almost zero in the gap. Ridgetron working mode is π-π, so the length of trajectory between two adjacent gap is $\beta\lambda/2$.

*Work supported by NSTS (2014BAA03B01) and CNNC (FA14000104)
lichunguang246@163.com

ISBN 978-3-95450-136-6

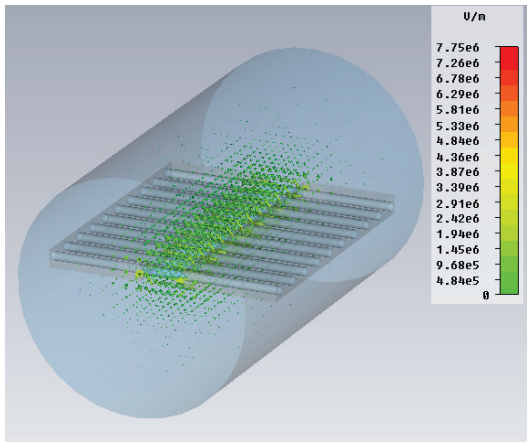

Figure 2: Ridgetron electric field distribution.

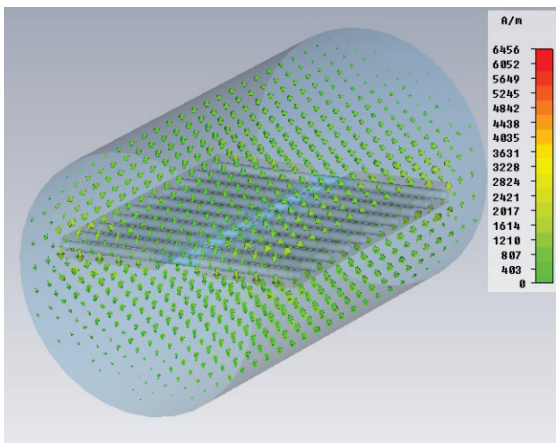

Figure 3: Ridgetron magnetic field distribution.

INFLUENT FACTORS' ANALYSIS OF SHUNT IMPEDANCE

There are several important factors that affect shunt impedance including cavity length, gap, electrode head. This section analyses influences of above factors on shunt impedance, to determine the cavity dimensions.

Figure 4 shows that as the length increases, shunt impedance increases and it is almost proportional with cavity length. Figure 5 shows that with the increase of gap, shunt impedance increases. But to meet the resonant frequency of 100 MHz, the greater the gap, the larger the cavity diameter. It is necessary to get a balance between shunt impedance and cavity dimension. Figure 6 shows that removing the electrode head can improve the shunt impedance at the same gap and cavity length. The electrode head helps to get uniform electric field in the gap [5, 6], to make sure the same energy gain per accelerating. If it has little influences on eventually energy gain, we can remove electrode head. So we have to analyse the influences of electrode head on energy gain.

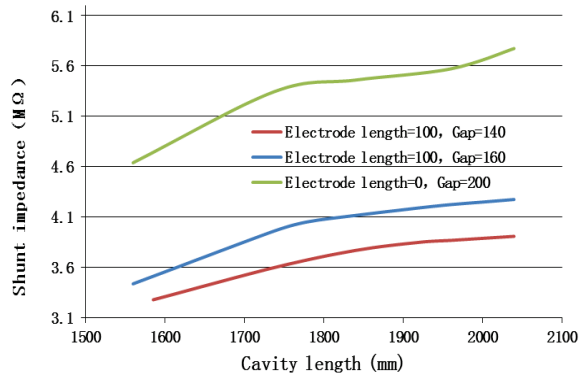

Figure 4: Influences of cavity length on the shunt impedance @f = 100 MHz.

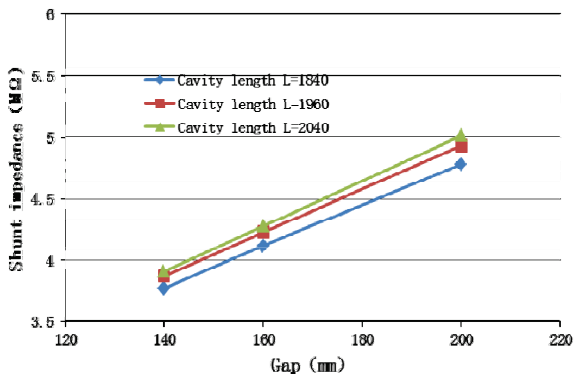

Figure 5: Influences of gap on the shunt impedance @f = 100 MHz, electrode length = 100 mm.

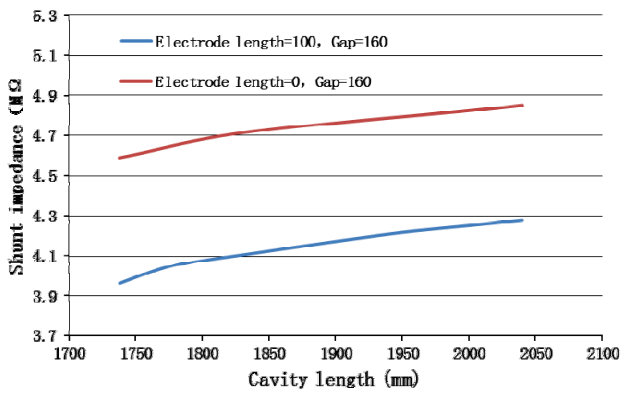

Figure 6: Influences of electrode head on the shunt impedance @f = 100 MHz.

Optimization of Electrode Head

This section makes a comparison of energy gain with electrode head and without. Electron beam is accelerated 10 times. The voltage in the gap is shown as Figure 7. It can figure out that with the same power loss, electron beam get more energy without electrode head. We make an integral of voltage in the gap, get the eventually energy gain of 5.2 MeV without electrode head and 4.74 MeV with electrode head.

ISBN 978-3-95450-136-6

Though electric field uniformity in the gap is bad without electrode head, the eventually energy gain is good. So we remove electrode head in our design.

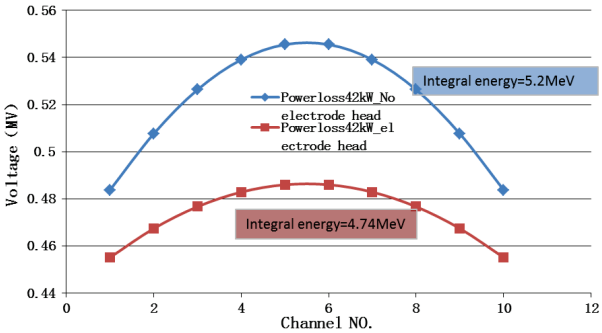

Figure 7: Voltage distribution in the gap in different channel @cavity length = 1960 mm, gap = 200, f = 100 MHz, power loss = 42 kW, distance_channel =120 mm.

Optimization of Acceleration Times

Through the above analysis, it shows that the shunt impedance is affected by cavity length with the same ridge length. Shunt impedance is larger with smaller proportion of ridge length to cavity, Ridge length is determined by acceleration times and distance between two adjacent channels. So we have to get short ridge as much as possible. Considering installing space and cooling structure, we set the distance between two adjacent channel 60 mm. Then we have to optimize acceleration times to make sure the final energy of 10MeV.

Acceleration times of 10, 14, 18, 20, 25 are taken into consideration. Power loss is 42 kW.

It can be figured out from Figure 8, when the cavity structure is determined, electron energy is higher with more acceleration times. We achieve 10.4 MeV after accelerating 20 times. So we set acceleration times to 20.

CONCLUSION

Shunt impedance is one of the important parameters. Large shunt impedance means low power loss. This paper gets Ridgetron structure with large shunt impedance by analyzing electromagnetic distribution, structure and energy. The largest shunt impedance is 5.77 MΩ with a cavity length of 2040 mm, gap of 200 mm, and an energy of 10.4 MeV at a frequency of 100 MHz

ACKNOWLEDGMENT

This work is support by National Science and Technology Support Program(NSTS) and China National Nuclear Corporation(CNNC).

REFERENCES

[1] A. Nguyen et al., Rhodotron's first operation, in; Pro. European Particle Accelerators Conf., Vol. 2, Nice, France (1990), pp. 1840.
[2] Y. Jongen et al., Nucl. Instr. and Meth. in Phys. Res. B 89 (1994), pp 60-64.
[3] N. Hayashizaki, T. Hattori, M. Odera, Nucl. Instr. and Meth. A 427 (1999) 28
[4] N.Hayashizaki et al., Nucl. Instr. and Meth. in Phys. Res. B 161-163 (2000)1159-1163.
[5] J .Pottier, Nucl. Instr. and Meth. B 40/41 (1989)943.
[6] K.G. Steffen, High-Energy Beam Optics, Interscience Monographs and Texts in Physics and Astronomy, vol.17, Wiley, New York, 1965, p.97

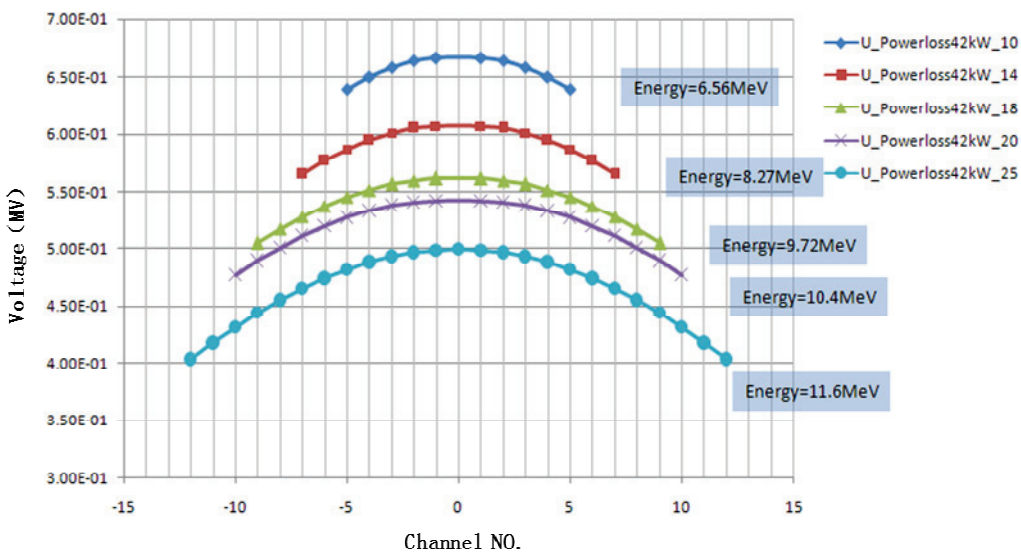

Figure 8: Voltage distribution at different acceleration times @cavity length = 2040 mm, gap = 200, f = 100 MHz, Total loss = 42 kW, distance_drift = 60 mm.

ISBN 978-3-95450-136-6

SIMULTANEOUS SIMULATION OF MULTI-PARTICLE AND MULTI-BUNCH COLLECTIVE EFFECTS FOR THE APS ULTRA-LOW EMITTANCE UPGRADE *

M. Borland, T. Berenc, L. Emery, R. Lindberg, ANL, Argonne, IL 60439, USA

Abstract

Next-generation storage ring light sources promise dramatically lower emittance due to the use of multi-bend achromat (MBA) lattices. The strong magnets required for such lattices entail small magnet and vacuum bores, which increases concerns about collective instabilities. In this paper, we describe detailed simulations undertaken for the APS MBA lattice using the parallel version of `elegant`. The simulations include short- and long-range geometric and resistive wakes, a beam-loaded main rf system including feedback, a passive harmonic bunch-lengthening cavity, higher-order cavity modes, and bunch-by-bunch feedback. Applications include insight into transients during filling, effects of missing bunches, evaluation of non-uniform fill patterns, and determination of feedback system requirements.

INTRODUCTION

Accurate modeling of instabilities is a challenging endeavor, yet it is vital if new accelerator designs are to deliver the expected performance. An example of a successful model of single-bunch effects in an existing ring is the impedance and instabilities model for the Advanced Photon Source (APS), a 7-GeV, third-generation storage ring light source. [1] Other noteworthy efforts are [2, 3].

Fourth-generation storage ring light sources are now being planned that will make use of multi-bend achromat lattices [4]. These lattices feature very strong quadrupoles and sextupoles, necessitating a significant reduction in the magnet bore and thus the vacuum bore radius r [5]. Since both geometric and resistive wakes scale like $1/r^2$ to $1/r^3$ [6], collective effects are expected to be more pronounced, although this is mitigated to some extent by the reduction in the beta functions. In the case of the proposed APS upgrade (APS-U) [7], the target single bunch current of 4.2 mA must be ensured (allowing 200 mA in 48 bunches). In addition, a passive higher-harmonic cavity (HHC) will be added to lengthen the bunch in order to reduce emittance growth due to intra-beam scattering and improve the Touschek lifetime. This cavity has difficult-to-determine implications for coupled-bunch instabilities [8]. Twelve of the 16 existing room-temperature 352-MHz rf cavities will also be retained. These considerations, coupled with the desire for a rapid return to user operations after the upgrade, motivate the creation of a model of collective instabilities that covers both single- and multi-bunch phenomena.

* Work supported by the U.S. Department of Energy, Office of Science, Office of Basic Energy Sciences, under Contract No. DE-AC02-06CH11357.

To be more specific, the model we have created encompasses (1) Storage ring single-particle dynamics including chromaticity, nonlinear momentum compaction, and synchrotron radiation. (2) Short-range geometric wakes. (3) Short-range resistive wakes. (4) Long-range (multi-turn) resistive wakes. (5) Beam-loading and rf feedback for the 12 main rf cavities. (6) Higher-order modes in the 12 main rf cavities. (7) Single-cell passive (i.e., beam-driven) higher-harmonic cavity. (8) Transverse and longitudinal bunch-by-bunch feedback.

MODELING METHODS

In this section, we briefly describe the modeling methods used for each of the simulation components in the context of modeling collective effects for APS-U.

Addition of collective effects to `elegant` [9] began in the early 1990s, when short-range impedances and rf cavity modes were included to model the APS Positron Accumulator Ring [10]. Coherent synchrotron radiation [11] and longitudinal space charge were added in the late 1990s and early 2000's for linac modeling for free-electron lasers, e.g., [12, 13]. A time-domain implementation of short-range wakes was also added (though it is equivalent to the frequency domain impedance). In the mid-2000's, these features appeared in the parallel version, `Pelegant`, [14, 15]. More recent additions include space-charge in rings [16], intrabeam scattering [17–19], and Touschek scattering [20,21], as well as more efficient simulation of long-range wakes and multi-bunch beams [19].

To control noise, modeling of collective effects requires many simulation particles. For the present case, the prominance of the microwave instability [22] motivates using at least 10,000 particles per bunch (10 kP/B). In addition, we must simulate all bunches to get accurate excitation of cavity modes, model feedback systems, etc., implying several million simulation particles in total. Given that the APS-U damping times are 3000~6000 turns, we must track for several tens of thousands of turns, and thus in excess of 10^{10} particle-turns. This would be very time-consuming if element-by-element modeling was performed. Hence, to the extent possible, both single- and multi-particle phenomena are simulated using lumped elements.

To accurately predict stability thresholds, simulations must include chromaticity, which can have a stabilizing effect. This is accomplished without element-by-element tracking using `elegant`'s `ILMATRIX` element, which computes a 6x6 linear matrix for each particle based on the particle's fractional momentum offset δ and transverse amplitudes. Path-length dependence on momentum, also im-

ISBN 978-3-95450-136-6

portant in collective effects, is supported up to third order in δ. `ILMATRIX` can model any periodic unit of the lattice, including the entire ring. In the present simulations, we use a full-ring method that includes chromaticity up to third order in δ and momentum compaction up to second order in δ. Lumped synchrotron radiation including quantum excitation is modeled using the `SREFFECTS` element.

Short-range geometric and resistive longitudinal and transverse wakes are modeled using the frequency-domain `ZLONGIT` and `ZTRANSVERSE` elements. The geometric wakes are computed using the programs GdfidL [23] and ECHO2D [24], while resistive wake potentials are computed using well-known analytical expressions [25]; These are added with appropriate weighting by the beta functions to obtain the total wake potential.

The longitudinal wake field is computed by convolving the longitudinal density with the wake potential. For transverse plane, dipole and quadrupole wakes are included. In brief, for a dipole wake the kick to a trailing particle depends on the longitudinal density of the leading particles weighted by their transverse position. For a quadrupole wake, the kick to a trailing particle depends on the longitudinal density of the leading particles multiplied by the transverse position of the *trailing* particle. For further details, see [1].

The long-range part of the resistive wall wake, defined as the part that acts on subsequent bunches or turns, is modeled using the `LRWAKE` element [19] This element is configured by time-domain wake potentials computed from analytical expressions [25]. It treats the bunches like point particles, which is a valid approximation since the space between bunches is large compared to the bunch lengths and since the long-range wake varies slowly over the length of a bunch. In the APS-U simulations, we used a long-range wake extending over 10 turns.

In addition to non-resonant short- and long-range collective effects, we must also include rf cavity modes. Beam-loading of resonant modes is modeled using the loss factor coupled with phasor addition, rotation, and damping. `elegant` models both monopole (accelerating) and dipole (deflecting) modes, using the `RFMODE` and `TRFMODE` elements, respectively. (For cavities with many modes, the `FRFMODE` and `FTRFMODE` elements are used, since they allow specifying the mode parameters in a separate SDDS file.) The monopole modes are modeled by first creating a histogram of the particle arrival times for the first bunch. Stepping through the histogram allows computing the voltage induced in the cavity by each beam slice, as well as the time-dependent cavity voltage within the bunch, which acts back on the bunch. Once the bunch has passed, the cavity phasor is propagated in a single step to the start of the next bunch using the cavity frequency and loaded Q. Dipole modes are handled in a similar fashion, except the histogram is weighted by the appropriate transverse coordinate of each particle.

Each APS rf cavity was constructed with a slightly different length in order to ensure that HOMs fell at slightly different frequencies, thus reducing the potential multi-bunch instability (MBI) growth rates. Since the exact frequencies for the HOMs for each cavity are not known, we use a Monte Carlo technique to randomize the frequencies and determine the growth rates for each configuration [8, 26]. We then selected one of these configurations that was expected, in the absence of feedback, to be unstable longitudinally but stable transversely.

For the main rf cavities, the generator and feedback system must be modeled in addition to the beam-induced voltage, as described in [27]. For the present simulations, the user-specifiable phase and amplitude feedback filters are configured to match the feedback systems in use today at APS.

The last component is the bunch-by-bunch transverse feedback (TFB) and longitudinal feedback (LFB), modeled using pairs of `TFBPICKUP` and `TFBDRIVER` elements. `elegant` allows specifying FIR filters for both signal processing (`TFBPICKUP`) and drive generation (`TFBDRIVER`). For the TFB, these are configured to mimic the existing APS system [28, 29].

The simulated LFB works by measuring the mean fractional momentum offset, $\langle\delta\rangle$, for each bunch, presumably via a BPM in a dispersion location, whereas a more common choice is to use bunch phase measurements. Such ϕ-LFB has several disadvantages compared to δ-LFB. The correcting kick cannot be delivered until 1/4 of a synchrotron oscillation after the measurement, which reduces the ability to damp fast instabilities. With δ-LFB, the feedback system can act promptly, before a significant fraction of a synchtron oscillation has occurred. In the presence of a harmonic cavity, the synchrotron tune is ill-defined and depends strongly on amplitude, so it is not clear how to design the filter for ϕ-LFB. Finally, in non-uniform fill patterns (e.g., while filling), ϕ-LFB will need a pattern- and current-specific setpoint for each bunch to compensate for phase slewing due to transient beam loading. This is not required in δ-LFB, since the equilibrium value of δ is always 0.

UNIFORM FILL PATTERNS

We start with results for the nominal uniform 48-bunch pattern proposed for APS-U. (A uniform 324-bunch pattern is also proposed, but will not be covered in this paper.) We simulated both with and without the bunch-by-bunch feedback systems.

The simulations require some care to avoid spurious instabilities from shock-excitation of the rf systems and beam. Hence, the simulated beam current is fictiously ramped from 0 to 200 mA over 5,000 turns. This provides time for the main rf cavity feedback system to respond and provide sufficient voltage. Following the ramp-up, another 7,000 turns are allowed for the beam to damp close to equilibrium parameters, after which the beam is kicked in the longitudinal and transverse planes to assess the ability of the feedback system to respond.

Tracking without feedback shows instability in *both* planes and significant beam loss, even prior to kicking the beam, as

ISBN 978-3-95450-136-6

illustrated in Fig. 1. It seems clear that feedback will be necessary. To confirm the feedback filter setup, we performed trial simulations with single-particle bunches, then tracked with 30 kP/B to confirm the results.

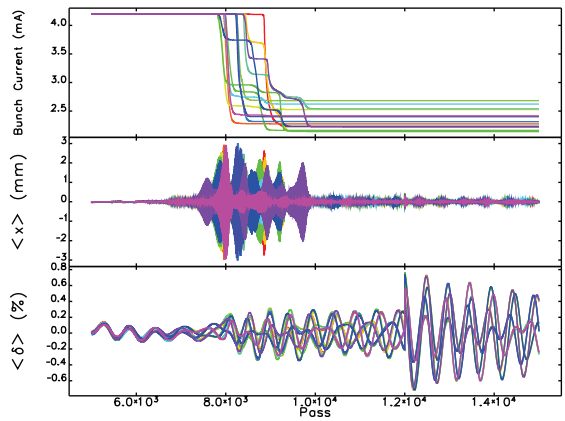

Figure 1: Multi-bunch instability resulting in beam loss in the absence of feedback. A selection of the 48 bunches is shown. See text for details. The beam is deliberately kicked at pass 12,000.

Turning on LFB alone is not sufficient to prevent instability. The cause appears to be the long-range transverse resistive wall wake, which is not covered by the mode-based analysis [8]. This was verified by removing first the transverse dipole modes, then the transverse long-range resistive wall wake. The former case still exhibited the instability, while the latter did not. This conclusion is confirmed by analysis of the bunch-by-bunch horizontal centroids for the unstable beam before particles are lost. This exhibits the expected horizontal tune signature [30], as shown in Fig. 2.

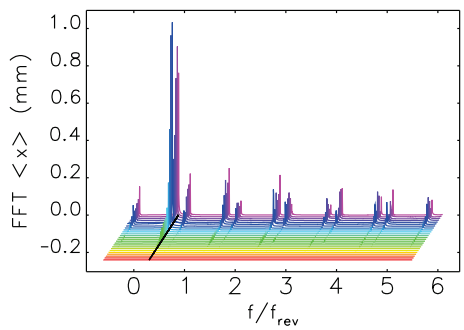

Figure 2: Evolution of Fourier transform of bunch-by-bunch horizontal centroids over 5000 turns, showing growth at $1 - \nu_x$ in the absence of transverse feedback.

With all effects included, the required peak (rms) feedback strength is 4.4 V (0.9 V) for horizontal, 1.6 V (0.3 V) for vertical, and 9.3 (2.6) kV for longitudinal. However, this is a relatively quiet situation and doesn't reflect the maximum effort that might be required from the feedback. Determining this requires looking at non-uniform fill patterns and transients during filling. As we'll see, it is possible to cap the longitudinal feedback strength and still preserve stability.

NON-UNIFORM FILL PATTERNS

Although uniform bunch patterns are the default, non-uniform patterns may be of value for some user programs. We've explored several alternatives in [31]. Here, we present a hybrid fill pattern created from the 48-bunch uniform pattern by removing two bunches on either side of a target bunch, creating an isolated bunch with twice the uniform gap on either side. Because of the low Q of the main rf cavities and the slow response of the main rf feedback, a voltage variation develops in the main rf cavities, causing the bunches to slew in phase. This impacts the induced voltage in the HHC and results in nonuniform lengthening of the bunches, as seen in Fig 3.

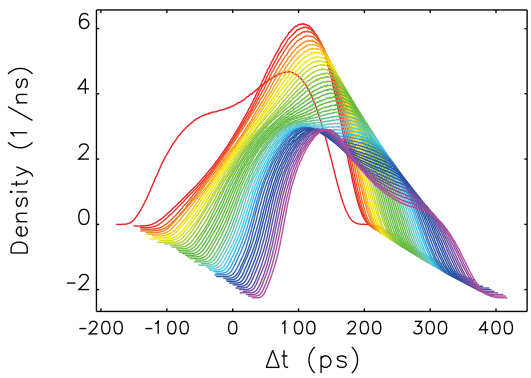

Figure 3: Bunch shapes for "1+45" hybrid mode pattern. Curves are offset in both dimensions for clarity. The isolated bunch is at the top.

As described above, the δ-based LFB employed in these simulations works without adjustment even in the case of nonuniform fill patterns. No stability issues are seen with LFB and TFB configured as for the uniform 48-bunch fill. With no strength limitations imposed and no disturbance to the beam, the peak (rms) feedback strength is 5.5 (1.0) V for horizontal, 0.5 (0.1) V for vertical, and 8.8 (2.4) kV for longitudinal. No particle losses are seen when limiting the longitudinal feedback strength to 1.8 kV (0.3 ppm of the 6 GeV beam energy). There is an increase in rms energy oscillation amplitude to 0.008%, which is negligible compared to the 0.1% energy spread of the beam. Reducing the strength cap to 0.1 ppm results in continuously growing longitudinal amplitude and partial beam loss.

IMPACT OF A LOST BUNCH

The injection method envisioned for APS-U is on-axis swap-out [32–34], which entails periodically extracting the weakest stored bunch and replacing it with a fresh, full-current bunch. It may well happen that a stored bunch will be extracted but the replacement bunch will not be injected. This will result in bunch phase, energy, and shape oscillations in the remaining bunches [31].

ISBN 978-3-95450-136-6

This could prove problematical for the LFB as it will attempt to damp the large transient phase oscillations resulting from such an event. If overwhelmed, the LFB may be unable to ensure stability and more beam loss may occur. If no limit is imposed, the LFB peak kick corresponds to 480 kV, which is about the same as a storage ring rf cavity. Limiting the kick to 6 kV (1 ppm of the beam energy) does not adversely impact stability, even though the feedback output is "railed" following the loss of the bunch. If the limit is reduced to 0.3 ppm (which worked for the 1+45 pattern just described), there is continuous growth of the longitudinal oscillation and ~50% beam loss. Figure 4 shows HOM voltage data for both cases along with the momentum centroid for one of the bunches.

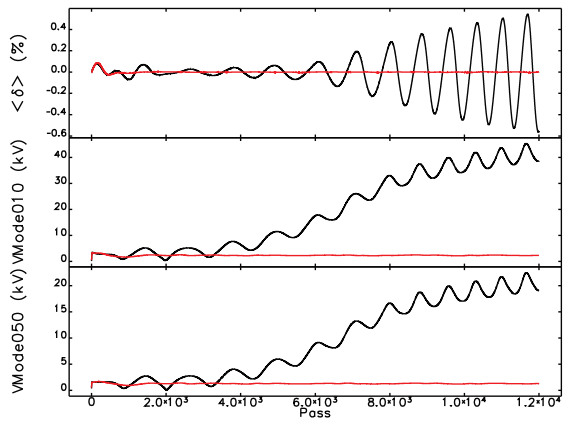

Figure 4: Centroid of bunch 0 (top) along with voltages in two monopole HOMs (923 MHz, 1.17 GHz), immediately following loss of one of 48 bunches. Black: LFB capped at 0.3 ppm. Red: LFB capped at 1 ppm.

SIMULATION OF FILLING FROM ZERO

Another situation in which transients may be important is when filling the ring from zero, particularly since on-axis injection requires injection of 15 nC shots. As in the case of a lost bunch, there will be transients whenever a new bunch is added. We previously simulated this [31] in the absence of bunch-by-bunch feedback and HOMs.

We simulated filling 48 bunches from zero using a "balanced" fill order to reduce transients [31]. The injection was accomplished using `elegant`'s `SCRIPT` element, which allows performing an essentially arbitrary periodic modification of the beam. In this case, at each injection time the beam is written to disk, modified by an external program, and then read back in for further tracking. A simple script using SDDS and Tcl/Tk was sufficient to add the next bunch with the appropriate time coordinates to simulate injection into a specific rf bucket.

Trial runs with 1 kP/B showed that the LFB strength was as high as 53 keV, which is about 15% of the voltage from one APS storage ring cavity. For production runs, we capped the LFB strength at 1 ppm (6 kV), which worked well in the simulations of a lost bunch reported in the previous section. To economize computer time, we used 10 kP/B and injected a new bunch every 5,000 turns (~18 ms), which is about one damping time. (The damping times, for reference, are 12, 20, and 14 ms in the horizontal, vertical, and longitidunal planes.) This is also about the response time (~ 20 ms) of the feedback on the main rf system.

Results show that without sufficient transverse feedback effort, the initial bunch is partially lost. The results depend somewhat on the number of particles used in the simulation: for 100 kP/B and above, a feedback cap of 60 nrad is consistent with full capture. If the cap is below this the initial bunch will suffer a ~30% loss. This continues for subsequent bunches with slowly decreasing losses. Eventually, all bunches are fully captured.

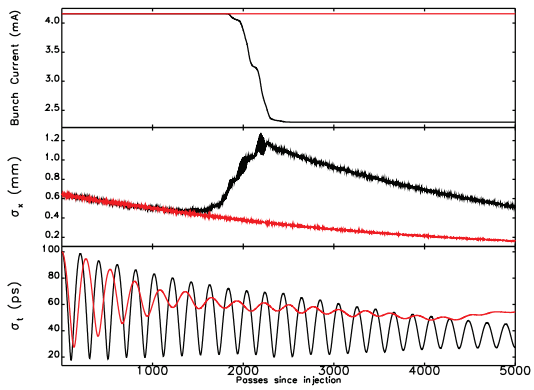

Figure 5: Turn-by-turn bunch current, bunch length, and bunch horizontal size for first (black) and 24^{th} bunches filled in a 48-bunch uniform fill, using 10,000 particles per bunch.

Although the required feedback effort is not a concern, it is interesting to simulate the behavior with marginal transverse feedback to understand the physics. As illustrated in Fig. 5, these losses apparently result from bunch-length oscillations that occur because of longitudinal mismatch of the injected bunch. As the early bunches tumble in the rf bucket in the absence of significant beam-driven harmonic-cavity voltage, they periodically become much shorter than normal, which amplifies the effect of the high-frequency part of the short-range dipole impedance. In particular, the horizontal beam centroid and size grow, resulting in particle loss. Inspection of the phase space data shows a clear head-tail instability, as shown in Fig. 6. As the harmonic cavity voltage builds up in response to the accumulation of beam, the minimum bunch length during these oscillations is increased, so the high-frequency part of the short-range impedance is not as influential.

The sensitivity of these results to the number of simulation particles suggests that the instability is seeded by noise. This implies that in a real system, jitter in the incoming beam position will be important. More simulations are planned to refine our understanding of this issue and the feedback requirements.

One possible solution is to fill in stages, i.e., fill to 100 mA in 48 equally-populated bunches, then to 200 mA by replac-

ISBN 978-3-95450-136-6

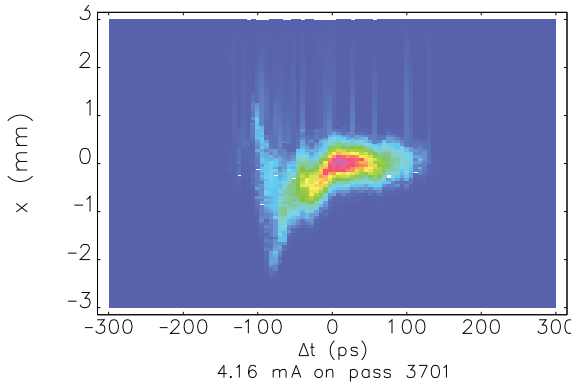

Figure 6: Tracking data from first injected bunch, showing head-tail instability.

ing each bunch with a bunch having twice the charge. With this approach we anticipate that the transients will be significantly reduced. Given that we intend injecting bunches at 1 Hz, this increases the fill time from 48 s to 96 s, which is a minor difference.

We modeled this using the same approach as described above, but with 10 kP per initial bunch and 20 kP per final bunch. We found no significant initial losses during the first pass of filling from 0 to 100 mA. Further, few losses were seen when replacing the damped 2.1 mA bunches with full-current 4.2 mA bunches. In one instance, injecting a bunch caused a loss in another previously-stored bunch, a phenomenon that remains to be understood.

CONCLUSIONS

Argonne is proposing to replace the APS storage ring with a multi-bend achromat lattice that would require much narrower vacuum chamber apertures. A sophisticated model of collective effects has been developed and is being used to understand issues related to single- and multi-bunch instabilities. The simulations include short-range longitudinal and transverse wakes, including the transverse quadrupole wakes; long-range resistive wall wakes; monopole and dipole resonant modes of the main cavities; beam-loading and rf feedback for the accelerating mode of the main cavities; a passively-driven higher-harmonic bunch lengthening cavity; and bunch-by-bunch feedback for the transverse and longitudinal planes.

So far, simulations have concentrated on the presumably more demanding few-bunch modes, primarily the 200-mA, 48-bunch uniform fill. Results include (1) The long-range transverse resistive wall impedance will result in beam loss in the absence of transverse feedback. (2) Non-uniform patterns, such as 1+45 hybrid mode, require considerable feedback effort to maintain longitudinal stability. (3) Even larger feedback effort is needed to prevent additional beam loss in the event of a failed swap out injection. (4) Filling from zero requires transverse feedback to suppress a horizontal head-tail instability. Filling to 100 mA in 48 bunches first, then going to 200 mA, will help reduce feedback strength requirements, although the latter do not appear onerous.

ACKNOWLEDGMENTS

Many of these simulations made use of the Blues cluster at Argonne's Laboratory Computing Resources Center.

REFERENCES

[1] R. Lindberg et al. *Proc. IPAC 2015*, 1822–1824 (2015).

[2] G. Bassi et al. *Proc. of IPAC 2012*, 1701 (2012).

[3] M. Klein et al. *Topical Workshop on Instabilities, Impedance and Collective Effects (TWIICE 2014)* (2014).

[4] D. Einfeld et al. *Proc. SPIE 2013*, 201–212 (1993).

[5] M. Borland et al. *J Synchrotron Radiation*, 21:912 (2014).

[6] K. Ng. *Physics of Intensity Dependent Beam Instabilities*. World Scientific (2005).

[7] M. Borland et al. *Proc. IPAC 2015*, 1776–1779 (2015).

[8] L. Emery et al. *Proc. IPAC 2015*, 1784–1786 (2015).

[9] M. Borland. ANL/APS LS-287 (2000).

[10] M. Borland. *PAC 1995*, 287 (1996).

[11] B. E. Carlsten et al. *Phys Rev E*, 51:1453 (1995).

[12] M. Borland. *PRSTAB*, 4:070701 (2001).

[13] Z. Huang et al. *PRSTAB*, 7:074401 (2004).

[14] Y. Wang et al. *AIP Conf Proc*, 877:241 (2006).

[15] Y. Wang et al. *Proc. PAC07*, 3444–3446 (2007).

[16] A. Xiao et al. *Proc. of PAC 2007*, 3456–3458 (2007).

[17] A. Xiao. *Proc. of Linac 2008*, 296–298 (2008).

[18] A. Xiao et al. *Proc. of PAC 2009*, 3281–3283 (2009).

[19] M. Borland et al. *Proc. IPAC 2015*, 549–552 (2015).

[20] A. Xiao et al. *Proc. of PAC 2007*, 3453–3455 (2007).

[21] A. Xiao et al. *Phys Rev ST Accel Beams*, 13:074201 (2010).

[22] K. Oide et al. 90-10, KEK (1990).

[23] W. Bruns. *Proc. of LINAC 2002*, 418–420 (2002).

[24] I. A. Zagorodnov et al. *Phys Rev ST Accel Beams*, 8:042001 (2005).

[25] A. Piwinski. CERN-HERA-92-11, CERN (1992).

[26] L. Emery. *Proc. of PAC 1993*, 3360 (1993).

[27] T. Berenc et al. *Proc. IPAC 2015*, 540–542 (2015).

[28] C. Yao et al. *Proc. of PAC 2007*, 440 (2007).

[29] C.-Y. Yao et al. *Proc. of IPAC 2010*, 2803 (2010).

[30] F. Sacherer. *9th Conf. on High Energy Accel.*, 347 (1974).

[31] M. Borland et al. *Proc. IPAC 2015*, 543–545 (2015).

[32] E. Rowe et al. *Part Accel*, 4.

[33] R. Abela. *Proc. EPAC 92*, 486–488 (1992).

[34] L. Emery et al. *Proc. of PAC 2003*, 256–258 (2003).

ISBN 978-3-95450-136-6

HYBRID METHODS FOR MUON ACCELERATOR SIMULATIONS WITH IONIZATION COOLING*

J. Kunz, Illinois Institute of Technology, Chicago, IL, USA
P. Snopok†, Illinois Institute of Technology, Chicago, IL, USA and Fermilab, Batavia, IL, USA
M. Berz, Michigan State University, East Lansing, MI, USA

Abstract

Muon ionization cooling involves passing particles through solid or liquid absorbers. Careful simulations are required to design muon cooling channels. New features are being developed for inclusion in the transfer map code COSY Infinity to follow the distribution of charged particles through matter. To study the passage of muons through material, the transfer map approach alone is not sufficient. The interplay of beam optics and atomic processes must be studied by a hybrid transfer map–Monte-Carlo approach in which transfer map methods describe the deterministic behavior of the particles, and Monte-Carlo methods are used to provide corrections accounting for the stochastic nature of scattering and straggling of particles. The advantage of the new approach is that the vast majority of the dynamics are represented by fast application of the high-order transfer map of an entire element and accumulated stochastic effects. The gains in speed are expected to simplify the optimization of cooling channels which is usually computationally demanding. Progress on the development of the required algorithms and their application to modeling muon ionization cooling channels is reported.

INTRODUCTION

A prime example of why matter-dominated lattices are relevant comes from the prospect of a neutrino factory or a muon collider [1]. As muon branching fractions are 100% $\mu^- \to e^- \bar{\nu}_e \nu_\mu$ and $\mu^+ \to e^+ \nu_e \bar{\nu}_\mu$, there are obvious advantages of a muon-sourced neutrino beam. Also, due to the fact that muons are roughly 200 times heavier than electrons, synchrotron radiation is not an issue, and as a result a high-energy muon collider ($\sqrt{s} \approx 6$ TeV) could be built on a relatively compact site where the collider ring is about 6 km in circumference. Such energy levels are experimentally unprecedented in the leptonic sector, since a circular electron accelerator would be restricted by vast amounts of synchrotron radiation. At lower energy, a muon collider could serve as a Higgs Factory ($\sqrt{s} \approx 126$ GeV), with possible new physics via the observation of Higgs to lepton coupling. This is advantageous since the Higgs coupling to leptons scales as mass squared.

However, muon-based facilities are not without their challenges. Synthetic muon creation comes from the collision of protons with a fixed target. The resultant spray of particles largely contains kaons (which decay primarily into pions and muons), pions (which decay primarily into muons), and rogue protons. High-intensity collection necessarily entails a large initial phase space volume. The resultant cloud of muons must be collected, focused, and accelerated well within the muon lifetime (2.2 μs at rest). Therefore, beam cooling (beam size reduction) techniques which are commonly used for protons and electrons cannot be used, as they are too slow. Ionization cooling technique [2], on the other hand, is fast enough to be relevant. The main idea is that muons traverse a certain amount of material where they lose energy in both longitudinal and transverse directions due to ionization. The energy is then restored in the longitudinal direction only by passing through a set of RF cavities, leading to an overall reduction in the transverse beam size (cooling). Schematically, this can be seen in Figure 1.

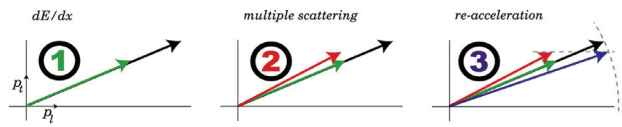

Figure 1: Ionization cooling schematics. 1) Energy loss in material, both transverse and longitudinal momenta are reduced. 2) Increase in the transverse momentum due to multiple scattering. 3) Re-acceleration through the RF cavity resulting in the net reduction in the transverse momentum.

The evolution of the normalized transverse emittance in the cooling channel can be described by the following equation [3]:

$$\frac{d\epsilon_n}{dz} \approx -\frac{1}{\beta^2}\langle\frac{dE_\mu}{dz}\rangle\frac{\epsilon_n}{E_\mu} + \frac{1}{\beta^3}\frac{\beta_\perp E_s^2}{2E_\mu mc^2 X_0}, \qquad (1)$$

where ϵ_n is the normalized emittance, z is the path length, E_μ is the muon beam energy, $\beta = v/c$ is the reduced velocity of the beam, X_0 is the radiation length of the absorber material, $\beta_\perp$ is the transverse betatron function, and E_s is the characteristic scattering energy. Here, two competing effects can be seen: the first term is the cooling (reduction of phase space beam size) component from ionization energy loss and the second term is the heating (increase of phase space beam size) term from multiple scattering. This highlights the importance of the stochastic terms, as the only deterministic term is the expected (Bethe-Bloch) energy loss, $\langle\frac{dE_\mu}{dz}\rangle$. It can also be seen that in order to minimize unavoidable heating from multiple scattering, low-Z materials with large radiation length X_0 are preferred, such as liquid hydrogen or lithium hydride; and $\beta_\perp$ has to be small.

For a neutrino factory only a modest amount of cooling is required, predominantly in the transverse plane. However,

* Work supported by the U.S. Department of Energy
† psnopok@iit.edu

ISBN 978-3-95450-136-6

neutrino factories could benefit from full six-dimensional cooling, where in addition to the transverse cooling emittance exchange is used to reduce longitudinal beam size in addition to transverse. Current muon collider designs assume significant, $O(10^6)$ six-dimensional cooling. An example of a cooling cell layout is shown in Fig. 2.

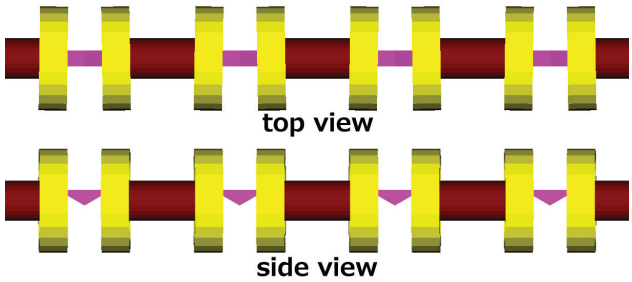

Figure 2: Cell schematics of a rectilinear vacuum RF six-dimensional cooling channel. Yellow: tilted magnetic coils producing solenoidal focusing and bending (to generate dispersion necessary for emittance exchange) fields; purple: wedge absorbers for ionization cooling, red: RF cavities for re-acceleration.

Cooling channels required for a high-energy high-luminosity muon collider could be up to a thousand meters long. Designing, simulating and optimizing performance of those channels involves using high-performance clusters and multi-objective genetic optimizers. Typically, the codes used for simulations belong to the class of particle-by-particle integrators, where each particle is guided through the length of the cooling channel independently. That takes its toll on genetic optimizers, especially with a large number of particles per run. Transfer map methods could solve this problem, since the nonlinear map of the system is calculated once, and then can be applied to any number of particles at very low computational cost. On the other hand, the transfer map approach alone is not sufficient to study the passage of muons through material. This study is an attempt to implement hybrid transfer map–Monte-Carlo approach in which transfer map methods describe the deterministic behavior of the particles, and Monte-Carlo methods are used to provide corrections accounting for the stochastic nature of scattering and straggling of particles. The advantage of the new approach is that the vast majority of the dynamics are represented by fast application of the high-order transfer map of an entire element and accumulated stochastic effects.

COSY INFINITY

COSY Infinity (COSY) [4] is a simulation tool used in the design, analysis, and optimization of particle accelerators, spectrographs, beam lines, electron microscopes, and other such devices, with its use in accelerator lattice design being of particular interest here. COSY uses the transfer map approach, in which the overall effect of the optics on a beam of particles is evaluated using differential algebra. Along with tracking of particles through a lattice, COSY has a plethora of analysis and optimization tools, including computation of Twiss parameters, tunes and nonlinear tune shifts, high-order nonlinearities; analysis of properties of repetitive motion via chromaticities, normal form analysis, and symplectic tracking; analysis of single-pass systems resolutions, reconstructive aberration correction, and consideration of detector errors; built-in local and global optimizers; and analysis of spin dynamics.

COSY is particularly advantageous to use when considering the efficient use of computational time. This is due to the transfer map methods that COSY employs. Given an initial phase space vector Z_0 at s_0 that describes the relative position of a particle with respect to the reference particle, and assuming the future evolution of the system is uniquely determined by Z_0, we can define a function called the transfer map relating the initial conditions at s_0 to the conditions at s via $Z(s) = \mathcal{M}(s_0, s) * Z(s_0)$. The transfer map formally summarizes the entire action of the system. The composition of two maps yields another map: $\mathcal{M}(s_0, s_1) \cdot \mathcal{M}(s_1, s_2) = \mathcal{M}(s_0, s_2)$, which means that transfer maps of systems can be built up from the transfer maps of the individual elements. Computationally this is advantageous because once calculated, it is much faster to apply a single transfer map to a distribution of particles than to track individual particles through multiple lattice elements.

Currently supported elements in COSY include various magnetic and electric multipoles (with fringe effects), homogeneous and inhomogeneous bending elements, Wien filters, wigglers and undulators, cavities, cylindrical electromagnetic lenses, general particle optical elements, and *deterministic* absorbers of intricate shapes described by polynomials of arbitrary order, with the last element being of particular interest for this study. The term *deterministic* is deliberately emphasized, since the polynomial absorber acts like a drift with the average (Bethe-Bloch) energy loss. The advantage of this is that the user must only specify six material parameters in order for COSY to calculate this energy loss: the atomic number, atomic mass, density, ionization potential, and two correction parameters. However, this element only takes into account deterministic effects (producing the same final result every time for a given initial condition), not stochastic effects (intrinsically random effects such as multiple scattering and energy straggling).

In order to carefully simulate the effect of the absorbers on the beam, one needs to take into account both deterministic and stochastic effects in the ionization energy loss. The deterministic effects in the form of the Bethe-Bloch formula with various theoretical and experimental corrections fit well into the transfer map methods approach, but the stochastic effects cannot be evaluated by such methods. It is easy to see why this is so. As previously stated, a transfer map will relate initial coordinates to final coordinates. This is generally a one-to-one relation. In other words, a transfer map is based on the *uniqueness* of the solutions of the equations of motion. However, stochastic effects such as scattering provide no uniqueness because, for example, Coulomb scattering is based on the probabilistic wave nature of the particle.

ISBN 978-3-95450-136-6

Therefore, two particles with identical initial coordinates will likely yield two very different final coordinates. Since the initial coordinates cannot uniquely be related to the final coordinates, no exact map exists.

Therefore, to take into account stochastic effects the transfer map paradigm needs to be augmented by implementing the corrections from stochastic effects directly into the fabric of COSY. Some of the fundamental ideas of the process were presented in [5] in application to quadrupole cooling channels, but the approximations used there were fairly basic. In this work, a more rigorous theoretical approach is presented along with the resulting validation.

STOCHASTIC PROCESSES

The stochastic processes of interest are straggling (fluctuation about a mean energy loss), angular scattering, transverse position corrections, and time-of-flight corrections (corresponding to the longitudinal position correction). The general outline to simulate these four beam properties is discussed and benchmarked against two other beamline simulation codes, ICOOL [6] and G4Beamline [7], and (in the case of angular scattering) against experimental data obtained by MuScat [8]. The simulation followed the beam properties cited in [8], which were a pencil beam with an iinitial momentum of 172 MeV/c through 109 mm of liquid hydrogen (LH) with cylindrical geometry. The step sizes for ICOOL and G4Beamline were chosen to be a modest 1 mm in order to ensure a quality simulation. The step size for COSY was chosen as the entire cell (109 mm), since its algorithms are largely insensitive to step sizes, as will be shown later. The simulations shown here were conducted with 5,000,000 particles through liquid hydrogen.

Straggling

As the momentum range of interest is 50–400 MeV/c through low Z materials, only ionization effects contribute to the mean energy loss. As such, Landau theory accurately describes the energy loss spectra, having the form [9]

$$f(\lambda) = \frac{1}{\xi} \cdot \frac{1}{2\pi i} \int_{c+i\infty}^{c-i\infty} \exp(x \ln x + \lambda x) dx, \qquad (2)$$

where $\xi \propto Z\rho L/\beta^2 A$, and $\lambda \propto dE/\xi - \beta^2 - \ln \xi$. Here, Z, A, and ρ are the atomic charge, atomic mass, and density of the material; L is the amount of material that the particle traverses; $\beta = v/c$; and dE is the fluctuation about the mean energy. The algorithm based on Eq. (2) has been implemented in COSY, and the results of comparison between COSY, ICOOL, and G4beamline for one particular material and muon momentum are shown in Fig. 3.

Angular Scattering

The derivation of the scattering function $g(u)$ (where $u = \cos\theta$) is done separately for small angles and large angles. For small angles, the shape is very nearly Gaussian in θ [10]. For large angles, the distribution follows the Mott scattering cross section, and is Rutherford-like [11]. The

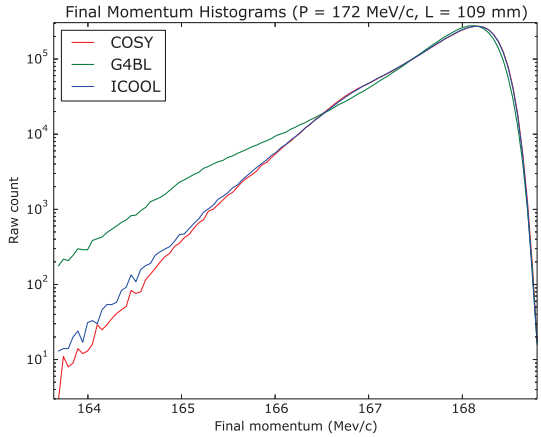

Figure 3: Straggling comparison between COSY (red), G4Beamline (green), and ICOOL (blue) for muons with the initial momentum of $P = 172$ MeV/c passing through 109 mm of liquid hydrogen.

resulting peak and tail are continuous and smooth at some critical u_0, which yields the final form of $g(u)$:

$$g(u) = \begin{cases} \exp\left(-\frac{1}{2}\frac{1-u}{1-u_\sigma}\right) & | \; u_0 < u \\ \zeta \cdot \frac{1 + \frac{1}{2}(\beta\gamma)^2(1+u-b)}{(1-u+b)^2} & | \; u \le u_0 \end{cases}. \qquad (3)$$

Here the parameters ζ and b are chosen to ensure continuity and smoothness. The familiar terms take their usual meaning: $\beta = v/c$ and $\gamma = 1/\sqrt{1-\beta^2}$; u_0 is a fitted parameter, and was chosen as $u_0 = 9u_\sigma - 8$; u_σ is the σ-like term for a Gaussian in θ. It is another fitted parameter based off [12] and takes the form

$$u_\sigma = \cos\left(\frac{13.6\text{ MeV}}{\beta pc}\left(\frac{L}{L_0}\left(1 + 0.103\ln\frac{L}{L_0}\right) + \right.\right.$$
$$\left.\left. +0.0038\left(\ln\frac{L}{L_0}\right)^2\right)^{\frac{1}{2}}\right).$$

The algorithm based on Eq. (3) has been implemented in COSY, and the results of comparison between COSY, ICOOL, and G4beamline for one particular material and muon momentum are shown in Fig. 4.

Transverse Position Corrections

Since there occur multiple scatterings in a given medium, one must account for the transverse position correction. A good starting point for these considerations is in [13]. If the scattered angle θ is known then the transverse displacement correction is generated from a Gaussian distribution with mean μ_T and standard deviation σ_T. These are chosen as

$$\mu_T = \frac{\theta \rho_c L}{\mu_w},$$

ISBN 978-3-95450-136-6

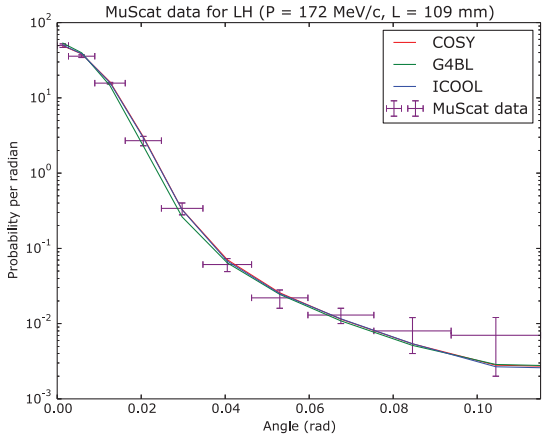

Figure 4: Angular scattering comparison between COSY (red), G4Beamline (green), ICOOL (blue), and the data points from [8] (purple) for muons with the initial momentum of $P = 172$ MeV/c passing through 109 mm of liquid hydrogen.

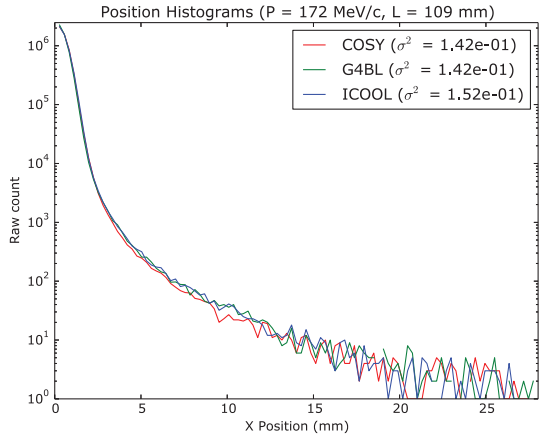

Figure 5: Transverse position comparison between COSY (red), G4Beamline (green), and ICOOL (blue) for muons with the initial momentum of $P = 172$ MeV/c passing through 109 mm of liquid hydrogen.

$$\sigma_T = \max\left(L\theta_\sigma\sqrt{\frac{1-\rho_c^2}{3}}, \left|\frac{LP_T/P_Z}{\sigma_w}\right|\right),$$

where $\rho_c = \sqrt{3}/2$ is the correlation coefficient; θ_σ corresponds to the aforementioned u_σ; P_T and P_Z are the particle's transverse and longitudinal momenta, and $\mu_w = 1+\sqrt{3}/2$ and $\sigma_w = 6$ are adjustable parameters. It should be further noted that μ_T must be given the proper sign, i.e. the same sign as the desired transverse momentum. Additionally, this fluctuation assumes an initially straight trajectory in the lab frame, and hence must be rotated accordingly and added to the mean (deterministic) transverse position deflection.

The results of comparison between COSY, ICOOL, and G4beamline for one particular material and muon momentum are shown in Fig. 5.

Perhaps more important than the raw histogram is the transverse phase space, see Fig. 6. This is because, for example, the raw histogram is insensitive to the σ_T changes, which describe the transverse position spread given a particular scattering angle.

Time-of-Flight Corrections

When particles traverse matter, the deterministic 'straight' path length differs from the 'true' path length due to many multiple scatterings within the material. The cases of straggling, angular scattering, and transverse position correction are largely insensitive to this. However, as the time-of-flight for these purposes is on the order of 1 ns for a single absorber, the true pathlength correction must be taken into account. Reference [14] gives a good approximation to the true path length t given the straight path length L and the scattered angle θ:

$$t = \frac{2L}{1+\cos\theta}.$$

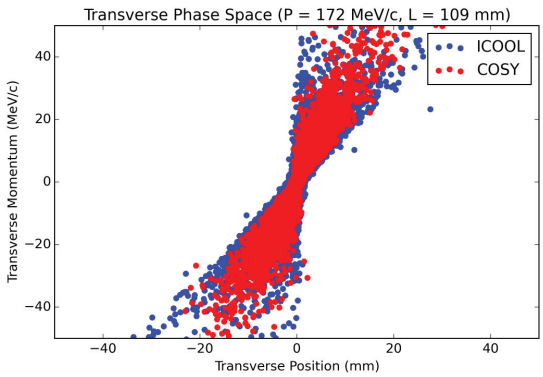

Figure 6: Transverse phase space comparison between COSY (red) and ICOOL (blue) for muons with the initial momentum of $P = 172$ MeV/c passing through 109 mm of liquid hydrogen.

Similar to the transverse position, the time-of-flight corrections have important implications for the overall shape of the longitudinal phase space, see Fig. 7.

SUMMARY

The addition of stochastic processes in COSY Infinity for the use of muon ionization cooling has been largely successful. While the straggling data in Fig. 3 agrees well with ICOOL, there is some discrepancy in the tail when compared to G4Beamline. This may be due to several factors which can be found in the physics reference manual of Geant4 [15] on which G4beamline is based. For example, the straggling model of Geant4 takes into account the cross sections for ionization and for excitation, whereas the Landau theory used in COSY only regards the ionization cross section. Moreover, Geant4 uses a synthetic width correction algorithm to the curve, which is not elaborated in detail in the manual. For future improvements, it is expected that COSY will use

ISBN 978-3-95450-136-6

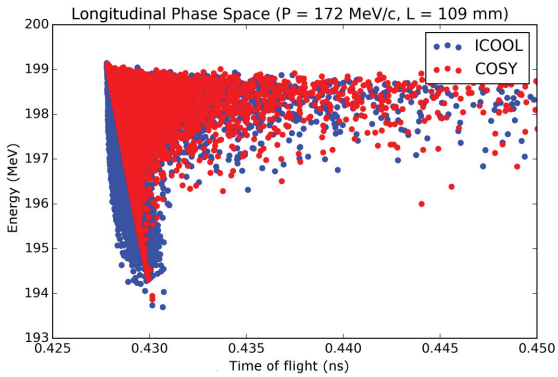

Figure 7: Longitudinal phase space comparison between COSY (red) and ICOOL (blue) for muons with the initial momentum of P = 172 MeV/c passing through 109 mm of liquid hydrogen.

the more general Vavilov theory [16], which converges to Landau theory for large energies or low absorber lengths.

The angular scattering algorithms appear to be functioning properly, as seen in Fig. 4. This is likely because ICOOL uses the Fano model with a Rutherford limit and G4Beamline uses the Urbán model, which also has a Rutherford tail. Then all of these codes agree that there should be some Gaussian-like behavior pieced together with a Rutherford tail. While not shown, it is reported here that good agreement has been achieved between COSY and other sets of data from MuScat [8] (i.e. 159 mm of liquid hydrogen, 3.73 mm of beryllium).

The transverse position histogram in Fig. 5 also shows that the algorithms in place appear to be largely in agreement with both ICOOL and G4Beamline. However, the phase space plot in Fig. 6 shows that COSY appears to be narrow. This may be misleading, since the discrepancy is not between the bulk of the data but rather the lengthy tails. A better parameterization of μ_T and σ_T could improve the agreement.

Similarly, the longitudinal phase space appears to agree fairly well between COSY and ICOOL. The discrepancy is on the order of 0.002 ns (roughly 0.5% of the mean time-of-flight). While the agreement is good, there can still be improvements made, possibly in the approximation of the true path length.

REFERENCES

[1] Muon Accelerator Program, http://map.fnal.gov/

[2] V. Parkhomchuk and A. Skrinsky, 12th Int. Conf. on High Energy Accel. (1983), p. 485, see also AIP Conf. Proc 352 (1996), p. 7

[3] Neuffer, D. (1983) Principles and Applications of Muon Cooling, *Part. Acc. 14,* p. 75

[4] K. Makino, M. Berz, COSY INFINITY Version 9, *Nuclear Instruments and Methods* **A558** (2005) 346-350, see also http://www.cosyinfinity.org

[5] D. Errede *et al.* Stochastic processes in muon ionization cooling, *NIM A,* 519 (2004) 466–471

[6] R. C. Fernow *et al.*, ICOOL Simulation Code,http://www.cap.bnl.gov/ICOOL/

[7] T. Roberts, G4beamline, http://www.muonsinternal.com/muons3/G4beamline

[8] D. Attwood *et al.* (2006), The scattering of muons in low-Z materials, NIM B251, p. 41

[9] L. Landau, On the Energy Loss of Fast Particles by Ionisation, J. Phys 8, p. 201

[10] S. Goudsmit and J. L. Saunderson (1940), Multiple Scattering of Electrons, Phys. Rev. 57, p. 24

[11] D. Griffiths (2008) Introduction to Elementary Particles, 2nd Ed.

[12] V. Highland, Some Practical Remarks on Multiple Scattering, NIM 129, p. 497

[13] J. Beringer *et al.* (PDG) (2013) PR D86, 010001 Ch. 31

[14] A. Bielajew and D.W.O. Rogers (1987) PRESTA: The Parameter Reduced Electron-Step Transport Algorithm for Electron Monte Carlo Transport, NIM B18 p. 165

[15] Geant4 User Documentation, http://geant4.cern.ch/support/userdocuments.shtml

[16] P. V. Vavilov (1957), Ionization Losses of High-Energy Heavy Particles, J. Exptl. Theoret. Phys. (U.S.S.R.) 5, p. 920

ISBN 978-3-95450-136-6

STRESS AND STRAIN ANALYSIS OF THE 10 MeV CYCLOTRON MAGNET

S.Sabounchi, H. Afarideh, R. Solhju, M.R. Asadi,
Energy engineering and physics department, Amirkabir University of Technology, Tehran, Iran
J.S. Chai, M. Ghegherehchi,
SKKU School of Information and Communication Engineering, Suwon, Republic of Korea

Abstract

In cyclotrons the heaviest part of the machine, is magnet system. In the 10 MeV cyclotron which is under construction At AmirKabir University of technology AISI 1010 is used for material because of its magnetic properties. AISI 1010 has got medium mechanical strength among steels. In detail engineering design for magnet system of 10 MeV cyclotron in amirkabir University of technology, because of drilling locations for joints and bolts and weight of magnet system, which is concentrated of specific parts, stress and strain analyze of some parts played an important role in insurance of mechanical stability of system. In this paper an attempt has been done for stress and strain simulation on detailed design of Magnet system for 10 MeV cyclotron using Ansys and Solidworks.

INTRODUCTION

The 10 MeV cyclotron which is under construction at AmirKabir university of technology for medical propose, is a compact AVF cyclotron. In this machine all parts specially magnet, are embedded in specific way in order to be compact [1]. In Table 1 parameters of magnet can be seen.

Table 1: Magnet Parameters

Parameter	Value
Material	AISI 1010
Weigh of one yoke System	5624 kg
Total number of pins	11
Total number of bolts	48
Type of bolts	M 10
Tensile strength: Yield (proof)	200 MPa

For insuring the stability of joints and bolts, stress and strain an analysis has been done on magnet structure. In Figure 1 magnet structure be shown. For simulation of stress and strain all parts modeled by solid works and Ansys workbench static structure has been used for simulation.

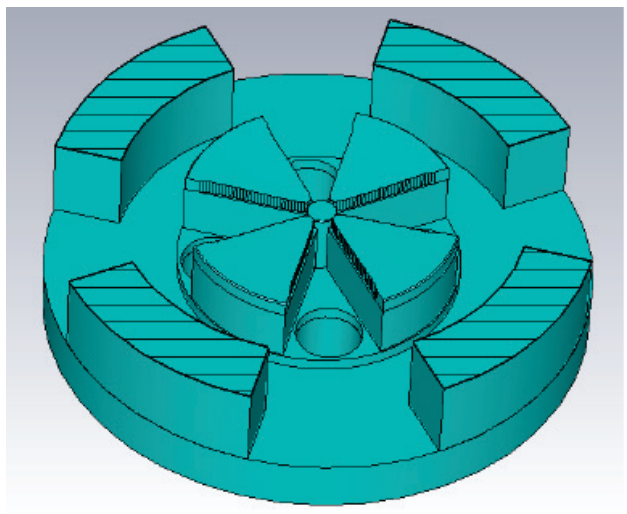

Figure 1: Magnet structure for the 10 MeV cyclotron.

In the structure of this magnet, there is a crucial part which joint poles to yokes, it is called extra part. In fact extra part is critical in way of stress and strain because it endures weight of all part except yokes and it is proportionally thin. In Figure 2 extra part can be seen.

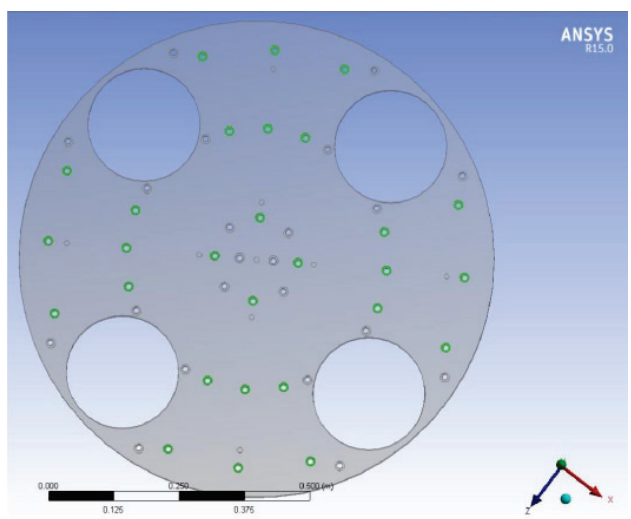

Figure 2: Extra part with drilling points.

As can be seen in Figure 2, there are some drilling points in extra part which can make it more [2].

ISBN 978-3-95450-136-6

SIMULATION

For simulation this structure all parts modeled in solid works and equivalent forces which caused by weight of RF Cavity and other parts applied of each structure. By considering priority of forces and weight all parts analyzed. Ansys static structure has been used for this simulation and because of applying details and considering all points, accuracy of simulation is significant. First step after providing geometry in Ansys is meshing [3]. Also suitable meshing can contribute proper simulation. For these simulations, an attain has been done in order to reach high quality of meshing as much as possible. In Figure 3 and Table 2, mesh characteristic for extra part can be seen.

Table 2: Mesh Characteristic for Extra Part

Parameter	Value
Method	Hex dominant
Total number of elements	383265
Total number of nodes	1523653
Maximum Aspect ratio	56
Average aspect ratio	1.325
Maximum skewness	0.86
Average skewness	0.3

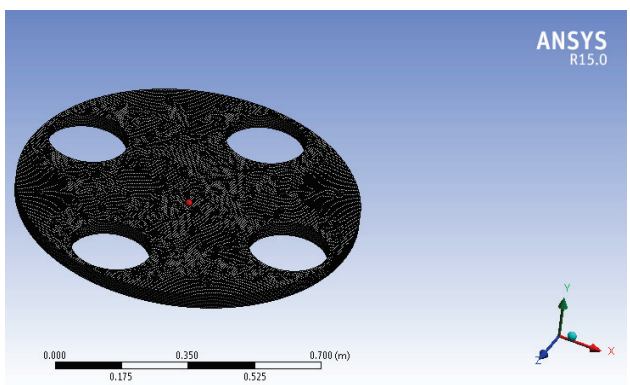

Figure 3: High quality meshing for extra part.

In Figure 4, Figure 5 and Figure 6 stress and strain distribution in magnet of the 10 MeV cyclotron is shown.

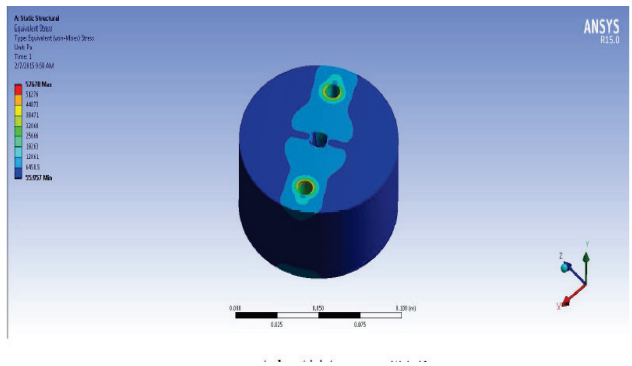

Figure 4: Stress distribution in central plug.

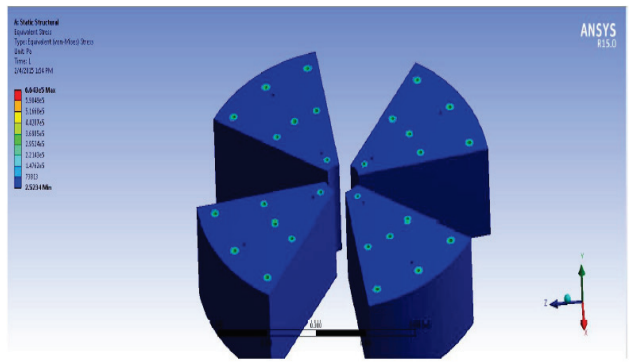

Figure 5 : Stress distribution in poles.

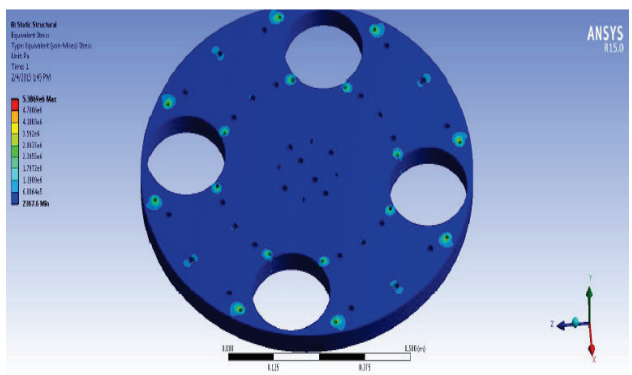

Figure 6: Stress distribution in extra part.

Because of the importance of extra part in structure stability of magnet system and accuracy of assembling, evaluating of total deformation in extra part is also essential. In Figure 7, deformation distribution in extra part is shown.

ISBN 978-3-95450-136-6

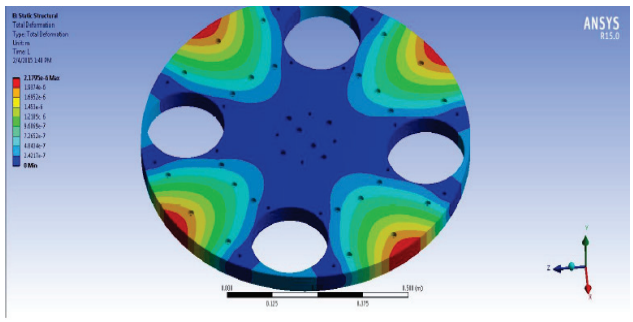

Figure 7: Deformation distribution in extra part.

CONCLUSION

In magnet structure, pins considered just for guiding and accuracy of assembly so they do not endure or apply any forces or pressure. As can be seen in Figure 6, maximum amount of stress (Von- mises) occurred in extra part bolts locations and its value is 5.369 MPa which is much less than Tensile strength. Also by considering deformation (Von -mises) in Figure 7, which has got maximum value of 2.170 μm, insurance safety and structure stability of magnet in time of working can be inferred. Also it indicates that the layout of drilling and joints is suitable for the 10 MeV compact cyclotron. This layout can help other parts of cyclotron in order to be compact and it is economical for manufacturing.

REFERENCES

[1] R. Solhju Masouleh, H. Afrideh, M. Ghergherehchi, S.J. Chai, "Magnet Design for the 10MeV AVF Cyclotron Accelerator", JOURNAL OF THE KOREAN PHYSICAL SOCIETY , Vol.63, No. 7, October 2, NO.7, PP.1347-1350, 05 October2013

[2] Shigley's mechanical engineering design 9th edition, P 451

[3] User Documents of ANSYS

ISBN 978-3-95450-136-6

TUNER SYSTEM OPTIMIZATION IN 10 MeV CYCLOTRON CAVITY

M. Mohamadian, M. Salehi, H. Afarideh, Energy Engineering and Physics Department, Amirkabir University of Technology, Tehran, Iran
M. Ghergherechi, J. Chai, Electronic and Electrical Engineering Department, Sungkyunkwan University, Republic of Korea

Abstract

Since fixed frequency cavities need fine tuning for the one operating frequency, their design require for the accurate tuning system to reach the best performance and quality factor. In the case of our cyclotron, the fine tuning device, capacitive trimmers, can be done by hydraulically squeezing the outer capacitive tuning disk to the inner disk which is connected to the cavity Dee part. This generates a Δf/f0 = 0.7% (Δf=500 kHz), sufficient to correct pressure changes, thermal effects acting on the cavity and any other supervention.

Computer model of the RF system was developed in the CST and double checked by HFSS. Necessary resonant frequency and increase of the voltage along the gaps were achieved. Optimization of the RF cavity parameters leads us into cavity with quality factor about 15000, and insertion loss about -0.06dB and also reflection power about -57dB, RF power dissipation is about 40 kW.

We have studied some models with different in accelerating gap, dimension of the Dee and Liner, and also optimization of the coupling and tuning capacitors. We analyzed the effect of the tuner and revealed that better diameter and gap space for the tuner is on the 60 and 2mm.

INTRODUCTION

Various small cyclotrons had successfully been developed with compact structure for isotope production from 1990s.[1] The conceptual design of the cyclotron systems is unchanged from that reviewed in the 1978 Conference, but many details have been modified. [2] RF cavity which is included Dee electrodes, couplers ant etc. is one of these parts that has had different structures. Our group has dedicated to the exploration of the cyclotron physics and key technologies with the compact structure for medical purpose recently. The cyclotron developed by our Lab began by referring to 10 MeV medical cyclotrons.

Our cyclotron has room temperature magnets, valley design with four sectors, two Dees in opposite valleys, external ion source and simultaneous beam extraction on opposite lines. The cyclotron is illustrated in Figure 1.

RF SYSTEM

The RF cavity as a resonator is composed of two λ/4 resonant cavities connected at the center. This option optimizes the resonator power dissipation with minimum Dee voltage off balance between the lower and upper Dee plates. [1]

The RF cavity has been simulated with the general purpose simulation software CST MWS and double checked by HFSS to optimize the resonator characteristics and continues with coupling and tuning optimization.

The coupling of the cavity adopts a fix capacitive method, which allows the simplicity and economy. Cylinder type ceramic is selected as an insulator to separate the vacuum and air. The shape of the inner/outer conductor of the coupling window is designed in a way to have good VSWR and also to prevent excessive multipacting at a certain power level. [3]

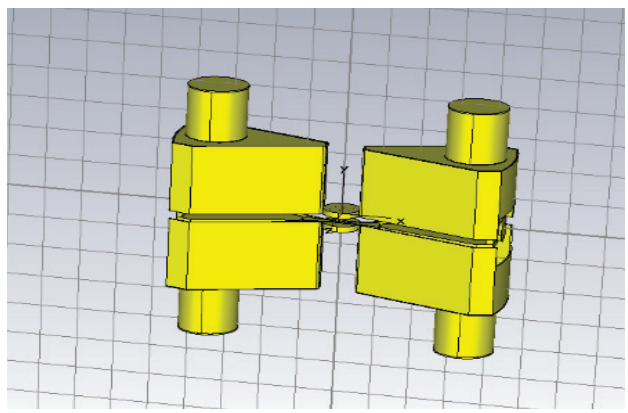

Figure1: RF cavity structure.

CAPACITIVE COUPLERS AND TUNERS

Capacitive coupling is widely used in double gap, coaxial type resonators, because the inner conductor presents an ideal opportunity to couple via a capacitance to the high voltage end (typically the 'Dee structure'); and be independent of geometry changes at the inductive end of the resonator especially if that end is used for frequency tuning. Matching the cavity to a 50 Ω transmission line with a suitable capacity usually presents no special problem; a further advantage can be that a variable capacity (=variable distance of the coupler to the 'Dee') is usually easier to design and operate reliable that a variable area (usually by rotation) inductive coupling loop [4].

SIMULATIONS IN CST MICROWAVE STUDIO AND HFSS

CST STUDIO SUITE is a general-purpose simulator based on the Finite Integration Technique (FIT). This numerical method provides a universal spatial discretization scheme applicable to various electromagnetic problems ranging from static field calculations to high frequency applications in time or frequency domain [5].

ISBN 978-3-95450-136-6

HFSS is an engineering simulation software which mainly relies on the Finite Element Method (FEM). These are general-purpose finite element modeling packages for numerically solving mechanical problems, heat transfer and fluid problems, as well as acoustic and electromagnetic problem [6]. Calculations of the created model were performed by means of Eigen mode JD loss-free solver (Jacobi Division Method) in CST Microwave Studio and Block LANCZOS solver in HFSS.

Voltage value was obtained by integrating the electric field in the median plane of the resonant cavity. To fit the frequency of the cavity to the project value after the first design and reach to a near value for resonant frequency, we had to examine the various coupling parameters. We revealed that variation of the coupler and tuner diameters and the gap between disks changes frequency by about 500 kHz, and the value of the voltage along radius does not change noticeably while fitting by less than 1 MHz.

Simulations show that the frequency of both programs is about, 71.5 MHz, for CST Microwave Studio and 72 MHz, from HFSS.

FITTING OF THE FREQUENCY OF THE CAVITY

We analyzed methods of fitting the frequency of the cavity. In order to decrease the resonant frequency it is possible to change the dimension of the coupler disks and its distance. It was shown earlier that simultaneous variation of the dimension of couplers changes the frequency without changing the voltage behavior along the radius. But there are other consideration and limitation to vary these dimensions.

First of all, we created the model with resonant frequency 71.5 MHz and examined the possibility of decreasing the resonant frequency of this model by modulation of the diameter of the stems, couplers and etc. Figure 2 illustrates the return loss for different stem diameters. The diameter of the couplers was changed from 30 to 130 mm and gap from 1.6 to 2.5. So as a result, the resonant frequency decreased from 71.5 to 70.954 MHz.

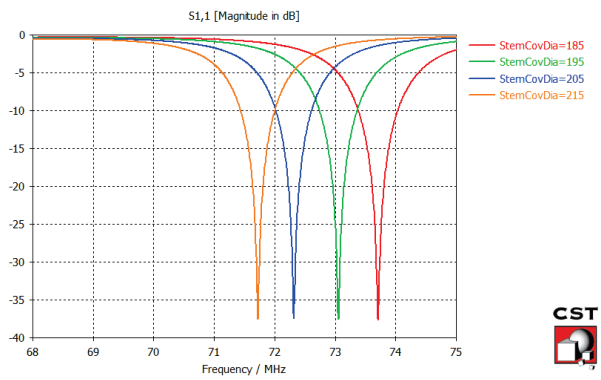

Figure 2: Return loss for different stem diameters.

Beside to reach the desired resonant frequency, the return loss is so significant parameters to consider. So after catching the desired result for resonant frequency, we try to optimize the model to minimum return loss. And, it's also necessary to know the effect of different dimension of the couplers on resonant frequency accurately to tune the system on practice. Therefore, we simulated these variations and analyzed the effects.

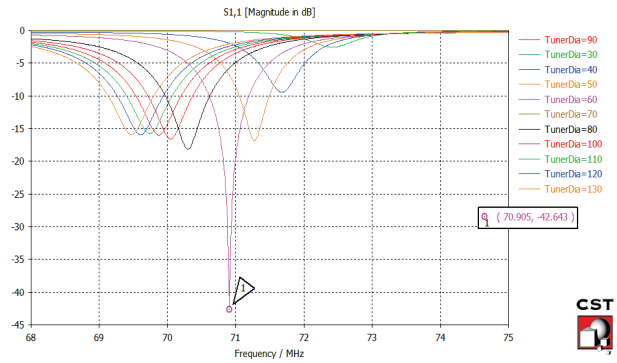

Figure 3: Return loss changes with different tuning parameters.

RESULTS AND CONCLUSIONS

Computer model of the cyclotron RF cavity with 4 stems was developed, simulated and analyzed in CST Microwave Studio and HFSS. The model had the frequency 71 MHz, necessary voltage distribution 40 kV (average). It was shown that the resonant frequency and return loss depends on the diameters and distance of coupler's disks. Figure 3 shows how the return loss changes with different tuning parameters.

Also, Figure 4 show how the return loss changes with different coupler parameters.

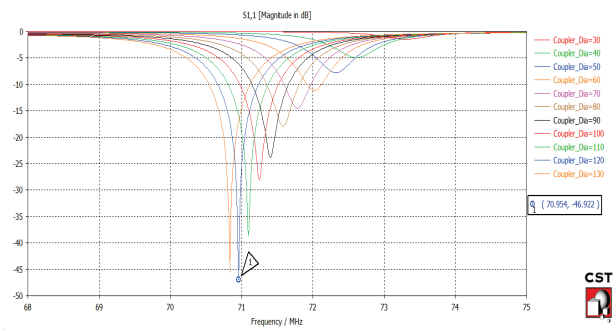

Figure 4: Return loss changes with different coupler parameters.

It was demonstrated that it is possible to change resonant frequency of the cavity and return loss of various diameters and distance of coupler's disks. Finally capacitance tuners at the end of the cavity structure with a diameter of about 60mm and gap distance of about 2mm will provide the necessary frequency tuning with fixed coupling capacitance, at the end of the transmission line with a diameter of about 130mm and gap distance of about 2mm. It should be noted that both tuner and coupler can change the disk's gap for the best tuning of the first installation. And also, tuner disk could have displacement during cyclotron working to fine tuning by hydraulically

ISBN 978-3-95450-136-6

squeezing. Figure 5 show the optimization results on return loss curve.

Table 1: Main Characteristics of the RF System

Frequency	71MHz, 4th harmonic
Dee angle	40º
Dissipated power	15 kW
Dee voltage	40kV
Quality factor	15000

Optimization of the RF cavity parameters leads us into the cavity with quality factor about 15000, RF power dissipation being about 40 kW per cavity. Table 1 illustrates our cyclotron parameters.

REFERENCES

[1] V. Sabaiduc et al., New high intensity compact negative hydrogen ions cyclotron, in Proceedings of Cyclotrons 2010, Lanzhou, China.

[2] Peter S. Miller and MSU Staff, Status Report on the 500 MeV Cyclotron, Proceedings of the 9th International Conference on Cyclotrons and their Applications September 1981, Caen, France, pp 191-195.

[3] M. Maggiore, A. Lombardi, L.A.C. Piazza, G. Prete, An intrinsically safe facility for forefront research and training on nuclear technologies -- An example of accelerator: the SPES cyclotron, EPJ Plus, 129 4 (2014) 69.

[4] Peter K. Sigg,, Cyclotron Cavities, Part II draft, Paul Scherrer Institute (PSI), Villigen, Switzerland.

[5] CST STUDIO SUITE. http://www.cst.com

[6] HFSS ANSYS. http://www.ansys.com

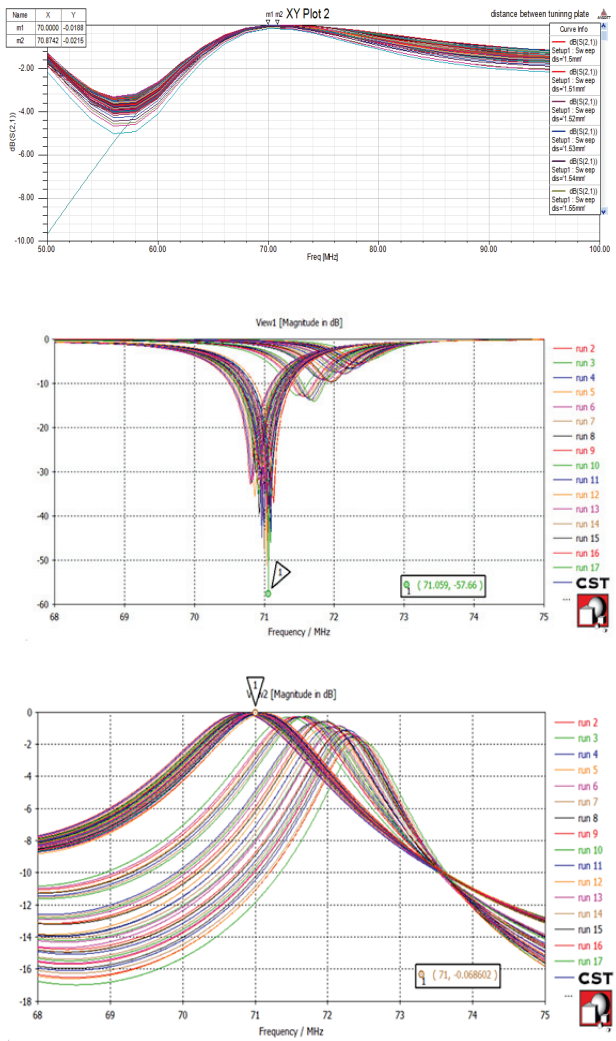

Figure 5: the optimization results on return and insertion loss curve of CST and HFSS simulations.

ISBN 978-3-95450-136-6

DESIGN AND SIMULATION OF 18 MeV CYCLOTRON MAGNET BY TOSCA CODE

N. Rahimpour Kalkhoran
Energy engineering and physics department, Amirkabir University of Technology, Tehran, Iran
H. Afarideh, R. Solhju, M. Ghergherechi
School of Information & Communication Engineering, Sungkyunkwan University, Suwon, Korea

Abstract

The 18MeV cyclotron magnet was designed for medical applications at Amirkabir University of Technology. In magnet simulation all other subsystems should be considered, because all of them are related with magnet. Designed magnet with 4 hills and valleys has AVF structure. The TOSCA (Opera-3D) code was used for simulation and analysis. Designing process summarize in tow steps: At first all theoretical calculation of magnetic field according to radius were done and it's curve which is named theoretical curve was plotted. In next step simulation in TOSCA code was done with a simple model of magnet and optimization process began until when the curve of the simulation result coincided with the theoretical curve. The result showed that at most radius, the isochronous magnetic field difference between simulated values and calculation is less than 10 Gauss, so designed magnet is optimized. Also the particle trajectories were illustrated. According to the results, work points of the cyclotron are far from the resonances region. With considering reliable mesh the accuracy of simulation result is sufficient high.

INTRODUCTION

According to various applications of cyclotrons in the world is increasing, research, study and manufacturing about cyclotrons is considered in the world. Magnet is one of the most important components of cyclotron that stimulates particle in spiral path until particle achieve to particular energy. Magnet design is very important in cyclotron design and is an iterative process. The structure of 18 MeV cyclotron magnet is Azimuthally Variable Field (AVF). Also for an ideal design all other subsystems in the cyclotron should be considered. Three goals are followed in this paper: first procedure of achievement to isochronous magnetic field, second working points of the cyclotron and the resonance regions are checked and at the end, dynamic of particle's closed orbits are presented. Also magnetic field in middle plane of the magnet and calculation of magnet weight are mentioned.

BASIC THEORETICAL CALCULATIONS

There are some parameters which should be estimated and calculated before the basic calculations. At first value of RF frequency should be estimated for primary calculations. After accurate studying 64.3 MHz was selected for RF frequency.

With considering RF frequency, magnetic field relation according to radius is [1]:

$$B_{iso} = \frac{B_0}{\sqrt{1-(\frac{300ZB_0r}{E_0})^2}}$$

Figure 1 shows isochronous magnetic field according to radius diagram. This is theoretical diagram.

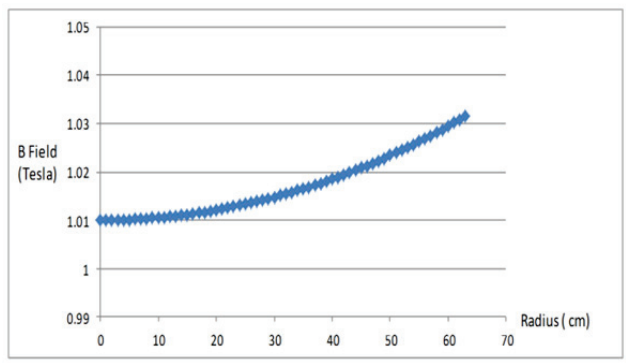

Figure 1: Isochronous magnetic field according to radius.

With using of cyclotron important equations, the relation between kinetic energy and radius is followed as [1]:

$$T(r) = \frac{938.27}{\sqrt{1-0.0000104\times r^2}} - 938.27$$

Figure 2 shows kinetic energy of particle according to radius diagram that suggests existence of particle in various radiuses with different energy [2].

ISBN 978-3-95450-136-6

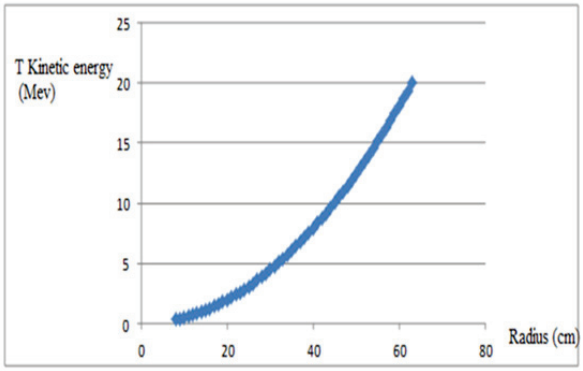

Figure 2: Kinetic energy of particle versus o radius.

Then magnet simulation was begun with simple model of magnet. Optimization process continued until that magnetic field according to radius diagram achieved from the simulation result coincided with theoretical diagram. For achieving to best coincidence, gap between poles was selected 3.66 up to 5.99 centimeter.

Then estimation of ampere-turn should be done with Ampere law [1], so 28Ka is selected for more coincidence between theoretical magnetic field curve and simulation curve. The coils are producer of magnetic field in the magnet.

All important specification of the designed magnet structure is shown in Table 1 and the whole structure is shown in Figure 3.

Table 1: Main Characteristics of the RF System

Parameter	Value
Total radius	120 cm
Pole radius	63 cm
Number of sector	4
Hill angle	46
Valley angle	44
Gap between poles	3.66-5.72 cm
Total height	116 cm

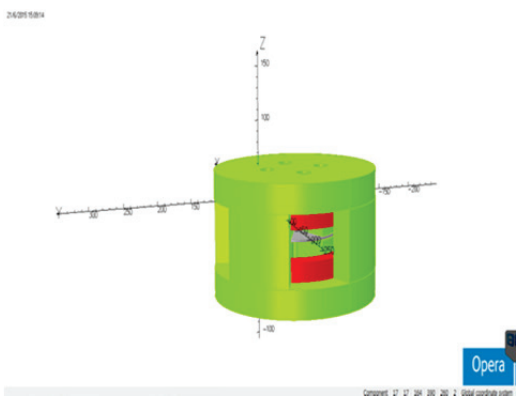

Figure 3: Overview of designed magnet in TOSCA code.

POLE RADIUS CALCULATION

All calculations of magnet design begin with magnetic rigidity relation from the following equation [3]:

$$B_{iso} \times R = \frac{\sqrt{T^2 + 2TE}}{300Z}$$

By using this equation and placement kinetic energy 18MeV, extraction radius is obtained 59 cm and with considering extraction element, pole radius increases to 63 centimeter.

SHIMMING OF POLE EDGE

For improvement of magnetic field process and approaching to theoretical state, shimming of pole edge was used. In design, same as the Figure 4, four triangle pieces with 10 angle was put in end of each pole. This design caused that magnetic field process in final positions was improved [4].

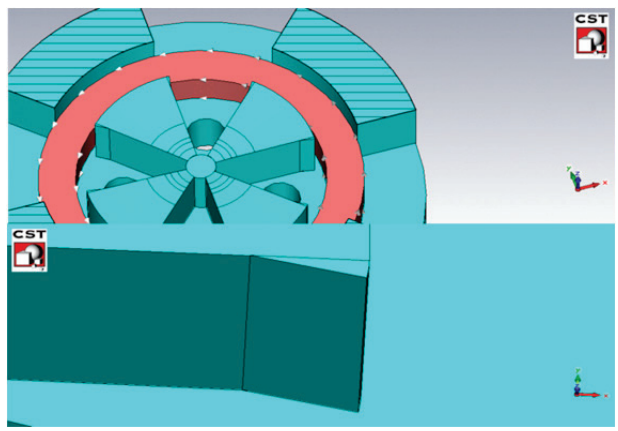

Figure 4: Shimming of pole edges in designed magnet.

SIMULATION RESULT

After early estimations and calculations simulation results are presented.

MAGNETIC FIELD DIAGRAM

All magnetic field calculations according to radius were done and its curve was plotted which is called theoretical curve. The final isochronous magnetic field curve is shown in Figure 5. As it is shown suitable coincidence is established between tow curves in small scale.

ISBN 978-3-95450-136-6

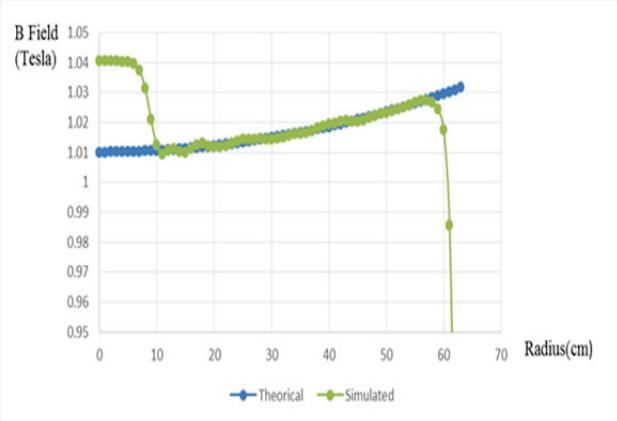

Figure 5: Isochronous magnetic field versus radius.

MAGNETIC FIELD IN MIDDLE PLANE

The magnetic field in middle plane (where particle orbits on it) is one of the most important parameters which should be checked after each simulation [5].

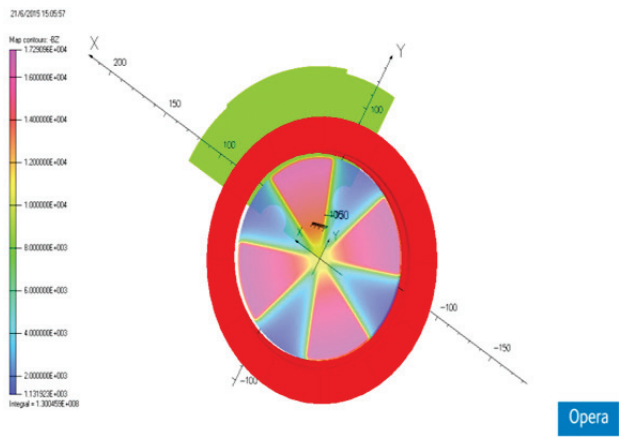

Figure 6: Distribution of magnetic field in middle plane.

As it is shown in Figure 6 maximum magnetic field in this plane is 1.72 Tesla that is less than saturated point of magnet material (AISI 10-10) 1.85Tesla.

MAGNETIC FIELD ERROR

The calculation of difference between tow curves in Figure 5 is magnetic field error in final designed magnet. This error is shown obviously in Figure 7 in small scale.

In ideal state theoretically, this difference should be about zero. But in simulation this value should be about 10^{-4}, as it is shown in Figure 7, magnetic field error in final design is less than 10 Gauss in more radiuses [4].

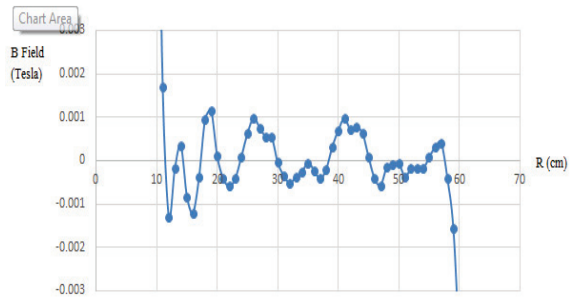

Figure 7: Magnetic field error.

BETATRON OSCILLATIONS

In particle motion at cyclotron, especially in final orbits, particle oscillates in vertical and radial exit. These are Betatron oscillations. From the following equations betatron oscillations factor obtained in each two directions [6]:

$$\upsilon_z = 1 - \gamma^2 + \frac{N^2}{N^2 - 1} F$$

$$\upsilon_r = \gamma^2 + \frac{3N^2}{(N^2 - 1) \times (N^2 - 4)} F$$

For more particle stability, vertical oscillations factor should be positive and radial oscillations factor should be more than one. As it is shown in Figure 8 in this designed magnet, these limits are respected.

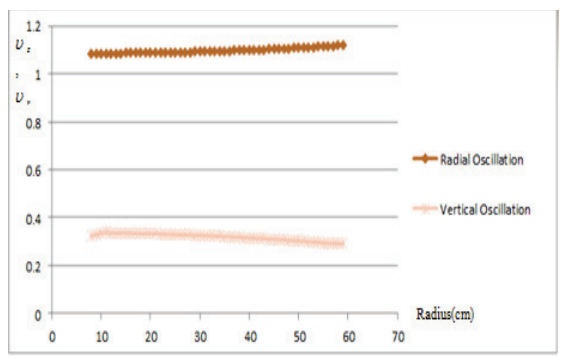

Figure 8: Betatron oscillations.

WORKING POINTS AND RESONANCE REGIONS

During cyclotron motion maybe some perturbations enter to particle. If frequency of these perturbations is same as particle revolution frequency, resonance will be happen. All resonances are destructive and destroy the particles. So working points of the cyclotron should be sufficient far from the resonance regions [7].

At first by using 4 and 5 equations, working points of the cyclotron are obtained, then with using following

ISBN 978-3-95450-136-6

equation that presents all vertical and horizontal oscillations, all resonance lines up to 3rd order

($|L| + |K| \leq 3$) were plotted, Figure 9 shows coincidence between these two results [8].

$$Kv_x + Lv_y = in$$

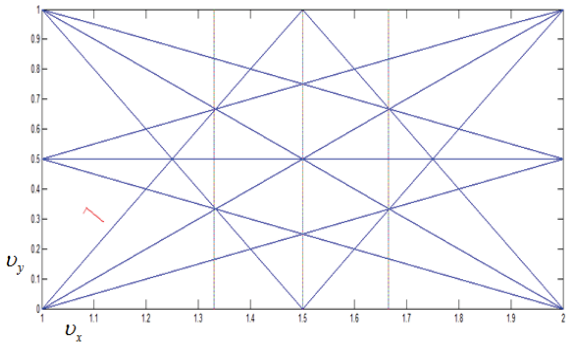

Figure 9: Resonance regions and working points.

As it is shown working points of cyclotron (red curve) are sufficient far from the resonance regions (blue lines).

CHECKING DYNAMIC OF CLOSED ORBITS OF PARTICLE MOTION

In TOSCA software can achieve to best particle tracks in various positions. Figure 10 shows accurate particle tracks in designed magnet [9].

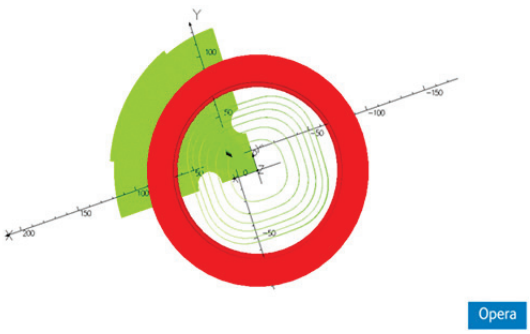

Figure 10: Tracks of particle.

Also in Table 2 energies and positions of particle in different radius is presented.

Table 2: Energies and Radiuses of Particle

Energy(MeV)	Radius(cm)
3	23
6	32
9	38.5
12	44
15	49
18	53

CONCLUSIONS

Design and simulation of 18 MeV cyclotron magnet has been followed accurately in this poster. Primary design calculation, initial estimation and all magnet specification was presented. The achieved result of the magnet contains isochronous magnetic field diagram, magnetic field in middle plane and magnetic field error in small scale were presented. Also betatron oscillations and destructive resonance regions for more particle stability were checked. In addition, dynamic of closed orbits of particle motion during accelerating was studied. At the end, magnet weight was calculated. Mesh factor I n running the software is sufficient small and reliable and ensure the result validity.

REFERENCES

[1] Y, Jongen and S. Zaremba, Cyclotron magnet calculation, IBA s.a, 2006.

[2] H.S. Kim and M. Ghergherechi, DESIGN STUDY OF 10 MeV H- CYCLOTRON MAGNET, Cyclotrons2013, Vancouver, 2013.

[3] J. Livingood, PRINCIPLES OF CYCLIC ACCELERATORS, D. Vannostrakd Company, Canada, 1960.

[4] S. Zaremba, Magnet for Cyclotrons, CERN Accelerator school Small accelerator, Netherlands, CERN-2006-012, 2005.

[5] R. Solhjou Masouleh, H. Afarideh and B. Mahdian, IMPROVEMENT IN DESIGN OF 10 MeV AVF CYCLOTRON MAGNET, Cyclotrons2013, Vancouver, 2013.

[6] F. Chautard, Beam dynamics for cyclotrons CERN accelerator school Small accelerators, Netherland, CERN, 2006.

[7] R. Solhju and H. Afarideh, Magnet Design for the 10MeV AVF Cyclotron Accelerator, Korean Physical Society, 2013

[8] H. Wiedemann, Particle Accelerator Physics, Berlin, Springer Science & Business Media, 2007.

[9] OPERA-3D User Guide, 2012.

ISBN 978-3-95450-136-6

DEMIRCI: AN RFQ DESIGN SOFTWARE*

B. Yasatekin†, G. Turemen, Ankara University, Department of Physics & SANAEM, Ankara, Turkey
E. Celebi, Bogazici University, Department of Physics, İstanbul, Turkey
G. Unel, University of California at Irvine, Department of Physics and Astronomy, Irvine, USA
O. Cakir, Ankara University, Department of Physics, Ankara, Turkey

Abstract

The development and production of radio frequency quadrupoles, which are used for accelerating low-energy ions to high energies, continues since 1970s. The development of RFQ design software packages, which can provide ease of use with a graphical interface, can visualize the behavior of the ion beam inside the RFQ, and can run on both Unix and Windows platforms, has become inevitable due to increasing interest around the world. In this context, a new RFQ design software package, DEMIRCI, has been under development. To meet the user expectations, a number of new features have been recently added to DEMIRCI. Apart from being usable via both graphical interface and command line, DEMIRCI has been enriched with beam dynamics calculations. This new module gives users the possibility to define and track an input beam and to monitor its behavior along the RFQ. Additionally, the Windows OS has been added to the list of supported platforms. Finally, the addition of more realistic 8 term potential results has been ongoing. This note will summarize the latest developments and results from DEMIRCI RFQ design software.

INTRODUCTION

The task of designing a radio frequency quadrupole (RFQ) necessitates the usage of dedicated design software packages [1]. Recently, the DEMIRCI project was started to supplement the existing such softwares [2, 3], with the goal of benefiting from modern concepts such as ROOT [4] environment and OO programming in order to make it easy to use and maintain. The initial version of this new program has been discussed previously [5]. During last year, the new version of DEMIRCI (v1.9) has been enriched with new design features which constitute the main subject of this note [6]. One of the new features is the ability of running beam dynamics simulations based on user selected beam types for a user selected number of particles. These simulations are expected to make the overall design experience more realistic by monitoring beam behavior in phase and normal spaces along the RFQ. One other feature of the new version is the support of Windows platform as a base operating system alongside Linux and Mac OSX. Amongst additional enhancements that will be also discussed below, one can count the realistic 2D profile definition of the RFQ cell and subsequent usage of SuperFish [7] for detailed studies.

NEW DEVELOPMENTS

The new developments mainly focus around the addition of the beam dynamics calculations and the addition of more terms to the potential function. As the latter is an ongoing effort, this note will focus on the former, the new supported platform and the enhanced interface to SuperFish. First of all, to define the particle beam at the entrance of the accelerator cavity, a new set of internal parameters were added to DEMIRCI. These are the beam distribution type, the beam emittance, the charge and mass of the particles under consideration and the total number of macro-particles to be used in the simulations. The enlarged setup window to set these new variables can be seen in Fig. 1 with their default values. One can also notice that language localization has been added to DEMIRCI, Turkish being the second language supported after English.

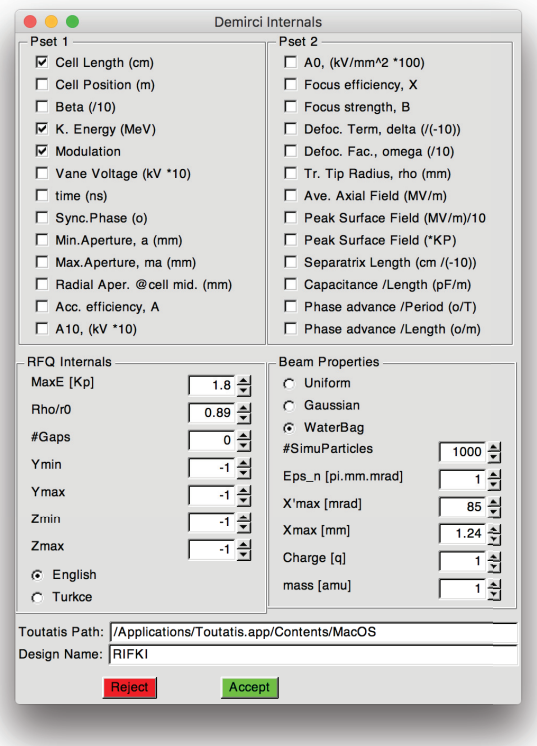

Figure 1: The enhanced setup window with beam parameters and their default values.

* Work supported by TUBITAK with 114F106 project number
† byasatekin@ankara.edu.tr

ISBN 978-3-95450-136-6

Beam Dynamics

At the initialization step, a number of macro particles are randomly generated in the phase space according to beam definitions just at the entrance of the RFQ. For individual particle motion, between the time based and position based approaches, DEMIRCI employs the former as it is more convenient for the user. In this approach, a small enough time step (δt) is selected to calculate the motion of particles according to the electric field ($\vec{E}$) values at the particle position, velocity and time. The relevant equations for position, velocity and kinetic energy at the next time interval ($t + \delta t$) are [8]:

$$\vec{x}^{t+\delta t} = \vec{x}^{t} + \vec{\beta}^{t} c\delta t + \frac{1}{2}\frac{Q}{\gamma^{t} M}\vec{E}^{t}\delta t^{2} \quad , \qquad (1)$$

$$\gamma^{t+\delta t}\vec{\beta}^{t+\delta t} = \gamma^{t}\vec{\beta}^{t} + \frac{1}{2}\frac{Q}{cM}\delta t(\vec{E}^{t} + \vec{E}^{t+\delta t}) \quad , \qquad (2)$$

$$E_{k}^{t+\delta t} = (\gamma^{t+\delta t} - 1)Mc^{2} \quad , \qquad (3)$$

where quantities with superscript t represent their values at time t, whereas Q and M are the charge and mass of the macro-particle. The DEMIRCI library has been enlarged with functions that calculate and plot the particle trajectories according to the above equations. For displaying the information, four beam dynamics tabs were added to the main DEMIRCI window. These become accessible once an RFQ description is loaded and its overall behavior is calculated using previously described methodology [9]. As seen in Fig. 2, each tab can only show four plots at a time, however up to four tabs were made available to the user for monitoring multiple distributions. The selection is made using the selection drop-down lists at the lower left side of the beam window. The bottom right hand side of the same window contains the buttons for initializing, starting and pausing the simulations which can also be executed stepwise. The selected time step of 0.1 ns and the large number of particles used in beam dynamics could be more than a CPU can handle. To overcome this problem, the graphics refresh rate is made user selectable using the scroll bar at the bottom center of the window. By adjusting it the user can play the simulation rapidly (up to 10 times) and slow it down when needed to examine in detail the important stages. One final visualization aid is the so called the OGL button, next to the speed adjustment slider. It was noticed that although the phase space plots like X-X' are great indicators while addressing issues related to beam dynamics plots, it is hard to visualize the overall beam behavior in 3D. Therefore the OGL button displays a new window in which 3D particles (with exaggerated volumes) are displayed for the relevant simulation step. Currently work focuses on using this tool to evaluate the performance of various RFQ designs and comparing the results of multi particle simulations to design equation results as can be observed in Fig. 3.

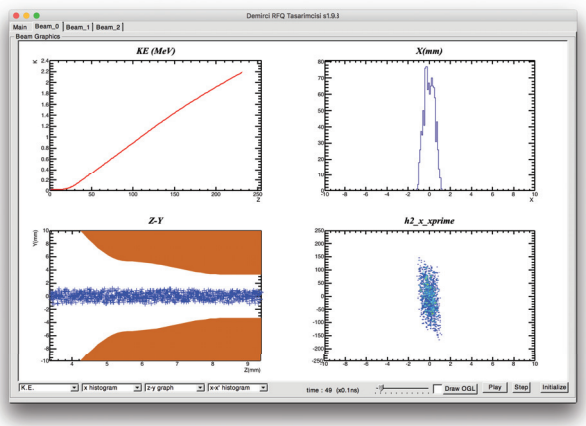

Figure 2: The new beam dynamics tab of DEMIRCI.

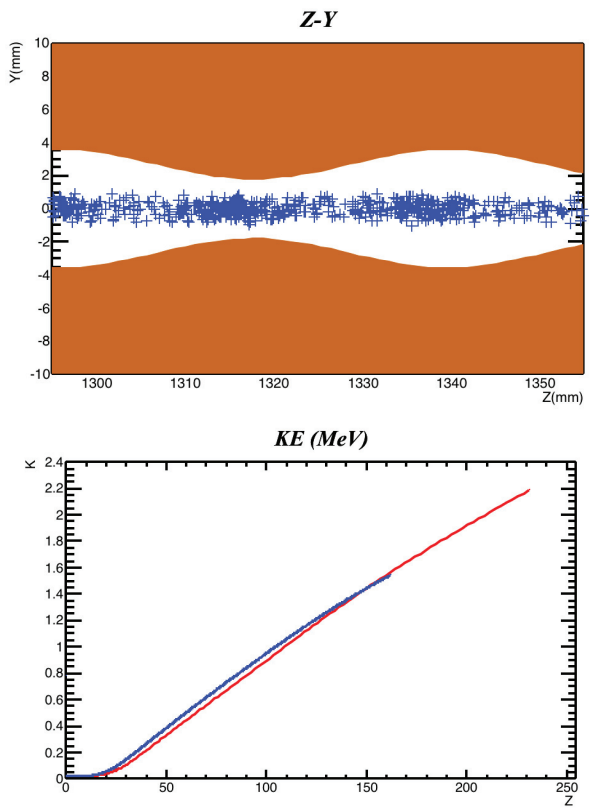

Figure 3: Top: bunching of particles in an RFQ becomes visible. Bottom: Average kinetic energy (in blue) of the macro particles obtained from dynamic equations in blue compared to estimations (in red) from averaged design equations in red.

2D Cross Section

In order to use the existing 2D EM design software SuperFish, the relevant parts of DEMIRCI have been updated as seen in Fig. 4. It is now possible to define the x-y cross section of any cell in a realistic way by specifying a total of 12 new parameters. These are vane skirt angles and distances together with connection angles to the RFQ wall. Their exact definitions can be found in the help menu accessible via the "?" button. The drawing routine also produces an output file

ISBN 978-3-95450-136-6

that can directly be read by SuperFish to calculate quantities like the power loss on the walls.

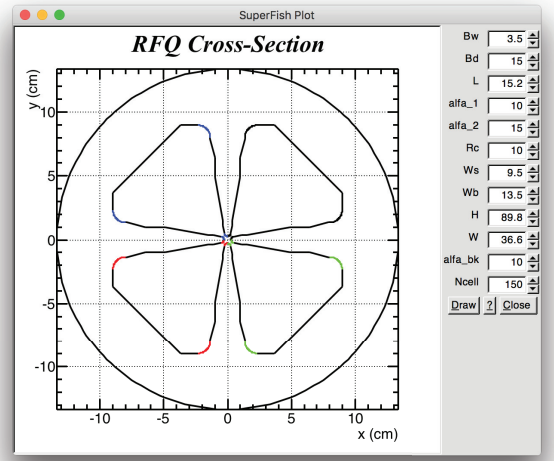

Figure 4: The RFQ cross section window.

A New Platform

Previously, DEMIRCI's base operating systems were only various Unix based platforms, such as Linux distributions and Mac OSX. A recent web based poll amongst the members of the accelerator community revealed a strong request to support the Windows operating system. To match this request, DEMIRCI has been ported to Windows with both graphical and command line interfaces. The minimum prerequisite libraries to run the Windows version of DEMIRCI are: Microsoft Visual Studio C++ version 2010 Express [10] and ROOT version 5.34/26 [4]. These software packages can be obtained free of charge. A screenshot of DEMIRCI running on Windows can be seen in Fig. 5. With this additional OS, it has become possible to interoperate DEMIRCI with other accelerator related software packages which are available on only Windows platforms, such as LIDOS [2] and SuperFish [7].

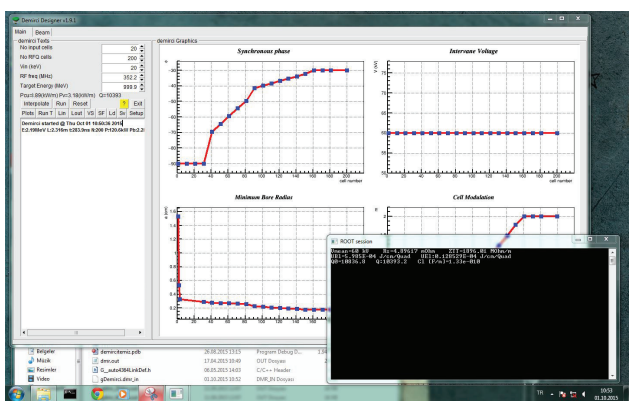

Figure 5: A screenshot of DEMIRCI v1.9, on Windows OS.

CONCLUSION

The development of the ROOT based RFQ design software DEMIRCI continues with the addition of many novelties like multi particle beam dynamics, new operating system and interoperability with other similar software. Performance comparison with similar software packages and the finalization of the 8-term potential implementation are also ongoing with the ultimate goal of delivering a reliable, user friendly and multi-platform solution to the RFQ design problem within 2016.

ACKNOWLEDGMENT

The authors would like to thank TUBITAK for their support under project number 114F106 and Dr. Sezen Sekmen for a careful reading of the manuscript.

REFERENCES

[1] I.M. Kapchinsky an V. A. Teplyakov, A Linear Ion Accelerator with Spatially Uniform Hard Focusing, ITEP-673, 1969.

[2] LIDOS.RFQ.DESIGNER Version 1.3, `http://www.ghga.com/accelsoft/`

[3] Kenneth R. Crandall, Thomas P. Wangler, Lloyd M. Young, James H. Billen, George H. Neuschaefer, and Dale L. Schrage, PARMTEQ-RFQ Design Codes.

[4] R. Brun and F. Rademakers, ROOT - An Object Oriented Data Analysis Framework, Proceedings AIHENP'96 Workshop, Lausanne, Sep. 1996, Nucl. Inst. & Meth. in Phys. Res. A 389 81-86, 1997.

[5] A. Alacakir, B. Yasatekin, G. Turemen and G. Unel, Design Studies with DEMIRCI for SPP RFQ, Proceedings of the Linear Accelerator Conference 2014 (LINAC'14), 31 Aug - 5 Sep 2014, TUPP139, p. 740.

[6] Demirci authors can be contacted by email at the following address: demirci.info@gmail.com

[7] J. Billen and L. M. Young, POISSON, SUPERFISH Reference Manual, LA-UR-96-1834.

[8] R. Duperrier, "TOUTATIS: A Radio Frequency Quadrupole Code", Phys. Rev. Vol.3, 124201, 2000.

[9] B. Yasatekin, G. Turemen and G. Unel, A Graphical Approach to Radio Frequency Quadrupole Design, Computer Physics Communications, Volume 192, 108-113, 2015.

[10] Microsoft Visual Studio website: `https://www.visualstudio.com/en-us/dn469161`

ISBN 978-3-95450-136-6

DIAGNOSING AND CONTROLS OF NSLS-II: A BRIGHT NEW LIGHT FOR SCIENCE*

Yong Hu#, Leo Bob Dalesio, BNL, NSLS-II, NY 11973, U.S.A.

Abstract

NSLS-II, the successor to NSLS (National Synchrotron Light Source) at Brookhaven National Lab, has been open to users worldwide since February 2015 as a world-class advanced synchrotron light source because of its unique features: its half-mile-circumference (792 m) Storage Ring provides the highest beam intensity (500 mA) at medium-energy (3 GeV) with sub-nm-rad horizontal emittance (down to 0.5 nm-rad) and diffraction-limited vertical emittance at a wavelength of 1 Å (<8 pm-rad). As the eyes of NSLS-II accelerators to observe fascinating particle beams, beam diagnostics and controls systems are designed to monitor and diagnose the electron beam quality so that NSLS-II could be tuned up to reach its highest performance. The design and implementation of NSLS-II diagnostics and controls are described. Commissioning results of NSLS-II accelerators, including Linac, Booster, and Storage Ring, are presented.

INTRODUCTION

The construction of NSLS-II (NSLS-2) began in Mar. 2009. Three years later, preliminary Linac commissioning started in Mar. 2012. Stored beam with 50mA in the Storage Ring was achieved in July 2014. The first light was delivered to one of the six project beam-lines on Oct. 23, 2014. And the NSLS-II project was dedicated and officially completed on Feb. 6, 2015. Recently, we have successfully tested and demonstrated the top-off injection. When the whole machine is fully tuned up, NSLS-II will be the most advanced third-generation light source in terms of the following parameters:

1) The lowest horizontal emittance at 0.5nm-rad;
2) The smallest beam size at ~3 μm;
3) The highest beam current (intensity) at 500mA;
4) The highest photon spectral brightness due to the lowest emittance, the smallest beam size, and the highest beam current as stated above.

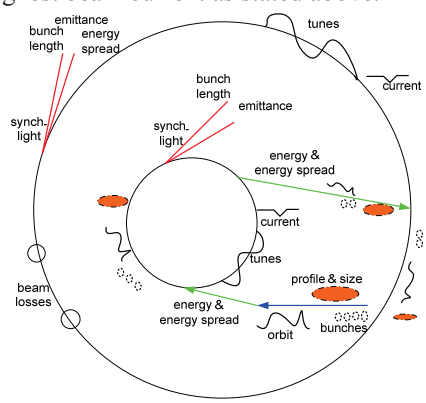

Figure 1: Beam Parameters Measured at NSLS-II

Machine commissioning and tuning up is all about diagnosing. To achieve the exceptional performance of NSLS-II, beam diagnostics and control systems are designed to monitor and diagnose the electron beam of NSLS-II accelerator complex. Diagnosing NSLS-II means measuring a variety of beam parameters (~10 types), including beam charge/current, filling pattern, beam position/orbit, beam size/profile, energy spread, tunes, emittance, bunch length, beam losses, etc., via a variety of beam monitors (~16 types, ~370 total device counts as shown in Table 1 below) distributed around the whole machine. Figure 1 briefly shows how the NSLS-II accelerators are diagnosed, i.e. what kind of beam parameters is measured from Linac to Storage Ring.

Effective diagnosing of NSLS-II accelerator depends on the effective combinations of a variety of beam monitors, control and data acquisitions (DAQ), and high level physics applications. Figure 2 shows how beam instrumentation, controls, and physics work together to diagnose the NSLS-II machine.

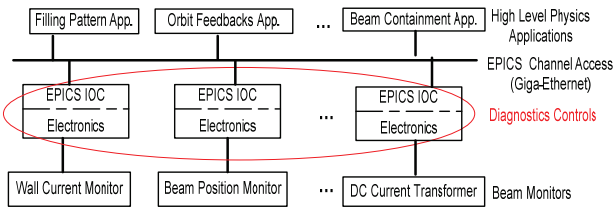

Figure 2: NSLS-II diagnostics and control architecture.

BEAM MONITORS AND SUBSYSTEMS

NSLS-II accelerators consist of one Injector and one Storage Ring (SR). According to the functionality as well as geographical distribution, the Injector is divided into 4 sub-accelerators: Linac, Linac to Booster (LtB) transfer line (including 2 beam dumps), Booster, Booster to Storage ring (BtS) transfer line (including 1 beam dump). Table 1 gives a summary of the beam monitors distributed over the whole machine.

From system functionality and application point of view, the variety of beam monitors as shown in Table 1 could be classified into a few subsystems such as beam position monitor (BPM), filling pattern (Wall Current Monitor, Fast Current Transformer), beam intensity (Integrating Current Transformer, DC Current Transformer), loss control and monitoring (Beam Loss Monitor, Scraper), beam profile (Screen, Visible Light Monitor, Streak camera), tunes, etc., as shown in Figure 3.

*Work supported by DOE contract No: DE-AC02-98CH10886
#yhu@bnl.gov

ISBN 978-3-95450-136-6

Table 1: Beam Monitors at NSLS-II

	Linac	Ltb	Booster	BtS	SR
WCM	5				
Screen/Flag	6	9	6	8	1
BPM	5	6	37	8	180
FCT / FPM		2	1	2	1
Bergoz ICT		2		2	
Energy Slit		1		1	
Faraday Cup	1	2		1	
Bergoz DCCT			1		1
Streak Camera					1
Visible Light Monitor			1		1
X-ray diag. beam-line					1
Tune Monitor			1		1
Transverse Feedback					1
Beam Loss Monitor					5
Beam Scrapers					5
Photon/x-ray BPM					1 or 2 per BL

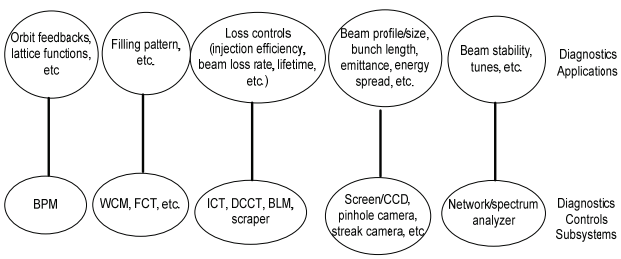

Figure 3: Diagnostics subsystems and applications.

CONTROLS AND DATA ACQUISITIONS

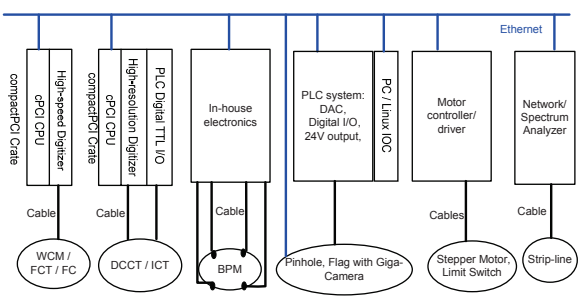

Figure 4: Diagnostics control interfaces.

NSLS-II beam diagnostics control system is completely EPICS-based [1]. Each type of beam monitor requires electronics to process its output signal. The electronics for beam monitors and associated EPICS IOC platform are listed in Table 2. Figure 4 shows the control interfaces for various beam monitors at NSLS-II.

Table 2: Diagnostics Electronics and IOC Platform

Beam Monitor	Diagnostics Electronics	IOC platform
WCM & FCT	Acqiris DC252 (2GHz bw, 10-bit, 4~8GS/s)	cPCI/Linux
DCCT & ICT	1)GE ICS-710-A (24-bit, 200KS/s, 8-ch) 2)Allen-Bradley PLC (DAC, Digital I/O)	cPCI/Linux
BPM	In-house BPM receiver [3]	PC/Linux
Profile / camera	PC/Linux	PC/Linux
Slit & scraper	Delta Tau GeoBrick LV	PC/Linux
Tune	Network analyzer	PC/Linux

PRELIMINARY DIAGNOSING NSLS-II

NSLS-II Storage Ring commissioning started in March 2014. A total of 50-mA stored beam in the Storage Ring was achieved with super-conducting RF recently (see Fig. 5). Although this is still far away from the designed value at 500 mA, it is a major milestone for the NSLS-II Project because the accelerators, including Linac, Booster, and Storage Ring, have been proven working in principle.

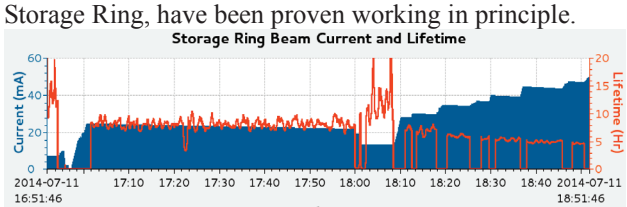

Figure 5: NSLS-II milestone -- 50-mA stored beam.

Beam Intensity Measurement

Beam intensity, also named beam charge (Q) or beam current (I_b), is one of the most important beam parameters for synchrotron light sources. 500-mA stored beam circulating in the Storage Ring is the ultimate goal, which is one of the factors making NSLS-II a world-class light source.

For single-pass accelerators including Linac and transfer-lines (LtB, BtS), the beam intensity is measured as beam charge (Q, nC) via the beam monitor Bergoz ICT. For ring-based circular accelerators including Booster and Storage Ring, the beam intensity is measured as beam current (I_b, mA) via the beam monitor Bergoz DCCT. The charge of circulating beam is actually the beam current multiplying the ring revolution period: $Q = I_b * T_{rev}$. In a sense, beam current and beam charge is interchangeable. Various injection efficiencies, such as Booster injection,

ISBN 978-3-95450-136-6

Booster ramping, Booster extraction, and Storage Ring injection, are calculated by the synchronized shot-by-shot charge ratio between two adjacent ICTs or DCCTs along the beam path.

During NSLS-II accelerator commissioning, the beam current monitors, i.e. Bergoz ICT and DCCT, have been proven very useful and reliable instruments for measuring absolute beam charge with accuracy ~1%. We had noise issues on the ICT & DCCT systems. But we managed to reduce the noise as low as possible by various methods such as adding ferrite beads around the cable, adding low-pass filter (50 Hz) for the Storage Ring NPCT / DCCT, adjusting trigger delay for the BCM / ICT, etc.

Filling Pattern

To achieve ultra-high stored beam current, i.e. 500 mA and meet various beam-line users' requirements, NSLS-II Injector is capable of delivering flexible filling patterns (also named bunch pattern or bunch structure): multi-bunch (80~150 bunches) beam with total charge up to 15 nC or single-bunch with beam charge up to 1 nC per shot. High-bandwidth beam monitors, such as Wall Current Monitors, Fast Current Transformers, together with high-speed digitizers (max. 8 GS/s) are used for filling pattern measurement, which provides data of number of bunches, bunch-to-bunch variation, turn-by-turn bunch charge, etc.

During NSLS-II Storage Ring commissioning, we successfully filled any RF bucket using different patterns as shown in Figure 6.

Figure 6: Storage ring filling pattern.

Beam Position Monitor

BPM is the largest as well as the key sub-system for NSLS-II beam diagnostics and controls. Eventually, NSLS-II Storage Ring will reach the lowest emmittance and the smallest beam size at ~3 µm, which requires BPM resolution at 0.3 µm (10% of beam size) to monitor beam position stability. This requirement for the BPM system is quite challenging. Huge efforts have been put in the development of in-house BPM electronics [2], which has demonstrated excellent long-term resolution performance and provided flexible data flows (see Table 2) for various physics applications during machine commissioning.

The BPM has played a vital role during NSLS-II machine commissioning: by using all BPMs' ADC raw data and turn-by-turn data, we made the first-turn beam in the Booster and Storage Ring quickly; by analysing BPMs' turn-by-turn sum signal drop, we found a hanging RF spring in the vacuum chamber, which resulted in the sudden beam loss [3]; The slow orbit feedback was tested and proved to be working as shown in Fig. 7.

Table 3: BPM Data & Physics Applications

Data Flow	Data Rate	Applications	Requirements
ADC	117 MHz	diagnostics, debugging	on demand; ~ 3.8K samples
TBT	378 kHz	tunes, phase advance, injection damping, etc.	on demand; 1 µm resolution; ~ 380K samples;
FA	10 kHz	fast orbit feedback, machine protection	continuous; 0.4µm resolution;
SA	10 Hz	beam-based alignment, response matrix, closed orbit, life-time	continuous; 0.3µm resolution;

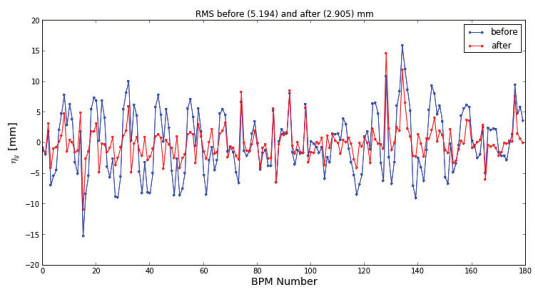

Figure 7: Preliminary test of slow orbit feedback.

CONCLUSIONS

Although we have made a very good start of commissioning and operation of NSLS-II accelerators, there are still lots of improvement opportunities for us to make the machine reach its highest performance and make it a world-class light source in the near future. Beam diagnostics and control systems have been tested with beam, proven to be functional, have played and will continue to play important roles for diagnosing NSLS-II.

REFERENCES

[1] http://www.aps.anl.gov/epics/
[2] Joe Mead, et al., "NSLS-II RF Beam Position Monitor Commissioning Update", Proceedings of IBIC14, Monterey, CA, USA.
[3] Weixing Cheng, et al., "NSLS2 Diagnostic Systems Commissioning and Measurements", Proceedings of IBIC14, Monterey, CA, USA.

ISBN 978-3-95450-136-6

SINGLE PARTICLE DYNAMICS SIMULATION AND CONTROL FOR NSLS-II COMMISSIONING

Lingyun Yang*, Yoshiteru Hidaka, Yongjun Li, BNL, Upton, NY, USA
Guobao Shen, FRIB, East Lansing, MI, USA

Abstract

NSLS-II is the 3 GeV low emittance sychrotron light source recently commissioned and in operation for users. We present some software developed for lattice simulations and machine commissioning. Majority of these tools are callable in a high level programming language Python. These new development and integration at both middle and high level has made our interactive and batch control very efficient.

INTRODUCTION

NSLS-II is the 3 GeV low emittance synchrotron light source recently commissioned and in user operations. From its design to commissioning and operations, we have used various accelerator phyiscs software available in the community and also developed some new tools. Those tools have contributed significantly to the NSLS-II project and many of them are not limited to our own facility, they are general tools that applicable to other accelerator beam dynamics or storage ring commissioning problems.

SINGLE PARTICLE DYNAMCIS

At the design stage, many good simulation software are available. They are well understood across the community and a few widely used ones have been used for decades. Many new tools are still being developed for various reasons: some are simple enough to fit one file, some are pursuing more realistic modeling, some are taking advantage of new technologies to improve performance or user experience. At NSLS-II, `elegant` [1], Tracy-2/3 [2] and TESLA [3] are used for lattice simulation and optimization [4, 5]. Some benchmarks were done on single particle trackings for these code [6]. A small first and second order linear lattice code was also developed in Python [7]. It is quick and versatile for any linear lattice matching. An example of FMA (Frequency Map Analysis) calculated with TESLA is shown in Fig. 1.

The local developed Tracy-2/3 [2] and TESLA [3] have also included the momentum dependant kickmap for insertion devices. Both code are symplectic integrator based tracking code and can do TPSA based map generation. Also, since they are developed as a library, the Python interface was implemented to call these `C++` routines and analyze/visualize the results in an IPython notebook. This is also an attractive way for interactive real machine control and modeling.

A virtual accelerator was also deveoped based on Tracy-2/3 for testing high level physics applications. An EPICS access layer is put on top of Tracy-2/3 simulator. The high level scripts can modify and retrieve magnet strength or beam dynamics information via EPICS protocol the exact same way as accessing the hardware. This virtual accelerator provided us an EPICS environment years before the real commissioning.

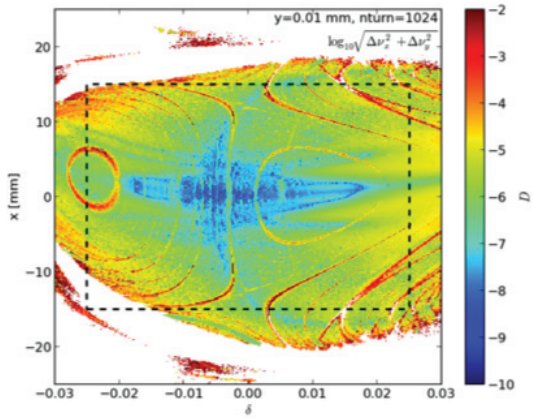

Figure 1: FMA (Frequency Map Analysis) including engineering tolerance such as misalignment, multipole errors.

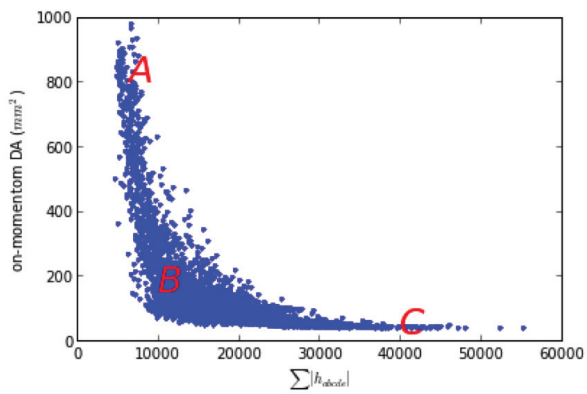

Figure 2: MOGA (Multi-Objective Genetic Algorithm) for NSLS-II lattice optimization. A, B and C are three regions that DA (dynamic aperture) correlates with nonlinear driving terms.

In the linear and nonlinear lattice optimizations, we have used MOGA (Multi-Objective Genetic Algorithm) to optimize the dynamic aperture at different working point and chromaticities [4,8,9]. The parallelized optimizer is efficient and has helped us explore many more candidate lattices that were not possible before (Fig. 2). MOGA and its variations with different strategies have been used as a standard tool for nonlinear lattice optimization.

* lyyang@bnl.gov

ISBN 978-3-95450-136-6

TOOLS FOR OPERATIONS

At the lower level controls, NSLS-II uses EPICS protocol [10]. Lots of general purpose tools, mostly lower and middle level, have been developed by the EPICS collabration and used in many accelerator facilities. For our facility, we developed some new middle layer services and a set of high level physics tools [11].

At the lower level we developed MASAR (machine snapshot save and restore) and new features in Control System Studio [12]. They are general tools that applicable to any EPICS based facilities.

MMLT (Matlab Middle Layer Toolkit) has been widely used in lots of accelerator facilities. Each facility can develop its own high level scripts on top. It was also chosen in the NSLS-II project and physicists can use and extend its features. In fact, other tools like SDDS are also installed to support interested users. But given the new infrastracture our controls system provides, developing a new middle layer could take more advantages of them. Python was chosen by one of our developers after careful comparison. It is a general purpose programming language, has good set of scientific and visualization packages, a major player in developing network services, a glue language for FORTRAN and C/C++, a good support on EPICS based controls at both server and client side, open and free. This means we can integrate simulation and controls more close and manipulate data at levels from low to high, server to client, desktop to cluster.

With the new middle layer services, we can map between hardware control channels, i.e. a PV (process variable) in EPICS, and accelerator models dynamically and globally. By querying the server, anyone knows a list of PVs associated to one particular instrument or a family of magnets, and vice versa. It is like a global address book for high level scripts who are looking for the hardware control PVs but only knows the high level element name. It is then easy to hide or disable one non-essential instrument, e.g. corrector or BPM, without disturbing the functioning of client scripts.

An advantage of using general purpose programming language for our high level script is that it is easier to make it a service which runs 24x7 for every client. For some applications, e.g. feedbacks, this single instance service is not optional but required. Programs in Python or C/C++ are trivial to be wrapped for EPICS soft-ioc and share the same code. An example is the ID (insertion device) local bump (Fig. 3). A script which generates orbit local bump was developed in Python is shown in Fig. 3a, and the same library called by the script is also used for an ID local bump IOC used by operators or beamline users is in Fig. 3b. The common part is retrieve a list of available or specified orbit correctors and BPMs, use the corresponding orbit response matrix to correct the orbit to target orbit. This is shared across high level scripts. In fact, even the general orbit correction is using this common routine by using all available BPMs, correctors with target orbit the golden orbit.

Recently Python programming language and its scientific libraries are heard frequently in scientific computing and

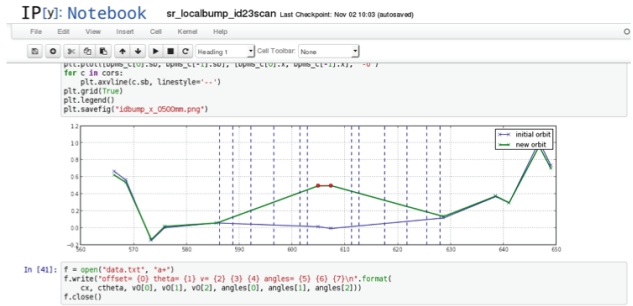

(a) IPython notebook on generating and plotting the orbit local bump.

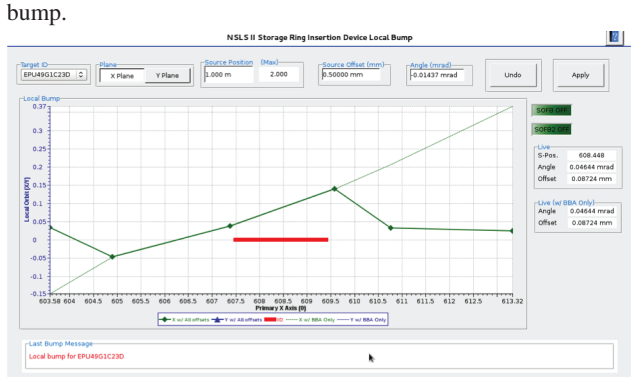

(b) CSS (Control System Studio) [13] Panel for insertion deivce (ID) radiation source point control, i.e. orbit local bump at the ID.

Figure 3: ID (Insertion Device) local bump control panel.

data science [14]. It has plenty of libraries for mathematical functions, optimization and visualizations. For our applications on NSLS-II commissioning and operations, a good support for both batch and interactive execution are convenient. Before deploying a formal batch mode script, we could easily start interactive control or testing in an IPython notebook where all code and results are in one place. These kind of notebook are easier to be understood when shared with other colleagues.

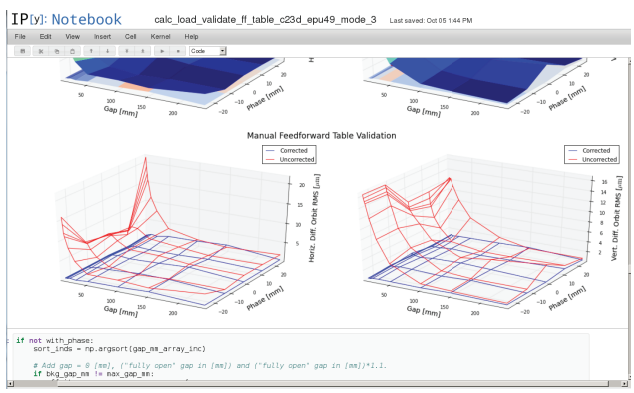

Figure 4: IPython notebook for 2D ID (Insertion Device) feedforward table.

The feedforward table for insertion devices are generated and analyzed in an IPython notebook (Fig. 4). In Python, accessing database like MySQL or SQLite is simple and part

ISBN 978-3-95450-136-6

of its standard library. Together with the hardware/model mapping [12], we can retrieve information from magnetic field measurement in the lab to temperature reading in the tunnel. Although there are 1D and 2D types of feedford tables depending on ID types, they can share a good amount of code and the high level script can query for the information easily.

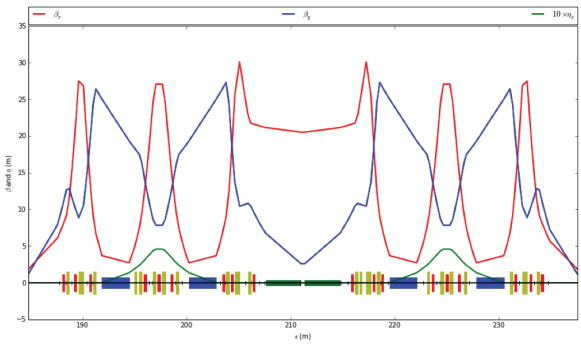

Figure 5: NSLS-II lattice from a simple Python linear lattice code [7].

For the design we would prefer a code modeling both physics dynamics, linear and nonlinear, and the engineering tolerance. But for the commissioning and operations, it might be more helpful to have a simple, fast and flexible code. The PyLat [7] we developed is a single file Python script (Fig. 5), but it only depends on standard library for first and second order linear lattice computing and lattice optimization (matching). Loading online machine data and convert unit with measured magnet field table to models and lattice properties are an integrated process. After tuning the model, its settings can be put back to the real machine again.

ACKNOWLEDGEMENT

We want to thank Dr. Samuel Krinsky (1945–2014) for his guidance and invaluable discussions, Bob Dalesio for his support of developing controls related toolset and his vision on system architecture. We are grateful for support from the NSLS-II. This work is supported in part by the U.S. Department of Energy (DOE) under contract No. DE-AC02-98CH1-886.

REFERENCES

[1] M. Borland, "Elegant: A Flexible SDDS-Compliant Code for Accelerator Simulation", LS-287, Advanced Photon Source, 2000.

[2] J. Bengtsson, "Tracy-2/3", unpublished.

[3] L. Yang, "Tracking Code Development for Beam Dynamics Optimization", PAC'11, New York, March 2011.

[4] L. Yang, Y. Li, W. Guo, S. Krinsky, "Multiobjective optimization of dynamic aperture", Phys. Rev. ST Accel. Beams 14 (2011) 5.

[5] W. Guo, S. Krinsky, L. Yang, "NSLS-II Lattice Optimization with Non-zero Chromaticity", IPAC'10, Kyoto, May 2010.

[6] J. Choi, unpublished.

[7] S. Krinsky, Y. Li, unpublished.

[8] Y. Li, L. Yang, Y. Hidaka, "Efficient MOGA for NSLS-II Ring Dynamic Aperture Optimization", Low Emittance Workshop 2014, INFN-LNF, Frascati, Italy, Sep. 2014.

[9] L. Yang, D. Robin, F. Sannibale, C. Steier, W. Wan, "Global optimization of an accelerator lattice using multiobjective genetic algorithms", NIM-A vol. 609 (2009) 1, 50–57.

[10] EPICS, `http://www.aps.anl.gov/epics/`.

[11] G.M. Wang etc., "Tools for NSLS-II Commissioning", IPAC'15, Richmond, May 2015.

[12] G. Shen, Y. Hu, M.R. Kraimer, K. Shroff, "NSLS II Middlelayer Services", ICALEPCS'13, San Francisco, October 2013.

[13] Control System Studio, `www.cs-studio.org`

[14] J. M. Perkel, "Programming: Pick up Python", Nature, Vol 518, Issue 7537, p 125, Feb, 2015

ISBN 978-3-95450-136-6

THE TPSA AND NORMAL FORM ANALYSIS IN TESLA

Lingyun Yang, NSLS-II, BNL, NY, USA

Abstract

TESLA is a single partile dynamics simulation code. In the recent development and following the algorithms in PTC [1], some normal form analysis and complex TPSA have been added to it. The lattice functions calculation based on symplectic integrator and normal form analysis are more general and robust. A Python module is also developed by wrapping the C++ code to make accelerator beam dynamics simulation and data analysis in both interactive and batch mode.

INTRODUCTION

TESLA is a single particle dynamics code. For the modeling of storage ring lattice, it follows the framework set in FPP/PTC [2, 3]. A nonlinear high order transfer map is first produced by truncated power series algebra (TPSA) [4, 5] and analyzed by normal form method to extract the lattice properties.

Althoug using C++ templates, the initial TPSA in TESLA was only instantiated with real numbers [5] to follow the FORTRAN77 implementation of normal form algorithm [6]. In fact, if there was a complex TPSA available in FORTRAN77, the implementation code would be much simpler and cleaner as the theory described in paper [7]. Since the TPSA algorithm in TESLA are general for any element type, complex or real, the only change needs to make is the instantiating type for the template, plus some functions specific to complex numbers, e.g. real, imag, abs, norm, arg, ...

- TPSA operations: +, -, *, /, +=, -=, *=, /=
- TPSA functions: compress, clear, truncate, exp, log, sin, cos, tan, sqrt, asin, acos, atan, pderivative, pbracket.
- TPSMap: *, +, -, substitute, partialInverse, inverse.
- CTPSMap (complex TPSA map): all functions in TPSMap, real, imag, conjugate.

As pointed out by E. Forest, once having a complex TPSA, the implementation of normal form is more clear. There is no need to simulate complex map operations with two real maps. This brings the new normalization routines in PTC and therefore followed by TESLA.

One example of complex TPSA instantiation is shown below:

```
const int NV = 2;
const int ND = 2;
TPST_<complex<double> > x(NV, ND), p(NV, ND);
x.setVariable(0, 0.0);
p.setVariable(1, 0.0);
TPST_<complex<double> > t1(NV, ND);
t1 = 0.5*x*x + p*p;
```

The output, i.e. the coefficient of power series expansion of $t1 = x^2/2 + p^2$ is simply 1/2 and 1 before x^2 and p^2.

```
t1=
 V : D= 2 L= 6           Base [ 6/6 ]
-------------------------------------
(0.000e+00,0.000e+00)     0 0     0
(5.000e-01,0.000e+00)     2 0     3
(1.000e+00,0.000e+00)     0 2     5
```

where $D = 2$ is the highest order, base is the exponent of each dependent variables x and p. The above data means $t1 = 0 * x^0p^0 + 0.5 * x^2p^2 + 1.0 * x^0p^2$. The imaginary part in the coefficients for each term in $t1$ are all zero.

Trignometric functions, derivatives and substitutions are also obtained in the same way as `TPST_<double>` for complex TPSA.

NORMAL FORM

The algorithm for normal form is described in early publications [2, 3, 6] and implemented in PTC. Here I am outline it briefly how TESLA normalizes the map with the same algorithm, but different TPSA library.

A full turn map is obtained first as $\mathcal{M}_0(z_1, z_2, \ldots, \delta)$. The closed orbit is the constant part of TPSA map. Then the δ-dependent part will be taken out by $\mathcal{M}_0 = \mathcal{A}_0 \circ \mathcal{M}_1 \circ \mathcal{A}_0^{-1}$. From closed orbit condition $z + \delta\eta = \mathcal{M}(z + \delta\eta) + \delta v$, we can solve for η [3],

$$\eta = (1 - \mathcal{M}_z)^{-1} v$$

where $\mathcal{M}_z$ is a map for all z_i, v takes out contributions from all z_i and $\mathcal{A}_0 = z + \delta\eta$. An example of $\mathcal{A}_0$ is

```
 V: D=3 L=56                                                  Base  [ 4/56 ]
-------------------------------------------------------------------------
  1.00e+00  0.00e+00  0.00e+00  0.00e+00   1 0 0 0 0 0    1
  0.00e+00  1.00e+00  0.00e+00  0.00e+00   0 1 0 0 0 0    2
  0.00e+00  0.00e+00  1.00e+00  0.00e+00   0 0 1 0 0 0    3
  0.00e+00  0.00e+00  0.00e+00  1.00e+00   0 0 0 1 0 0    4
  1.56e-03  1.82e-03 -8.76e-03 -8.13e-03   0 0 0 0 0 1    5
  4.96e+00 -1.79e-01  7.06e-01  6.96e-01   0 0 0 0 0 2   20
 -1.20e+02  1.89e+01 -8.77e+01 -8.84e+01   0 0 0 0 0 3   55
```

In this perturbative approach its inverse map is $A_0^{-1} = z - \delta\eta$ with sign reversed for the δ-dependent coefficients.

The linear map is diagonalized by $\mathcal{A}_2$ from the eigenvectors of $\mathcal{M}$. We have chosen the convension $A_2(0, 1) = A(2, 3) = 0$. The current residual map $\mathcal{M}_2$ has a rotation map R in its linear part. An example $\mathcal{A}_2$ is in the following:

```
 V: D= 4 L= 5                                  Base  [ 4 / 126 ]
-------------------------------------------------------------
  2.18e+00  1.39e-12  1.34e-01  3.57e-04  1 0 0 0 0  1
  0.00e+00  4.58e-01 -3.00e-04  1.60e-01  0 1 0 0 0  2
  3.20e-01 -4.91e-05 -9.16e-01  1.42e-12  0 0 1 0 0  3
  2.34e-04  6.73e-02 -3.61e-17 -1.09e+00  0 0 0 1 0  4
```

and the diagonalized map $\mathcal{M}_2$ (shown only up to second order) is

ISBN 978-3-95450-136-6

```
V: D= 4 L= 126                                          Base [ 5/126 ]
-------------------------------------------------------------------
-9.80e-01 -1.98e-01 -1.34e-16 -7.75e-17  0.0  1 0 0 0 0  1
 1.98e-01 -9.80e-01  1.14e-16  2.49e-16  0.0  0 1 0 0 0  2
-1.16e-16  3.14e-18 -9.80e-01 -1.98e-01  0.0  0 0 1 0 0  3
 4.16e-17 -4.71e-16  1.98e-01 -9.80e-01  0.0  0 0 0 1 0  4
-1.42e-23 -2.75e-23  5.56e-23  3.84e-22  1.0  0 0 0 0 1  5
 7.81e-06 -9.77e-05  5.70e-06 -2.08e-05       2 0 0 0 0  6
-1.91e-05  2.01e-05 -4.17e-06 -5.02e-06       1 1 0 0 0  7
 1.23e-05 -4.16e-05 -3.01e-05  3.29e-05       1 0 1 0 0  8
-4.29e-06 -4.34e-06 -5.92e-07  2.32e-05       1 0 0 1 0  9
 3.89e+00 -1.92e+01 -1.29e-04 -7.84e-02       1 0 0 0 1 10
-9.59e-05 -1.19e-05 -1.46e-05 -3.16e-06       0 2 0 0 0 11
 1.22e-06 -3.76e-06 -2.82e-07  2.32e-05       0 1 1 0 0 12
-2.99e-05 -8.33e-07 -6.60e-08 -4.45e-06       0 1 0 1 0 13
 1.91e+01  3.89e+00 -7.84e-02  1.29e-04       0 1 0 0 1 14
-1.50e-05  1.64e-05 -6.71e-06  2.02e-06       0 0 2 0 0 15
-2.92e-07  2.33e-05  3.88e-06  1.29e-05       0 0 1 1 0 16
-4.42e-05 -7.84e-02  3.89e+00 -1.87e+01       0 0 1 0 1 17
-4.31e-08 -2.07e-06 -1.58e-07 -3.20e-06       0 0 0 2 0 18
-7.84e-02  4.42e-05  1.96e+01  3.89e+00       0 0 0 1 1 19
 1.70e-25  2.23e-22 -4.81e-26 -1.51e-21       0 0 0 0 2 20
 ...
```

The linear map has tow rotation matrix at the diagonal and zeros (machine precision) at the off-diagonal. Since at this stage the δ-dependence is removed, the coefficient for base `00001` is identity. If we plot the coordinates by applying $\mathcal{M}_2$ on the initial coordinates iteratively, it is a circle up to the linear order.

The residual nonlinear map becomes $\mathcal{M}_{\rm nl} = \mathcal{M}_2 \circ R^{-1}$, and $\mathcal{M}_0 = \mathcal{A}_0 \circ \mathcal{A}_1 \circ \mathcal{M}_{\rm nl} \circ \mathcal{R} \circ \mathcal{A}_1^{-1} \circ \mathcal{A}_0^{-1}$. The further normalization is done order-by-order in a perturbative approximation. However, depends on what quantities we are interested, we may not need go high order normalizations. A method of calulating some twiss functions from averaging is proposed in Ref. [3], e.g. beta function is an average of x^2. The normalized map makes averaging straight forward.

For the map starting at a different s-location s_2, the full turn map is

$$\mathcal{M}_2 = \mathcal{M}_{1\to 2} \circ \mathcal{M}_1 \circ \mathcal{M}_{2\to 1} \equiv \mathcal{M}_{12} \circ \mathcal{M}_1 \circ \mathcal{M}_{12}^{-1}$$

Once we have normalized $\mathcal{M}_1 = \mathcal{A} \circ \mathcal{M}_{\rm nl} \circ \mathcal{R} \circ \mathcal{A}^{-1}$, then we can have

$$\mathcal{M}_2 = (\mathcal{M}_{12} \circ \mathcal{A}) \circ \mathcal{M}_{\rm nl} \circ \mathcal{R} \circ (\mathcal{M}_{12} \circ \mathcal{A})^{-1}$$

i.e. $\mathcal{B} \equiv \mathcal{M}_{12} \circ \mathcal{A}$ normalized the full turn map $\mathcal{M}_2$ starting at s_2. It simply means if we can transport the map $\mathcal{A}$ from s_1 to s_2, we can normalize the full turn maps starting at any s-locations. In TESLA or any polymorphic code this is trivial, transporting a particle coordinates are same as transporting a map. We know that $\mathcal{R}$ has the tune (rotation) information and $\mathcal{A}$ has the s-dependant β functions. In this way we can get β around the ring.

PYTHON BINDINGS

Python is a high level programming language convenient for both interactive or batch scripting. Wrapping a C/C++ simulation code as Python library is well supported. Such an API is also developed for TESLA. A short Python script which loads the lattice and normalize the one turn map is given in the following:

```
import tesla
ring = tesla.Ring("fodo_02.tslat", "RING")
# six phase space varialbe, 4 independent
m = tesla.TPSMap(5,5,2)
m.resetI()
m.c=[1e-6, 0, 0, 0, 1e-2, 0]
print m
err = ring.trackTPSMap(m, \
    0, ring.elements(), tesla.AP_TRK_DEFAULT)
print m
nf = tesla.NormalForm()
nf.normalize(m, 4)
print nf.A0()
print nf.A1()
```

ACKNOWLEDGEMENT

I want to thank Dr. Samuel Krinsky (1945–2014) for his encouragement, E. Forest for sharing his various notes and FORTRAN code. I am grateful for support from the NSLS-II. This work is supported in part by the U.S. Department of Energy (DOE) under contract No. DE-AC02-98CH1-886.

APPENDIX

A lattice input for TESLA is like the following. The format is close to MAD-8 [8] but in a former grammar.

```
MKBPM: Marker;
QH1G2C30A: Quadrupole, L= 0.275, K1= -0.633;
SQHHG2C30A: Quadrupole, L= 0.1;
QH2G2C30A: Quadrupole, L= 0.448, K1= 1.477;
...
B1G5C01B: Dipole, L= 2.62, ANGLE= 0.1047198,
  E1= 0.05236, E2= 0.05236;
DH02G1A: Drift, L= 4.29379;
...
CELL: LINE=(DH02G1A, ..., DH01G1A);
RING: LINE=(MK0, 15*CELL);
setup, line="RING", shared=false;
#
update, name="B.*", type="Dipole",
  property="SLICE", value=15;
update, name="Q[LHM].*", type="Quad.*",
  property="SLICE", value=10;
update, name="S[LHM].*", type="Sext.*",
  property="SLICE", value=5;

save_lattice, h5group="ring_lat";
basic, h5group = "basic";

frequency_map, nturn=256,
  x=(-0.025, 0.025, 150),
  dp=(-0.03, 0.03, 120), y=1e-5, ppn=20,
  naff_iter=30, h5group="fma_xdp";
```

REFERENCES

[1] E. Forest, Y. Nogiwa, F. Schmidt, "The FPP documentation", ICAP'06, Chamonix, France, 2006.

[2] E. Forest, "Beam dynamics: a new attitude and framework", Harwood Academic Publishers, 1998.

[3] E. Forest, "Implementation and Illustration of Perturbation Theory in a Tracking Code", unpublished.

ISBN 978-3-95450-136-6

[4] M. Berz, "Differential Algebraic Description of Beam Dynamics to Very High Orders", Particle Accelerators, p. 109–124, 1989.

[5] L. Yang, "Array Based Truncated Power Series Package", ICAP'09, p. 371–373, San Francisco, CA, USA.

[6] E. Forest, M. Berz, J. Irwin, "Normal form methods for complicated periodic systems", Particle Accelerators, p. 91–107, 1989.

[7] E. Forest, private communications.

[8] "MAD: Methodical Accelerator Design V8", http://mad.home.cern.ch/mad/mad8web/mad8.html

ISBN 978-3-95450-136-6

THE SIMULATION OF THE ROOM TEMPERATURE CROSS-BAR H TYPE DRIFT TUBE LINAC*

Jinhai Li#, Shuoyu Zheng, China Institute of Atomic Energy, Beijing, China
Zhihui Li, Institute of Nuclear Science and Technology, Sichuan University, Chengdu, China

Abstract

The room temperature Cross-bar H Type Drift Tube Linac (CH-DTL) is one of the candidate acceleration structures working in CW mode. In order to optimize the parameters, the 3 dimensional electromagnetic field of the CH-DTL cavity is simulated. The method of parameter sweeping with constraint variable is better than the method of parameter sweeping with only one variable during the optimization. In order to simplify the manufacture, the drift tube surface can be designed as spherical shape. The effective shunt impedance of the CH-DTL cavity with cylinder end cup is better than that with cone cup.

INTRODUCTON

An industrial scale ADS will require a 10 MW proton beam having an energy between 600 and 1500 MeV. To achieve the required power at this energy will require an average beam current of ≥10 mA. In2010, a study program was initiated to develop the design a 10 mA, 1.5 GeV, CW superconducting proton linac for ADS. The Institute of High Energy Physics (IHEP) and the Institute of Modern Physics (IMP) are both developing superconducting accelerating structures which would follow an RFQ [1].

Although low AC power consumption and a large aperture favour superconducting structures following a 2-3.5 MeV RFQ, normal-conducting accelerating structures have some advantages [2-5]. While the technology for normal-conducting structures in the energy range from 2 to a few tens of MeV is relatively mature, superconducting structures in this energy range are still under development. Normal-conducting structures in this energy range are more efficient than superconducting cavities and, when located downstream of the RFQ, can serve as a beam filter to reduce the potential for beam loss at higher energies.

Under the support of the National Nature Science Foundation of China, we have initiated the design of a 10 MeV CW proton injector, based on normal-conducting Cross-Bar H-type (CH) structure. The CH structure, initially proposed by IAP, Frankfurt University [6, 7] belongs to the π-mode family of accelerating structures and is typically characterized by a high shunt impedance, low stored energy and a stable geometry that is relatively easy to cool. We are evaluating this structure as a potential candidate for CW operation. In this paper we present the results of geometry optimization of the CH structure using the method of parameter sweeping with constraint variable (PSCV).

*Work supported by NSFC (91126003)
#lijinhai@ciae.ac.cn

OPTIMIZATION PHILOSOPHY

The final energy of modern proton RFQs is typically 3MeV, corresponding to a relativistic velocity β=0.08. The room-temperature CH-DTL can be used to accelerate the beam starting at this velocity. The CH structure belongs to the π-mode family of structures in which the cells are βλ/2 long, the cell length at β=0.08 being about 37mm. To save simulation time, the geometry of a single cell was first optimized followed by the optimization of the complete multi-cell cavity. The parameters of a single cell are shown in Fig. 1. The outer drift tube radius (TR) and the radius of the drift tube aperture (HR) are fixed during the optimization.

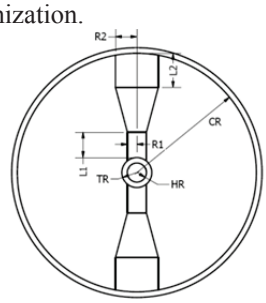

Figure 1: Geometry of a CH single cell.

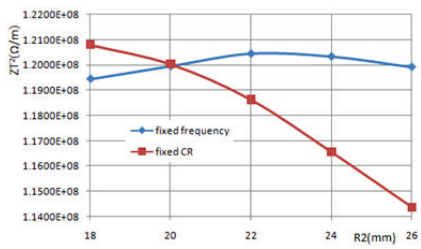

Figure 2: Shunt impedance as a function of outer stem radius using two methods of parameter sweeping.

Typically we would sweep a single parameter while monitoring the cavity's RF properties. For example, we know that changing the length of a drift tube causes a corresponding change in the cavity's Q value [6]. However, by changing the length of a drift tube, the resonant frequency changes. Our objective is to optimize the cavity geometry at a fixed frequency (325 MHz). If the frequency changes during the optimization, the optimized value of the swept parameter will differ from the value corresponding to the correct frequency as shown in Fig. 2. In Figure 2 we have swept the radius of the drift-tube stem base (R2) while fixing the cavity radius (CR). We see that the effective shunt impedance decreases with increasing R2 while the resonant frequency increases from 321.7 to 333.5MHz. It is convenient to use the cavity radius (CR) as a "constraint variable" to fix the resonant frequency to 325 MHz. By doing so we find that the maximum effec-

ISBN 978-3-95450-136-6

tive shunt impedance at the correct frequency occurs at R2=22. We refer to this method as "parameter sweeping with constraint variables" (PSCV). Other parameters can be selected as constraint variables, but we find that the resonant frequency is more sensitive to cavity radius than it is to other geometrical parameters.

DRIFT TUBE GEOMETRY

The drift tube in CH-DTL is typically much smaller than drift tubes in a conventional DTL, and there is little possibility to optimize the drift tube length and outer radius (TR). The small drift tubes have much smaller capacitance resulting in a higher shunt impedance however, because they are so small they are difficult to manufacture with integral cooling channels [7]. Traditional drift tubes are nominally cylindrical. By modifying the design to have a spherically shaped drift tube, the stem and drift tube can be manufactured (turned) in one step without welding or brazing. In Figure 3 we can see that axis of revolution for the stem is coaxial with that of the drift tube. The effective shunt impedance of the spherical drift tube is only slightly lower than that of the cylindrical drift tube (<1%) as shown in Fig. 4.

Figure 3: Spherical drift tube.

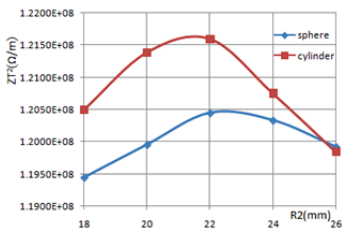

Figure 4: Shunt impedance for two different drift tube shapes as a function of the stem-base radius.

OPTIMIZATION OF A SINGLE CELL

The CH single cell is shown in Fig. 5, and is composed of one acceleration gap and two half stems and half drift tubes. The TE_{210} mode is established in the single cell, by imposing the boundary condition that the magnetic field, that encircle the stems, be perpendicular to the end planes.

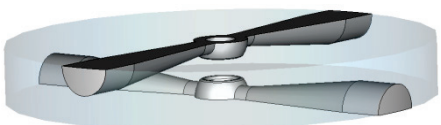

Figure 5: 3-D geometry of a single cell.

To optimize the shunt impedance of the single cell, we have adjusted the lengths of the inner and outer cylindrical stem segments, L1 and L2, as well as the radius of the stem base, R2, while using the cavity radius, CR, as the constraint variable to maintain the resonant frequency. The inner stem radius, R1, is physically constrained by the drift tube radius and can't be changed. For this calculation we have fixed the axial length of the single cell to be 37 mm, corresponding to a beam velocity β=0.08. We first swept the value of R2 from 18 to 26 mm as shown in Fig. 4, to find that the maximum effective shunt impedance is obtained at R2=22 mm.

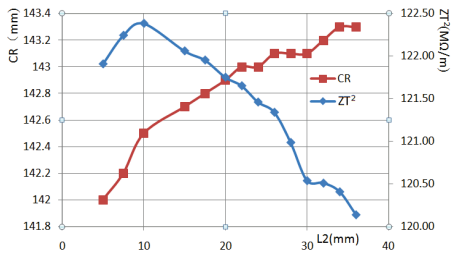

Figure 6: Shunt impedance and cavity radius at a fixed frequency as a function of L2.

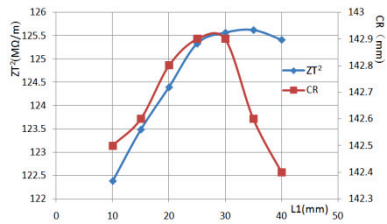

Figure 7: Shunt impedance and cavity radius at a fixed frequency as a function of L1.

Setting R2 to 22 mm we then swept L2 to find that the highest value for shunt impedance occurs for L2=10 mm as shown in Fig. 6. Finally, setting L2 to 10 mm, we swept L1 to find that the maximum effective shunt impedance occurs for L1=35 as shown in Fig. 7.

In each of these procedures we see that the maximum shunt impedance occurs at a different cavity radius, CR, which has been constrained to assure resonance at 325 MHz. Because the values of L2 and L1 have been changed, we sweep R2 again, to find that the maximum effective shunt impedance occurs at R2=27mm as shown in Fig. 8. Comparing Figs. 4 and 8 we can see that the maximum effective shunt impedance has increased from 121 to 128 MΩ/m while the optimized value of R2 has increased from 22 to 27 mm. We found that iterating this procedure a third time yields minimal improvement in the shunt impedance.

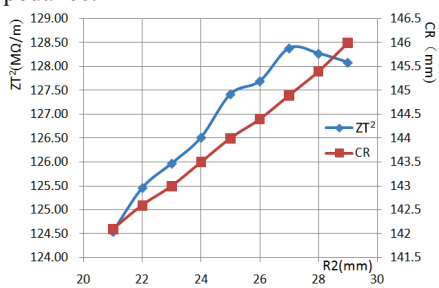

Figure 8: Shunt impedance and cavity radius at a fixed frequency as a function of R2.

ISBN 978-3-95450-136-6

OPTIMIZING THE MULTI-CELL CAVITY

Our multi-cell CH-DTL cavity model includes four drift tubes and five gaps as shown in Fig. 9. In addition to the parameters optimized above, the multi-cell cavity contains two additional geometrical features requiring optimization. These include the length and radius of the end cups (EL and ER). We first swept ER to find that the effective shunt impedance is inversely proportional to ER as shown in Fig. 10.

In this calculation we have considered only the central portion of the cavity containing the drift tubes. In other words, the cavity is assumed to be only 5 times the length of a single cell or 185 mm and only the faces of the end cups are included. In order to accommodate the magnetic elements needed for beam focusing, ER should not less than 60 mm.

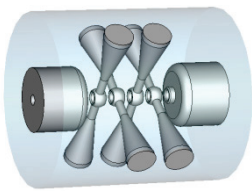

Figure 9: 3-D geometry of the 5-cell CH-DTL cavity model.

As we increase the end cup length(EL) we see that the effective shunt impedance(ZT^2) decreases rapidly due to the power dissipated in the end regions where no acceleration occurs as shown in Fig. 11.

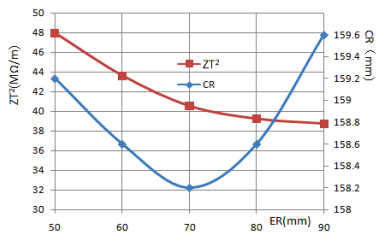

Figure 10: ZT^2 and cavity radius at a fixed frequency as a function of ER for a 5-cell cavity without end cups.

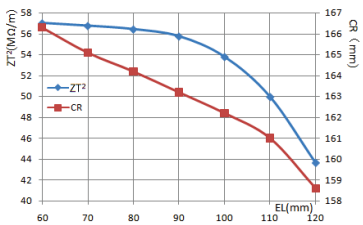

Figure 11: ZT^2 and cavity radius at a fixed frequency as a function of EL for a 5-cell cavity with end cups.

THE MANUFACTURE OF THE CAVITY

The material of the whole cavity is made of copper. The cavity wall, the end cell and the drift tube with the stem have been made as shown from Figs. 12 to 14.

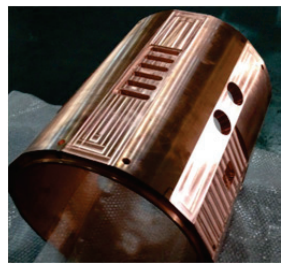

Figure 12: The CH-DTL cavity wall.

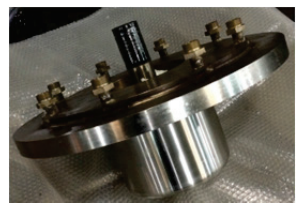

Figure 13: The CH-DTL end cell.

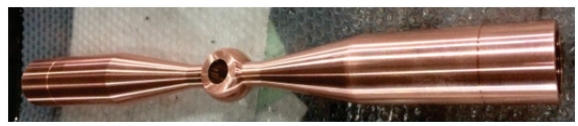

Figure 14: The drift tube with stem.

We will weld the drift tube to the cavity wall later and measure the RF property of the low power.

ACKNOWLEDGMENT

This work is supported by the National Natural Science Foundation of China (NSFC). I would show my best thanks to James Edward Stovall for his kind help.

REFERENCES

[1] WeimingYue, X. L. Guo, S. He, Y. He, R. X. Wang, P. R. Xiong, M. X. Xu, B. Zhang,S. H. Zhang, S. X. Zhang, H. W. Zhao, R&D of IMP Superconducting HWR for China ADS, proceedings of LINAC2012, 2012, TUPB055, pp 600-602.

[2] L. Ristori, G Apollinari, I. Gonin, T. Khabiboulline, G. Romanov, design of normal conducting 325 MHz crossbar H-type Resonators at fermilab, proceedings of LINAC2006, 2006, THP057, pp 710-712.

[3] L. Ristori, G. Apollinari, I. Gonin, T. Khabiboulline, G. Romanov, fabrication and test of the first normal-conducting crossbar H-type accelerating cavity at fermilab for HINS, Proceedings of PAC07, New Mexico, 2007, WEPMN110, pp. 2292–2294.

[4] W-M. Tam,G. Apollinari, T. Khabiboulline, R. Madrak, A. Moretti, L. Ristori, G. Romanov, J. Steimel, R. Webber, D. Wildman, proceedings of LINAC2008, Victoria, 2008, MOP012, pp 79-81.

[5] R.C. Webber,G. Apollinari, J. P. Carneriro, I. Gonin, B. Hanna, S. Hays,T. Khabiboulline, G. Lanfranco, R. L. Madrak, A. Moretti, T. Nicol, T. Page, E. Peoples, H. Piekarz, L. Ristori, G. Romanov, C.W. Schmidt, J. Steimel, W. Tam, I. Terechkine, R. Wangner, D. Wildman, proceedings of LINAC2008, Victoria, 2008, MO301, pp 36-40.

ISBN 978-3-95450-136-6

[6] Gianluigi Clemente, The room temperature CH-DTL and its application for the FAIR Proton injector, Ph.D. dissertation, University Frankfurt, 2007, p52.
[7] U. Ratzinger, R. Tiede, H. Podlech, G. Clemente, B. Hofmann, A. Schempp,L. Groening, W. Barth, S. Yaramishev, Z. Li, and S. Minaev, The 70 MeV p-Injector Design for FAIR, AIP Conference Proceedings 773, (2005), p249-253.

ISBN 978-3-95450-136-6

THE DEVELOPMENT OF INJECTION AND EXTRACTION SOFTWARE IN THE RAPID CYCLING SYNCHROTRON

L. Huang*, Y. An, H. Ji, S. Wang, CSNS/IHEP, CAS, Dongguan, 523803, China

Abstract

The Rapid Cycling Synchrotron is widely used in medicine, materials and biology. The software, which studies injection and extraction of the synchrotron and is widely applied in almost all those synchrotrons, is useful to design of the new synchrotron. In this paper, the development of the software is introduced and an example is presented.

INTRODUCTION

The Rapid Cycling Synchrotron is widely used in medicine, materials and biology. High-energy, ionising radiation has proved to be effective in the treatment of cancerous tumours by causing double-strand breaks in the cell DNA. In particular, hadrons have the advantageous property of penetrating the body easily and then depositing their energy at a depth determined by their initial energy [1]. The characteristic of some materials will be changed as it is irradiated by high energy proton beam. It is specially used in aerospace, the spacecraft and all the detectors in universe may be broken with the action of cosmic high ray. The ion synchrotron helps researchers predict uncharted phenomenon of the spacecraft in outer space and adopted novel method to improve the lifetime of the spacecraft. The synchrotron also offers the micro-beam which is used in biology [2]. The biologist uses the micro-beam to study the single cell of the biology. It promotes the development of the biology and medicine.

The rapid cycling synchrotron is widely studied and constructed in all over the world now, it is different for every synchrotron and the software of injection and extraction study is also different, thus a lot of repetitive work is done again and again. A rapid cycling synchrotron is firstly designed and the software of injection and extraction design is development based on matlab/AT [3]. Then, according to the software, the widely software which can simulate injection and extraction for all the synchrotron is plan to develop. The software will help researchers to design and construct new synchrotron.

THE RAPID CYCLING SYNCHROTRON

The typical rapid cycling synchrotron is designed to accumulated proton beam and accelerates it from 7 MeV to 300 MeV with the repetition rate of 0.5 Hz. The layout of the synchrotron is shown in Fig. 1. The beam injects the synchrotron by two bumps, injection magnets septum (IMS) and injection electrostatic inflector (IEI). The beam is slow extracted by sextupoles, RF knockout (RFK), extraction magnets septum (EMS) and extraction electrostatic septum (EES) for micro beam, material and biology study. The lattice of the rapid cycling synchrotron adopts a FODO cell based 2-fold structure. The main parameter of the synchrotron is given in Table 1.

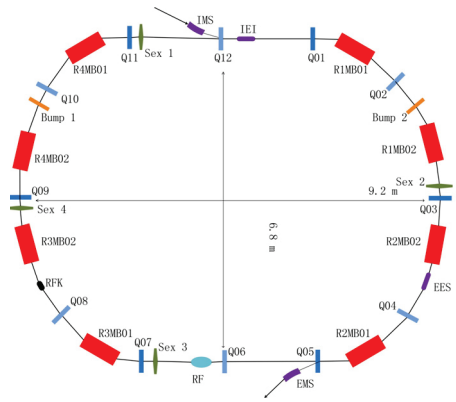

Figure 1: The schematic view of the synchrotron

Table 1: The Main Parameters of the Synchrotron

Parameters	Units	Values
Circumference	m	35
Inj. Energy	MeV	7
Ext. Energy	MeV	300
Tunes(H/V)		1.72/1.28
Repetition rate	Hz	0.5
Emittance	π mm-mrad	150/50
Particle Number		$2*10^{11}$

INJECTION

The proton beam, which is pre-accelerated by linear accelerator, is injected into synchrotron by multi-turns injection method. Injection energy of 7 MeV is decided in consideration of space charge limitation for proton.

The linear beam passes through the IMS and the IEI and arrives injection point, thus injection beam joins circular beam and ramps with circular beam together. The orbit of the linear beam is easily given in injection region. The lowest aperture of the synchrotron is generally the EES, and the circular beam may lose at EES and EMS, so it has to judge the loss beam in extraction region before every ramping turn. Furthermore, the circular beam ramps one turn and arrives in injection region, it may enter and hit the IMS and IEI, thus the beam loses, so the beam also

#huangls@ihep.ac.cn

ISBN 978-3-95450-136-6

should be judged at them. The closed orbit is bumped by two bump magnets, and the intensity of the bump steps down. Injection beam is painted around 200 π.mm.mrad in horizontal phase space by sweep of magnetic field of the two bump magnets.

According to the physical consideration, the injection software based on AT is developed, and injection process is simulated. The linear beam is injected in synchrotron with 50-turn injection and 100 particles per turn in the simulation. Fig. 2 gives the change of the closed orbit, the circular beam and linear beam at injection point and injection efficiency. The height of the closed orbit in the injection region decreases from 36 mm to 24 mm. The efficiency of the injection is over 98% with 50-turn injection. Injection beam is adiabatically captured into buckets for acceleration.

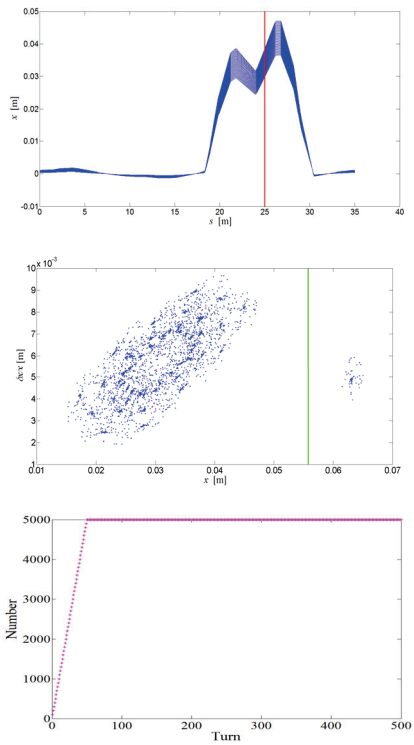

Figure 2: The closed orbit in injection (top), injection beam and circular beam in injection point (middle) and injection efficiency (bottom).

EXTRACTION

The layout of extraction is shown in Fig. 1, the components of extraction include four sextupoles, the RFK, EMS and EES. The resonance sextupole (Sex 1) is placed in a dispersion-free region before the arc, and the other resonance sextupole (Sex 3) is symmetrical with Sex 1. Sex 2 and Sex 4 correct chromaticity for the Hardt condition.The accelerated beam is extracted by slow extraction scheme using a third order resonance ν_x = 5/3 by the transverse RFK [4][5]. The phase advance to the EES is well above the permissible minimum of 230 degree and close to the ideal of 225 degree, the phase advance to the EMS is a comfortable 81.5 degree, which gives 98% of kick that would be available if the phase advance were 90 degree. The dispersion function are configured with $D_x>0$ and $D'_x<0$ at EES for the Hardt condition. Stabilities of extraction beam parameters, for example beam position, beam size, momentum deviation and extraction efficiency, are very important issue for particle beam therapy, material and biology study. In the RFK method, the separatrix is kept constant whole extraction, so the control of extraction is very easy, and it makes extraction beam position and extraction efficiency more stable.

The software of extraction checks the reasonable of the lattice design, and simulates the beam loss and beam stability. The accelerated beam is completely extracted at several million turns, even several ten million turn. The study of extraction also includes several kilo turns, even more. The tune of the synchrotron firstly adjusts to 1.67. The code can analyze the beam loss at IMS, IEI and EMS, then, the accelerated beam passes through the synchrotron with reasonable intensity of the sextupole and RFK. The particles are judged when they arrive at EES. Some particles hit the EES and lose, some particles enter in EES and EMS and are extracted, even some lose in pipe, but many particles per turn pass through the extraction region and ramp again. In order to stability and uniformity of the extraction efficiency, the intensity of the resonance sextupole and RFK should be considered carefully. To decrease beam loss in extraction, the component of EES and EMS should be designed reasonably, including its location, gap, length and intensity. The aperture of the magnets in the extraction region should be given through the software. Furthermore, the orbit of the extraction beam is also given. In fact, only the first and third quadrants are usable to extraction beam, the software compares advantage of two quadrants. The spiral step and spiral kick are also confirmed in the simulation.

To check the software, the extraction of the designed synchrotron is simulated. 20 kilo particles ramp 0.2 million turns. Fig. 3 gives the distribution of the extraction beam at the EES, and the loss rate is about 7%. The extraction beam is referred to as the rayleigh distribution when only the resonance sextupole, but it change uniformity as the effect of the sextuple and the RFK shown in Fig. 4. The parameters of the EES and EMS are shown in Table 2. The efficiency of the extraction is over 90% in the simulation.

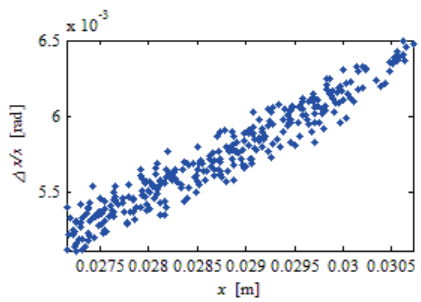

Figure 3: The extraction beam at the EES.

ISBN 978-3-95450-136-6

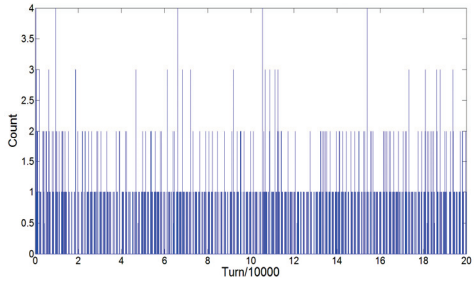

Figure 4: The extracted efficiency with the sextupole and the RFK.

Table 2: The Main Parameters of EES and EMS

Parameters	Units	Values
Length(EES)	m	0.5
Gap(EES)	mm	10
Kick(EES)	mrad	5
Electric filed(EES)	kV/mm	0.3
Length(EMS)	m	0.8
Gap(EMS)	mm	20
Thickness(EMS)	mm	15
Kick(EMS)	rad	0.1
Magnet filed(EMS)	T	0.675

SUMMARY

The simulated software of the injection and extraction design for rapid cycling synchrotron based on matlab/AT is developed, which treats with injection and extraction design particularly, and is the wide software for this entire type synchrotron. The program is check by the designed synchrotron, and it shows it is usable. The software will be improved so as to a wholesome software.

REFERENCES

[1] Proton-ion medical machine study (PIMMS), CERN – PS Dicision, CERN/PS 99-010, Geneva, Switzerland, 1999, p. 1.

[2] L. Sheng, Intermediate energy heavy ion microbeam irradiation facility, Ph. D Thesis (2010), p.4.

[3] http://als.lbl.gov/als_physics/portmann/MiddleLayer/Release/at/doc_html/, retrieved 10th Aug. 2015.

[4] N. Carmignani, RF-KNOCKOUT EXTRACTION SYSTEM FOR THE CNAO SYNCHROTRON, Proceedings of IPAC'10, Kyoto, Japan, p. 3891.

[5] T. Furukawa, Nuclear Instruments and Methods in Physics Research A 489 (2002): 59 – 67.

ISBN 978-3-95450-136-6

DISCUSSION ON THE PROBLEMS OF THE ONLINE OPTIMIZATION OF THE LUMINOSITY OF BEPCII WITH THE ROBUST CONJUGATE DIRECTION SEARCH METHOD

Hongfei Ji#, Sheng Wang. CSNS/IHEP, CAS, Dongguan, 523803, P.R. China
Yi Jiao, Daheng Ji, Chenghui Yu, Yuan Zhang. IHEP, CAS, Beijing 100049, P.R. China
XiaoBiao Huang. SLAC, Menlo Park, California 94025, USA

Abstract

The robust conjugate direction search (RCDS) has high tolerance to noise in beam experiments, and it is an efficient experimental technology for online optimization with multi-dimensional variables. This method has been used to optimize the machine performance of the SPEAR3 storage ring online. In this paper, we discuss the problems and developments of the online optimization of the luminosity of BEPCII with this method. To apply the method in BEPCII, the objective function, optimization time and experimental applications require careful consideration based on the analysis of the real machine situation.

INTRODUCTION

A particle accelerator is a complex system that is made up of many components, e.g., beam transport, control, diagnostic, acceleration systems. There are many variables to be tuned, which are typically coupled. So we have to optimize the performance of an accelerator in a multi-dimensional variable space. To meet the design requirements of the machine, we need to optimize parameters to meet the demands in different phases: design, commissioning, and operation.

Generally, in an accelerator that is built already, optimization algorithms are rarely used. There inevitably exist effects of error which make some differences between the fact and the theoretical model. The optimized parameters from theoretical analysis and numerical calculation may not work very well in real operation. Therefore more efforts are needed in beam tuning and operation to achieve better performance. In most cases, physicists can only repeatedly tune and scan parameters according to the actual situation of the accelerator observed directly, starting from theoretic design values. Although this method usually works, it is time-consuming and the effectiveness decreases as the number of parameters increases.

Along with the unceasing development of computer technology and optimization algorithms, applications of online optimization algorithms of multi-dimensional variables on accelerators have become imperative. Several optimization algorithms have been proposed for different purposes in different accelerator labs, the downhill simplex method [1-3], Rotation rate tuning [4], Random walk optimization [5], Robust conjugate direction search (RCDS) [6] and so on. Among these methods, the algorithm RCDS has high tolerance to noise in beam experiments and high convergence speed, which can reduce effects of noise and lead to optimal solution. RCDS method can be used as an online optimization algorithm to optimize the performance of an accelerator and it is effective in optimizing a single-objective function of several variables with a certain level of noise. This method has been successfully applied to the SPEAR3 storage ring for realistic accelerator optimization problems, including the minimization of the vertical emittance with skew quadrupoles and the optimization of the injection kicker bump match. But it has not been applied to colliders.

The most important measure of performance of colliders is the luminosity. The peak luminosity of BEPCII [7] at IHEP now is 8.0×10^{32} $cm^{-2}s^{-1}$. It is an essential subject for physics study of BEPCII to ensure the stability operation and to achieve a higher luminosity by further optimization of parameters. Luminosity is considered as a multivariable function with more than 20 variables to be tuned, such as the transverse offset in displacement and angular deviation (x, x', y, y') at the interaction point (IP), the x-y coupling parameters (R_1, R_2, R_3, R_4), working point, RF parameters, and optical parameters at the IP. At present, operators mainly tune and scan parameters manually. That is, they manually scan one parameter to get a value which corresponds to a higher luminosity, and then scan the next with the first parameter fixed. All parameters can be manually optimized in a similar fashion. Because the actual situation of the collider changes as beam current decreases, operators always have to repeat the process. Moreover, because of the complexity of the collider, optimization results vary with each person and time.

So it makes sense to set up an online optimization process based on the RCDS method and establish a standard operation system for optimization of luminosity of BEPCII by scanning parameters in a standardized and routine way. It is expected to reduce operators' work and contribute to increasing the peak luminosity using the online algorithm. A flowchart of RCDS for online luminosity tuning in BEPCII is shown in Fig. 1.

jihf@ihep.ac.cn

ISBN 978-3-95450-136-6

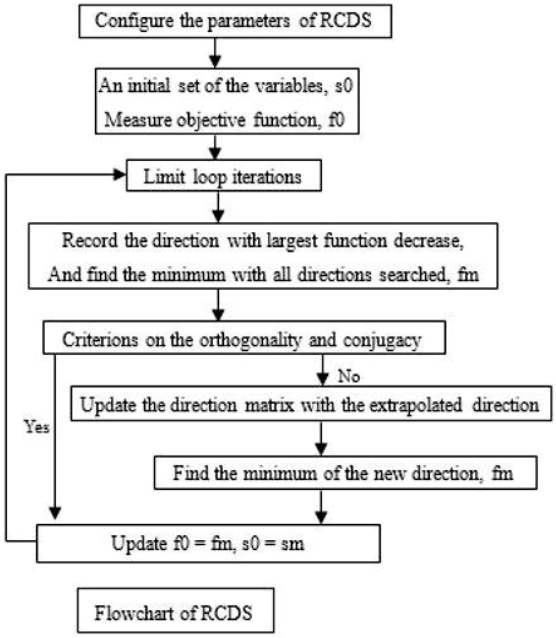

Figure 1: flowchart of RCDS for online luminosity tuning in BEPCII.

The online control program at the BEPCII is SAD, which is a computer program complex for accelerator design and operation. So we developed the algorithm code of the RCDS method in SAD program, and the optimization algorithm is combined with the operating system as needed. The luminosity is considered as an objective function with multi-dimensional variables to be tuned. The set of parameter values produced by the RCDS method is used to set up the collider. Then we get the luminosity from the database of BESIII. As needed, the value of objective function is calculated from the luminosity and introduced into the RCDS method to continue the iterator.

CHOICE OF THE OBJECTIVE FUNCTION

It is very critical to choose an appropriate objective function in order to achieve high optimization efficiency and effectiveness. The luminosity of BEPCII determined by the BESIII End-cap Electro-Magnetic Calorimeter is actually an integral average luminosity value of luminosity values in 30 seconds. So it has a long response time. Moreover, the decrease of beam current has a significant effect on the luminosity both in theory and in practice such that the same parameter set may lead to different luminosity values over time, which will directly affect the efficiency of optimization. Theoretically, luminosity can be expressed as

$$L\left[cm^{-2}s^{-1}\right] = L_0 R = 2.17\times10^{34}(1+r)\xi\frac{E[GeV]k_b I_b[A]}{\beta_y^*[cm]}R \quad , \qquad (1)$$

where L_0, r, ξ, E, k_b, I_b, β^*_y represent the nominal luminosity, the aspect factor, the beam-beam parameter, the energy, the number of bunches, the bunch current, and the value of the vertical beta function at IP, respectively. R is a reduction factor which may come from a non-zero horizontal crossing angle, coupling, tune and so on. It is expected that the optimization algorithm can find an optimized set of parameter values, which can lead to a higher luminosity value with the factor R closer to 1.

So we have to choose another objective function which can well represent the collision luminosity, has a short response time and would be less affected by the decrease of beam current. To this end, the objective function (with a minus sign) is chosen to be the so-called specific small-angle luminosity (SSAL),

$$L_{SpeLumP} = \frac{L_{ZeroLumP} / N_{bCollide}}{(I_{BER} / N_{bBER}) * (I_{BPR} / N_{bBPR})} \quad , \qquad (2)$$

where $L_{ZeroLumP}$ is the small-angle luminosity given by a zero-degree detector [8], $N_{bCollide}$ is the number of collision bunches, I_{BER} and I_{BPR} are the electron and positron beam current respectively, and N_{bBER} and N_{bBPR} are the number of electron bunches and positron bunches respectively. As a result, the decay of the beam current during the RCDS scan has a very weak effect on the SSAL.

SHORTENING OPTIMIZATION TIME OF THE APPLICATION

Electron beam current and positron beam current both decay in time due to the limited beam lifetime in BEPCII. So the state of the machine also changes with time. Time between two injections is limited, which means time for optimization is also limited. Thus shortening optimization time becomes very important.

The optimization time depends primarily on the response speed for setting parameters and the data acquisition speed from the database, which in fact determines the time needed to get an evaluation. Because the luminosity of BEPCII is sensitive to the vertical displacement, we estimate the response time requirement by setting the y offset to a fixed value. The results of a series of measurements show that the state of the machine becomes stable again 7 seconds after a deviation. Thus, to obtain a trust worthy response for the luminosity for a changed variable, it is best to take more than 7 s to complete an evaluation.

FOUR VARIABLES WERE USED AS KNOBS IN THE EXPERIMENTS

As a preliminary test of the effectiveness of this method in a collider, only the 4 offset variables were considered, i.e., (x, x', y, y') at the IP. We set an optical model of BEPCII, which was already found by manual tuning, as the reference state, with SSAL of about 51 mA^{-2}. The variables were deliberately set to deviate from the

ISBN 978-3-95450-136-6

reference and then the RCDS scan was performed to observe the increase in luminosity.

Right from the reference, we deliberately set the offset with a deviation. The SSAL decreased to be only 4.3 mA^{-2}. The corresponding state of the machine was used as the initial state to run the RCDS algorithm. During the run, the objective was calculated from an individual reading of the luminosity. Finally, the objective is tuned to about -50 mA^{-2}, with a total of 138 evaluations taking about 24 minutes. The evolution of the luminosity recorded by BESIII is shown in Fig. 2, and further verifies the experimental effectiveness.

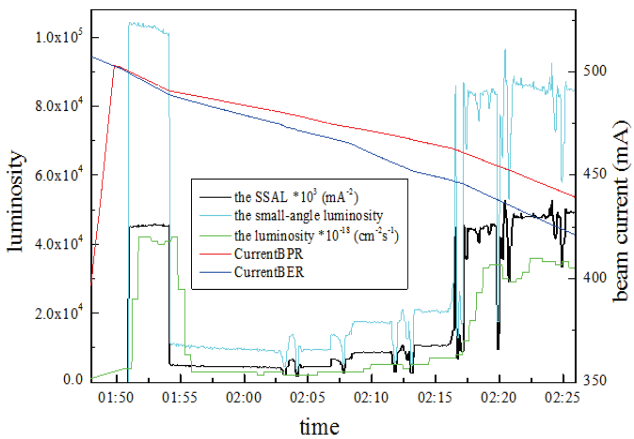

Figure 2: Evolution of the luminosity recorded by BESIII. Unlike the recovery of the SSAL, both the small-angle luminosity and the luminosity recorded by BESIII achieve a partial recovery, which results from the effect of the decay of the beam current.

DISCUSSION

The paper states the major problems of the online optimization of luminosity with RCDS. Taking the SSAL as objective function, we have explored the feasibility of online luminosity tuning using the RCDS method in machine experiments with the BEPCII collider. Four variables of orbital offset were used as knobs in the experiments. They were first deviated from the reference standard, which led to a reduced luminosity. An automatic scan of these knobs was then launched with the RCDS method. Convergence was reached within a few iterations, and a recovery of luminosity was also observed.

Only 4 variables are tuned among the more than 20 variables affecting the luminosity in the experiments. As we know, an actual luminosity optimization requires delicate tuning of all the related variables.

The more variables are tuned, the more evaluations are taken and the longer time is needed. Then it is difficult to tune more variables simultaneously during a collision period. Fortunately, the more than 20 variables scanned for the luminosity tuning are controlled by different machine components (e.g. correctors for orbital offset and skew quadrupoles for coupling factors). So the variables can be divided into several groups (orbital tuning, coupling factors). Then one RCDS scan may be done in turn for each group, or even in different collision periods, until all the optimal values of the variables were found.

Moreover, when some sensitive parameters are tuned online, great care will be required to ensure the stability of the machine. For example, the present working point of the collider is around (6.513, 5.583) (as shown in Fig. 3). The reasonable tuning ranges of the working point for a higher luminosity are extremely limited.

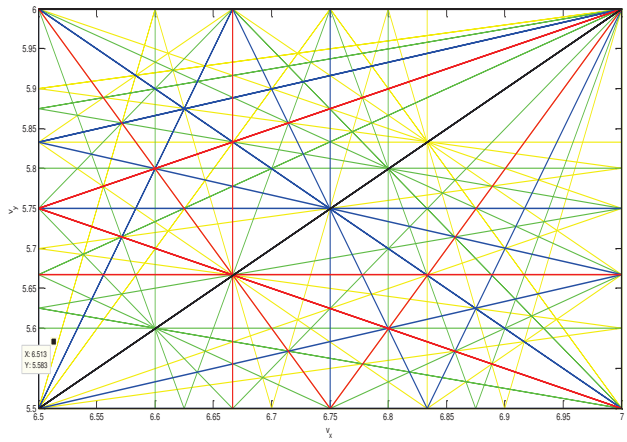

Figure 3: The available tuning ranges of the working point.

ACKNOWLEDGEMENT

The authors would like to thank the members of the BEPCII physics group for various suggestions and practical experience. We also would like to acknowledge the support in experiments of the members of the BEPCII operation group.

REFERENCES

[1] Emery L et al. PAC03, Portland, Oregon, 2003
[2] Nelder J, Mead R. Computer Journal 7, 1965, 308
[3] Funakoshi Y et al. EPAC2008, Genoa, Italy, 2008, p.1893
[4] Scheinker A et al. Phys. Rev. ST Accel. Beams, 2013, **16**: 102803
[5] Aiba M et al. IPAC2012, New Orleans, Louisiana, USA, TUPPC033
[6] Huang X, Corbett J, Safranek J, Wu J. Nucl. Instrum. Methods Phys. Res., Sect. A, 2013, **726**: 77-83
[7] IHEP-BEPCII-SB-03-3, 2003. (in Chinese)
[8] Xue Zhen et al. Chinese Physics C, 2011, **35**(1): 1-5

ISBN 978-3-95450-136-6

3D NUMERICAL SIMULATION OF EXTRACTION OF A LARGE-POWER NEGATIVE ION SOURCE

Zhe Zhang#, DeZhi Chen, Dong Li, RuiMin Pan, Chen Zuo
State Key Laboratory of Advanced Electromagnetic Engineering and Technology (AEET)
College of Electrical and Electronic Engineering
Huazhong University of Science and Technology (HUST), Wuhan 430074, China

Abstract

A driver of the RF negative ion source has been finished at Huazhong University of Science and Technology (HUST) last year, and then the extraction system of negative ion source will be finished in the next stage. The extraction system has important influence on the extraction beam. This paper presents a 3D numerical modelling to simulate the extraction system, considering the space charge effect. The electric field is calculated by solving Poisson equation with finite difference method (FDM). The particle transport process is simulated with particle-in-cell (PIC) method, considering the electrodes field, the electron deflection magnetic field, as well as the field of the space charge. The influences of the shape of electrodes and the electron deflection magnetic field on the quality of extraction beam are studied. These results provide useful guidance for the design of a negative ion source.

INTRODUCTION

The radio frequency (RF) driven negative hydrogen ion source is the reference source for the ITER neutral beam injection (NBI) system [1,2]. RF driven negative hydrogen ion source can be divided into three parts: driver, exp-ansion region and extraction system (see Fig. 1)[3,4].

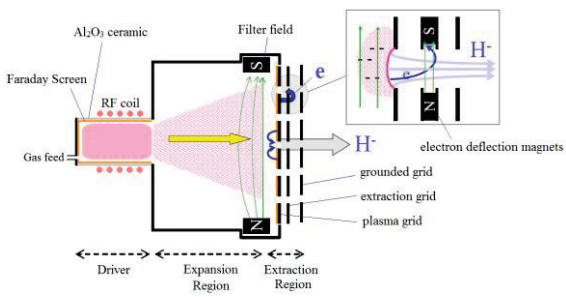

Figure 1: Schematic view of negative ion source.

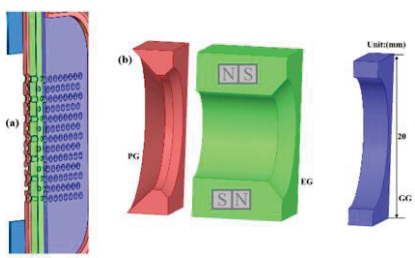

Figure 2: Schematic view of extraction system.

This paper presents a 3D numerical modelling to simulate the extraction system. As shown in Fig. 2, the extraction system consists of three grids: the plasma grid (PG), which separates the plasma from the beam region; the extraction grid (EG), where the co-extracted electrons are filtered out of the beam by the fields from the permanent magnets embedded in the extraction grid; and the grounded grid (GG)[5, 6]. The extraction system of the test facility BATMAN [7] (a test facility at IPP, Carching) is used as an example in this paper.

SIMULATION MODEL

Model Description

The simulation domain is restricted to a single extraction aperture of the grids due to the periodicity of the structure, as shown in Fig. 3. The particles can only move in the space without grids, as shown in Fig. 4.

The CoSm permanent magnets are embedded in EG to deflect the co-extracted electrons out of the beam.

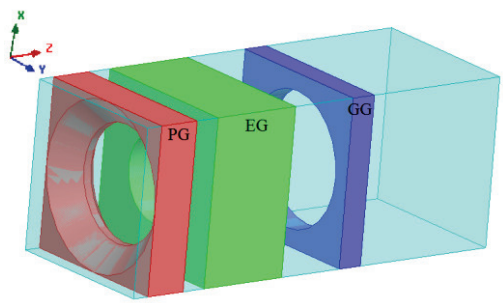

Figure 3: Computational domain.

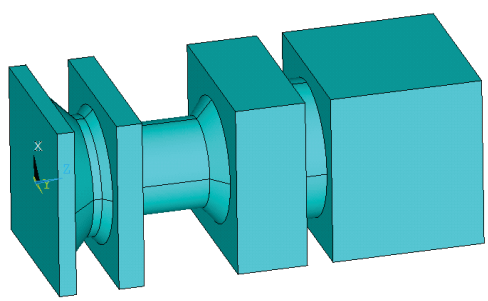

Figure 4: Domain without electrodes.

The plane $z=z_{min}$ with the plasma potential (approximately equal to potential of PG) is the emitting surface that a prescribed number of particles are injected every time step from this plane uniformly in x and y

zhzhang@hust.edu.cn

ISBN 978-3-95450-136-6

directions. The plane $z=z_{max}$ satisfies the natural boundary conditions. And the periodical boundary conditions are used in the x and y directions.

Flow Chart of Simulation Code

The general flow of simulation is shown in Fig. 5:

(1) Initialize: input the electron density ne, the electron temperature Te, the ion density ni and the ion temperature Te; define the type of the particle location and velocity distributions; import the data of the reflecting magnetic field.

(2) Calculate emitting surface: this is a complex step including the interaction between plasma and electromagnetic field, the collisions of the particles. We have not complete this step up to now, so in this paper, the location and velocity of electrons and ions are assumed in uniform distribution.

(3) Calculate electric field: the finite difference method is used to solve Poisson equation.

(4) Calculate particle trajectories: tracking the particle trajectories from their starting points to their leaving points of the calculate domain.

(5) Calculate charge density: the space charge density is calculated on the grid based on the ray-traced trajectories, the charge deposition is based on the method used in the more established PIC codes, where the space charge is assigned to the grid from particles at each time step.

(6) Convergence criterion: the evolution of the transverse rms emittance has been chosen to be used for estimating the convergence.

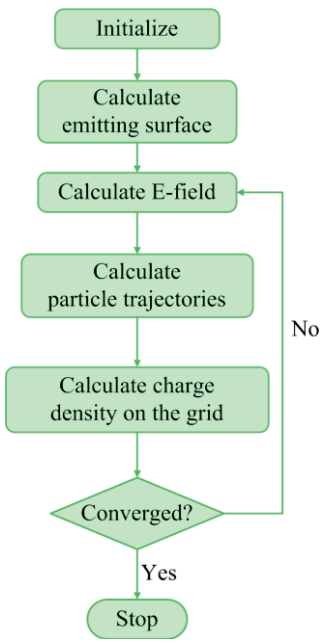

Figure 5: General flow chart of the simulation.

RESULTS AND DISCUSSION

This paper calculated two different extraction systems of BATMAN (CEA and LAG), as shown in Fig. 6. The size of computational domain is shown in Table 1.

Every step in Fig. 5 has been finished except for the calculation of emitting surface. This paper presents the preliminary results, which is agree well with the IPP results, electrons are almost filtered out of the beam.

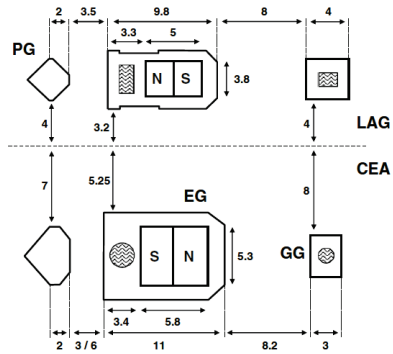

Figure 6: Geometry of the two different extraction systems (unit: mm).

Table 1: Size of CEA and LAG

	LAG	CEA
X_{min}(mm)	0	0
X_{max}(mm)	12	20
Y_{min}(mm)	0	0
Y_{max}(mm)	11.5	20
Z_{min}(mm)	0	0
Z_{max}(mm)	45	50
PG(kV)	-26.4	-26.4
EG(kV)	-16.8	-16.8
GG(kV)	0	0

The equipotential lines for the two different extraction system is shown in Fig. 7 and Fig. 8. The potential of grids is PG: -26.4kV, EG: -19.2kV, GG: 0V.

The vertical magnetic field strength Bx of the electron deflection field along the aperture center is shown in Fig.9 and Fig. 10. The samarium cobalt magnet is used, the relative permeability is 1.07, and residual magnetism is 1.1T.

The negative ion (in blue) and electron (in red) trajectories for the two different extraction systems is shown in Fig. 11 and Fig. 12. The initial temperature of electron and negative ion are both 9eV.

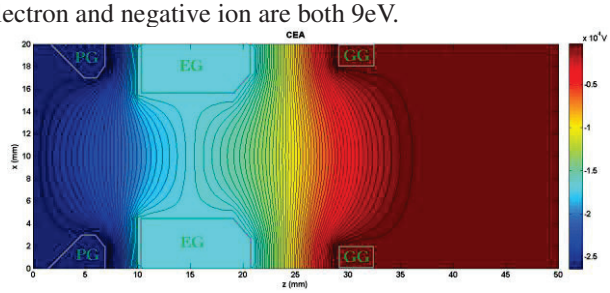

Figure 7: Equipotential lines of the extraction system CEA.

ISBN 978-3-95450-136-6

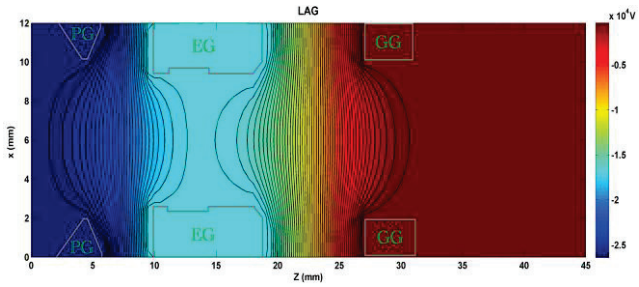

Figure 8: Equipotential lines of the extraction system LAG.

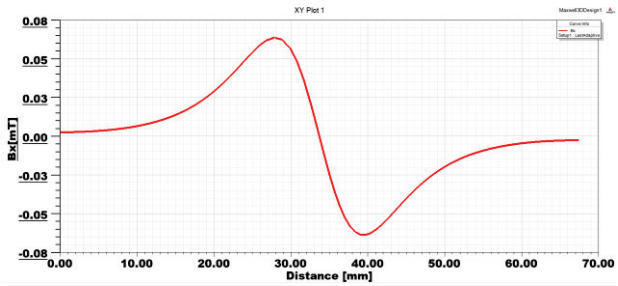

Figure 9: Vertical magnetic field strength Bx of the electron deflection field (CEA).

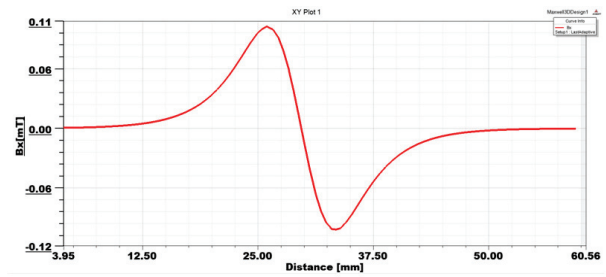

Figure 10: Vertical magnetic field strength Bx of the electron deflection field (LAG).

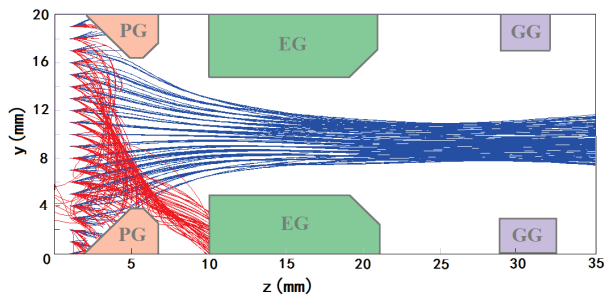

Figure 11: Negative ion (in blue) and electron (in red) trajectories for the extraction system CEA.

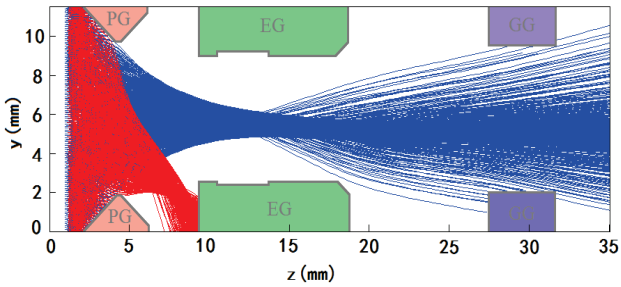

Figure 12: Negative ion (in blue) and electron (in red) trajectories for the extraction system LAG.

CONCLUSION

This paper presents a 3D numerical modelling to simulate the extraction system of negative ion source based on finite difference method. CEA and LAG (two different extraction systems of BATMAN have been used to check this numerical modelling. The results prove a very good agreement with the IPP results. In the future work, the calculation of the emitting surface will be finished, the simulation model and the code will be improved to get the more realistic results.

REFERENCES

[1] Heinemann B, Falter H, Fantz U, et al. "Design of the "half-size" ITER neutral beam source for the test facility ELISE". Fusion Engineering and Design, 84(2): 915-922, 2009.

[2] Speth E, Falter H D, Franzen P, et al. "Overview of the RF source development programme at IPP Garching". Nuclear Fusion, 46(6): S220, 2006.

[3] Bandyopadhyay M. "Studies of an inductively coupled negative hydrogen ion radio frequency source through simulations and experiments." Max Planck institut for plasma physics, 2004.

[4] Mochalskyy S, Lifschitz A F, Minea T. "3D modelling of negative ion extraction from a negative ion source". Nuclear Fusion, 50(10): 105011, 2013.

[5] Franzen P, Wünderlich D, Fantz U, et al. "On the electron extraction in a large RF-driven negative hydrogen ion source for the ITER NBI system." Plasma Physics and Controlled Fusion, 56(2): 025007, 2014.

[6] Taccogna F, Minelli P, Capitelli M, et al. "Plasma grid shape and size effects on the extraction of negative ions." Third International Symposium on Negative Ions, Beams and Sources (NIBS 2012). AIP Publishing, 1515(1): 3-11, 2013.

[7] Franzen P, Gutser R, Fantz U, et al. "Performance of multi-aperture grid extraction systems for an ITER-relevant RF-driven negative hydrogen ion source." Nuclear Fusion, 51(7): 073035, 2011.

ISBN 978-3-95450-136-6

MAGNET SORTING OF THE CSNS/RCS DIPOLES AND QUADRUPOLES *

Y. An[1,2,#], S. Xu[1,2], S. Wang[1,2], L. Huang[1,2]
[1]Institute of High Energy Physics, Chinese Academy of Sciences(CAS), Beijing 100049, China
[2]Dongguan Neutron Science Center, Dongguan 523803, China

Abstract

As a key component of the China Spallation Neutron Source (CSNS) Project, the Rapid Cycling Synchrotron (RCS) accumulates and accelerates the proton beams from 80MeV to 1.6GeV for extracting and striking the target with a repetition rate of 25Hz. RCS demands low uncontrolled loss for hands on maintenance, and one needs a tight tolerance on magnet field accuracy. Magnet sorting can be done to minimize linear effects of beam dynamics. Using closed-orbit distortion (COD) and beta-beating independently as the merit function, and considering maintaining the symmetry of the lattice, a code based on traversal algorithm is developed to get the dipoles and quadrupoles sorting for CSNS/RCS.

INTRODUCTION

The CSNS accelerator consists of a low energy H^- Linac and high energy RCS. H^- beam with energy of 80MeV is scraped and transformed into proton beam by the carbon foil located in the injection region. After around four hundred turn accumulation, the proton beam is accelerated to 1.6GeV and then extracted to strike the target with the design power of 100 kW. For the convenience of maintenance and high power requirements, the uncontrolled beam loss should be less than 1 Watt/m. In order to achieve this goal, the expected magnet errors are designed to lower 10^{-3} for main dipoles and quadrupoles. Table 1 shows the main parameters of RCS [1].

Table 1: Main Parameters of RCS

Parameters	Units	Values
Circumference	m	227.92
Repetition Rate	Hz	25
Average current	μA	62.5
Inj. Energy	MeV	80
Ext. Energy	GeV	1.6
Beam Power	kW	100
Quad		48
Dipole		24
Corrector		16/16
BPM		32/32
Nominal Tunes(H/V)	1	4.86/4.78

*Work supported by National Natural Science Foundation of China (11405189)
#anyw@ihep.ac.cn

As a key component of CSNS, RCS consists of 4-fold symmetric structure, and each of which is constructed by a triplet cell. Figure 1 shows the twiss parameters of RCS [2]. The long drift is reversed for the installation of cavities, collimator, injection elements and extraction elements, and the dispersion function in this area is designed to be zero. The short drift in the arc of the accelerator is reserved for installation of BPMs, correctors, sextupoles, and so on.

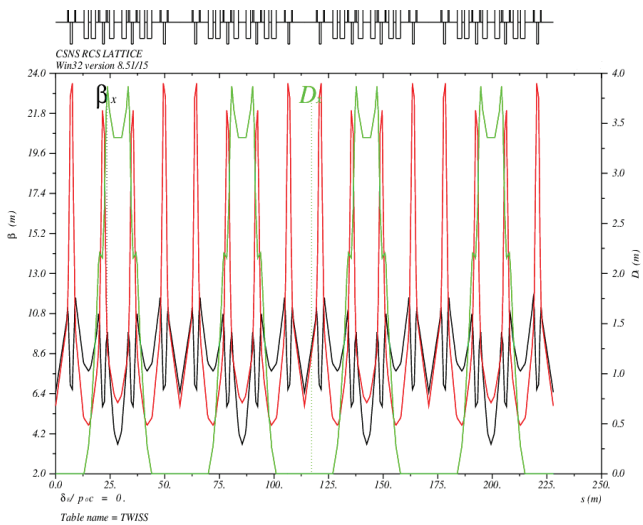

Figure 1: Twiss parameters of CSNS/RCS.

SORTING STRATEGIES

Algorithm Description

A simple script is developed to calculate the permutations of a given vector, and then embedded in our code based on Accelerator Toolbox [3]. By setting the closed orbit distortion or beta-beating as the merit function, the best sorting result can be picked from a lot of reasonable results according to the symmetry structure of the Lattice. However, it seems difficult and time consuming to get the sorting results when all of the dipoles errors and quadrupole errors calculated simultaneously, so we get it step by step.

Dipole Sorting Strategies

There are 24 dipoles located along the azimuth of the ring, and can be divided into type-A and type-B dipoles, a. Type-A and type-B dipoles are powered by one power

ISBN 978-3-95450-136-6

supply system but with different water cooling system. As shown in Figure 2, the yellow column depicts type-A dipoles while the green column depicts type-B dipoles. In order to get a good arrangement of the dipoles, one needs to compare the closed orbit distortion (COD) caused by dipoles field errors and pick up the smallest closed orbit distortion. The process of the dipole sorting was to be done in two steps. Firstly, type-B dipoles were arranged for its corresponding smallest COD. And then, after the type-B dipoles were given, and the arrangement for type-A dipoles was figured for the evaluation of the COD. The dipoles field measurement was done in DC mode and AC mode, however, the DC dipoles field error was not conformed to AC dipoles field error very closely, and the most important that, the repeatability of field measurement in DC mode is about 2E-4 while that in AC mode is about 5E-4. So the arrangement of the dipoles was determined by DC field measurement.

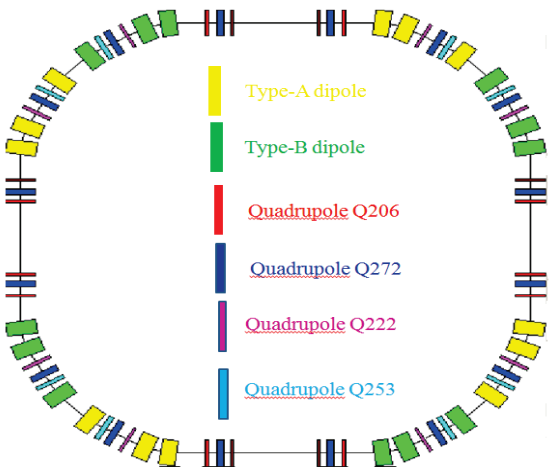

Figure 2: Magnet distribution along the CSNS/RCS ring.

Quadrupole Sorting Strategies

There are 48 quadrupoles located along the ring, and powered by 5 group power supplies as follows: two strings of eight Q206 (diameter 206mm) quadrupoles, one string of sixteen Q272 (diameter 272mm) quadrupoles, one string of eight Q222 (diameter 222mm) quadrupoles, and one string of eight Q253 (diameter 253mm) quadrupoles. The quadruple distribution along the CSNS/RCS ring is also shown in Figure 2. The red column depicts quadrupole Q206 with two power supplies, the blue column depicts quadrupole Q272, the pink column depicts quadrupole Q222, and the cyan column depicts quadrupole Q253. So far, the field measurements of one strings of eight Q206, one string of sixteen Q272 and one string of eight Q222 finished. Table 2 shows the RMS values of the quadrupoles discretization field errors from the quadrupole field measurements in DC mode.

Table 2: RMS Values of the Quadrupoles Discretization Field Errors from Field Measurement in DC Mode

Quadrupoles	RMS Values
one string of eight Q206	5.62E-4
one string of sixteen Q272	7.95E-4
one string of eight Q222	3.03E-4

For an early installation in tunnel, the sorting results should be followed by the results of the field measurement. The quadrupole field measurement is a three step process as follow: one string of sixteen Q272, one string of eight Q222 and one string of eight Q206.The field measurements of the quadrupoles are also carefully taken both in DC mode and in AC mode. However, as descripted in dipole sorting section, the repeatability of the field measurement in AC mode is much worse than that in DC mode, so we just used the field measurement data in DC mode. The process of sorting is simultaneous with the filed measurement, so the quadrupole Q272 should be figured out firstly, quadrupole Q222 is followed and quadrupole Q206 is at last. Sorting of the quadrupoles is a little different than the dipoles sorting. When sorting quadrupole Q272, it is important to choose a result with good lattice symmetry, so the arrangement of quadrupole Q272 didn't mean a smallest beta beating. But in the sorting process of quadrupole Q222 and quadrupole Q206, we picked up the smallest beta beating that is because the non-uniformity of quadrupole Q272 is larger than that of quadrupole Q222 and quadrupole Q206.

DIPOLES SORTING RESULTS

The field errors of dipoles can cause large closed orbit distortion, and that will make the central of beam oscillate close to the vacuum chamber. On one hand, scattering along the vacuum chamber can make beam loss. On the other hand, the quantity of the magnet field is a little worse than that in the centre of the magnet. So the dipoles should be sorted carefully. Firstly, one of the type-B dipoles was installed in the tunnel. Secondly, the left eleven type-B dipoles were carefully sorted by founding the smallest closed orbit distortion. Lastly, after the positions of the type-B dipoles fixed, the left twelve type-A dipoles were carefully sorted again by founding the smallest closed orbit distortion. Figure 3 shows the closed orbit distortion comparison after 24 dipoles sorting. The red line indicates the closed orbit distortion caused by random arrangement of the dipoles, and the dark line indicates the closed orbit distortion caused by carefully sorting arrangement of the dipoles, and the closed orbit distortion decreased from 8mm to 1.5mm.

ISBN 978-3-95450-136-6

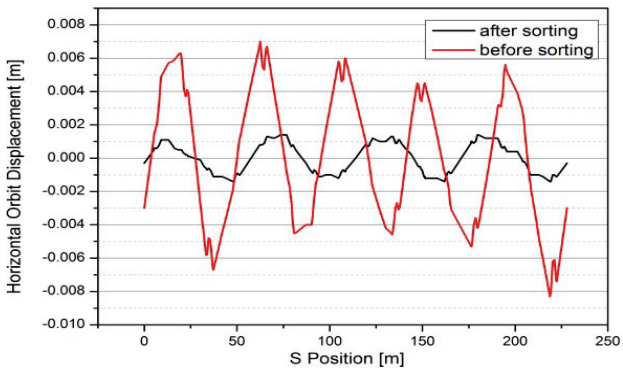

Figure 3: The comparison of the horizontal closed orbit distortion from dipoles sorting.

QUADRUPOLES SORTING RESULTS

The field errors of the quadrupoles can cause beta beating, destroy symmetry of the lattice structure, and make beam emmittance growth. On the one hand, the lattice symmetry should be well restored. On the other hand, beta beating caused by quadrupoles should be well compensated by quadrupoles itself. When doing the sorting of the quadrupoles Q272, the sixteen magnet are divided into two groups according to their absolute non-uniformity field errors, and one group with larger non-uniformity field errors while the other group with smaller non-uniformity field errors. Firstly, the eight quadrupoes in the larger non-uniformity field errors group are carefully arranged. One thousand of the quadrupoles sorting patterns with small beta beating are saved, and then according to the symmetry of lattice structure, a reasonable sorting pattern is adopted. Secondly, the left eight quadrupole Q272 are carefully sorted, not considering the lattice symmetry. After the quadrupole Q272 arrangement is fixed, the quadrupole Q222 and quadrupole Q206 are carefully sorted. Figure 4 shows the comparison of the horizontal beta beating from quadrupoles sorting, and the red line depicts the beta beating with random quadrupole arrangement while the dark line depicts the beta beating with sorting quadrupole arrangement.

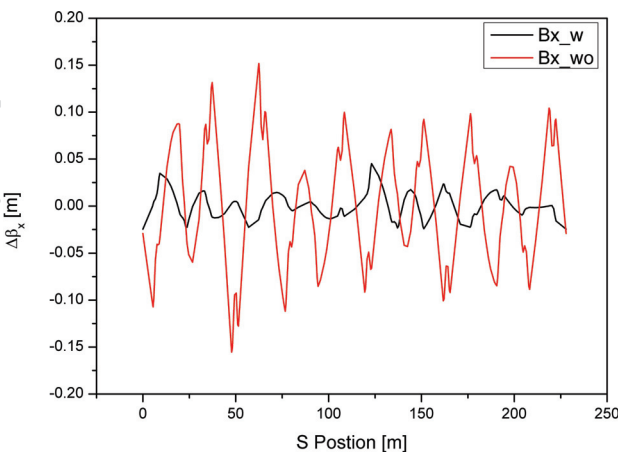

Figure 4: The comparison of the horizontal beta beating from quadrupoles sorting.

Figure 5 shows the comparison of the vertical beta beating from magnet sorting; the red line depicts the random arrangement while the dark line depicts the sorting arrangement respectively.

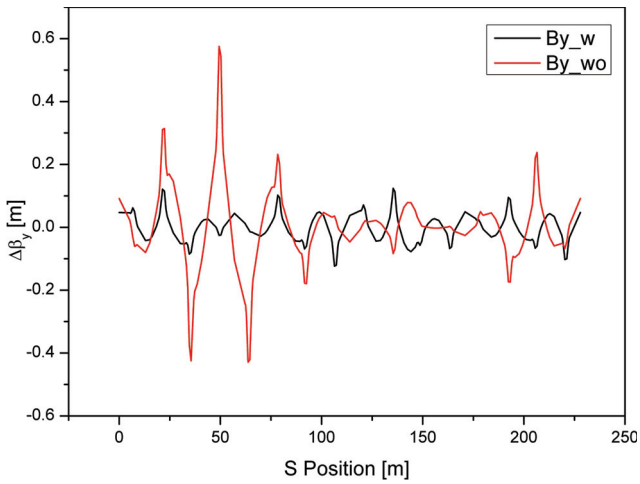

Figure 5: The comparison of the vertical beta beating from quadrupoles sorting.

CONCLUSIONS

For the requirements of the high power, the main dipoles and quadrupoles of CSNS/RCS should be carefully arranged along the azimuth of the accelerator. A code based on traverse algorithm is well developed to get all permutation results of sorting and to pick the best result according to lattice symmetry, small beta beating and small closed orbit distortion. After dipoles and quadrupoles sorting, the beta beating and closed orbit distortion are decreased, and the lattice symmetry are restored.

REFERENCES

[1] Wang S, An Y W, Fang S X, et al., "An overview of design for CSNS/RCS and beam transport", SCIENCE CHINA Physics, Mechanics & Astronomy 54 (Suppl 2): s239-s244, 2011
[2] URL http://mad.home.cern.ch/mad/.
[3] URL http://www.slac.stanford.edu/~terebilo/at/

ISBN 978-3-95450-136-6

DESIGN STUDIES OF A COMPACT SUPERCONDUCTING CYCLOTRON FOR PROTON THERAPY

G. Karamysheva, O. Karamyshev, S. Kostromin, N. Morozov, E. Samsonov, G. Shirkov, JINR, Dubna, Russia
Yanfang Bi, Yuntao Song, ASIPP, Hefei, China

Abstract

The ASIPP (Hefei, China)-JINR (Dubna, Russia) collaboration is developing a superconducting cyclotron SC200 for proton therapy. The cyclotron will provide acceleration of protons up to 200MeV with maximum beam current of 1 μA. In 2015 Institute of Plasma Physics, Chinese Academy of Sciences, ASIPP, (Hefei, China) and Joint Institute for nuclear research, JINR (Dubna, Russia) started collaboration to develop a superconducting cyclotron for proton therapy. The first prototype of SC200, tuned and tested in Dubna, will remain at JINR and will be used for further research and development of cancer therapy by protons. The results of testing will be used by ASIPP for a serial SC200 manufacturing.

The 200 MeV final energy has been chosen for this accelerator based on statistics for China for necessary depth of treatment and experience of work of the medical department in Laboratory of Nuclear problems on the base of JINR Phasotron. Mean magnetic field will be in the range of 2.9T-3.5T (center-extraction).

The results of conceptual design study of a 200 MeV superconducting isochronous cyclotron are presented. Computer modeling results for the magnetic, accelerating and extracting systems are given. Simulations of the beam dynamics are also presented.

INTRODUCTION

SC200 is an isochronous superconducting compact cyclotron. Superconducting coils will be enclosed in cryostat, all other parts are warm. Internal ion source of PIG type will be used. It is a fixed field, fixed RF frequency and fixed 200 MeV extracted energy proton cyclotron. Extraction will be organized with an electrostatic deflector and magnetic channels. Currently for proton acceleration we are planning to use 2 accelerating RF cavities, operating on the 4-th harmonic mode.

SUPERCONDUCTING (SC) MAGNET SYSTEM OF CYCLOTRON SC-200

Preliminary conceptual designs of SC magnet and cryogenic system are finished. Main parameters are presented in Table 1.

Figure 1: View of the SC200 Cyclotron.

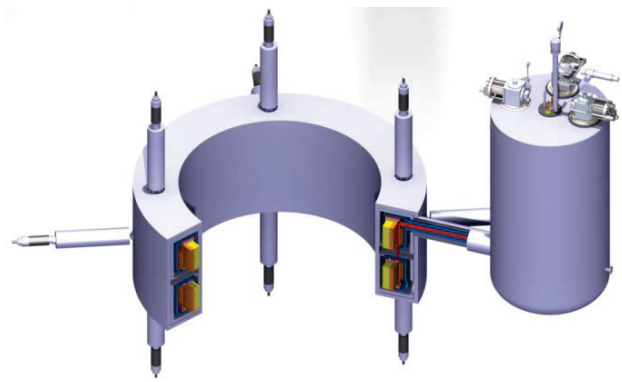

Figure 2: View of the SC coil and cryogenic system.

Table 1: The Parameters of Refrigerator

Cooling method	immersion
GM refrigerator	3
50K thermal shield	3*45W @50K
Thermal coupling with magnet	Thermal siphon

The simulation and design of the SC-200 magnetic system is based on its main characteristics:

- Four-fold symmetry and spiral sectors
- Deep-valley concept with RF cavities placed in the valleys
- Pole diameter less than 150 cm.

ISBN 978-3-95450-136-6

- Average field ($R_{extraction}$) ~ 3.5 T.
- Magnetic induction inside yoke less 2-2.3 Tesla.
- Magnet (yoke) weight less 30 tons
  During the magnet simulation the following design goals should be achieved:
- Optimization of the magnet sizes.
- Realization of the vertical focusing (Qz) at the extraction region as close to 0.4 as possible (to decrease the vertical beam size and minimize the median plane effects).
- Keeping optimal value of the spiral angle of the sectors (minimize total sectors phase angle change).
- Average magnetic field shaping by variation of the sectors azimuth width and by pole profiling.
- Minimization iron weight, keeping the stray field at an acceptable level.
- Avoiding dangerous resonances.
- Optimal solution for SC coil design.
- Realisation of optimal design of electrostatic and magnetic elements for the extraction channels.

The magnet modelling has been performed in 2D POISSON code and 3D ANSOFT MAXWELL one. VECTOR FIELDS TOSCA software [1] will be used for future optimization of the magnet design.

The sectors of the computer model have the edge radius 62 cm. The average line of the sector is the Archimedes spiral φ=R(cm)/25. The vertical sectors gap is described by the ellipsis with semi axis of 3/62 cm and cut at the edge at the distance of 0.75 cm from median plane. The magnet's main parameters are presented in the Table 2.

Table 2: Parameters of the Magnet System of the SC200 Cyclotron

Magnet type	Compact, SC coil, warm yoke
Pole diameter ,m	1.24
Magnet diameter, m	2.2
Magnet height, m	1.22
Hill gap, m	0.06-0.015
Valley gap, m	0.6
Yoke material	St.1010
Yoke weight, t	25
Extraction radius, m	0.6
Average magnetic field (R_o/$R_{extr.}$),T	2.9/3.5
Excitation current (1 coil), A*turns	1 000 000
Excitation current density, A/mm^2	70
Magnetic field in the coil (max), T	4.5
Cryostat and coils weight, t	5
Total magnet weight, t	30

Profiling of the pole shape and vertical profile of the sectors was used to shape the required isochronous magnetic field. The magnet's computer model after realization of these steps is shown in Fig.3.

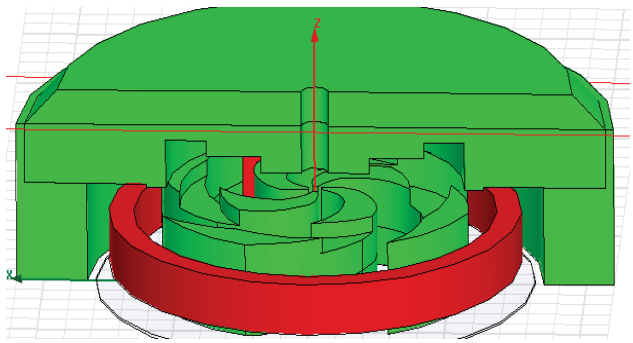

Figure 3: Computer model of the magnet with profiling its geometry.

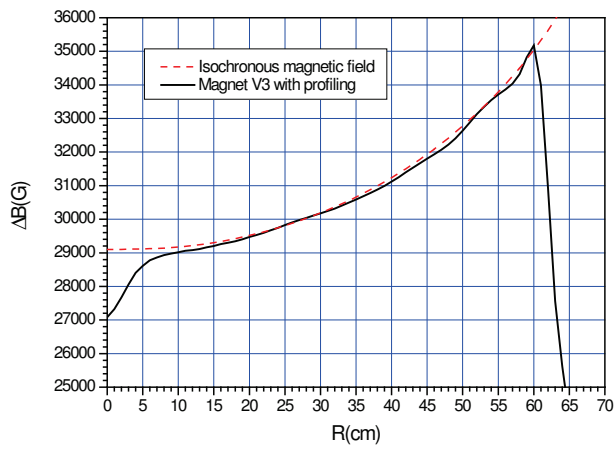

Figure 4: Magnetic field for the model with profiling pole and sectors.

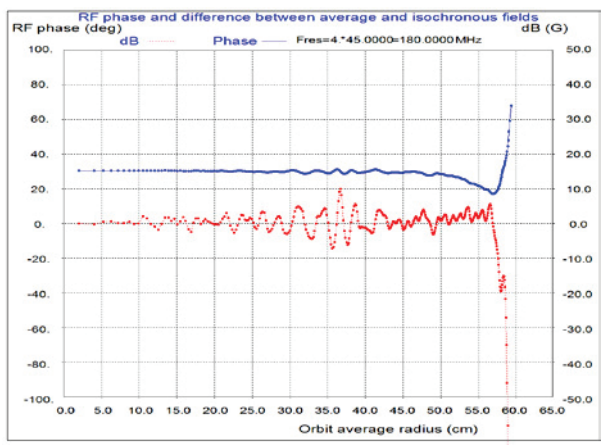

Figure 5: RF phase of the central proton during acceleration and difference between used average field and exact isochronous field.

The difference between fields was calculated using a deviation of proton orbital frequency from the resonance value 45 MHz. Starting phase 30°RF was assumed in order to provide the beam axial focusing in central region of the cyclotron. The code PHASCOL [2] was used for particle dynamics simulation.

ISBN 978-3-95450-136-6

ACCELERATION SYSTEM

Magnetic field modelling and beam dynamics have determined orbital frequency of the ions equal to about 45 MHz. To operate on 4-th harmonic, the RF system has to achieve frequency of 180 MHz. We are planning to use two normal conducting RF cavities for ion beam acceleration in the SC200 cyclotron.

The geometry of the RF cavity is restricted by the size of the valley of the magnet. We have fitted the double gap delta cavity inside the valley of the magnet. Azimuth extension of the cavity (between middles of accelerating gaps) is 45 degrees. We have chosen the accelerating gap to be equal to 7 degrees, and not less than 5mm in the center, where 7 degrees is less than 5mm to avoid the sparking.

Main parameters of the RF system are presented in Table 3.

Table 3: Parameters of Accelerating System

RF cavities	warm
Number of cavities	2
Operating frequency, MHz	180
Harmonic number	4th
Radial dimension, m	0.62
Vertical dimension, m	0.6
Number of stems	3

As the first step of our simulations we have used COMSOL Multiphysics RF module [3] to simulate the cavity. In the future in order to improve the accuracy of simulations and to avoid possible numerical errors we will use several software packages such as CST Microwave studio [4] and ANSYS [5]. To check if the 180 MHz frequency can be achieved with such geometry of the valley we have decided to build a model with 3 stems (see Fig.6). Similar cavity design [6] was proposed for the project of the superconducting cyclotron C400 [7] for hadron therapy.

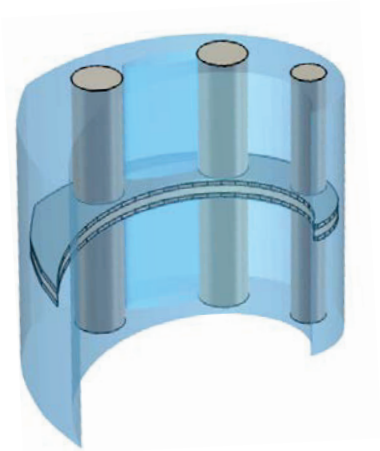

Figure 6: View or the RF cavity computer model.

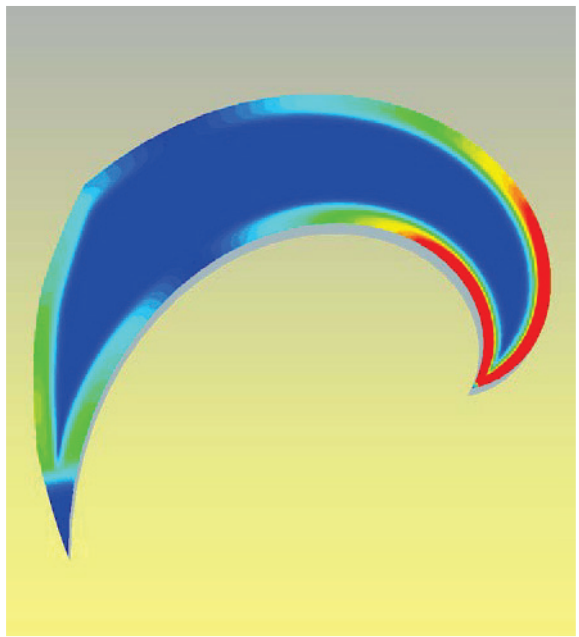

Figure 7: Electric field distribution in the median plane.

Frequency of the cavity with 3 stems reaches 186 Mhz. However the work still has to be done to optimize the field distribution, to optimize number of stems, their sizes, shapes and positions.

CONCLUSION

The work on design of the proton superconducting cyclotron SC200 continues. Manufacturing of SC200 systems and elements will be done during the 2017. Assembling, tuning and testing SC200 should be finished in 2018.

REFERENCES

[1] http://www.vectorfields.co.uk/
[2] Onischenko L. M., Samsonov E. V. Code PHASCOL for Computation of Space Charge Effects in the Cyclotrons and Synchrocyclotrons // Vopr. At. Nauki Teh., 5 (2001) pp.163-165
[3] https://www.comsol.com/
[4] https://www.cst.com/Products/CSTMWS
[5] http://www.ansys.com/
[6] Y. Jongen et al. Compact Superconducting Cyclotron C400 for Hadron Therapy // Nuclear Instruments and Methods in Physics Research Section A. 2012. V. 624, Issue 1. P. 47–53
[7] Y. Jongen, et al. RF Cavity Design for Superconducting C400 Cyclotron // Physics of Particles and Nuclei, Letters. 2011. V. 8, № 4. P. 386–390.

ISBN 978-3-95450-136-6

SIMULATION OF THE DISTRIBUTION OF PARASITIC IONS IN THE POTENTIAL OF AN ELECTRON BEAM*

E. Brentegani†, U. van Rienen, Rostock University, Germany
D. Sauerland, W. Hillert, ELSA, Bonn University, Germany
A. Meseck, Helmholtz-Zentrum Berlin, Germany

Abstract

In an electron machine, positively charged ions are generated by direct collision between the beam and the residual gas molecules or by synchrotron radiation. If no countermeasure is employed, they can be trapped in the beam potential and accumulate over time until the full beam neutralization is reached [1]. Ion clouds can cause incoherent tune shifts and coherent beam instabilities, therefore they are a performance limiting factor for high current electron storage rings as well as Energy Recovery Linacs (ERLs). In order to give a detailed estimation of their effects on the beam dynamics and to further optimize the existing ion clearing techniques, accurate knowledge on the ion density distribution is required. In the following we present numerical studies on the distribution of ionized gas while interacting with electron bunch trains. The simulations have been performed with the software MOEVE PIC Tracking developed at the University of Rostock.

INTRODUCTION

An analytical model describing the equilibrium distribution of ions trapped in the beam potential is already available [2]. In addition, the distribution of the ions has been computed numerically in [3], where also the self-space charge of the cloud was taken into account.

Nevertheless, since the residual gas which populates the vacuum chamber of an accelerator is composed by many chemical species, further insight on the transverse behavior of each component is required. Knowledge about the regions occupied by different ionized chemical species is important because of its implication on the clearing techniques. Regardless of which particular technology is employed, these techniques have to be optimized considering that each species has its own dynamics, depending on the mass-to-charge ratio.

Furthermore, measurements of the so-called "Beam Transfer Function" (BTF) have been performed at the Electron Stretcher Accelerator (ELSA) in Bonn, in order to estimate the incoherent tune shift and therefore to obtain preliminary information about the average density of trapped ions [4]. The simulations presented here are also intended to enforce the development of the new applications of the BTF method by computing the evolution of the ion density around the beam on a time scale which is too short to allow experimental investigations.

Therefore, the simulated system has been chosen very similar to the one of the related measurements and a realistic ionized gas mixture has been employed.

SIMULATED PHYSICAL SYSTEM

The simulations focused on the behavior of parasitic ions in a drift session of the ELSA stretcher ring and were carried out with the 3D Particle-In-Cell code MOEVE PIC Tracking developed at the University of Rostock [5]. The operating parameters of the machine which are relevant for the numerical studies are shown in Table 1. As it can be seen, four different fill patterns have been chosen. When present, the clearing gaps were added all together after the bunches: for instance, in the scheme with a gap of 220, 54 bunches were followed by 220 empty buckets.

Table 1: Parameters of the ELSA Storage Ring

Parameters	Values
Beam energy	1.7 GeV
Bunch charge	27.4 pC
Bunch horiz. rms size	2.258 mm
Bunch vert. rms size	0.2253 mm
Bunch rms length	9.57 mm
Harmonic number	274
RF period	2 ns
Clearing gaps	220, 150, 70, 0 buckets
Ion cloud temperature (initial)	300 K
Neutralization level (initial)	50 %
Vacuum chamber, hor. diameter	103 mm
Vacuum chamber, vert. diameter	44 mm

The bunches were modeled with $2 \cdot 10^4$ macro-particles each, distributed according to a 3D Gaussian distribution. The ion cloud was also composed by $2 \cdot 10^4$ macro-particles, which were loaded all at once at the beginning of the simulation. Their initial distribution was chosen to be Gaussian in the transverse plane, with the same horizontal and vertical standard deviations as the bunches. In the longitudinal direction they were uniformly distributed. This initial distribution is the one that is considered to best resemble the ion generation map due to direct collisions of the beam electrons with the residual gas molecules. The composition of the cloud was chosen in accordance with the spectrometric measurements and is presented in Table 2.

* Work supported by BMBF, Germany under contract 05K13HRC
† emanuele.brentegani@uni-rostock.de

ISBN 978-3-95450-136-6

Table 2: Ion Cloud Composition

Species	Mass number	Mole-fraction
H_2^+	2	0.5
CH_4^+	16	0.08
OH^+	17	0.03
H_2O^+	18	0.1
CO^+	28	0.1
CO_2^+	44	0.16
Others	-	0.03

RESULTS

For each fill pattern, the interaction of the beam with the positively charged cloud was simulated for more than ten thousands radio-frequency periods. The settings with 0 and 70 gaps were simulated for 24 µs, whereas for the cases with 150 and 220 gaps the tracking time was 55 µs. The required computational time was in the order of two weeks per computation, on a machine with a 3.40GHz processor and 256GB of RAM.

Transverse macro-ion distributions around the beam at the end of the tracking have been computed and are shown in Fig. 1 and 2.

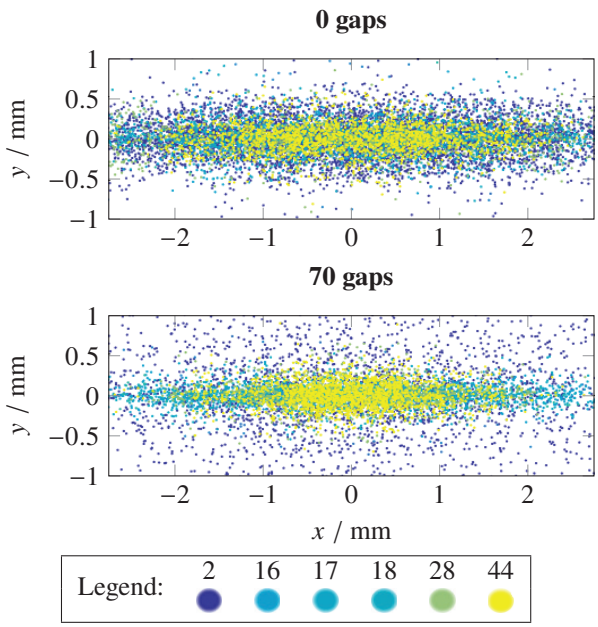

Figure 1: Transverse distribution of the macro-ions zoomed at the center of the beam pipe, after 24 µs, for the machine configuration with 0 and 70 gaps. The legend shows the correspondence between the dot colors and the ion masses in atomic mass units.

It is clear from these plots that the heavier components of the cloud seem to concentrate closer to the beam axis than the lighter ones. This is especially true for the yellow macro-particles, corresponding to the ions of carbon dioxide, which are mostly located at the center of the plots, whereas the dark blue macro-particles, corresponding to the hydrogen ions, are much more spread out.

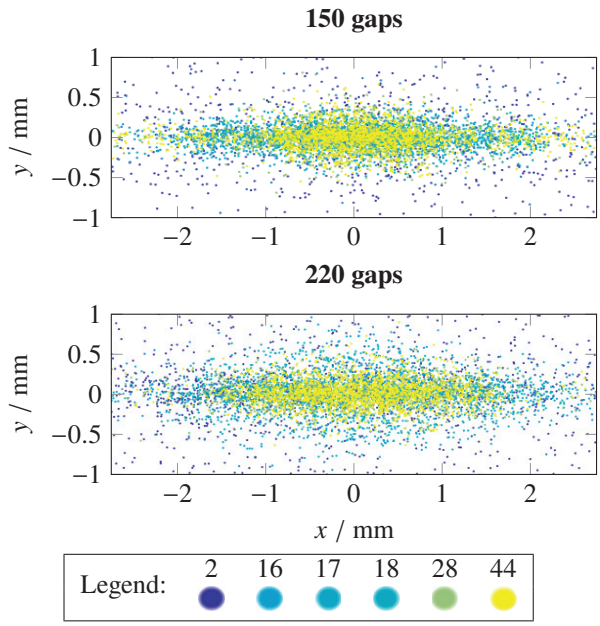

Figure 2: Transverse distributions of the macro-ions zoomed at the center of the beam pipe, after 55 µs, for the machine configuration with 150 and 220 gaps. The legend shows the correspondence between the dot colors and the ion masses in atomic mass units.

Furthermore, as a meaningful parameter for the ion density in the vicinity of the beam, it has been chosen the number of macro-ions which are transversally located inside an elliptic cylinder defined by the following equation:

$$C_n = \left\{ (x, y, z) : \frac{x^2}{(n\sigma_x)^2} + \frac{y^2}{(n\sigma_y)^2} \leq 1 \right\}, \qquad (1)$$

where σ_x and σ_y are the transverse root mean square sizes of the beam and $n = 1, 2, 3$. This quantity is then normalized to the total number of macro-ions present at the beginning of the simulation. Figure 3 and 4 show the values of the mentioned density parameter during the evolution of the cloud interacting with the beam, for $n = 1$ (blue line), $n = 2$ (red line) and $n = 3$ (yellow line).

CONCLUSION AND OUTLOOK

The transverse distribution of parasitic ions in a drift section of the ELSA stretcher ring has been computed. According to these studies, the component of the ionized gas mixture with the higher molecular mass tends to stay closer to the beam axis with respect to the region occupied by the lighter one. This result triggers speculations on the accumulation of heavy ions in the vicinity of the beam and its implications on the clearing efficiency.

Moreover, the dynamics of the charge density of the ion cloud has been presented. These simulations represent a step

ISBN 978-3-95450-136-6

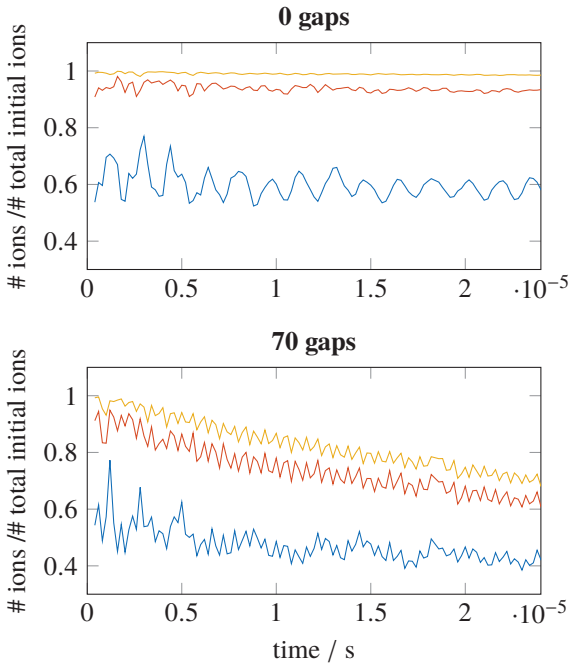

Figure 3: Time evolution of the number of ions inside the elliptic cylinder C_1 (blue), C_2 (red), C_3 (yellow), for the fill patterns with 0 and 70 gaps.

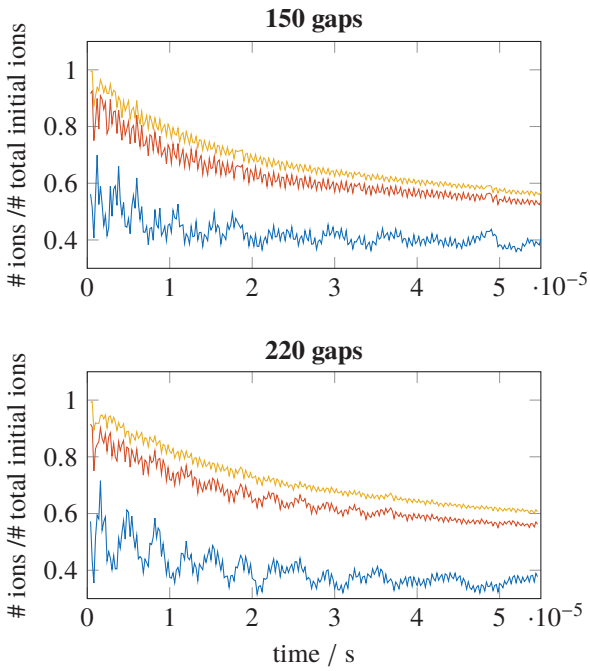

Figure 4: Time evolution of the number of ions inside the elliptic cylinder C_1 (blue), C_2 (red), C_3 (yellow), for the fill patterns with 150 and 220 gaps.

forward towards a deeper understanding of the incoherent tune shift due to parasitic ions and its characterization via BTF measurements.

Further numerical and experimental studies will follow, to map the ion density under different beam currents and in other locations of the ELSA. This will eventually allow for an accurate assessment of the ion cloud contribution to the machine tune and for a study of the distribution of the different ionized gas components also in the beam optics.

REFERENCES

[1] Y. Baconnier et al., "Neutralisation of accelerator beams by ionisation of the residual gas", CERN-PS-94-40-LP, 1994.

[2] L. Wang, Y. Cai, T.O. Raubenheimer, and H. Fukuma, "Suppression of beam-ion instability in electron rings with multi-bunch train beam fillings", Phys. Rev. ST Accel. Beams 14, 084401 (2011).

[3] G. Pöplau, U. van Rienen, A. Meseck, "Numerical studies of the behavior of ionized residual gas in an energy recovering linac", Phys. Rev. ST Accel. Beams 18, 044401 (2015).

[4] D. Sauerland, W. Hillert, A. Meseck, "Estimation of the ion density in accelerators using the beam transfer function technique", Proceedings of IPAC'15, Richmond, VA, USA (2015).

[5] A. Markovik, "Simulation of the interaction of positively charged Beams and electron clouds", PhD thesis, Rostock University, 2013.

ISBN 978-3-95450-136-6

6D TRACKING WITH COMPUTE UNIFIED DEVICE ARCHITECTURE (CUDA) TECHNOLOGY

S. Glukhov, E. Levichev, S. Nikitin, P. Piminov, D. Shatilov, S. Sinyatkin
BINP, Novosibirsk 630090, Russia

Abstract

A program code TrackKing for a 6D fully-coupled particle tracking in circular accelerators has been developed with the usage of parallel computations on Graphics Processing Units (GPU) with Compute Unified Device Architecture (CUDA). We can track several thousands of particles in parallel providing optical functions calculation, dynamic aperture and energy acceptance study, intrabeam scattering, radiation effects (including their realistic distribution along the lattice), etc. In the paper we discuss the code arrangement and compare its performance with PTC module of MAD-X.

INTRODUCTION

Various tools for beam tracking allow computing trajectories of beam particles in the given lattice. Coordinate transformation from initial to final coordinates is generally the same for each particle. Thus, simulation algorithm can be paralleled using SIMD principle (Single Instruction Multiple Data). This approach has been successfully implemented in GPU. There are several software-hardware complexes for GPGPU (General Purpose Computing on Graphics Processing Units), one of them is CUDA by NVIDIA company [1].

TrackKing is the program complex for particle tracking in circular accelerators, which has been developed with the usage of CUDA technology. Two main goals were set: on the one hand, tracking should be as fast as possible, on the other hand, the program code should be comprehensive and extendable. To achieve this, a clear division of labor between CPU (Central Processing Unit) and GPU has been implemented: all the preliminary work on lattice and results processing are performed on CPU, while GPU is assigned only to the tracking, because this part of the work can be most effectively paralleled. Also two-stage compilation is used: source code of CUDA kernel (central part of tracking code) is generated on CPU during runtime (first stage), then passed to nvcc compiler (developed by NVIDIA) and then the resulting code is executed on GPU (second stage).

Such an approach allows one to perform a task with lots of tracking involved (e.g. dynamic aperture study) on a single PC with CUDA enabled graphics card in a reasonable period of time. Usually such tasks are performed on CPU clusters at data processing centers, but the ability to perform calculations locally is very important when remote clusters are unavailable or overburdened.

PROGRAM LOGIC

Both CPU and GPU parts of TrackKing are implemented on C++ language, an extension to C++ provided by CUDA Toolkit [1] is also used in the GPU part. The logic of the program is shown in (Fig. 1), where parts of TrackKing code are denoted by gray rectangles.

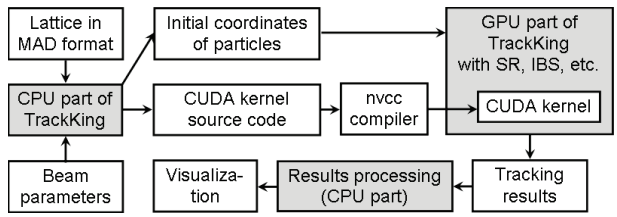

Figure 1: Scheme of TrackKing simulation program.

Reading Input Files

TrackKing accepts beamlines and sequences saved with SAVELINE or SAVE commands in MAD-8 [2] and MAD-X [3] formats. Non-saved beamlines and sequences described within a single file are also accepted. In this case all the mathematical expressions will be correctly parsed, but action commands (MATCH, CORRECT, SURVEY, etc.) will be ignored. After reading of the structure TrackKing saves parameters of beamline elements using its own class library.

Calculating Optical Functions and Structure Integrals

All necessary optical functions and structure integrals are calculated inside the CPU part of the program. TrackKing uses Twiss parameterization for non-coupled motion; for transversally coupled motion Teng — Edwards [4] or Lebedev — Bogasz [5] parameterizations can be used. TrackKing also has its own parameterization for fully coupled motion, which is a 6D extension of 4D Lebedev — Bogasz parameterization.

Generating Initial Coordinates of Particles and Source Code of CUDA Kernel

Usually the computational power is insufficient to track every particle in a beam, but one can track a sample (small ensemble of particles with the same distribution). The data obtained on the previous step can be used to inject matched beam (sample) with equilibrium emittance and energy spread, but also a beam with any other initial distribution can be injected.

Generated source code of CUDA kernel is highly optimized in view of the features of the lattice and the effects taken into account in the forthcoming tracking run. To improve tracking performance, separate functions are generated not only for each type of beamline elements (except DRIFT), but for each different element of the same type. For huge lattices with thousands of elements the CUDA kernel can

ISBN 978-3-95450-136-6

be splitted into several kernels to reduce compilation time and the amount of virtual memory used by nvcc compiler during the compilation.

Compiling and Performing Tracking

Now neither CPU nor GPU part of TrackKing has user interface, because the program is still under development. So, each tracking run means recompilation of the both parts with manual start of the compilers. But in the future we plan to convert the CPU part into an executable module with console interface, which will automatically start nvcc compiler after parsing the lattice and then launch the tracking on the GPU part. Other constituents of the GPU part, except the CUDA kernel (which depends on the lattice), will be precompiled to speed up the compilation process.

Visualization of the Results

6D phase space trajectories of the tracked particles are recorded into file at one or more observation points along the lattice. Observation points can be arranged automatically or manually, each of them has adjustable resolution (turns between two successive records) and selectivity (subset of particles, whose coordinates are recorded). This allows one to study beam distribution, its Poincaré sections, moments and related values (beam sizes, emittances, etc.) depending on time and coordinate along the lattice. Tools for Fourier analysis of the trajectories, dynamic aperture and energy acceptance study and analysis of particle losses are also implemented in TrackKing. In the case of insufficient disk space substantial part of data processing can be performed on-the-flight, when only distribution moments and other averaged values are recorded to disk instead of the full trajectories.

Results are exported as simple text files that can be processed with any data analyzing and plotting tool.

PHYSICAL EFFECTS TAKEN INTO ACCOUNT

Magnetic and Electric Fields of Beamline Elements

For each type of beamline elements TrackKing uses the same symplectic map as PTC module of MAD-X. Identity of the maps was carefully checked for various lattices containing all types of beamline elements possible in MAD [6]. The maps are obtained from expanded hamiltonian, all linear elements are thick, nonlinear elements can be splitted into any desired number of slices using drift-kick-drift scheme. Multipole fringe fields can be simulated in the hard-edge approximation [7].

Synchrotron Radiation

Two methods of SR simulation are implemented in TrackKing. On the one hand, radiation damping and quantum exitation due to SR can be simulated once per turn [8]. On the other hand, these effects can be taken into account in each beamline element, where beam particles follow curved trajectories. In high energy rings distributed radiation energy losses result in variation of equilibrium energy along the lattice (sawtooth effect) and closed orbit distortion. To preserve closed orbit magnet tapering is introduced (variation of magnetic field strength in beamline elements along the ring in proportion to the equilibrium energy). In TrackKing tapering can be introduced automatically. SR from quadrupoles and higher multipoles, as well as from dipoles, can affect beam dynamics. The techniques used in TrackKing for SR simulations allow taking these effects into account [9].

IBS and Touschek Effect

Simulations of IBS and Touschek effect in TrackKing are based on the theory described in [10]. Now these effects can be simulated once per turn as well as in each beamline element (previous version of algorithm was described in [11]). The new algorithm has shown the same results for various lattices and beam energies as the previous one.

BENCHMARKING

Tracking performance of TrackKing and PTC module of MAD-X were measured for various lattices and different numbers of tracked particles (N_p), results are summarized in Table 1 and Fig. 2. Initial conditions and coordinate transformations were exactly the same for each particle, all stochastic effects (SR, IBS) were switched off. Measurements were performed on a standard PC with the following characteristics:

- OS: Microsoft Windows XP SP3,
- CPU: Pentium Dual Core E5300 (2.60 GHz),
- GPU: NVIDIA GeForce GT 520,
- RAM: 3.25 GB.

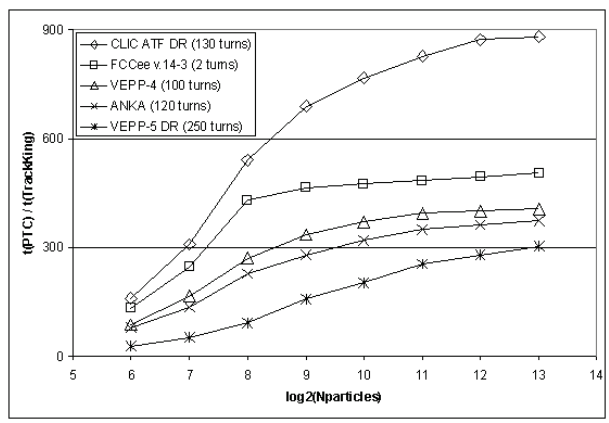

Figure 2: Tracking performance ratio of PTC and TrackKing for different lattices.

So, for sufficiently large number of tracked particles (>2000) TrackKing shows 200—900 times better performance than PTC, depending on lattice. This advantage is due to paralleling of the tracking process. But even if we assume that PTC tracking code can be fully paralleled on CPU (i.e. total PTC tracking time can be decreased N_p times), then for some lattices TrackKing still has an advantage for

ISBN 978-3-95450-136-6

Table 1: Time Elapsed for Tracking (in Seconds) with TrackKing (Upper) and PTC (Lower)

N_p	ATF	FCC	V4	ANKA	V5
64	0.25 40	0.16 21	0.22 19	0.22 17	0.24 6.5
128	0.26 80	0.17 42	0.23 38	0.23 31	0.25 13
256	0.3 162	0.2 86	0.28 76	0.27 61	0.28 26
512	0.48 331	0.39 181	0.47 157	0.44 123	0.34 53
1024	0.84 644	0.73 347	0.84 311	0.77 246	0.52 105
2048	1.55 1283	1.44 696	1.58 623	1.42 495	0.84 214
4096	2.98 2605	2.83 1397	3.05 1220	2.73 992	1.53 427
8192	5.84 5148	5.61 2829	5.98 2430	5.34 1989	2.86 868

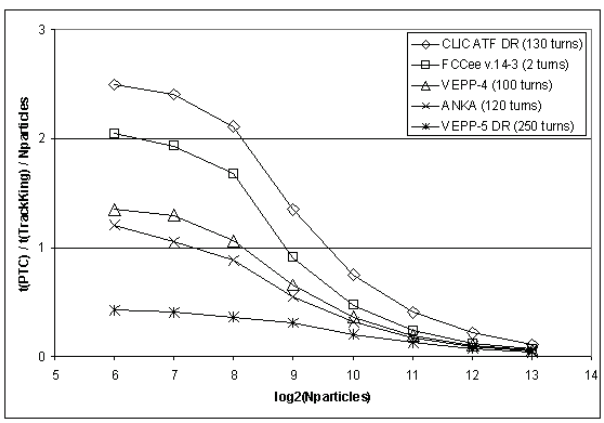

Figure 3: Tracking performance ratio of PTC and TrackKing per particle for different lattices.

$N_p < 10^9$ (Fig. 3). If a special GPGPU device (such as Tesla or Kepler graphics card by NVIDIA) is available for benchmarking, then the variety of lattices and range of N_p to see this advantage will increase substantially. This means that single particle tracking is on average faster in TrackKing than in PTC due to highly optimized CUDA kernel code.

FUTURE PLANS

Improvements to be done in the near future are the following: implementation of advanced tapering options, adding a module for dynamic aperture and energy acceptance optimization by sextupole adjustment, taking misalignments and field errors into account. Also the code for beam-beam and beamstrahlung simulations by D. Shatilov (BINP) is to be added to the program. The work on documentation and user interface part is being carried out in parallel.

CONCLUSION

New tracking tool based on CUDA technology has been developed, which is substantially faster than PTC code used in MAD-X. On the available hardware performance gain is up to 2.5 times per particle due to automatically generated highly optimized CUDA kernel code and up to 900 times totally due to paralleling. On the one hand, the new program named TrackKing has a big potential as an independent tracking tool. On the other hand, techniques used in TrackKing can be integrated into MAD-X to increase tracking performance considerably.

REFERENCES

[1] A. Boreskov, A. Kharlamov, Basics of working with CUDA technology. — DMK Press, 2010.

[2] H. Grote, F. C. Iselin, "The MAD program (methodical accelerator design) version 8.4: User's reference manual", CERN-SL-90-13-AP-REV.2, CERN-SL-90-13-AP (1991).

[3] H. Grote et al., "The MAD-X program (methodical accelerator design) version 5.02.06: User's reference manual", `http://madx.web.cern.ch/madx/madX/doc/latexuguide/madxuguide.pdf`

[4] D. A. Edwards, L. C. Teng, "Parametrization of linear coupled motion in periodic systems", IEEE Trans. Nucl. Sci. **20** (1973) 885.

[5] S. A. Bogacz, V. A. Lebedev, "Betatron motion with coupling of horizontal and vertical degrees of freedom", eConf C **010630** (2001) T511.

[6] R. De. Maria, M. Fjellstrom, "SixTrack physics manual (draft)", August 2015, `http://sixtrack.web.cern.ch/SixTrack/doc/physics_manual/sixphys.pdf`

[7] E. Forest, J. Milutinovic, "Leading Order Hard Edge Fringe Fields Effects Exact (1 + Delta) and Consistent With Maxwell's Equations for Rectilinear Magnets", Nucl. Instrum. Meth. A **269** (1988) 474.

[8] K. Ohmi, K. Hirata and K. Oide, "From the beam envelope matrix to synchrotron radiation integrals", Phys. Rev. E **49**, 751 (1994).

[9] S. Glukhov, E. Levichev, S. Nikitin, P. Piminov, D. Shatilov, S. Sinyatkin, "6D Tracking with Compute Unified Device Architecture (CUDA) Technology", these Proceedings.

[10] J. Le Duff, "Single And Multiple Touschek Effects", In *Berlin 1987, Proceedings, Advanced accelerator physics* 114-130 and Orsay Lin. Accel. Lab. - L.A.L.-RT-88-08 (88,rec.Sep.) 17 p.

[11] S. Glukhov, E. Levichev, S. Nikitin, P. Piminov, D. Shatilov, S. Sinyatkin, "IBS Simulations with Compute Unified Device Architecture (CUDA) Technology", Proceedings of IPAC'14.

ISBN 978-3-95450-136-6

PARALLEL OPTIMIZATION OF ACCELERATOR TOOLBOX BY OpenMP AND MPI*

K. Wang#, C.M. Luo, S.Q. Tian, M.Z. Zhang, Q.L. Zhang, B.C. Jiang
SINAP, Shanghai, China

Abstract

Parallel computing adopted in the simulation program of accelerators improves the computational efficiency, especially tracking with multi-particle and multi-turn which always takes a lot of time. Through investigating the operational principle and running flow of Accelerator Toolbox(AT) embeded in Matlab for accelerator design and simulation, Open Multi-Processing (OpenMP) and Message Passing Interface (MPI) were studied on and adopted in the parallel computing. The key code of particle tracking in AT has been transplanted and test with OpenMP-MPI as well as estimated reasonably, which improve the calculation efficiency largely. It is indicated that OpenMP-MPI hybrid parallel structure is in good agreement with AT programs by avoiding the internal communication and improving load balance. A multi-core computing platform based on OpenMP-MPI has been developed and contributed to the deep optimization of accelerators. And it shows good extensibility, which could speed up by adding computing nodes.

INTRODUCTION

Accelerator Toolbox(AT), developed by Stanford Synchrotron Radiation Light source (SSRL), is a toolbox embedded in Matlab for accelerator design and simulation [1]. The experiment measurements agreed well with AT has been carried out using a plenty of functions and applications assisted by Matlab. In recently years, AT has been used for the design and operation at Shanghai Synchrotron Radiation Facility (SSRF), which is one of the advanced 3rd light sources worldwide [2, 3]. In order to calculate the dynamic aperture and optimize the lattice design of synchrotrons, computation-intensive algorithms are required. Based on the progress of the programme, we can improve the computational efficiency largely. Because of the abundant repeated calls of particle tracking functions used in AT, the computing speed will be postponed without parallel computing. It is expected that we propose the parallel optimization of AT [4].

The two common methods for parallel optimization are as follows. One is based on using GPU. The other one is using multi-core CPU with multi-thread. Due to the frequently data exchange between computer memory and GPU in particle tracking assisted by cache operations, the speed-up efficiency cannot be effective obviously with a few data such as a small number of particles. As a result, it is verified that parallel optimization with multi-core CPU is a better choice.

*Work supported by National Natural Science Foundation of China under Grant No. 11105214
wangkun2013@ sinap.ac.cn

OpenMP is a standard model of share memory computing, which supports C/C++ compiler. With a local qual-core computer, the speed-up can be almost 4 times. Based on the message passing model, MPI is used for a dual CPU server to speed up further. And it shows good extensibility that the speed grows linearly along with the number of computing nodes.

EXPERIMENTAL

Accelerator Physics and Optimization Analysis

Considering that a particle can be represented in AT with a point in 6-dimension phase space, particles transport from one accelerator element to the next can be computed by a second-order transport matrix. It is assumed that the particles are relativistic and there are no interaction with each other, which obtain the parallel computing request [5]. With particle tracking assisted by different *passmethod* functions, AT can calculate the particles trajectories by *ringpass* function. The *passmethod* functions have million calls in particle tracking process and the calculation of multi-particle with multi-turn through accelerator elements is called as Single Instruction Multiple Data (SIMD) operation, which has a good agreement with OpenMP and MPI processing [6]. Parallel computing can work simultaneously for the different part of the same programme by the use of multiple computing resources, which increase the computing speed efficiently [7]. However, it is expected that the parallel computing is compatible with OpenMP and MPI.

OpenMP is an Application Programming Interface (API) for multi-thread programming with C/C++ and FORTRAN, which offers a highly abstract description for parallel computing. OpenMP includes compiler directives, library routines and environment variables which affect the run-time behavior [8]. Using OpenMP routines and directives for the existing AT source code, AT adopts the Uniform Memory Access (UMA) model which all the cores of processors share the same physical memory uniformly. With the moderate changes to the *passmethod* functions written in C, OpenMP can be carried out by Matlab MEX compiling function [9].

MPI is a standard of distribution model adopted in the control of parallel computing by explicit ways. Matlab MPI is a Matlab implementation of the MPI standard, which allows any Matlab program to exploit the multiple processors [10]. It is called NUMA architecture model built with OpenMP and MPI that multi machines run independently with local memory and communicate each other with Bus Interconnect. Figure 1 shows the NUMA model schematic diagram.

ISBN 978-3-95450-136-6

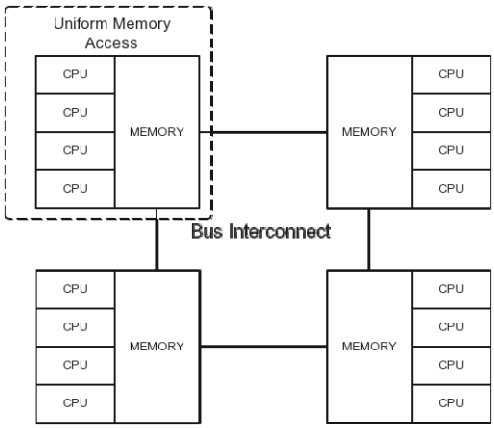

Figure 1: The NUMA schematic diagram.

Here we use a general distributed memory model. The upper computers use Matlab MPI for controlling the parallel computing and communication. And the lower computers use OpenMP for compute. The data is distributed to the lower computers with message-passing functions. And then the computing results from the lower computers can be transferred to the upper computers. Finally, they are combined into the final result. The local task distribution for every CPU can be managed by the shared memory computing interface, so that a global distributed memory model is adopted in AT. Through the way, the data conflict caused by two processors access to the same memory can be avoided. Only with UMA model, the CPU spin time will be raised up. And sometimes the data conflict delay takes two-processor working time longer than that one-processor.

Parallel AT with OpenMP and MPI

OpenMP and MPI are used to the parallel computing of the *passmethod* functions, which can increase the increase the speed mentioned above. To find sections of the codes processed simultaneously, OpenMP and MPI program can be created with existing code. The changings and the compilation of the codes are in the appendix. Library functions *omp_get_num_threads()* and *omp_get_thread_num()* can be used for the parallel part of the function to obtain the number of threads and the id of the working thread numbered from zero. The start_index is the offset of each computing core. Based on the thread id number, different thread works on different data., which realize the paralleling of data and tasks.

For instance, the DriftPass.c [2] can be used to calculate the particle tracking through a drift element. Intel VTune Amplifier [11] is adopted to test the efficiency of the parallel DriftPass.c. The test number of the particles is 3920, with 500000 loops on a qual-core computer. The result is shown in Fig. 2 and Table 1.

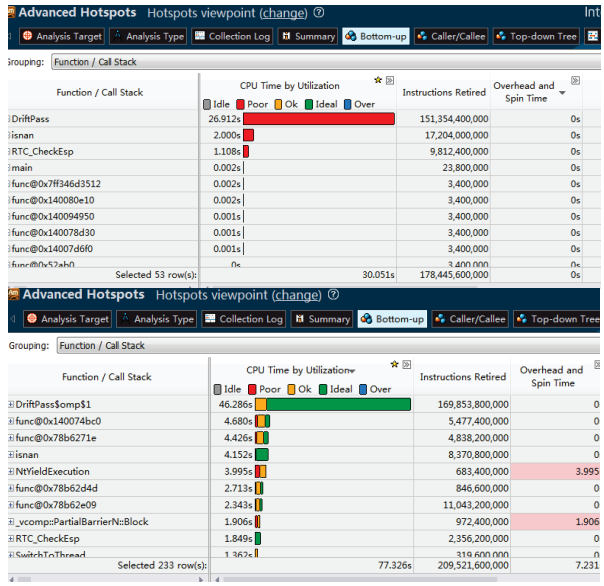

Figure 2: Compute times for parallel and non-parallel DriftPass.

As seen in Fig. 2, the CPU have a large free time during the non-parallel compute because only one core is used for compute, others are free. The parallel compute has some extra time for multi-thread open and so on.

Table 1: Compute Times for Parallel and Non-parallel DriftPass

	Elapsed time/s	CPU time/s	Overhead & Spin time/s
Parallel	10.28	77.83	7.22
non-parallel	30.09	30.05	0.00

CPU time is the sum time for all threads; Overhead & Spin Time is the time which an active thread takes to get a synchronization construct. They take over the most CPU time. Overhead & Spin Time takes about 9.3% of all CPU time. So the speedup of the parallel program is 2.98. And it is not reach the limit value 4. All the *passmethod* functions called in *ringpass* can be parallelized by OpenMP, so that *ringpass* is a parallel program.

RESULTS AND DISCUSSION

Frequency map analysis (FMA) is an analysis method for a dynamic aperture to find the amplitude of frequency shifts. The FMA works as follows: (1) the program flow carry out particle tracking, (2) then through N turns and gets the particles output data, (3) finally uses a first-order Hamming filter and filter the data [12]. It is a frequency scanning tool which is used to reveal information about nonlinear resonances and guide frequency optimization [13]. It is takes lots of time that particle tracking computing. As a result, OpenMP is used to save time and improve the efficiency. Figure 3 shows the result that the time costs when using parallel and non-parallel methods

ISBN 978-3-95450-136-6

to compute FMA with different number of particles. An Intel i7-3770 CPU was used with 4G RAM.

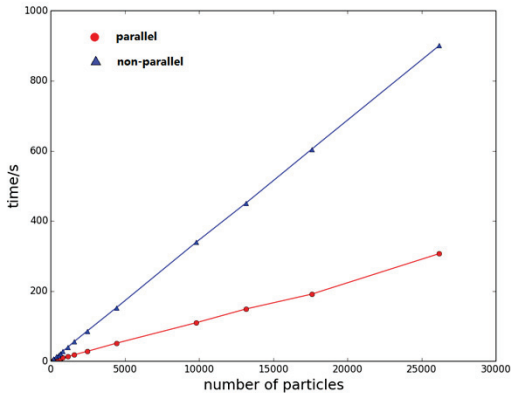

Figure 3: FMA execution time for non-parallel and parallel computing using different numbers of particles.

The number of particles is shown on the x axis and the execution time on the y axis. It is indicated that the time grows almost linearly with the number of particles. The time of non-parallel method takes up to 3.16 times as long as that of the parallel method, so that the speed using parallel computing is at most 3.16 times the speed using non-parallel computing. Based on Amdahl's law [14]:

$$S = \frac{1}{f_{par}/P + (1 - f_{par})}, \quad (1)$$

where f_{par} is the parallel fraction of the program. P is the speedup of the parallel part and S is the speedup of all programs. The formula is used to calculate the times for the parallel and non-parallel parts of the program flow. The parallel part of the program is the *ringpass* function and the main non-parallel part is the FMA function. The results for the parallel and non-parallel programs is shown in Table 2 and Table 3, where N is the number of particles, T_f is the time taken by the FMA function and T_{all} is the time of all program.

Table 2: Time Profile Using Parallel Computing

N	T_f /s	T_{all}/s	T_f/T_{all}/s
512	1.19	5.87	0.202
1128	2.66	12.58	0.207
2450	5.75	28.04	0.205
4418	10.18	51.28	0.206
9800	22.47	109.74	0.207
177578	50.57	191.24	0.212

Table 3: Time Profile Using Non-parallel Computing

N	T_f /s	T_{all}/s	T_f/T_{all}/s
512	1.25	17.52	0.071
1128	2.82	39.11	0.072
2450	6.16	85.92	0.071
4418	11.01	152.52	0.072
9800	24.40	339.43	0.072
177578	43.50	604.51	0.072

As listed in Tables 2 and Table 3, the value Tf/Tall is almost constant for both types of computing. From Eq. (1), the speedup of the parallel part can be calculated as follow:

$$3.16 = \frac{1}{(1 - 0.07)/P + 0.07}. \quad (2)$$

From Eq. (2), 0.07 is the non-parallel part of the computing process and the value of P is about 3.77. Along with the number of particles increasing, P will be close to 4, but not never equal to 4 because of the quad-core CPU with 4 threads. And the synchronization between threads of different cores reduces the compute speed.

A Dell R720 server platform has been developed to use the speedup raised by OpenMP and MPI. R720 has 2 processors with 16 CPU cores each, which can be regard as two compute nodes during the computing process. The speedup of one node is 6.23. And the speedup of 2 nodes is 12.18, which is almost double of one node. It is obvious that because the computing process is independent each other, the communication costs about 2.3% of the total time. The speedup of the computing process can grow linearly with the number of CPU using OpenMP and MPI, which shows good extensibility.

CONCLUSION

This paper describes parallel and non-parallel results with use of OpenMP and MPI, which the parallel optimization of AT improves the computational efficiency. OpenMP and MPI can be carried out to the similar way for other accelerator physics programs if the program parallelized. A multi-core computing platform has been developed and contributed to the deep optimization of accelerators, which is convenient to speed up by adding computing nodes.

APPENDIX

```
#include<omp.h>
…… some computation and initialization
Omp_set_num_threads(4)
#pragma omp parallel private(i) share(start_index,n)
{
thread_id=omp_get_thread_num();
num_threads=omp_get_num_threads();
start= start_index + n*thread_id /num_ threads;
if(thread_id==num_threads-1)
end=n-1;
else
end=n*(thread_num+1)/ num_threads-1;
for(i=start;i<=end;i++){
…computation
}
}
```


ISBN 978-3-95450-136-6

REFERENCES

[1] Terebilo. A, “SLAC-PUB-8732”, 2001.
[2] S.Q. Tian et al., Nuc. Sci. Tech. 25 (2014): 10102-010102
[3] B.C. Jiang et al., HIGH ENERGY PHYSICS AND NUCLEAR PHYSICS. 31(2007):956-961.
[4] X.Y. Yan et al., Journal of South China University of Technology (Natural Science Edition), 40(2012):71-78. DOI:10.3969/j.issn.1000-565X.2012.04.011.
[5] H. Grote et al., “The MAD Program (Methodical Accelerator Design) Version 8.13/8 User’s Reference Manual”, Geneva, Switzerland. January, 1994, 18.
[6] M.D. Salt et al., “Beam Dynamics using Graphical Processing Units”, 2008.
[7] G. L. Chen et al., Chinese Science Bulletin. 54(2009): 1845-1853.
[8] L. Dagum et al., Computational Science & Engineering, IEEE. 5(1998): 46-55.
[9] Y. Zhang, Optimization Methods and Software. 10(1998): 1-31.
[10] J. Kepner et al., arXiv preprint astro-ph/0107406, 2001.
[11] Marowka.Ami, “On Performance Analysis of a Multithreaded Application Parallelized by DiKerent Programming Models Using Intel Vtune Parallel Computing Technologies”, 2011:317-331.
[12] J. Laskar, “Frequency map analysis and particle accelerators”, Particle Accelerator Conference, Portland. 2003: 12-16.
[13] S.Q. TIAN et al., Chinese Physics C. 533(2009): 224
[14] Chandra, “Parallel programming in OpenMP”, Morgan Kaufmann, 3(2001):16-17.

ISBN 978-3-95450-136-6

NUMERICAL CALCULATION OF EIGENMODES IN PETRA 7-CELL CAVITY UNDER PRECISE CONSIDERATION OF COUPLER STRUCTURES*

C. Liu†, W. Ackermann, H. De Gersem, W.F.O. Mueller, and T. Weiland
Technische Universitaet Darmstadt, Institut fuer Theorie Elektromagnetischer Felder (TEMF)
Schlossgartenstr. 8, 64289 Darmstadt, Germany

Abstract

The PETRA accelerator [1], which served originally as a pre-accelerator for the large HERA facility, is nowadays the world's best storage-ring-based X-ray radiation source. It provides the scientists experimental opportunities with X-rays radiation. The PETRA accelerator is based on a 7-cell normal conducting copper cavity operating at 500 MHz and delivers a particle beam with energy up to 6 GeV. To enable proper beam dynamics simulations, it is important to determine the eigenmodes in the accelerating cavities with high precision. In the real installation, the input coupler is required to transfer the energy from the sources to the particle beam. For this reason, a complex-valued eigenmode solver can be applied to properly calculate the eigenmodes. At the Computational Electromagnetics Laboratory (TEMF) a robust parallel eigenmode solver based on complex-valued finite element analysis is available. In this paper, the real-valued and complex-valued eigenmode solver have been applied to the PETRA 7-cell cavity to determine the resonance frequency, the quality factor and the corresponding field distribution of eigenmodes.

INTRODUCTION

As shown in earlier studies [2], the higher order modes (HOMs) can cause instabilities of the particle beam in the accelerating cavities. For this reason, during the design phase of the accelerating cavities, a challenging and difficult task is to determine the eigenmodes inside the accelerating cavities with the help of proper computer simulations. So far, the most efficient commercially available eigenmode solvers are based on real-valued analysis, which is sufficient to describe the entire electromagnetic field in the lossless acceleration structure. But in reality, the PETRA 7-cell cavity requires the input coupler to transfer energy from the sources to the beam. Therefore, a complex-valued eigenmode solver can be applied to calculate the eigenmodes efficiently [3]. In this paper, we used the real-valued and complex-valued eigenmode solver to calculate the eigenmodes in the PETRA 7-cell cavity.

THEORETICAL BACKGROUND

Generally, Maxwell's equations are the mathematical foundation of the eigenmode analysis for accelerating structures. To determine the eigenmodes with high precision, the continuous Maxwell's formulation has been transformed to a suitable matrix equation with the help of the Finite Element Method (FEM) [4]. For the FEM discretization the tetrahedral grids and higher order curvilinear elements (see Fig. 1) have been applied to satisfy the demand for high-precision modeling of the curved geometry [5].

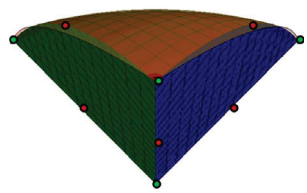

Figure 1: Curvilinear tetrahedral element [5].

Real-valued Eigenmode Solver

The real-valued eigenmode solver is applying the idealized boundary conditions (the perfect electric conductive material (PEC) or the perfect magnetic conductive material (PMC)) and utilizes the basis functions up to third order on curved tetrahedral elements. The determination of the eigenmodes for the accelerating structures by the real-valued eigenmode solver is performed with CST MICROWAVE STUDIO [6].

Complex-valued Eigenmode Solver

In the real installation, energy transfer can occur with the help of dedicated couplers of the accelerating cavity. To represent this fundamental behavior in the computational model, a complex-valued eigenmode solver applies the port boundary condition as one of the lossy boundary conditions, which can be applied to formulate the necessary energy exchange in the port plane [4].

For implementation of the complex-valued eigenmode solver, the geometric modeling of the accelerating structure with the tetrahedral meshing is performed with CST MICROWAVE STUDIO [6], then the essential information will be delivered to the complex-valued eigenmode solver by means of ASCII or binary file transfer. The eigenmode solver is generally computationally demanding due to the precision modeling of elliptical cavities with curved tetrahedral meshes as well as the complex-valued calculation process. To achieve a good performance on simulation time, a distributed memory architecture using MPI parallelization strategy has been utilized for the implementation [5].

* Work supported by DESY Hamburg
† liu@temf.tu-darmstadt.de

ISBN 978-3-95450-136-6

COMPUTATION OF EIGENMODES WITH REAL-VALUED EIGENMODE SOLVER

Firstly, the real-valued eigenmode solver has been applied to the unperturbed PETRA 7-cell cavity (see Fig. 2) to determine the characteristic values (resonance frequency and shunt impedance R/Q) for all modes in the 1st monopole passband. The electric boundary condition (PEC) is applied on the entire surface. In addition, the magnetic boundary condition (PMC) is used to realize the symmetry planes to reduce the computational costs.

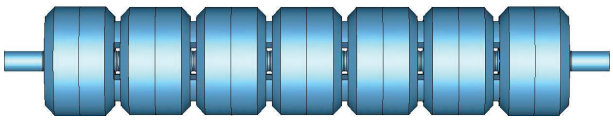

Figure 2: The PETRA 7-cell cavity (500 MHz) with beam tubes.

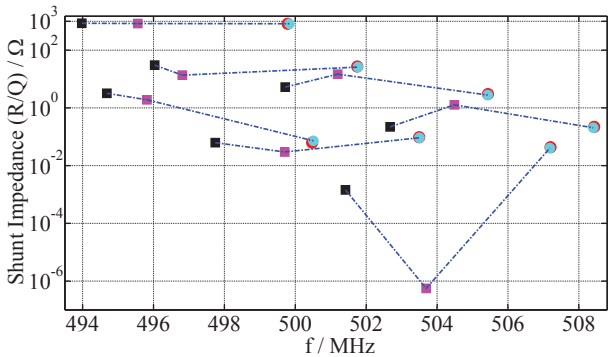

Figure 3: Shunt impedance (R/Q) versus frequency for the monopole modes in the 1st monopole passband for different discretizations. The squares denote the values obtained from the MAFIA calculations. The MAFIA calculations are performed on meshes with 94.231 and 698.412 'hexahedrons' in cylindrical coordinate system indicated by black and magenta squares. The results obtained with the PMC symmetry planes from the real-valued FEM (CST MWS) calculations using basis functions up to the second order on second order curved tetrahedral elements are marked by cyan data points, while the red points mark the results obtained with the PMC symmetry planes from CST MWS calculations using basis functions up to the third order on fourth order curved tetrahedral elements. The CST MWS calculations are performed on meshes with 307.200 tetrahedrons.

A graphical representation of the shunt impedance (R/Q) as a figure of merit for the calculated monopole modes using the electromagnetic field solver MAFIA based on the real-valued Finite Integration Technique (FIT) [7] as well as on the real-valued FEM eigenmode solver is given in Fig. 3. According to Fig. 3, the colored data points obtained with various tetrahedral meshes indicate a robust calculation of frequency and shunt impedance for the eigenmodes in the 1st monopole passband. The eigenmode solver on the basis of real-valued finite element analysis is sufficient to describe the entire electromagnetic field in the lossless PETRA cavity. In addition, with the increase of the hexahedral mesh cells, the difference between the eigenfrequencies from the MAFIA and CST MWS calculations becomes smaller.

The simulation results summarized in Fig. 3 have shown a remarkable competence of the real-valued eigenmode solver for the PETRA 7-cell cavity. Starting from the design values, the green curve in Fig. 4 indicates a bad field flatness of the longitudinal electric field component E_z in the PETRA 7-cell cavity for the TM_{010}, π mode. According to the fundamental operating principle of the PETRA accelerating cavity, a homogeneous field distribution is desirable.

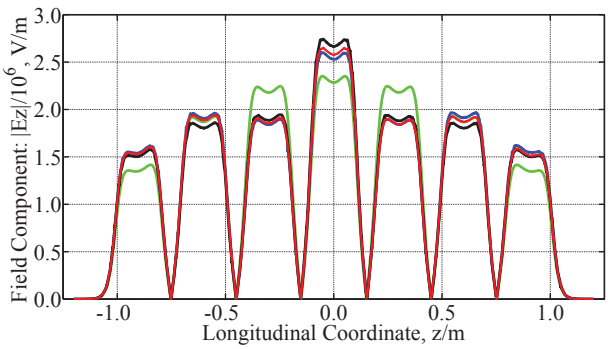

Figure 4: Evaluation of the longitudinal electric field component E_z along the cavity axis. Green curve: unperturbed 7-cell cavity. Black curve: the penetration depth of the plunger is set to -20 mm, while the length of the pump is set to 120 mm. Red curve: the penetration depth of the plunger is set to -50 mm, while the length of the pump is set to 120 mm. Blue curve: the penetration depth of the plunger is set to -80 mm, while the length of the pump is set to 120 mm. All calculations are performed with 0.5 million curvilinear tetrahedrons.

COMPUTATION OF EIGENMODES WITH COMPLEX-VALUED EIGENMODE SOLVER

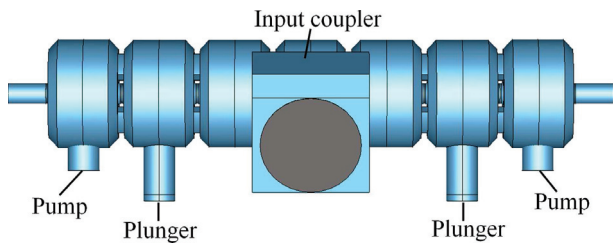

Figure 5: PETRA 7-cell cavity (500 MHz) equipped with beam tubes, plungers, pumps as well as the input coupler.

In reality, the PETRA acceleration cavity is equipped with two vacuum pumps, two plungers as well as an input coupler (see Fig. 5). The input coupler is installed onto the central cell of the PETRA cavity and required as an additional extension to transfer the energy from the sources to the

ISBN 978-3-95450-136-6

particle beam. Therefore, the complex-valued eigenmode solver, which utilizes basis function up to the second order on curved tetrahedral elements, has been applied to the PETRA cavity to determine the characteristic values (resonance frequency, quality factor and shunt impedance) for all modes in the 1st monopole passband. A port boundary condition is used to define the boundary condition for the input coupler.

Firstly, by means of adjusting the penetration depth of the plungers, the field flatness of the PETRA cavity has been adjusted, as is shown in Fig. 4. In the future, the field flatness will be adjusted to a homogeneous level.

In Fig. 6, the colored markers indicate the values of frequency, external quality factor for all eigenmodes in the 1st monopole passband for a specific geometric setup where the penetration depth of the plungers is set to -80 mm, while the length of the pumps is set to 120 mm. According to Fig. 6, the quality factor of the accelerating mode TM_{010}, π is about $2.3 \cdot 10^3$, while the quality factors of three monopole modes can reach to about 10^8. The reason for those large values is that the electric fields of the three monopole modes in the central cell of the PETRA cavity are so weak that the energy transfer between the cavity and input coupler is restricted. Furthermore, a graphical representation of the shunt impedance (R/Q) for all modes in the 1st monopole passband are given in Fig. 7. The calculated results in Fig. 7 have shown a robust calculation of the shunt impedance.

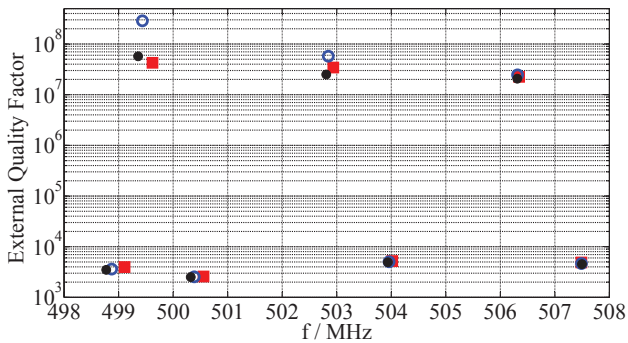

Figure 6: Quality factors for the monopole modes in the 1st monopole passband for various mesh resolutions. The calculations are performed on meshes with 117.012, 347.427 and 1.145.408 tetrahedrons indicated by red squares, blue circles and black points.

CONCLUSION

In this paper, the eigenmodes in the PETRA 7-cell cavity have been preliminary calculated by using the real-valued and complex-valued eigenmode solver. Firstly, the fundamental monopole modes in the unperturbed 7-cell cavity has been computed with different tetrahedral meshes by using the real-valued eigenmode solver. The obtained results are in good agreement with the values of the eigenfrequency and shunt impedance. Due to the bad field flatness of the

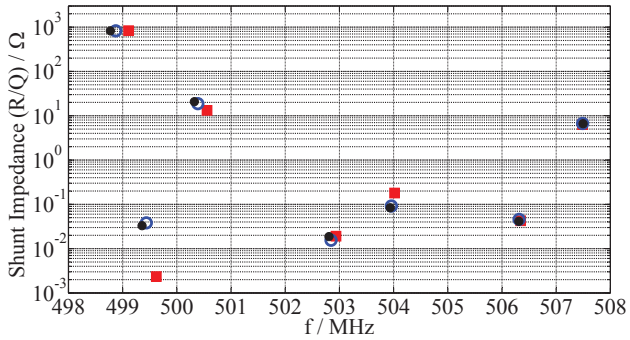

Figure 7: Shunt impedances (R/Q) for the monopole modes in the 1st monopole passband for various mesh resolutions. The calculations are performed on meshes with 117.012, 347.427 and 1.145.408 tetrahedrons indicated by red squares, blue circles and black points.

longitudinal electric field components in the unperturbed PETRA 7-cell cavity, the penetration depth of the equipped plungers has to be set properly. Finally, a robust parallel eigenmode solver on the basis of complex-valued finite element analysis, has been successfully applied to calculate the eigenmodes inside the PETRA 7-cell cavity.

In the future, the eigenfrequency, the quality factor as well as the shunt impedance of the fundamental monopole modes and higher order modes in the PETRA 7-cell cavity will be calculated by using the complex-valued eigenmode solver, thereby the eigenmodes, which impair the stability of particle beam, can be discovered.

REFERENCES

[1] K. Balewski, "STATUS OF PETRA III", Proceedings of EPAC08, Geno, Italy, 2008, WEPC001.

[2] H. Padamsee, J. Knobloch and T. Hays,"RF Superconductivity for Accelerator", Second Edition, Wiley-VCH, Weinheim, 2008.

[3] L.-Q. Lee, Z. Li, C. Ng, K. Ko, "Omega3P: A Parallel Finite-Element Eigenmode Analysis Code for Accelerator Cavities", SLAC-PUB-13529, Menlo Park, USA, February 2009.

[4] W.Ackeramnn and T.Weiland, "High Precision Cavity Simulation", ICAP2012, Rostock-Warnemuende, Germany, 2012, MOADI1.

[5] W. Ackermann, G. Benderskaya and T. Weiland, "State of the Art in the Simulation of Electromagnetic Fields based on Large Scale Finite Element Eigenanalysis", International COMPUMAG Society Newsletter, Vol. 17(2), 2010.

[6] CST MICROWAVE STUDIO 2015, CST AG - Computer Simulation Technology, Darmstadt, Germany. http://www.cst.com.

[7] T. Weiland "A discretization model for the solution of Maxwell's equations for six-component fields." Archiv Elektronik und Uebertragungstechnik, 31: 116-120, 1977.

ISBN 978-3-95450-136-6

OFF-AXIS BEAM DYNAMICS STUDY IN RF PHOTOCATHODE ELECTRON SOURCES *

R. Huang†, Q. Jia
NSRL, University of Science and Technology of China, Hefei, Anhui, 230029, China
C. Mitchell, C. Papadopoulos, F. Sannibale, H. Qian, M. Venturini, J. Qiang, D. Filippetto, J. Staples
Lawrence Berkeley National Laboratory, Berkeley, CA 94720, USA

Abstract

We report on simulations and analysis of off-axis electron emission in a high-field VHF electron gun and beam dynamics in the photoinjector downstream. The electron gun is the core of the Advanced Photoinjector Experiment at Lawrence Berkeley National Laboratory, aimed toward the development of a novel source for a high repetition rate Free Electron Laser. People may operate the drive laser away from the cathode center in some special cases. However, off-axis emitted beam will result in a growth of the projected transverse emittance due to correlations between the transverse and longitudinal degrees of freedom. In this paper, we will evaluate the off-axis beam characteristic and describe simulation results which indicate that a realistic implementation of correction procedure would compensate this source of emittance growth. A multi-objective genetic optimizer tool is induced for beam property improvement.

INTRODUCTION

RF photocathode electron guns are built to generate high brightness beams with low emittance and large charge. Typically on RF cathode, a laser excites photo-emission in the center area to get the best performance in terms of emittance. However, in some cases, it is necessary to operate off-axis electron emission, such as the quantum efficiency (QE) depletion in the cathode center after hours of center emission. The challenge in using off-axis emission at the cathode is controlling emittance growth that can be induced in RF guns. This is because the time-dependent focusing effects lead to distribution asymmetries and longitudinal-transverse correlations, which will finally increase the beam emittance.

In this paper, we evaluate this effect as an example on the the VHF gun of Advanced Photoinjector Experiment (APEX) at Lawrence Berkeley National Laboratory (LBNL), and define a correction procedure that can largely compensate for the emittance growth. A useful computational tool to optimize multi-objective is applied in order to enable global optimization of high brightness injector parameter and correct off-axis emission. The introduction to the APEX and the recent status can be found in [1, 2]. Figure 1 shows the schematic layout based on VHF gun that will be used in simulations. A 100 pC charge bunch is emitted in a 186 MHz normal-conducting VHF gun, accelerated to 800 keV at the gun exit, and further boosted to 95 MeV by eight 9-cell 1.3 GHz TESLA-type cavities. The beam out of the cathode has a bunch length of 33 ps with plateau distribution and rms beam size of 192 μm with uniform distribution. The two solenoids between the gun and TESLA cavities are tuned to optimized emittance compensation setting, and a 1.3 GHz Buncher cavity is applied for proper bunch compression. The off-axis emitted beam will result in great emittance increase and misalignment propagation through the beamline. Correcting the beam to on-axis downstream the gun exit does not solve the problem because the emittance growth is produced by time-dependent defocusing force in the gun cavity. We will introduce an effective correction procedure to mostly compensate the emittance growth. Space charge effect is not considered in this paper for simplify, further calculation and analysis will be discussed in [3].

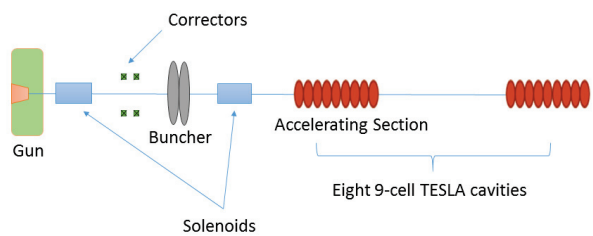

Figure 1: Schematic of the beamline based on the VHF gun. The injector exit is located at 15 m downstream from the cathode.

MULTI-OBJECTIVE GENETIC OPTIMIZATION

In this section, we will introduce a multi-objective genetic optimizer as a useful tool to optimize high-brightness injector parameters.

The method of multi-objective genetic optimization is an effective approach to solve the problem with multiple competing goals. The optimizer was written by integrating the multi-objective genetic algorithm NSGA-II [4] together with the beam dynamics tool ASTRA [5], in order to enable global optimization of high-brightness injector parameters. It has been actively used in injector design for APEX with two objectives of minimizing the emittance and the bunch length. The optimizer is written primarily in C language and typically run in parallel on about 100 processors. Once the optimizer is converged after adequate generations, a

* Work supported by Director of the Office of Science of the US Department of Energy under Contract no. DEAC02-05CH11231
† hruixuan@mail.ustc.edu.cn

ISBN 978-3-95450-136-6

population of good solutions can be obtained in a Pareto front, showing trade-offs between the emittance and bunch length. Detail optimization procedure to obtain the settings for the gun, the solenoid, and RF cavities is reported in [6], which determines the nominal settings used in this paper.

CORRECTION OF EMITTANCE GROWTH

Previously, we have introduced the method of multi-objective genetic optimization to obtain optimal settings in the injector. Based on the nominal settings, a possible correction procedure for off-axis beam is investigated to finally reduce the off-axis beam emittance growth.

Assume that a beam with 2.0 mm misalignment in horizontal, ten times of rms laser spot, is emitted on the cathode of the VHF gun. The beam will maintain offset downstream, go as far as 7.3 mm offset in the first solenoid and 4.1 mm at injector exit. The misalignment is transferred from horizontal to vertical due to the two solenoids that rotate the beam by roughly 90 degrees. Compared with on-axis beam, the final emittance of the 2.0 mm offset beam is increased by 2.6% and 147.9% in the horizontal and vertical, respectively. If we further investigate particle distribution at the injector exit, we can see an evident correlation between the vertical plane and longitudinal position, and the beam's cylindrical symmetry is destroyed by transverse RF kicks in RF cavities.

Before introducing the correction optimization, we will adjust the first solenoid to enforce the beam passing through the symmetry axis, for the purpose of future emittance compensation. Since the solenoid is equipped with remotely controlled motors, it can be adjusted for both its position and orientation angle. For 2 mm off-axis beam, the first solenoid is shifted to 8 mm off-center and rotated in the $x - z$ plane by 22 mrad, which can be found by ASTRA simulation.

Simulation indicates that steering the beam back into axis alignment results in a beam with a larger projected emittance. In order to obtain a minimum emittance solution at the injector exit, the bending radii of the two pairs of correctors before the buncher cavity are adjusted to vary the beam alignment. Based on the full injector optimized setting, the four bending radii are set as knobs, the normalized horizontal rms emittance and the vertical rms emittance are chosen as two objectives to be minimized. As described previously, the result is not a single solution, but instead a set of solutions that are optimal in a Pareto sense Fig. 2. It is a trade-off between horizontal and vertical emittance. The final decision on the correction procedure is the one that gives the minimum value of the emittance geometric mean ε_G:

$$\varepsilon_G = \sqrt{\varepsilon_x \varepsilon_y} \tag{1}$$

where ε_x and ε_y are the horizontal and vertical normalized emittances. The minimum ε_G attained along the Pareto front is 0.207 mm-mrad, while the corresponding values are 0.312 mm-mrad for the off-axis uncorrected beam and 0.196 mm-mrad for the on-axis emitted beam, respectively. This indicates that the optimization scheme can almost remove the emittance growth due to off-axis emission.

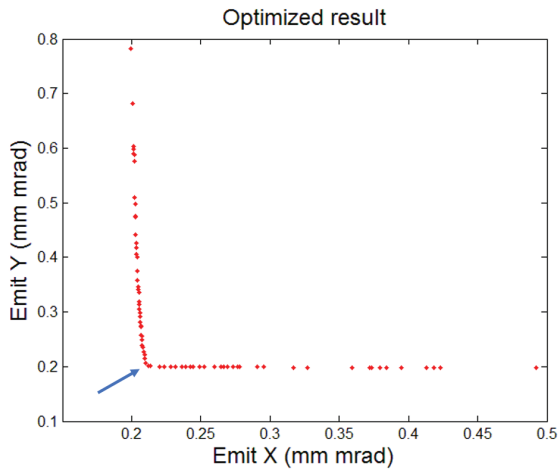

Figure 2: Pareto front of correction for off-axis emitted beam. The solution with minimum ε_G is marked as an arrow.

The bending radii of the correctors corresponding to this optimized solution are listed in Table 1. A negative bending radius represents a bending direction opposite the bends with positive radii. In Fig. 3, it has compared along the injector the evolution of the transverse beam centroid and the rms beam emittance between the optimized beam and the uncorrected beam. It is notable that the optimized beam is not steered into axis alignment by the correctors, shown in black of the upper graph. Instead, the beam propagates off-axis through the buncher and accelerating cavities, and it remains off-axis at the exit of the injector (15 m). Compared with uncorrected beam, the optimized corrected beam has a noteworthy decrease in emittance.

Table 1: Correctors Bending Radii for 2 mm Off-axis Beam Emittance Optimization

Parameter	Value
1^{st} corrector in horizontal	0.659 m
1^{st} corrector in vertical	6.447 m
2^{nd} corrector in horizontal	14.672 m
2^{nd} corrector in vertical	-32.992 m

Although the off-axis emitted beam remains off-center at the exit of the present stage of the injector, one may still align the beam on-center before downstream acceleration to higher energy. More correctors should be applied downstream to steer the beam to on-axis, proceeding with further accelerating sections. One may notice that the beam at the second series of correctors has larger rigidity than at the first one, because of the higher energy. The bending radii for the second series of correctors, which can also be evaluated by similar ways as in previous section, are still practical. At the end of the second accelerating section, the final beam emittance and other parameters are nearly identical to those of a beam emitted on-axis at the cathode.

ISBN 978-3-95450-136-6

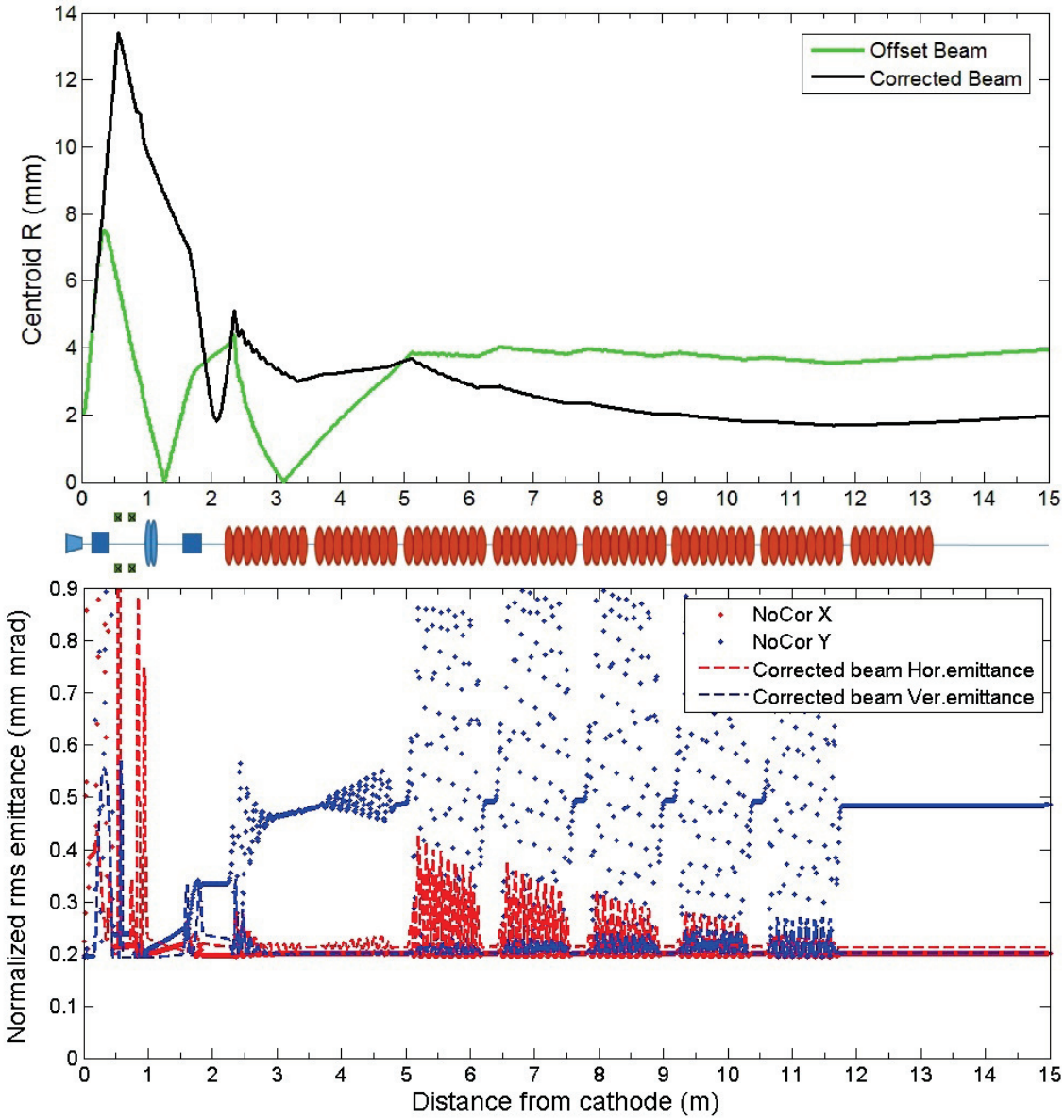

Figure 3: Centroid and emittance evolution of optimized corrected beam. Optimized and uncorrected beam centroid are plotted with black and green lines respectively in upper graph. Transverse emittance for optimized beam and uncorrected one are plotted with dash lines and dots. Red color stands for horizontal plane and blue one represents vertical plane.

CONCLUSION

By using a proper setting for the corrector dipoles, the emittance growth of a beam emitted off-axis in an RF photoinjector can be compensated to achieve an emittance similar to that of a beam emitted on-axis. By further alignment, the beam can be made to return on-axis with acceptable emittance growth at high energy. The emittance growth of off-axis emitted beam is due to time-dependent RF effect, which is independent of space charge effect. Although the space charge effect was not taken into consideration above, the correction procedure is still practicable. Further space charge calculation will be included in the future [3].

REFERENCES

[1] F. Sannibale et al., Phys. Rev. ST Accel. Beams **15**, 103501 (2012).

[2] F. Sannibale et al., MOPRI053, IPAC14, Dresden.

[3] R. Huang,et al., (to be published).

[4] K. Deb, IEEE Trans. Evol. Comp. 6, pp. 182-197 (2002).

[5] K. Flottman, ASTRA: A space charge tracking algorithm, `http://www.desy.de/~mpyflo/astradokumentation/`

[6] C. Papadopoulos, SLAC-PUB-16210 (2014).

ISBN 978-3-95450-136-6

SEARCHING ELECTRIC DIPOLE MOMENTS IN STORAGE RINGS – CHALLENGES, STATUS AND COMPUTATIONAL NEEDS –*

A. Lehrach# on behalf of the JEDI Collaboration
Institut für Kernphysik, Forschungszentrum Jülich, 52425 Jülich, Germany
III. Physikalisches Institut B, RWTH Aachen University, 52074 Aachen, Germany
JARA-FAME (Forces and Matter Experiments)

Abstract

Full spin tracking simulations of the entire experiment are absolutely crucial to explore the feasibility of the planned storage ring EDM (Electric Dipole Moment) experiments and to investigate systematic limitations. For a detailed study during the storage and buildup of the EDM signal, one needs to track a large sample of particles for billions of turns. Existing spin tracking programs have to be extended to properly simulate spin motion in presence of an EDM. In addition, benchmarking experiments are performed at the Cooler Synchrotron COSY to check and to further improve the simulation tools. Finally, the layout of a dedicated storage ring has to be optimized by a full simulation of particle and spin motion.

INTRODUCTION

Permanent EDMs of fundamental particles violate both time invariance *T* and parity *P*. Assuming the *CPT* theorem this implies *CP* violation. The Standard Model (SM) predicts non-vanishing EDMs. Their magnitudes, however, are expected to be unobservably small with current experimental techniques. Hence, the discovery of a non-zero EDM would be a signal for new physics and could explain the matter-antimatter asymmetry observed in our Universe.

Different approaches to measure EDMs of charged particles are proposed with an ultimate goal to reach a sensitivity of 10^{-29} e·cm in a dedicated storage ring [1,2,3]. The Jülich-based JEDI Collaboration (Jülich Electric Dipole moments Investigations) has been formed to exploit and demonstrate the feasibility of such a measurement and to perform the necessary R&D work towards the design of a dedicated storage ring [4]. As a first step R&D work at the Cooler Synchrotron COSY is pursued. Subsequently, an EDM measurement of a charged particle will be performed at COSY with limited sensitivity [5]. On a longer time scale, the design and construction of a dedicated EDM storage ring will be carried out.

EXPERIMENTAL METHOD

The principle of every EDM measurement (e.g., neutral and charged particles, atoms, molecules) is the interaction of the particles' electric dipole moment with an electric field. In the center-of-mass system of particles electric dipole moments $\vec{d}$ couple to the electric fields, whereas magnetic dipole moments $\vec{\mu}$ (MDM) couple to magnetic fields.

The spin precession in presence of both electric and magnetic fields is given by:

$$\frac{d\vec{S}}{dt} = \vec{d} \times \vec{E}^* + \vec{\mu} \times \vec{B}^*. \quad (1)$$

$\vec{E}^*$ and $\vec{B}^*$ denote the electric and magnetic fields in the rest frame of a particle.

In case of moving particles in a circular accelerator or storage ring, the spin motion is covered by the Thomas-BMT equation and its extension for EDM [6]:

$$\frac{d\vec{S}}{dt} = \vec{S} \times (\vec{\Omega}_{\mathrm{MDM}} + \vec{\Omega}_{\mathrm{EDM}}),$$

$$\vec{\Omega}_{\mathrm{MDM}} = \frac{q}{m}\left[G\vec{B} - \frac{\gamma G}{\gamma+1}\vec{\beta}(\vec{\beta}\cdot\vec{B}) - \left(G - \frac{1}{\gamma^2-1}\right)\frac{\vec{\beta}\times\vec{E}}{c}\right],$$

$$\vec{\Omega}_{\mathrm{EDM}} = \frac{\eta q}{2mc}\left[\vec{E} - \frac{\gamma}{\gamma+1}\vec{\beta}(\vec{\beta}\cdot\vec{E}) + c\vec{\beta}\times\vec{B}\right]. \quad (2)$$

$\vec{S}$ in this equation denotes the spin vector in the particle rest frame in units of $\hbar$, t the time in the laboratory system. β and γ are the relativistic Lorentz factors, q and m the charge and mass of the particle, respectively. $\vec{E}$ and $\vec{B}$ denote the electric and magnetic fields in the laboratory system. Two angular frequencies $\vec{\Omega}_{\mathrm{MDM}}$ and $\vec{\Omega}_{\mathrm{MDM}}$ are defined with respect to the momentum vector. The gyromagnetic anomaly $G=(g-2)/2$ with the Landé g-factor and η are dimensionless and related to the magnetic and electric dipole moments of the particle as follows:

$$\vec{\mu} = 2(G+1)\frac{q\hbar}{2m}\vec{S}, \vec{d} = \eta\frac{q\hbar}{2mc}\vec{S}. \quad (3)$$

*Work supported by BMBF International Cooperation (Grant Number RUS 11/043) and Jülich-Aachen Research Alliance JARA-FAME (http://www.jara.org/de/research/jara-fame/)
#a.lehrach@fz-juelich.de

ISBN 978-3-95450-136-6

In a planar storage ring the spin precession in the horizontal plane is governed by the MDM. If an EDM exists, the spin vector will experience an additional torque. The resulting vertical spin component, proportional to the size of the EDM, will be measured by scattering the particles of the stored beam at an internal target and analyzing the azimuthal distribution of the scattered particles. A coherent buildup of the vertical polarization only takes place within the time the spins of the particle ensemble stays aligned. Since the spin tune is a function of the betatron and synchrotron amplitudes of the particles in the six-dimensional phase space, spin decoherence is caused by beam emittance and momentum spread of the beam and leads to a gradual decrease of the polarization buildup rate in the vertical direction. To reach the anticipated statistical sensitivity of 10^{-29} e·cm a spin coherence time (SCT) of 1000 s has to be reached.

The major challenge of such kind of experiment is a very small expected vertical component of the spin excited by the EDM and the relatively large contribution by false spin rotations via the MDM due the field and misalignments errors of accelerator elements.

Starting from Equation (2), different approaches are possible to excite spin rotations via the electric dipole moment:

1. Frozen-spin method [7], where the electrostatic and magnetic bending fields in a storage ring are adjusted according to the particle momentum in such a way that the longitudinally polarized spins of the particle beam are kept aligned ("frozen") with their momenta. For protons pure electrostatic bending fields are sufficient to freeze the spin at a magic momentum of roughly 701 MeV/c [1]. If the particle has an EDM along its spin direction, the electrostatic fields in the rest frame of the particles will rotate the spin into the vertical direction. This change of the vertical component of the beam polarization from early to late storage times is the signature of the EDM signal.
2. Quasi-frozen-spin method [8], where the anomalous magnetic moment of the particles has to have a small negative value like for deuterons. In this case electric and magnetic field deflectors can be spatially separated. The spins oscillate around the momentum direction in the horizontal plane back and forth every time the particle passes through a magnetic or an electrostatic field. The spin oscillations of individual particles compensate each other with respect to the momentum vector in the magnetic and electrostatic part of the ring. Due to the low value of the anomalous magnetic moment of deuteron, an effective contribution to the expected EDM effect is reduced only by a few percent compared to the frozen-spin method.
3. Resonant method [5,9], were an RF ExB dipole runs at a frequency tuned to the spin tune ($\gamma G \pm K$, K integer). In Wien filter mode the ratio of the electric and magnetic fields are chosen in a way that the Lorentz force cancels: $\vec{E}/c = -\vec{\beta} \times \vec{\mathrm{B}}$. This means, that the RF Wien filter will not influence the EDM directly. It does, however, modulate the horizontal spin precession via the MDM turn by turn. Together with the interaction of the EDM with the motional electric field in the rest of the ring, this frequency modulation is able to rotate the spin around the radial axis and leads to an accumulation of the EDM signal.

BEAM AND SPIN DYNAMICS

For a detailed study during the storage and buildup of the EDM signal, one needs to track a large sample of particles for billions of turns. Given the complexity of the tasks, particle and spin tracking programs must be benchmarked and simulation results compared to beam experiments, to ensure the required accuracy of the obtained results. The COSY Infinity [10] and MODE [11] simulation programs are utilized for this purpose, both based on map generation using differential algebra and the subsequent calculation of the spin-orbital motion for an arbitrary particle. In a first step the development and implementation of time-dependent transfer maps as well as the EDM extension to spin motion were benchmarked and used to investigate the resonant method and its systematic limitations. Integrating programs, solving equations of particle and spin motion in electric and magnetic fields using Runge-Kutta integration, have also been used for benchmarking [12].

To achieve the unprecedented precision of the EDM measurement robust and advanced numerical tracking codes are required for exploring various systematic effects. Also sophisticated lattice design tools for storage rings with all electrostatic elements as well as combined magnetic and electric elements have to be applied. To identify the best approach using numerical simulation codes a satellite meeting during the International Particle Accelerator Conference IPAC'15 in Richmond (VA, USA) has been organized [13]. The aim of this meeting was to review different advanced numerical tracking codes for exploring various systematic effects. In addition various lattice design codes with all electrostatic as well as combined magnetic and electric elements have been discussed. The following capabilities are required:

- Accurate description of all ring elements including fringe fields.
- Allowing various error inputs for systematics investigation.
- Accurate implementation of RF spin manipulation elements.
- Calculation of orbital and spin motion with a high accuracy for billion orbital revolutions.
- User friendly graphic interfaces for extracting physical information from tracking data (e.g., orbit, betatron tune, and spin tune from tracking data).

ISBN 978-3-95450-136-6

The discussions at this meeting included benchmarking of simulation codes against first principle based models as well as experimental results. A second meeting will be organized during International Particle Accelerator Conference IPAC'16 in South Korea to further discuss extensions and benchmarking of the various simulation programs.

Experimental and Theoretical Studies of Spin Coherence Time

Effective measures to counteract spin decoherence is phase space cooling, beam bunching and multipole correction. Especially the adjustment of beam chromaticity by sextupole magnets at the Cooler Synchrotron COSY has been studied theoretically and experimentally [14,15]. For the measurements and the results discussed below a common experimental setup of COSY has been used with a polarized deuteron beam of roughly 10^9 particles, electron-cooled beams to reduce the equilibrium beam emittance and momentum spread, accelerated to a beam momentum of 970 MeV/c and bunched by an RF cavity. An RF solenoid induced spin resonance was employed to rotate the spin by 90° from the initially vertical direction into the horizontal plane. Three different families of sextupole magnets located in the arcs of COSY were adjusted to find the best setting for long SCT. It has been demonstrated experimentally that the SCT of a horizontally polarized deuteron beam at COSY can be substantially extended to more than 1000 s through a combination of sextupole fields by adjusting the beam chromaticities $\xi_{x,y}$ together with beam bunching and electron cooling [15].

Simulations with COSY Infinity confirmed the experimental results [14]. Highest SCT can be reached by adjusting the beam chromaticities $\xi_{x,y}$. This way the path length change induced by the betatron motion is reduced. In addition the path length change due to second order momentum deviations has to be minimized. Both chromaticities and the second order momentum compaction factor can be adjusted accordingly by the three sextupole families in the arcs of COSY.

Investigations of Systematic Effects Studies for the Resonance Method

Main sources of systematic errors for the resonance method are the alignment of the RF Wien filter with respect to the invariant spin field, opening angle of spin ensemble, field quality (fringe fields), the relative frequency slip of the RF Wien filter and the closed orbit deviation of the beam due to misalignments and field errors of ring magnets. The spin motion including these systematic errors has been investigated for the resonance method in detail [16,17]. The resulting closed orbits can be corrected by the orbit correction system of COSY to suppress false spin rotations via the MDM [16]. From these simulations the present estimate for the systematic EDM limit utilizing the resonance method at the Cooler Synchrotron COSY is in the order of $d = 10^{-19}$ e·cm for a remaining orbit excitations below the millimeter level, a rotation of the RF Wien filter of 10^{-4} rad and relative mismatch between the operating frequency of the RF Wien filter and the spin resonance frequency of less than 10^{-5} [17]. In order to improve the systematic EDM limit for this method the closed orbit correction system of COSY has to be improved significantly, the relative frequency slip of the RF ExB dipole stabilized and the RF Wien filter aligned to the invariant spin axis with the maximum achievable precision.

Lattice Design of a Dedicated Storage Ring

Presently, the two different approaches to design a dedicated deuteron EDM ring are investigated, the frozen and the quasi-frozen-spin method. The proposed quasi-frozen-spin lattice leads to a simplified design of electrostatic and magnetic bending elements [18], because magnetic and electric bending elements can be spatially separated. Additional systematic spin rotations due to this separation of bending elements have to be carefully studied. In addition a frozen-spin lattice is under investigation with combined magnetic and electrostatic field deflectors. Presently different lattice configurations are investigated ranging for bending radii between 30 and 20 m. The required electric field strength for a 1 GeV/c deuteron beam reaches 4 to 8 MV/m with a magnetic field of roughly 0.15 to 0.3 T.

To confirm the feasibility of the different lattice structures, beam and spin tracking simulation are performed using COSY Infinity and MODE.

CONCLUSION

Different proposals to perform a first direct EDM measurement at the Cooler Synchrotron COSY will be further investigated by spin tracking simulations in order to quantify the systematic limits and finally perform a first EDM measurement at COSY.

For the design study of a dedicated EDM storage ring, lattice design and spin tracking to identify the systematic EDM limit of the experimental method in conjunction with the design of all accelerator elements are a major task for the JEDI collaboration in the upcoming years. This requires dedicated tools for lattice design with electrostatic and magnetic field elements.

A very accurate description of all ring elements including fringe fields are indispensable for beam and spin tracking simulations in order to achieve the intended accuracy of the planned EDM measurements.

ACKNOWLEDGMENT

The author would like to thank all members of the JEDI and srEDM collaborations for fruitful discussions. I'm especially very grateful to M. Berz and K. Makino for supervised the upgrades of COSY Infinity and S. Andrianov, A. Ivanov and Yu. Senichev for developing the MODE simulation program.

ISBN 978-3-95450-136-6

REFERENCES

[1] V. Anastassopoulos et al. (srEDM Collaboration), "A proposal to measure the proton electric dipole moment with 10^{-29} e cm sensitivity", proposal as submitted to DOE, October 2011; http://www.bnl.gov/edm/Proposal.asp

[2] D. Anastassopoulos et al., (srEDM Collaboration), "Search for a permanent electric dipole moment of the deuteron nucleus at the 10^{-29} e cm level", proposal as submitted to the BNL PAC, April 2008; http://www.bnl.gov/edm/Proposal.asp

[3] JEDI Collaboration web page: http://collaborations.fz-juelich.de/ikp/jedi

[4] A. Lehrach, "Project Overview and Computational Needs to Measure Electric Dipole Moments at Storage Rings", Proc. of 11th International Computational Accelerator Physics Conference (ICAP'12), Rostock-Warnemünde, Germany, MOAAI1, p. 7 (2012), ISBN 978-3-95450-116-8.

[5] A. Lehrach, B. Lorentz, W. Morse, N. Nikolaev, F. Rathmann, "Precursor Experiments to Search for Permanent Electric Dipole Moments (EDMs) of Protons and Deuterons at COSY", Proc. of XIV Advanced Research Workshop on High Energy Spin Physics (DSPIN'11), Dubna, Russia, p 287 (2012); http://arxiv.org/abs:1201.5773

[6] T. Fukuyama, A.J. Silenko, "Derivation of Generalized Thomas-Bargmann-Michel-Telegdi Equation for a Particle with Electric Dipole Moment". International Journal of Modern Physics A, 28(29):1350147 (2013).

[7] F.J.M. Farley et al., Phys. Rev. Lett. 93, 052001 (2004); http://arxiv.org/abs/hep-ex/0307006

[8] Yu. Senichev et al., "Quasi-frozen-spin method for EDM deuteron search", Proc. of the 6th International Particle Accelerator Conference (IPAC'15), Richmond, Virginia, USA, p. 213 (2015); http://accelconf.web.cern.ch/AccelConf/IPAC2015/papers/mopwa044.pdf

[9] W. Morse et al., Phys. Rev. ST Accel. Beams 16, 114001 (2013).

[10] K. Makino, M. Berz, Nucl. Inst. and Meth. in Phys. Res. A 558 (2005).

[11] A. Ivanov, Yu. Senichev, "Matrix Integration of ODEs for Spin-.Orbit Dynamics Simulation", Proc. of 5th International Particle Accelerator Conference (IPAC'14), Dresden, Germany, MOPME011, p. 400 (2014), ISBN 978-3-95450-132-8.

[12] Yu. Senichev, "Storage Ring EDM Simulation: Methods and Results", Proc. of 11th International Computational Accelerator Physics Conference (ICAP'12), Rostock-Warnemünde, Germany, TUADI1, p. 99 (2012), ISBN 978-3-95450-116-8.

[13] "Topical meeting of Spin Tracking for Precision Measurements", satellite meeting of 6th International Particle Accelerator Conference (IPAC'15), Richmond, Virginia, USA, May 2015, organized by M. Bai, A. Lehrach. H. Stroeher, Y. Semertzidis, and E. Stephenson https://indico.cern.ch/event/368912/

[14] M. Rosenthal, "Investigation of Beam and Spin Dynamics for EDM Measurements at COSY", Proc. of 9th International Conference on Charged Particle Optics (CPO-9), Brno, Czech Republic, September 2014, published in the Cambridge Journals Online - Microscopy and Microanalysis.

[15] G. Guidoboni, "Spin coherence time studies of a horizontally polarized deuteron beam at COSY", Proc. of 9th International Conference on Nuclear Physics at Storage Rings (STORI'14), Sankt Goar, Germany, published in Physica Scripta (2015).

[16] M. Rosenthal, A. Lehrach, "Spin Tracking Simulations towards EDM Measurements at COSY", Proc. of the 6th International Particle Accelerator Conference (IPAC'15), Richmond, Virginia, USA, p. 3467 (2015); http://accelconf.web.cern.ch/AccelConf/IPAC2015/papers/thpf032.pdf

[17] S. Chekmenev, "Estimation of Systematic Errors for Deuteron Electric Dipole Moment Search at COSY", Proc. of the 21st International Symposium on Spin Physics (Spin'14), Peking University, Beijing, China, October 2014, International Journal of Modern Physics: Conference Series.

[18] Yu. Senichev et al.," Investigating of Lattice for Deuteron EDM Ring", presented at ICAP'15, Shanghai, China, MODBC4, these proceedings.

ISBN 978-3-95450-136-6

PRECISION SPIN TRACKING FOR ELECTRIC DIPOLE MOMENT SEARCHES

M. Gaisser[1,2,*], S. Hacıömeroğlu[1,2], Y.I. Kim[1,2], S. Lee[1,2], Y.K. Semertzidis[1,2,3]
[1]Center for Axion and Precision Physics (CAPP), Daejeon, South Korea
[2]Institute for Basic Science (IBS), Daejeon, South Korea
[3]Korea Advanced Institute of Science and Technology (KAIST), Daejeon, South Korea

Abstract

Several proposed storage ring electric dipole moment (EDM) searches as well as muon g-2 experiments require a precise understanding of the evolution of the spin during the experiment, both theoretically as well as experimentally in order to understand systematic errors. Here we present the computational challenges of these experiments, our way of dealing with them and a comparison of analytical benchmarking cases with simulation results. In the end we give a short overview of future improvements of our program.

INTRODUCTION

Spin is probably the least used particle property in accelerator physics although it offers paths to precision physics that can yield information about physics beyond the Standard Model. For both, muon g-2 as well as storage ring electric dipole moment (EDM) experiments, the relevant physical information is encoded in the speed and direction of the spin rotation and proper beam preparation, beam control and polarization measurements are therefore crucial for the measurements. Furthermore it is essential to understand all unwanted sources of spin rotation (systematic errors), their magnitude and possible ways of their elimination. Because of the complexity of the equations, this can in general only be achieved with simulations and it has to be shown that their results are reliable.

SPIN EVOLUTION

The spin evolution of a particle with magnetic moment $\vec{\mu}$ and electric dipole moment $\vec{d}$ in the particles rest frame is given by

$$\frac{d\vec{S}}{dt} = \vec{\mu} \times \vec{B}^* + \vec{d} \times \vec{E}^*,$$

where $\vec{B}^*$ and $\vec{E}^*$ are the magnetic and the electric field in the particles rest frame. Using Lorentz transformations for the fields and taking the acceleration of the rest frame into account, one arrives at the famous T-BMT equation which in accelerator coordinates parametrized by the arc-length s looks as follows:

$$\begin{aligned}
\frac{d\vec{S}}{ds} &= \left(\frac{1}{\dot{s}}\left(\vec{\Omega}_\mu + \vec{\Omega}_d\right) - \vec{\kappa} \times \vec{e}_s\right) \times \vec{S} \\
\vec{\Omega}_\mu &= \frac{q}{m}\left(\left(G + \frac{1}{\gamma}\right)\vec{B} - \frac{G\gamma}{\gamma+1}(\vec{\beta}\cdot\vec{B})\vec{\beta}\right) \\
&\quad - \frac{q}{m}\left(G + \frac{1}{\gamma+1}\right)\frac{\vec{\beta}\times\vec{E}}{c} \\
\vec{\Omega}_d &= \frac{\eta q}{2m}\left(\vec{\beta}\times\vec{B} + \frac{\vec{E}}{c} - \frac{\gamma}{\gamma+1}\frac{\vec{\beta}\cdot\vec{E}}{c}\vec{\beta}\right)
\end{aligned}$$

Almost every quantity depends on the position and/or time: The fields $\vec{E}$ and $\vec{B}$, the relativistic factors $\vec{\beta} = \vec{v}/c$ and $\gamma = 1/\sqrt{1-\beta^2}$ (only in electric fields) as well as the curvature $\vec{\kappa} = (1/R(s), 0, 0)$ (for flat rings of bending radius $R(s)$) and the longitudinal unit vector $\vec{e}_s$. $G = (g-2)/2$ is the anomalous magnetic moment while the dimensionless parameter η is given by $\vec{d} = \eta\frac{q}{2mc}\vec{S}$ in analogy to the g-factor for the magnetic dipole moment. Its magnitude is about $\eta \approx 2 \cdot 10^{-15}$ for an assumed proton EDM of 10^{-29}e · cm. $1/\dot{s} = 1/(ds/dt) = dt/ds$ is the inverse of the longitudinal velocity of the particle. The fields have to be evaluated at the respective position of the particle which introduces an additional dependence on the transversal coordinates and closely couples this equation to the equation of motion. All of that, together with a possible explicit time-dependence for rf-fields, makes this a very complicated equation which in general cannot be solved analytically.

SYSTEMATIC ERRORS IN PROTON EDM EXPERIMENT

The proton EDM experiment is proposed for an all-electric ring with the proton momentum at its "magic" value $p = \frac{mc}{\sqrt{G}} \approx 0.7$ GeV/c such that there are no spin rotations due to the magnetic dipole moment in the rest frame of the ideal particle [1]. A possible electric dipole moment will cause a spin rotation out of the horizontal plane with an expected rate of a few nrad/s for an assumed value of $d = 10^{-29}$ e · cm. A net radial magnetic field of only a few aT would cause a similar effect. Shielding to this level is not possible and additional strategies have been developed to deal with the issue, most notably the use of counter-rotating beams with a low and modulated vertical tune such that the oscillating vertical beam separation caused by the radial B-field could be measured with SQUID-based beam position monitors. In case of strong local spin rotations, e.g. due to misalignments

* gaiwa84@ibs.re.kr

ISBN 978-3-95450-136-6

or field errors, that may almost average out along the ring, one also has to consider the "geometric phase effect", i.e. the fact that rotations do not commute and hence a sequence of rotations around different axes generally does not cancel completely. Other systematic errors might be caused by a possible polarization profile of the beam or an unsuitable extraction scheme.

OUR APPROACH

Several codes based on different ideas like mapping codes using differential algebra or truncated power series algebra, kick-bend algorithms or Romberg integration are in use around the world. Some of these codes have difficulties with explicitly time-dependent fields or difficult field configurations. In general every code has to make various approximations and this typically originates either in a difficulty to model the real world or a trade-off between accuracy and speed.

In order to force as little approximations as possible, we choose a very simple but general approach and integrate the equation of motion as well as the T-BMT equation numerically. To this end many different algorithms are available with different characteristics. In our program we implement several of them with the aim of testing and benchmarking them with respect to accuracy and speed. Standard algorithms like the fourth order Runge-Kutta algorithm will be compared to newer ones and great emphasis is placed on the modular implementation in C++ for maximal flexibility. VexCL [2] (Vector Expression Template Library for OpenCL/CUDA) is used for parallelization with either CUDA or OpenCL as backends for a wide range of different hardware. VexCL is a header-only library that strives to reduce boilerplate code and supports multi-device and multi-platform computations. OpenCL has the advantage of being able to run on different hardware from various manufacturers while CUDA may be faster but depends on NVIDIA GPUs. Furthermore, VexCL is easy to learn and was demonstrated to work with Boost-Odeint [3, 4].

Our program also comes with the option of changing the data type for all floating point operations and allows the use of arbitrary precision numbers via the Boost-Multiprecision library with various backends in order to investigate errors caused by limitations of the machine precision.

CHOICE OF ALGORITHMS

Currently our program uses several algorithms from the Boost-Odeint library, some of which can be used with step size control or as dense output steppers meaning that a large step size can be used for the calculation while output at intermediate points is obtained via interpolation. Both concepts can help to speed up the calculation and improve the accuracy. Not all solvers from the library can be used however, since we currently use the hard edge approximation for fields which causes discontinuities that cannot be dealt with by some algorithms. This excludes for example the class of multistep solvers which can be very fast and accurate because they require very few (possibly costly) evaluations of the right hand side of the differential equation while they may still be of high order. Fortunately, A. Nordsieck discovered another way of expressing the same concept which solves all the problems associated with multistep methods [5]. This may become implemented in our program in the future.

So far also the symplectic solvers have to be excluded since our equation of motion is based on the Lorentz force equation and the physical fields, while symplectic solvers make use of the Hamiltonian approach with the potentials of the fields. This issue will certainly be addressed in the near future and both ways of expressing the differential equation may coexist within the code.

SYMPLECTICITY

All of our currently implemented algorithms are not symplectic meaning they neither conserve energy nor angular momentum. For short term simulations this is not a real concern since one can enforce approximate correctness with smaller step sizes. It however seriously limits the capabilities for precise long term tracking since the errors add up over time and small step sizes make the program slow. On the other hand it offers an additional path to estimating the accuracy of the result by looking at the energy or angular momentum drift.

The issue generally originates in the formulation of these algorithms where a new state vector $\vec{x}_{n+1}$ is calculated from an old one $\vec{x}_n$ by a scheme like

$$\vec{x}_{n+1} = \vec{x}_n + \Delta\vec{x}, \tag{1}$$

whereas mathematically the evolution is described by a rotation $\mathbf{R}$ in a suitable space such that a new point of the solution is obtained via a scheme like

$$\vec{x}_{n+1} = \mathbf{R} \cdot \vec{x}_n. \tag{2}$$

In eq. 1 the numerical errors will grow over time while they will average out for the symplectic case in eq. 2. It should be noted however that symplectic methods only guarantee that the length of a vector remains constant while its direction may still be off. Nonetheless, for long term simulations symplectic methods seem to be a crucial requirement since the spin evolution is tightly tied to the orbital motion. Errors in the solution of the phase space coordinates will therefore directly radiate into the spin part and the nonlinear behavior there may make things even worse.

PERFORMANCE

Some previous integration codes made use of cartesian coordinates with time as independent parameter, see e.g. [6]. This required very small step sizes of $dt \leqslant 10^{-11}$ s for precise results. It is however known that the arc length parametrization (of the individual particle) has much more favorable properties [7] and one may expect that the accelerator coordinates come close to this. Our new program employs these coordinates and tests show that generally a step size

ISBN 978-3-95450-136-6

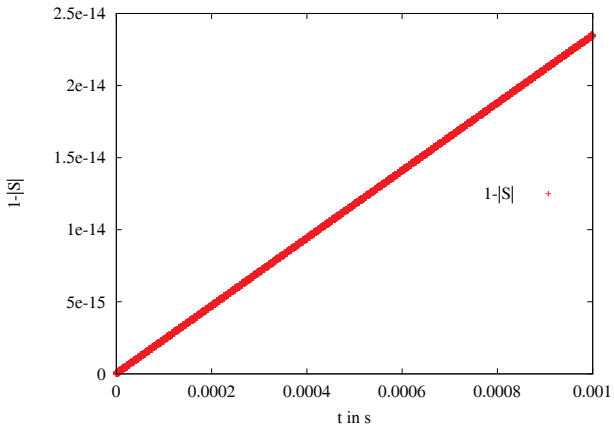

Figure 1: Loss of spin of a muon during the simulation of one millisecond with the 8th order Runge-Kutta algorithm with a step size $dt = 10^{-8}$ s and data type *long double* in the Fermilab muon g-2 ring. For a step size of $dt = 3 \cdot 10^{-9}$ s (not shown) the error remains below $3 \cdot 10^{-16}$ for the complete time interval.

corresponding to $dt = 10^{-8}$s yields very good results, see Fig. 1. This almost directly corresponds to a performance gain of a factor of thousand. With this parametrization it generally takes a few seconds to simulate a particle for one millisecond when a native C++ data type like *double* or *long double* is used. Using arbitrary precision data types makes the code several times slower, e.g. by approximately a factor of 4 for data type *float128* (quad precision) and a factor of 10-15 for *mpfr<N>* data types with N significant digits.

The parallel version of the program cannot use arbitrary precision data types yet and is far from optimal performance. It is however still possible to simulate 10.000 particles for a millisecond on two Intel Xeon E5-2630 hexacore processors in the course of a few hours. Significant improvement on this can be expected from using VexCLs kernel generation capability and the use of GPUs as accelerators.

BENCHMARKING

Every precision tracking program has to be tested very accurately. A recent paper [8] describes several high precision benchmarks with effects that can be calculated analytically which makes them ideal test cases for precision codes. One of the most precise tests of the correctness of an algorithm solving the T-BMT equation is the so-called pitch effect. This is a frequency change of the g-2 precession of the spin in a magnetic field when the particle undergoes vertical betatron oscillations, i.e. when there is a component of the B-field parallel to the velocity. The effect was first considered in [9] for a muon g-2 experiment and it was shown in [8] that our tracking programs are so precise that second order terms have to be included in the analytical calculation and the obtained results are matched to sub-ppb level, see Table 1.

Table 1: Comparison of Pitch Correction: in ppb between analytical estimates and tracking results for a muon with $\gamma = 29.3$ in a magnetic ring of radius $r = 7.112$ m with vertical focusing index n and maximal pitch angle $\theta_0 = 0.5$ mrad.

n	Estimated (ppb)	Tracking (ppb)
0.01	1.1	1.0
0.02	2.4	2.4
0.03	3.7	3.6
0.05	6.4	6.4
0.08	10.7	10.8
0.10	13.7	13.7
0.137	19.7	19.9
0.237	38.7	38.8

Table 2: Comparison of Tracking Results and Analytical Calculations of the EDM Signal and the Systematic Error (both in rad/s) Due to a Misalignment of the RF Wien Filter of an Angle $\theta = 0.1$ mrad for the Deuteron Case

p [GeV/c]	EDM tracking	EDM analytical	Syst. error tracking	Syst. error analytical
0.7	-1.00	-1.00	0.41	0.41
1.4	-0.74	-0.73	0.175	0.17
2.1	-0.50	-0.51	0.096	0.097
2.8	-0.36	-0.35	0.063	0.06

Another test described in detail in [10] is a systematic error estimation for a magnetic ring with an rf Wien filter that is operated at the $g-2$ frequency and tilted by a small angle versus the ideal vertical direction. With perfect alignment, the Wien filter produces a vertical magnetic field and a radial electric field such that the Lorentz force cancels. In the presence of an EDM it would however cause an approximately linear build-up of a vertical component of the spin that is proportional to the EDM. In the non-ideal case when the Wien filter is misaligned with respect to the vertical direction, the B-field produced by the Wien filter also has a radial component which also causes a spin rotation out of the plane. Both effects were estimated analytically and were also simulated for the proton and deuteron case. Table 2 shows the results for the deuteron case with an estimated EDM of $d = 10^{-18}$ e $\cdot$ cm and an angular misalignment of $\theta = 0.1$ mrad of the rf Wien filter of 0.1 m length and 30 MV/m electric field strength.

FUTURE WORK

There are great perspectives for the new program described above but there also remains a lot of work to be

ISBN 978-3-95450-136-6

done in the future. Conceptually one of the most important improvement is the inclusion of geometric algorithms to enforce symplecticity. Algorithms based on the Magnus expansion [11] appear to be very efficient and precise at the same time and can be constructed of high order. These will be implemented in the near future.

Another very interesting option for precise long term tracking is the use of algorithms with global error estimation or control. So far, only algorithms are used that can adjust their step size such that a local error requirement set by the user is met. This feature can significantly increase the execution speed of the program but the local errors still build up over time. Recent developments [12–14] show that significantly better results may be obtained with different classes of algorithms when global error control algorithms are used in step size adjustment schemes. Although this decreases the speed of the method it may prove very useful for our purpose and will be implemented later.

A third issue that requires some work will be the optimization of the parallel program version with the help of VexCLs kernel generation facility. Currently each command is compiled during the execution of the program into a so-called compute kernel. Together with the cost of starting these kernels this is a major source of overhead. VexCL offers however the possibility to record a sequence of commands and build a kernel from the combined command sequence which then can be run with much less total overhead. This may accelerate the parallel program version significantly although the approach works only when there are no data dependent conditions. One therefore needs a smart way of implementation or a split of a command sequence into different kernels with the if-condition in between.

Last but not least, the program will be used for accuracy studies of the used methods and studies of systematic errors for muon g-2 and EDM experiments. Some simple initial tests show for example that the accuracy of the code depends on many details. In one test a solution for the simple initial value problem

$$dy/dx = 1.0 \cdot y, \quad y(0) = 1, \quad x \in [0, 10] \qquad (3)$$

with the analytical solution $y(x) = e^x$ was calculated with the Boost implementation of the 4th order Runge-Kutta algorithm with different optimization levels of the gcc compiler. The calculation was performed for different step sizes $dx = 10^{-k}$, $k = 1...10$ with *double* as the chosen data type. No difference of the solutions for optimization levels *O0* to *O3* could be observed but the option *Ofast* produces different results than all others, see Fig. 2. This may generally be not that surprising since the option *-ffast-math* is switched on but since the Runge-Kutta algorithm requires only the basic arithmetic operations $(+, -, *, /)$ for this problem, it actually is a surprise. For more complicated equations with trigonometric functions etc. significantly worse results may be expected. In this respect, a possible future symbolic math capability of compilers may prove very useful. Expression trees built with the use of expression templates could be simplified and optimized which would not only reduce execution time but could at the same time increase accuracy.

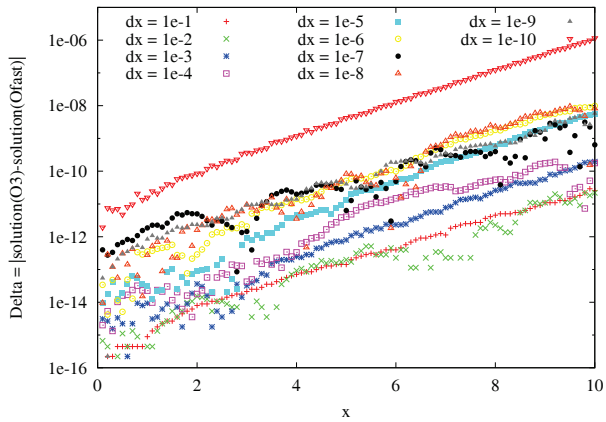

Figure 2: Difference of the solution of eq. 3 obtained with the 4th order Runge-Kutta algorithm from the Boost library when the code is compiled either with the *-O3* option or the *-Ofast* option.

REFERENCES

[1] V. Anastassopoulos et al., arXiv preprint, arXiv:1502.04317 (2015).

[2] VexCL website: `https://github.com/ddemidov/vexcl`

[3] Boost website: `www.boost.org`

[4] D. Demidov et al., SIAM Journal on Scientific Computing **35.5**, C453 (2013).

[5] A. Nordsieck, Mathematics of Computation **6.77**, 22 (1962).

[6] S. Hacıömeroğlu, Y.K. Semertzidis, Nucl. Instrum. Methods Phys. Res., Sect. A **743**, 96 (2014).

[7] E.B. Kuznetsov, Journal of the Franklin Institute, **344**, 658 (2007).

[8] E.M. Metodiev et al., Nucl. Instrum. Methods Phys. Res., Sect. A **797**, 311 (2015).

[9] F.J.N. Farley, Physics Letters B **42.1**, 66 (1972).

[10] W.M. Morse et al., Phys. Rev. ST Accel. Beams **16**, 114001 (2013).

[11] S. Blanes et al., Physics Reports **470**, 151 (2009).

[12] G.Yu. Kulikov, R. Weiner, J. Comp. App. Math. **233** 2351 (2010).

[13] G.Yu. Kulikov, Russ. J. Numer. Anal. Math. Modelling, **28.4**, 321 (2013).

[14] G.u. Kulikov, IMA J. Numer. Anal., **33**, 136 (2013).

ISBN 978-3-95450-136-6

ESTABLISHING A CONSISTENT BASIS FOR BEAM PHYSICS, ACCELERATOR MAGNET DESIGN, AND MAGNETIC MEASUREMENTS

Stephan Russenschuck
CERN, 1211 Geneva 23 , Switzerland

Abstract

In mathematics, C^3 denotes 3-times continuous differentiable functions. We use this as shorthand for establishing a consistent basis for beam physics simulations and machine requirements, magnet design and manufacture, and magnetic measurements.

Magnetic field measurements serve for the quality assurance of the magnet production, both at an early stage in the production process and after the reception of the magnets in the laboratory. Measurements are also performed for validating numerical field simulation (FEM) tools and magnet design techniques. In order to study the performance of the accelerator and to allocate a budget for magnet misalignment in the tunnel, the beam physicists require the field maps and multipole field errors of the magnet system, either from validated numerical models or from magnetic measurements. Field measurements are also done for on-line monitoring of the magnet behavior and thus providing direct feedback to the accelerator control room for adjusting the magnet current cycles, and to tune the high-frequency accelerator cavities.

This paper describes the approaches and techniques in magnetic field measurements, discusses their limitations and attempts to make them consistent with the requirements from beam physics and magnet design.

INTRODUCTION

For the LHC magnet system [1], it was relatively easy to establish C^3. The aperture of the superconducting magnets is round and the beam is pencil shaped with respect to the dimensions of the magnet aperture. The LHC beam is ultra-relativistic and stiff, that is, the main dipole magnets exert only a small kick to the particle trajectory, even though their magnetic lengths is 14.3 meters. Moreover, the betatron amplitude changes only very slightly within the arc magnets (the beam is in good approximation paraxial with the magnetic axis of the magnets), so that the magnets can be represented as a set of thin lenses in the beam tracking codes.

A classical method for describing the magnetic flux density in accelerator magnets is to develop the eigenfunctions of the 2D Laplace equation (expressed in cylindrical coordinates) into the Fourier components of the magnetic flux density, calculated or measured at a given reference radius; usually 2/3 of the aperture, or 17 mm in case of the LHC [2]. This method works well for long, straight magnets and is perfectly in line with magnetic field measurements using rotating search coils. The Fourier coefficients of the field solution, known in the accelerator community as field harmonics, serve for the integrated field reconstruction and are the direct interface between the magnet "owners" and the beam physicists. Extensive beam tracking studies during the LHC design and construction phase, gave a good knowledge of the effect of multipole field errors and the role (and limitations) of a correction system to compensate their effect on the particle beam. The magnetic measurements were therefore based on rotating search coils assembled in long shafts and driven by a motor unit [3]. An angular encoder and a digital integrator [4] were used to re-parametrize the measured voltage (over time) into flux increments measured as a function of the coil's angular position. In this way the requirements on the uniform motion of the drive unit could be relaxed.

The design of the magnet system for the LHC could be based on the experience with the Tevatron and HERA machines [5]. In particular, the dynamic effects in superconducting magnets were intensively studied and brought under tight control during the magnet construction period. A strategy could therefore be developed to monitor the production process with field measurements at ambient temperature. Using a well established cold-warm relationship, the magnetic measurements at cryogenic conditions could be reduced to about 10% of the magnets [6]. Recently, a large number of magnetic measurement requests has arisen from new accelerator projects, such as SESAME, HIE-ISOLDE, ELENA, and Linac4, at CERN, as well as the magnet system for MedAustron and the FAIR superFRS [7] magnets that require more than just the measurement of the integrated bending strength. Limited resources and a narrow time slots impose optimized procedures and instrumentation. Standardization of measurement equipment becomes essential in order to increase efficiency in terms of installation time and workflow. Large efforts have been undertaken to optimize CERN measurement resources while keeping a stringent measurement quality. This resulted in a flexible control and acquisition software, a standard drive system, rotating-coil systems with standard assembly of tangential search coils, and multipurpose measurement benches. Moreover, an increasing number of measurement have been based on the stretched wire techniques, as these techniques are very universal and do not require magnet-specific probes and instrumentation.

However, the most important savings on material and resources are made on a different level: it is important to establish a consistent basis for beam physics, the magnet system, and the magnetic measurements in order limit the development of dedicated instrumentation and reduce the measurement time, while providing exactly the feedback needed. In this respect, the new projects are very challenging

ISBN 978-3-95450-136-6

as magnets with small bending radii and large aspect ratios of the air gap will be built.

A well established measurement method consists of mapping the field with a 3D Hall probe, which is inaccurate compared to the rotating search coils and very time consuming. For fast-cycling magnets the field is often measured only on the mid-plane using a stationary fluxmeter which is expensive to fabricate in printed-circuit board (PCB) technology. While fluxmeter measurements yield a relatively fast feedback on the magnet-to-magnet reproducibility, the measurements are of limited relevance for beam simulations because they require ramping the magnet and deliver only the integrated field strength. However, in machines that are operated as storage rings, the highest precision of the magnet measurements is required at steady state, i.e., injection and/or high-energy plateau of the beam.

When the magnet is operated in steady state condition, the only meaningful measurement with a fluxmeter consists of moving the entire fluxmeter from a field-free region into a final position within the magnet, while integrating the induced voltage. This yields the total flux intercepted by the conductor, but requires a large support at the extremities of the magnet.

Components of an approach towards C^3 include the expansion of the field solution into bipolar (for curved magnets) and plane elliptic coordinates (for magnets with narrow gaps), the local description of field errors in the magnet ends, and the post-processing of measurement data using numerical field computation methods. For example, 3D hall probes can be calibrated by imposing that the measured magnetic flux density must be divergence free. The raw data (fluxes or fields) can be used as Dirichlet and Neumann data of the boundary element technique, and the positioning errors of the mapper can be corrected on boundary element mesh [8].

MAGNETIC MEASUREMENT TECHNIQUES

When magnets must be measured in fast-ramping conditions a flux meter at fixed position delivers a voltage signal in a pulsed field. Modern integrators with large bandwidth and time resolution connected to such a coil can give the full $B(t)$ curve and measure saturation effects of the iron yoke. Hysteresis and eddy current effects can be separated by measurements at different ramp rates. One precaution must be taken for the remanent field of the magnet, i.e., the field at zero current value. Possible measures are to use a bipolar power supply and perform symmetric sweeps from negative to positive maximum current. Other methods include demagnetizing the magnet with a bipolar power supply or measure the remanent field using flip coils or Hall probes.

Search coils are the standard method for measuring multipole field errors in accelerator magnets [9]. However, the measurement of magnets with small apertures of less than 20 mm in diameter is a challenging task [10]. Consider a rotating coil inside a bore of radius r, then the maximum number of coil turns that can be wound with a conductor of given diameter is proportional to r^2 and, consequently, the coil sensitivity factor scales with r^{-2}. The impact of mechanical tolerances and calibration errors increases drastically and the measurement uncertainty can be expected to be one to two orders of magnitude higher than in typical synchrotron magnets with an aperture radius of 50 to 100 mm. Moreover, experience has shown that the coils are affected by manufacturing tolerances resulting in a longitudinal non-uniformity of the width and radius of about 0.6%. This resolution must be compared to the beam dynamics requirements for the LHC, where both the absolute integrated magnet length as well as the field contribution from higher harmonics must be measured and controlled on a level of 10^{-5} of the main field, which is 8.3 T in the straight section.

When measuring a magnet that is shorter than the search coil, such variations imply that standard calibration of the average geometry becomes problematic and a in-situ calibration must be performed.

A method to circumvent these problems is based on displaced or vibrating wires [11–13]. A conducting wire is displaced inside the magnetic field by precision displacement stages at which the two end-points of the wire are fixed. Copper-Beryllium (CuBe) wires, 0.1 mm thick, are commonly used because of their high tensile strength and low martensitic contaminations. The return wire must be routed through a field-free region. The integrated voltage at the connection terminals of the wire is a measure for the flux linked with the surface that is traced out by the wire. This so-called single stretched wire method is commonly used to measure the magnetic field strength and magnetic axis. It can also be used in a vibrating mode when it is excited with an alternating current at resonance frequencies. The latter operation mode is very sensitive to determine the magnetic axis in solenoidal magnets [14].

The stretched wire method has recently been extended to measure multipole field errors in accelerator magnets by exciting the wire with an alternating current well below the natural resonance frequency. In this way we make use of the linear relationship between wire oscillation amplitude, integrated field, and current amplitude. To distinguish the wire methods we speak of vibrating (resonant) and oscillating (non-resonant) wires although these terms are often used synonymously [14, 15].

A classical method for measuring magnetic fields is the mapping with hall probes. The challenges here are the calibration of the probes, which are very sensitive to temperature variations. The accuracy of the measurement strongly depends on the mechanical stability of the displacement stage, as often a long shaft is required to enter into the aperture of the magnet. Typical specifications for such systems require ranges of about one meter in the transversal directions and up to five meters in longitudinal direction with an accuracy on the order of 0.1 mm. Mapping of fields is thus very time consuming even if the data acquisition can be done "on the fly".

ISBN 978-3-95450-136-6

ISSUES IN ESTABLISHING C^3

To establish a consistent basis for accelerator physics, magnet design, and magnetic measurements for a large verity of accelerator magnets is no easy task. All parties involved must be aware about the risk of over-specification. Computational beam dynamics, based on tracking codes for simulating the effect of higher-order field harmonics on the stability of the stored particle beam, results in specifications of the field homogeneity on the order of one unit in 10000. This yields tight (and costly) tolerances on the coil manufacture, yoke-material, punching of laminations, and assembly of the magnets. This, in turn, leads to even higher demands on measurement probe calibration and data acquisition techniques for magnetic measurements. A classification of consistency issues can be done according to the main user of magnetic measurements. Measurements driven by beam physics requirements must deal with the appropriate definition of the good-field region and the field homogeneity. This will depend on the specific application of a magnetic element. For example, a curved, normal-conducting dipole magnet may be used as a bending magnet in a synchrotron, as a spectrometer, or as a bending magnet in a beam transfer line. Will it be sufficient to measure the longitudinally integrated field errors or will local field measurement be needed in the magnet extremities? We must also ask what are the systems variables of the beam tracking codes (multipole field errors, field maps, Taylor approximations, integrated strength values) and how can they be derived from the magnetic measurement raw data.

A large number of software packages have been developed to study the dynamics of charged particles in accelerators. For many applications it is sufficient to track an ensemble of single particles through the magnetic elements of the machine. Such codes include MADX [22], SixTrack [17], and PTC [18], among others. Self interactions between the particles in the beam (space charge) can cause emittance growth and beam loss. Special purpose codes to simulate space charge effects in linear and circular accelerators are pyORBIT [21] and Synergia [23], for example. In contrast to single particle codes, the numerical accuracy in space charge codes is limited by finite particle and grid effects.

MADX consists of different routines for (single) particle tracking, beam optics (twiss parameters and beam envelopes) as well as symplectic integrators. For tracking, thin and thick lens descriptions of dipoles and quadrupoles are used as elementary magnetic elements. PTC has been added to MADX in order to enable thick-element tracking with arbitrary order [19]. In general, MADX is used for the layout of the accelerator considering the integrated dipole field of the bending magnets and, eventually the feed-down [2] from misaligned quadrupole magnets, so defining the design orbit. With respect to this, the effect of all other elements, including higher order multipoles in the magnets, is computed. For the study of the beam envelope and long term stability in synchrotrons, as well as light sources employing wigglers and undulators, the higher order imperfections (or harmonics) in the magnetic field play an essential role. While the pattern of pure dipole and quadrupole fields establish a strictly linear particle oscillation, unwanted higher harmonics that are present in any real magnetic field create distortions on the particle dynamics and can lead to growing oscillation amplitudes and finally particle loss. Consequently, tolerance limits for these higher field harmonics must be established. They will depend on the beam size, the required storage time and the particle species (electrons, protons heavy ions). Tracking codes are used for this purpose, where the effect of a higher multipole field on the particle dynamics is described explicitly by the Lorentz-force acting on the particle.

The description of the magnet elements must be symplectic, that is, the integral operators acting on these elements must preserve the particle density in the phase space of all possible values of position and momentum variables. This is automatically the case as long as the magnetic field in a magnet can be described by a series of thin lenses with an equivalent kick. Only a few codes, such as PTC [18] and COSY INFINITY [20] can accurately handle a displacement of the design orbit in the magnet element itself. The field and its derivatives are required around the design orbit. The order is defined by the specific beam physics requirements, for example by the storage time or the maximum emittance of the beam. As long as the design orbit is not deviating too much from the central orbit, and the multipole field expansion is valid, the calculation of these fields is straightforward. This is, however, not the case in the magnet extremities, where highly non-linear field distributions are encountered and the multipole coefficients do not constitute a complete orthogonal function set for the field solution. This gives rise to so-called pseudo-multipoles which result from the magnet field variation in axial direction [16].

Especially in the case of solenoids a considerable influence on the dynamics of the particles is observed as they lead to coupling between the horizontal and vertical planes, which usually will have to be compensated either by compensating solenoids or an arrangement of skew quadrupoles. Measured or calculated fields on a grid are only appropriate to first and second order in the grid spacing because of the discretization errors. Often, the field description relies on measurements on the mid plane of the magnetic element. Out-of-plane field expansions therefore depend strongly on the accuracy of the field derivatives in the mid plane. This is not a problem for computed but indeed for measured fields. In this case it is advantageous to measure the field on a closed volumetric domain and to represent the field by integrals based on the Kirchhoff theorem. For this reason, the magnetic measurement section at CERN is developing a transversal-field transducers based on a short measurement coil, a non-magnetic piezoelectric motor and a longitudinal displacement mechanism. Because of its resemblance, this transducer is nicknamed as the "toy train".

When measurements are driven by modeling capabilities of the employed magnet design codes (usually based on structural and electro-magnetic finite-element FEM packages) it is important to check the necessary model reduction

ISBN 978-3-95450-136-6

(omitting details like welding seams) and measure the effect of shims, chamfers, welds and other material parameters [2]. An iterative process is often required to distinguish manufacturing or modeling errors from measurement artifacts and to decide on corrective actions for the magnet design. It is here where a strong link between the magnet designer and the magnetic measurement engineer can yield improvements on both the measurement techniques and the modeling capabilities of the design codes. If the consistence is established, beam simulations can often be based on computed rather than measured data. It will then also be possible to simulate the effects of manufacturing tolerances and in this way arrive at a technical specification for the production of the magnets. When measurements are driven by (series) magnet manufacturing, the aim is to check the magnet-to-magnet reproducibility and to arrive at acceptance criteria for the delivered magnets. Often inverse field computations are needed in order to relate the measured field errors to manufacturing errors. During the series production of the magnets, a reduced set of magnetic measurements will be sufficient as long as there are no sudden changes in the built quality of the delivered magnets.

Accelerator Operation

When magnetic measurements are driven by the accelerator operation, the demands are much more challenging. In some cases the magnets exceed the model capabilities of the FEM codes. For some legacy equipment incomplete information on the design makes it impossible to set up such a precise model. Different machine cycles may result in a coupling of dynamic and hysteretic effects which are difficult to compute. Magnetic measurements employing search coils as well as NMR and ferromagnetic resonance probes are therefore required for on-line monitoring of the magnetic field in reference magnets that are excited at the same current as the magnets in the machine [24].

SOLENOID MAGNETIC MEASUREMENTS

We will now take the example of a solenoid to explain the above-mentioned issues in establishing C^3. Solenoids are used to focus charged particle beams in the low energy section of accelerators. Particles moving exactly along the magnetic axis of the solenoids do not experience any force, while off-axis particles are azimuthally accelerated by the radial field components in the fringe field region of the magnet. The resulting helical particle motion in the longitudinal field region of the magnet yields a focusing effect due to the radial Lorentz force. Solenoid magnets are not compatible with the standard measurement equipment optimized for accelerator magnets. Solenoids are therefore routinely tested with general-purpose instruments such as 3D Hall probe mappers. Field mapping makes no sense as long as the magnet is not perfectly aligned with the stages, because an apparent asymmetry results in the fringe field regions, which is due to misalignment and not due to magnet manufacturing errors or intrinsic limitations in the magnet design.

We have therefore developed magnetic measurement techniques for solenoids based on vibrating/oscillating wires as well as field transducers based on solenoidal search coils. Figure 1 defines the reference frames for the solenoid magnet and the stages of the stretched-wire system. The figure also indicates the position of the drive unit when rotating field probes are employed. Because of the radial symmetry of the field, we can assume, without lack of generality, that the two wire stages (Stages A and B) are perfectly aligned in the longitudinal direction such that the wire moves parallel to the z-axis.

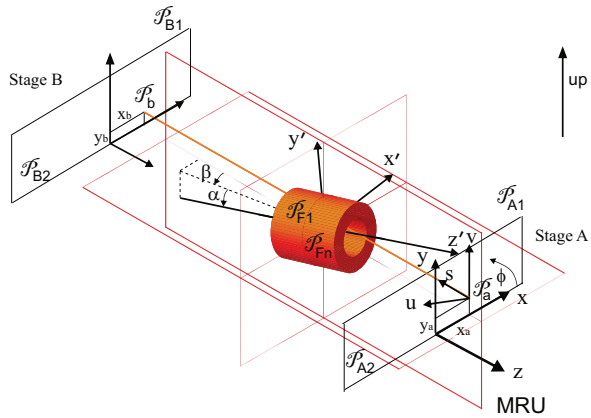

Figure 1: Coordinate systems of the magnet and the stages of the stretched-wire system. Definition of pitch (tilt) α and yaw (swing) β angles. Position of the motor unit (MRU) when rotating search coils are used.

A method for the alignment of solenoids, based on the oscillation wire method, has been developed at CERN [15]. Exciting the wire at its second resonance yields a wire motion in phase with the Lorentz forces due to the fringe fields on both sides of the magnetic center. When the wire is misaligned with respect to the magnet center, the fringe fields in the horizontal plane of the magnet give rise to Lorentz forces as shown schematically in Fig. 2.

The wire displacements are measured by means of phototransistors arranged in orthogonal directions at a longitudinal position z_0 close to Stage A [15]. When the wire is centered, the two fringe fields have the same direction and therefore the wire oscillation amplitude takes its minimum. But there may still be a swing and tilt misalignment with respect to the wire axis. In this case the fringe field components point into the same direction on either side of the magnet center. To align the stages with the magnetic axis, we must therefore switch to the first resonance frequency so that the wire motion will be in phase with the transversal component of the field. The magnet alignment consists of solving iteratively a minimization problem with two objectives (the oscillation amplitudes d_x and d_y in the horizontal and vertical planes) and two design variables (the x and y positions of the wire fixation points at both stages). The minimization method

ISBN 978-3-95450-136-6

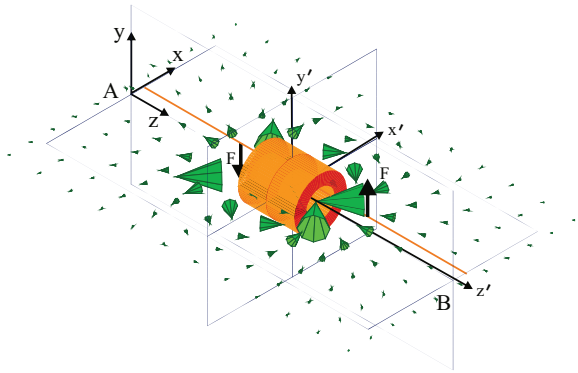

Figure 2: Stray field on the horizontal plane and direction of the Lorentz force acting on the off-centered stretched wire (no tilt and swing misalignment).

by Gauss-Seidel (also known as coordinate search) is used in combination with a linear regression of the measurement data in each coordinated direction. The linear regression is motivated by the fact that for small displacements from the magnetic center the Cartesian components of the fringe fields decrease linearly in the coordinate directions. After the magnet is aligned, the field homogeneity can be mapped in the coordinate system of the wire. To this end, we switch again to the second resonance, and map out the oscillation amplitudes for different angular positions on the same radius. A small azimuthal asymmetry is present because of the layer jumps of the conductor in multilayer solenoids.

The longitudinal field profile can then be measured with an instrument based on moving search coils. In thin lens approximation, the focusing effect in a solenoid is described by the following expressions of the rotation of the beam about the z-axis φ_L (the so called Larmor angle) and the focusing strength $1/f$ [26]:

$$\varphi_L = \frac{e}{2\gamma m v_z} \int B_z \mathrm{d}z := \frac{e}{2\gamma m v_z} F_1 \qquad (1)$$

$$\frac{1}{f} = \frac{e^2}{4\gamma^2 m^2 v_z^2} \int B_z^2 \mathrm{d}z := \frac{e^2}{4\gamma^2 m^2 v_z^2} F_2 \qquad (2)$$

The integrals, occurring in these expressions, are defined as the field integrals F_1 and F_2. It turns out that these field integrals are independent of the alignment. This can be understood by the theory of the magnetic double layer [2]. This double layer gives rise to a jump in the magnetic scalar potential, that is constant all across a plane coil loop.

As proposed in [27], the instrument for measuring the first and second field integrals consists of two coaxial search coils slightly spaced apart longitudinally. The flux variation in the search coils induces a voltage across the coil terminals, which will be integrated with a digital integrator. When the search coils are connected in series, the longitudinal field component can be calculated up to first order, deviding the flux by the calibrated coil surface. The coils can also be connected in series in opposite orientation. Because of flux preservation, the integrated voltage is a measure of the radial flux between the two coils, from which the radial field component can be calculated.

CONCLUSIONS

In an ideal world, a magnet is built to perfection, without any systematic manufacturing error, and without variations in the material parameters. The numerical field computation model is able to predict all static and dynamic phenomena, and the magnetic measurements, without systemic errors from calibration or any random errors, confirm the prediction of the magnet designer. In the real world, however, an iterative process is often required to distinguish manufacturing or modeling errors from measurement artifacts and to decide on corrective actions for the magnet design. In some cases, hysteresis and eddy current effects in the magnets require on-line monitoring of the field strength for the optimization of the accelerator performance.

In an accelerator project, the field measurements are often on the critical path, because delays in the performance or interpretation of these measurement lead to a late release of the series production or a late installation of the components in the accelerator tunnel. For the LHC, magnetic measurements at ambient temperatures were performed at the magnet manufacturers premises in order to identify manufacturing errors at a very early stage. A good knowledge on the correlation between measurements at ambient and cryogenic temperatures made it possible to limit the number of time-consuming measurements after the electrical tests at CERN.

For smaller accelerator projects, such an approach is hardly feasible; either because there is a considerably shorter R&D phase or because of the low number of magnet units. In these cases, the magnetic measurements must be well chosen and limited to the methods that yield the required feedback to the magnet designers and beam physicists at minimum cost of time and resources.

REFERENCES

[1] L. Evans, "The Large Hadron Collider: a Marvel of Technology", EPFL Press, Lausanne, Switzerland, 2009

[2] S. Russenschuck, "Field Computation for Accelerator Magnets: Analytical and Numerical Methods for Electromagnetic Design and Optimization", Wiley, 2011.

[3] L.Walckiers, "Magnetic measurement with coils and wires" in CERN Accelerator School CAS 2009: Specialized Course on Magnets, Bruges,16-25 June, CERN, Bruges, 2009.

[4] P. Arpaia, L. Bottura, L. Fiscarelli, L. Walckiers, "Performance of a fast digital integrator in on-field magnetic measurements for particle accelerators, Review of scientific instruments 83, 2012

[5] B. H. Wiik, "Progress with HERA", IEEE Transactions on Nuclear Science, 32, 1985

[6] L.Bottura, "Standard Analysis Procedures for Field Quality Measurements Part I:Harmonics", Document.LHC-M-ES-0007 rev 1.0, CERN, Geneva, Switzerland 2001

ISBN 978-3-95450-136-6

[7] H. Muller, H. Leibrock, M. Winkler, P. Schnizer, E. Fischer, "Status of the super FRS magnet development for FAIR", Proceedings of the IPAC2013 Conference, Shanghai, China, 2013

[8] M.B. Giles, N. Pierce, E. Süli, "Progress in adjoint error correction for integral functionals", Computing and Visualization in Science, 2004

[9] A . K. Jain, "Harmonic Coils", CERN Accelerator School on Measurement and Alignment of Accelerator and Detector Magnets, Anacapri, Italy, April 11-17, 1997, CERN Report 98-05

[10] J. DiMarco et al., "Application of PCB and FDM Technologies to Magnetic Measurement Probe System Development", IEEE Transactions on Applied Superconductivity, Vol. 23, No.3, June 2013.

[11] A. Temnykh, "Vibrating wire field-measuring technique", Nuclear Instruments and Methods in Physics Research Section A: Accelerators, Spectrometers, Detectors and Associated Equipment, Vol. 399, 1997.

[12] T. Lei, X. Wang, M. Wang, "Pulsed wire magnetic field measurement on the permanent magnet focusing device of millimeter-wave traveling wave tube", Journal of Applied Physics, 05/2008

[13] Z. Wolf, "A Vibrating Wire System For Quadrupole Fiducialization", SLAC National Accelerator Laboratory, Technical Note LCLS-TN-05-11, Menlo Park, 2005

[14] P. Arpaia, M. Buzio, J. Garcia Perez, C. Petrone, S. Russenschuck, L. Walckiers, "Measuring field multipoles in accelerator magnets with small-apertures by an oscillating wire moved on a circular trajectory", Jinst May 8, 2012.

[15] P. Arpaia, C. Petrone, S. Russenschuck, L. Walckiers, "Vibrating-wire measurement method for centering and alignment of solenoids", Journal of Instrumentation, 2013

[16] B. Erdelyi, M. Berz, M. Lindemann, "Differential algebra based magnetic field computation and accurate fringe field maps", American Physical Society, abstract #P19.005, 2001

[17] F. Schmidt, "SixTrack, User's Reference Manual, CERN/SL/94-56, 2012

[18] E. Forest, Y. Nogiwa, F. Schmidt, "The FPP and PTC Libraries", Proceedings ICAP, p.17, 2006

[19] P. K. Skowronski, F. Schmidt, R. de Maria, "New Developments of MAD-X using PTC, Proceedings ICAP, p. 209, 2006

[20] K. Makino, M. Berz, Cosy infinity version 9, Nuclear Instruments and Methods in Physics Research, Section A, Vol 558, 2006

[21] Python/C++ implementation of the ORBIT (Objective Ring Beam Injection and Tracking) code, http://code.google.com/p/py-orbit/

[22] MAD- Methodical Accelerator Design, CERN - BE/ABP web pages, http://madx.web.cern.ch/madx/

[23] Synergia, Fermilab, http://web.fnal.gov/sites/Synergia

[24] M. Buzio, R. Chritin, D. Cornuet, P. Galbraith, D. Giloteaux, "Status and outlook of B-train systems for magnetic field control", private communication, CERN, ATC/ABOC days, 2008

[25] V. Kumar, "Understanding the focusing of charged particle beams in a solenoid magnetic field", American Journal of Physics, 77 (8), 2009.

[26] M. Reiser, "Theory and Design of Charged Particle Beams", Wiley, 2008.

[27] P. Arpaia, M. Buzio, M. Kazazi, S. Russenschuck, "A fluxmeter based on translating coils for axially symmetric magnets, IMEKO, Benevento, 2014

ISBN 978-3-95450-136-6

SURFACE METHODS FOR THE COMPUTATION OF CHARGED-PARTICLE TRANSFER MAPS FROM MAGNETIC FIELD DATA

C. E. Mitchell*, Lawrence Berkeley National Laboratory, Berkeley, CA 94729, USA
A. J. Dragt, University of Maryland, College Park, MD 94720, USA

Abstract

The behavior of orbits in charged-particle beam transport systems, including both linear and circular accelerators as well as final focus sections and spectrometers, can depend sensitively on nonlinear fringe-field and high-order-multipole effects in the various beam-line elements. Surface fitting algorithms provide a robust and reliable method for extracting this information accurately from 3-dimensional field data provided on a grid. Based on these realistic field models, Lie or other methods may be used to compute accurate design orbits and high-order symplectic maps about these orbits. We describe the implementation of a general method for treating magnetic elements with curved reference trajectories that is especially well-suited for extracting symplectic transfer maps for large-sagitta bending dipoles with fringe fields.

INTRODUCTION

Successful design of high-performance free-electron lasers, storage rings, and colliders relies heavily on charged-particle optics codes with high-order nonlinear tracking and map capabilities. To compute design orbits and high-order transfer maps (in Lie or Taylor form) that accurately include the effects of asymmetries, nonlinear fringe-fields and high-order multipoles not well-captured by idealized magnet and cavity models, realistic 3-dimensional electric and magnetic field information for various beam-line elements is needed. Realistic field data can be provided on a grid by 3D finite element codes, sometimes spot checked against measured data. However, the computation of high-order transfer maps requires high derivatives of the fields or corresponding potentials, and the direct calculation of high derivatives based only on grid data is intolerably sensitive to noise (due to truncation or round-off) in the grid data.

The effect of numerical noise can best be overcome by fitting onto a bounding surface far from the beam axis and continuing inward using the Maxwell equations [1–4]. While the process of differentiation amplifies the effect of numerical noise, the process of continuing inward using the Maxwell equations is *smoothing*. For beam-line elements such as quadrupoles, sextupoles, octupoles, wigglers, and RF cavities, well-established algorithms exist that employ cylindrical fitting surfaces with circular, elliptical, or rectangular cross section [1, 3–5] to extract transfer maps to high order. These algorithms are robust and insensitive to noise in the underlying grid data, but are limited to beamline elements with straight or nearly-straight reference trajectories.

In this paper we describe a parallel code (BMAP3D) designed to extract symplectic transfer maps in Lie-algebraic form from 3D field data associated with curved magnetic elements, such as dipoles with large design-orbit sagitta. The data is fitted onto a bent box with straight ends that extends into the fringe-field regions outside the beam-line element, and the resulting map takes into account all fringe-field effects as well as all linear and nonlinear effects up to the desired order. We work with the canonical equations of motion based on a computed vector potential $\mathbf{A}$. If instead one wishes to integrate noncanonical equations employing the magnetic field $\boldsymbol{B}$, it can be obtained using $\boldsymbol{B} = \nabla \times \boldsymbol{A}$. The technique described is quite general, and can be applied to magnetic elements with complex reference trajectories (which need not be known exactly) and more complex surface-fitting geometries.

SURFACE REPRESENTATION OF FIELDS AND POTENTIALS

Consider a volume V free of electromagnetic sources and contained within the beam-line element of interest, and let S denote its boundary surface. The solution of Maxwell's equations for a single mode with time dependence $\exp(-i\omega t)$ can be represented in terms of field values on the surface S. Defining a function Φ by

$$\Phi(\mathbf{r}, \mathbf{r}') = \frac{e^{ik|\mathbf{r}-\mathbf{r}'|}}{4\pi|\mathbf{r}-\mathbf{r}'|}, \qquad k = \omega/c, \tag{1}$$

we have for points $\mathbf{r}$ interior to V that [6]:

$$\begin{aligned}\mathbf{E}(\mathbf{r}) &= -\int_S \{i\omega(\mathbf{n}\times\mathbf{B})\Phi + (\mathbf{n}\times\mathbf{E})\times\nabla'\Phi + (\mathbf{n}\cdot\mathbf{E})\nabla'\Phi\}\, dS',\\ \mathbf{B}(\mathbf{r}) &= \int_S \left\{i\frac{\omega}{c^2}(\mathbf{n}\times\mathbf{E})\Phi - (\mathbf{n}\times\mathbf{B})\times\nabla'\Phi - (\mathbf{n}\cdot\mathbf{B})\nabla'\Phi\right\} dS',\end{aligned} \tag{2}$$

where $\mathbf{n}$ is the outward-directed normal at each point $\mathbf{r}'$ on the surface S. The representation (2) is smooth (analytic), and convergent Taylor series for $\mathbf{E}$ and $\mathbf{B}$ about any point interior to V may be obtained by expanding the integral kernel Φ in the unprimed variables $\mathbf{r}$. In this way, each coefficient in the Taylor series is represented as an integral over the boundary surface S.

Magnetic Vector Potential

In this paper, we consider only magnetic elements (with $\omega \to 0$, $\mathbf{E} \to 0$), and employ canonical equations of motion

* ChadMitchell@lbl.gov

ISBN 978-3-95450-136-6

for which we require a vector potential $\mathbf{A}$ such that $\mathbf{B} = \nabla\times\mathbf{A}$. Using (2) and results related to Dirac monopoles, it can be shown [7, 8] that one can represent the vector potential in the volume V in the form $\mathbf{A} = \mathbf{A}^n + \mathbf{A}^t$, where:

$$\mathbf{A}^n(\mathbf{r}) = \int_S [\mathbf{n}\cdot\mathbf{B}(\mathbf{r}')]\mathbf{G}^n(\mathbf{r};\mathbf{r}',\mathbf{m})dS',$$
$$\mathbf{A}^t(\mathbf{r}) = \int_S \psi(\mathbf{r}')\mathbf{G}^t(\mathbf{r};\mathbf{r}',\mathbf{n})dS'. \quad (3)$$

Here ψ denotes a magnetic scalar potential with the property $\mathbf{B} = \nabla\psi$, which we assume to be known on the boundary surface. (If ψ is not known, it can be recovered from the components of $\mathbf{B}$ tangent to the surface.)

Here $\mathbf{n}$ denotes the unit normal at each surface point $\mathbf{r}'$, and $\mathbf{m}$ is an outward-directed unit vector at $\mathbf{r}'$ with the property that the ray $\{\mathbf{r}' + \lambda\mathbf{m} : \lambda > 0\}$ does not intersect the volume V. The vector-valued integration kernels $\mathbf{G}^n$ and $\mathbf{G}^t$ are given by [5, 8]

$$\mathbf{G}^n(\mathbf{r};\mathbf{r}',\mathbf{m}(\mathbf{r}')) = \frac{\mathbf{m}\times(\mathbf{r}-\mathbf{r}')}{4\pi|\mathbf{r}-\mathbf{r}'|(|\mathbf{r}-\mathbf{r}'| - \mathbf{m}\cdot(\mathbf{r}-\mathbf{r}'))},$$
$$\mathbf{G}^t(\mathbf{r};\mathbf{r}',\mathbf{n}(\mathbf{r}')) = \frac{\mathbf{n}\times(\mathbf{r}-\mathbf{r}')}{4\pi|\mathbf{r}-\mathbf{r}'|^3}. \quad (4)$$

It can be verified that each kernel $\mathbf{G}^\alpha$ has the two properties $\nabla\cdot\mathbf{G}^\alpha = 0$ and $\nabla\times\nabla\times\mathbf{G}^\alpha = 0$ within the region of interest, where derivatives are taken with respect to the variable $\mathbf{r}$. As a result, the vector potential $\mathbf{A}$ given by (3) shares these properties. It follows that $\nabla\cdot\mathbf{B} = 0$ and $\nabla\times\mathbf{B} = 0$, and $\mathbf{A}$ satisfies the Coulomb gauge condition, for any surface values $\mathbf{n}\cdot\mathbf{B}$ and ψ, even if these values are noisy and the surface integrals are only evaluated approximately. Furthermore, $\mathbf{G}^n$ and $\mathbf{G}^t$ are analytic within the region of interest, and convergent Taylor series for $\mathbf{A}$ about any point interior to V may be obtained by expanding the integral kernels $\mathbf{G}^\alpha$ in the unprimed variables $\mathbf{r}$.

EXTRACTING MAPS USING BMAP3D

Consider a bending magnet with large design-orbit sagitta, and suppose that the values B_x, B_y, and B_z and ψ are provided on a 3D grid that lies within the magnet and extends into the magnet fringe field regions. We surround the design trajectory by a bent box with straight ends that encloses no iron or other sources (Fig. 1). If the data $\mathbf{B}$ and ψ are interpolated onto the boundary of the box, the result (3) allows one to construct a corresponding vector potential and its Taylor coefficients about any point in the interior via surface integrals, without the need for numerical differentiation. Knowledge of these quantities allows one to construct the Hamiltonian and its Taylor series near the design trajectory, which are sufficient to compute a symplectic transfer map through the magnet [9].

The code BMAP3D uses this technique to compute the design orbit and an associated transfer map about this orbit in Lie-algebraic form through third order for a given set of data B_x, B_y, B_z and ψ on a regular Cartesian grid. The

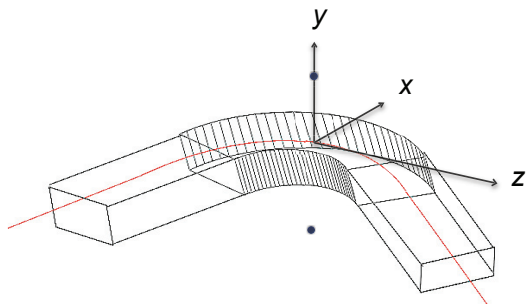

Figure 1: A bent box surrounding a reference trajectory (red) through the magnetic field of a bending dipole. The dots above and below the midplane illustrate the monopole doublet used to generate the magnetic field described in (6).

equations of motion for the design trajectory are integrated simultaneously with the equations for the Lie generators of the nonlinear map [9] using the global Cartesian coordinate system shown in Fig. 1, with z chosen as the independent variable. At each numerical step in z, the code uses efficient truncated power series algebra (TPSA) algorithms to compute the Taylor coefficients of the integral kernels (4) about the design point, which are used to extract the Taylor coefficients of $\mathbf{A}$ (through degree 4) by surface integrals of the form (3). In addition to the final transfer map, Taylor coefficients of $\mathbf{A}$ and $\mathbf{B}$ along the design trajectory are provided as numerical output.

Each Taylor coefficient of the vector potential $\mathbf{A}$ at a fixed value of z requires a single integration of the field and potential data over the surface S. Due to the computational cost associated with the number of Taylor coefficients required, the code has been parallelized using a domain decomposition by partitioning the surface of the bent box into disjoint regions. During the surface integration required for a given Taylor coefficient, integration over each region is performed on a separate processor core. This parallelization allows a large number of maps (~100) to be computed from distinct 3D data sets within a reasonable time (~hours), allowing for statistical studies or optimization of magnet design.

Benchmarks

The code is benchmarked using an exactly-soluble Maxwellian field that captures many features of a physical dipole. Suppose two magnetic monopoles having strengths $\pm g$ are placed at the (x, y, z) locations

$$r^+ = (0, a, 0),\ r^- = (0, -a, 0). \quad (5)$$

These monopoles generate a source-free magnetic field ($\nabla\times\mathbf{B} = 0$ and $\nabla\cdot\mathbf{B} = 0$) away from the two points (5). The field is given by $\mathbf{B} = \nabla\psi$ with:

$$\psi(x,y,z) = \psi_+(x,y,z) + \psi_-(x,y,z) =$$
$$-g[x^2 + (y-a)^2 + z^2]^{-1/2} + g[x^2 + (y+a)^2 + z^2]^{-1/2}. \quad (6)$$

In our test, $a = 2.5$ cm and $g = 1$ Tesla-(cm)^2. We set up a regular grid in x, y, z space, where $x \in [-4.4, 4.4]$

ISBN 978-3-95450-136-6

with spacing $h_x = 0.1$, $y \in [-2.4, 2.4]$ with $h_y = 0.1$, and $z \in [-300, 300]$ with $h_z = 0.125$ (in units of cm). The values of B_x, B_y, B_z, and ψ are computed and stored at each grid point.

We choose an 8.65 MeV electron reference trajectory that lies in the midplane, which makes a 30 degree bend and passes directly through the midpoint joining the two monopoles (Fig. 1). We surround this reference trajectory by a bent box with height 4 cm and width 8 cm and a bending angle of 30 degrees. (The length of the arc segment is 10 cm, and the length of each straight leg is 3.054 m.) Using the code BMAP3D, power series for the components of **A** and **B** about each reference point $\mathbf{r}_d$ are computed from grid data and compared to the analytically known Taylor coefficients of the field.

The computed vector potential is shown in Fig. 2, and Fig. 3 illustrates the error in two third-order Taylor coefficients of the corresponding magnetic field. In each case, this error is measured relative to the maximum value attained by the coefficient along the reference trajectory. The increase in error near the endpoints $z = \pm 20$ cm is due to the fact that the contribution of the magnetic field and magnetic scalar potential on the two end faces of the bent box have been omitted, and this error can be reduced by allowing the straight legs of the box to extend farther into the fringe field region.

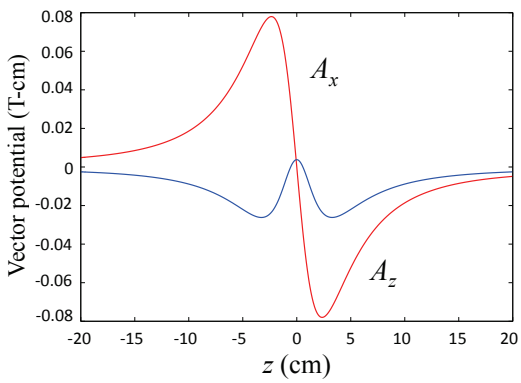

Figure 2: The vector potential for the monopole doublet for the case $a = 2.5$ cm and $g = 1$ Tesla-(cm)^2 at points along the reference trajectory, shown as a function of the longitudinal coordinate z. (Red) The component A_x. (Blue) The component A_z. Note that $A_y = 0$.

To benchmark the transfer map, a vector potential for the monopole doublet can be explicitly constructed in one simple gauge [5, 9]. Using this exactly-known vector potential, a reference trajectory can be computed and the transfer map determined using numerical integration of the map equations. This map can then be compared to the map obtained using the surface method just described. In this case, we find that the relative difference in each coefficient of the third-order transfer map is 10^{-4} or smaller.

Smoothing

The key feature of this technique is that results are relatively insensitive to numerical errors (noise) in the underlying grid data. To examine the effect of numerical noise, we generate random magnetic field errors $\Delta\mathbf{B}$ and potential errors $\Delta\psi$ at each grid point that are proportional, at the 1% level, to the magnetic field **B** and scalar potential ψ of the monopole doublet (6). At each mesh point (x_j, y_j, z_j) we set:

$$\Delta B_{x,y,z}(x_j, y_j, z_j) = \epsilon B_{x,y,z}(x_j, y_j, z_j)\delta_{x,y,z}(j), \quad (7a)$$

$$\Delta\psi(x_j, y_j, z_j) = \epsilon\psi(x_j, y_j, z_j)\delta_\psi(j). \quad (7b)$$

Here $\delta_x(j)$, $\delta_y(j)$, $\delta_z(j)$, and $\delta_\psi(j)$ are uniformly distributed random variables taking values in the interval $[-1, 1]$, and $\epsilon = 0.01$. Using the code BMAP3D, the values (7) are interpolated onto the surface of the bent box described in the previous Section, and the vector potential and its Taylor coefficients are computed about the reference trajectory shown in Fig. 1. The resulting vector potential components A_x and A_z are shown in Fig. 4 for six distinct random seeds (red). This procedure was performed for a total of 160 random seeds, and the rms values of A_x and A_z at each value of z are shown in blue, indicating maximum rms values that are 6×10^{-5} and 3×10^{-4} relative to the maximum values of A_x and A_z shown in Fig. 2. Thus, in the case of the monopole doublet, random noise of order 1% in the grid values produces a relative error in the computed vector potential that is only of order 10^{-4} along the reference

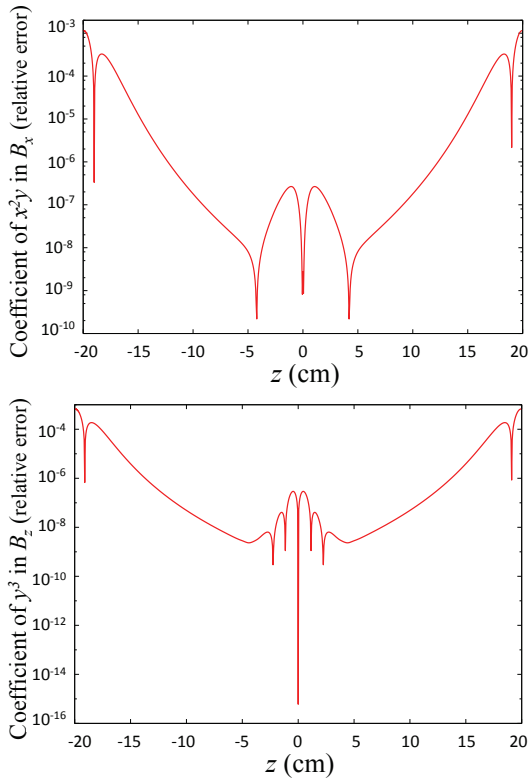

Figure 3: The error in the Taylor coefficients of the computed magnetic field of the monopole doublet (6) for the case $a = 2.5$ cm and $g = 1$ Tesla-(cm)^2 is shown along the reference trajectory as a function of the longitudinal coordinate z.

ISBN 978-3-95450-136-6

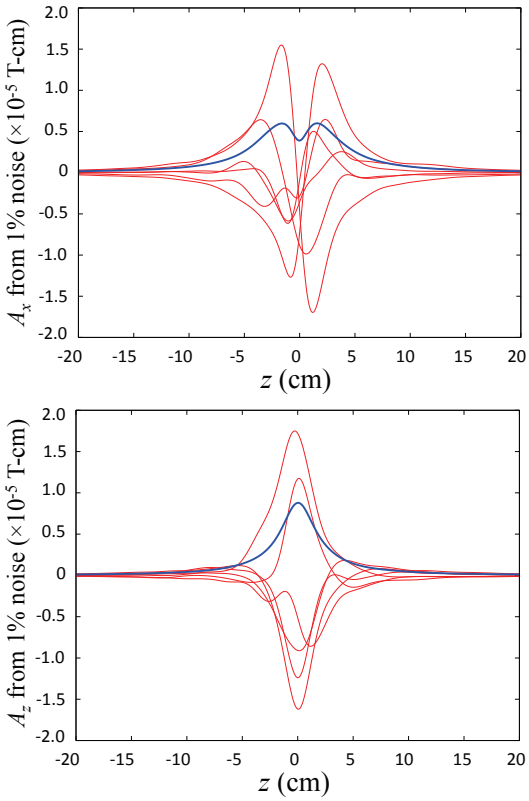

Figure 4: Vector potential components A_x and A_z computed from 1% random noise for the case $a = 2.5$ cm and $g = 1$ Tesla-(cm)^2. (Red) Results are shown for 6 distinct random seeds. (Blue) The rms value as computed using 160 random seeds.

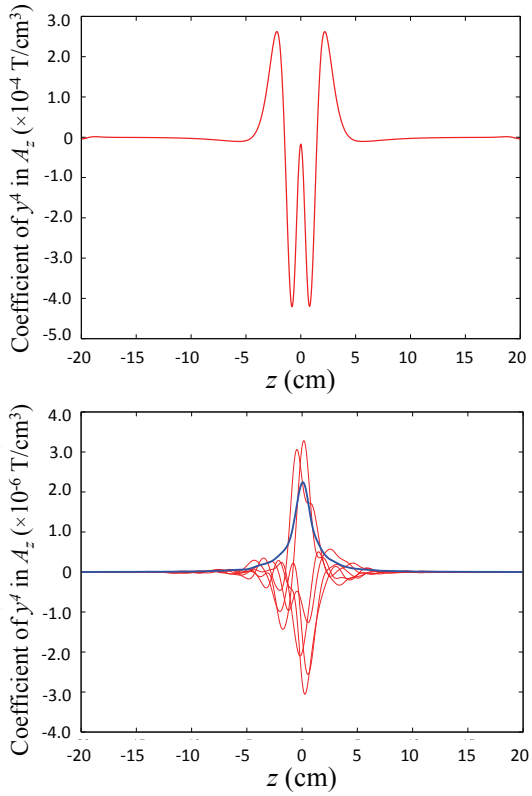

Figure 5: (Upper) The coefficient of the monomial y^4 in the Taylor series for A_z computed for the monopole doublet (6) for the case $a = 2.5$ cm and $g = 1$ Tesla-(cm)^2. (Lower) The same coefficient computed from 1% random noise. The blue line denotes the rms value as computed using 160 random seeds

trajectory. This is a result of *numerical smoothing*, by which random errors in the values of the magnetic field and scalar potential on the bent box surface are damped as one moves inward toward the reference trajectory.

The same phenomenon also occurs for high-order Taylor coefficients of the vector potential. As an example, one fourth-degree Taylor coefficient for the vector potential of the monopole doublet (6) is shown in the upper plot of Fig. 5. The corresponding Taylor coefficient as computed from 1% relative noise (7) is also shown, which attains a maximum rms value that is 5×10^{-3} relative to the maximum value appearing in the upper figure.

APPLICATION

As an application of this technique, we performed a study of the 35-mm gap design of the Brookhaven NSLS-II dipoles. The dipole is designed to provide 3 GeV electrons with a bend of 6 degrees. Based on the use of Opera 3D, Brookhaven provided data for both the field $\boldsymbol{B}$ and the scalar potential ψ on a grid with

$$x \in [-0.06, 0.06], \quad y \in [-0.016, 0.016], \quad z \in [-1.8, 1.8]$$

and spacing

$$h_x = h_y = h_z = .002.$$

Here all quantities are in meters.

The map computation in BMAP3D was performed using a bent box with height 0.024 m and width 0.1 m. The length of the arc segment was 3.22 m, and the length of each straight leg was 0.1 m. For preliminary fitting, the box was taken to be nearly straight (with a bending angle of 0.6 degrees). As a numerical test, the interior magnetic field was computed in BMAP3D (using $\mathbf{B} = \nabla \times \mathbf{A}$) at several interior grid point locations. This solution for the interior field, which is obtained using only field and potential data on the surface of the bent box, was then compared to the original data at each grid point. Figure 6 displays the computed value of the vertical field B_y off-axis at $(x, y) = (0, 0.2)$ cm along the length of the dipole. Note that the fitted field correctly captures the fringe-field behavior, and the maximum error obtained along the line shown was $|\mathbf{B}_{data} - \mathbf{B}_{fit}|/|\mathbf{B}|_{peak} = 4 \times 10^{-4}$.

As a second test, Fig. 7 shows the reference trajectory through the dipole as computed using BMAP3D, together with a reference trajectory that is computed using numerical integration based on magnetic field data interpolated from the grid. Using the numerically determined Taylor coeffi-

ISBN 978-3-95450-136-6

cients of A_x, A_y, and A_z, a transfer map was computed about this reference trajectory through third order.

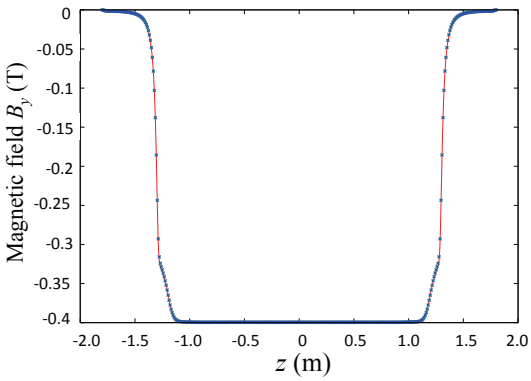

Figure 6: Fit obtained to proposed NSLS-II dipole vertical field using the bent box of Fig. 1. The solid line is a linear interpolation through numerical data provided by OPERA-3d. Dots indicate values computed from surface data using BMAP3D.

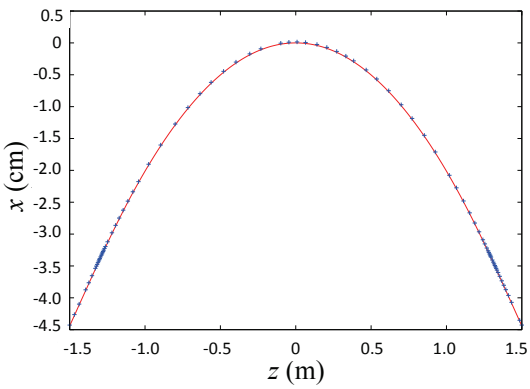

Figure 7: Reference trajectory through the NSLS-II dipole vertical field. (Solid) Reference trajectory computed by BMAP3D using data on the surface of a bent box. (Dots) Reference trajectory computed by numerical integration through magnetic field data on a mesh.

CONCLUSIONS

A parallel code BMAP3D has been developed for computing third-order symplectic transfer maps based on 3-dimensional magnetic field data on a grid, as provided by various 3-D finite element field codes. The method involves fitting field data onto a boundary surface and continuing inward to obtain **A** and its Taylor coefficients in a neighborhood of the beam design trajectory. If desired, the code can produce both **A** and **B** at any interior point, together with Taylor coefficients about this point through 4th and 3rd order, respectively. These quantities can be exported for use with other charged-particle optics codes. The surface-fitting procedure has several distinct advantages:

- The method is based on a smooth (analytic) representation of the interior magnetic field that exactly satisfies Maxwell's equations. One may verify that $\nabla \cdot \mathbf{B} = 0$ and $\nabla \times \mathbf{B} = 0$ at each interior point to within machine precision.
- The error is globally controlled. Each component B_x, B_y, and B_z of both the exact and computed fields satisfies the Laplace equation. Therefore their difference, the error field, also satisfies the Laplace equation, and must take its extrema on the boundary. The fitting error on the boundary is controlled, and the interior error must therefore be even smaller.
- Interior values inferred from surface data are relatively insensitive to errors/noise in the surface data. In general, the sensitivity to noise in the data decreases rapidly (as some high inverse power of distance) with increasing distance from the surface, and this property improves the accuracy of the high-order interior derivatives needed to compute high-order transfer maps.
- Unlike a truncated Taylor map, the computed transfer map in factorized Lie form is exactly symplectic [9].

Using tools such as BMAP3D and those described in [1]-[4], one may obtain a realistic high-order transfer map for an entire accelerator or storage ring without the uncertainties associated with the use of only approximate field models.

ACKNOWLEDGMENTS

This work is partially supported by the U.S. Department of Energy and made use of computer resources at the National Energy Research Scientific Computing Center.

REFERENCES

[1] M. Venturini and A. Dragt, Nucl. Instrum. and Meth. A 427, 387 (1999).

[2] S. Manikonda and M. Berz, IJPAM **23**, 365 (2005).

[3] D. Abell, Phys. Rev. ST Accel. Beams 9, 052001 (2006).

[4] C. Mitchell and A. Dragt, Phys. Rev. ST Accel. Beams 13, 064001 (2010).

[5] C. Mitchell, "Calculation of Realistic Charged-Particle Transfer Maps," Ph. D. thesis, University of Maryland, College Park (2007), `http://www.physics.umd.edu/dsat/`.

[6] J. Stratton and L. Chu, Phys. Rev. **56**, pp. 99-107 (1939); J. Stratton, *Electromagnetic Theory*, McGraw-Hill Book Co., Inc. New York (1941).

[7] C. Mitchell and A. Dragt, in Proceedings of PAC2011, New York, NY, March 2011 (2011).

[8] A. Dragt, T. Stasvevich, and P. Walstrom, in Proceedings of PAC2001, Chicago, IL, June 2001, p. 1776 (2001).

[9] A. Dragt, *Lie Methods for Nonlinear Dynamics with Applications to Accelerator Physics*, University of Maryland Technical Report (2009), `http://www.physics.umd.edu/dsat/`.

ISBN 978-3-95450-136-6

REALISTIC APPROACH FOR BEAM DYNAMICS SIMULATION WITH SYNCHROTRON RADIATION IN HIGH ENERGY CIRCULAR LEPTON COLLIDERS

S. Glukhov, E. Levichev,
BINP, Novosibirsk 630090, Russia

Abstract

In extremely high energy circular lepton collider correct consideration of synchrotron radiation (SR) is important for beam dynamics simulation. We developed fast, precise and effective method to track the paricles in the lattice (including nonlinearities) when the radiation effects — classical damping and quantum emittance excitation — are distributed along the beam orbit. As an example we study beam dynamics in the FCC-ee lepton collider which is now under development at CERN [1]. Radiation effect on beam optics, dynamic aperture and momentum acceptance is discussed.

CONCENTRATED SR

Usual way to simulate SR in a circular lattice is to apply the following transformation to the coordinates of all particles once per turn at arbitrary azimuth s_0 [2] (the formulae are simplified for the case of flat lattice without betatron coupling)

$$\begin{aligned} x &\mapsto a_x(x-\eta_x\delta)+\eta_x\delta+b_x\hat{r}_1 \\ p_x &\mapsto a_x(p_x-\eta'_x\delta)+\eta'_x\delta+b_x(\hat{r}_2-\alpha_x\hat{r}_1)/\beta_x \\ y &\mapsto a_y y+b_y\hat{r}_3 \\ p_y &\mapsto a_y p_y+b_y(\hat{r}_4-\alpha_y\hat{r}_3)/\beta_y \\ \delta = \Delta E/E_0 &\mapsto e^{-\frac{T_0}{2\tau_\delta}}\delta+\sigma_\delta\sqrt{1-e^{-\frac{T_0}{\tau_\delta}}}\,\hat{r}_5 \end{aligned} \quad , \quad (1)$$

where

$$a_u = e^{-\frac{T_0}{2\tau_u}}, \quad b_u = \sqrt{\varepsilon_u\beta_u\left(1-e^{-\frac{T_0}{\tau_u}}\right)},$$

E_0 — reference energy, T_0 — revolution period, τ_u — damping times ($u = x, y$), ε_u — emittances, β_u, α_u, η_x, η'_x — optical functions at s_0, and $\hat{r}_1 \ldots \hat{r}_5$ — random values with standard distribution.

DISTRIBUTED SR

If the energy loss per turn is very large, then the technique described above may provide erroneous results. So, we developed an algorithm, which takes into account realistic distribution of SR along the lattice.

Radiated Energy

In a dipole magnet of the length L and bending angle θ an electron with relativistic factor γ follows an arc with radius $\rho = L/\theta$ and radiates amount of energy equal to

$$W_0 = \frac{2\theta e^2}{3\rho}\gamma^4 .$$

Spectral power density is the following

$$\frac{dW}{d\omega} = \frac{W_0}{\omega_c} S\left(\frac{\omega}{\omega_c}\right), \quad \text{where} \quad \omega_c = \frac{3c}{2\rho}\gamma^3,$$

or

$$\frac{dW}{dy} = \frac{W_0}{y} S(y), \quad \text{where} \quad y = \frac{\omega}{\omega_c}.$$

$S(y)$ is so called spectral function

$$S(y) = \frac{9\sqrt{3}}{8\pi} y \int_y^\infty K_{5/3}(t)dt .$$

Then spectral photon density can be written as follows

$$s(y) = \frac{dN}{dy} = \frac{1}{y} S(y) .$$

Mean number of photons emitted during single passage through the magnet is

$$\bar{N} = \frac{W_0}{\hbar\omega_c}\int_0^\infty s(y)dy = \frac{5\sqrt{3}}{6}\alpha\gamma\theta,$$

where α is the fine structure constant. Then average photon energy is

$$\bar{E} = \frac{W_0}{\bar{N}} = \frac{4\sqrt{3}}{15}\frac{\lambda\!\!\!^{-}_e}{\rho} E_e\gamma^3,$$

where E_e is the electron rest energy, $\lambda\!\!\!^{-}_e$ is the reduced electron wavelength.

All radiation acts are independent, hence the number of actually emitted photons N has Poisson distribution with the parameter $\bar{N}$. To obtain energy of the i-th photon one should generate random value y_i with the following distribution density function

$$f(y_i) = \frac{3}{5\pi}\int_{y_i}^\infty K_{5/3}(t)dt, \quad (2)$$

where K is a modified Bessel function of the second kind. Such a distribution will be referred to as SR-distribution, notation $y_i \in SR$ means that y_i obeys this distribution (a method for generation of this distribution will be described in the next subsection). After emission of the i-th photon coordinate δ is changed by

$$\Delta_i\delta = -\frac{3\lambda\!\!\!^{-}_e}{2\rho}\frac{\gamma^3}{\gamma_0}y_i, \quad i = 1\ldots N,$$

where γ_0 is the relativistic factor of the reference particle. It should be noted that

$$\frac{\gamma}{\rho} = \frac{e}{E_e}B, \quad \gamma = \gamma_0(1+\delta),$$

ISBN 978-3-95450-136-6

where B is on-axis magnetic field. Then

$$\bar{N} = \frac{5\sqrt{3}}{6}\frac{\alpha e}{E_e}BL, \quad \Delta_i\delta = -\frac{3}{2}\frac{e\lambda_e}{E_e}\gamma_0 B(1+\delta)^2 y_i\,. \quad (3)$$

Particle's path in the bending magnet depends on its initial horizontal coordinate x_0 (at the entrance pole face) and pole face rotation angles. If the magnet has quadrupole field of strength $k_1 = \frac{1}{B\rho}\frac{\partial B}{\partial x}$, then off-axis particles travel in different magnetic field. To take these effects into account we make the following substitutions in (3)

$$B \mapsto B\,(1 + k_1\rho x_0)\,,$$
$$L \mapsto L\,(1 + x_0/\rho) - x_0(\tan\varphi_1 + \tan\varphi_2)\,,$$

where φ_1, φ_2 are the rotation angles for the entrance and exit pole face of the dipole. We should also substitute δ in (3) by its value δ_0 at the entrance pole. Finally

$$\bar{N} = \frac{5\sqrt{3}}{6}\alpha\theta\gamma_0\,(1 + k_1\rho x_0)\,(1 + h^* x_0)\,,$$
$$\Delta_i\delta = -\frac{3\lambda_e}{2\rho}{\gamma_0}^2\,(1+\delta_0)^2\,(1 + k_1\rho x_0)\,y_i\,,$$

where

$$h^* = \frac{1}{\rho} - \frac{\tan\varphi_1 + \tan\varphi_2}{L}\,.$$

Generation of SR-Distribution

Given the distribution density (2) and the integral representation of K-function

$$K_\nu(z) = \int_0^\infty e^{-z\cosh t}\cosh(\nu t)dt\,, \quad \mathrm{Re}\,(z) > 0\,,$$

we can find distribution function of SR-distribution

$$F(z) = 1 - \frac{3}{5\pi}\int_0^\infty \frac{\cosh\left(\frac{5}{3}t\right)}{\cosh^2 t}e^{-z\cosh t}dt\,.$$

$y \in SR$ can be generated using inversion method [3], its main idea is the following: if ξ has uniform distribution over $[0;1]$ segment, then $F^{-1}(\xi) \in SR$. We will use analytical approximation of $F^{-1}(\xi)$, which will be denoted as $\widetilde{F}^{-1}(\xi)$. Its asymptotics should be the same as for $F^{-1}(\xi)$. Given asymptotics for $F(z)$

$$F(z) \underset{z\to 0}{\longrightarrow} const\cdot z^{1/3}\,, \quad F(z) \underset{z\to\infty}{\longrightarrow} const\cdot\frac{e^{-z}}{\sqrt{z}}\,,$$

we may take the following expression for $\widetilde{F}^{-1}(\xi)$

$$\widetilde{F}^{-1}(\xi) = C\,(-\ln(1-\xi^a))^{3/a}\,.$$

So, instead of y we will generate $\widetilde{y}$, which has the distribution function $\widetilde{F}(z)$. Thus $\widetilde{F}(z)$ should be close to $F(z)$, this can be achieved by appropriate choice of C and a values. Let the first two moments of y be the same as for $\widetilde{y}$. Also we have an expression for the n-th distribution moment

$$\langle y^n\rangle = \int_0^1 \left(F^{-1}(\xi)\right)^n d\xi$$

Table 1: Relative Deviation of the First Four Moments of Energy Distribution from Theoretical Value $\langle y^n\rangle$ for the simulation Techniques Proposed in the Present Paper ($\langle\widetilde{y}^n\rangle$) and the One Proposed in [5] ($\langle {y_t}^n\rangle$).

n	$\langle y^n\rangle$	$\Delta\langle\widetilde{y}^n\rangle$, %	$\Delta\langle {y_t}^n\rangle$, %
1	$8\sqrt{3}/45$	$-3\cdot10^{-8}$	$-6\cdot10^{-5}$
2	$11/27$	$1\cdot10^{-7}$	-0.5
3	$224\sqrt{3}/405$	1.56	-1.8
4	$1309/405$	4.83	-5.1

and similar expression for $\langle\widetilde{y}^n\rangle$. Using computer algebra system Maple 9.5 [4], we obtain $C = 0.5770253543282$, $a = 2.535608814842$.

Two another techniques for SR-distribution generation were proposed in [5]. The first of them also involves inversion method, but its accuracy is poor because $F(z)$ is approximated with an inversible function instead of direct approximation of $F^{-1}(\xi)$. The second one involves lookup table and has much better accuracy. Let $\langle {y_t}^n\rangle$ be the values of the first four distribution moments for the lookup table method from [5]. Table 1 summarizes relative deviations for $\langle\widetilde{y}^n\rangle$ and $\langle {y_t}^n\rangle$ from theoretical values $\langle y^n\rangle$. So, our method is significantly more accurate. From now on we will assume that $\widetilde{F}(z) \equiv F(z)$ and $\widetilde{y} \equiv y$.

Transversal Motion

Energy deviation due to SR photons emission affects particle's motion in the bending plane. In a flat lattice all bends are horizontal, hence x and p_x are to be changed along with δ. Radiation damping in the magnet in both transversal planes is proportional to the magnet's contribution to I_2 integral, squared quantum exitation amplitude is proportional to the contribution to I_{5x}. Equilibrium distribution of the horizontal coordinates is gaussian, so we can apply transformations (1) to x and p_x in each bending magnet separately, assuming that the addition due to quantum exitation in each magnet is also gaussian. So, all radiation acts in the magnet can be simulated at once at its exit pole face. Finally, the following transformation should be applied to the coordinates of each particle after tracking through each bending magnet

$$\begin{aligned} x &\mapsto e^{c_{1x}\Delta\delta}(x - \eta_x\delta) + \eta_x(\delta + \Delta\delta) + c_{2x}\hat{r}_1\sqrt{\Delta^2\delta}\,,\\ p_x &\mapsto e^{c_{1x}\Delta\delta}(p_x - \eta'_x\delta) + \eta'_x(\delta + \Delta\delta) + c_{2x}\tfrac{\hat{r}_2 - \alpha_x\hat{r}_1}{\beta_x}\sqrt{\Delta^2\delta}\,,\\ y &\mapsto e^{c_{1y}\Delta\delta}y\,, \quad p_y \mapsto e^{a_y\Delta\delta}p_y\,, \quad \delta \mapsto \delta + \Delta\delta\,, \end{aligned} \quad (4)$$

where

$$\Delta\delta = \textstyle\sum_{i=1}^N \Delta_i\delta\,, \quad \Delta^2\delta = \sum_{i=1}^N (\Delta_i\delta)^2\,,$$
$$c_{1x,1y} = \frac{3T_0}{2\tau_{x,y}r_e{\gamma_0}^3 I_2}\,,$$
$$c_{2x} = \sqrt{\frac{24\sqrt{3}}{55}\frac{\varepsilon_x\beta_x\langle H_x\rangle}{\alpha{\gamma_0}^5{\lambda_e}^2 I_{5x}}\left(1 - e^{-\frac{T_0}{\tau_x}}\right)},$$

I_2, I_{5x} — radiation integrals, $\langle H_x\rangle$ — horizontal dispersion invariant averaged over the magnet, $\beta_x, \alpha_x, \eta_x, \eta'_x$ — horizontal optical functions at the exit pole of the magnet, $\hat{r}_1$,

ISBN 978-3-95450-136-6

$\hat{r}_2$ — random values with standard distribution. Quantum excitation in the vertical plane can be simulated once per turn, as in (1).

SAWTOOTH EFFECT AND TAPERING

Distributed energy losses lead to variation of equilibrium beam energy $\langle\delta\rangle$ along the lattice: it drops in bending magnets and rises in RF cavities. This is so called sawtooth effect, which also leads to the closed orbit distortions, $\Delta x_{co} \approx \eta_x \langle\delta\rangle$, therefore, reference particle becames off-axis in quadrupoles and higher multipoles. So, in high energy rings all the optics will be completely distorted, dynamic aperture and energy acceptance will drop significantly due to sawtooth effect. It can be cured by a variation of magnetic field in beamline elements in proportion to varying equilibrium energy (magnet tapering). To make optics in tapered and original lattice as close as possible, one should change steering field and multipole gradients in each beamline element in proportion to $(1 + \langle\delta\rangle)$. Then, to take into account the effect of the dipoles on the closed orbit, the following transformation should be applied to the horizontal coordinates after each dipole

$$x \mapsto x + \rho(1 - \cos\theta)\,\Delta\langle\delta\rangle\,,$$
$$p_x \mapsto p_x + \sin\theta\,\Delta\langle\delta\rangle\,,$$

where $\Delta\langle\delta\rangle = W_0/E_0$ is the variation of equilibrium energy in the dipole.

SR FROM QUADRUPOLES

Particle follows curved trajectory and therefore emits SR photons not only in dipoles but also in other beamline elements. Additional energy loss due to this effect, averaged over beam particles, is small compared to total losses even for high energy rings. Hence radiation integrals and beam sizes stay unchanged, but coordinate dependent losses, especially in strong final focus quadrupoles, distort optics for particles with large amplitudes, which leads to decrease in dynamic aperture [6].

The simpliest way to study this effect is to consider each strong quadrupole as a "variable strength dipole" with parallel pole faces and no quadrupole gradient. This fictitious dipole acts in both transversal planes and has different bending angle and radius of curvature each turn for each particle. These values will be different for horizontal and vertical planes

$$\theta_x = |p_{x1} - p_{x0}|\,, \quad \theta_y = \left|p_{y1} - p_{y0}\right|\,, \quad \rho_{x,y} = L/\theta_{x,y}\,,$$

where p_{x0}, p_{y0} are the transversal momenta at the entrance pole face, p_{x1}, p_{y1} are the transversal momenta at the exit pole face of the quadrupole. So, radiation in both transversal planes should be simulated independently

$$\bar{N}_{x,y} = \frac{5\sqrt{3}}{6}\alpha\theta_{x,y}\gamma_0\,, \quad N_{x,y} \in Poisson\left(\bar{N}_{x,y}\right)\,,$$
$$(\Delta_i\delta)_{x,y} = -\frac{3\lambda_e}{2\rho_{x,y}}\gamma_0{}^2\,(1+\delta_0)^2\,y_i\,, \quad i = 1\ldots N_{x,y}\,,$$

$$\Delta\delta = \sum_{i=1}^{N_x}(\Delta_i\delta)_x + \sum_{i=1}^{N_y}(\Delta_i\delta)_y\,,$$
$$\Delta^2\delta = \sum_{i=1}^{N_x}((\Delta_i\delta)_x)^2 + \sum_{i=1}^{N_y}\left((\Delta_i\delta)_y\right)^2\,.$$

Then the transformation (4) should be applied.

SIMULATION RESULTS FOR FCC-ee

The simulation technique described above was implemented as part of TrackKing simulation program [7]. N-turn DA at the given azimuth is defined as 3D region in (x, y, δ) coordinates visited by particles, which survived N turns of tracking. Initial particle distribution is uniform over these 3 coordinates with other 3 zeroed and wide enough to span the whole stability region. DA can be plotted as 3 projections of this region.

FCC-ee is 100 km e+e- collider with beam energy 45–175 GeV. Simulations were performed for preliminary version of 175 GeV FCC-ee lattice with 4 different algorithms: without SR; with concentrated SR; with distributed SR and tapering; with distributed SR, tapering and SR from final focus quadrupoles. DA borders (in units of beam sizes) are shown in Fig. 1.

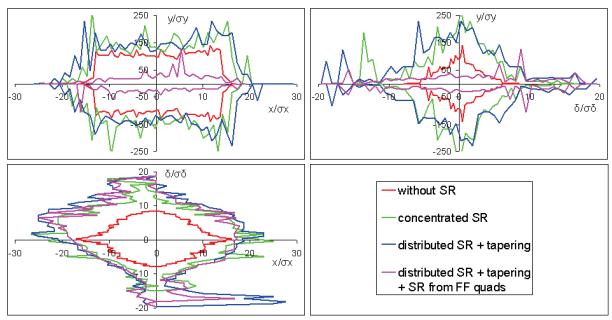

Figure 1: 500-turns DA of 175 GeV FCC-ee lattice.

Introducing SR into simulations increases energy acceptance considerably and also increases transversal DA slightly. At this point concentrated and distributed algorithms of SR simulation give similar results, but vertical DA decreases dramatically, when SR from quadrupoles is added (only distributed algorithm has this option). Further studies are required to explain the results correctly.

CONCLUSION

Dynamic aperture and energy acceptance of FCC-ee depends strongly on the choice of SR simulation technique, so, the most realistic one should be taken. The method described in this paper includes simulation of radiation damping and quantum excitation in longitudinal and both transversal planes. It contains procedure for precise generation of SR photons spectrum and takes into account realistic distribution of emission points along the lattice. The only assumption is that the addition to horizontal coordinates due to quantum excitation has gaussian distribution in each bending magnet. The important advantage of this method is the possibility of simulating SR from quadrupoles and studying of the magnet tapering options.

ISBN 978-3-95450-136-6

REFERENCES

[1] cern.ch website: http://tlep.web.cern.ch

[2] K. Ohmi, K. Hirata and K. Oide, "From the beam envelope matrix to synchrotron radiation integrals", Phys. Rev. E **49**, 751 (1994).

[3] L. Devroye, "Non-Uniform Random Variate Generation", (New York: Springer-Verlag, 1986), 27.

[4] maplesoft.com website: http://www.maplesoft.com

[5] G. J. Roy, "A New method for the simulation of synchrotron radiation in particle tracking codes", Nucl. Instrum. Meth. A **298** (1990) 128.

[6] G. Guignard and J. M. Jowett, "Damping Aperture Of Lep", CERN-LEP-NOTE-407.

[7] S. Glukhov, E. Levichev, S. Nikitin, P. Piminov, D. Shatilov, S. Sinyatkin, "6D Tracking with Compute Unified Device Architecture (CUDA) Technology", presented at ICAP'15, Shanghai, China, paper WEP34, these proceedings.

ISBN 978-3-95450-136-6

THEORY AND SIMULATION OF EMITTANCE GROWTH CAUSED BY SPACE CHARGE AND LATTICE INDUCED RESONANCES

Kazuhito Ohmi, KEK, Tsukuba, Japan

Abstract

Emittance growth and beam loss in high intensity circular proton accelerators are one of the most serious issue which limit their performance. The emittance growth is caused by linear and nonlinear resonances of betatron/synchrotron oscillation due to lattice and space charge nonlinear force. We should first understand which resonances how are serious. Tune shift and resonance strength induced by space charge and lattice nonlinearity is discussed with integrals along a ring like the radiation integrals. Emittance growth is discussed using so-called standard model, in which the resonance width has an important role.

INTRODUCTION

Particles move with experience of electro-magnetic field of lattice elements and space charge. We study slow emittance growth arising in a high intensity circular proton ring. We assume that the beam distribution is static, and each particle moves in the filed of the static distribution. As a practical issue, we concern about beam loss of 0.1-1% during a long term ($\approx 10,000$ turns) in J-PARC MR. A halo is formed by the nonlinear force due to the electro-magnetic field. The halo, which consists of small part of whole beam, does not affect the field. Particle motion is described by a single particle Hamiltonian in the field.

Hamiltonian is separated by three parts for (1) linear betatron motion (μJ) (2) nonlinear component of the lattice magnets (U_{nl}) and (3) space charge potential (U_{sc}).

$$H = \mu J + U_{nl} + U_{sc}. \tag{1}$$

where Hamiltonian is represented by action variables J and ϕ, which are Courant-Snyder invariant ($W = 2J$) and betatron phase, respectively. Betatron motion is expressed by the action variables as,

$$\begin{aligned} x(s)_\beta &= \sqrt{2\beta_x(s)J_x}\cos(\phi_x(s)) \\ y(s)_\beta &= \sqrt{2\beta_y(s)J_y}\cos(\phi_y(s)). \end{aligned} \tag{2}$$

where dispersion is subtracted in x and y. Betatron phase advance per turn ($\tilde{\mu}_i = 2\pi\tilde{\nu}_i, i = x, y$), which depends on J_i due to U's, is given by

$$\begin{aligned} \tilde{\mu}_i(\boldsymbol{J}) &= \phi_i(s+L) - \phi_i(s) \\ &= \frac{\partial H}{\partial J_i} = \mu_i + \frac{\partial (U_{nl}+U_{sc})}{\partial J_i}. \end{aligned} \tag{3}$$

where $\boldsymbol{J} = (J_x, J_y)$. Synchrotron motion is treated as external given motion for s,

$$z = z_0 \cos(2\pi\nu_s s/L). \tag{4}$$

Hamiltonian is expanded by Fourier series [1],

$$H = \mu J + U_{00}(\boldsymbol{J}) + \sum_{m_x,m_y \neq 0} U_{m_x,m_y}(\boldsymbol{J}) \exp(-im_x\phi_x - im_y\phi_y) \tag{5}$$

First and second terms in RHS characterize shift, spread and slope of tune.

$$\tilde{\mu}_i = \frac{\partial H}{\partial J_i} = \mu_i + \frac{\partial U_{00}}{\partial J_i} \tag{6}$$

Third term is averaged out for the tune shift due to the betatron phase variation. Resonance condition is expressed by

$$m_x\tilde{\mu}_x(\boldsymbol{J}) + m_y\tilde{\mu}_y(\boldsymbol{J}) = 2\pi n. \tag{7}$$

where n is an integer. The resonance condition Eq.(7) gives a line in (J_x, J_y) space. $\boldsymbol{J}$ satisfying Eq.(7) is expressed by $\boldsymbol{J}_R$.

Hamiltonian is expanded near $\boldsymbol{J}_R$ as

$$\begin{aligned} U_{00}(\boldsymbol{J}) = U_{00}(\boldsymbol{J}_R) &+ \left.\frac{\partial U_{00}}{\partial \boldsymbol{J}}\right|_{\boldsymbol{J}_R} (\boldsymbol{J}-\boldsymbol{J}_R) \\ &+ (\boldsymbol{J}-\boldsymbol{J}_R)^t \frac{1}{2} \left.\frac{\partial^2 U_{00}}{\partial \boldsymbol{J}\partial \boldsymbol{J}}\right|_{\boldsymbol{J}_R} (\boldsymbol{J}-\boldsymbol{J}_R) \end{aligned} \tag{8}$$

Third term in RHS is characterized by the tune slope

$$\frac{\partial \nu_i}{\partial J_j} = \frac{\partial \nu_j}{\partial J_i} = \frac{\partial^2 U_{00}}{\partial J_i \partial J_j} \tag{9}$$

Canonical transformation for new variable $\boldsymbol{P}$ and $\boldsymbol{\psi}$ is considered

$$\begin{aligned} F_2(\boldsymbol{P}, \boldsymbol{\phi}) = &(J_{x,R} + m_x P_1 + m_{x,2} P_2)\phi_x \\ &+ (J_{y,R} + m_y P_1 + m_{y,2} P_2)\phi_y \end{aligned} \tag{10}$$

Choise of $(m_{x,2}, m_{y,2})$ is arbitrary under independent of (m_x, m_y). Choosing $m_{x,2} = 0, m_{y,2} = 1$,

$$P_1 = \frac{J_x - J_{x,R}}{m_x} \qquad \psi_1 = m_x\phi_x + m_y\phi_y \tag{11}$$

$$P_2 = (J_y - J_{y,R}) - \frac{m_y}{m_x}(J_x - J_{x,R}) \qquad \psi_2 = \phi_y$$

Hamiltonian for $\boldsymbol{J}$ dependent terms is now given by

$$H_{00} = U_{00} \approx \frac{\Lambda}{2} P_1^2, \tag{12}$$

where

$$\Lambda \equiv m_x^2 \frac{\partial^2 U_{00}}{\partial J_x^2} + m_x m_y \frac{\partial^2 U_{00}}{\partial J_x \partial J_y} + m_y^2 \frac{\partial^2 U_{00}}{\partial J_y^2}. \tag{13}$$

ISBN 978-3-95450-136-6

The resonance term, which is third term of RHS in Eq.(5), drives resonances. The resonance strengths $U_{\boldsymbol{m}}$ as function of $\boldsymbol{J}$ are approximated to be those at $\boldsymbol{J}_R$

$$U_{\boldsymbol{m}}(\boldsymbol{J}) \approx U_{\boldsymbol{m}}(\boldsymbol{J}_R) \qquad \boldsymbol{m} = (m_x, m_y). \tag{14}$$

Hamiltonian for the standard model is given as

$$H = \frac{\Lambda}{2} P_1^2 + U_{\boldsymbol{m}}(\boldsymbol{J}_R)\cos\psi_1. \tag{15}$$

Phase space structure near resonances are characterized by the resonance width. The resonance width is given by

$$\Delta P_1 = 4\sqrt{\frac{U_{\boldsymbol{m}}}{\Lambda}} \qquad \Delta J_x = 4m_x\sqrt{\frac{U_{\boldsymbol{m}}}{\Lambda}}. \tag{16}$$

EVALUATION OF RESONANCE WIDTH

Resonances Due to Space Charge Force

We first discuss the space charge potential U_{sc} [2]. Beam distribution is assumed to be Gaussian in transverse determined by emittance and Twiss parameters. U contains linear component, which gives a tune shift and Twiss parameter distortion.

$$U_{sc}(s) = \int ds' U_{sc}(s', s) = -\frac{\lambda_p r_p}{\beta^2\gamma^3}\oint ds' \int_0^\infty \frac{1 - \exp\left(-\frac{x(s',s)^2}{2\sigma_x^2+u} - \frac{y(s',s)^2}{2\sigma_y^2+u}\right)}{\sqrt{2\sigma_x^2+u}\sqrt{2\sigma_y^2+u}} du \tag{17}$$

x and y are sum of betatron coordinates dispersion orbit at s' as

$$x(s', s) = \sqrt{2\beta_x(s')J_x}\cos(\varphi_x(s', s) + \phi_x(s)) + \eta(s')\delta(s)$$

$$y(s', s) = \sqrt{2\beta_y(s')J_y}\cos(\varphi_y(s', s) + \phi_y(s)). \tag{18}$$

where $\varphi_{x,y}(s', s)$ is the betatron phase difference between s and s' and η is the dispersion. δ is a given function of s,

$$\delta(s) = \delta_0 \sin \mu_s s/L \tag{19}$$

The synchrotron motion is slow $\nu_s \approx 0.002$ for J-PARC MR. We consider δ changes addiabatically in the evaluation of the tune shift and resonance terms: i.e. they are evaluated at a given δ. We introduce follwing variables.

$$\begin{aligned} \frac{x^2}{2\sigma_x^2+u} &= w_{x\eta} + w_x\cos 2(\varphi_x+\phi_x) + v_x\cos(\varphi_x+\phi_x) \\ \frac{y^2}{2\sigma_y^2+u} &= w_y + w_y\cos 2(\varphi_y+\phi_y) \end{aligned} \tag{20}$$

where

$$w_x = \frac{\beta_x J_x}{2\sigma_x^2+u}. \qquad w_{x\eta} = \frac{\beta_x J_x + \eta^2\delta^2}{2\sigma_x^2+u}. \tag{21}$$

$$v_x = \frac{2\sqrt{2\beta_x J_x}\eta\delta}{2\sigma_x^2+u} \qquad w_y = \frac{\beta_y J_y}{2\sigma_y^2+u}. \tag{22}$$

Using

$$e^{-w\cos\psi} = \sum_{k=-\infty}^{\infty}(-1)^k I_k(w)e^{-ik\psi}, \tag{23}$$

the exponential term is expressed by modified Bessel functions,

$$\begin{aligned} \exp\left(-\frac{x^2}{2\sigma_x^2+u} - \frac{y^2}{2\sigma_y^2+u}\right) &= e^{-w_{x\eta}-w_y} \\ &\sum_{k,l=-\infty}^{\infty}(-1)^{k+l} I_k(w_x)I_l(v_x)e^{-i(2k+l)(\varphi_x+\phi_x)} \\ &\sum_{k'=-\infty}^{\infty}(-1)^{k'} I_{k'}(w_y)e^{-2ik'(\varphi_y+\phi_y)}. \end{aligned} \tag{24}$$

The Fourier component, which correspond to resonance strength, is given by

$$\begin{aligned} U_{m_x,m_y}(J_x, J_y) = -\frac{\lambda_p r_p}{\beta^2\gamma^3}\oint ds \int_0^\infty \frac{du}{\sqrt{2\sigma_x^2+u}\sqrt{2\sigma_y^2+u}} \\ \left[\delta_{m_x 0}\delta_{m_y 0} - \exp(-w_{x\eta} - w_y)\sum_{l=-\infty}^{\infty}(-1)^{(m_x+l+m_y)/2} \right. \\ \left. I_{(m_x-l)/2}(w_x)I_l(v_x)I_{m_y/2}(w_y)e^{-im_x\varphi_x - im_y\varphi_y}\right]. \end{aligned} \tag{25}$$

where $m_x + l$ and m_y are even numbers.

The tune slope $\partial^2 U_{00}/\partial J_x^2$ induced by space charge potential is evaluated by $U_{00}(J_x, J_y)$ in Eq.(27).

$$\begin{aligned} U_{00}(J_x, J_y) = -\frac{\lambda_p r_p}{\beta^2\gamma^3}\oint ds \int_0^\infty \frac{dt}{\sqrt{2+t}\sqrt{2r_{yx}+t}} \\ \left[1 - e^{-w_{x\eta}-w_y}\sum_{l=-\infty}^{\infty}(-1)^l I_{l/2}(w_x)I_l(v_x)I_0(w_y)\right]. \end{aligned} \tag{26}$$

where $t = u/\sigma_x^2$ and $r_{yx} = \sigma_y^2/\sigma_x^2$ and

$$\frac{\partial}{\partial J_x} = \frac{\beta_x/\sigma_x^2}{2+t}\frac{\partial}{\partial w_x}. \qquad \frac{\partial}{\partial J_y} = \frac{\beta_y/\sigma_x^2}{2r_{yx}+t}\frac{\partial}{\partial w_y}. \tag{27}$$

The tune shift for on energy particle ($\delta = 0$) is given by derivative of U_{00} for J_{xy} as follows,

$$\begin{aligned} 2\pi\Delta\nu_x &= \frac{\partial U_{00}}{\partial J_x} \\ &= -\frac{\lambda_p r_p}{\beta^2\gamma^3}\oint ds\frac{\beta_x}{\sigma_x^2}\int_0^\infty \frac{e^{-w_x-w_y}dt}{(2+t)^{3/2}(2r_{yx}+t)^{1/2}} \\ &\left[(I_0(w_x) - I_1(w_x))I_0(w_y)\right], \end{aligned} \tag{28}$$

$$\begin{aligned} 2\pi\Delta\nu_y &= \frac{\partial U_{00}}{\partial J_y} \\ &= -\frac{\lambda_p r_p}{\beta^2\gamma^3}\oint ds\frac{\beta_y}{\sigma_x^2}\int_0^\infty \frac{e^{-w_x-w_y}dt}{(2+t)^{1/2}(2r_{yx}+t)^{3/2}} \\ &\left[I_0(w_x)(I_0(w_y) - I_1(w_y))\right], \end{aligned} \tag{29}$$

ISBN 978-3-95450-136-6

The tune slope for $\delta = 0$ is given by second derivative of U_{00} as follows,

$$\frac{\partial^2 U_{00}}{\partial J_x^2} = 2\pi \frac{\partial \nu_x}{\partial J_x} \tag{30}$$
$$= -\frac{\lambda_p r_p}{\beta^2\gamma^3} \oint ds \frac{\beta_x^2}{\sigma_x^4} \int_0^\infty \frac{e^{-w_x - w_y} dt}{(2+t)^{5/2}(2r_{yx}+t)^{1/2}}$$
$$\left[\left\{ \frac{3}{2} I_0(w_x) - 2I_1(w_x) + \frac{1}{2} I_2(w_x) \right\} I_0(w_y) \right],$$

$$\frac{\partial^2 U_{00}}{\partial J_x \partial J_y} = 2\pi \frac{\partial \nu_x}{\partial J_y} \tag{31}$$
$$= -\frac{\lambda_p r_p}{\beta^2\gamma^3} \oint ds \frac{\beta_x \beta_y}{\sigma_x^4} \int_0^\infty \frac{e^{-w_x - w_y} dt}{(2+t)^{3/2}(2r_{yx}+t)^{3/2}}$$
$$\left[(I_0(w_x) - I_1(w_x))(I_0(w_y) - I_0(w_y)) \right],$$

$$\frac{\partial^2 U_{00}}{\partial J_y^2} = 2\pi \frac{\partial \nu_y}{\partial J_y} \tag{32}$$
$$= -\frac{\lambda_p r_p}{\beta^2\gamma^3} \oint ds \frac{\beta_y^2}{\sigma_x^4} \int_0^\infty \frac{e^{-w_x - w_y} dt}{(2+t)^{1/2}(2r_{yx}+t)^{5/2}}$$
$$\left[I_0(w_x) \left\{ \frac{3}{2} I_0(w_y) - 2I_1(w_y) + \frac{1}{2} I_2(w_y) \right\} \right],$$

where formulae $I_0(x)' = I_1(x)$, $I_0(x)'' = (I_0(x) + I_2(x))/2$ are used.

The integral is performed using linear lattice information of J-PARC MR. Figure 1 shows tune spread ($\Delta\nu_{x,y}(J_x, J_y)$), slope ($\partial^2 U_0/\partial J_x^2$).

Figure 2 shows the tune slope ($U_{ij} = \partial^2 U_{00}/\partial J_i \partial J_j$).

Figures 3 and 4 show the resonance strengths of U_{30} and U_{40} for $(\nu_x, \nu_y) = (21.39, 21.43)$ and $(22.40, 20.75)$, respectively. For U_{30}, $l = 1$ term is taken with an energy deviation $\delta = \sigma_\delta = 0.1\%$. The resonance strength is an order of 10^{-7} m.

Resonance Strength Taking Into Account of Superperiodicity

J-PARC MR ring has superperiodicity of three, therefore resonances without $m_x\nu_x + m_y\nu_y = 3n$ is suppressed. It is sufficient to consider 1/3 ring under the perfect superperiodicity. New operating point, $(\nu_x, \nu_y) = (21.39, 21.43)$, $(\nu_x/3, \nu_y/3) = (7.13, 7.143)$. While present operating point, $(\nu_x, \nu_y) = (22.40, 20.75)$, $(\nu_x/3, \nu_y/3) = (7.4667, 6.9167)$, Higher order resonances are concerned now.

Figure 5 and 6 shows resonance strengths for $(\nu_x/3, \nu_y/3) = (7.13, 7.143)$ and $(\nu_x/3, \nu_y/3) = (7.4667, 6.9167)$, respectively. The resonance strengths are order of 10^{-9} m, while they are 10^{-7} m in above case of Figs.3 and 4. Since the resonance width scales square root of the strength, the width is one order smaller than that of above case.

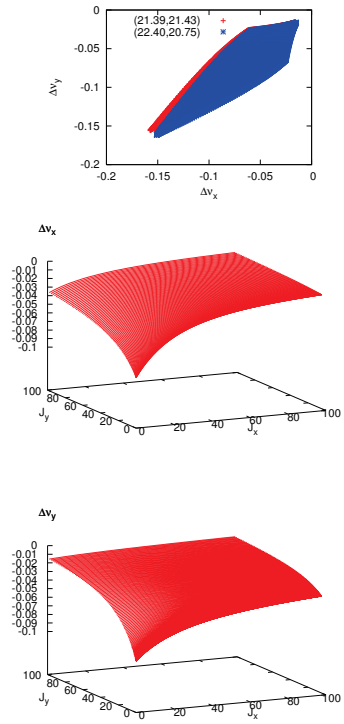

Figure 1: Tune spread ($\Delta\nu_{x,y}(J_x, J_y)$) due to space charge force.

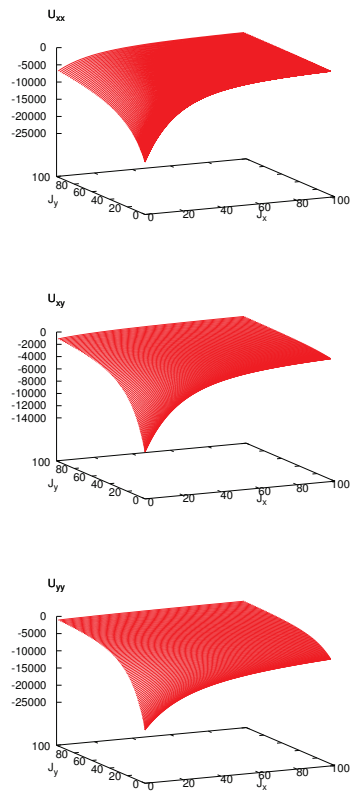

Figure 2: Tune slope ($U_{ij} = \partial^2 U_{00}/\partial J_i \partial J_j$) due to space charge force.

ISBN 978-3-95450-136-6

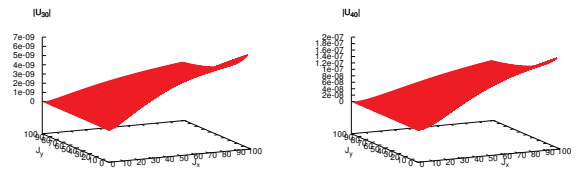

Figure 3: Resonance strengths (U_{30} and U_{40}) for $(\nu_x, \nu_y) = (21.39, 21.43)$ due to space charge force. $l = 1$ is taken into account for $m_x = 3$, where $\delta = \sigma_\delta = 0.1\%$.

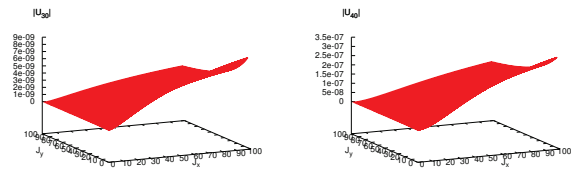

Figure 4: Resonance strengths (U_{30} and U_{40}) for $(\nu_x, \nu_y) = (22.40, 20.75)$ due to space charge force. $l = 1$ is taken into account for $m_x = 3$, where $\delta = \sigma_\delta = 0.1\%$.

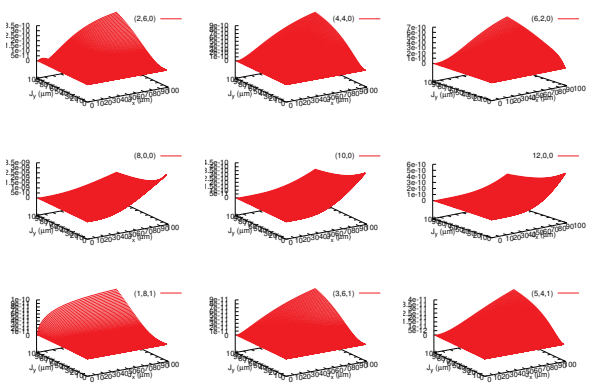

Figure 5: Resonance strengths under superperiodicty 3 for $(\nu_x, \nu_y) = (22.40, 20.75)$ due to space charge force. $l = 1$ is taken into account for odd m_x, where $\delta = \sigma_\delta = 0.1\%$.

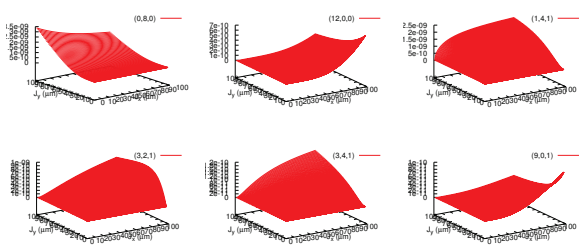

Figure 6: Resonance strengths under superperiodicty 3 for $(\nu_x, \nu_y) = (22.40, 20.75)$ due to space charge force. $l = 1$ is taken into account for odd m_x, where $\delta = \sigma_\delta = 0.1\%$.

Resonances Due to Nonlinear Magnets

Tune spread/slope and esonances are also induced by nonlinear magnets. One turn map is expanded by 12-th order polynomials for J-PARC MR. Taking at phase independent term, U_{00} is obtained as

$$\begin{aligned} U_{00}(\boldsymbol{J}) &= 3.43103\times10^{14}J_x^6 + 7.36914\times10^{14}J_x^5J_y + 7.17029\times10^{11}J_x^5 + 2.34124\times10^{15}J_x^4J_y^2 \\ &+ 1.70991\times10^{12}J_x^4J_y + 1.43961\times10^{8}J_x^4 + 4.48931\times10^{15}J_x^3J_y^3 + 2.20917\times10^{12}J_x^3J_y^2 \\ &+ 2.50211\times10^{8}J_x^3J_y + 613899.J_x^3 + 3.33998\times10^{15}J_x^2J_y^4 + 1.79716\times10^{12}J_x^2J_y^3 \\ &+ 7.07531\times10^{8}J_x^2J_y^2 + 809323.J_x^2J_y + 1095.71J_x^2 + 7.58773\times10^{14}J_xJ_y^5 \\ &+ 5.7438\times10^{11}J_xJ_y^4 + 4.55828\times10^{8}J_xJ_y^3 + 650655.J_xJ_y^2 + 2096.06J_xJ_y \\ &+ 4.11283\times10^{13}J_y^6 + 4.00294\times10^{10}J_y^5 + 5.3027\times10^{7}J_y^4 + 79924.4J_y^3 + 1106.98J_y^2 \end{aligned} . \quad (33)$$

Figure 7 shows the tune shift and slope. Typical tune slope is $\partial^2 U_{00}/\partial x^2 = 1000 \sim 3000$. Tune slope of space charge ($\sim 10{,}000$) is dominant for that of lattice nonlinearity at $J < 9\varepsilon(3\sigma)$, while it is similar for $U_{sc,00}$ at $J_x = 100\mu$ m.

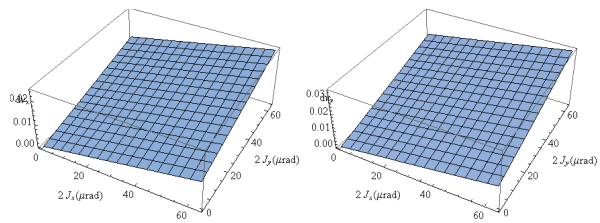

Figure 7: Tune spread ($\Delta\nu_{x,y}(J_x, J_y)$) induced by lattice nonlinearity.

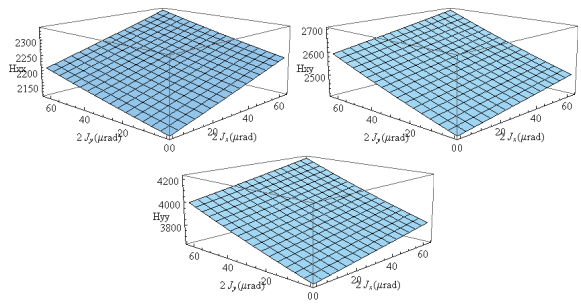

Figure 8: Tune slope ($\partial^2 U_{00}/\partial J_x^2$, $\partial^2 U_{00}/\partial J_x \partial J_y$ and $\partial^2 U_{00}/\partial J_y^2$) due to lattice nonlinearity.

Resonance strength due to lattice nonlinearity is also obtained by the one turn map. Table 1 shows the resonance strength $U_{m_x,m_y}(J)$. up to 4-th. Superperiodicity is not taken into account. The resonance strength, which is order of 10^{-7} m, is similar as the space charge induced resonances.

SIMULATION USING THE RESONANCE HAMILTONIAN

Without Synchrotron Motion

We study emittance growth for an accelerator model with a given tune slope and resonance strength. Hamiltonian is written explicity by real and imaginary parts of $U_{\boldsymbol{m}}$,

$$\begin{aligned} H &= \mu_x J_x + \mu_y J_y + U_0(J_x, J_y) \\ &+ U_{m,c}(J_x, J_y)\cos \boldsymbol{m}\cdot\boldsymbol{\phi} + U_{m,s}(J_x, J_y)\sin \boldsymbol{m}\cdot\boldsymbol{\phi}. \end{aligned} \quad (34)$$

ISBN 978-3-95450-136-6

Table 1: $U_{m_x,m_y}(J)$ for Lattice Nonlinearity. U's are evaluated at J 3rd and 4-th column. The suffix, B0,B and BR means lattices without errors, lattice with measured beta and measured beta and coupling [3].

mx	my	Jx	Jy	|Um| (B0)	|Um| (B)	|Um| (BR)
1	0	3.6E−05	0.0E+00	4.84E−08	1.88E−07	1.86E−07
2	0	3.6E−05	0.0E+00	2.47E−08	4.55E−08	4.66E−08
1	1	1.8E−05	1.8E−05	1.28E−25	1.67E−26	4.01E−09
0	2	0.0E+00	3.6E−05	5.55E−09	3.91E−09	2.69E−09
3	0	3.6E−05	0.0E+00	5.46E−08	1.29E−07	1.32E−07
2	1	1.8E−05	1.8E−05	2.09E−25	1.42E−26	1.42E−07
2	−1	1.8E−05	1.8E−05	2.16E−25	4.52E−27	7.96E−08
1	2	1.8E−05	1.8E−05	4.66E−08	1.78E−07	1.83E−07
1	−2	1.8E−05	1.8E−05	1.48E−07	2.72E−07	2.72E−07
0	3	0.0E+00	3.6E−05	1.42E−25	1.59E−26	1.10E−07
4	0	3.6E−05	0.0E+00	2.50E−07	2.51E−07	2.51E−07
3	1	1.8E−05	1.8E−05	1.93E−26	2.52E−27	6.80E−09
3	−1	1.8E−05	1.8E−05	1.61E−26	4.97E−27	7.04E−10
2	2	1.8E−05	1.8E−05	2.49E−08	5.90E−09	5.58E−09
2	−2	1.8E−05	1.8E−05	1.27E−08	8.40E−09	8.03E−09
1	3	1.8E−05	1.8E−05	2.52E−26	5.66E−27	3.56E−09
1	−3	1.8E−05	1.8E−05	1.63E−26	1.10E−26	8.42E−10
0	4	0.0E+00	3.6E−05	1.20E−08	1.45E−08	1.42E−08

where $m\phi = m_x\phi_x + m_y\phi_y$. Symplectic transformation for above Hamiltonian is expressed by

$$\begin{aligned} \bar{\phi}_i &= \phi_i + \frac{\partial U_0}{\partial J_i} + \frac{\partial U_{m,c}}{\partial J_i}\cos m\phi - \frac{\partial U_{m,s}}{\partial J_i}\sin m\phi \\ J_i &= \bar{J}_i - m_i(U_{m,c}\sin m\phi - U_{m,s}\cos m\phi). \end{aligned} \quad (35)$$

where $\bar{J}$ and $\bar{\phi}$ are those after the transformation, and U_m's are function of $\bar{J}_i$ and ϕ_i. Second equation of Eq.(35) is implicit relation. To solve $(\bar{J},\bar{\phi})$, Newton-Raphson method is used.

$$f_x = \bar{J}_x - J_x - m_x(U_{m,c}\sin m\phi - U_{m,s}\cos m\phi) = 0$$

$$f_y = \bar{J}_y - J_y - m_y(U_{m,c}\sin m\phi - U_{m,s}\cos m\phi) = 0. \quad (36)$$

Iteration of Newton method is expressed by

$$\begin{pmatrix} \bar{J}_x \\ \bar{J}_y \end{pmatrix}_{n+1} = \begin{pmatrix} \bar{J}_x \\ \bar{J}_y \end{pmatrix}_n - F^{-1}\begin{pmatrix} f_x \\ f_y \end{pmatrix}_n. \quad (37)$$

where F is Jacobian matrix for f_i; $F_{ij} = \partial f_i/\partial J_j, i,j = x,y$.

The resonance width is estimated by the tune slope and resonance strength seen in Figs.2, 3 and 4. The estimeted resonance width agrees well with the width seen in Figure 9.

$$\Delta J_x = 4\sqrt{\frac{U_m}{\partial^2 U_{00}/\partial J_x^2}} = 4\sqrt{\frac{10^{-7}}{10^4}} = 12\times10^{-6}\mathrm{m} = 12\mu\mathrm{m} \quad (38)$$

With Synchrotron Motion

Synchrotron motion is treated as an external force oscillation

$$z = z_0\cos(\mu_s s/L) = z_0\cos(\mu_s n_{turn}) \quad (39)$$

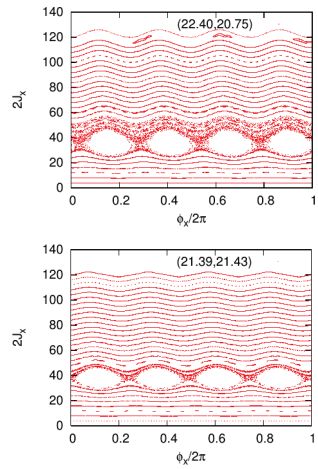

Figure 9: Phase space trajectory for the model map with U_{40}. No synchrotron motion. Left and right plots correspond to tune (22.40,20.75) and (21.39,21.43), respectively.

Beam charge density depends on z.

$$\lambda(z,s) = \frac{N_p}{\sqrt{2\pi}\sigma_z}\exp\left(-\frac{z(s)^2}{2\sigma_z^2}\right) \quad (40)$$

The resonance amplitude ($\boldsymbol{J}_R$) and width (ΔJ are modulated by the synchrotron motion. The resonance structure moving and changing width in the phase space. Phase space lower amplitude than the resonance structure in Fig.9 is filled in chaotic area [4]. Therefore emittance growth is enhanced by the synchrotron motion. Figure 10 shows phase space plot with synchrotron motion.

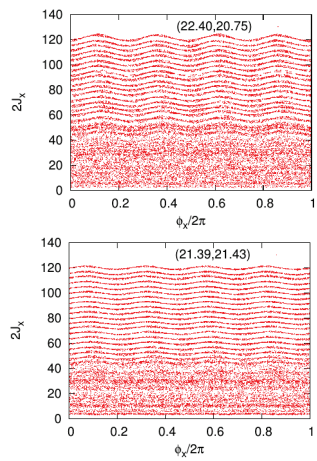

Figure 10: Phase space trajectory for the model map with U_{40}. Synchrotron tune, $\nu_s = 0.002$, $z_0 = \sigma_z$. Left and right plots correspond to tune (22.40,20.75) and (21.39,21.43), respectively

Diffusion of J characterizes emittance growth. To calculate of diffusion rate of J, initializing $\delta(\boldsymbol{J}-\boldsymbol{J}_0)$ and uniform $\boldsymbol{\phi}$, an evolution of spread of $\boldsymbol{J}$ is calculated. Figure 11 shows evolution of the spred of J_x. Top and bottom are given for without and with synchrotron motion. Diffusion of J with

ISBN 978-3-95450-136-6

synchrotron motion is larger than those without synchrotron motion. All particles $J_x < 40\mu$m diffuse for finite ν_s, while limited particles $J_x = 30$ and 40 have large ΔJ, but not diffusive.

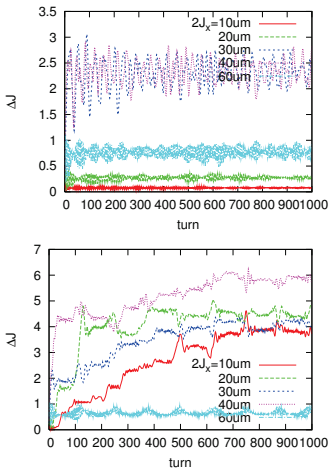

Figure 11: Diffusion of J. Top is for no synchrotron moiton. Bottom is for Synchrotron tune, $\nu_s = 0.002$, $z_0 = \sigma_z$.

SUMMARY

- Emittance growth based on chaos near resonances.
- Tune shift and slope for space charge and lattice is evaluated.
- Resonance terms for space charge and lattice is evaluated.
- Resonance fixed point and width are determined by the tune slope and resonance strength.
- Simulation of a model baed on the tune and resonance information is being performed.
- Emittance growth is evaluated by combination with Synchrotron motion
- Simulations for Multi-resonances will be performed.
- Simulations taking into account of superperiodicity and erros of beta.will be performed.

REFERENCES

[1] J. L. Tennyson, AIP Conference proceedings, 87, 345(1982).

[2] K. Ohmi et al., WEO2LR03, proceedings of HB2014.

[3] K. Ohmi et al., THO1B03, proceedings of HB2012.

[4] K. Ohmi and K. Oide, Phys. Rev. ST-AB **10**, 014401 (2007).

ISBN 978-3-95450-136-6

MODELING AND SIMULATION OF PHOTOEMISSION BASED ELECTRON SOURCES*

Y. Chen†1), E. Gjonaj1), H. De Gersem1), T. Weiland1),
M. Krasilnikov2), C. Hernandez-Garcia2)4), F. Stephan2), M. Dohlus3)

1) TEMF, Technische Universitaet Darmstadt, Schlossgartenstraße 8, 64289 Darmstadt, Germany
2) DESY, Platanenallee 6, 15738 Zeuthen, Germany
3) DESY, Notkestraße 85, 22607 Hamburg, Germany
4) Jefferson Lab, Newport News, VA 23606, USA

Abstract

Photoemission based electron source allow producing electron beams with precisely controlled temporal and spatial profiles, high current and high brightness. Their development is critical to future short-wavelength light sources. To accurately characterize electron beams generated by the source, a full electromagnetic emission modeling is carried out in a self-consistent manner. It takes into account the Schottky-like modulation of the cathode quantum efficiency (QE). In pulsed operation, this effect causes the QE of the cathode to be time dependent. Thus, the electron bunch temporal profile is not the same as the laser pulse profile and it should be corrected according to this model. As an application, the PITZ injector installed at the DESY site in Zeuthen is considered. The emission process is modeled in the QE- and SC-limited (space-charge) regimes, respectively. Simulation results are in good agreements with the measurement data.

INTRODUCTION

Photoemission based electron sources are widely used to generate high brilliance electron beams for coherent light sources [1–3]. Photoemission is a highly nonlinear process depending on the properties of the photocathode as well as on the dynamics of the charged particle beam in immediate vicinity of the cathode. These effects are, furthermore, mutually dependent. Specifically, the nonlinear space-charge (SC) field during photoemission can modulate the quantum efficiency (QE) of the semiconductor layer due to Schottky effect [4], while the cathode QE modifies the electron bunch distribution thereby influencing the beam dynamics in the gun. Thus, the approach used in beam dynamics simulations assuming a fixed particle distribution at the cathode may be inaccurate.

The main goal of this paper is to resolve this modeling issue, by developing a nonlinear SC field dependent dynamic emission model. The model takes into account the work function modification of the emitting layer due to the total field applied at the cathode. This includes the dc- (or rf-) cavity field of the gun as well as the SC field of the beam. In particular, in pulsed source operation this model results in a time-dependent QE of the photocathode. Thus, the longitudinal profile of the emitted electron beam is no longer the same as the temporal profile of the cathode-illuminating laser pulse. Yet another effect is that, the near-cathode SC effects also affect the QE map of the cathode thus modifying the transverse distribution of the extracted electron beam. All these effects should be considered in the emission modeling and beam dynamics simulations.

As an application, the PITZ photoinjector [1–3] offers a good opportunity to validate our theoretical model and numerical simulation with measurement data. In the PITZ injector a Cs_2Te photocathode is illuminated by a UV laser at the wavelength of 257 nm. In the following, we will describe the simulation procedure and then show the results obtained for the PITZ gun in the QE- and SC-limited emission regimes, respectively.

PHOTOEMISSION MODELING

Schottky-like Effect

This effect results from the reduction of the work function of the cathode material due to the presence of high electric fields applied. The QE of the cathode including the Schottky-like effect is given by [4]:

$$QE\,(x,y,t) = \eta\{h\nu - [\Phi_w \mp \beta\Delta\Phi\,(x,y,t)]\}^2. \quad (1)$$

$$\Delta\Phi\,(x,y,t) = \sqrt{\frac{e^3}{4\pi\epsilon_0}E_{cath}\,(x,y,z=0,t)}. \quad (2)$$

where $h\nu$, Φ_w and $\Delta\Phi$ are the laser photon energy, the cathode work function with no applied fields, and its reduction due to Schottky effect, respectively. E_{cath} represents the total normal electric field at the cathode. β is known as the field enhancement factor which is used to characterize surface conditions of the emission area. η is a form factor depending on material properties such as absorption coefficient, density of states and transition probability.

The total electric field at the cathode E_{cath} is a superposition of all dc and rf fields within the gun including the SC field of the beam. These fields are time and space dependent. Thus, the resulting QE of the cathode will generally vary with time as well as along the cathode surface.

Given expressions (1) and (2) for the cathode QE, the total emitted charge is given by [4]:

* Work supported by DESY Hamburg and Zeuthen. PITZ: the Photo Injector Test Facility at DESY in Zeuthen, Berlin, Germany
† chen@temf.tu-darmstadt.de

ISBN 978-3-95450-136-6

$$Q_{tot}(\eta; x, y, t) = \eta \int_{t_0}^{t} \int_x \int_y e \frac{P_{las}(\tau)}{h\nu} \times \{h\nu - \left[\Phi_w - \beta \sqrt{\frac{e^3}{4\pi\epsilon_0}} E_{cath}(x, y, z = 0, t)\right]\}^2 dx dy d\tau. \quad (3)$$

where P_{las} is the power of the laser pulse.

As seen from Eq. (3), due to the Schottky effect, the emitted charge profile is generally not identical with the laser pulse shape. Likewise, the transverse distribution of the electron bunch, $Q_{tot}(x, y)$ is no longer uniform over the emission area, because the QE map is modified by the nonuniform space-charge field at the cathode. In order to calculate the total extracted bunch charge, however, the characteristic cathode factor is needed. This parameter can be determined by contrasting simulation and measurement results for a selected set of operation parameters as described below.

Cathode Characterization

The cathode characterization is conducted based on measurement data to take into account the contributions of the cathode material properties to the emission process. A self-consistent numerical approach has been designed to determine the cathode factor, η. The main procedure is shown in Fig. 1. Essentially, the emission process is computed iteratively starting with a guess value for the cathode factor. In every step of the iteration, the cathode factor is corrected such that the total predicted charge is the same as a measured value Q_{meas}. This procedure is repeated until numerical converge is reached. The cathode factor determined from this approach is used for simulations involving different sets of gun and beam parameters.

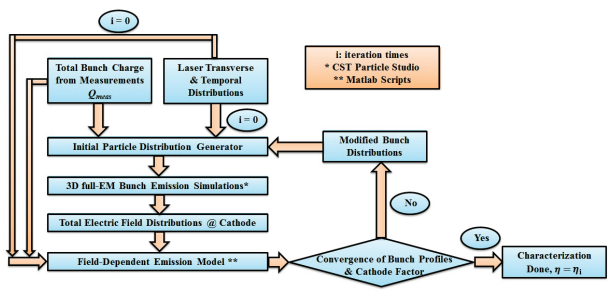

Figure 1: Iterative simulation scheme for photocathode characterization.

Model Implementation

For model implementation, a 3D full electromagnetic tracking code is used, taking into account multiple effects of space-charge, image-charge and also relativistic field effects during photoemission [5, 6]. The code is based on a Lienard-Wiechert (LW) Particle-Particle (PP) interaction approach. It stores particle history and searches at every time step retarded times and positions for all beam particles [7]. In addition, the total rf and particle fields at the cathode are computed on-the-fly as a new particle is emitted. This allows to compute the individual (macro-) particle charges according to the modified emission model (3).

APPLICATION

Using the above simulation approach, a series of electron bunch emission simulations are performed for the Cs_2Te photocathode 1.6-cell copper rf photogun of PITZ and compared with measurements [2, 3, 8].

Figure 2 shows the dynamic Schottky-like modulation of the cathode QE on the right axis (blue curve) in comparison to the case without Schottky effect (dashed grey curve). Accordingly, time-dependent QE-induced modification of the transient bunch current distribution (red curve) is shown for a flattop-shaped cathode laser temporal profile of about 27 ps in total length (black curve). The maximum field gradient is about 46 MV/m. The QE slightly increases during moments of emission due to the fact that the applied rf field in the cavity reduces the work function of the cathode material. Then it gradually drops as the SC field of the beam is built up. Likewise, the QE tends to increase again at the end of emission as the SC density declines with more emitted particles escaping from the cathode region. This results in a corresponding modification of the emitted charge profile (red curve).

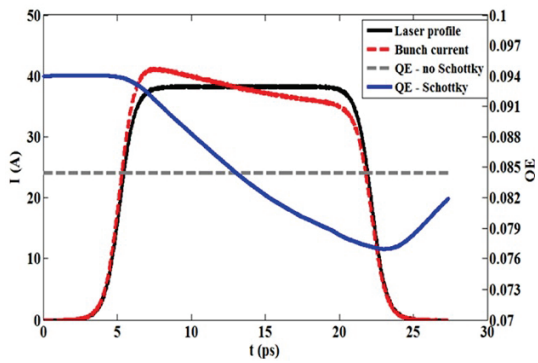

Figure 2: Dynamic QE-modulation due to Schottky effect and transient bunch current for a flattop laser profile.

Figure 3 shows the Schottky modification of the QE map on the transverse plane at different time instants. Note that this transverse QE modification is only due to the space charge field of the bunch at the position of the cathode. The QE map is homogeneous in the beginning of emission. As seen in the figure, a stronger SC field in the central area of the beam reduces the total field over this area of the cathode. This causes a relative decrease in the QE of the central area (left). This effect leads to QE variations between the center and the edge of the emission area by approximately 9% (right) by the end of emission for the extraction of 1 nC bunch charge using an rms cathode laser spot size of 0.4 mm.

Figure 4 shows comparisons for the total extracted bunch charge between measurements and simulations in terms of the cathode laser pulse energy. This is conducted for three

ISBN 978-3-95450-136-6

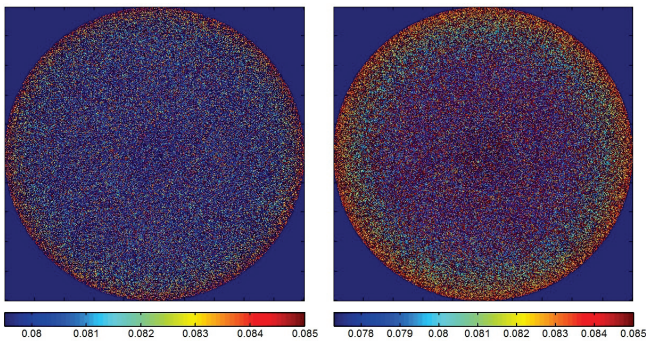

Figure 3: Transverse modulation of QE due to the dynamic Schottky effect at the cathode at different time instants. The total emission time is about 30 ps. Left: t =16 ps; Right: t = 30 ps.

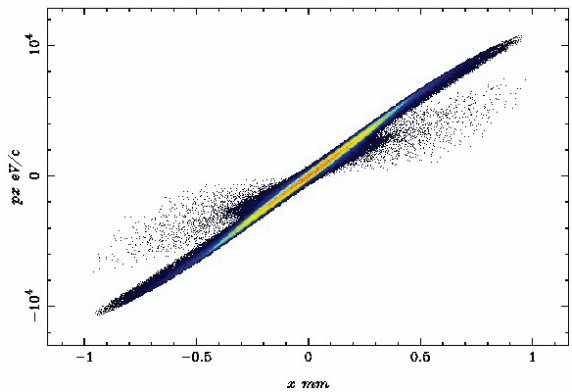

Figure 5: Transverse phase space for a 0.1 nC electron bunch at the first emittance measurement station.

photocathodes in different conditions using two rf gun powers of 7.75 and 1.5 MW, and two temporal cathode laser profiles of 17 ps (FWHM) flattop and 1.5 ps (RMS) Gaussian, respectively. In all cases the total produced charge increases nearly linearly with the laser pulse energy. This is consistent with the charge extraction mechanism in the QE-limited emission regime [6]. Good agreements are reached between measurements and simulations. That is, the Schottky-based dynamic emission model is able to well predict the total extracted bunch charge from the cathode.

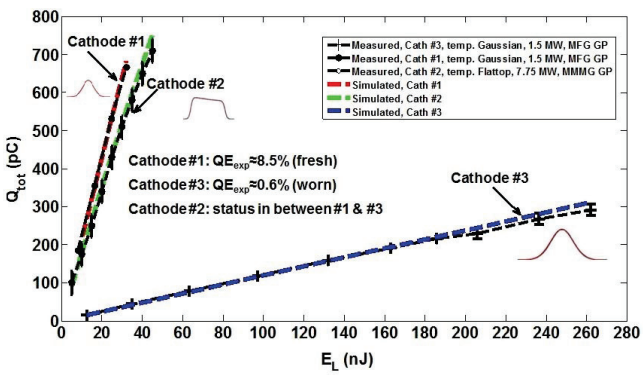

Figure 4: Total bunch charge versus laser pulse energy for three cathodes in different conditions using various machine parameters. MMMG: maximum mean momentum gain. MFG: maximum field gradient. GP: gun phase.

To further verify the emission model, a comparison of the bunch transverse emittance between simulation and measurement is performed. Using this model, a 0.1 nC electron bunch is extracted from the cathode and tracked to the first emittance measurement station at z = 5.74 m, as shown in Fig. 5. A flattop temporal profile of the cathode laser pulse with 21.5 ps FWHM is applied. The rms laser spot size is 0.102 mm. The peak rf electric field at the cathode is about 60 MV/m. The simulation shows an optimized transverse bunch emittance of 0.19 mm mrad, which agrees with the measured minimum transverse emittance of about 0.21 mm mrad [2].

CONCLUSIONS

A Schottky-based dynamic photoemission model is proposed and implemented with the 3D LW PP code. This model is able to modify the temporal and transverse distributions of the emitted electron bunch from cathode in transient emission process, by modulating the photocathode QE through Schottky effect. The SC effects in the gun cavity are included in the modeling which allows to take into account the transverse modification of the QE map. For validation, the model has been used in the photoemission studies of the PITZ injector. The total extracted bunch charges calculated from simulations coincide with measurements in the QE-limited emission regime for different photocathodes under distinct experimental conditions. A comparison of the bunch transverse emittance for a 0.1 nC bunch charge also shows a good agreement with measurement. Further modelings and simulations using this model for the SC-limited emission regime are still in progress.

REFERENCES

[1] Frank Stephan, Technical report: High Brightness Photo Injectors for Brilliant Light Sources, DESY, Germany (2014).

[2] M. Krasilnikov et al., PRST-AB 15, 100701 (2012).

[3] F. Stephan et al., PRST-AB 13, 020704 (2010).

[4] I. Copper et al., Phys. Rev. 185 882 (1969).

[5] Y. Chen et al., IPAC'14, Dresden, p. 391 (2014).

[6] Y. Chen et al., IPAC'15, Richmond, VA, USA, p. 162 (2015).

[7] E. Gjonaj, DESY-TEMF Meeting, Hamburg (2011).

[8] M. Krasilnikov, DESY-TEMF Meeting, Darmstadt (2013).

ISBN 978-3-95450-136-6

DISTRIBUTED MATCHING SCHEME AND A FLEXIBLE DETERMINISTIC MATCHING ALGORITHM FOR ARBITRARY SYSTEMS

Yu-Chiu Chao, TRIUMF, Vancouver BC V6T 2A3, Canada

Abstract

Paradigm complementary to conventional betatron matching is explored, with matching distributed over the entire line. This can have varying degrees of advantage over a conventional scheme.

In conjunction, a matching algorithm was developed for any line configuration, coupled 4D included, giving deterministic, rigorous optimal solutions spanning entire tradeoff curve between mismatch and quad strength, thus allowing insight and control pre-implementation. It also shows promise of attaining global optimum. Combined with distributed matching this algorithm displays further advantages of speed, determinism and flexibility.

DISTRIBUTED MATCHING AND INTERPOLATED SOLUTION

Matching either beam ellipse or optical transport to design, in either XY coupled or uncoupled environments, has been one of the most important accelerator operation topics inspiring constant algorithmic investigation [1]. A configuration premise common to all these approaches is that the matching occurs locally, within a dedicated matching section of quadrupoles and skew quadrupoles. The current report aims to free the control paradigm from this premise and develop a supporting algorithm to enable this paradigm shift. Its implication can extend beyond matching.

Distributed vs Local Matching Configuration

Control of accelerator and beam properties follows two distinct paradigms in terms of geometrical configuration: Distributed and Localized. These two paradigms are often characterized and justified by cost vs performance.

Localized Control

- Limited/Costly/Bulky hardware (monitor and actuator)
- Little chance of cumulative/compounded error
- Damage mostly confined to local areas
- Example: Dispersion, Bunch length, Energy Spread

Distributed Control

- More affordable and compact monitors and actuators
- Errors accumulate & compound throughout entire line
- Damage arises everywhere and is irreversible
- Example: Transverse orbit

Transverse matching shares almost all characteristics with parameters controlled in a distributed scheme, given the following features of modern accelerator systems:

- Beam profile diagnostics often form adequate coverage throughout a beam line.
- Even more dense BPM coverage has been exploited to provide AC or DC measurements of optical transport in accelerators [2].
- Quadrupoles, the actuators for matching, typically far outnumber orbit correctors.
- Beam and optical mismatch is not a local problem. It emerges and compounds at all locations and from all sources, and its adverse effects impact all sections of a beam line.

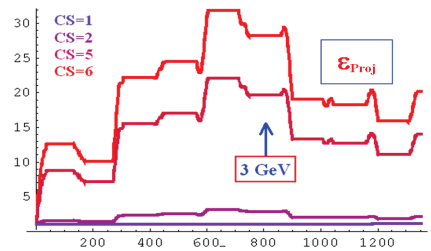

Figure 1: Projected Emittance for Various Initial Mismatch Propagated through 5 Pass CEBAF

Of the last point, cumulative mismatch not only results in excessive beam envelope and tail, it can cause more subtle damages as shown in Figure 1 [3], in which are plotted evolution paths of beam projected emittance in the Jefferson Lab CEBAF accelerator under different mismatch parameters (CS), with CS=1 for completely matched beam. Due to slight un-cancelled skew quad terms in the linac HOM couplers, the projected emittance inevitably grows. However this growth can be kept under control with a globally matched beam (CS=1). Once the projected emittance grows out of bound, no amount of quadrupole matching can bring it down. Other factors that can be exacerbated by mismatch include geometrical aberrations, nonlinear dispersive effects such as T_{512}, etc.

The reason for matching to become a localized control process, apart from specific functionality concerns, may be that historically anything less than fully matched optics out of a matching process is considered unacceptable, with no systematic procedure to evaluate its consequence or identify the follow-up action. Thus the problem is resolved by designed-in sections that must achieve 100% matching within themselves, and nowhere else. The following issues can arise with this paradigm:

- Design flexibility is limited by matching sections
- Cumulative mismatch causes problem everywhere, but is addressed only near matching sections.
- Cumulative mismatch causes excessive quad strengths.
- Excessive matching quad strengths cause local blowup.
- With all matching concentrated in localized places, there is no recourse if the solution fails.

A side product of the localized matching paradigm is often a black box optimization engine responsible for matching the beam or optics to 100%. Depending on the engine, further issues can be introduced:

- (Beam) time consuming

ISBN 978-3-95450-136-6

- Unpredictable/Inconsistent outcome
- Lack of option/insight/control on the user's part

By allowing the possibility of partial matching spread over the entire beam line, coupled to an interpolation scheme that does away with inefficiency and uncertainty, a distributed matching scheme may prove competitive where the above issues are acute, and it also leads to a rigorous and deterministic matching algorithm with physically consistent and unambiguous interpretation.

Segmentation of Matching Sections

In a distributed matching scheme the entire beam line is segmented into sections, all contributing to the reduction of mismatch in an adiabatic manner. The segmentation is flexible and the sections need not be contiguous. Any special-purpose modules, such as RF or dispersion suppressor, can be either left out or embedded inside a matching section, as indicated in Figure 2.

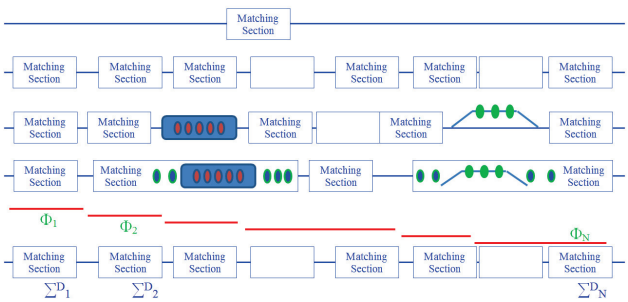

Figure 2: Concept of distributed matching. Top to bottom: (a) Localized matching (b) Segmentation into distributed matching sections, (c) Special modules left out, (d) Special modules embedded, (e) Adiabatic reduction of mismatch Φ by partially matching to design beam covariance Σ^D at end of each section.

Interpolation Scheme

The design twiss Σ^D at end of each section in Fig. 2 is a constant. This begs the question of why matching has to be done repeatedly, and likely haphazardly, by a black box engine using beam time. Thus we look into implementing the distributed matching scheme via interpolation on pre-calculated partial matching solutions for each section. This has the following advantages:

- Speed: No online optimization needed
- Determinism: Best solution worked out a priori
- Flexibility/Controllability: User options on matching scenario such as profile of tapering mismatch Φ
- Insight into the problem can be gained given a competent offline process.

A competent algorithm will be introduced later in the note. But firstly this concept using a more naïve algorithm is demonstrated in Figure 3 for a FODO lattice with 120° phase advance. Each matching section contains 3 quads. With initial mismatch factor as high as 9, in 7 sections the beam is totally matched. Due to the large phase advance between quads, this process is not overly demanding numerically.

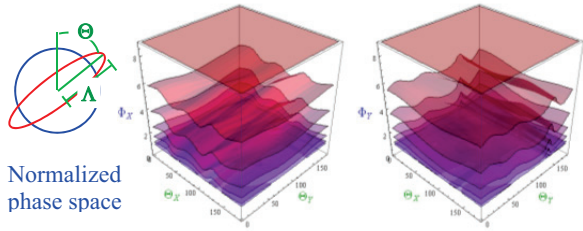

Figure 3: Applying distributed matching to a 120° lattice. Initial mismatch of Φ=9 in both X & Y is launched into the line, with mismatch angle Θ covering entire range of 0 to π. The color sheets represent the evolution of $\Phi_{X/Y}$ at all initial $\Theta_{X/Y}$ through 7 distributed matching sections. Solution at each section is interpolated from offline table.

RIGOROUS DETERMINISTIC MATCHING ALGORITHM

Trade-off Between Objective and Constraint

By allowing the possibility of partial matching solutions we have the opportunity of rigorously examine the interplay between matching objective and other factors limiting it. The canonical approach for studying this interplay is that due to Lagrange

$$\begin{cases}\nabla F = \lambda\cdot\nabla H \\ H = h\end{cases} \rightarrow \; k_1^o, k_2^o, k_3^o, \ldots k_N^o, \lambda^o \rightarrow \; F = f(h)$$

where an objective function F of k_m to be optimized is subject to constraint function H of the same k_m. The solution is obtained by imposing the tangency condition with an arbitrary variable λ, and specifying the particular value of H=h. This amounts to asking what the optimal value is for F as a function of h. By scanning over h we get a complete picture of the objective F played against the constraint H in a locally optimal sense everywhere. Equivalently, one can scan f, or even λ, to get an alternative view of the same trade-off [4].

$$\begin{cases}\nabla F = \lambda\cdot\nabla H \\ F = f\end{cases} \rightarrow \; k_1^o, k_2^o, k_3^o, \ldots k_N^o, \lambda^o \rightarrow \; H = h(f)$$

$$\nabla F = \lambda\cdot\nabla H \rightarrow \quad k_1^o, k_2^o, k_3^o, \ldots k_N^o \rightarrow \begin{cases}F = f(\lambda) \\ H = h(\lambda)\end{cases}$$

The three formulations above for mapping out trade-off between objective and constraint can be shown to lead to differential relations between the optimal solution $\boldsymbol{k} = (k_1^o, k_2^o \ldots k_N^o)$ and f, h or λ:

$$\left.\frac{d\boldsymbol{k}}{df}\right| = \frac{1}{\lambda}\cdot\frac{\boldsymbol{M}^{-1}\cdot\boldsymbol{R}}{\boldsymbol{R^T}\cdot\boldsymbol{M}^{-1}\cdot\boldsymbol{R}} = \frac{1}{\lambda}\cdot\frac{Adj(\boldsymbol{M})\cdot\boldsymbol{R}}{\boldsymbol{R^T}\cdot Adj(\boldsymbol{M})\cdot\boldsymbol{R}}$$

$$\left.\frac{d\boldsymbol{k}}{dh}\right| = \frac{\boldsymbol{M}^{-1}\cdot\boldsymbol{R}}{\boldsymbol{R^T}\cdot\boldsymbol{M}^{-1}\cdot\boldsymbol{R}} = \frac{Adj(\boldsymbol{M})\cdot\boldsymbol{R}}{\boldsymbol{R^T}\cdot Adj(\boldsymbol{M})\cdot\boldsymbol{R}}$$

$$\left.\frac{d\boldsymbol{k}}{d\lambda}\right| = \boldsymbol{M}^{-1}\cdot\boldsymbol{R}, \;\; \boldsymbol{k} = \left(k_1^o(\lambda), k_2^o(\lambda), \ldots k_N^o(\lambda)\right)$$

$$\boldsymbol{M_{ij}} = \frac{\partial^2(F(\boldsymbol{k}) - \lambda\cdot H(\boldsymbol{k}))}{\partial k_i \partial k_j}, \;\; \boldsymbol{R_i} = \frac{\partial H(\boldsymbol{k})}{\partial k_i}$$

$$Adj(\boldsymbol{M}) = Cof(\boldsymbol{M})^{\boldsymbol{T}} = Det(\boldsymbol{M})\cdot\boldsymbol{M}^{-1}$$

where the vertical bar limits the derivative to be taken only along the 1-dimensional curve of optimal tradeoff. The above formulas in principle make possible a

ISBN 978-3-95450-136-6

deterministic program of integration from optimal constraint to optimal objective and vice versa, including all optimal tradeoff solutions in between. Of the 3 differential relations, the one w.r.t. λ is most crucial:

- This formulation has universal starting (-∞) and ending (0) values for λ, independent of problem detail, thus giving unequivocal start and end points of the process.
- Integration over f and h alone will encounter singularities ($\boldsymbol{R^T} \cdot Adj(\boldsymbol{M}) \cdot \boldsymbol{R}$ =0) that can be resolved only by complementary process over λ at these points.

Betatron Matching Algorithm

For the most generic 4D betatron matching problem under constraint of minimal RMS deviation of N_Q quadrupole strengths from design, we take

$$F = \frac{1}{4} Tr\left(\Sigma_D^{-1} \cdot M(k_m) \cdot \Sigma_R \cdot M^T(k_m)\right)$$

$$m = 1, 2, \ldots N_Q$$

$$\Sigma^{ij} = \frac{1}{n}\sum_{k=1}^{n} x_k^i \cdot x_k^j \quad i,j = 1,2,3,4$$

$$H = \sum_{m=1}^{N_Q} (k_m^R - k_m^D)^2 = \sum_{k=1}^{N_Q} \delta k_m{}^2$$

where Σ_D and Σ_R are the design and real beam covariance and M the transfer matrix of the N_Q quad section. F can be regarded as a 4D extension of the 2D mismatch factor. The generic formulation allows using other performance objectives and constraints, although the example above is very well behaved even for very difficult optics. Figure 4 shows a representative case where the entire tradeoff is mapped out for a 6 quad, 30° per cell FODO lattice. This is a much more difficult problem numerically than the 120° case numerically due to low phase advance. Robustness and ability to reach the final optimum of the algorithm are explained in the caption. The true power of this algorithm is revealed in Figure 5 showing the same solution plotted in the *h–f* plane. While a typical local optimization algorithm might have stopped at f=1.00013 (C2 of Fig. 4) and declared success, it is clear from the current algoithm that the optimization as not stopped until λ=0, and we are rewarded with a much lower RMS quad strength. This characteristic property of the algorithm allows us to extract a simple subset of the complex solution path that corresponds to the "global" optimum for both objective and constraint, as shown in Fig. 5.

Additional tests of the algorithm, including restoring transport error causing mismatch factor up to several 1000 further demonstrate its robustness, self-consistency, and very low demand for human intervention in terms of fine tuning run parameters, an important feature if this algorithm is to be used for generating massive interpolation tables. We are also looking into expanding the repertoire of objectives and constraints, to functions such as weighted mismatch factor, weighted or absolute quad RMS, phase advance, matrix elements, etc. Even if the optima for these functions are not known a priori, the algorithm introduced here can take advantage of the known trivial optimum for H, at $\delta k_m = 0$, to integrate to the optima at either the new objective or constraint [4].

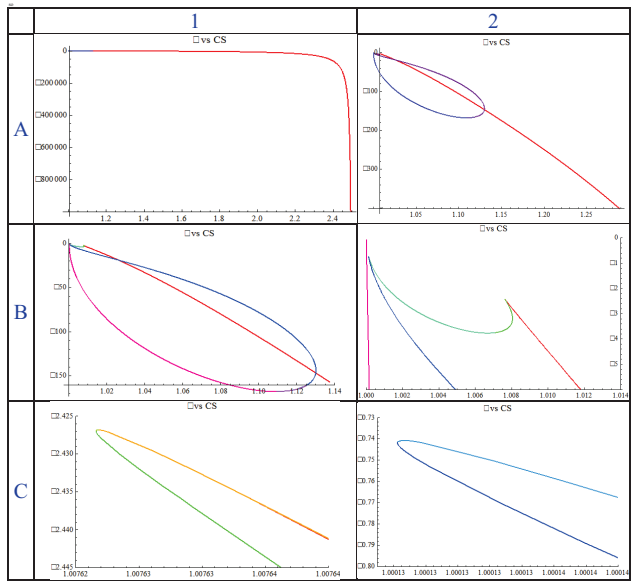

Figure 4: Entire solution path in the *λ–f* plane for a 6-quad 30° per cell FODO lattice, zoomed at different locations. A1: Global solution path starting at (f=2.5, $\lambda \to -\infty$), ending at (f=1, λ=0). A2: Zoomed in for detail toward the end. B1: Further zoom. B2: Near the point λ=0 and f=1: The path first approaches absolute optimum near f=1.0076, then at f=1.00013 (!), then executing a loop all the way down to f=1.14 before turning around and reaching the true f=1 point, shown by the red line on the extreme left.. C1: Zoom in around f=1.0076, the turn-around on the right in B2. C2: Zoom in around f=1.00013, the turn-around on the left in B2.

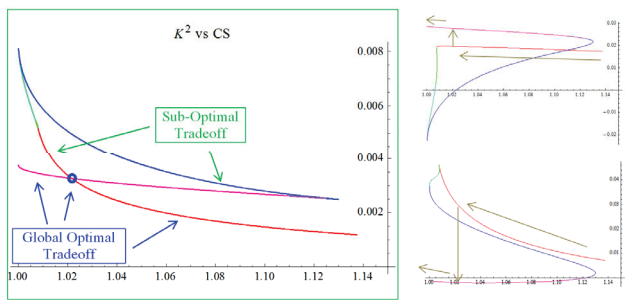

Figure 5: Left: Solution path in the h–f plane roughly corresponding to B1 in Figure 4. By insisting on not stopping at f=1.00013 and press on to λ=0, we reached the true `global` optimum with a much lower RMS quad strength. This illustrates how a globally optimal tradeoff curve can be extracted by joining the red section with the magenta section at the intersection (blue circle), and discard everything above and to the right.
Right: Examples showing two quadrupole k vs f plots with the path of globally optimal tradeoff indicated by gold arrows. Start with the red curve, then jump to the magenta curve at f(CS)=1.02, the blue circle location on the left plot. The fact that λ is negative everywhere makes this process unambiguous for both f and h.

ISBN 978-3-95450-136-6

REFERENCES

[1] See for example Y. Chao, "A Full-Order, Almost-Deterministic Optical Matching Algorithm", Proceedings of the 2001 Particle Accelerator Conference.

[2] V. Lebedev et al., "Linear Optics Correction in the CEBAF Accelerator," Proceedings of the 1997 Particle Accelerator Conference.
Y. Chao, "Measuring and Matching Transport Optics at Jefferson Lab," Proceedings of the 2003 Particle Accelerator Conference.
R. Bodenstein et al., "Real Beam Line Optics from a Synthetic Beam", Proceedings of the 2010 International Particle Accelerator Conference.

[3] Y. Chao, "Generation and Control of High Precision Beams at Lepton Accelerators", Proceedings of the 2007 Particle Accelerator Conference.

[4] Y. Chao, "A Deterministic Program for Obtaining Optima under Constraints for Any Analytical System", ARXIV:1508.01846V2 [MATH.OC]

ISBN 978-3-95450-136-6

A NOVEL OPTIMIZATION PLATFORM AND ITS APPLICATIONS TO THE TRIUMF ENERGY RECOVERY LINAC*

C. Gong and Y. C. Chao
TRIUMF, 4004 Wesbrook Mall, Vancouver V6T 2A3, Canada

Abstract

A software platform for global optimization was developed to study the TRIUMF Energy Recovery Linac. The platform is parallel capable and allows for combinations of accelerator modeling tools such as MADX and Genesis. Many parameters are coupled, including RF parameters which are shared for all linac passes. The platform can study dynamic relationships between different processes, a practice not easily performed with standalone optimization. Tradeoffs are presented to give insights on how objectives are related and the repercussions of design decisions.

INTRODUCTION

The TRIUMF E-linac is a 50 MeV, 10 mA average current CW driver for rare isotope beams (RIB). The E-linac can be upgraded to an Energy Recovery Linac (ERL) for simultaneous ERL and RIB operations.

The design of the upgrade is complicated. Many parameters are coupled, including RF parameters which are shared between three beams (RIB pass and two ERL passes). Our goals are:

- Create a computational platform for multiobjective optimization (MOO), capable of massively parallel computation.
- Capable of using different modeling tools, or engines, in combination to produce global models of machines.
- Use the platform to set up a global ERL model.
- Use the platform to study the physics of the TRIUMF ERL.
- Create a baseline from optimization results, complete with layout coordinates and optics requirements.

More details on the capabilities of the platform can be found in [1, 2]. The complete platform design and implementation can be found in [3], with a description of MOO.

OPTIMIZATION METHOD

Objectives and constraints used in the optimization are

- Maximize gain, therefore FEL power.
- Energy recovery: $E_{dmp} = E_{in}$ =7.5 MeV, or equivalently, $p_{dmp} = p_{in}$ =7.5 MeV/c - dump energy same as injection energy.
- $\sigma_x \leq 3$ mm, $\sigma_y \leq 3$ mm - minimize beam loss via beam scraping by restricting transverse beam size everywhere.
- $\sigma_{x,EDBT} \leq 3$ mm, $\sigma_{y,EDBT} \leq 3$ mm - constrain beam size in the dump section EDBT. This is complicated by the large energy spread δ obtained from lasing and deceleration, which is converted to beam size by the EDBT dipole. This constraint overlaps with the previous, but is listed again for emphasis.
- beam loss $\leq 10^{-5}$ - lasing creates a momentum tail which can cause beam loss in the return arc.
- $\sigma_{x,dmp} = 7$ mm, $\sigma_{y,dmp} = 7$ mm - blow up beam at the dump to reduce radiation heating.
- $\alpha_x = \alpha_y = \eta_{x'} = 0$ at both arc centers - look for designs with arc symmetries in β_x, β_y, and η_x. Symmetries make tuning easier. The layout of the arc optics is symmetric to accommodate these conditions. η_y is zero everywhere and does not need to be considered.
- Maximize E_{RIB} - high energy is desired for RIB transport.

Free parameters in the optimization are:

- RF phases and amplitudes (four independent cavities)
- Drift lengths (25 cm minimum separation between elements to support diagnostics)
- Quad gradients (upper limit set by existing TRIUMF magnet designs)
- Chicane dipoles bend angle

The main linac geometry is designed and not subject to optimization. Care is also taken to make sure the ERL fits in the TRIUMF E-hall.

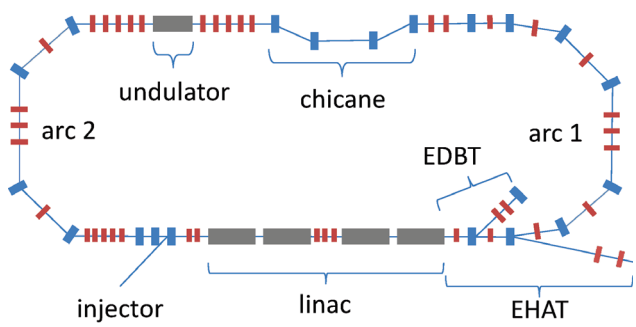

Figure 1: Dual ERL-RIB layout.

Layout of the ERL is shown in Fig. 1. Modeling of the machine starts at the linac. After acceleration an RF separator kicks the ERL beam into the recirculation loop. The beam lases and is then decelerated by a second pass. The energy recovered beam is kicked to EDBT for disposal. The RIB pass is modeled as well, with the RF separator kicking the beam into RIB transport EHAT.

Components of the ERL are modeled by a combination of engines: MADX, DIMAD, Genesis, and the Empirical Model (EM) [4]. EM is a TRIUMF code for modeling cavities. The optimization platform handles all transitions between engines and distribution of work on parallel clusters.

* Work supported by Natural Sciences and Engineering Research Council of Canada and National Research Council of Canada

ISBN 978-3-95450-136-6

Engines can be easily switched because the platform treats them as independent modules.

RESULTS

Most plots shown in this section represent either the optimization population, or a subset of the population. Each point in the plots should be interpreted as an instance of the ERL, i.e. a particular machine design created by the optimization platform.

The RF can have a significant impact on bunch compression and therefore the gain. Figure 2 shows the effects of the acceleration phase ϕ_1 on the gain. The data forms the typical shape of the RF curve, demonstrating the important role of RF in shaping the bunch for compression and lasing. Note that in EM convention, phases denote when the bunch centroid is at the cavity entrance. 335°/155° represents the RF crest/trough. Figure 2 shows the best bunch compression occurs when the beam is accelerated several degrees before crest.

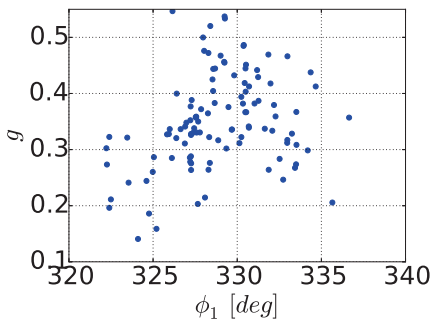

Figure 2: FEL gain vs acceleration phase ϕ_1. Slices made on parameters at the undulator entrance: $\beta_x \leq 2$ m, $\beta_y \leq 2$ m, $-0.5 \leq \alpha_x \leq 0.5$, and $0.5 \leq \alpha_x \leq 1.5$. These slices are centered around the optimal transverse matching conditions for the undulator (Eq. (1)) to isolate longitudinal effects. The solution set encompasses physics of the linac, arc transport, and lasing. No single simulation tool can provide all the physics modeling necessary.

We follow the evolution of the energy spread δ in the machine. δ increases as a result of lasing (Fig. 3), by several 10^{-3}. The larger δ can cause problems for the return transport, where arc dipoles can convert δ into beam size, potentially resulting in beam loss.

δ also increases significantly after linac pass 2 due to anti-damping (Fig. 4). This causes problems for transport in the dump section EDBT, where again δ can be converted into beam size and beam loss. Notice that δ increases by an order of magnitude before and after acceleration.

Lasing also induces non-Gaussian effects in the bunch. Figure 5 shows the distribution of bunch particles' energy deviation after lasing. A slight tail can be observed. Its effects need to be tracked in the second transport arc, where the tail can be turned into beam size by the dipoles and cause beam loss.

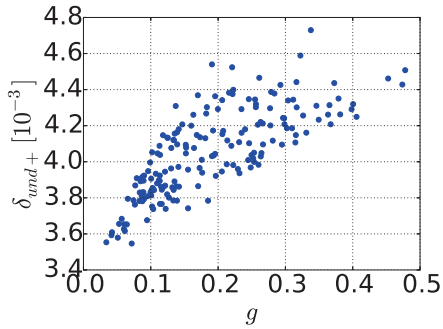

Figure 3: Increase in δ due to lasing.

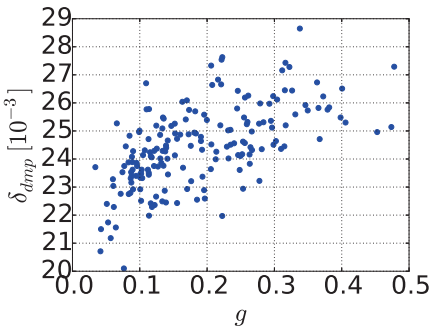

Figure 4: Effects of gain on δ and beam disposal.

In addition to constraining beam sizes σ_x and σ_y, we also require beam loss $\leq 10^{-5}$ through particle tracking to observe effects of the momentum tail.

Figure 6 shows maximum horizontal and vertical beam sizes in the return arc. Blue solutions satisfy beam size constraints $\sigma_x \leq 3$ mm and $\sigma_y \leq 3$ mm. Red solutions satisfy both beam size constraints and beam loss $\leq 10^{-5}$. The red solutions are a subset of the blue. The momentum tail tightens the maximally allowed beam sizes to $\sigma_x \leq 2.9$ mm and $\sigma_y \leq 2.8$ mm.

Figure 7 shows the importance of the RF deceleration phase ϕ_2. Both momentum p and energy spread δ are greatly affected. The closer the bunch enters the linac on-crest, the greater deceleration it experiences, but this leads to a decrease in RF slope and therefore less control of δ. This coupling leads to a tradeoff.

Figure 8 shows the tradeoff, or Pareto front, between energy recovered p and δ at the dump. For energy recovery,

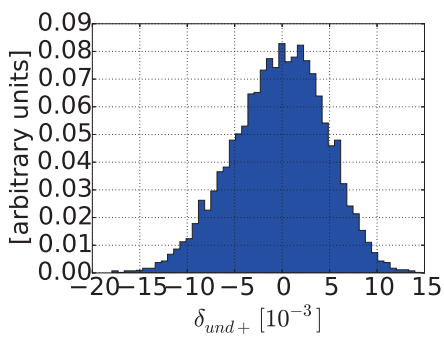

Figure 5: Energy deviation of particles in bunch after lasing.

ISBN 978-3-95450-136-6

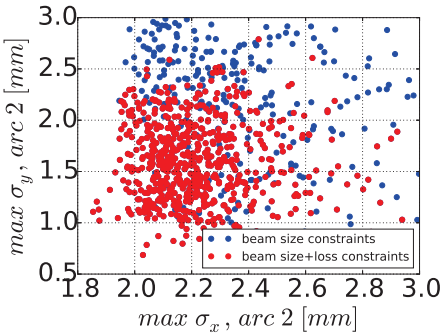

Figure 6: Tracking beam loss after lasing.

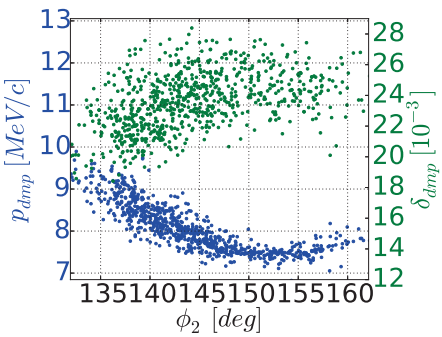

Figure 7: Effects of ϕ_2.

we wish to move left towards the vertical red line, which shows the desired injection $p = 7.5$ MeV/c. At this momentum only a 0.021 minimum δ_{dmp} is achievable. To lower δ_{dmp}, we wish to move to the right. The two parameters are fighting against each other because they are both coupled to ϕ_2. If δ at the dump becomes an issue, it is possible to sacrifice energy recovery to achieve smaller δ.

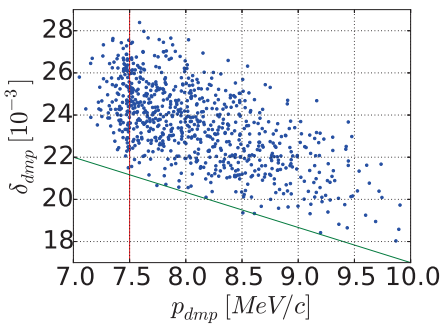

Figure 8: Pareto front between energy recovered momentum p_{dmp} and energy spread at dump δ_{dmp}.

The theoretical matching conditions for the undulator are given by [5]. Horizontally the undulator resembles a drift so we want the incoming beam to be focusing and form a symmetric waist at the center. Vertically, the B-field is sinusoidal with $B_y \approx B \cos k_u z$, where $k_u = 2\pi/4$ cm is the undulator wavenumber. The field can be averaged over the undulator period λ_u to create a section of constant focusing strength $K/(\sqrt{2}\gamma_r \lambda_u)$ where $K = .7$ is the undulator parameter and $\gamma_r \approx 90$ is the Lorentz factor of the bunch. Thus we would

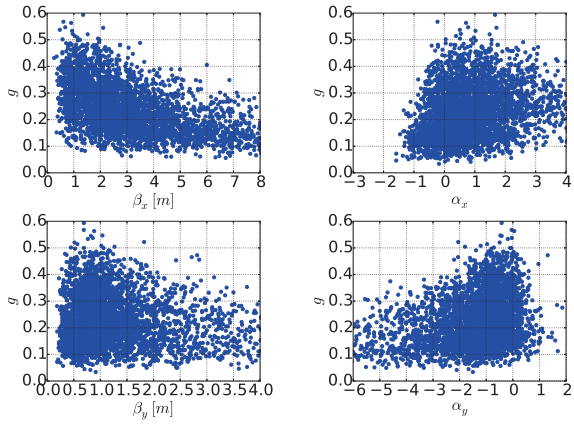

Figure 9: Undulator matching conditions from optimization match well with Eq. (1).

like a coasting beam. The matching parameters are

$$\begin{aligned} \beta_{x,match} &= Z_R + (L_u^2/4Z_R) = 1 \text{ m} \\ \alpha_{x,match} &= L_u/(2Z_R) = 1 \\ \beta_{y,match} &= \sqrt{2}\gamma_r/(K k_u) \approx Z_R = .5 \text{ m} \\ \alpha_{y,match} &= 0 \end{aligned} \tag{1}$$

where $Z_R = .5$ m is the Rayleigh length and $L_u = 1$ m is the undulator length. Optimization results supports these conditions (Fig. 9).

BASELINE

An ERL baseline is chosen from the optimization population. Important values are displayed in Table 1.

Table 1: ERL Engine Topology

Parameter	Value
Gain	0.5 m^{-1}
Initial momentum	7.5 MeV
EDBT momentum	7.7 MeV
σ_x	$\leq$ 3 mm everywhere
σ_y	$\leq$ 3 mm everywhere
EDBT energy spread	0.029
EDBT max σ_x	3.0 mm
EDBT max σ_y	1.9 mm
Dump σ_x	5.5 mm
Dump σ_y	6.0 mm
Beam loss	$\leq 10^{-5}$

The design has a gain of 0.5 m^{-1}. This is near the top of the optimization search space for gain and satisfies our maximize lasing objective.

The EDBT max σ_x is within our beam size constraint, demonstrating that energy spread is contained and should not be an issue.

Further physics and baseline results can be found in [3].

ISBN 978-3-95450-136-6

REFERENCES

[1] C. Gong and Y.C. Chao, "A New Platform for Global Optimization," IPAC12, New Orleans, 2012.

[2] C. Gong and Y.C. Chao, "The TRIUMF Optimization Platform and Application to the E-Linac Injector," ICAP12, Rostock, 2012.

[3] C. Gong, "A Novel Optimization Platform and Its Applications to the TRIUMF Energy Recovery Linac," PhD Dissertation, University of British Columbia, 2015.

[4] Y.C. Chao et al., "Low-Beta Empirical Models used in Online Modeling and High Level Applications," IPAC11, San Sebastian, 2011.

[5] Y.C. Chao, "Wiggler Parameters and Matching Conditions," Unpublished TRIUMF note, 2014.

ISBN 978-3-95450-136-6

COMPUTATION OF NONLINEAR FIELDS AND ORBIT AND SPIN TRANSFER MAPS OF ELECTROSTATIC ELEMENTS USING DIFFERENTIAL ALGEBRAS*

K. Makino†, E. Valetov, M. Berz, Michigan State University, East Lansing, MI 48824, USA

Abstract

Traditionally most large storage rings for nuclear and high energy physics use magnetic elements for focusing and bending. However, recent interest in the study of the possible existence of an electric dipole moment (EDM) of protons, deuterons and others requires the use of electrostatic elements in rings, and would even greatly benefit from the use of purely electrostatic lattices without any magnetic elements. Indeed the classical Thomas-BMT equation describing the motion of the spin due to a magnetic dipole moment coupling to magnetic fields can be augmented to analogously also describe the effects of a possibly present electric dipole moment coupling to electric fields, and the additional term would lead to detectable effects. We discuss how to address and resolve various problems appearing in the simulation of such lattices. We begin with methods that allow the computation of nonlinear fields of elements, and in particular their fringe fields, using DA-based PDE solvers, and proceed to the computation of high-order transfer maps, typically up to order 7 or 9. We also discuss a problem arising in these rings, especially the possible nonconservation of the particle energies.

THE DA PDE FIELD SOLVER

The electric and magnetic rigidities $\chi_e = pv/q$ and $\chi_m = p/q$ describe the strengths of coupling to the electric and magnetic fields [1]. Due to the additional factor v, the practically achievable bending in electrostatic elements is less than in magnetic elements, which limits their use to moderate energies, and their desired use in storage ring EDM studies [2] represents a new frontier. Beam dynamics simulations of systems containing electrostatic elements encounter various undesirable effects that do not arise in magnet based systems. We start the discussion with a differential algebra (DA) based field solver, which provides an efficient mechanism to compute 3D nonlinear fields while computing a high-order nonlinear transfer map [3].

We outline the principle of the DA PDE solver using a general form of the Laplace equation. We first bring the equation into a fixed point form:

$$V = V|_{y=0} + \int_0^y \frac{1}{b_2}\left[\left(b_2\frac{\partial V}{\partial y}\right)\Big|_{y=0}\right] dy - \int_0^y \frac{1}{b_2}\int_0^y \left(\frac{a_1}{b_1}\frac{\partial}{\partial x}\left(a_2\frac{\partial V}{\partial x}\right)+\frac{c_1}{b_1}\frac{\partial}{\partial z}\left(c_2\frac{\partial V}{\partial z}\right)\right) dy dy,$$

where a_i, b_i, c_i are functions of x, y, z. Viewing it as a DA fixed point problem, we provide the boundary conditions $V|_{y=0}$ and $(b_2 \cdot \partial V/\partial y)|_{y=0}$ as DA quantities, which represents the field description in the midplane, as analytical functions of x and z. The right hand side is contracting with respect to y in the DA framework [3], and we obtain V as a function of x, y, z by calculating the equation in the DA arithmetic iteratively in finitely many steps. The field components can be obtained also by DA arithmetic as the first derivatives of V [3,4].

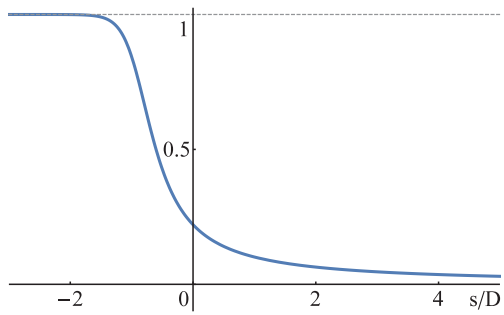

Figure 1: The normalized profile of the fringe field falloff of an electrostatic deflector consisting of two infinitely long capacitor plates, computed by conformal mapping techniques. The effective field boundary is marked by the vertical line. The electric field falls off very slowly on the outside (rightward). s: arclength, $D = 2d$: full aperture.

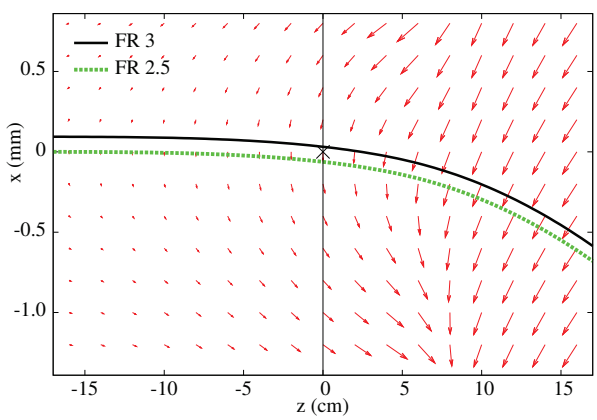

Figure 2: The field distribution in the entrance fringe region of a cylindrical electrostatic deflector; the default falloff, $d = 5$ cm, $R = 24.7$ m, E_z is multiplied by 10^4 for emphasis. The reference trajectories by fringe field modes FR 3 and FR 2.5 are shown. "×" marks the entrance position of the hard edge model (no fringe field).

* Work supported by the U.S. Department of Energy.
† makino@msu.edu

ISBN 978-3-95450-136-6

One carefully attempts to keep the main field of an electromagnetic element constant along the reference trajectory. However in the fringe field region, unavoidable nonlinearity in the motion and hence aberrations are introduced. Figure 1 shows an example fringe field falloff in the midplane along the reference orbit arclength s. The fringe field nonlinearity affects particles at different locations from reference orbit differently due to the curvature of field lines. The DA PDE solver is utilized to obtain the full 3D fringe fields from a suitable analytical function of only s describing the field falloff along the reference orbit in the midplane. The fields of the entire element now can be obtained via the DA PDE solver by supplying the necessary boundary conditions, for example, the DA multiplication of the s-dependent Enge function and the midplane main field. The field shown in Fig. 2 is computed in such a way.

TRANSFER MAP COMPUTATION

Once the fields are known, the equations of motion determine the final status of the coordinate variables $\vec{Z}_f$ depending on the initial status $\vec{Z}_i$. Except for simplified models of electromagnetic elements, one may resort to numerical integration of the differential equations. Using the DA method, one can readily obtain a nonlinear high-order transfer map $\vec{Z}_f = \mathcal{M}(\vec{Z}_i)$ including spin dynamics [3, 5] necessary for the EDM studies. The DA PDE solver is the main mechanism to supply the 3D fields including the derivatives at any position along the transfer map flow integration for nontrivial electromagnetic elements in the code COSY INFINITY [6], and it frees the code from the need to rely on the conventional field computation methods such as FEM and BEM as well as subsequent numerical interpolation and numerical differentiation.

In the hard edge model of the example cylindrical deflector in Fig. 2, the field is zero before the effective field boundary $z = 0$, so the reference trajectory approaches from the left and enters the deflector at $(z, x) = (0, 0)$. However in practice, when considering the unavoidable fringe field, the non-zero field before the boundary already bends the trajectories of the particles. Even the reference trajectory becomes different from the ideal hard edge model; the green dashed curve labeled "FR 2.5" shows the reference trajectory when it approaches from far left at $x = 0$, traveling parallel to the z axis, having quite an offset from $(0, 0)$ due to the influence of the fringe field. This can have far reaching consequences especially in electrostatic elements with their generally slower field falloff, and in particular introduces discrepancies in the resulting transfer maps [7].

The fringe field computation mode FR 2.5 in COSY INFINITY calculates the transfer map along the reference trajectory as described above. This is the easiest way to utilize to treat nonlinear fringe fields, though the reference trajectory throughout the element does not form the expected mirror symmetry about the middle of the element. In order to enforce this symmetry, one can first integrate the reference orbit backwards from the middle of the element, and then shift and rotate the element to account for the resulting deviations. This is done in the mode FR 3, and the resulting reference trajectory in the 22.5° deflector, which has an arc length of ~ 10 m, is shown in the black curve in Fig. 2, resulting in ~ 0.1 mm offset from the FR 2.5 case.

Besides the problem of the trajectory offset, there is another major problem since particle optical elements with fringe fields are usually described by three separate parts, namely the entrance fringe field, the main field, and the exit fringe field. In electrostatic elements, at the end of the entrance fringe fields there are nonzero potentials affecting the particle's energy. If this is followed by a shift or rotation of the reference orbit to line up with the subsequent main field, as is usually done, this leads to a discontinuity

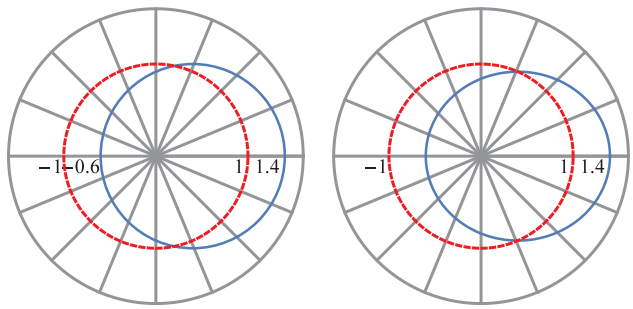

Figure 3: The reference orbit of radius 1 m (dashed red) and an orbit starting at the position displaced rightward by 0.4 m (blue). The system consists of 16 sectors. (left) In the uniform magnets, the displaced orbit is circular with radius 1 m. (right) In the electrostatic spherical deflectors, the displaced orbit is Keplerian elliptic if nonrelativistic.

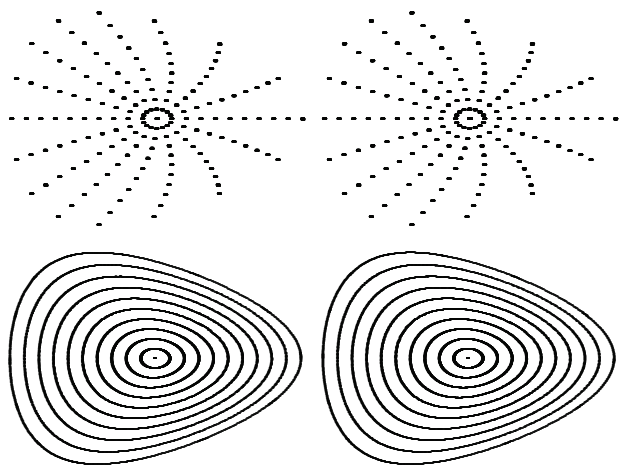

Figure 4: Tracking particles long term through a 22.5° electrostatic spherical deflector around the circular reference orbit with deflection radius 1 m (see Fig. 3) for 160,000 times by (left) pushing through a high-order transfer map, (right) integrating via an 8th order Runge Kutta integrator – this figure and Figs. 5, 6. Particles are launched horizontally up to $x_{\mathrm{ini}} = 0.4$ m, and the x-a phase space motion is shown for nonrelativistic (top) and relativistic (bottom) cases. $|a|$ reaches to 0.46.

ISBN 978-3-95450-136-6

in the potential, and thus a violation of energy conservation. While seemingly small, these effects can very detrimentally build up in repetitive systems. Thus different from common particle optical practice, the discussed fringe field computation modes FR 3 and FR 2.5 carry the computation throughout the entire element including the entrance and exit fringe field regions in a single operation.

A BENCHMARK EXAMPLE

Electrostatic deflectors, while presenting difficulties in particle optical simulations, allow interesting and far-reaching cross checks [6, 7]. Here we study spherical deflectors in detail, where the electrostatic potential is $\propto 1/r$, so the system represents a Kepler problem. In the nonrelativistic case, the motion returns to the exact original state after one full revolution, independent of initial conditions. Thus the transfer map of such a spherical deflector of 360° is an identity map [7].

We perform a challenging long term tracking test based on knowing that the field is radial and nonlinear $\propto 1/r^2$, so the nonrelativistic particles follow Kepler orbits. We pick a circle with radius 1 m as the reference orbit, and consider a system consisting of 16 of 22.5° deflectors as shown in Fig. 3. We study the long term motion of displaced particles up to 0.4 m in the radial direction ($x_{\rm ini}$; Fig. 4) and in the vertical direction ($y_{\rm ini}$; Figs. 5, 6), each having 10 equidistantly displaced particles. We note that a particle with any radial position displacement follows a 1 m radius circle in uniform magnets (left, Fig. 3), and follows a Kepler ellipse in the spherical electrostatic deflectors (right, Fig. 3).

We performed tracking through the electrostatic spherical deflectors for 160,000 iterations, corresponding to a total of 10,000 orbital revolutions, by the transfer map method with and without symplectification [8], and compared the performance with the numerical integrations using a highly accurate 8th order Runge Kutta (RK) integrator with automatic step size control. In case of the $x_{\rm ini}$ test, the majority of the interesting aspects is seen in the x-a phase space plots corresponding to the radial motion. On the other hand, the $y_{\rm ini}$ test shows interesting aspects in both the x-a and the vertical y-b phase spaces. To represent the motion covering the range of this stress test, nonlinear transfer maps of high order are necessary. In Figs. 4, 5, 6 we used maps of order 19, and no visible difference is observed compared to the plots by RK. One tracking run of 160,000 elements required $\sim$ 400 s by RK. The corresponding computation by the transfer map method requires the computation of a high order transfer map for one 22.5° deflector in the beginning, and the remaining task is to apply the transfer map repeatedly for 160,000 times. This is very fast using the DA method; the 2D $x_{\rm ini}$ test takes $\sim$ 7 s, while the 4D $y_{\rm ini}$ test takes $\sim$ 140 s. To cross check the results, we also performed the transfer map tracking computations with symplectification [8], where the $x_{\rm ini}$ test takes $\sim$ 40 s and the $y_{\rm ini}$ test takes $\sim$ 950 s, and it results in complete agreement in the resulting plots.

Nonrelativistic particles follow closed Kepler ellipses, so each of 10 displaced particle leaves 16 breadcrumbs at the exactly same 16 phase space positions in every revolution. If the motion were linear, all breadcrumbs would line up straight and symmetrically. However, in reality the motion is very nonlinear, resulting in the curved structure seen in the top plots in Fig. 4. The plots in the $y_{\rm ini}$ test look straightforward at first glance, but a careful inspection reveals the complication due to the 3D elliptic motion. For example, the top plots in Fig. 5 stretch out leftward less than they do on the right. In the relativistic case, the orbits are no longer closed due to precession of perihelion resulting from the relativistic change of mass during the revolution, corresponding to Einstein's precession of the perihelion of Mercury. The bottom plots in Fig. 5 show the effect of this precession, and coupling effect arise in the x-a plots in Fig. 6.

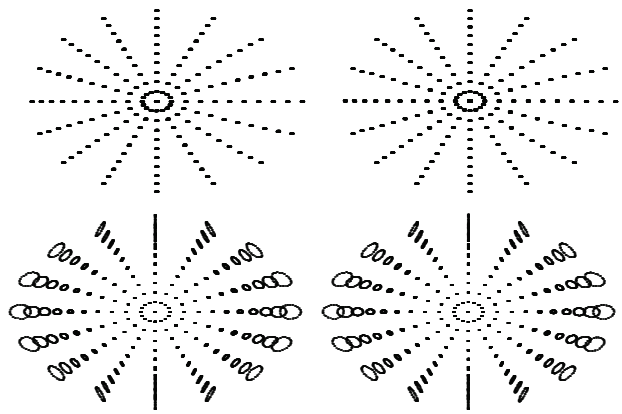

Figure 5: Particles are launched vertically up to $y_{\rm ini} = 0.4$ m. The y-b projection of the motion is shown for nonrelativistic (top) and relativistic (bottom) cases. $|b|$ reaches to 0.43. (left) map, (right) RK.

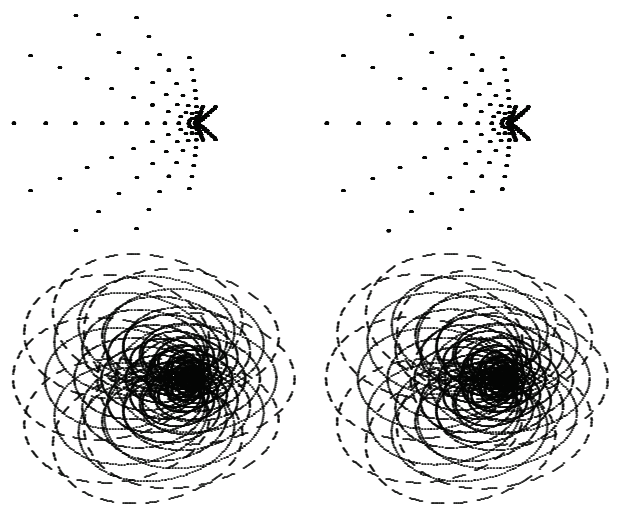

Figure 6: Particles are launched up to $y_{\rm ini} = 0.4$ m as in Fig. 5. The x-a projection of the motion is shown. x and a, initially 0, reach to the range $-0.15 \le x \le 0.02$, $|a| \le 0.13$ (top, nonrelativistic), and $-0.15 \le x \le 0.08$, $|a| \le 0.15$ (bottom, relativistic). (left) map, (right) RK.

ISBN 978-3-95450-136-6

REFERENCES

[1] M. Berz, K. Makino, W. Wan, *An Introduction to Beam Physics*. CRC Press, Taylor & Francis Group, London, Boca Raton (2014).

[2] Storage Ring Electric Dipole Moment Collaboration. http://www.bnl.gov/edm/. JEDI Collaboration (Jülich Electric Dipole Moment Investigations). http://collaborations.fz-juelich.de/ikp/jedi/.

[3] M. Berz, *Modern Map Methods in Particle Beam Physics*. Academic Press, San Diego (1999).

[4] K. Makino, M. Berz, C. Johnstone, "High-order out-of-plane expansion for 3D fields," International Journal of Modern Physics A **26**, 1807 (2011).

[5] M. Berz, K. Makino, "Advanced computational methods for nonlinear spin dynamics," IOP Journal of Physics **295**, 012143 (2011).

[6] M. Berz, K. Makino, "COSY INFINITY version 9.2 beam physics manual," Technical Report MSUHEP-151103, Michigan State University (2015).

[7] K. Makino, M. Berz, "Dynamics in electrostatic rings via high-order transfer maps," Microscopy and Microanalysis **21** Suppl. **4**, 36 (2015).

[8] B. Erdélyi, M. Berz, "Optimal symplectic approximation of HHamiltonian flows," Physical Review Letters **87,**11, 114302 (2001).

ISBN 978-3-95450-136-6

SEARCH FOR THE OPTIMAL SPIN DECOHERENCE EFFECT IN A QFS LATTICE

E. Valetov*, M. Berz, Michigan State University, East Lansing, MI 48824, USA
Yu. Senichev, IKP, Forschungszentrum Jülich, Germany
on behalf of the JEDI Collaboration

Abstract

Measurement of electric dipole moment (EDM) in a storage ring requires the spin decoherence in a particle bunch to be less than 1 rad in 1000 s, which corresponds to about 1 billion turns. The quasi-frozen spin (QFS) method [1] has been proposed for deuteron EDM search. In a QFS lattice, spin direction turn in magnetic bend sections is compensated by spin direction turn in electrostatic bend sections, and thus the spin direction at a point in the lattice is approximately constant. We consider two QFS lattices, each with an RF cavity and a family of sextupoles. In *COSY INFINITY*, calculations were done using transfer maps of the 7th order, with symplectic tracking using the Extended Poincaré (EXPO) generating function and the most accurate *COSY INFINITY* fringe field mode. We have optimized the sextupole strengths to minimize the spin decoherence. Using these sextupole strengths, we have done spin tracking of the lattice and analyzed the growth of spin decoherence as a function of the number of turns. Within their scope, our results indicate the feasibility of the QFS method.

INTRODUCTION

Frozen spin method has been previously proposed for EDM search. It is characterized by the spin vector of particle being aligned with its momentum while the particle moves within the lattice. The radial electrostatic field effects torque on the spin, causing it to rotate out of the midplane.

Quasi-Frozen Spin Method and Lattices

In quasi-frozen spin (QFS) method, the average projection of the spin vector on the momentum vector is approximately one. The mechanism for detection of the EDM is the same in QFS, but the implementation becomes simpler and more flexible [2].

We recall the Thomas-BMT equation:

$$\frac{d\vec{S}}{dt} = S \times \left(\vec{\Omega}_{MDM} + \vec{\Omega}_{EDM}\right)$$

where

$$\vec{\Omega}_{MDM} = \frac{e}{m}\left[G\vec{B} - \left(G - \frac{1}{\gamma^2 - 1}\right)\frac{\vec{E} \times \beta}{c}\right]$$

and

$$\vec{\Omega}_{EDM} = \frac{e}{m}\frac{\eta}{2}\left[\frac{\vec{E}}{c} + \beta \times \vec{B}\right]$$

* valetove@msu.edu

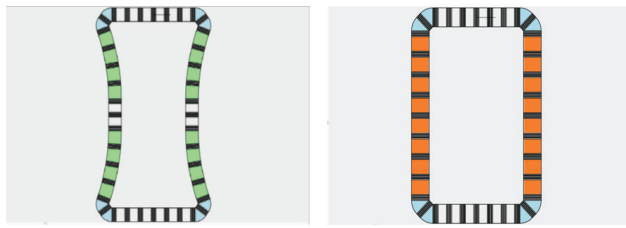

(a) *Senichev 6*. Structure includes 4 straight sections (light gray), 4 magnetic sections (blue), and 4 electrostatic sections (green). Lattice length is 16667 cm.

(b) *Senichev E+B*. Structure includes 4 straight sections (light gray), 4 magnetic sections (blue), and 4 E+B sections (orange). Lattice length is 14921 cm.

Figure 1: QFS Lattices.

The QFS condition is

$$\gamma G \Phi_B = \left[\frac{1}{\gamma}(1 - G) + \gamma G\right]\Phi_E$$

where Φ_B and Φ_E are the angles of momentum rotation in magnetic and electric bend parts of the ring correspondingly.

Yu. Senichev has proposed two QFS lattices, which we codenamed as *Senichev 6* and *Senichev E+B* [3](see Fig. 1). Both lattices operate with deuterons at the kinetic energy 270 MeV.

The RF cavity suppresses the 1st and partially the 2nd order of spin decoherence by mixing the particles relatively to the average field strength, and therefore, averaging out $\triangle\gamma G$ for each particle. Sextupoles are used to suppress the remaining 2nd order component, which is due to the average $\triangle\gamma G$ being different for each particle.

In *Senichev E+B* lattice, E+B static Wien filter elements are used instead of the electrostatic deflectors. This removes the respective nonlinear components and simplifies that lattice from the engineering perspective.

Fringe Fields of the Electrostatic Deflector

Senichev 6 lattice uses cylindrical electrostatic deflectors among other elements. Fringe fields of magnetic dipoles were previously studied extensively, but fringe fields of electrostatic deflectors were not studied in detail in the context of beam physics.

In 2015, we have calculated fringe fields of semi-infinite capacitors with solid metal plates in *MATLAB* using *Schwarz-Christoffel Toolbox* v.2.3 [4] and analyzed the results in *Mathematica*. In this analysis, we have compared the field falloffs with those of finite rectangular metal capacitors obtained in *Coulomb* by H. Soltner (IKP, Forschungszentrum Jülich, Germany).

ISBN 978-3-95450-136-6

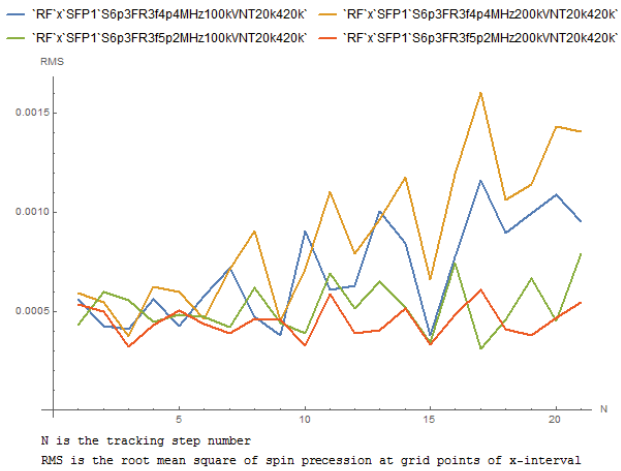

(a) Optimization by SFP1 sextupole family.

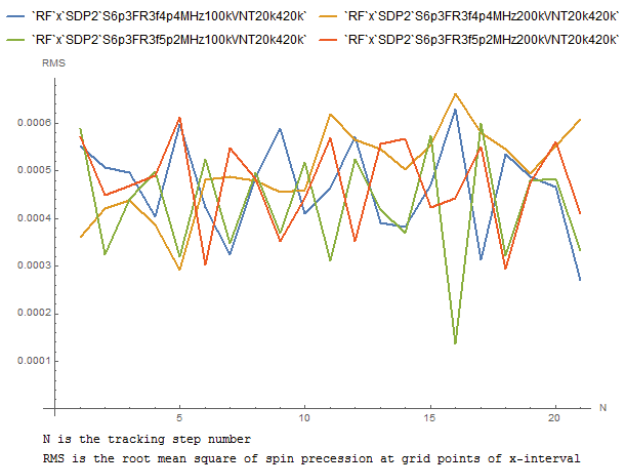

(b) Optimization by SDP2 sextupole famil.y

Figure 2: Spin decoherence in *Senichev 6* vs. number of turns up to 420k, FR 3 mode, $x - a$ plane.

(a) Optimization by SFP1 sextupole family.

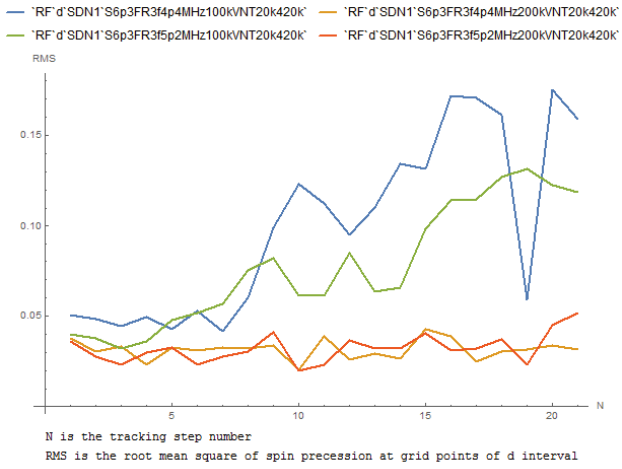

(b) Optimization by SDN1 sextupole family.

Figure 3: Spin decoherence in *Senichev 6* vs. number of turns up to 420k, FR 3 mode, $l - \delta$ plane.

For *Senichev 6* lattice, we used Enge coefficients for a semi-infinite electrostatic deflector with rounded edges and with $d/10$ plate thickness, where d is the distance between a plate and the midplane (see Table 1).

METHODS

Analytic relations (quadratic, etc.) show the general character of the system. Numerical methods, such as system tracking in *COSY INFINITY*, give the final understanding of which orders are needed for spin decoherence to be less than 1 rad in 1000 s, i.e. 1 billion turns.

Table 1: Enge Function Coefficients for Electrostatic Deflectors in *Senichev 6* lattice.

Coefficient	Value
h_0	1.0614024399605924
h_1	1.6135741290714967
h_2	−0.9401447081042862
h_3	0.4781500036872176
h_4	−0.14379986967718494
h_5	0.017831089071215347

We have developed a solution, which consists of *COSY INFINITY* and *Mathematica* programs.

In *COSY INFINITY* programs, we manually and automatically optimize the sextupole strengths and perform long-term tracking of the resulting lattice. For effective energy averaging of particles, RF cavity frequency is set to a sufficiently high multiple of the $l - \delta$ motion frequency for effective energy averaging. Optimization and tracking data is saved in text and graphics files. Calculations are done using transfer maps of the 7th order. For tracking, the motion is symplectified using the Extended Poincaré (EXPO) generating function. Although it is considerably slower, we do final calculations in the most accurate fringe field mode FR 3.

The output of *COSY INFINITY* programs is used as input to the *Mathematica* programs, where data arrays are stored, processed, and QA checked. Context selector list is used to generate reports that consist of plots and tables. We analyze and compare the data using these reports.

ISBN 978-3-95450-136-6

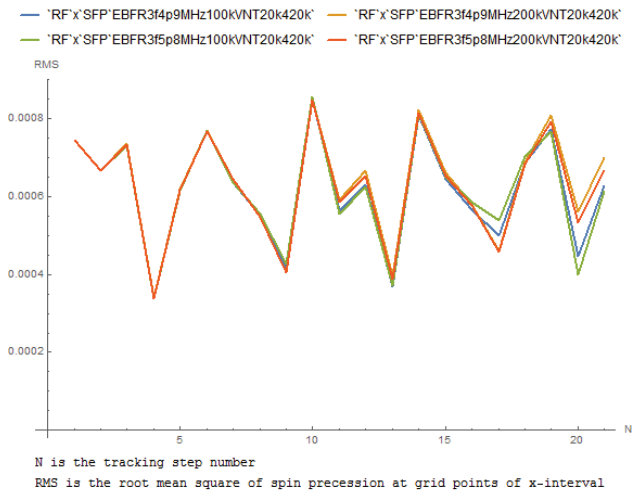

(a) Optimization by SFP sextupole family.

(b) Optimization by SDP sextupole family.

Figure 4: Spin decoherence in *Senichev E+B* vs. number of turns up to 420k, FR 3 mode, $x - a$ plane.

SUMMARY OF RESULTS

At 20 thousand turns, the order of spin decoherence in both systems was sufficiently large for 5×10^{-3} beam apertures in $x - a$ and $l - \delta$ planes of *COSY INFINITY*'s particle optical coordinate system [5] to require study of its longer term behavior. At present, we have studied its evolution up to 420 thousand turns in FR 3 mode and up to 1 million turns in FR 0 (no fringe fields).

With some input parameters (RF cavity frequency and voltage, sextupole settings), spin decoherence evolution has strong periodic minima, which can be explained by periodicity of RF modulation.

Spin decoherence evolution can be roughly classified into two types: (1) growing and (2) remaining in the same range. A necessary condition for the latter is the RF cavity being on.

With no fringe fields, spin decoherence as a function of a spacial coordinate is often bounded by two slanted lines.

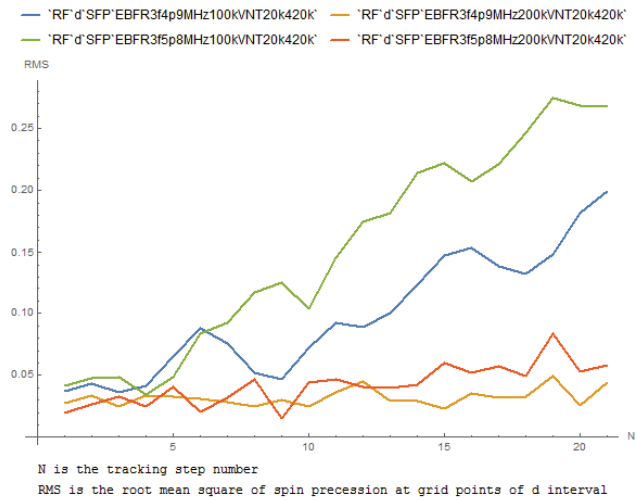

Figure 5: Spin decoherence in *Senichev E+B* vs. number of turns up to 420k, FR 3 mode, $l - \delta$ plane, optimization by SFP sextupole family.

We think that this illustrates the forced oscillations induced by the RF cavity. Turning fringe fields on distorts these lines to a various, but usually not very significant, extent.

DISCUSSION

Spin decoherence remaining in the same range for some parameters is indicative of the feasibility of the QFS method.

Spin decoherence should be optimized using the RF cavity and the sextupoles in all planes simultaneously. We may need to add octupoles to achieve spin decoherence of less than 1 rad in 1 billion turns. Tracking for more than 1 million turns is desirable for an optimal balance between computation time and confidence level, subject to any limits imposed by computational errors.

We will try to obtain a better optimization objective function by tracking a differential algebra (DA) vector-valued particle rays for multiple turns using modified *COSY INFINITY* tracking functionality.

REFERENCES

[1] Yu. Senichev et al., Quasi-frozen Spin Method for EDM Deuteron Search, in Proc. 6th International Particle Accelerator Conference, Richmond, VA, USA, pp. 213215, 2015.

[2] Yu. Senichev, A. Lehrach, B. Lorentz, R. Maier, S. Andrianov, A. Ivanov, S. Chekmenev, M. Berz, and E. Valetov. Quasi-frozen spin method for EDM deuteron search. *Proceedings of IPAC'2015, Richmond, VA*, 2015.

[3] Yu. Senichev, M. Berz, E. Valetov, S. Chekmenev, S. Andrianov, and A. Ivanov. Investigation of lattice for deuteron EDM ring. *presented at ICAP'2015, Shanghai, China*, MODBC4, 2015.

[4] Tobin A. Driscoll. Algorithm 756: A MATLAB toolbox for Schwarz-Christoffel mapping. *ACM Trans. Math. Softw.*, 22(2):168–186, June 1996.

[5] M. Berz. *Modern Map Methods in Particle Beam Physics*. Academic Press, 1999.

ISBN 978-3-95450-136-6

EFFICIENT PLASMA WAKEFIELD ACCELERATION SIMULATIONS VIA KINETIC-HYDRO CODE ARCHITECT

F. Massimo[1,2], A. Marocchino[1,2], E. Chiadroni[3], M. Ferrario[3],
A. Mostacci[1,2], L. Palumbo[1,2], A.R. Rossi[4]
[1]Dipartimento SBAI, "Sapienza" University of Rome, Rome, Italy
[2]INFN-ROMA 1, Rome, Italy
[3]INFN, Laboratori Nazionali di Frascati, Frascati, Italy
[4]INFN, Milano, Italy

Abstract

Start-to-end simulations are needed for sensitivity studies and online analysis of experimental data of the Plasma Wakefield Acceleration experiment COMB at SPARC_LAB facility, Frascati (Italy). *Ad hoc* tools are needed for the plasma section modeling. Particle in cell codes are the most widely used tools for this purpose, but they suffer from the considerable amount of computational resources they require. We seek for a simple, portable, quick-to-run approach. For this purpose we introduce a time-explicit cylindrical hybrid fluid-kinetic code: *Architect*. The beam particles are treated with PIC-like kinetic approach, while the plasma wake is treated as a fluid. Since the number of computational particles used by the hybrid model is significantly reduced with respect of full PIC codes with the same number of dimensions, the time required for a simulation is reduced as well.

INTRODUCTION

The use of accelerating electromagnetic fields in the wake of a perturbation of the neutrality of a plasma channel appears as one of the most promising ways to overcome the conventional accelerators' limits [1]. In particular in the Plasma Wakefield Acceleration (PWFA) scheme high energy driving particle beams created in a conventional beam line are injected into a plasma channel, to excite wakefields used to accelerate a witness bunch injected in the proper phase of the wake [2]. The most widely used technique to study the underlying physics and to guide the experimental efforts in PWFA is the Particle in Cell method [3]. The amount of computational resources (i.e. number of cores and simulation time) required for 3D full PIC simulations of typical experimental setups of plasma acceleration is still too high to use PIC codes for systematic scans. For this reason much interest has been devoted to reduced models, to perform faster simulations. In particular the codes using the quasi-static (QSA) approximation [4–6] proved to significantly reduce the computational time required to simulate plasma acceleration when the characteristic timescales of the beam evolution are significantly greater than the characteristic timescales of the plasma evolution.

An alternative efficient technique is the hybrid kinetic-fluid approach, which treats the relativistic beams kinetically and the background plasma electrons as a fluid. The reduced number of computational particles needed in this technique drastically reduces the simulation time with respect to a PIC code of the same dimensions. This approach has been proven successful for the Laser Wakefield Acceleration scheme (e.g. INF&RNO [7]) and for the PWFA with QSA (LCODE [8]). We present the 2D time-explicit hybrid kinetic-fluid code *Architect*, developed to aid the preliminary parameter skimming for the PWFA experiments planned at at SPARC_LAB facility in Frascati, Italy [9]. The time-explicit formulation of the code allows to initialize the bunch electromagnetic fields in vacuum and to investigate the transient phase of the beam entrance in the plasma channel.

IMPLEMENTATION OF A HYBRID MODEL FOR PWFA

Architect simulates PWFA treating the relativistic electron beams as an ensemble of macroparticles as in a PIC code and the background plasma electrons as a relativistic cold fluid. The plasma ions are treated as a uniform immobile background. The current densities of the two species are projected on the grid, using PIC techniques [3] and computing the fluid current on the grid respectively. The sum of the current densities acts as a source for the evolution equations of the electromagnetic fields, i.e. Faraday's Law and Ampere-Maxwell equation. The macroparticle positions and momenta in the 6D space evolve using the updated electromagnetic fields as source terms. The plasma background fluid density and momentum on the grid evolve using the updated electromagnetic fields as source terms.

For each particle of the kinetic bunch(es) we identify a position, $\mathbf{x}_{\text{particle}}$, a velocity, $\boldsymbol{\beta}_{\text{particle}}c$ and a relativistic momentum, $\mathbf{p}_{\text{particle}} = m_e\boldsymbol{\beta}_{\text{particle}}c/\sqrt{1-|\boldsymbol{\beta}_{\text{particle}}|^2}$ (m_e is the electron mass).

Thus, the the macroparticle positions and momenta evolve following the equations of motion:

$$\begin{aligned} d_t\mathbf{x}_{\text{particle}} &= \boldsymbol{\beta}_{\text{particle}}c \\ d_t\mathbf{p}_{\text{particle}} &= q\left(\mathbf{E} + c\boldsymbol{\beta}_{\text{particle}} \times \mathbf{B}\right) \end{aligned} \quad (1)$$

where q is the electron charge, $\mathbf{E}$ is the electric field, $\mathbf{B}$ the magnetic field, c the speed of light.

ISBN 978-3-95450-136-6

The background plasma electron density n_e and momentum $\mathbf{p}_e$ evolve according to [10]:

$$\begin{aligned} \partial_t n_e + \nabla \cdot (\boldsymbol{\beta}_e c\, n_e) &= 0 \\ \partial_t \mathbf{p}_e + c\boldsymbol{\beta}_e \cdot \nabla \mathbf{p}_e &= q(\mathbf{E} + c\boldsymbol{\beta}_e \times \mathbf{B}), \\ \boldsymbol{\beta}_e &= \frac{\mathbf{p}_e}{m_e c\sqrt{1+|\mathbf{p}_e/m_e c|^2}}. \end{aligned} \quad (2)$$

The first equation is the mass conservation equation; the second equation is the momentum conservation equation.

The electromagnetic fields, induced by both the beam particles and the fluid background, evolve according to Faraday's Law and Ampere-Maxwell's equation:

$$\begin{aligned} \nabla \times \mathbf{E} + \partial_t \mathbf{B} &= 0 \\ \nabla \times \mathbf{B} - c^{-2}\partial_t \mathbf{E} &= q\mu_0 c\,(n_e\boldsymbol{\beta}_e + n_b\boldsymbol{\beta}_b), \end{aligned} \quad (3)$$

where $\boldsymbol{\beta}_b c$ the velocity for the electron bunch and n_b the bunch density.

The fluid Eqs. (2) and the evolution equations for the electromagnetic fields, i.e. Eqs. (3) are integrated on a cartesian $r-z$ grid assuming cylindrical symmetry, i.e. the partial derivatives along the poloidal direction are all zero. To save memory and reduce the simulation time, the fluid and electromagnetic quantities are only integrated in a window around the beam (depicted in Fig. 1), which moves with the beam center of mass. The direction of propagation for the beam is z. Cylindrically symmetric boundary conditions are assumed on the window boundary corresponding to the z axis; free flux conditions are assumed on the other window edges. The code loop for each timestep is composed as follows; the

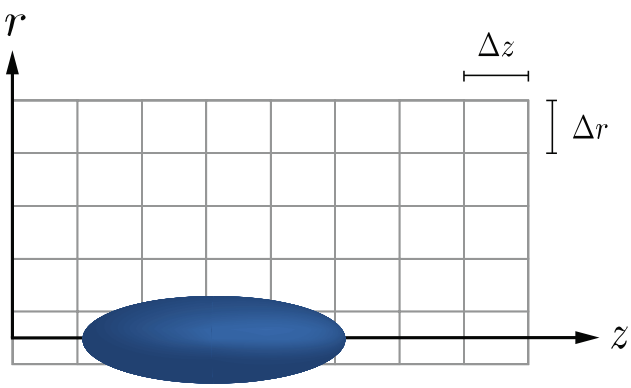

Figure 1: Architect $r-z$ grid. In blue a gaussian electron bunch, which moves in the z direction.

beam particles' position $\mathbf{x}_{\text{particle}}$ and momentum $\mathbf{p}_{\text{particle}}$ are used to project the beam current $\mathbf{J}_\text{b} = n_\text{b}\boldsymbol{\beta}_\text{b}c$ by means of PIC techniques [3]. The fluid current $\mathbf{J}_\text{e} = n_e\boldsymbol{\beta}_e c$ is then computed on the grid. The sum of the two currents is then used as a source term to integrate Eqs. (3) through the Finite Difference Time Domain (FDTD) method [3]. The updated fields are then used as source terms to integrate the equations of motion for every macroparticle, i.e. Eqs. (3), with a second order leap-frog with Boris rotation around the magnetic field [3]. The fields acting on each macroparticle are extrapolated from the grid through PIC techniques [3]. The updated fields are used also as source terms to integrate the fluid Equations (3). Such integration is performed through the Flux Corrected Transport (FCT) scheme [11, 12], a simplified shock-capturing scheme to catch the shock-like features of the ion bubble closing-up region. Once the fluid quantities and the macroparticle positions and momenta are updated the loop of the code timestep, summarized in in Fig. 2, is iterated. The self-consistent simulation of the beam-plasma

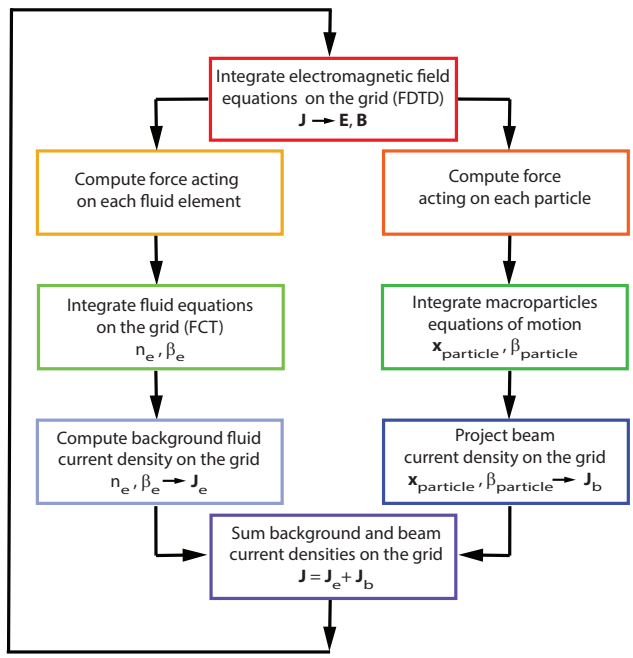

Figure 2: Architect Loop. On the left branch are the steps which involve the fluid quantities; on the right branch are the steps involving the beam macroparticles, identical to the steps of a standard PIC code.

interaction requires the correct initialization of the beam electromagnetic field in vacuum before it enters the plasma channel, which is initially at rest. Typical COMB simulations have an initial beam energy spread of 0.1%, thus all the beam particles move initially with a nearly equal velocity. The electromagnetic fields induced by the electron beam can thus be computed solving Poisson's equation in the beam rest frame and transforming the fields back in the laboratory frame. Poisson's equation is solved in Architect through finite differences, and using a Successive Over Relaxation (SOR) method to accurately solve the Poisson associated problem. Appropriate optimizations reduces the required computation time down to seconds even with very refined meshes.

RUNNING TIME

To highlight the speed of the hybrid approach, we report the time required for a 1 cm-simulation of an electron beam injected in a uniform plasma channel of density $n_0 = 10^6\,\text{cm}^{-3}$. The initial beam parameters, chosen from a realistic SPARC_LAB scenario, are: charge $Q = 113\,\text{pC}$, rms-lengh $\sigma_z = 50\,\mu\text{m}$, rms-transverse size $\sigma_x = \sigma_y = 8\,\mu\text{m}$,

ISBN 978-3-95450-136-6

energy $E_0 = 100$ MeV, energy spread $\Delta\gamma/\gamma = 0.1\%$, transverse normalized emittance $\varepsilon_x = \varepsilon_y = 1$ mm-mrad. Such benchmark is in the weakly nonlinear regime [13, 14]. The simulation parameters are: integration timestep $\Delta t = 0.88$ fs, mesh cell size $\Delta z = 2\,\mu$m in the z direction and $\Delta z = 0.8\,\mu$m in the r direction. The colormap of the beam and background electron density after 0.1 cm of propagation are shown in Fig. 3. The simulation reported in the figure used 50000 particles to model the electron beam.

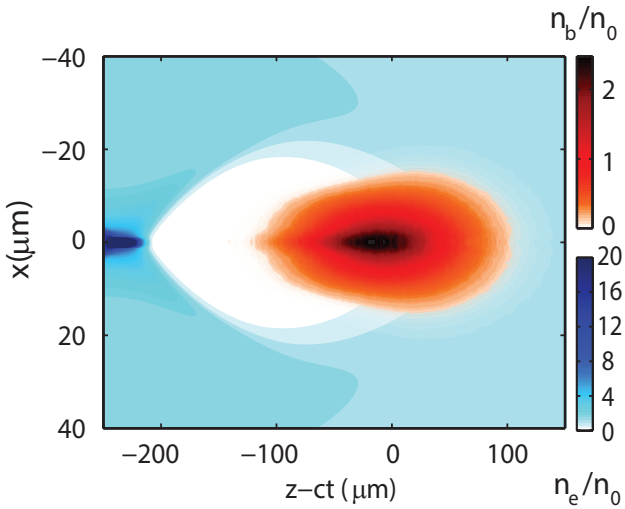

Figure 3: Beam and background electron density for the considered benchmark, after a 0.1 cm beam propagation.

The time scaling of the described benchmark, varying the number of beam particles is reported in Table 1. The reported running times are referred to a single cpu, since the code does not need parallelization. From the table we note that a preliminary run of 1 cm in the plasma channel, with the same number of beam particles of Fig. 3, needs less than one hour on a single cpu.

Table 1: Benchmark Simulation Time, Referred to an 1 cm-Run on a Single CPU

Number of beam particles	Running time (hours/cm)
30000	0.25
50000	0.38
70000	0.51
100000	0.71
200000	1.37
500000	3.34
1000000	6.63

ACKNOWLEDGMENT

This work has been partially funded by the Italian Minister of Research in the framework of FIRB- Fondo per gli Investimenti della Ricerca di Base, Project no. RBFR12NK5K.

REFERENCES

[1] I. Blumenfeld et al., Nature **445** 741-744 (2007).

[2] M. Litos et al., Nature, **515** 92-95 (2014).

[3] C. K. Birdsall, A. B. Langdon, Plasma Physics Via Computer Simulation, CRC Press, Boca Raton (2004).

[4] P. Mora, T.M. Antonsen, Phys. Rev. E, **53** R2068 (1996).

[5] D.H. Whittum, Phys. Plasmas, **4** 1154 (1997).

[6] P. Sprangle, E. Esarey, A. Ting, Phys. Rev. A, **41** 4463 (1990).

[7] C. Benedetti, C.B. Schroeder, E. Esarey, C.G.R. Geddes, W.P. Leemans, AAC 2010 Proc., **56** 084012 (2010).

[8] K. V. Lotov, Phys. Plasmas, **5** 785 (1998).

[9] M. Ferrario et al., Nucl. Instr. and Meth. B 309, 183 (2013).

[10] L. Rezzolla and O. Zanotti, Relativistic Hydrodynamics, Oxford University Press (2013).

[11] J.P. Boris, D.L. Book, J Comput Phys, **11** 38 (1973)

[12] S.T. Zalesak, J Comput Phys, 1-28 (1979)

[13] J.B. Rosenzweig, N. Barov, M. Thompson, R. Yoder, Phys. Rev. ST Accel. Beams., **7** 061302 (2004).

[14] P. Londrillo, C. Gatti, M. Ferrario, Nuclear Inst. and Methods in Physics Research, A, **740** 236-241 (2014).

ISBN 978-3-95450-136-6

NUMERICAL CALCULATIONS OF WAKE FIELDS AND IMPEDANCES OF LHC COLLIMATORS' REAL STRUCTURES *

O. Frasciello†, M. Zobov, INFN-LNF, Frascati, Rome, Italy

Abstract

The LHC collimators have very complicated mechanical designs including movable jaws made of higly resistive materials, ferrite materials, tiny RF contacts. Since the jaws are moved very close to the circulating beams their contribution in the overall LHC coupling impedance is dominant, with respect to other machine components. For these reasons accurate simulation of collimators' impedance becomes very important and challenging. Besides, several dedicated tests have been performed to verify correct simulations of lossy dispersive material properties, such as resistive wall and ferrites, benchmarking code results with analytical, semi-analytical and other numerical codes outcomes. Here we describe all the performed numerical tests and discuss the results of LHC collimators' impedances and wake fields calculations.

INTRODUCTION

The Large Hadron Collider (LHC) has a very sophisticated collimation system used to protect the accelerator and physics detectors against unavoidable regular and accident beam losses [1, 2]. The system has a complicated hierarchy composed of the primary (TCP), secondary (TCS) and tertiary (TCT) collimators and the injection protection collimators.

Since the collimators are moved very close to the circulating beams they give the dominant contribution in the collider beam coupling impedance, both broad-band and narrow band. The electromagnetic broad-band impedance is responsible of several single bunch instabilities and results in the betatron tunes shift with beam current, while the narrow band impedance gives rise to the multibunch instabilities and leads to vacuum chamber elements heating.

The impedance related problem has been recognized already in the present LHC operating conditions [3] and is expected to be even more severe for the High Luminosity LHC upgrade [4], where one of the principal key ingredients for the luminosity increase is the beam current increase. For this reason the correct simulation of the collimator impedance becomes very important and challenging.

In order to simulate the collimators as close as possible to their real designs, we used CAD drawings including all the mechanical details as inputs for the high performing, parallelizable, UNIX-platform FDTD GdfidL code [5]. A very fine mesh, typically, of several billions mesh points, was required to reproduce the long and complicated structures, described in huge .stl files, and to overcome arising numerical problems. In order to be sure that the code reproduces correctly properties of lossy dispersive materials (resistive walls, ferrites) used in the collimators we have carried our several dedicated numerical tests comparing the GdfidL simulations with available analytical formulae, other numerical codes and semi-analytical mode matching techniques.

The only way to afford such a huge computational task was to use the GdfidL dedicated cluster at CERN, engpara, which has allowed us to study the wake fields and impedances for several types of collimators without using any model simplifications: secondary collimators, new collimators with incorporated beam position monitors and injection protection collimators. In such circumstances, GdfidL wake fields computation up to wake length of hundreds times the typical devices lengths (~ 1m) took several days or two weeks at maximum.

In this paper we describe GdfidL tests of the resistive walls and ferrites simulations, discuss the calculated collimator impedances comparing the obtained results with available experimental data.

RESISTIVE WALL SIMULATION TEST

Only recently a possibility to carry out simulations with resistive walls (RW), implementing the impedance boundary conditions, was made available in GdfidL. So it has been decided to perform a numerical test comparing the simulation results with known analytical formulas. For this purpose we calculated both the longitudinal and the transverse loss factors (the latter known also as kick factor) of a Gaussian bunch passing inside a round beam pipe having an azimuthally symmetric thick resistive insert. The insert was enough long in order to be able to neglect the contribution of the insert ends, as shown in Fig. 1.

Figure 1: GdfidL model for the azimuthally symmetric beam pipe with resistive insert. The choosen length was L = 30 cm, the insert thickness a = 5 mm, the pipe radius plus the insert thickness b = 10 mm, and the electrical conductivity σ_c=7.69 · 10^5 S/m for Carbon Fiber Composite (CFC).

In this case the loss factors can be found analytically:

$$k_{\parallel} = \frac{cL}{4\pi b\sigma^{3/2}}\sqrt{\frac{Z_0\rho}{2}}\Gamma\left(\frac{3}{4}\right), \qquad (1)$$

* Work supported by HiLumi LHC Design Study, which is included in the High Luminosity LHC project and is partly funded by the European Commission within the Framework Programme 7 Capacities Specific Programme, Grant Agreement 284404.

† oscar.frasciello@lnf.infn.it

ISBN 978-3-95450-136-6

for the longitudinal one and

$$k_{\perp} = \frac{cL}{\pi^2 b^3}\sqrt{\frac{2Z_0\rho}{\sigma_z}}\Gamma\left(\frac{5}{4}\right) \qquad (2)$$

for the transverse one, where $c = 2.997925 \times 10^8$ m/s is the speed of light, L is the length of the pipe, $\rho = \sigma_c$ is the electrical resistivity, σ_z the bunch length and Γ the Euler gamma function. Figure 2 shows a comparison between the analytical formulas and the numerical data. As it is seen the agreement is quite satisfactory.

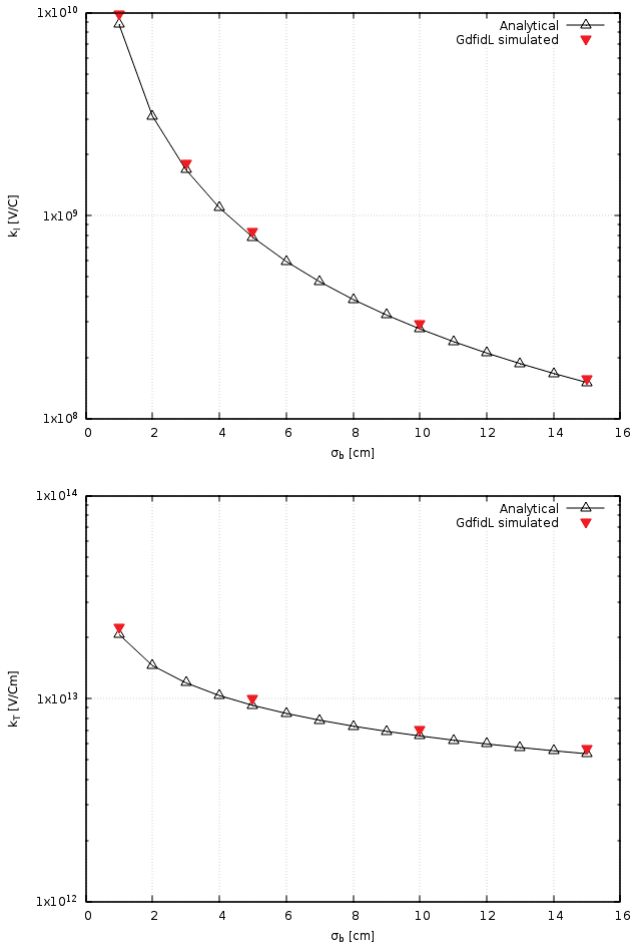

Figure 2: Loss and kick factors benchmark between GdfidL and analytical formulas Eq. (1) and Eq. (2).

However, the loss factors are somewhat "averaged" values characterizing the beam impedance. In order to check the impedance frequency behavior the RW impedance of the insert has been calculated using the semi-analytical mode-matching method (MMM) [6]. In turn, numerically the impedance till rather low frequencies has been obtained by performing a Fourier transform of a long wake behind a long bunch obtained by Gdfidl, and also by CST for comparison. As it is seen in Fig. 3 also the impedance frequency behavior is reproduced well by GdfidL.

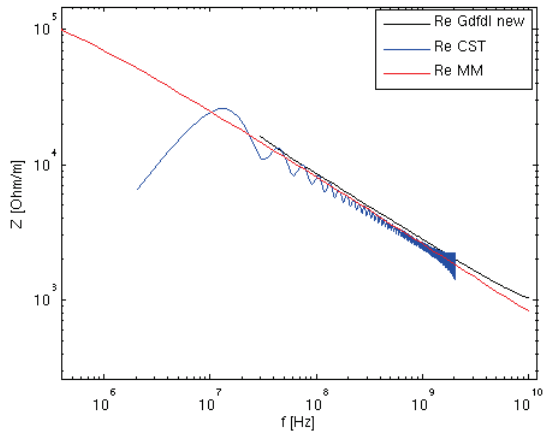

Figure 3: Dipolar transverse impedance benchmark between GdfidL, CST and MMM outcomes.

FERRITE MATERIAL SIMULATION TEST

In order to damp parasitic higher order modes (HOMs) in the new collimators with embedded BPM pickup buttons, special blocks made of the TT2-111R lossy ferrite material are used. For this reason we have carried out a comprehensive numerical study to test the ability of GdfidL to reproduce frequency dependent properties of the lossy ferrite in calculations of wake fields, impedances and scattering matrix parameters [7].

For this purpose, we have a) simulated a typical coaxial-probe measurement of the ferrite scattering parameter S_{11}; b) compared the computation results of CST, GdfidL and Mode Matching Techniques by calculating impedances of an azimuthally symmetric pill-box cavity filled with the TT2-111R ferrite in the toroidal region; c) benchmarked GdfidL simulations against analytical Tsutsui model for a rectangular kicker with ferrite insert [8, 9] and CST simulations for the same device.

All the comparative studies have confirmed a good agreement between the results obtained by GdfidL and the results provided by other numerical codes, by available analytical formulas and by the mode matching semi-analytical approach. As an example, Fig. 4 shows a simplified sketch of a set-up for the ferrite material properties measurements: just a coaxial line filled with a ferrite material under test. For such a simple structure the reflection coefficient S_{11} is easily measured and can be found analytically as in Eq. (3).

$$S_{11} = \frac{\Delta \cdot \tanh(\gamma L) - 1}{\Delta \cdot \tanh(\gamma L) + 1}, \qquad (3)$$

with $\gamma = j\omega\sqrt{\epsilon\mu}$ and $\Delta = \sqrt{\frac{\mu_r}{\epsilon_r}}$. Figure 5 shows the S_{11} coefficient calculated for the TT2-111R material in a very wide frequency range, from 10^6 to 10^{12} Hz. As it is seen, despite the complicated S_{11} frequency dependence the agreement between GdfidL, HFSS and the analytical formula is remarkable.

ISBN 978-3-95450-136-6

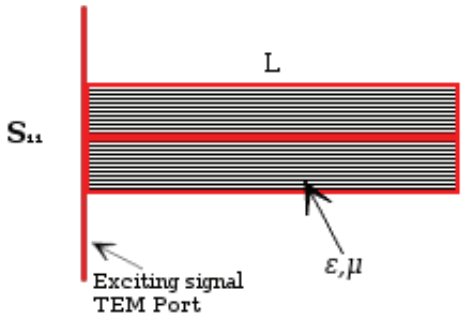

Figure 4: Coaxial probe measurement model for GdfidL S_{11} simulations.

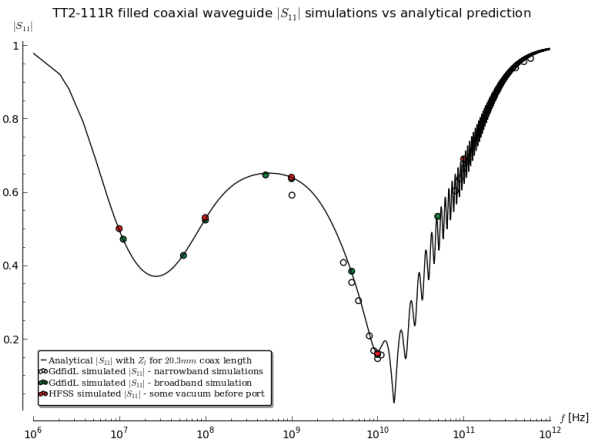

Figure 5: Reflection coefficient S_{11} results for the arranged simulation setup. The solid line is the analytical trend from Eq. (3).

IMPEDANCE OF LHC RUN I TCS/TCT COLLIMATORS

In the 2012 LHC impedance model, collimators played the major role ($\sim$ 90%) over a wide frequency range, both for real and imaginary parts, but the model was essentially based on the resistive wall impedance of collimators, the resistive wall impedance of beam screens and warm vacuum pipe and a broad-band model including pumping holes, BPMs, bellows, vacuum valves and other beam instruments. The geometric impedance of collimators was approximated only by that of a round circular taper [10].

However, several measurements were performed in 2012 of the total single bunch tune shifts vs. intensity, both at injection and at 4 TeV, the results coming out to be higher than predicted ones with numerical simulations by a factor of $\sim$ 2 at top energy and of $\sim$ 3 at injection [11]. This fact led to the need for an LHC impedance model refining which, first of all, required a careful collimator geometric impedance calculation. For this purpose, we carried out numerical calculations of the geometric impedance of the LHC Run I TCS/TCT collimator, whose design is shown in Fig. 6, and evaluated its contribution to the overall LHC impedance budget.

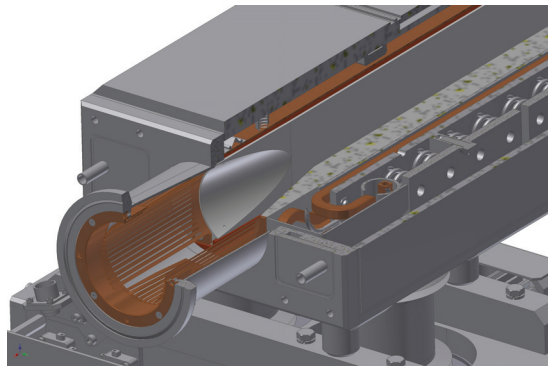

Figure 6: LHC Run I TCS/TCT collimator design.

In order to verify whether the geometric collimator impedance could give a noticeable contribution to the betatron tune shifts, we suggested to compare transverse kick factors due to the resistive wall impedance and the geometric one, showing that the tune shifts are directly proportional to the kick factors [12].

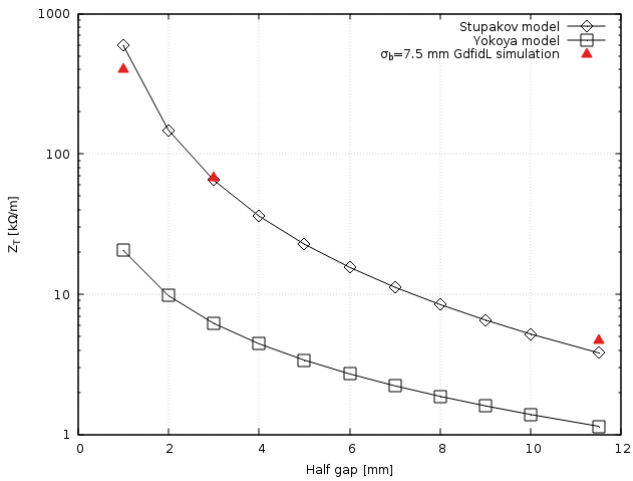

Figure 7: Effective transverse impedances of theoretical Stupakov flat taper model, Yokoya round taper model) and GdfidL simulations of TCS/TCT collimator, as a function of the jaws' half gap.

In Fig. 7 and Fig. 8 the main results about the transverse broad-band impedance and kick factors are reported, showing that the geometric impedance is better approximated by a flat taper model than by a round taper one and that the geometric contribution is not negligible with respect to the resistive wall one. In particular, for CFC made collimator, the geometrical kick starts to be comparable to resistive wall one at about 8 mm half gap. In turn, for W made collimators, the geometrical kick dominates almost for all the collimator gaps.

The study contributed to the refinement of the LHC impedance model. It has also been shown that the geometrical collimator impedance accounts for approximately 30% of the total LHC impedance budget, at frequencies close to 1 GHz.

ISBN 978-3-95450-136-6

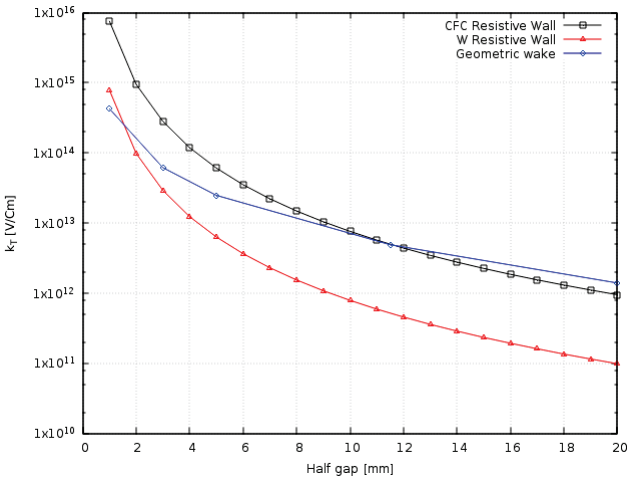

Figure 8: Comparison between geometrical kick factor and RW kick factors for CFC and W, as a function of the jaws' half gap.

IMPEDANCE OF LHC RUN II TCS/TCT COLLIMATORS

During the last LHC Long Shutdown I (LSI), 2 TCS CFC and 16 TCT Tungsten (W) collimators were replaced by new devices with embedded BPM pickup buttons, whose design is shown in Fig. 9. RF fingers were removed from the

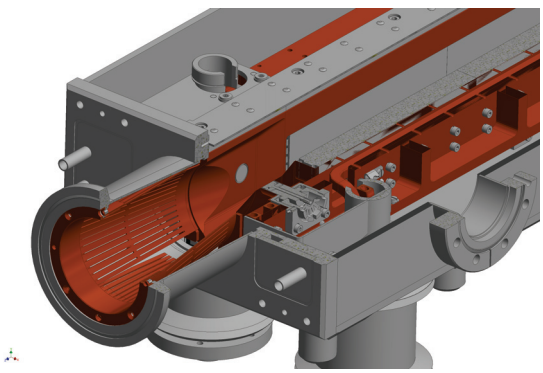

Figure 9: LHC Run II TCS/TCT collimator with embedded BPM pickup buttons.

previous LHC Run I TCS/TCT design and HOMs damping was entrusted to the TT2-111R ferrite blocks. By means of GdfidL broad band impedance simulations of the new collimators' real structure, we gained the results for the kick factors in Tab. 1, showing that an increase of about 20% is expected for the transverse effective impedance, with respect to LHC RUN I type collimator's design.

In order to study the impedance behaviour of the new collimators and the effect of the ferrite blocks on HOMs, we performed detailed GdfidL wake fields simulations of the whole real structures. We set into GdfidL input file the finite conductivity of W and the frequency-dependent permeability of TT2-111R. As a first result, an overall impedance damping feature was shown to be proper of the structure with

Table 1: Geometric Transverse Kick Factors Due to the Two TCS/TCT Geometries, Calculated at Different Half Gap Values

	w/ BPM cavity	w/o BPM cavity
Half gaps (mm)	k_T ($\frac{V}{Cm}$)	k_T ($\frac{V}{Cm}$)
1	$3.921 \cdot 10^{14}$	$3.340 \cdot 10^{14}$
3	$6.271 \cdot 10^{13}$	$5.322 \cdot 10^{13}$
5	$2.457 \cdot 10^{13}$	$2.124 \cdot 10^{13}$

resistive W jaws plus ferrite blocks at all frequencies [13], as clearly visible from the plot in Fig. 10. There, the red curve represents the collimator simulated as a whole Perfect Electrical Conductor (PEC), without any resistive and dispersive material, while the black one represents the real collimator with W jaws and ferrite blocks. The effect of ferrite results also in the shift of HOMs characteristic frequencies toward lower frequencies. As an example, the first HOM frequency shifts from ≈ 95 MHz to ≈ 84.5 MHz, at exactly the same frequency measured experimentally at CERN with loop technique [14]. It is clear that the computed impedance spectrum resolved very well the low frequency HOMs, whose characteristic frequencies are in excellent agreement with those found experimentally. Moreover, under these simulation

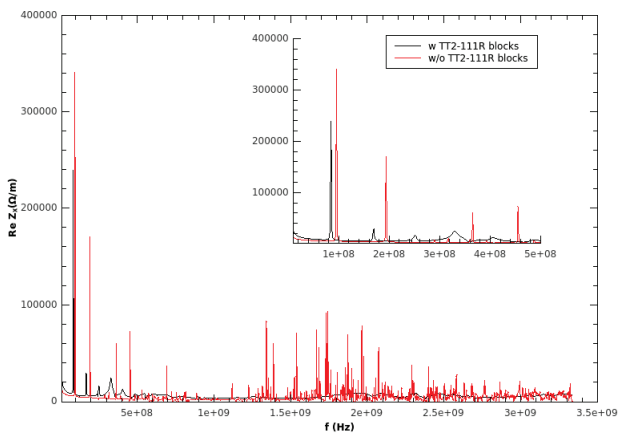

Figure 10: Real part of the impedance spectrum of LHC Run II TCS/TCT collimators, the inset layer focusing on low frequency HOMs.

circumstances, the computed shunt resistance of the first HOM at ≈ 84 MHz is in remarkably agreement, within a factor of 2, with that measured experimentally with the wire technique at CERN [15], being $R_s^{sim} \approx 237\,\mathrm{k\Omega/m}$ and $R_s^{meas} \approx 152\,\mathrm{k\Omega/m}$ [16].

CONCLUSIONS

Calculations of wake fields and beam coupling impedance have been performed for the LHC TCS/TCT collimators, by means of GdfidL electromagnetic code. We performed, for the first time in the field of impedance computations, a complete and detailed simulation campaign of collimators'

ISBN 978-3-95450-136-6

real structures, including the properties of real and lossy dissipative materials.

For LHC Run I collimators, the comparison of the transverse kick factors calculated for five different jaws' half gaps, has shown that the geometric impedance contribution is not negligible with respect to the resistive wall one. The study has contributed to the refinement of the LHC impedance model, as a result of the geometrical collimator impedance accounting for approximately 30% of the total LHC impedance budget, at frequencies close to 1 GHz.

The performed numerical tests have confirmed that GdfidL reproduces very well the properties of the lossy dispersive materials. The simulation test results for the resistive walls and the lossy ferrites are in a good agreement with available analytical formulae and the results of other numerical codes and semi-analytical models. The tests have made us confident in the results of our impedance studies carried out for the real structures of the new Run II TCS/TCT collimators with incorporated BPMs. Several important results have been obtained conducting these studies. First, we found that there are no dangerous longitudinal higher order modes till about 1.2 GHz. This is important for the heating reduction of the collimators in the multibunch regime (for the nominal LHC bunches 7.5 long). Second, the TT2-111R ferrite resulted to be very effective in damping both longitudinal and transverse parasitic modes for frequencies above 500 MHz. However, the modes at lower frequencies are less damped, residual transverse HOMs at frequencies around 100 MHz and 200 MHz with non-negligible shunt impedances still existing. The calculated frequencies of the modes are in remarkable agreement with the loop measurements. The shunt impedances of the modes obtained numerically agrees within a factor of 2 with the experimental data of the wire measurements performed at CERN. Finally, the broad-band transverse impedance of the new LHC Run II double taper collimators are evaluated to be approximately by 20% higher with respect to that of the LHC Run I TCS/TCT collimators.

ACKNOWLEDGMENTS

We are grateful to W. Bruns for his invaluable support.

We would like to thank also the CERN EN-MME and BE-ABP departments, for the providing of the collimators' CAD designs and S. Tomassini, of INFN-LNF, for his accurate handling and adjusting the CAD designs to serve as inputs for GdfidL simulations. In particular special thanks are addressed to the E. Metral, on behalf of the whole CERN LHC impedance group, for the support and profitable discussions, to N. Biancacci for the MMM simulations' data and, together with F. Caspers, J. Kuczerowski, A. Mostacci and B.Salvant for the information on the collimators' impedance measurements side.

REFERENCES

[1] R.W. Assman et al. Requirements for the LHC collimation system. *Proceedings of the 8th European Particle Accelerator Conference*, pages 197–199, 2002.

[2] R.W. Assman et al. An improved collimation system for the LHC. *Proceedings of the 9th European Particle Accelerator Conference*, pages 536–538, 2004.

[3] E. Metral et al. Transverse Impedance of LHC Collimators. *Proceedings of Particle Accelerator Conference PAC07*, pages 2003–2005, 2007. CERN-LHC-PROJECT-REPORT-1015.

[4] The HL-LHC collaboration. HL-LHC Preliminary Design Report Deliverable: D1.5. Technical report, 2014. CERN-ACC-2014-0300.

[5] W. Bruns. GdfidL web page. `http://www.gdfidl.de`.

[6] N. Biancacci, V. G. Vaccaro, E. Métral, B. Salvant, M. Migliorati, and L. Palumbo. Impedance studies of 2d azimuthally symmetric devices of finite length. *Phys. Rev. ST Accel. Beams*, 17:021001, Feb 2014.

[7] O. Frasciello et al. Wake fields and impedances calculations with GdfidL, MMM and CST for benchmarking purposes, 2014. Contributed talk at BE-ABP Impedance meeting, February 2nd, CERN, Geneva, Switzerland.

[8] H. Tsutsui et al. Transverse Coupling Impedance of a Simplified Ferrite Licker Magnet Model. Technical report, 2000. LHC-PROJECT-NOTE-234.

[9] H. Tsutsui. Some Simplified Models of Ferrite Kicker Magnet for Calculations of Longitudinal Coupling Impedance. Technical report, 2000. CERN-SL-2000-004 AP.

[10] N. Mounet. The LHC Transverse Coupled-Bunch Instability. PhD thesis, Ecole Polytechnique, Lausanne, Mar 2012.

[11] N. Mounet et al. Beam stability with separated beams at 6.5 tev. In *LHC Beam Operation Workshop Evian 17-20 December 2012*, 2012.

[12] O. Frasciello et al. Geometric beam coupling impedance of LHC secondary collimators. In *Proceedings of IPAC 2014*.

[13] O. Frasciello et al. Present status and future plans of LHC collimators wake fields and impedance simulations, 2015. Contributed talk at BE-ABP Impedance meeting, March 23rd, CERN, Geneva, Switzerland.

[14] N. Biancacci et al. Impedance bench measurements on TCTP collimator with ferrite, 2014. Contributed talk at BE-ABP Impedance meeting, August 8th, CERN, Geneva, Switzerland.

[15] N. Biancacci et al. Impedance bench measurements on TCTP and SLAC collimators, 2014. Contributed talk at BE-ABP Impedance meeting, April 14th, CERN, Geneva, Switzerland.

[16] O. Frasciello et al. Beam coupling impedance of the new LHC collimators, 2015. Contributed talk at 101st National Congress of the Italian Physical Society (SIF), September 24th, Rome, Italy.

ISBN 978-3-95450-136-6

ADVANCES IN MASSIVELY PARALLEL ELECTROMAGNETIC SIMULATION SUITE ACE3P*

Oleksiy Kononenko#, Lixin Ge, Kwok Ko, Zenghai Li, Cho-Kuen Ng, Liling Xiao
SLAC, Menlo Park, CA 94025, USA

Abstract

ACE3P is a 3D parallel electromagnetic simulation suite that has been developed at SLAC National Accelerator Laboratory for the past decades. Effectively utilizing supercomputer resources with advanced computational algorithms, ACE3P has become a unique modeling tool for the research and design of particle accelerators. Newly developed capabilities are presented, including the calculation of RF eigenmodes in large-scale accelerator structures using state-of-the-art scalable linear solvers, the enhanced multi-physics solutions for coupled electromagnetic, thermal and mechanical problems, the integration of ACE3P with the beam dynamics code IMPACT, as well as the interface of ACE3P to the particle-material interaction code Fluka for evaluating radiation effects in accelerators.

INTRODUCTION

The ACE3P (Advanced Computational Electro- magnetics 3D Parallel) simulation suite has been developed at SLAC for the past decades consisting of modules in frequency and time domains for the research and design of particle accelerators [1]. This massively parallel set of codes is based on the finite-element method so that geometries of complex structures can be represented with high fidelity through conformal grids, and high solution accuracies can be obtained through high-order basis functions. Using high performance computing, ACE3P has provided a unique capability for large-scale simulations for the design, optimization and analysis of accelerating structures and systems. Running on DOE state-of-the-art supercomputers, parallel electromagnetics computation has enabled the design of accelerating cavities to machining tolerances and the analysis of accelerator systems to ensure operational reliability. The modeling effort has supported many of the accelerator projects within the DOE accelerator complex and beyond such as LHC upgrade and PIP-II, CEBAF upgrade, FRIB and e-RHIC, as well as LCLS and LCLS-II at SLAC [2,3].

ACE3P consists of the following modules:

- Omega3P, an electromagnetic eigensolver;
- S3P, a frequency-domain S-parameter solver;
- T3P, a time-domain solver for transients and wakefield computations;
- Track3P, a particle tracking code for multipacting and dark current studies;
- Pic3P, a particle-in-cell code for self-consistent particle and field interactions;
- TEM3P, a multi-physics code for integrated electromagnetic, thermal and mechanical effects.

A typical ACE3P simulation workflow also includes preprocessing of model and mesh building in Cubit [4] as well as post-processing results in Paraview [5], see Fig. 1. While preprocessing and postprocessing procedures can be both performed on a local desktop, ACE3P solvers run on supercomputers at the National Energy Research Scientific Computing Center (NERSC) [6], which is a major facility for scientific computing in the US.

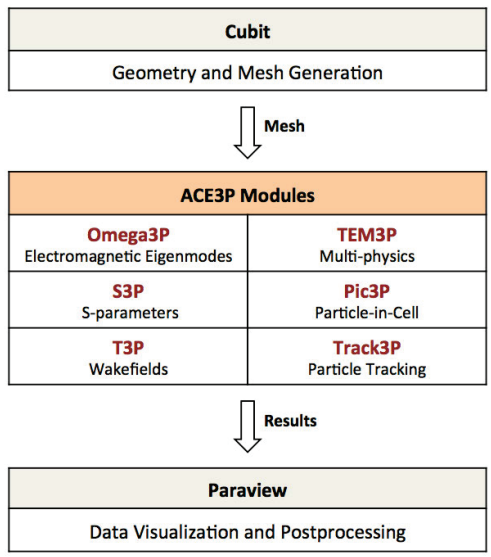

Figure 1: A typical simulation workflow for ACE3P.

Recent advances in the development and application of ACE3P include

- State-of-the-art hybrid linear solver [7] implementation in Omega3P for fast electromagnetic eigenmodes analysis;
- Accurate determination of temperature distribution for realistic 3D accelerator components using the thermal solver in TEM3P [8];
- Development of an eigensolver in TEM3P to determine mechanical modes of a superconducting (SRF) cavity facilitating the investigation of microphonics [9];
- Development of a harmonic response solver in TEM3P to calculate damped and undamped mechanical responses of an SRF cavity to external harmonic excitations [10];
- Development of an electro-mechanical analysis tool to decompose structural displacements into those of the mechanical modes of an SRF cavity required for

*Work supported by DOE Contract No. DE-AC02-76SF00515
#Oleksiy.Kononenko@slac.stanford.edu

ISBN 978-3-95450-136-6

the design of feedback control loop ensuring operational reliability of particle accelerator;

- Integration of the ACE3P suite with the beam dynamics code IMPACT-T [11] for realistic calculations of beam emittance in accelerators;
- Interface of ACE3P to the particle-material interaction code Fluka [12] for evaluating radiation effects.

The corresponding simulation results are presented in the following sections in details.

IMPLEMENTATION OF HYBRID LINEAR SOLVER IN ACE3P

In collaboration with Lawrence Berkeley National Laboratory, the parallel domain decomposition Schur complement based linear solver (PDSLin) [7] was implemented in ACE3P's eigensolver Omega3P and applied to calculate higher-order modes (HOMs) in the Project X (and later PIPI-II) 650 MHz cryomodule [13]. Compared with direct solvers, the hybrid linear solver PDSLin uses less memory per core per run, and hence can utilize most of the resources in a NERSC compute node. The monopole HOMs above the beampipe cutoff calculated using PDSLin in Omega3P are shown in Fig. 2. It took about 3 minutes to calculate each mode using 300 cores in 25 nodes and a total of 1.1 TB of memory on NERSC Edison supercomputer.

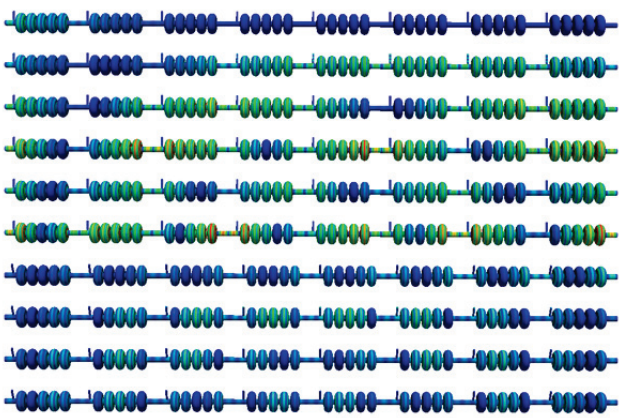

Figure 2: HOMs in Project X 650 MHz cryomodule.

In comparison, a similar calculation, performed several years ago, took about 1 hour per mode on NERSC Seaborg system using the direct solver MUMPS [14]. On average, the memory usage per process for PDSLin is five times less than MUMPS, allowing the solution of large problem sizes that cannot be handled by direct solvers.

THERMAL CALCULATIONS FOR LCLS-II COUPLER

The LCLS-II project [15] at SLAC National Accelerator Laboratory adopts the TTF3 coaxial fundamental power coupler (FPC) with modest modifications to make it suitable for continuous-wave operation. The coupler consists of a cold and a warm sections made of different types of materials with a thin copper coating at the warm side. The fully 3D geometry of the coupler is simulated using TEM3P to determine the temperature distribution along the feedthrough of the coupler [8].

First, electromagnetic fields are calculated in the FPC vacuum and ceramic regions using S3P. Then, the corresponding power losses on the metal walls as well as in the ceramic window are used as the heat load input for TEM3P thermal simulation. The RF and thermal models share a common geometrical interface, so that the heat flux information can be easily converted into the proper boundary condition, see Fig. 3.

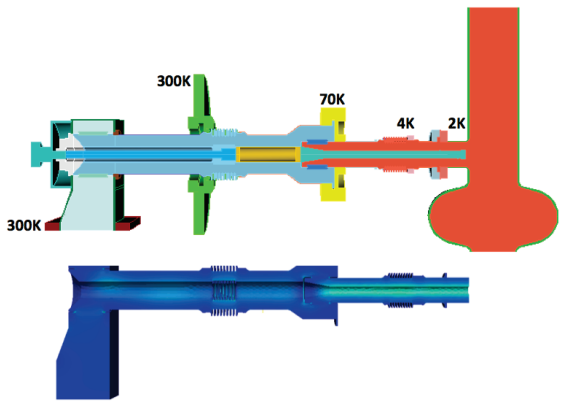

Figure 3: FPC model for TEM3P thermal simulation (top) and RF field distribution calculated with S3P in the vacuum/ceramic regions (bottom).

The temperature distribution shown in Fig. 4 is obtained using 6 kW power for the standing wave on resonance. The maximum temperature is found at the bellows near the central region of the coupler (red zone in Fig. 4) and agrees well with the value from high power tests at Fermilab [16], as shown in Fig. 5.

Fully 3D analysis is essential here as the 2D COMSOL desktop simulations (green and blue curves in Fig. 5) have both discrepancies compared to the measured data and significantly underestimated the maximum temperature.

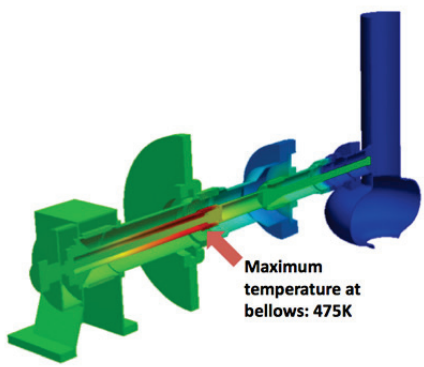

Figure 4: Temperature distribution in TTF3 coupler calculated using TEM3P.

ISBN 978-3-95450-136-6

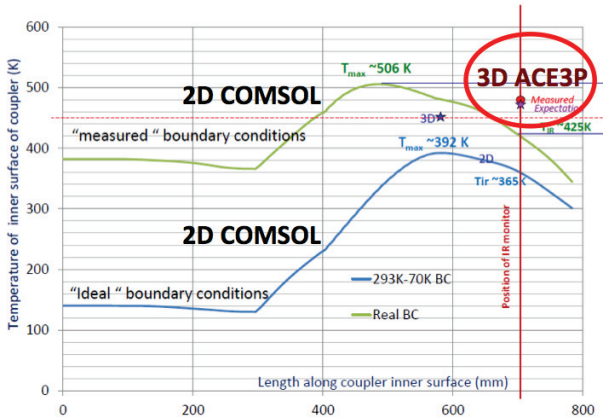

Figure 5: Temperature along the inner conductor with the red dot showing the agreement of ACE3P simulation and measurement (Courtesy of A. Hocker, Fermilab).

The simulation has been made feasible by the availability of shell elements in TEM3P, which enables the modeling of the thin copper coating on the conductor wall without the use of extremely small elements. In addition, 3D parallel computation through the use of multiple processors allows for high-resolution simulation by taking advantages of large memory resources and speedup.

ELECTRO-MECHANICAL SIMULATIONS FOR SRF CAVITY

RF fields in superconducting accelerating structures exert pressure upon all the surfaces exposed to electromagnetic radiation. Unless carefully studied and controlled, it may significantly affect the operational reliability of a particle accelerator. To mitigate this adverse effect (Lorentz force detuning) a corresponding feedback loop must be developed to tune the cavity during the operation.

Equation (1) describes how the cavity RF frequency is affected by a particular mechanical mode excited by the the changes in field amplitude and/or external noise sources [17].

$$\Delta\ddot{\omega}_\mu + \frac{2}{\tau_\mu}\Delta\dot{\omega}_\mu + \Omega_\mu^2\Delta\omega_\mu = -k_\mu\Omega_\mu^2 V(t)^2 + n(t). \quad (1)$$

where $\Delta\omega_\mu$ is an RF circular frequency shift due to a μ-th mechanical mode, τ_μ is the mode decay time, Ω_μ is the mechanical eigenfrequency, k_μ is the coupling coefficient between the RF field and mechanical mode μ, $V(t)$ is the accelerating voltage and $n(t)$ is a driving term due to external vibrations or microphonics.

Mechanical Eigenmode Calculations

To determine the mechanical eigenmodes of the LCLS-II SRF TESLA cavity, an eigensolver has been developed in TEM3P [9]. In Fig. 6 the simulation model for the TEM3P mechanical calculation is shown for the TESLA cavity positioned in a helium tank.

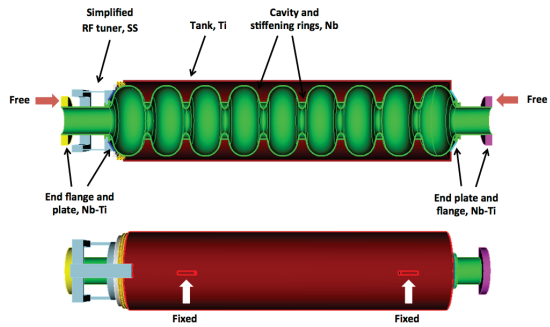

Figure 6: Simulation model for the TEM3P mechanical calculation of the TESLA cavity in a Helium tank.

A fully 3D eigenmode calculation involving multiple materials was performed to determine dressed cavity eigenfrequencies. Table 1 shows that they are in good agreement with the dominating modes determined in measurements [18-19].

Table 1: Eigen Frequencies of the Dressed TESLA Cavity Calculated Using ACE3P and Measured at Fermilab

ACE3P	Measurement	Strength
233	235	0.65
176	168	0.1
473	471	0.09

Electro-Mechanical Simulations

The determination of Lorentz force detuning requires a coupled electro-mechanical calculation, where the electromagnetic field is first calculated using Omega3P in the vacuum region of the cavity and then the Lorentz force on the cavity surface serves as the boundary condition for TEM3P to determine deformations of the cavity wall. For simplicity and demonstration purposes we consider a model of the undressed SRF cavity in the following calculations.

Figure 7 shows the Lorentz force displacement for the TESLA structure using an accelerating gradient of 16 MV/m, with a free and a fixed boundary condition imposed on the left and the right ends of the cavity, respectively. The displacement is largest at the free end and falls off gradually towards the fixed end.

Figure 7: Lorentz force displacement of the TESLA cavity using a quarter model of the geometry.

Using TEM3P's mechanical eigensolver, the first three eigenmodes for the quarter model subject to the same boundary constraints are shown in Fig. 8. Because of the boundary conditions imposed on the symmetry planes, only longitudinal modes are modeled.

The coupling of Lorentz force displacement to individual mechanical modes is computed by a modal decomposition. In this regard, the displacement shown in Fig. 7 is expressed as a linear combination of a complete set of displacements from the orthogonal modes, three of those are shown in Fig. 8:

ISBN 978-3-95450-136-6

$$\vec{u}(x,y,z)=\sum_{\mu=0}^{\infty} q_\mu \vec{u}_\mu(x,y,z)$$

where q_μ is the coupling cofficient of the μ-th mechanical mode, from which one can determine the contribution to the frequency shift by this mode if it is excited.

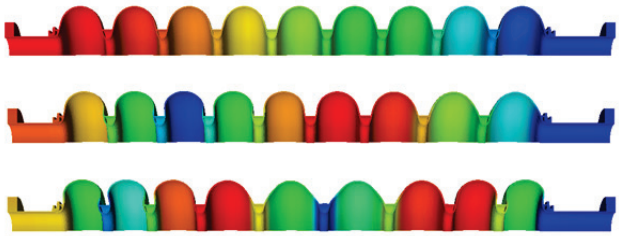

Figure 8: Mechanical modes of the TESLA cavity with frequencies 96 Hz, 296 Hz and 496 Hz (from top to bottom).

Assuming a specific accelerating voltage V, the Lorentz force coefficient k_μ for the μ-th mechanical mode is calculated as

$$k_\mu = \frac{\Delta f_\mu^{RF}}{V^2}.$$

Table 2: Lorentz Force Coefficients for the Ten Lowest Mechanical Modes of the LCLS-II SRF Cavity

Mode	Ω[Hz]	q	Δf^{RF}[Hz]	k [Hz/MV^2]
1	99	-4.8E-06	-930	-2.21
2	297	7.51E-07	-145	-0.34
3	497	3.38E-07	-43	-0.1
4	695	2.59E-07	-36	-0.09
5	890	1.91E-07	-15	-0.04
6	1075	1.68E-07	-18	-0.04
7	1246	1.37E-07	-6	-0.01
8	1393	1.22E-07	-10	-0.02
9	1493	6.03E-08	0	0
10	1585	2.65E-07	-33	-0.08
Total	–	–	**-1236**	**-2.93**
Static LF	–	–	**-1192**	**-2.83**

Table 2 lists the decomposition of the Lorentz force displacement into the first ten longitudinal modes. It can be seen that the major contributions to the total RF frequency shift are from the several lowest mechanical modes and the summation of Δf_i^{RF} by them is very close to the value of static Lorentz force.

The eigenfrequencies and k-coefficients of the mechanical eigenmodes will provide useful information for studying microphonics effects using a feedback control algorithm [20] based on Eq. (1).

INTEGRATION OF ACE3P AND IMPACT

IMPACT-T[11] is a parallel, 3D space-charge tracking code to study beam dynamics in photo-injectors and linear accelerators. The code can track particles using its built-in beamline element models, or using the external field maps of beamline elements provided by users for more accurate modeling of 3D effects.

Integrating ACE3P with IMPACT-T presents a new parallel capability that combines 3D electromagnetic simulation with beam dynamics calculation so that accelerator cavities and beamline elements can be modeled on a system scale with high accuracy. The representations of field data (in terms of 3D and transfer maps) in the two simulation software packages have been standardized to enable the transfer of cavity RF fields from ACE3P to IMPACT-T for particle tracking.

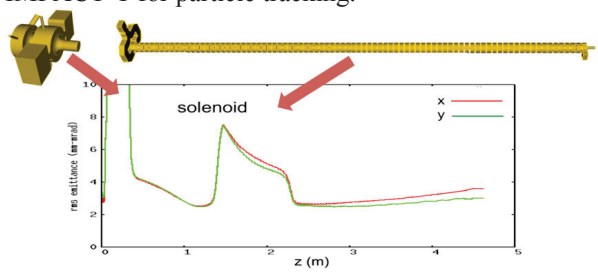

Figure 9: Beam emittances in the transverse directions as a function of the longitudinal position for the FACET-II injector (Courtesy of J. Qiang, LBNL).

The beam emittances in the transverse directions calculated by the integrated simulation as a function of the longitudinal position for the FACET-II injector, which includes an RF gun, an S-band accelerating structure and a solenoid between them, are shown in Fig. 9. The electromagnetic fields of the accelerating modes of the RF gun and the accelerating structure to produce the respective 3D field maps are calculated using Omega3P and then read into IMPACT-T for particle tracking of a low energy beam using the field maps for the full length of the injector. This integrated simulation at the system scale has been performed using the NERSC supercomputers.

INTERFACE OF ACE3P TO RADIATION CALCULATION

Accelerator cavities operating at high gradients are subject to damage from high-energy electrons hitting the surface of the cavity wall. These electrons are believed to originate from certain locations of the cavity surface due to field emission, and then accelerated under the RF field before impacting the cavity wall. Interacting with the certain materials, they produce electromagnetic radiation that can affect the performance of the accelerator. For instance, during the commissioning of cryomodule at Jefferson Lab, strong radiation dosages along the cryomodules were observed during the processing period, regardless of the presence of the beam [21].

ISBN 978-3-95450-136-6

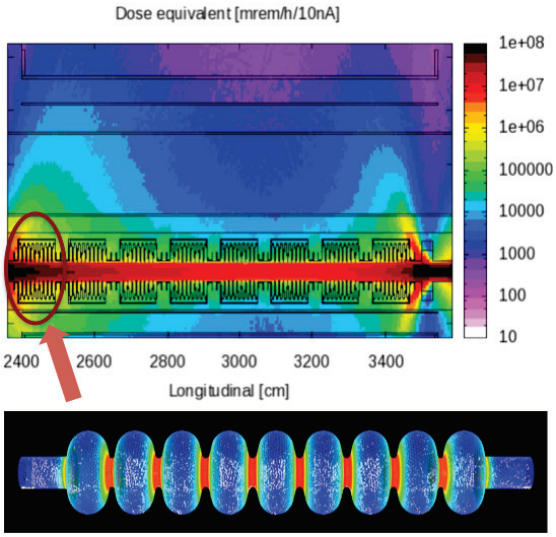

Figure 10: The radiation dose for the LCLS-II cryomodule as calculated in Fluka (top) and a snapshot of the electron distribution in the coupled Track3P calculation for one SRF cavity (top) (Courtesy of M. Santana, SLAC).

ACE3P provides simulation modules that model the 3D electromagnetic fields in an accelerator cavity (Omega3P, S3P and T3P), generate the initial field emission electrons and track the electrons in the vacuum region of the cavity (Track3P). When the electrons hit the surface of the cavity wall, their phase space information are transferred to the particle-material interaction code Fluka [12] for radiation calculation.

Figure 10 shows the calculation of the radiation dose for the LCLS-II cryomodule. Track3P is used to simulate dark current in a LCLS-II cavity, and an interface has been developed to transfer particle data on the cavity surface from Track3P to Fluka to calculate radiation produced by the interaction of the electrons with the wall materials [22].

CONCLUSIONS

Under SLAC and DOE SciDAC [23] program support, new modeling capabilities have been developed in ACE3P in recent years and successfully benchmarked against measurements. Through high performance computing, simulation using ACE3P has enabled the solution of challenging computational problems for a wide range of applications in accelerator projects, accelerator science and development. With ongoing development and enhancement of its multi-physics capabilities including integration with other accelerator codes and implementation of state-of-the-art scalable numerical algorithms, ACE3P can be used to facilitate optimized accelerator design and reliable machine operation, thus reducing costs and saving time.

ACKNOWLEDGEMENTS

We would like to thank A. Hocker, J. Qiang and M. Santana for collaborations. This research used resources of the National Energy Research Scientific Computing Center, which is supported by the Office of Science of the U.S. Department of Energy under Contract No. DE-AC02-05CH11231.

REFERENCES

[1] Massively parallel electromagnetic ACE3P Simulation Suite, https://portal.slac.stanford.edu/sites/ard_public/acd/
[2] K. Ko et al., "Advances in Parallel Computing Codes for Accelerator Science and Development," Proc. LINAC2010, Tsukuba, Japan, 2010.
[3] L. Ge, K. Ko, O. Kononenko, Z. Li, C.-K. Ng, L. Xiao, "Advances In Parallel Finite Element Code Suite ACE3P,"
[4] " Proc. IPAC15, Richmond, VA, USA May 3-8, 2015.
[5] The CUBIT Geometry and Mesh Generation Toolkit, https://cubit.sandia.gov/
[6] Paraview, http://www.paraview.org/
[7] National Energy Research Scientific Computing Center, https://www.nersc.gov/
[8] I. Yamazaki, PDSLin User Guide, 2012.
[9] L. Xiao et al., "TTF Power Coupler Thermal Analysis for LCLS-II CW Application," Proc. IPAC15, Richmond, USA, 2015.
[10] O. Kononenko et al., "A Massively Parallel Finite-Element Eigenvalue Solver for Modal Analysis in Structural Mechanics," Technical Report SLAC-PUB-16229, SLAC, 2014.
[11] O. Kononenko, "A Massively Parallel Solver for Mechanical Harmonic Analysis of Accelerator Cavities," Technical Report SLAC-PUB-15976, SLAC, 2015.
[12] IMPACT-T: A 3D Parallel Particle Tracking Code in Time Domain, Official webpage, http://amac.lbl.gov/~jiqiang/IMPACT-T/index.html
[13] Fluka, https://www.fluka.org/
[14] A. Saini, et al., Design of Superconducting CW Linac for PIP-II, Proc. IPAC15, Richmond, USA, 2015, pp. 565-567.
[15] M. Paszyński, D. Pardo, A. Paszyńska, "Parallel multi-frontal solver for p adaptive finite element modeling of multi-physics computational problems," Journal of Computational Science, 1(1), 2010. pp. 48-54.
[16] Linac Coherent Light Source II, Official web page, https://portal.slac.stanford.edu/sites/lcls_public/lcls_ii/Pages/default.aspx
[17] A. Hocker, "LCLS-II Coupler Test Results," FNAL presentation, 2014.
[18] J. Delayen, Ponderomotive instabilities and microphonics–a tutorial, Proceedings of the 12th International Workshop on RF Superconductivity, Cornell University, Ithaca, New York, USA.
[19] W. Schappert et al., "Resonance Control for Narrow-Bandwidth, Superconducting RF Applications," Proc. SRF2015, Whistler, Canada, 2015.
[20] Y. Pischalnikov et al., "Design and Test of Compact Tuner for Narrow Bandwidth SRF Cavities," Proc. IPAC15, Richmond, USA, 2015.
[21] Z. Li et al., "Multi-Physics Analysis of CW Superconducting Cavity for the LCLS-II Using ACE3P," Proc. IPAC14, Dresden, Germany, 2014.
[22] F. Marhauser et al., "Field Emission and Consequences as Observed and Simulated for CEBAF Upgrade Cryomodules," Proc. of SRF 2013, Paris, Sep 23-27, 2013.
[23] C. Adolphsen, "High Power RF Status," LCLS-II DOE Review, April 7-9, 2015, SLAC.
[24] DOE SciDAC, http://www.scidac.gov/

ISBN 978-3-95450-136-6

SPACE OF MOTION INTEGRALS IN PROBLEMS ON SELF-CONSISTENT CHARGED PARTICLE DISTRIBUTIONS*

O.I. Drivotin†, D.A. Ovsyannikov
St.-Petersburg State University, 7/9 Universitetskaya nab., St. Petersburg, 199034 Russia

Abstract

A new approach for investigation of self-consistent distributions for charged particle beam in magnetic field is presented. According to this approach, the space of motion integrals is introduced. Specifying charged particles density in the space of motion integrals provides a self-consistent distribution for charged particle beam under some conditions, which are formulated. This approach allows simple graphical representation of various distributions by means of a special diagram.

INTRODUCTION

In the particle beam physics, dynamics of a charged particle beam is commonly described by the Vlasov Equation [1]. Its solutions are called self-consistent distributions, because the particles move in a field which is created by them. To find solutions of the Vlasov equation is very complicated problem due to nonlocal nonlinearity of the equation. Despite of complexity, there are founded various solutions of the Vlasov equation for a charged particle beam in magnetic field. The most known solution is the Kapchinsky-Vladimirsky distribution [2]. Another well-known solution is the Brillouin flow [3]. Both of them are degenerate distributions. The so called waterbag distribution is an example of nondegenerate distributions [4, 5].

In the present work we formulate a new approach of investigation of self-consistent distributions of charged particles. This approach can be applied for all problems on self-consistent distributions, but in this work we apply it only for a charged particle beam in longitudinal magnetic field.

We follow ideas formulated in previous works of the authors [6-15]. The space of integrals of motion integrals is introduced, and particle distribution density is specified as a density in this space. Under some conditions, which are specified further, the phase density can be expressed through the distribution density in the space of motion integrals. This approach equally works for cylindrical longitudinally uniform beam propagating through longitudinal uniform magnetic field and for nonuniform beam in magnetic and electric fields that can vary along beam axis.

Making use of this approach gives a possibility to construct new solutions of the Vlasov equation. They can be obtained taking a linear combination of known distributions, for example, rigid rotor distributions [16-18]. New solutions can be also found using some integral equation.

* Work supported by St.-Petersburg State University grant #9.38.673.2013
† o.drivotin@spbu.ru

PROBLEM FORMULATION

Consider stationary axially symmetric longitudinally uniform beam propagating in a uniform longitudinal magnetic field **B**. Assume that longitudinal velocity components of all particles $v_z = \beta c$ are the same, and that transverse velocity components much less than longitudinal. In this case the phase space is four-dimensional, and the Vlasov equation can be written in the form

$$\mathbf{v}\frac{\partial f}{\partial \mathbf{x}} + \frac{e}{m\gamma}\left(-\frac{1}{\gamma^2}\frac{\partial u}{\partial \mathbf{x}} + e\mathbf{v}\times\mathbf{B}\right)\frac{\partial f}{\partial \mathbf{v}} = 0. \qquad (1)$$

Here $f = f(\mathbf{x}, \mathbf{v})$ is the distribution function, **x** and **v** are particle position and velocity, e, m, γ are particle charge, mass and reduced energy, u is self potential of the beam satisfying to the Poisson equation and the boundary conditions

$$\Delta u = -\frac{\varrho}{\varepsilon_0}, \quad u(0) = 0, \quad du/dr|_{r=0} = 0. \qquad (2)$$

under assumption that beam is propagating in coaxial tube or in empty space. Further, ϱ is particle density in the configuration space, normalized as follows

$$\int f(\mathbf{x}, \mathbf{v})\, d\mathbf{x}\, d\mathbf{v} = \int \varrho(\mathbf{x})\, d\mathbf{x} = \frac{I}{e\beta c}, \qquad (3)$$

where I is the beam current.

Considering differential equations for particle trajectories in the self field of the beam, we obtain from one of them that

$$M = r^2(\dot{\varphi} + \omega_0), \qquad (4)$$

is conserves along the trajectories. The other equation takes the form

$$\frac{d\dot{r}}{dt} = -\omega_0^2 r + \frac{M^2}{r^3} - \varepsilon\frac{\partial U}{\partial r}, \qquad (5)$$

Equation (5) has the integral

$$H = \dot{r}^2 + \omega_0^2 r^2 + \frac{M^2}{r^2} + 2\varepsilon U. \qquad (6)$$

Here $\omega_0 = eB_z/(2m\gamma)$ $\varepsilon = e/(m\gamma^3)$, M, H are azimuthal component of momentum and energy of transverse motion with an accuracy up to multiplier. Integral M is well known as the Bush integral.

The particle radial motion is shown in Fig. 1. Line 2 represents effective potential function

$$V_M(r) = M^2/r^2 + \omega_0^2 r^2 \qquad (7)$$

for a particle with $M \neq 0$. If H is given, motion is possible only on the segment $[r_{\min}, r_{\max}]$, corresponding to this M, H.

ISBN 978-3-95450-136-6

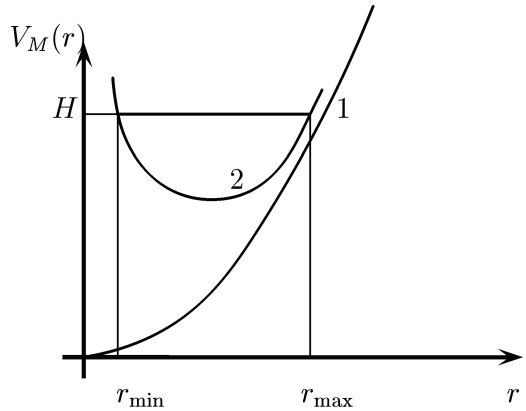

Figure 1: Radial motion of particles.

Line 1 represents effective potential function corresponding to $M = 0$. It can be shown that if the function $V_0(r)$ is strictly convex then the particle trajectories are confined and for each pair of admissible values of M and H there exists a unique radial trajectory. In configuration space, a radial trajectory corresponds to a set of particle trajectories such that any trajectory of this set can be obtained by rotating of any other trajectory by some angle.

THE SPACE OF INTEGRALS OF MOTIONS

Let us introduce the space of integrals of motion Ω_R for a cylindrical beam with radius R, as such set of values of the integrals of motion M, H that corresponding particle trajectory does not go out the boundary of the beam. That means that for all particles the inequality $r \le R$ holds.

It can be shown that the space of integrals of motion Ω_R is defined by the inequalities

$$\min_r V_M(r) < H \le M^2/R^2 + \omega_0^2 R^2 + 2\varepsilon U(R). \quad (8)$$

and $|M| < M^*$, where M^* is such M that the left and the right hand sides in inequality Eq. (8) are equal.

The set $\Omega(r)$ of admissible values of M and H such that trajectory with these M and H passes through points with coordinate r is defined as follows

$$\frac{M^2}{r^2} + \omega_0^2 r^2 + 2\varepsilon U(r) \le H \le \frac{M^2}{R^2} + \omega_0^2 R^2 + 2\varepsilon U(R). \quad (9)$$

$$|M| \le rR\sqrt{\omega_0^2 + 2\varepsilon \frac{U(R) - U(r)}{R^2 - r^2}}. \quad (10)$$

The space of integrals of motion Ω_R for radially confined beam and the set $\Omega(r)$ are represented on Figure 2. Upper and the low bounds of Ω_R Eq. (8) are marked as 1 and 2.

PARTICLE DISTRIBUTION DENSITY

In the previous section we described the particle distributions with making use of the distribution function. Commonly, it is defined as number of particles per a unit of the phase volume.

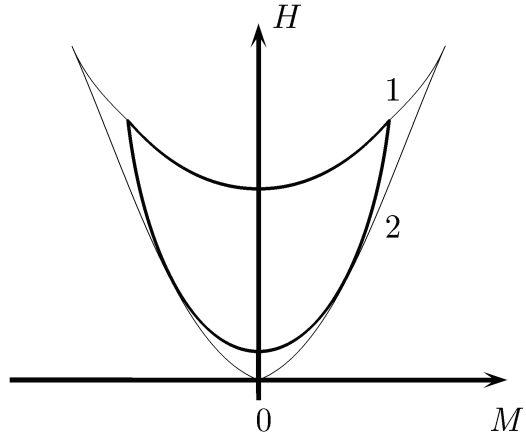

Figure 2: The space of integrals of motion Ω_R and the set $\Omega(r)$.

Let us introduce the concept of particle distribution density following the approach suggested in works [19, 20] As distinct from the distribution function, the definition of the distribution density does not require the notion of the phase volume.

Firstly, consider the nondegenerate case. Take a cell in a region occupied by particles. Let the edges of this cell can be described by increments of coordinates in this region δq^i $i = 1, \ldots, m$ where m is dimension of the region. Then the value that put in correspondence to this cell a number of particles in it will be called the particle density. From mathematical point of view, such value is differential form. It can be written in the form $n = n_{1,\ldots,m}\, dq^1 \ldots dq_m$ (product of differentials is regarded as external product).

For example, if we consider density of particles in the phase space (the phase density) then m is dimension of the phase space, and q^i are coordinates in it.

When particles are distributed on some surface in the phase space, their distribution is degenerate, because in this case the concept of the distribution function cannot be applied. Degenerate distributions can be described by forms of lower degree, which can be defined analogously to the form of top degree, corresponding to a nongenerate distribution.

The phase density satisfies to the Vlasov equation in the covariant form

$$n(t + \delta t, F_{w\,\delta t} q) = F_{w\,\delta t} n(t, q), \quad (11)$$

which was written down in the works [19, 20]. Here $F_{w\,\delta t}$ denotes the operation of Lie dragging along the vector field w defined by particles trajectories by the parameter t increment δt. If phase density is described by a form of top degree Equation (11) can be rewritten in the form

$$\frac{\partial n}{\partial t} = -\mathcal{L}_w n(t, q). \quad (12)$$

Here $\mathcal{L}_w$ denotes the Lie derivative along the vector field w.

ISBN 978-3-95450-136-6

PARTICLE DISTRIBUTIONS IN THE SPACE OF INTEGRALS OF MOTION

Let us introduce the particle distribution density in the space of integrals of motion and $f(M,H)\,dM\,dH$ (further we use the letter f for designation of this density, instead of distribution function). Under conditions formulated in previous section, such distribution corresponds to some distribution in the phase space. To find the relation between them, let us note that M and H can be considered as coordinates in the phase space. Azimuthal angle φ and the phase of a particle on the trajectory θ can be regarded as other two coordinates. As it was assumed, particles are uniformly distributed on φ and θ. Therefore,

$$n_{\varphi\theta MH} = \frac{f(M,H)}{4\pi P(M,H)},$$

where $P(M,H)$ is:

$$P(M,H) = \int\limits_{r_{min}(M,H)}^{r_{max}(M,H)} \frac{dr}{|\dot r|} =$$

$$= \int\limits_{r_{min}(M,H)}^{r_{max}(M,H)} \frac{dr}{\sqrt{H-\omega_0^2 r^2 - M^2/r^2 - 2\varepsilon U(r)}}. \qquad (13)$$

Substituting $\tilde n = n_{\varphi\theta MH}$ to the Equation (12), we get

$$\frac{\partial \tilde n}{\partial t} = -\frac{\partial \tilde n}{\partial \varphi}\dot\varphi - \frac{\partial \tilde n}{\partial \theta}\dot\theta - \frac{\partial \tilde n}{\partial M}\dot M - \frac{\partial \tilde n}{\partial H}\dot H = 0.$$

It means that uniformity of the distributionon on the trajectory phases θ ensures its stationarity.

To compute the particle density in the configuration space, take into account that

$$n_{xyMH} = n_{\varphi\theta MH}\cdot det\left|\left(\frac{\partial(\varphi,\theta)}{\partial(x,y)}\right)\right| = \frac{n_{\varphi\theta MH}}{r|\dot r|}.$$

Then we get that

$$\varrho(r) = 2\int\limits_{\Omega(r)} n_{xyMH}\,dM\,dH =$$

$$= \frac{1}{2\pi r}\int\limits_{\Omega(r)} \frac{f(M,H)\,dM\,dH}{P(M,H)(H - M^2/r^2 - \omega_0^2 r^2 - 2\varepsilon U(r))^{1/2}}. \qquad (14)$$

It can be obtained also that the particle distribution function is

$$n_{xy\dot x\dot y} = \frac{f(M(\mathbf{x},\mathbf{v}),H(\mathbf{x},\mathbf{v}))}{2\pi P(M(\mathbf{x},\mathbf{v}),H(\mathbf{x},\mathbf{v}))}. \qquad (15)$$

In many problems specifying of component $n_{xy\dot x\dot y}$, which is distribution function, is more convenient because Integral (14) can be taken in analytical form.

For example, if consider the distribution with uniform phase density $n_{xy\dot x\dot y} = n_0$. specified in Ω_R under sufficient condition

$$H \le H_0 = \omega_0^2 R^2 + 2\varepsilon u(R), \qquad (16)$$

we obtained the "waterbag" distribution [4,5]. In this case the Poisson equation takes the form

$$\frac{1}{r}\frac{dU}{dr}r\frac{dU}{dr} = -\frac{\pi e f_0}{\varepsilon_0}\Big(\omega(R^2-r^2) + 2\varepsilon(U(R)-U(r)\Big).$$

Its solution can be expressed through the modified Bessel function I_0. Beam profile for this distribution is described by the expression

$$\varrho(r) = \varrho_B\left(1 - \frac{I_0(\sqrt{\lambda r/R})}{I_0(\sqrt{\lambda})}\right), \quad \lambda = 2\pi e n_0 \varepsilon R^2/\varepsilon_0,$$

where $\varrho_B = \varepsilon_0 B_z\gamma/2m_0$ is density of the Brillouin flow which will be considered further.

Generalization of the waterbag distribution was considered in works [6, 10, 12–15]. This distribution has uniform density component $n_{xy\dot x\dot y}$ in all space Ω_R without restriction $H < H_0$.

Wide classes of self-consistent distributions can be obtained with making use of the density inversion theorem [21] which can be formulated as follows. Let $n_{xy\dot x\dot y}$ depends only on H, particles are situated inside the surface (16) in Ω_R, and $\varrho(r)$ is monotonic decreasing function.

Then the phase density can be found according to the expression

$$n_{xy\dot x\dot y}(V_0(r)) = -\frac{1}{dV_0/dr}\cdot\frac{d\varrho}{dr}, \qquad (17)$$

where $V_0(r)$ is the function defined by Eq. (7).

UNIFORMLY CHARGED BEAM

Let us find such phase distributions that particle density in the configuration space is uniform inside the beam cross-section $\varrho_{xy}(r) = \varrho_0$, $r \le R$. Then the Poisson equation yields $U(r) = -e\varrho_0 r^2/4\varepsilon_0$.

Firstly, consider the case when particle are distributed on the two-dimensional surface $M = 0$, $H = 0$, and assume that the phase density does not depend of φ. In this case the phase density is described by the form of the second order defined on the surface. As particle always lie on this surface it can be regarded as a phase space and the Vlasov Equation (11) can be written in the form (12):

$$\frac{\partial n_{r\varphi}}{\partial t} + \dot r\frac{\partial n_{r\varphi}}{\partial r} + \dot\varphi\frac{\partial n_{r\varphi}}{\partial \varphi} = 0.$$

This equation is satisfied as the distribution is stationary, $\dot r = 0$, and particles are evenly distributed on φ.

The solution under consideration corresponds to wide known Brillouin flow [3], when particle rotates around beam axis with the same angular velocity $\dot\varphi = -\omega_0$. As can be seen from (6), $\varrho_B = 2\varepsilon_0\omega_0^2/(e\varepsilon) = \varepsilon_0 B_z\gamma/(2m)$ is the spatial density of the Brillouin flow. In what follows, it is assumed that $\varrho_0 < \varrho_B$.

For uniformly charged beam the inequalities defining ω_R Eq. (8) take the form

$$2\omega|M| < H \le M^2/R^2 + \omega^2 R^2,$$

ISBN 978-3-95450-136-6

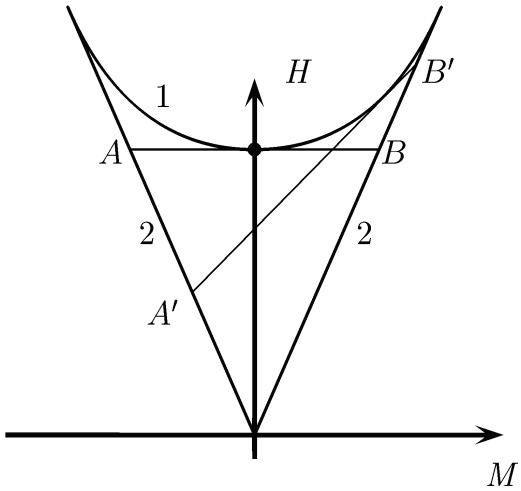

Figure 3: The space Ω_R for a uniformly charged beam.

where $\omega^2 = \omega_0^2 - e\varrho_0\varepsilon/(2\varepsilon_0)$ (see Fig. 3).

Let all particles are uniformly distributed on the straight line segment S_k, which is tangent to upper boundary of the set Ω_R :

$$S_k : H = kM + H_0, \quad H_0 = R^2(\omega^2 - k^2/4),$$

$|k| < 2\omega$, $(M, H) \in \Omega_R$ (segment $A'B'$ on Fig. 1). In this case, the particle density in the space of integrals of motion is described by the differential form of the first degree $f_0 dM$, $f_0 > 0$. In the phase space, density of such distribution is described by the form of degree 3 defined on a three dimensional surface corresponding to segment S_k. Analogously to previous case, we get

$$n_{\varphi\theta M} = \frac{f_0}{4\pi P(M,H)}, \qquad n_{xyM} = \frac{n_{\varphi\theta M}}{r|\dot{r}|}.$$

Then spatial density does not depend of r :

$$\varrho_0 = 2\int_{M_1}^{M_2} n_{xyM}\, dM = \frac{\omega f_0}{\pi} = const.$$

Here M_1, M_2 are roots of the denominator in the integrand.

This distribution is known as the rigid rotor distribution [16–18]. Here we offer simple geometrical representation of it in the space of integrals of motion.

At $k = 0$ (segment AB on Fig. 1), this distribution represents wide known Kapchinsky-Vladimirsky distribution [2], for which all particles are uniformly distributed on the segment AB (Fig. 1).

All distributions corresponding to various k give uniformly charged beam with the same radius R. Therefore any linear combinations of these distributions

$$f(M,H) = \sum \alpha_k f_k(M,H), \tag{18}$$

or their integral on the parameter k

$$f(M,H) = \int_{-2\omega}^{2\omega} f_k(M,H)\, dk, \quad f_k > 0. \tag{19}$$

give the uniform charged beam with radius R.

As an example of nontrivial distribution which can be obtained as integral, cite the distribution

$$f(M,H) = \frac{\pi\varrho_0}{2\omega^2(M^2 - HR^2 + \omega^2R^4)^{1/2}}.$$

This nondegenerate distribution was found for the first time in the work [6]. It was mentioned also in the work [22].

Wide classes of self-consistent distributions can be found if Poisson equation is regarded as integral equation for $f(M,H)$ [10-15].

LONGWISE NONUNIFORM BEAM

Consider stationary azimuthally symmetric beam in longitudinal magnetic field in which all particles have the same longitudinal velocity v_z. Let R and ω_0 slow change along beam axis: $d\omega_0/dz \ll \omega_0/R$. Assume also that the spatial density is uniform within each cross-section: $\varrho_{xy} = \varrho_0(z)$, $r < R$.

In this case, M is also integral of motion. To get another integral, consider equation of radial motion

$$\frac{d^2r}{dt^2} = -\omega_0^2 r + \frac{M^2}{r^3} + \lambda\frac{r}{R^2}. \tag{20}$$

Assume that at some instance particles lie inside an ellipse $r^2/a_0^2 + \dot{r}^2/c_0^2 = 1$, and that the beam envelope is defined only by particles with $M = 0$. Then it can be shown [8-14] that equation for the beam envelope $R(z)$ has the form [23]

$$\frac{d^2R}{dt^2} = -\omega_0^2 R + \frac{\lambda}{R} + \frac{a_0^2c_0^2}{R^3}, \tag{21}$$

which holds under assumption that at initial instance particles lie inside the ellipse $r^2/a_0^2 + \dot{r}^2/c_0^2 = 1$ in the phase space of the transverse motion. Here $\lambda = eJ/(2\pi\varepsilon_0 m\gamma^3 v^z)$.

It is easy to show that the system of Equations (20), (21) is particular case of the generalized Ermakov system, considered in the work [24]. Using the expression for its integral [24], one can show that the value

$$I = (\frac{dq}{d\tau})^2 + \frac{M^2}{q^2} + a_0^2c_0^2q^2. \tag{22}$$

is an integral of motion. Here $q = r/R$, $d\tau = ds/R^2$. The integral (22) was introduced for the first time in the work [8] and after that was used in the works [9-14] for description of self-consistent distributions for a charged particle beam. When $M = 0$, integral (22) coincides with the Courant-Snyder invariant [25], which is well-known in charged particle beam physics, and which is integral for the Ermakov system also [26]. Thus, instead of integral H, we introduced another integral of motion I, which depends not only from motion of a particle, but from motion of a beam as a whole.

As previously, let us introduce the space of integrals of motion and denote it by $\tilde{\Omega}_1$. It is easy to see that $\tilde{\Omega}_1$ is determined by inequalities

$$2a_0c_0|M| < I \le M^2 + a_0^2c_0^2, \tag{23}$$

ISBN 978-3-95450-136-6

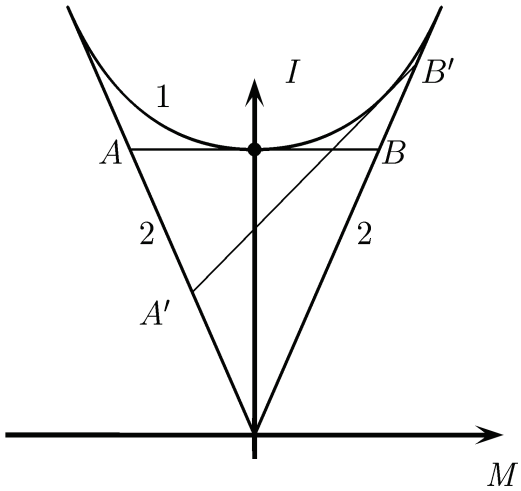

Figure 4: The space Ω_R for a uniformly charged beam.

and, therefore, looks like the set Ω_R for radially confined beam on Fig. 1, where H should be replaced by I.

Consider a particle distribution of some thin layer moving along beam axis. The phase space is four-dimensional, and M, I, φ and θ can be taken as coordinates. As previously, assume that particle uniformly distributed on phases θ and azimuthal angle φ.

At first, consider a case when particles are distributed on the two-dimensional surface $M = 0$, $I = 0$. Equation (12) yields

$$\frac{\partial n_{q\varphi}}{\partial t} + \dot{q}\frac{\partial n_{q\varphi}}{\partial q} + \dot{\varphi}\frac{\partial n_{q\varphi}}{\partial \varphi} = 0.$$

Therefore, such distribution is a stationary solution of the Vlasov equation. From physical point of view, it corresponds to a beam with radius changing along beam axis according to Equation (21), and rotating in each cross-section with angular velocity that also depends on z. Such distribution is analogue to the Brillouin flow, and can be called the generalized Brillouin flow.

Consider also a distribution when all particles are uniformly distributed on the segment S_k, which is tangent to upper boundary of the set $\tilde{\Omega}_1$:

$$S_k : I = kM + I_0, \quad I_0(k) = a_0^2 c_0^2 - k^2/4,$$

$|k| < 2a_0c_0$, $(M, I) \in \tilde{\Omega}_1$ (segment $A'B'$ on Fig. 1). Describe the particle density in the space of the integrals of motion by the differential form of the first degree $f_0 dM$, $f_0 > 0$. In the initial four-dimensional phase space such density is described by the form of degree 3 defined on the segment S_k. Analogously to the previous case, we get

$$n_{\varphi\theta M} = \frac{f_0}{4\pi P(M,I)}, \qquad n_{\tilde{x}\tilde{y}M} = \frac{n_{\varphi\theta M}}{q|\dot{q}|},$$

where $\tilde{x} = x/R$, $\tilde{y} = y/R$,

$$P(M,I) = \int_{q_{\min(M,I)}}^{q_{\max(M,I)}} (I - \frac{M^2}{q^2} - a_0^2 c_0^2 q^2)^{1/2}\, dq = \frac{\pi}{2a_0c_0}.$$

For spatial density we get

$$\varrho_{\tilde{x}\tilde{y}M} = \int_{M_1}^{M_2} n_{\tilde{x}\tilde{y}M}\, dM = \frac{a_0c_0f_0}{\pi} = const.$$

When $k = 0$ (segment AB on Fig. 1), we have analogue of the Kapchinsky-Vladimirsky distribution for nonuniform beam. It is easy to understand that taking a linear combination of such distributions with various k we also get a solution of the Vlasov equation.

Analogous approach can be also used for beam in external electric field [20, 27].

CONCLUSION

As a conclusion, list the main results of this work The spaces of integrals of motion are introduced for a longitudinally uniform beam and for nonuniform ("breathing") beam. The densities of particle distribution in these spaces are defined. The relations between these densities and the phase density, the spatial density, and the distribution function are established. It is shown that new self-consistent distributions can be obtained as linear combinations of the rigid rotor distributions. New integral I for longitudinally nonuniform beam is presented. New self-consistent distributions are also presented.

Self-consistent distributions written down in analytical form can be used as a beam models in optimization problems [14, 28, 29] and as test problems for beam simulation software.

REFERENCES

[1] R.L. Liboff, Introduction to the Theory of Kinetic Equations, New York: John Wiley&Sons, 1969.

[2] I.M. Kapchinsky, Particle Dynamics in Resonant Linear Accelerators, (Moscow: Atomizdat, 1966) (in russ.).

[3] L. Brillouin, Phys.Rev., 67, 260-266 (1945).

[4] I. Hofmann, "Transport and focusing of high intensity unnetralized beams", In: Applied charged particle optics / Ed. A.Septier. Part C: Very- high-density beams. New-York, 1983. C. 49-140.

[5] M. Reiser, Theory and design of charged particle beams New York: John Wiley & Sons, 1994.

[6] O.I. Drivotin, D.A. Ovsyannikov, USSR Comp. Math. Math. Phys., 27 (2), 62-70 (1987).

[7] O.I. Drivotin, D.A. Ovsyannikov, USSR Comp. Math. Math. Phys., 29 (4), 195-199 (1989).

[8] O.I. Drivotin, D.A. Ovsyannikov, Dokl. Phys., 39(5), 1-4 (1994).

[9] O.I. Drivotin, D.A. Ovsyannikov, "New Classes of Uniform Distributions for Charged Particles in Magnetic Field", PAC'97, Vancouver, Canada, 1997, 1943-1945.

[10] O.I. Drivotin, D.A. Ovsyannikov, Vestnik Sankt-Peterburgskogo Universiteta, Ser.10: Applied Math., 1-2, 3-15;70-81 (2004) (in russ.).

ISBN 978-3-95450-136-6

[11] O.I. Drivotin, D.A. Ovsyannikov, Nucl. Instr. Meth. Phys. Res., A 558, 112-118 (2006).

[12] O.I. Drivotin, D.A. Ovsyannikov, Int. J. Modern Phys., A 24 (5), 816-842 (2009).

[13] O.I. Drivotin, D.A. Ovsyannikov, Izvestiya Irkutskogo Gosudarstvennogo Universiteta, Ser. Math., 6(4), 2-22 (2013) (in russ.).

[14] D.A. Ovsyannikov, O.I. Drivotin, Modeling of Intensive Charge Particle Beams, St.-Petersburg: Publ. Comp. of St.-Petersburg State Univ., 2003 (in russ.).

[15] O.I. Drivotin, D.A. Ovsyannikov, Proc. Linear Accel. Conf. LINAC2014, Geneva, 2014. http://accelconf.web.cern.ch/accelconf/LINAC2014/papers/mopp135.pdf

[16] R. C. Davidson, Physics of nonneutral plasmas. Reading, Massachusetts: Addison-Wesley Publishing Co., 1990.

[17] R. C. Davidson, H. Quin, Physics of intense charged particle beams in high energy accelerators. Singapore: World Scientific, 2001. 242 p.

[18] R.C. Davidson, N.A. Krall, "Vlasov equilibria and stability of an electron gas", Phys.Fluids, 1970. Vol.13. N 6. C. 1543-1555.

[19] O.I. Drivotin, "Covariant Formulation of the Vlasov equation," IPAC'2011, San-Sebastian, September 2011, accelconf.web.cern.ch/ accelconf/ IPAC2011/ papers/ wepc114.pdf

[20] O.I. Drivotin, "Degenerate Solutions of the Vlasov Equation", RUPAC'2012, St.-Petersburg, September 2012, http://accelconf.web.cern.ch/accelconf/rupac2012/papers/tuppb028.pdf

[21] R.C. Davidson, C. Chen, "Kinetic description of high intensity beam propagation through a periodic focusing field based on the nonlinear Vlasov-Maxwell equations", Particle Accelerators, 1998. Vol.59. C. 175-250.

[22] V. Danilov., S.Cousineu, S.Henderson, J.Holmes, "Self-consistent time dependent two-dimensional and three-dimensional space charge distributions with linear force", Phys.Rev. Special Topics – Accelerators and Beams, 2003. Vol. 6, N 9. C.094202-1 – 094202-12.

[23] E.P. Lee, R.K. Cooper, "General envelope equation for cylindrically symmetric charge particle beams", Particle Accelerators. 1976. Vol. 7. N 2. C. 83-95.

[24] J.R. Ray, J.L. Raid, "More exact invariants for the time-dependent harmonic oscillator", Phys.Lett., V.71 A, N 4. pp.317-318.

[25] E.D. Courant, H.S. Snyder, Annals of Physics, 1958. Vol. 3, N 1.

[26] V.P. Ermakov, Univ. Izvestiya (Kiev), 20(9), 1-25 (1880) (in russ.).

[27] O.I. Drivotin, D.A. Ovsyannikov, "Particle Distributions for Beam in Electric Field," PAC'99, New York, 1999, 1857-1859.

[28] O.I. Drivotin et al., Problems of Atomic Science and Technology, Ser. Nuclear Physical Investigations, 29,30, 93-95 (1997).

[29] O.I. Drivotin et al., "Mathematical Models for Accelerating Structures of Safe Energetical Installation" EPAC'98, June 1998, Stockholm, Sweden.

ISBN 978-3-95450-136-6

List of Authors

Bold papercodes indicate primary authors

ISBN 978-3-95450-136-6

ISBN 978-3-95450-136-6

ISBN 978-3-95450-136-6

Institutes List

Ankara University, Faculty of Sciences
Ankara, Turkey
- Cakir, O.
- Turemen, G.
- Yasatekin, B.

ANL
Argonne, Ilinois, USA
- Berenc, T.G.
- Borland, M.
- Emery, L.
- Ha, G.
- Lindberg, R.R.

ASIPP
Hefei, People's Republic of China
- Bi, Y.F.
- Song, Y.

AUT
Tehran, Iran
- Afarideh, H.
- Mohamadian, M.
- Rahimpour Kalkhoran, N.
- Sabounchi, S.
- Salehi, M.
- Solhju, R.

BINP SB RAS
Novosibirsk, Russia
- Glukhov, S.A.
- Levichev, E.B.
- Nikitin, S.A.
- Piminov, P.A.
- Shatilov, D.N.
- Sinyatkin, S.V.

Bivio Software Inc.
Boulder, USA
- Moeller, P.

BNL
Upton, Long Island, New York, USA
- Cheng, W.X.
- Dalesio, L.R.
- Hao, Y.
- Hidaka, Y.
- Hu, Y.
- Li, Y.
- Yang, L.
- Zhu, Y.

Bogazici University
Bebek / Istanbul, Turkey
- Celebi, E.

CAPP/IBS
Daejeon, Republic of Korea
- Gaisser, M.
- Haciomeroglu, S.
- Kim, Y.I.
- Lee, S.
- Semertzidis, Y.K.

CERN
Geneva, Switzerland
- Bruce, R.
- Fiscarelli, L.
- Koester, O.
- Redaelli, S.
- Russenschuck, S.
- Wagner, J.F.

China Institute of Atomic Energy
Beijing, People's Republic of China
- Li, J.H.

CIAE
Beijing, People's Republic of China
- Li, C.G.
- Li, J.H.
- Lv, Y.L.
- Wang, C.
- Wang, F.
- Wei, S.M.
- Yang, J.J.
- Zhang, T.J.
- Zheng, S.
- Zheng, X.

CIPS
Boulder, Colorado, USA
- Cary, J.R.

CQU
Shapingba, Chongqing, People's Republic of China
- Feng, J.
- Liu, J.Z.
- Sun, J.G.
- Tang, W.X.
- Wan, W.
- Wei, Z.
- Wu, S.J.
- Yang, X.D.
- Yu, L.
- Zhu, L.

ISBN 978-3-95450-136-6

DESY Zeuthen
Zeuthen, Germany
- Krasilnikov, M.
- Stephan, F.

DESY
Hamburg, Germany
- Dohlus, M.

ELSA
Bonn, Germany
- Hillert, W.
- Sauerland, D.

Euclid TechLabs, LLC
Solon, Ohio, USA
- Antipov, S.P.
- Baryshev, S.V.
- Jing, C.-J.
- Qiu, J.Q.

Fermilab
Batavia, Illinois, USA
- Nagaitsev, S.
- Prebys, E.
- Valishev, A.

FRIB
East Lansing, Michigan, USA
- He, Z.Q.
- Shen, G.

FZJ
Jülich, Germany
- Lehrach, A.
- Senichev, V.

Huazhong University of Science and Technology, State Key Laboratory of Advanced Electromagnetic Engineering and Technology,
Hubei, People's Republic of China
- Chen, D.Z.
- Li, D.
- Pan, M.R.
- Zhang, Z.
- Zuo, C.

HZB
Berlin, Germany
- Meseck, A.

IBM T. J. Watson Center
Yorktown Heights, New York, USA
- Tromp, R.M.

IHEP
Beijing, People's Republic of China
- An, Y.W.
- Huang, L.
- Ji, H.F.
- Wang, S.
- Xu, S.Y.
- Zhou, Z.S.

IIT
Chicago, Illinois, USA
- Kunz, J.D.

Illinois Institute of Technology
Chicago, Illlinois, USA
- Snopok, P.

INFN-Roma
Roma, Italy
- Marocchino, A.
- Massimo, F.
- Mostacci, A.
- Palumbo, L.

INFN/LNF
Frascati (Roma), Italy
- Chiadroni, E.
- Ferrario, M.
- Frasciello, O.
- Zobov, M.

Instituto Superior Tecnico
Lisbon, Portugal
- Fiuza, F.
- Fonseca, R.A.
- Silva, L.O.
- Vieira, J.

Integrated Dynamic Electron Solutions
Pleasanton, California, USA
- Reed, B.

Istituto Nazionale di Fisica Nucleare
Milano, Italy
- Rossi, A.R.

JINR
Dubna, Moscow Region, Russia
- Karamyshev, O.
- Karamysheva, G.A.
- Kostromin, S.A.
- Morozov, N.A.
- Samsonov, E.V.
- Shirkov, G.

ISBN 978-3-95450-136-6

JLab
Newport News, Virginia, USA
- Hernandez-Garcia, C.
- Lin, F.
- Morozov, V.S.
- Roblin, Y.
- Zhang, H.

KAIST
Daejeon, Republic of Korea
- Semertzidis, Y.K.

KEK
Ibaraki, Japan
- Ohmi, K.

KIRAMS
Seoul, Republic of Korea
- Chai, J.-S.

Laboratoire de Physique des Gaz et des Plasmas, Universite Paris-Sud
Orsay, France
- Lee, P.

LANL
Los Alamos, New Mexico, USA
- Pang, X.
- Russell, S.J.

LBNL
Berkeley, California, USA
- Feng, J.
- Filippetto, D.
- Lehé, R.
- Mitchell, C.E.
- Ng, E.G.
- Papadopoulos, C. F.
- Qian, H.J.
- Qiang, J.
- Ryne, R.D.
- Sannibale, F.
- Staples, J.W.
- Vay, J.-L.
- Venturini, M.
- Vincenti, H.
- Wan, W.

MIT
Cambridge, Massachusetts, USA
- Winklehner, D.

Monash University, Faculty of Science
Clayton, Victoria, Australia
- Tang, W.X.
- Zheng, C.X.

Monash University
Clayton, Victoria, Australia
- Liu, J.Z.

MSU
East Lansing, Michigan, USA
- Berz, M.
- Hipple, R.
- Makino, K.
- Valetov, E.

NIST
Gaithersburg, Maryland, USA
- Lau, J.W.

ODU CS
Norfolk, Virginia, USA
- Arumugam, A.
- Ranjan, D.
- Zubair, M.

ODU
Norfolk, Virginia, USA
- Terzić, B.

PPRC
Tehran, Iran
- Asadi, M.R.

PSI
Villigen PSI, Switzerland
- Adelmann, A.
- Baumgarten, C.
- Frey, M.
- Gsell, A.
- Ineichen, Y.
- Locans, U.
- Metzger-Kraus, C.J.
- Rizzoglio, V.
- Suter, A.

RadiaBeam
Marina del Rey, California, USA
- Andonian, G.

RadiaSoft LLC
Boulder, Colorado, USA
- Bruhwiler, D.L.
- Cook, N.M.
- Kishek, R.A.
- Nagler, R.
- Webb, S.D.

ISBN 978-3-95450-136-6

Rostock University, Faculty of Computer Science and Electrical Engineering
Rostock, Germany
- Brackebusch, K.
- Brentegani, E.
- van Rienen, U.
- Zheng, D.

RWTH
Aachen, Germany
- Chekmenev, S.

SCU
Chengdu, People's Republic of China
- Li, Z.

Shanghai Jiao Tong University
Shanghai, People's Republic of China
- Xiang, D.

SINAP
Shanghai, People's Republic of China
- Chen, J.H.
- Jiang, B.C.
- Liu, B.
- Luo, C.M.
- Tian, S.Q.
- Wang, D.
- Wang, K.
- Zhang, M.Z.
- Zhang, Q.L.
- Zhang, T.

SKKU
Suwon, Republic of Korea
- Chai, J.-S.
- Ghergherehchi, M.

SLAC
Menlo Park, California, USA
- Ge, L.
- Ko, C.
- Kononenko, O.
- Li, Z.
- Marcus, G.
- Ng, C.-K.
- Xiao, L.

SNRTC
Ankara, Turkey
- Yasatekin, B.

SPECS GmbH
Berlin, Germany
- Kaiser, A.
- Schaff, O.S.

St. Petersburg State University
St. Petersburg, Russia
- Andrianov, S.N.
- Drivotin, O.I.
- Ivanov, A.N.
- Ovsyannikov, D.A.

STFC/RAL/ASTeC
Chilton, Didcot, Oxon, United Kingdom
- Rogers, C.T.
- Sheehy, S.L.

Tech-X
Boulder, Colorado, USA
- Abell, D.T.
- Cary, J.R.
- Cowan, B.M.
- Higuera, A.V.
- Meiser, D.

TEMF, TU Darmstadt
Darmstadt, Germany
- Ackermann, W.
- Boine-Frankenheim, O.
- Chen, Y.
- De Gersem, H.
- Gjonaj, E.
- Kazantseva, E.S.
- Liu, C.
- Müller, W.F.O.
- Niedermayer, U.
- Weiland, T.

The University of Texas at Austin
Austin, Texas, USA
- Downer, M.
- Fazel, N.
- Weichman, K.J.

TRIUMF, Canada's National Laboratory for Particle and Nuclear Physics
Vancouver, Canada
- Chao, Y.-C.
- Gong, C.
- Planche, T.
- Rao, Y.-N.

TUB
Beijing, People's Republic of China
- Lu, W.
- Tang, C.-X.
- Xu, X.L.
- Zhang, Z.

ISBN 978-3-95450-136-6

UC Davis
Davis, USA
- Ma, K.

UCI
Irvine, California, USA
- Unel, G.

UCLA
Los Angeles, California, USA
- An, W.
- Davidson, A.W.
- Decyk, V.K.
- Mori, W.B.
- Tableman, A.
- Tsung, F.S.
- Xi, Y.
- Yu, P.

UMAN
Manchester, United Kingdom
- Appleby, R.B.
- Tygier, S.C.

UMD
College Park, Maryland, USA
- Dragt, A. J.
- Godfrey, B.B.
- Haber, I.

University of Huddersfield
Huddersfield, United Kingdom
- Barlow, R.J.
- Rafique, H.

University of Kaiserslautern
Kaiserslautern, Germany
- Wei, Z.

University of Latvia
Riga, Latvia
- Locans, U.

University of Rome La Sapienza
Rome, Italy
- Marocchino, A.
- Massimo, F.
- Mostacci, A.
- Palumbo, L.

University of the Punjab, Centre in High Energy Physics
Lahore, Pakistan
- Abdul, M.R.
- Iqbal, M.

USTC/NSRL
Hefei, Anhui, People's Republic of China
- Huang, R.
- Jia, Q.K.

USTRAT/SUPA
Glasgow, United Kingdom
- Hidding, B.

YSU
Yerevan, Armenia
- Kotanjyan, A.
- Saharian, A.A.

ISBN 978-3-95450-136-6